FACTORS AFFECTING LOW TEMPERATURE PERFORMANCE OF ZIRCONIA GAS SENSORS

J. A. PAGE

Ph.D. 2001

Factors affecting low temperature performance of zirconia gas sensors

A thesis submitted to Middlesex University
in partial fulfilment of the requirements for the degree
of Doctor of Philosophy

Julian Page

School of Manufacturing Systems
Energy Technology Centre

Middlesex University

December 2001

ABSTRACT

A reduction in the operation temperature of zirconia ceramic gas sensors is highly desirable for a number of practical reasons. This work seeks to investigate the factors that prevent a reduction in operation temperature and propose methods by which these may be resolved.

A novel approach to sensor fabrication has been developed and employed with the advantage of reduced device complexity that should lead to subsequent cost and reliability benefits. Leakage rates in these devices have been shown to be small and electrochemical in origin. Leakage was greater than reported for gold seal devices, partly due to increased electrode activity. The flexibility of device configuration allows a variety of sensor geometries and functions to be realised. This flexibility led to the characterisation of sensors at the upper and lower ends of measurement range and the identification of deviations from theoretical performance. These deviations have been reconciled with theory extended to cover these limits.

Such sensors are known to be sensitive to reducible gas species such as CO_2 and H_2O with a second limiting plateau allowing quantification of these gases. Such analysis capabilities have been found to be extended by incorporating a second pair of electrodes. These effects have not previously been reported. Sensors have been shown to be more sensitive to H_2O than to CO_2.

To investigate the low temperature response of sensors, a variety of techniques and analyses have been developed and are employed with varying success. Impedance spectroscopy was by far the most useful and revealing tool but this is a function of the highly developed hardware and sophisticated control and analysis software bought as a complete system. Gas step changes and current / voltage sweeps were also useful as comparative techniques but could not separate out component mechanisms. Scanning electron microscopy proved to be a vital tool as it allowed vital information to be obtained concerning electrode and electrolyte microstructure. Again this is a function of a highly developed and sophisticated instrument. The techniques of pressure and concentration modulation were limited in terms of ease of use, measurement range and results interpretation. The main drawbacks were limited frequency ranges and laborious data collection and analysis. They do both however show large potential for improvement. Both

amperometric and potentiometric sensors response rates were analysed with a variety of noble metal electrodes using each technique.

Electrode material proved to have a marked effect on sensor performance with the best results obtained with silver and electro-deposited platinum. Scanning electron microscopy of silver showed that a finely divided and openly porous electrode was not required for high performance contrary to expectations. This is thought to be due to the solubility of oxygen in this metal. With platinum however, the improved microstructure is thought to be a significant factor in electro-deposited and cermet electrode performance.

Response rates in amperometric sensors did not show any significant temperature dependence although a restriction in measurement range was observed. Response rates were suspected to be mainly influenced by sensor geometry whilst measurement range was a function of sensor geometry, electrolyte conductivity and electrode activity. Improved electrolytes will provide improvements and may come in the form of attention to the YSZ system or by employing an alternative ion conductor such as ceria. Close attention to sensor dimensions provides possibility for enhancements. In amperometric devices for instance a long, thin diffusion barrier is required leading to a small internal cavity with a large electrode surface area and a thin electrolyte membrane.

CONTENTS

CHAPTER 2

EXPERIMENTAL

CHAPTER 3
RESPONSE RATE MEASUREMENT TECHNIQUE DEVELOPMENT
RESULTS & DISCUSSION

CHAPTER 4
TECHNIQUE APPLICATION TO A Pt/YSZ SYSTEM
RESULTS & DISCUSSION

CHAPTER 5
ELECTRODE MATERIALS INVESTIGATION
RESULTS & DISCUSSION

CHAPTER 6
CONCLUSIONS

APPENDICES

LIST of FIGURES

CHAPTER 1

INTRODUCTION

1 Introduction

1.1 Statement of purpose

The purpose of this work is to investigate the factors affecting the low temperature operation of zirconia gas sensors. This is to be realised using accepted techniques and by development of novel, generic techniques for investigating gas sensors response rates.

The aims of this research have been identified as:

- To investigate the factors affecting low temperature performance of zirconia gas sensors.
- To develop and assess methods of sensor response rate measurement and improvement.
- To develop amperometric sensors using plastic/ceramic technique.

1.1.1 Nature of problem

Zirconia gas sensors have to be operated at elevated temperatures, typically 500 to 800°C. Currently, operation at lower temperatures restricts the measurement range, lengthens response times and results in greater measurement inaccuracies. There are several advantages to be gained by lowering this temperature requirement which would enhance the marketability of these devices. Firstly there would be a reduced power consumption of the heating facility. The power consumption is not great at present but is sufficient to prevent inclusion in portable systems limiting, opportunities for sensor employment. Secondly there would be a benefit in terms of sensor life-expectancy. Current fabrication materials are able to withstand the elevated operation temperatures required but, over time, they do degrade and become more liable to failure. Sensors are particularly vulnerable through thermal shock during temperature ramping. Exposure to high temperatures will also lead to an acceleration of device ageing with a performance deterioration from electrodes, electrolyte and connecting components. Reduced temperatures would mean a reduction in thermal stresses leading to increased reliability and reduced system maintenance costs. Finally fabrication options for both sensors and supporting structures are currently limited by the high temperature requirement. Reducing the temperature requirement would open further possibilities concerning the materials and techniques used in construction. Maskell & Steele [1] reviewed solid electrolyte potentiometric sensors. They identified the areas of reducing costs, miniaturisation and lower operation temperatures as areas for further research. They also suggested however that, for boiler

systems, a response of 1 to 2 minutes might be beneficial for damping out system oscillations. A reduction in device response is easily achieved artificially through the control components but such alterations cannot be used to increase response rates. Their review covered details of sensor applications, electrolytes, electrodes, temperature effects, measurement range, reference systems, sampling, design and future developments.

1.1.2 Scope of problem

The problem with reducing the operation temperature of these devices is that they suffer a performance drop off in several areas. Firstly we see that the response time increases dramatically from a fast response (ms) to slow response (hours) between 600 and 400°C. This is most apparent in potentiometric and pump-gauge devices. The second effect is that of increasing inaccuracy. Inaccuracies can be reduced by careful design but their effects are amplified as temperature drops. Finally we see a reduction in measurement range. This is most notable in amperometric devices as the upper limit of measurement is lost through device inactivity

These problems have been attributed to a variety of mechanisms taking place in the sensor components and their vacinity. Ioannou & Maskell [2] reviewed the factors affecting the response times in zirconia oxygen gas sensors. Factors affecting potentiometric sensors were identified as double layer capacitance, electrode interface resistance and hydrodynamics. Electrode three phase boundary length, presence of glassy phases, type of electrolyte, gas transfers and electrode porosity were all reported as influential. In amperometric sensors the diffusion barrier dimensions were identified as critical whilst in pump gauges it was the method of operation that proved most influential. Materials modification or dimensional optimisation of the devices may overcome these phenomena. Winnubst et al [3] investigated response times of solid state potentiometric sensors and concluded that electrochemical response rates were affected by both electrode and electrolyte components. Maskell [4] attributed the non-instantaneous response of potentiometric sensors to the following factors:

1. The double layer at the electrode/electrolyte interface acting as a capacitor requiring the transfer of charge when the sensor EMF responds to a change in oxygen pressure.

2. The electrode potential cannot stabilise until the stoichiometry of the electrolyte in the double layer has achieved equilibrium with the gas phase.

3. Changes in stoichiometry throughout the electrolyte result in overvoltages due to charge transfer and perturbation of the oxygen partial pressure at the gas-solid interface.

4. A low electrode resistance to charge transfer reduces the response time of the sensor by minimising the RC time constant.

5. The hydrodynamics in the gas phase influence the rate at which a P_{O2} (Oxygen Partial Pressure) change in bulk gas is transmitted to the sensor interface.

1.1.3 Method of investigation

Only by fully understanding the nature of these problems can we hope to propose viable solutions. With this in mind it is the purpose of this work to focus on the low temperature problems, to shed light on the causes and explore routes to improvements. This has been achieved by operating sensors over a range of operating conditions, especially temperatures, to get a good view of problems encountered. The sensors were then broken down into component parts to assess the contribution of each to the problem. A series of techniques were employed to assess these individual components, using both existing and novel techniques. These techniques are then used to examine some proposed solutions for reducing temperature requirement. Techniques employed in this research include current / voltage characterisation, electrochemical gas pumping analyses, frequency response analysis, scanning electron microscopy, step concentration changes, concentration modulation experiments and pressure modulation experiments. In applying these analyses, a large part of this work has entailed the fabrication, assembly and verification of test apparatus and sensors.

1.2 Background

1.2.1 Applications of zirconia sensors

Sensors are the vital interface between a system or process and its environment, sensors for gaseous species make an important contribution to this technology. Gas detection has found a role with necessity for both monitoring and control of economic and environmental effects of a process. Applications are found in hazard monitoring, industrial hygiene, pollution monitoring, process control, combustion control and in medical applications. They are used in mines, sewerage systems, chemical plants, automotive applications with monitoring of the environment and emission levels becoming

increasingly mandatory. The majority of pollution originates in heavy industry, power generation and in combustion engines thus these are the natural markets for gas detectors. Pollutants are rarely evolved as a single gas but as a mixture of many components. For this reason a good selectivity of sensors is required along with a knowledge of the system under analysis. Detection is required for oxygen to ensure breathable atmosphere and in combustion to maintain efficiency and minimise pollution. Sensors are also required to monitor flammable and toxic gases in terms of system safety. Applications of gas sensors have been reviewed [5, 6].

1.2.1.1 Automotive

The vast quantities and cost of fossil fuels consumed in transportation lead to a significant contribution to pollution and the opportunity for savings through increased efficiency. In heavy industry, pollution is generally concentrated at source and therefore simply dealt with using expensive and sophisticated systems where necessary. With transportation however, the number of vehicles in use make small cost effective solutions vital. In addition automotive sensors must be able to operate under harsh conditions dependent upon the application. Typical conditions include high / low temperatures, harsh vibrations, mud, water, salt, oil, electrical interference, pressure fluctuations and combustion products. Ideally the measurements are taken as close to the point of combustion to obtain readings close to real time and with close relation to combustion products. This however entails exposure to a very harsh environment. Flemming [7] reported that exhaust gases contain a plethora of oxidizable gas residuals including CO and H_2 and up to 200 species of hydrocarbons. Figure 1.1 gives an indication of exhaust emission levels with air to fuel ratio. Logothetis [8] stated that the independence of gas sensors to barometric pressure in exhaust pipes is desirable as these pressures can vary appreciably with engine operation conditions. In addition a minimum life of 5 years or tens of thousands of miles and the low cost criteria must be met. One common automobile sensor is the lambda sensor (a potentiometric zirconia sensor for determination of air to fuel A:F ratio). This device is inserted into the exhaust gases to monitor oxygen levels and thus provide closed loop control of A:F ratio. This is necessary for the engine to run efficiently, as well as to allow 3 way catalytic converters to reduce pollution effectively and efficiently. The 3 way catalytic converter passes the combustion products over a high temperature, high surface area precious metal catalyst to ensure the complete oxidation and reduce the harmful components. In addition to A:F ratio, sensors may also be employed in exhaust gas re-circulation control systems. Exhaust gas re-circulation is a common system used to reduce

the NO_x produced by the engine. By feeding an amount of exhaust gases back into the cylinder, the combustion temperatures can be reduced resulting in lower NO_x emissions. With car exhaust sensors a fuel savings of 15 - 20% is achievable compared to an unregulated system [9]. The stoichiometric point (lambda point) is the A:F ratio where the mixture is suitable for complete combustion to occur. The lambda sensor experiences a large step change in output as stoichiometry is traversed. If run rich of this point, fuel will be wasted, resulting in unburned hydrocarbons which poison the catalytic converter, contaminate oil, foul sparking plugs and are damaging to health and the environment. If run too far lean of stoichiometry, knocking and detonation will occur and the engine will run hot, damaging the engine components and causing poor running. The engines are most efficient when run slightly lean of stoichiometry, which is slightly excess air ensuring complete combustion but not incurring damage or poor running. To ensure that engines are run in the lean region without resulting in damage to components requires exact combustion management. For this exacting criterion to be met with potentiometric or semi-conductor sensors, a precise temperature control is required. Potentiometric sensors do not operate well at lean A:F ratios because of the logarithmic oxygen dependence. Saji et al [10] used an amperometric zirconia sensor with a porous diffusion layer to demonstrate limiting current variation with A:F ratio in the lean range. Amperometric sensors are particularly useful lean of stoichiometry as output is linear whereas potentiometric devices become insensitive in this region. Sensor systems are also necessary so that engine mapping may be used in conjunction with fuel injection to provide additional performance / efficiency improvements. Although sensor response is an important factor, response can be too fast in certain circumstances and requires matching to control systems. Reviews of A:F zirconia sensors, potentiometric and based on oxygen pumping, in automotive applications are available [8, 11].

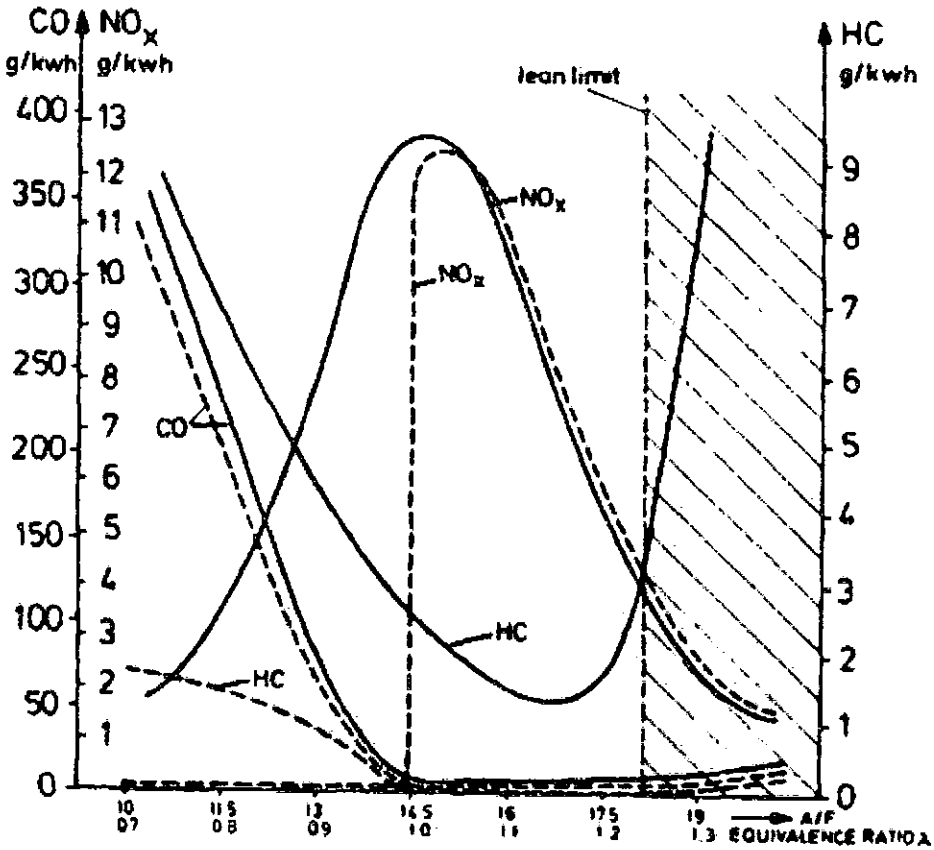

Figure 1.1 A:F ratio exhaust emissions taken from Dietz [12] (p.74).

1.2.1.2 Combustion

The above section related to internal combustion in which fuel and oxygen are mixed prior to combustion. In this section we examine external combustion systems where fuel is fed into and oxygen atmosphere before combustion. Combustion control is required in boilers, fossil fuel powered furnaces and in metallurgical and glass tank furnaces. Again the most efficient and least polluting operation is at approximately 0.5% excess air, however they are often run using 25 - 50% excess air to ensure complete and safe combustion. The heating of this additional air is the cause of poor efficiency as this effectively dilutes the heat generated. This effect is further emphasised where temperatures are high. The introduction of sensors to boiler systems allows safe operation at the optimal efficiency and can achieve up to 30% fuel savings [9]. Copcutt & Maskell [13] showed that amperometric oxygen sensors without an external reference cannot be used to resolve the sides of stoichiometry as the EMFs generated at the stoichiometry point move the pump potential into the CO_2/H_2O reduction region (see appendix B1.3). Vitter et al [14] suggested the use of a zirconia potentiometric mini-gauge for use in domestic boiler systems. The external reference requirement was circumvented by use of an internal

Pd/PdO solid reference. The benefits of using such a device were shown to be a significant efficiency saving, lower maintenance and safe operation using a range of fuels without physical adjustment. Whilst inclusion of sensors allow proper control of A:F ratio so that conditions may be optimised they also allow an additional flexibility in furnace / boiler design. A full description of which is given by Benammar & Maskell [15]. A further advantage is that a variety of fuel compositions would be acceptable without requiring modification or adjustment for correct operation. Such fuel composition variations are experienced when fuel suppliers are switched and traditionally require burner adjustments from a service technician. This is a significant consideration in the supply of domestic boiler systems to overseas markets where the fuel supply can be significantly different to that of the regulated domestic market. One important consideration in the use of sensors operating at high temperatures is the inclusion of a flame trap to eliminate the risk of igniting explosive gases [4]. Another consideration is the reversion to a fail-safe mode in event of sensor failure. Typical measurands in flue gas analysis are O_2, CO, CO_2, SO_2, NO_x, NH_3 and dust.

1.2.1.3 Atmospheric

Gas sensors have been widely employed in both domestic and industrial applications for atmospheric gas detection. These are primarily as means of warning of the presence of toxic or flammable gases. Maximum exposure limits (MEL) for toxic gaseous components are annually published by the Health and Safety Executive. For flammable gases it is the lower explosion limit (LEL) that is of primary interest. When a material is heated or burned, a variety of gases are commonly evolved. Detection of this can be used to sense the onset of combustion. These safety limits mainly lie between several ppb and hundreds of ppm so it is in this range where detection is often required. Yamazoe [16] reviewed the various atmospheric pollutants and sensing elements available for environmental gas sensing.

Atmospheric oxygen analysis is often required as a part of process control e.g. monitoring of oxygen levels and also required in food packaging where oxygen presence will lower storage life. Oxygen is also essential for life support and measurement may be necessary in applications such as aircraft, spacecraft, sub-marine applications and in medical breathing apparatus. In heat treatment of metals the amount of oxygen present affects the quality of product produced. Janke [17] reviewed the use of zirconia sensors in iron and steel making. Detection of oxygen activities of 0.1 to 0.00005 are required for the various metals. In the production of aluminium, the presence of hydrogen can cause embrittlement

of the product and requires monitoring. In most cases a quick immersion in the melt is used and therefore a high thermal shock resistance required as temperatures of 1600°C are reached.

1.2.1.4 Domestic

Domestic applications are typically less harsh than industrial ones but devices must be low cost, small, robust and easy to use. Typical domestic applications for gas sensors are in appliances such as washing machines, smoke and carbon monoxide alarms and gas burning domestic boilers (see combustion systems). A domestic application for humidity sensors lies in microwave ovens where large amounts of humidity are released as the food approaches boiling point. Whilst oxygen sensors are commonly employed in medium to large scale boilers, so far the inclusion in domestic boilers has been limited by the cost of sensors. Domestic consumers are traditionally very purchase price sensitive. Reduction in sensor costs would open this extensive market, as would legislation that proved the driving force behind the inclusion in automotive markets.

1.2.2 Electrolyte properties

1.2.2.1 Mechanical

Zirconia is a ceramic with typical ceramic physical properties. It has a crystal structure of tetravalent zirconium ions and divalent oxygen ions held together in a lattice by covalent bonds. The material is obtained from its ore of zircon sands and undergoes a series of purification processes before the pure oxide is obtained. Single crystals of zirconia may be grown by slow cooling from molten, primarily for jewellery (similar in appearance and feel to diamond). These are also used for materials investigation purposes. Zirconia has a high hardness and strength with good corrosion, wear and thermal resistance with a low expansion coefficient. It is however brittle, susceptible to thermal shock and should be used in compression where used structurally as failure is unpredictable and sudden. The structural properties of zirconias are affected by the size of grains of the electrolyte which in turn are affected by the sintering time, temperature and purity. Ioannou & Maskell [18] investigated the electrolyte microstructure of thick films of partially stabilised zirconia with film thickness and substrate purity. Larger grains were found in electrolytes due to adsorption of impurities from substrate sintering aids. These effects were not seen when printing on top of electrode material so contaminants were not thought to be transmitted through the gas phase. Winnubst et al [19] examined the mechanical properties of yttria stabilised zirconia ceramics. They found the Young's modulus is grain size independent

but porosity dependent. Young's modulus is given by the equation $E(GPa)=221exp^{-2.7P}$. A linear relation of fracture energy to (average grain size)$^{-1/2}$ was found.

Zirconia physical properties include:

Density	= 5.9g/mm^3
Hardness (Rockwell A)	= 87
Price (dependent upon specification)	= £225/Kg
Thermal conductivity	= 0.6Wm^{-1}K^{-1}
Thermal expansion coefficient	= 10^{-6}K^{-1}.

(Information taken from Tosoh information sheet for 8mol% YSZ)

Terblanche [20] reported the effects of yttria stabilisation on the expansion coefficients of YSZ ceramics and found a virtually linear increase in lattice parameter with mol% yttria content measurements were taken using x-ray diffraction (XRD) patterns for 9.4 to 24mol% YSZs over temperatures from ambient to 1270K. The resulting equation was proposed:

$$A = 5.1208 + 0.00231y + 4.6468\times10^{-5}\,(t-273) + 7.6613\times10^{-9}\,((t-273) \qquad \text{Equation 1.0}$$

where t = temperature in Kelvin, A = lattice parameter, y = mol% yttria

Lattice parameter is related to expansion coefficient by Z_{exp} = 1/A dA/dT. Terblanche's work gives a value of dA/dT at approximately 4.65×10^{-5}. The result is an expansion coefficient of 1.04E^{-5} K^{-1} virtually independent of temperature or yttria content.

1.2.2.2 Thermal

As mentioned, zirconia has a high thermal resistance, it is a good thermal insulator and has a high melting temperature. In its pure form it undergoes structural transitions from the monoclinic to tetragonal to cubic structure at 1170 and 2370°C respectively, before melting at 2680°C. The monoclinic to tetragonal transition is accompanied by a 3% volume change that will lead to structural disintegration upon thermal cycling. The expansion coefficient of zirconia is high for a ceramic although still low. This high expansion coefficient along with the poor thermal conduction gives the material its susceptibility to thermal shock. This means care must be exercised upon heating and cooling to avoid fast temperature variations. Powder particle size has a marked effect on

sintering temperature, with <0.3μm sintering at 1180°C whilst an 8μm powder will take >1900°C for full sintering. Information courtesy of TOSOH Corporation, Tokyo, Japan.

1.2.2.3 Electrical

At room temperature, zirconia is a good electrical insulator with breakdown only occurring under the application of very high electrical potentials. As the temperature of the sample is raised above 300°C, the ceramic develops a certain degree of conductivity. This conductivity is not however electronic conductivity as achieved in metals through the passage of free electrons, but rather charge is passed by the movement of negatively charged oxygen ions through the structure and is therefore termed ionic conduction. It is the ability of oxygen ion conduction that enables the use of zirconia as an ion selective solid electrolyte in high temperature electrochemical devices. The ionic conduction rises with temperature, whilst electronic conduction remains low in comparison until temperature exceeds 900°C, then a non-negligible degree of semi-conduction is obtained. Electronic conduction in the electrolyte provides an internal short circuit which will allow permeability [12]. Prolonged use at high pump potentials where electronic conduction is substantial will result in ceramic embrittlement and reduced life [21]. This electronic conduction is accompanied by a darkening of the zirconia as the electrolyte itself is reduced. The darkening can be removed by heating in an oxidising atmosphere. Guo et al [22] investigated, using XRD, the problem of zirconia electrolyte darkening which is known to occur in reducing atmospheres. They observed no phase change in the material but did see that the darkening was accompanied by an increase in the semi-conduction and followed by electronic conductivity. The darkening did not indicate any detrimental structural change in the electrolyte and the role of reducing gases were considered trivial. Zirconia displays neither magnetic nor peizo-electrical properties.

1.2.2.4 Stabilisation

In order to combat the catastrophic effects of the monoclinic to tetragonal transition, zirconia is often doped with an oxide of a lower valency metal such as CaO, Y_2O_3, Sc_2O_3 or MgO_2. This has the effect of reducing the transition temperature (monoclinic to tetragonal or tetragonal to cubic dependent on dopant concentration) below ambient, taking the transition lower than the normal operation temperature of the material.

Haaland [23] used yttria and calcia stabilised zirconias for his work on pump gauges. He found that the calcia stabilised zirconias required higher operating temperatures, >700°C,

for sufficient ionic conduction. Ramaswamy & Agarwal [24] investigated the sintering of calcia stabilised zirconia in low oxygen atmospheres. Metallic zirconium was identified in pockets between the grains, which was proposed to have precipitated out as the maximum concentration of vacant anion sites was reached (21%).

1.2.2.5 Oxygen vacancies

The effects of doping are not however limited to the mechanical properties. An additional benefit is an enhancement of the ion conduction characteristics. The dopant has the effect (by its lower valency) of introducing additional oxygen vacancies, effectively giving some room for manoeuvre for the oxygen ions within the rigid structure therefore making conduction easier. It should be noted that it is the oxygen ions that dominate the conduction process, with zirconium ions having diffusion coefficient 6 orders of magnitude lower than that of oxygen ions. Ionic conductivity increases with dopant content with higher conduction in yttria than calcia stabilised zirconia due to the smaller dopant cation allowing easier movement.

1.2.2.6 Zirconia phases

By controlling the dopant level within the structure some control of electrolyte properties can be achieved. By restricting the dopant, e.g.<4 mole percent yttria, the zirconia is stabilised in the tetragonal phase to give a material with a higher mechanical strength and resistance to thermal shock, but low ionic conductivity. This material is known as partially stabilised zirconia (PSZ). PSZ is one of the toughest ceramics at 200 Tm^{-2}, only 3 to 4 orders of magnitude less than most metals [25].

Alternatively if a higher dopant concentration, e.g. >6 mole percent, is used the material is stabilised in the cubic phase, with the benefit of improved conductivity but at the expense of increasing the costly yttria fraction and lowering of mechanical properties. This material is termed fully stabilised (FSZ). Kobayashi et al [26] investigated the mechanical and electrical properties of partially and fully stabilised zirconias. Measurements of percentage monoclinic phase, microstructure, bend strength, thermal shock resistance and conductivity were examined. PSZ was found to be mechanically stronger with little change on ageing. With ageing the percentage of monoclinic phase increased accompanied by a drop in conductivity. Monoclinic phase was reduced well below 1% between 5 and 6mol% yttria, dependent on sintering time and temperature. Bend strength reached a maximum just under 5% yttria. Thermal shock resistance decreased with increasing yttria content.

Conductivity increased with yttria content over the range examined, from 4 to 8mol% yttria. Kuwabara et al [27] used impedance spectroscopy to measure conductivities of zirconia with yttria doping variation. Conductivity reached a maximum at 8mol% YSZ for both grain and grain boundary conductivity with 1450 and 1600°C sintered specimens. After allowing for grain size however maximum grain conductivities were achieved at 3mol% YSZ. Badwal & Swain [28] investigated the conductivities of zirconias with varying yttria stabilisation using impedance spectroscopy. They found that for temperatures above 600°C, increased yttria content gave a higher conductivity but that this reversed at lower temperatures.

An alternative to PSZ and FSZ is tetragonal zirconia polycrystals or TZP. This material is composed of very small particles of partially stabilised zirconia with the benefit of higher conductivity and high physical strength. On the down side the smaller grain sizes can give problems of large grain boundary resistance and so must be of high purity. Slotwinski et al [29] used impedance spectroscopy to examine the effects of mixed dopants calcia / yttria and magnesia / yttria stabilised zirconias. They found that grain boundary impedance was eliminated when zirconia polycrystals contained magnesia doping but no such effect resulted using calcia stabiliser. Badwal & Swain [28] also found a lower conductivity in TZP due to significant grain boundary impedance. They measured activation energies for the grain of 12 mol% YSZ at 1.19eV (116 kJ mol^{-1}) and 0.91eV (88.7 kJ mol^{-1}) for 2.8 mol% YSZ.

At the other end of the grain size spectrum, it is possible to use single crystal samples that have no grain boundary resistance but are mechanically very weak. Ikeda et al [30] investigated the conductivity of single crystal zirconia electrolytes with varying yttria stabilisation using impedance spectroscopy and Ag paste electrodes. They found that maximum electrolyte conductivity occurred at 14 mol% but a plateau occurred at 8-12mol%. Activation energy generally increased with yttria content, as did the conductivity until 18mol%. Arrhenius plots showed a high and low temperature regions with differing activation energies.

1.2.2.7 Alternative electrolytes

Zirconia is not alone in its ability for oxygen ion conduction. Alternative electrolytes include Bi_2O_3, ThO_2 and CeO_2 all of which display greater levels of conductivity. Zirconia remains the material of choice due to its excellent mechanical characteristics. Fouletier &

Henault [31] examined the applicability of using alternative electrolytes for oxygen sensing applications. The most highly conducting oxygen ion conductors are Bi_2O_3 based with conductivities 2 orders of magnitude better than zirconia but these are easily reduced when oxygen is scarce. CeO_2 gives better conductivity than zirconia but suffers electronic conduction that leads to measurement errors when employed as a sensor. Maskell & Steele [2] reviewed solid state gas sensor technology and gave a comparison of temperature / conductivity of various ion conductors including ZrO_2, CeO_2, ThO_2, Bi_2O_3 with various dopants and dopant levels. Conductivities were found to vary with type of dopant in the order $Yb_2O_3 > Y_2O_3 > CaO > MgO$ and reach a maximum with minimum dopant to reach full stabilisation. Takeuchi & Takahashi [32], in their review of sensors for A:F control, advocated the use of Nb_2O_5 electrolyte for its small temperature dependence of electrolyte resistance. Yamazoe et al [33] employed a LaF_3 electrolyte as a substitute of zirconia in a potentiometric cell to give a low operation temperature with Nernst response at 25°C with a 2-minute response time determined by step concentration response. A platinum black measuring electrode was used with a reference of Sn/SnF_2 sealed with epoxy. Huggins [34] reviewed solid state ion conductors, principally β aluminas and non-oxide membranes but some reference to Nernst and the early work on solid electrolyte systems.

Often it is the electrode/electrolyte interface that is of interest rather than the bulk electrode or electrolyte properties as this region is widely identified as the limiting factor in cell performance. Vohrer et al [35] investigated reducing electrode interface impedance by doping the YSZ electrolyte with titania to obtain mixed conduction. The results was an increase in electrolyte grain impedance but a reduction in grain boundary impedance, reaching a minima at 5mol% titania which was attributed to improved sintering of the electrolyte. Above very low oxygen partial pressures, the effect on electrode interface impedance was not substantial.

1.2.3 Electrode properties

1.2.3.1 Materials

In order to apply and measure electrical signals to the ceramic electrolyte, it is necessary to apply electrically conductive electrodes to act as current collectors and to supply electrons. Electrodes can be identified as those of the first kind, where a potential is developed according to direct partial pressure of the gas, or of the second kind, where the potential is determined by a preceding chemical equilibrium. Electrodes of the second kind will be more temperature sensitive than those of the first kind [12]. Whilst the common materials

are costly noble metals or highly refined and prepared composites, cost is not a greatly significant factor due to the low quantities used per sensor in relation to electrolyte and fabrication costs.

The measuring electrode should be inert to the electrolyte and gas but electrocatalysis is essential for selectivity, sensitivity and short response times [9]. The most common electrode material used is platinum. This is largely due to its chemical inertness, good conductivity, high melting temperature and not least due to its strongly catalytic behaviour. Gold and silver are also commonly employed with higher conductivities and good inertness but lower melting temperatures. Their non-catalytic behaviour may however be advantageous dependent upon application. Haaland [23] recommended gold or silver electrodes to reduce the oxidation catalysis of CH_4, C_3H_6, CO and H_2 for the measurement of non-equilibrium oxygen levels. Silver electrodes have been shown to give a better performance, in terms of faster response, than platinum at lower temperatures [36]. However, whilst giving improved response rates sensors, Fouletier et al [37] found silver electrodes were subject to large errors at low oxygen partial pressures. Alternative electrode materials have been suggested and recommended such as Ni, UO and $LaSrCoNiO_2$ and are reported to have advantages over simple noble metal electrodes. Inoue et al [38] used 4 probe DC measurements to research alternative electrode materials. They found that, at 600°C, 90% of cell resistance was due to the Pt electrode on zirconia. This dropped to 30% with the use of a perovskite electrode (see figure 1.2). They measured the lowest temperatures at which Nernstian EMFs were obtained (see section 1.2.5.1) for potentiometric sensors using various electrodes. The results indicated Pt = 500°C, Au = 450°C, Ru = 620°C, Ni = 720°C, Ag = 280°C, Pd = 600°C, Cu = 700°C, Fe = 750°C, $La_{0.6}Sr_{0.4}Co_{0.98}Ni_{0.02}O_3$ = 200°C. Xiang & Sheng [39] also reported a zirconia potentiometric sensor that gave Nernstian EMFs to temperatures as low as 200°C. The sensor incorporated electrodes of $Bi_3Ru_3O_{11}$-YSZ painted onto the electrolyte at a thickness of 100μm. Badwal & Ciacchi [40] investigated urania/metal non-stoichiometric oxide electrodes in comparison with platinum paste and electroplated electrodes in order to achieve a low temperature operation of potentiometric sensors. They concluded that urania electrodes could be used to realise Nernstian EMFs at 350°C compared to 450°C with platinum electrodes with less sensitivity to gas flows or pressure changes.

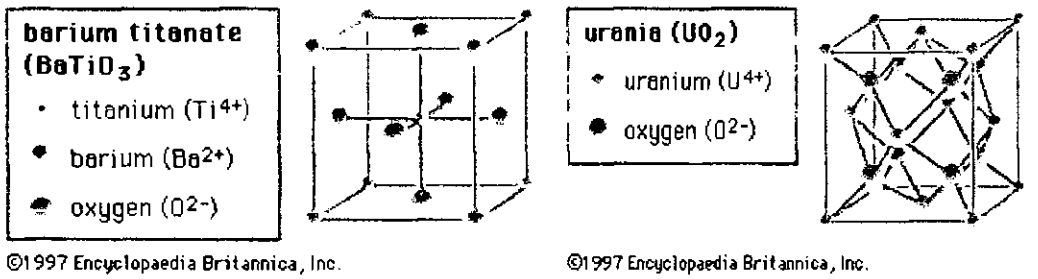

Figure 1.2 Crystal structures of a) fluorite and b) perovskite.

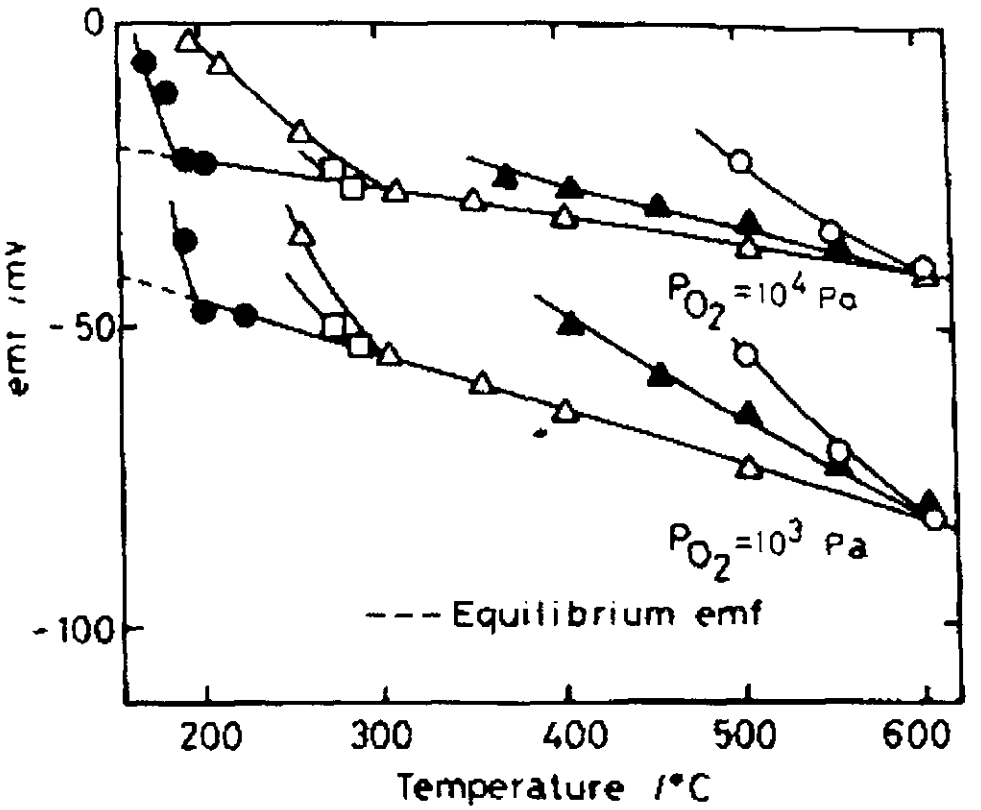

Figure 1.3 Temperature required for Nernstian response. Inoue et al [38]

● $La_{0.6}Sr_{0.4}Co_{0.98}Ni_{0.02}O_3$, ▲$LaCoO_3$, ○ Pt, □ Ag, △$La_{0.6}Sr_{0.4}CoO_3$

Kaneko et al [41] used impedance spectroscopy to investigate palladium and rhodium cermet electrodes over a range of temperature and oxygen partial pressure and observed a two stage behaviour corresponding to metal oxidation / reduction. These two systems gave similar behaviour, corresponding to similarities in their characteristics. A hysteresis in their impedance spectra was explained by the requirement of excess oxygen potential to give reduction of the metal oxide. The decomposition occurred at approximately 850-900°C for Rh and 650-700°C for Pd in 1×10^{-2} atm oxygen pressure. Adler et al [42] investigated various mixed conducting electrodes such as $La_{0.6}Ca_{0.4}Fe_{0.8}Co_{0.2}O_{3-\delta}$ to extend the active three phase boundaries to make more efficient use of the electrode.

Haaland [43] attempted free oxygen measurements in reactive gas mixtures of CH_4, C_3H_6, CO and H_2 using electrodes of Pt, Au, Ag and Pt poisoned with Pb or S for sensing with zirconia pump-gauges in oxygen / nitrogen atmospheres. Silver was found to be non-catalytic to methane but slightly so for carbon monoxide whilst its oxygen solubility caused measurement errors and hysteresis. Use of thin silver electrodes reduced the solubility problems but the slight catalytic behaviour remained. A thin Ag layer, vapour deposited on Pt, reduced catalytic characteristics of Pt whilst retaining oxygen pumping capability. Silver appeared to remain on the surface as Ag has a strong surface segregation on Pt-Ag alloys at high temperature. Au was found to be more catalytic than Ag but less so than Pt and that oxygen is not soluble or adsorbed onto Au. Au however performed poorly as pump electrodes below 700°C (see section 1.2.5.3). Pb poisoned Pt electrodes did show catalytic behaviour below 500°C. H_2S poisoned platinum electrodes proved non-catalytic to methane whilst retaining pumping characteristics but retained their CO oxidation catalytic activity. The H_2S poisoning was removed and catalytic properties restored when sulphur desorbed at temperatures of approximately 800°C. This effect may be used to reactivate performance of electrodes of sulphur poisoned sensors.

Chen & Saltsburg [44] measured exchange currents with a zirconia potentiometric sensor to examine the behaviour in SO_2/SO_3 using Pt, Ag and Au electrodes and explained observations using a mixed potential theory. They found that reaction rates in the order Ag>Pt>Au following the same order of oxygen affinity on electrode surfaces.

1.2.3.2 Microstructure

At least as important as electrode material to performance is its microstructure. The porous nature of electrode microstructure determines the sensitivity and performance of sensors which is particularly of interest at low temperatures [45]. In order for an external gas to interact with the zirconia ion conduction phenomenon, it is necessary to bring oxygen molecules to the zirconia surface and dissociate them into O^{2-} ions whilst supplying electrons. In Kroger-Vink notation:

$$^1/_2O_2 + 2e' + V_o^{\cdot\cdot} \leftrightarrows O_o^x$$

This means that the three components of electrolyte, gas and electrode (for electron supply) must exist together for the interaction to occur. This is widely reported to happen at, or very close to, the so-called three phase boundaries (TPB). Under zero current

conditions surface diffusion leads to a homogeneous oxygen coverage of platinum electrodes, this is depleted near the three phase boundaries upon current application [45]. This means that it is critical to performance to keep the electrode porous, to allow diffusion to the TPB, with a finely divided form, to give a large TPB length, whilst maintaining electrical contact over the whole electrode area. Usmen et al [46] used methanation of adsorbed CO using H_2 to measure the surface area of platinum electrodes on a selection of commercial zirconia gas sensors. In all sensors they found that platinum dispersion was very low with around only 1.3 atoms in 10^3 directly available to the gas phase. According to Adler et al [42] reaction beyond the TPB is only a few μm in the best electrodes, therefore electrodes of over 10μm thickness are mostly inert but may give a benefit in structural terms. Wang & Nowick [47] studied foil and paste electrodes of Pt, Au and Ag on calcia stabilised ceria electrolyte by current interruption. Activation energies were given as 1.1 eV and 1.69 eV for silver and gold respectively. Charge transfer was found to occur in the 2 phase electrode / electrolyte region unless the rate of surface diffusion is lower than the local charge transfer rate in which case the reaction occurred near the TPB with the majority of the electrode material blocked. It would appear that the improved electrode performance of silver is due to the high oxygen solubility compared to the low solubility of platinum. This allows the whole silver electrode/electrolyte contact to be used as TPB rather than the just edges of the platinum contact area.

Robertson & Michaels [48] used steady state and transient experiments to examine the O_2/Pt/YSZ system to demonstrate that oxygen dissociation occurs at the three phase boundaries and not at the electrode/electrolyte interface. They inferred that only a small fraction of the interface was active. Oxygen permeable electrodes such as perovskites show a greater electrode efficiency and therefore support this hypothesis. Oxygen solubility in silver means silver may also benefit in this respect.

Reactions at the three phase boundaries mean that the performance of platinum electrodes is highly dependent on microstructure. This microstructure suffers sintering and grain growth upon exposure to high temperatures which reduces porosity and three phase boundaries, thus adversely affecting low temperature behaviour. Badwal et al [36] found that UO electrodes are better able to resist microstructural changes when exposed to high temperatures.

Whilst it is most common for simple single metal electrode to be used, work has been done using mixed electrodes, layered electrodes and cermets. In addition to three-phase boundary length and electrode porosity, it is important for the electrode to have a good adhesion to the electrolyte surface since the high temperatures and thermal expansion mismatches will tend to separate these two vital components. The use of cermets (an intimate mix of metal electrode and ceramic electrolyte powder) give improved adhesion of electrodes to the electrolyte and are commonly employed. Mineral binders in electrode aid electrode adhesion but can make response very slow [37]. Maskell & Steele [1] pointed out that good electrode adhesion, porosity and a long three phase boundaries are key to electrode performance whilst mineral binders, glassy phases and high temperatures should be avoided. Young [49] noticed that fritted electrodes gave a poor performance but found that this could be restored by rinsing with acid.

1.2.3.3 Deposition

Having established the importance of electrode microstructure, it is useful to know something of the deposition methods employed to achieve the desired characteristics. There are a number of ways to lay down the electrode material dependent upon device configuration and facilities available. The most common methods are painting of metallic inks using brushes, and sputtering which gives greater control but at greater cost and limited flexibility. Haaland [23] found that superior performance with greatly improved oxygen transport could be obtained from thin sputtered rather than thick sputtered or paste platinum electrodes. Bauerle [50] used sputtered and paste platinum metal electrodes in his analysis of solid electrolyte systems. These were fired at 1400°C. The paste electrodes became non-porous and showed poor performance. He found that passing a current of 1A/cm2 for several minutes at 800°C could rectify this, producing porosity due to the high gas pressures attained within the electrodes. Electrode porosity was deemed essential for oxygen reduction in platinum, as it is virtually impermeable to oxygen even at 1425°C. Electrode porosity was detected by adsorption of a liquid droplet.

Alternative methods of electroplating and screen-printing are also used, plating requiring deposition on an already conducting layer. Screen-printing on the other hand is a very laborious process best suited to large batch production where it becomes highly efficient. This method has been employed by Ioannou & Maskell [18, 51] and Gopaul et al [52] who used it to deposit thick film platinum / YSZ cermets on thick-film zirconia electrolytes. Kinoshita & Stonehart [53] reviewed the catalytic activity of highly dispersed metals. A

good platinum black electrode would have a surface area of $20m^2g^{-1}$ but a theoretical $280m^2g^{-1}$ is possible. From this it is clear that even finely deposited electrodes have substantial room for improvement. They give references for the preparation of finely divided Ru, Au, Rh, Pd, Ir, Pt and Ag electrodes. The term platinum black refers to platinum deposited with a sufficiently high surface roughness that little light is reflected from the surface, giving a black rather than the usual silver appearance. Weng & Landau [54] proposed a method for electroplating onto a non-conducting substrate. The method was demonstrated by palladium deposition onto a substrate by seeding with metal clusters by dipping into a $Pd/SnCl_2$ solution. This then allowed a plated layer to grow from a metallic contact to non-conducting areas. Etsell & Flengas [55] applied platinum electrodes by application of a solution of chloroplatinic acid and formaldehyde and heating to 600°C to obtain a platinum black electrode. They did also obtain potentiometric readings of oxygen from simple platinum foil and wire electrodes although these performed poorly and required high temperatures.

Feltham & Spiro [56] reviewed the electro-deposition of platinum to form electrodes. They suggested that the adhesion of platinum black to platinum may be enhanced by the presence of Cu or Pb. Use of these materials may run the risk of introducing a catalytic poisoning of the electrode. The reduction of chloroplatinic acid occurs as two separate processes

$$Pt^{IV}Cl_6^{2-} + 2e^- \leftrightarrows Pt^{II}Cl_4^{2-} + 2Cl^- \qquad \text{Equation 1.1}$$

$$Pt^{II}Cl_4^{2-} + 2e^- \leftrightarrows Pt + 4Cl^- \qquad \text{Equation 1.2}$$

But may be simplified to one single reaction for the complete process

$$Pt^{IV}Cl_6^{2-} + 4e^- \leftrightarrows Pt + 6Cl^- \qquad \text{Equation 1.3}$$

at 25°C this will occur at 0.7 to 0.76V. The electrolyte may be observed to turn from yellow to red before platinum is deposited due to the formation of $PtCl_4^{2-}$ particularly at higher temperatures.

Surface roughening or heat treatment of the electrode before plating may provide improved electrode adherence. AC plating was reported using a 60 and 30Hz sine and square waves and reported that time until electrode blackening reduced with frequency.

There is scope for further investigation. Reproducibility can be as good as 2% but literature indicates that it is dependent upon conditions. A decrease in surface area is reported as significant with very noticeable effects reported in days even at room temperature and dependent on storage conditions. Badwal & Ciacchi [40] compared platinum paste and electroplated electrodes but concluded that electroplated electrodes gave only a slight improvement over the paste electrodes although no details of the deposition were given.

Many workers pay particular attention to the electrolyte surface to ensure good adhesion by polishing with a diamond paste, or etching using aggressive chemicals such as hydrofluoric acid. Electrode shape will also affect the device performance. If electrodes extend out of the furnace hot zone, for instance, local thermocells are set up leading to errors in measurement [21].

1.2.4 Configuration of sensors

1.2.4.1 Two electrode amperometric

Two electrode amperometric sensors are usually made from discs of zirconia fabricated to enclose an internal volume which is linked to the external atmosphere by means of a diffusion hole. These devices include two metal electrodes between which a voltage may be applied to electrochemically pump oxygen from the internal volume.

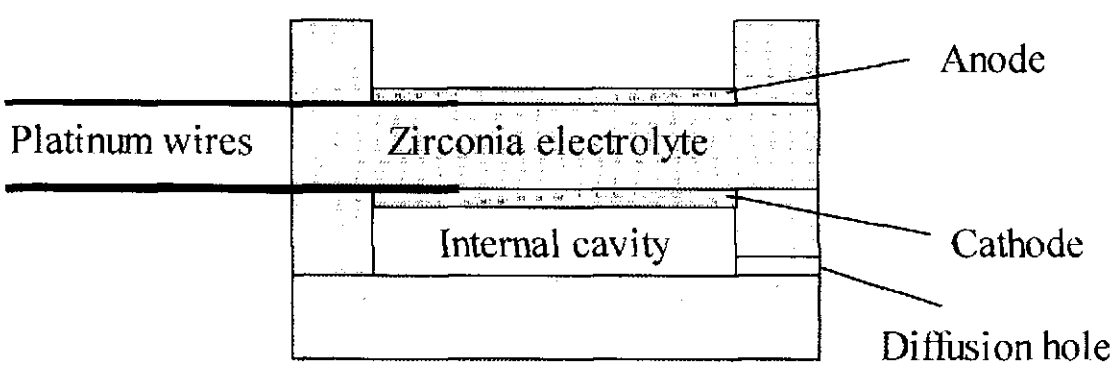

Figure 1.4 Two electrode amperometric sensor

1.2.4.2 Four electrode amperometric

These devices are identical to the devices mentioned above with the exception that they include a second pair of electrodes. This forms a second cell that acts as a potentiometric sensor (see below) to give information on the ratio of partial pressures inside and outside the device. Maskell & Steele [57] used an amperometric sensor with an additional pair of

electrodes to obtain additional information for device characterisation. Their devices were fabricated from FSZ using gold seals and laser drilled diffusion pores with platinum sputtered or paste electrodes. This information may be used to enhance readings or for problem diagnosis.

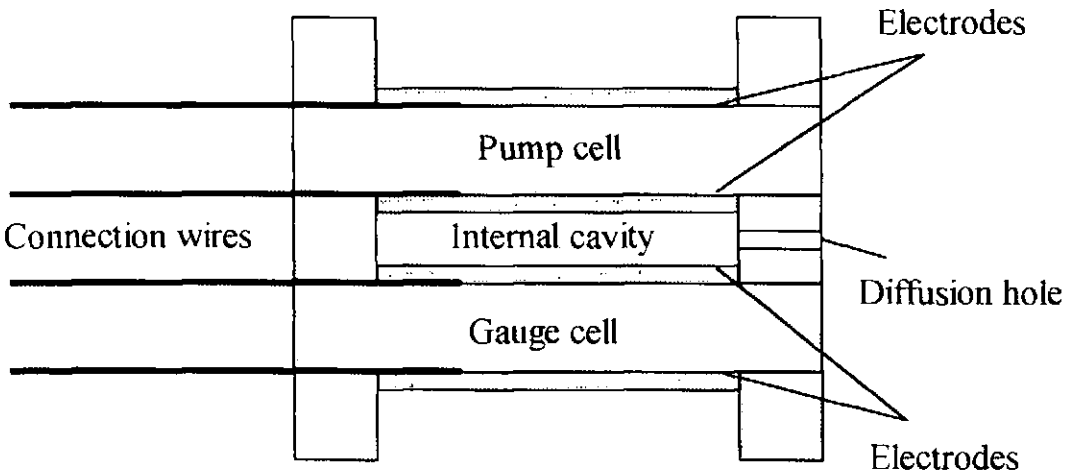

Figure 1.5 Four-electrode amperometric sensor

Logothetis et al [58] constructed an amperometric pump-gauge in which the external gauge electrodes were exposed to an external reference gas, allowing oxygen to be pumped into the sensor from the reference. This gives a sensor that works in excess fuel or air, has a low temperature dependence, pressure independence and a linear output.

1.2.4.3 Pump-gauges

Pump-gauges are similar again to the four electrode amperometric sensors, but may be made fully sealed (no diffusion pore). This allows operation of the device using different principles all based upon pumping oxygen into / out of the internal volume whilst observing the effects on the gauge cell. Operation modes are discussed in section 1.2.5.2.

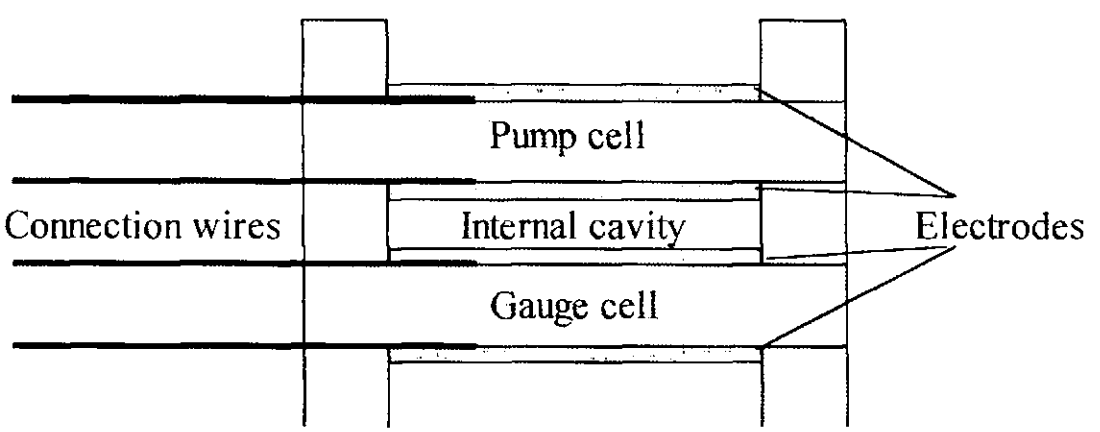

Figure 1.6 Pump-gauge device

1.2.4.4 Split electrode sensors

Split electrode sensors are a novel aspect of this work. They were developed to examine a deviation from the predicted theory of amperometric sensors at high oxygen partial pressures. The design is similar to that of the four electrode amperometric cells but the internal gauge electrode has been split to give multiple readings of internal partial pressure across the electrode area to form an array of cells perpendicular to the diffusion hole. External electrodes and may be split, however this adds complexity and oxygen levels would not be expected to vary across these surfaces. Pump cells could be split to achieve various oxygen profiles across the sensor cavity.

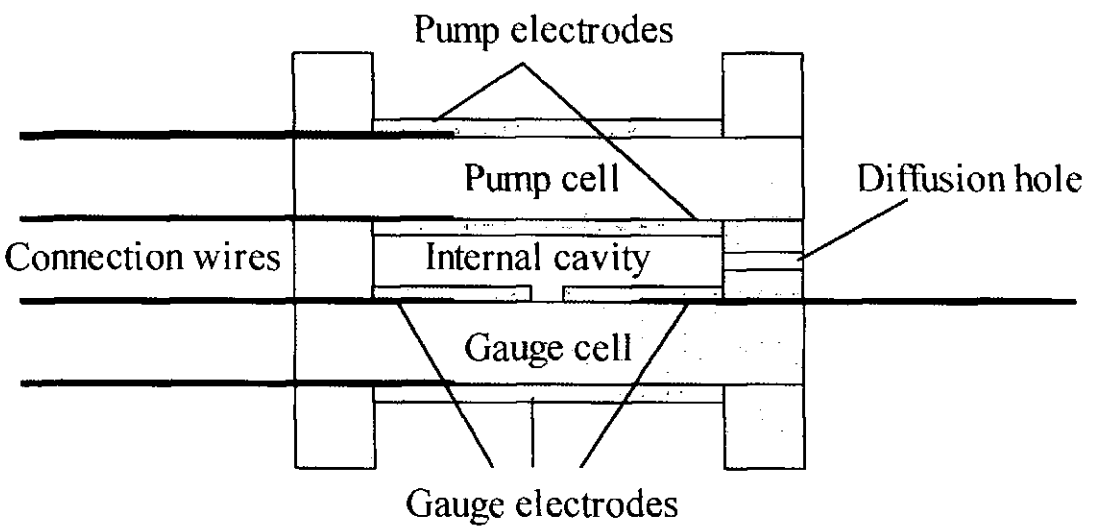

Figure 1.7 Split electrode amperometric sensor

1.2.4.5 Potentiometric cells

These are the simplest devices, consisting usually of a closed end tube of zirconia with electrodes applied to the inner or outer faces. A reference gas is fed to, or generated at, one of these electrodes whilst the other is exposed to the gas to be analysed. This forms a concentration cell whose operation is described below.

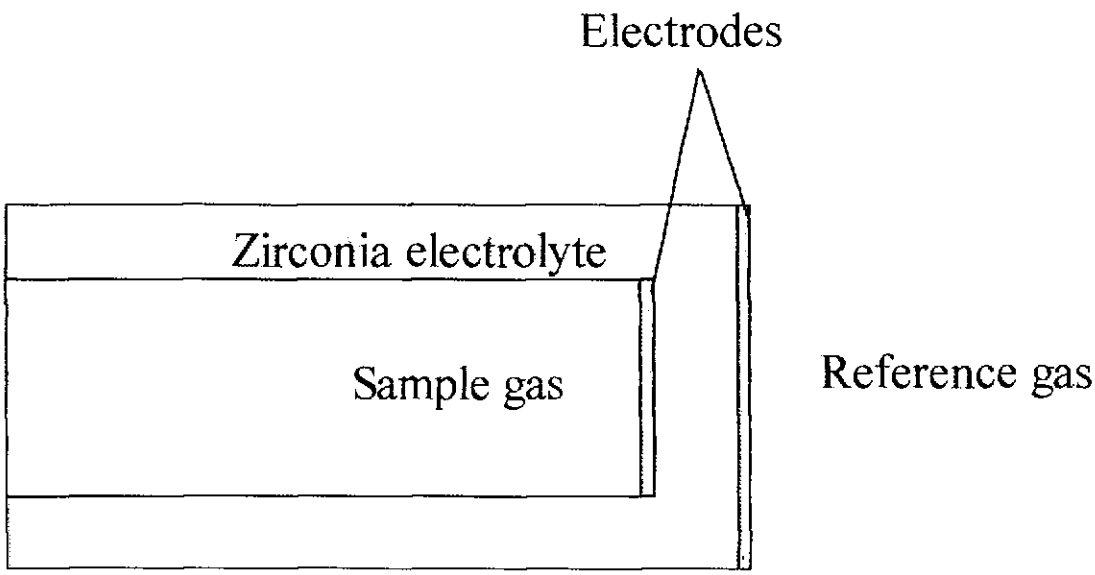

Figure 1.8 Potentiometric sensor

Each of the above mentioned sensor configurations require the electrolyte to be impermeable to species in the gas phase. Ceramic porosity would allow gas diffusion to occur through adjoining pores which is likely to occur if density does not exceed 95% [12]. The exception to this rule is in the manufacture of amperometric devices that incorporate a porous membrane rather than a cylindrical hole to limit gas diffusion. An example is thick film devices where a porous electrolyte is deposited directly onto the cathode to act as both electrolyte and diffusion barrier.

Other considerations reflected in construction of various sensors are the method of heating, temperature control, flame traps, electrical / thermal insulation, connections, gas feed (whether reference or measured) and sensor mounting.

1.2.5 Sensor operation theory

1.2.5.1 Potentiometric

A potentiometric sensor uses an electrode / electrolyte / electrode cell to separate two gases containing different oxygen partial pressures. We now have, in effect, a concentration cell and an EMF is developed across the electrolyte according to the Nernst equation:

$$E = \frac{RT}{4F} \times \ln \frac{P'}{P''} \qquad \text{Equation 1.4}$$

where R, T and F are the molar gas constant, operation temperature and Faraday's constant respectively. Whilst P' and P'' are the oxygen partial pressures on either side of the cell. If

one of the atmospheres is a reference gas of known composition and barometric pressure, then the second partial pressure may be calculated from the measured EMF. Equally, if an identical oxygen concentration is present on each side of the cell, the cell will indicate a pure barometric pressure differential reading. These sensors are very simple in operation and construction, with a wide measurement range of over 20 orders of magnitude under appropriate conditions [1, 4]. They are currently widely employed especially in automotive applications and large-medium sized boilers (Lambda sensor).

It is important to have a good gas tight seal if there is to be no cross contamination of reference / measurement gases, the solid electrolyte must be close to full density and free of cracks to prevent physical diffusion. These requirements lead to the design problems of achieving a gas tight seal given the thermal expansion coefficient and elevated temperature required for operation. One solution is the use of closed end zirconia tubes extending beyond the hot region. Whilst being mechanically sound and the low thermal conductivity giving low heat losses it does lead to manufacturing difficulties and is not an efficient use of the expensive electrolyte material. Sealing is often avoided by extending electrodes out of the furnace hot zone however these can result in significant errors that arise through thermo-electric EMFs where the metal and electrolyte contact [37].

The use of gold or platinum metal seals can give strong gas tight seals if formed under pressure near the melting temperature for the metal. They also provide a route for electrical contacts through the electrolyte. The seals produced between zirconia and alumina parts are able to withstand thermal expansion stresses by nature of the metal's ductility. Fabrication through this method requires the use of expensive and complex high temperature presses, and also gives rise to a route for electrochemical leakage of oxygen between the two separated gases. Whelan & Borbidge [59] used this method, reaction bonding zirconia parts to an alumina tube using a Pt foil washer. Gold seals have been employed extensively Benammar & Maskell, [60], Kaneko et al, [61], Fouletier et al, [21]. Suganuma et al [62] reported a method for joining ceramic discs (Si_3N_4) to hard metal tubes (Steel) using a soft metal interlayer (Invar) to avoid problems of thermal expansion mismatch. Hao et al [63] used a filler metal alloy of Ag, Cu and Ti to braze zirconia to steel using temperatures of 850°C.

By careful selection of expansion coefficients, it is possible to select a suitable glass, which may be applied as a paste and fired to give a good seal. Glass seals must be kept

away from the electrode if contamination is to be avoided (see section 1.2.3.2). It is also possible for glasses to evolve oxygen dependent upon operation temperature and exact glass composition. A further restriction is the limiting of use to temperatures below the melting point of the glass used. Glass seals also have been widely employed both independently and in conjunction with other methods to ensure seal integrity.

Other workers have achieved the sealing of a zirconia part to an alumina tube by varying the composition from zirconia to alumina over the length of the joint. Varying the composition gradually spreads the stresses arising from thermal expansion mismatch. Badwal & Ciacchi [40] used high temperature eutectic welding to join a scandia stabilised zirconia disc to an alumina tube. This method requires careful preparation, also the joint would be particularly prone to thermal shock.

Temperature has major effects on the behaviour of potentiometric sensors and so careful design must be implemented to avoid measurement errors. A tight control and monitoring of device temperature must be maintained if an accurate measurement is to be obtained. Potentiometric sensors work well between 600 and 800°C. Below 600°C they exhibit increasing response times as electrode interface impedance provides increasing RC time constants. Fouletier [9] suggested that total cell resistance must be much less than that of the measuring voltmeter with 1MΩ usually considered to be the upper limit.

The sensors also develop increasing errors in measurement EMF and they become very sensitive to gas flows. Dietz et al [12] reported that potentiometric sensors develop errors at low temperature due to electrode polarisation arising through transfer, diffusion and reaction overvoltages which reduce with temperature. Badwal et al [36] found potentiometric cells suffered increasing errors as temperatures reduced below 400°C and that cell performance at low temperature was influenced more by the electrode than the electrolyte. At temperatures exceeding 800°C, the degree of electronic conduction starts to become significant. Dietz et al [12] suggested that deviations from the Nernst potential arise if electronic conduction exceeds 1%. Kleitz & Fouletier [64] investigated the accuracy of potentiometric zirconia sensors. They found that careful design considering the heating and feeding of reference gases are essential for high accuracy measurements. They also found that for measurements of less than 10^{-5} atm, zirconia tube semi-permeability is not negligible.

Taimatsu et al [65] investigated transient abnormal EMFs observed in zirconia potentiometric sensors upon variation in temperature. EMFs were found to be generated temporarily upon a change in temperature and were attributed to a change in oxygen leakage rate or oxygen being released or adsorbed from the electrolyte upon temperature change. EMFs were present over a time scale of minutes following a temperature change.

Another important design factor is the elimination of temperature differentials between the two electrodes. These differentials can lead to large errors, especially where there are large partial pressure differentials between reference and measured gases. Temperature differentials arise through cooling, where the gases are pumped to the electrodes to ensure a constant composition at the reference and measuring electrodes. Fouletier et al [66] traced errors in gauges to thermo electric electrode temperature differentials which arose through cooling by the gas flow.

Differentials can also arise where there is heat drain away through connecting pipes or where the furnace hot zone has to be kept small. Kocache et al [67] researched design considerations for potentiometric zirconia sensors with proposed design to eliminate or minimise problems. A number of problems were identified including: electrolyte fracture, seal breakage, electrode peeling, electrode blocking thermal EMF errors, temperature differential errors, non-uniform electrode temperatures, gas flow electrode cooling, diaphragm sealing. These were all solved by careful design of components and assembly.

Air is most commonly used as reference gas since it has a consistent composition and plentiful supply. For accurate work however it must be cleaned and dried before use. Bottled gases may be used and have the advantage that they may be selected with a composition close to that expected to be measured this reduces inaccuracies that may occur when large differentials exist especially at low temperatures. Bottled gases are also bulky, incur additional expense and require piping to the reference electrode. Alternatively a second zirconia cell may be used to generate an internal gaseous reference atmosphere (see pump-gauges devices). An alternative to a gaseous reference is the use of solid reference metal / metal oxide couple. These may be placed in intimate contact with the reference electrode. They have the advantage of reference piping elimination, simplifying design and improving flexibility. Examples include Pd / PdO, Pb / PbO, Cu / Cu_2O, Ru / RuO_2. Maskell & Steele [1] presented data on the oxygen pressures developed in equilibrium for a variety of metal / oxide couples over a range of temperature. Fouletier et

al [66] & Vitter et al [14] proposed a potentiometric sensors which used a zirconia tube with Pd/PdO solid reference (named microgauges) for use in domestic boiler systems. Kaneko et al [68] developed a potentiometric sensor with internal metal/metal oxide reference system to operate at low temperature. The cell was similar to a 2 electrode amperometric cell but filled with the reference metal/oxide and including silver / $La_{0.85}Sr_{0.15}MnO_3$ electrodes. They used solid reference metal / oxides of Cu / Cu_2O and Pd / PdO with an 8 mol% YSZ electrolyte. Nernstian EMFs were obtained to temperatures as low as 280°C but response times were not reported. Temperature dependence is accentuated where a solid reference is used since the partial pressure evolved is also temperature dependent. Reference whether gas or solid must give a constant EMF despite disturbances [9]. Fouletier et al [69] investigated the use of potentiometric sensors to measure low oxygen concentrations. They used a differential gauge and a guard gas to ensure that there was no contamination of the measured gas from the reference. This enabled them to obtain an agreement with Nernst EMFs for concentrations as low as 1ppm and for temperatures from 400 to 800°C. Above this temperature, significant errors arose from the electrolyte semi-permeability.

Potentiometric sensors are also affected by the presence of reducing gases. These effects are particularly noticed around the stoichiometric point and indeed it is this effect that gives the Lambda sensor its characteristic step. Flemming [70] analysed the non-ideal behaviour of zirconia potentiometric A:F sensors. He pointed out that EMFs generated during the stoichiometric step indicated oxygen levels as low as 10^{-25} atm, which equates to a single oxygen molecule per cubic meter. Clearly this is not a feasible measurement and the real cause is that the EMF is set by the equilibrium of reducible species present. Relative O and CO magnitudes adsorbed on the anode determine sharpness of the step. EMF established depends upon standard cell potentials at rich and lean tails of the curves [7]. Departures from the ideal behaviour are:

1. Reduced slope at the stoichiometric transition

2. Pronounced drop of the voltage level over the entire A:F range

3. Shifting of the step like transitions toward rich A:F with increased temperature

In addition electrode active sites (TPBs) may be blocked by CO adsorption, at low temperatures, that prevents the access of oxygen to the three phase boundaries, this is however a temporary effect that may be cleared by heating to desorb the CO [71]. Okamoto et al [72] utilised this by converting a zirconia sensor to a CO sensor by applying a coating of CO catalyst to the measuring electrode. In addition to CO, many aggressive gases can poison the platinum electrodes of the sensor and reduce the device performance. This can be a particular problem in industrial applications. Whelan & Borbidge [59] placed a ceramic muffle over the measuring electrode and pumped oxygen from the reference. This gave a protective atmosphere that shielded the electrode from reducing and electrode poisoning gases. As previously mentioned, platinum electrodes will not measure free oxygen in reducing gases due to its catalytic properties. Silver, gold and poisoned platinum are much less catalytic and therefore may used to measure free oxygen in these gases [9]. Takahashi et al [73] studied the effects of reducing and oxidising gases on the output of amperometric sensors. The devices utilised a porous layer and a Yb_2O_3 stabilised zirconia electrolyte with platinum electrodes. Secondary current limits increased as reducible gases were added but reducing gases had the effect of reducing the primary currents as oxygen was consumed. Limiting currents were linearly effected by all reducing and oxidising gases added to O_2 / N_2 mixtures

1.2.5.2 Pump-gauge

The pump-gauge device first described by Haaland [23] (fig. 1.3) is fabricated from two electrode / electrolyte / electrode cells. With this device he demonstrated its use as an oxygen sensor that did not require an external reference and operated from 400 to 1000°C in 0.2 to 21% oxygen atmospheres. In this device one cell is used as a potentiometric sensor, the other acts as an electrochemical oxygen pump. Between the two cells, an internal cavity exists, either fully sealed from the external atmosphere, or connected with a leakage pore. The gauge cell records the Nernst potential between the internal and external atmospheres whilst the internal cavity is maintained at a certain partial pressure using the pump cell. The two cells may be constructed identically and their applications are interchangeable. Several designs have been proposed utilising zirconia tubes [21] but the most common is a device constructed from discs and rings of electrolyte. Again the seals between components may be achieved using gold [74] or platinum metal seals [23], ceramic-ceramic seals or seals utilising high temperature glass [75]. Fouletier et al [66] found that errors in pump-gauges could arise from electrical coupling of the two cells

through the electrolyte. These could be eliminated using a non-conducting layer such as a glass seal or by separating the two cells with a cold electrolyte region.

Pump-gauge devices may have similar constructions but differ mainly in mode of operation. Benammar [76] reviewed techniques for oxygen and A:F ratio measurement using zirconia sensors with particular concentration on methods involving pump-gauge devices. The various operation modes are discussed below.

The first proposed use of a pump-gauge was by Heyne [77] in 1970. This included a deliberate leak (four-electrode amperometric sensor) for the coulometric assessment of oxygen partial pressure. In this operation mode, the internal cavity of known volume was pumped free of oxygen. The pump current was then cut and the time recorded for the gauge voltage to settle back to zero as the internal / external equilibrium was re-established. From the required time and the dimensions of the pore, a value for partial pressure could be calculated.

Haaland [23] continued this work, in 1977, using a fully sealed device. In his operation mode, the internal cavity is drained of oxygen using the pump cell. The gauge cell recording a high EMF shows oxygen depletion. The pump cell is then reversed to pump oxygen back into the cavity at a controlled rate until the gauge again reads zero EMF, indicating that internal and external partial pressures are equal. The Faraday law may now be invoked to calculate the required amount of oxygen pumped for equilibrium to be attained, and with the internal volume, give a calculated figure for external partial pressure. Used in this mode, these devices gave a measurement with low temperature sensitivity and no external reference gases. On the other side, the measurements obtained have to be discrete due finite time required for the measurement cycle and errors can arise through leakages and electronic conduction.

In 1982 Hetrick et al [75] used a pump-gauge in an oscillatory mode. In this mode a constant pump current is applied. Upon application of this current, oxygen is pumped from the cell until a set maximum gauge voltage is obtained, which triggers the automatic switching of pump current sign whilst magnitude is constant. Again this current is applied until a set minimum gauge voltage is attained, and again the current sign is switched. Provided the difference between maximum and minimum currents is kept small, the

resultant gauge EMF signal will be triangular, the slope of which will be dependent upon diffusion pore dimensions and oxygen partial pressure.

In 1987 Maskell et al [78] introduced the AC mode of operation. In this mode a sinusoidal modulation of pump current is used to induce a pseudo sinusoidal gauge EMF variation that follows external oxygen partial pressure. A $\pi/2$ radian (90^{o}) phase shift between EMF and current was expected. Good agreement to theory was obtained, provided internal oxygen partial pressure was greater than 0.01atm, otherwise response times of electrodes were suspected to be excessive. This device allows continuous rather than discreet monitoring. Maskell et al [79] investigated operating a zirconia pump-gauge using a continuous operation through sinusoidal pumping to obtain a stable reference. The sinusoidal component was removed to reveal oxygen variation. This paper focused on a description of the sensor, techniques and instrumentation.

Benammar & Maskell [74] further developed this idea, in 1993, with feedback to modulate the pump current such that a sinusoidal gauge EMF is obtained. In the AC mode, gauge EMF could be separated into AC and DC components, of which, the AC component was dependent upon internal partial pressure alone. The external partial pressure can be calculated from the DC component and Nernst law. They gave experimental results for a leaky pump gauge operated in the AC mode which gave the same advantage as that of a fully sealed device operated in this mode, but with simplified calculation of the oxygen partial pressure. This device was fabricated from discs of sintered ceramic and assembled using a gold seal with a further glass coating to minimise leakage. The leak was in the form of laser drilled holes. Benammar & Maskell [80] demonstrated a pump-gauge operated in the AC mode to generate its own internal reference for use in the potentiometric mode whilst also allowing continuous monitoring. The device demonstrated a fast response of 65mS at 800°C, measured using a gas concentration step change

Logothetis et al [81] reviewed the use of zirconia chemical and physical sensors based on pumping to show the versatility of zirconia sensors. They also demonstrated a double cell device as a sensor for combustibles such as CH_4 and C_3H_8 with a faster response than SnO_2 devices. Pumping techniques also suggested for flow or pressure measurement. Benammar & Maskell [82] showed that a double chamber device could be used for unambiguous determination of A:F ratio operated either side of stoichiometry. In this device two

pumping cells were incorporated with a third gauge cell that was not essential for operation. Diffusion holes were present connecting each internal chamber to the external atmosphere. The device was operated by pumping oxygen from the external atmosphere into one chamber using a constant current whilst the other pumping cell pumped oxygen from the second chamber into this first one using a constant potential. The second cell and chamber then operated as an amperometric sensor whilst the first cell and chamber gave an oxygen rich atmosphere to the second pump anode to pin its potential. Operated at sufficiently high constant current, this device gave an unambiguous current with respect to A:F ratio although not a linear one. Operation was reconciled with existing theory.

Fouletier et al [37, 66, 69] and Canerio et al [83] used a zirconia tube including electrodes for a pump and a gauge to monitor and alter the oxygen levels in a flowing inert gas. The measurement was achieved using an external reference to give an EMF dependent upon the internal gases partial pressures. This EMF maybe fed back to control the partial pressure by pumping oxygen in / out using the pump cell. Vizethum et al [84] used a zirconia pump to generate oxygen atmospheres in N_2, H_2O and CO_2 gas streams. The system flowed the gas streams through a 12mm diameter, 600mm long tube of calcia stabilised zirconia. The system was linked to a DAQ system to enable computer control of gas mixtures produced. As mentioned previously Whelan & Borbidge [85] used the application of a current through a potentiometric sensor to provide a protective atmosphere for hostile gases. The current was stepped through the electrolyte to pump oxygen to the exposed electrode, a porous ceramic overlayer helped to maintain this atmosphere. A stepped EMF was generated which could be analysed to provide information for sample gas measurement. Caneiro et al [83] used a solid electrolyte zirconia tube to prepare gases of various CO / CO_2 and H_2 / H_2O composition by electrochemical pumping of oxygen into or out of flowing gas streams.

Three leakage mechanisms have been identified by Kaneko et al [61] as, physical leakage, electrochemical leakage and semi-permeability. Experimental details of this work are reported in Appendix B1.2.

Physical leakage arises through structural flaws in the device. These flaws may arise through cracks in the ceramic originating from thermal shock, physical damage or from stresses arising from mismatched thermal expansion. Another source may be porosity introduced through insufficient sintering temperature or time, contamination,

agglomeration or large particle size in the green state. The final cause of physical leakage is imperfect seals between sensor components. The causes will depend upon the type of seal used but likely causes are poor fabrication, deterioration or thermal / physical abuse. Poor sealing may also arise in the novel plastic / ceramic devices proposed in this work. They may arise through the inclusion of large contaminants, insufficient wetting of the electrolyte prior to fabrication, insufficient pressing force or by volume changes in the connecting wires during firing.

Electrochemical leakage occurs by ion migration through the electrolyte. This may only occur where an electrical short circuit allows electrons to pass between internal and external three phase boundaries (TPBs). Short circuits exist where the internal electrode connection wire has to pass through the ceramic to exit the sensor. Electrochemical leakage may also arise through a track of electrode material traversing the seal. These short circuits allow oxygen dissociation to proceed at TPBs with the passage of electrons through the short circuit and oxygen ions through the neighbouring electrolyte. The leakage is driven by the partial pressure gradient established across the electrolyte upon oxygen pumping. The degree of electrochemical leakage will be affected by the TPB length of the connection, the catalytic behaviour of the metal used, the oxygen gradient present and electrolyte resistance.

Semi-permeability arises in YSZ this occurs where the electrolyte electronic conduction is no longer insignificant, at high pump potentials, particularly at high temperatures and low oxygen partial pressures. The mechanism is then similar to electrochemical leakage but the electrons are transferred through the electrolyte via electronic conduction rather than through the metal. The transport is a function of partial pressure, and as well as being electrolyte dependent, is also a thermally activated process. Electronic conduction proceeds through the formation of electron / hole pairs, and in amperometric sensors can lead to an overestimation of the oxygen partial pressure through increased currents. This leakage mechanism can be avoided only by use of reduced temperature and pump potentials.

1.2.5.3 Amperometric

Amperometric sensors are very simple in terms of design, the requirements being a membrane of zirconia electrolyte with attached electrodes, and a method for electrically joining these electrodes to external circuitry. An internal volume and a diffusion barrier

with known dimensions are required to restrict to passage of gas from the sensor exterior and present this to the internal measuring electrode. In practise we find similar problems to those discussed previously for potentiometric sensors of obtaining a gas tight seal with thermal expansion mismatches, and in precise control of the diffusion hole dimensions.

The common approach to sensor assembly is as detailed here:

1. Press zirconia powder under high isostatic pressure of several tonnes per square inch to form a 'green' pellet.

2. Fire this pellet at 1500°C for several hours to attain sintering and high density.

3. Use a hollow diamond drill to cut a rod of ceramic from this pellet.

4. Slice the rod into two discs using a diamond saw and polish surfaces to obtain a flat smooth surface.

5. Laser drill a hole through one component to act as the diffusion barrier.

6. Apply metal electrodes by painting or sputtering and attach wires by spot welding.

7. Join components using either a glass or metal seal as detailed above to form internal cavity with a gas tight seal.

8. Fire to cure joint, if necessary under pressure and in an inert atmosphere. Often an external coating of glass paste is applied to maintain seal integrity and reduce electrochemical leakage.

This is a lengthy process involving complex and expensive techniques. These are necessary due to the hardness of the material and the high temperatures it must operate under. Also the finished sensors are not particularly robust, with seals affected by ageing and ill-defined characteristics due to the inaccuracies of laser drilling hard materials. The devices first proposed by Dietz [86] were constructed using 7.5m%YSZ with platinum electrodes using a laser drilled cap, microporous cap or paste diffusion layer. They were sealed using high temperature glass. An alternative approach has been detailed by Maskell

& Page [87] who introduced the fabrication of sensors constructed from plastic-ceramic material. Sensors gave linear output from 21 to 0.4% oxygen at temperatures from 500 to 800°C. In addition leakage rates were shown to be low indicating low ceramic porosity and high integrity seals (see sensor construction). Similar fabrication procedures may be employed for the production of pump-gauge devices. Saji et al [10] made use of a spinel porous layer in place of a single diffusion hole to achieve a limiting current with a roughly linear output with respect to air/fuel ratio.

A simplification of the pump-gauge with the deliberate introduction of a diffusion pore, amperometric sensors allow gas to leak from the external atmosphere into the internal cavity of the device. The electrode / electrolyte / electrode cell is now used solely as a pump to remove the oxygen from the internal cavity, a low impedance ammeter may be used to record the rate of oxygen removal using Faraday's law:

$$I = nF \qquad \text{Equation 1.5}$$

where dn/dt is the molar rate of removal, I is the current drawn and F is Faraday's constant. A factor of 4 comes from the fact that four electrons are required for the dissociation of one O_2 molecule to two O^{2-} ions. Under typical conditions a current of 1A will produce around 3.5mlmin^{-1} of gaseous oxygen

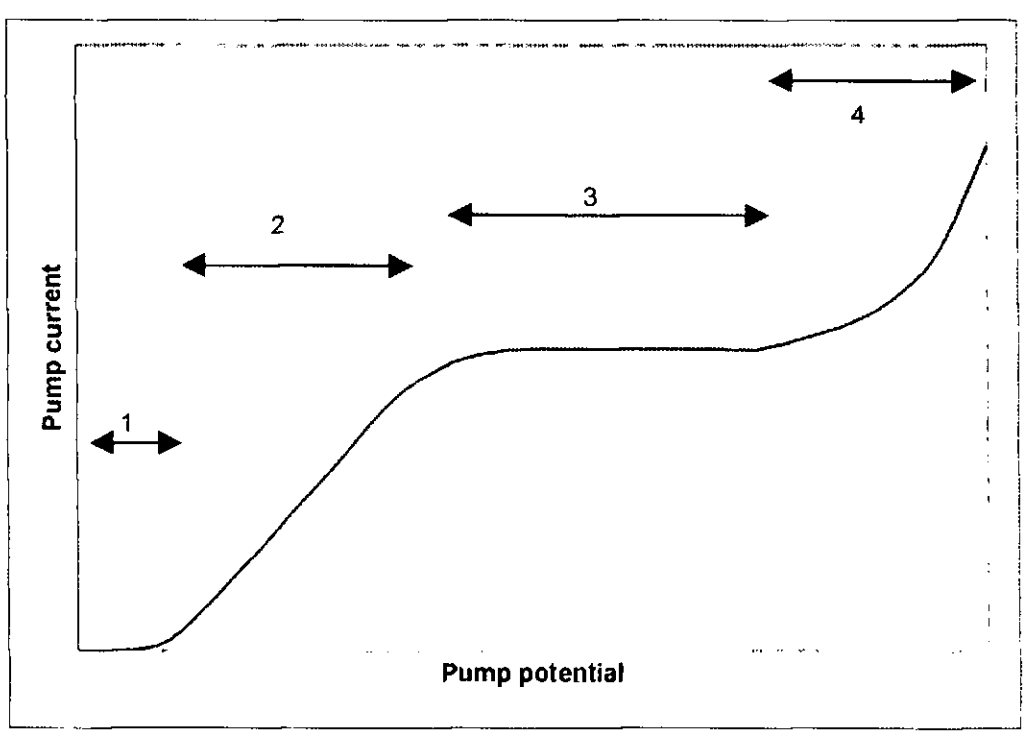

Figure 1.9 Typical current / voltage curve

Figure 1.9 shows a typical current / voltage curve for an amperometric sensor. The curve may be split into four areas, according to the dominating mechanism at a given pump potential. Area 1, at low pump potentials the electrode kinetics for the oxygen dissociation reaction are low so only a small current is drawn. This is most notable at low temperatures. Area 2, resistances within the cell determine the current that may be drawn. These are resistances due to internal electrolyte resistances and show an ohmic behaviour. Area 3, if the diffusion of gases through the diffusion hole to the negative electrode can be severely restricted, then it is this diffusion mechanism that dominates the current. The diffusion mechanism effectively gives an upper limit to the current, seen as a plateau, as the inner volume becomes depleted of oxygen. Area 4, at high pump potentials the electrolyte can suffer a breakdown where oxygen is stripped from the ceramic itself resulting in an additional current. Electrolyte breakdown occurs at higher temperatures especially in atmospheres low in oxygen. It results in embrittlement of the ceramic and a darkening in colour. The electrolyte reduction is reversible but the damage caused may not be.

Area 3, the diffusion controlled plateau is the main area of interest as it relates directly to the oxygen concentration in the external atmosphere. By combining Fick's first law of diffusion with Faraday's law we are able to obtain an expression relating the level of this current limit to the oxygen partial pressure.

$$I_{Lim} = \frac{4\ F\ D\ S\ P}{R\ T\ L} \qquad \text{Equation 1.6}$$

where D, P, L and S are the gas diffusion coefficient, oxygen partial pressure and effective length and cross sectional area of the diffusion pore respectively. This equation shows the limiting current is inversely proportional to temperature and proportional to barometric pressure. In practise we see that the current is actually proportional to temperature and independent of barometric pressure. This is due to the fact that the diffusion coefficient is not a constant but is inversely proportional to barometric pressure, which cancels out, and proportional to temperature that then counteracts the inverse proportionality. The result is a device that is fairly insensitive to temperature variations and independent of barometric pressure. The Fujikura amperometric sensor has been examined by Usui & Asada [88, 89, 90, 91, 92, 93 & 94] they demonstrated that the nature of the inert carrier gas has a large influence on the limiting current due to variations in diffusion coefficients. At fixed

temperature we now see the device has a limiting current which is virtually linear to the oxygen mole fraction. This gives an advantage over the potentiometric sensor's logarithmic response in that the degree of signal processing is reduced. Sensors may contain a single pumping cell (fig. 1.4), a double cell including both pump and gauge (fig. 1.5) or a more complex electrode arrangement (fig. 1.7). Further advantages of both the pump-gauge and amperometric sensors are that they do not require a piped reference gas. One draw back of amperometric devices is that they are unable to distinguish the two sides of stoichiometry.

1.2.6 AC Impedance theory

Impedance analysis is a commonly used and well-developed tool for investigating electrochemical materials and properties. With modern electronics and computing systems, powerful instrumentation exists, specifically designed for their measurements. These modern instruments have the advantages of good noise rejection, automated measurement and simulation capabilities. It was such a system that was used in the frequency response work presented here. Impedance spectroscopy has uses in characterising chemical processes, analysing materials for ageing, moisture incursion, dielectric properties, and flaw detection. Flaws in rubber gloves, water in concrete, curing of adhesives, metals corrosion, effectiveness of paints, oxygen levels in biological applications, quality assurance and drugs testing are just a few of the applications. In some systems, Fast Fourier Transform (FFT) analysis is employed so that many frequencies can be analysed at once saving test time however this is inherently less accurate and was not employed here. AC impedance analysis is a high precision technique that, over a small range of excitation amplitude, approximates I/V characteristics to linear. The technique returns values for R and C that are interpreted to provide information on interfacial phenomena.

Whilst many electrochemical techniques drive the system from equilibrium and then monitor system response, AC impedance perturbs the system with a small AC signal in order to observe the system following the perturbation. Impedance analysis monitors changes in the impedance (AC resistance) to an applied signal with varying frequency. This is achieved by measuring the phase difference and signal amplitude at fixed frequency intervals. The principle behind the impedance measurement technique may be illustrated (fig. 1.10 & 1.11) using phasor and Argand diagrams. A sinusoidal EMF (ε) is applied to the system under investigation, which results in the passing of a sinusoidal current (or vice versa) of identical frequency ($1/\omega$) but with modified amplitude (a) and

phase (f). Provided the system can be characterised by an RC circuit the phase and amplitude will change with frequency. The rates of change will depend upon the values of R and C. The result is plotted in a complex diagram (fig. 1.11) plotting the capacitive (imaginary) resistance Z" versus the real resistance Z'. Using such plots each RC component will be revealed as a semicircle from which R and C values may be extracted. Macdonald [95] gave an overview of impedance spectroscopy in analysing solid and liquid electrolyte systems. He advocated the use of 3d plots for identifying data for rejection. His review took a non-specific but detailed examination of the analysis and interpretation of impedance spectra. Solid electrolyte systems were first investigated using this method by Bauerle [50] in 1969. Before his work, the technique was used in the analysis of liquid electrolytes and electronic networks. An electrode / solid electrolyte / electrode system such as Pt / ZrO_2 / Pt has been shown to reveal three polarisations, one at high frequencies identified as electrolyte grain resistance, one at intermediate frequencies identified as the grain boundary impedance and one at low frequency identified as the electrode interface impedance. The system may be modelled as an equivalent circuit as shown as three, parallel RC circuits in series. More advanced models have been proposed however this was deemed suitable for our requirements since we were using the technique for a comparative study rather than a detailed microstructural investigation. The resistance component is given by the semi-circle diameter of each complex impedance polarisation plot, with the capacitance revealed by the frequency at the semi-circle maxima as:

$$f = 1/2\,\pi RC \qquad \text{Equation 1.7}$$

A more complete explanation of impedance spectroscopy technique applied to electrochemical systems may be found [96]. Impedance spectroscopy applications, theory and instruments have been reviewed by Evans [97]. Appendix B1.4 contains details of solid electrolyte impedance measurements from the literature.

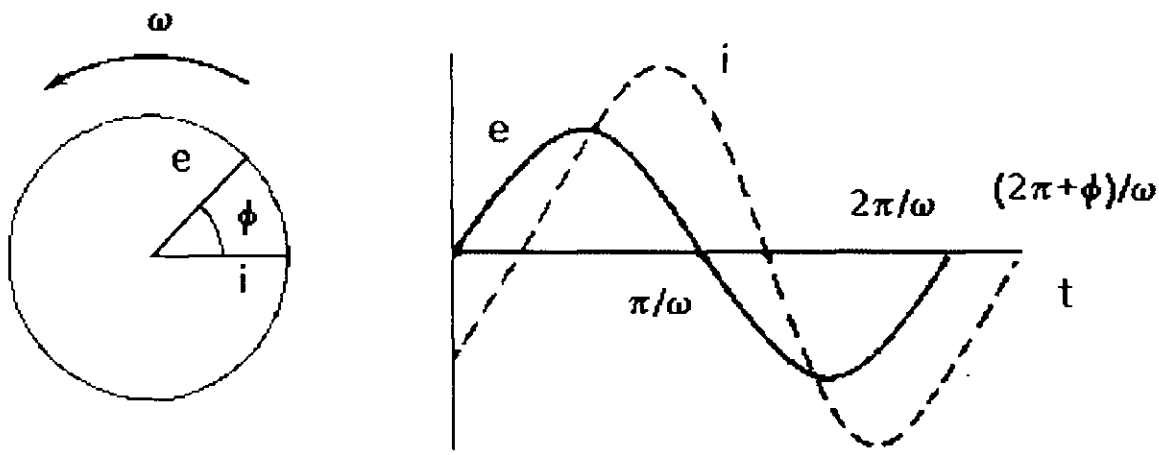

Figure 1.10 Phasor diagram of out of phase voltage and current components

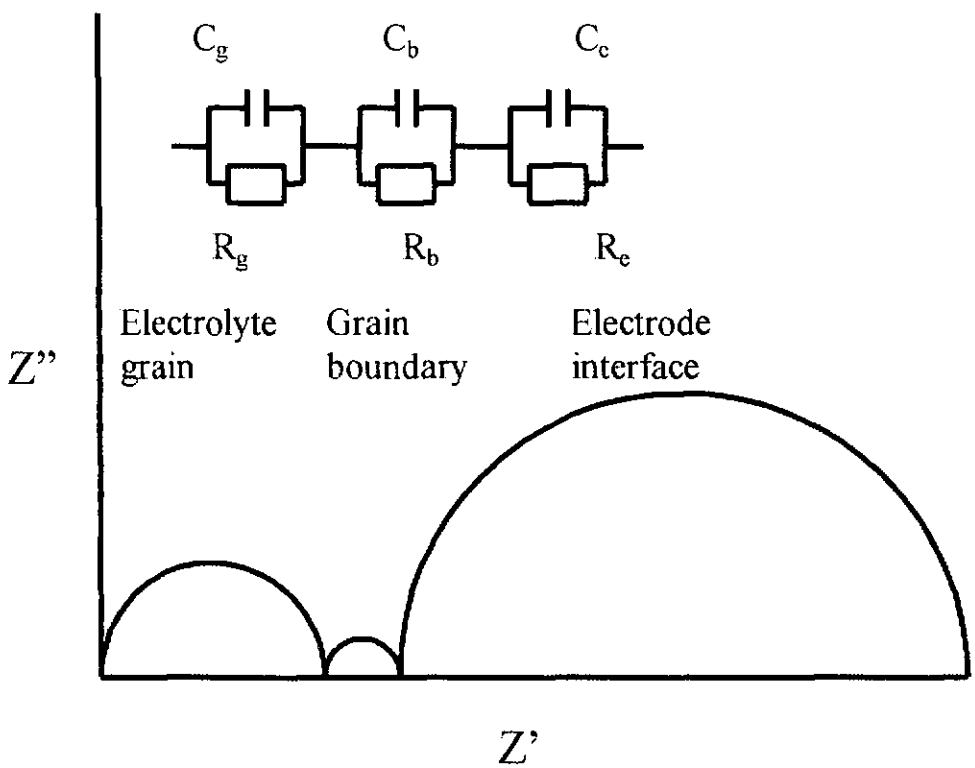

Figure 1.11 Complex impedance diagram showing separate impedance components

1.2.7 Scanning electron microscopy

Another highly developed technique employed is that of scanning electron microscopy. The use of electron examination for microscopy was proposed by Louis de Broglie in 1924 and the first electron microscope was constructed in 1933. Electron beam wavelengths are some 5 orders of magnitude shorter than that of light. This has since become a common laboratory technique widely employed to visually examine the microstructure of a sample. Other variations in electron microscopy include transmission electron microscopy and

tunnelling electron microscopy. Electron microscopy is similar in concept to optical microscopy but uses electrons rather than photons to "illuminate" the surface. A tungsten filament cathode heated by an electrical current is used to generate the electrons that are then accelerated towards the sample by a high electrical potential (5 to 30 kV). Controlling the current in a series of electromagnetic lenses focuses the beam. Upon the primary electron beam striking the sample, a secondary electron beam (which generally is used for analysis), back-scattered electrons, x-rays, specimen current and cathode luminescence are emitted. In SEM the electron beam is then scanned across the sample surface to build an image of surface structure. Secondary electrons are collected and passed to a scintillator that produces light when bombarded by electrons. The light is amplified by a photo-multiplier then converted back to an electrical signal. Amplification in this manner allows an effective gain in excess of ×10,000. The resultant is interpreted electronically to give an image on screen or as a micrograph whose brightness is directly related to the number of electrons emitted from each point. A number of considerations include:

- Magnifications of 20 to 20,000 times are achievable. by concentrating the scan on a small area.
- Electrons cannot travel any significant distance in air at atmospheric pressure, so the whole system has to be kept under vacuum during operation.
- The use of a vacuum would cause vaporisation of liquids so samples must be dry.
- Sample size is dictated by the dimensions of the analysis chamber (typically 10 cm in each direction).
- Loose samples may be dislodged and should be restrained.
- The use of a strong beam may damage the sample so care must be taken.
- Heavy atoms are more effective at scattering electrons from which the image is formed so a thin coating of gold is applied at 50 to 100 angstroms thick which is sufficiently thin so as not to hide surface detail.
- Non-conductive specimens will tend to charge as they cannot conduct away excess electrons.
- The gold layer prevents this charging which would prevent a sharp picture.

The main advantage of electron microscopy is higher resolution but it also provides a greater depth of field than optical techniques. Disadvantages lie in the cost of purchase, operation and maintenance along with the degree of sample preparation required (sample mounting and sputtering) and the complexity of operation.

In addition, an elemental analysis may be performed through Energy Dispersive X-ray analysis. The EDX system is a bolt-on facility to the SEM which allows distribution and proportion analysis of elements within the specimen surface. The system uses the various energies of x-rays emitted by the sample upon bombardment with the electron beam. Each element has a characteristic set of energies, which enable identification upon analysis. As x-rays strike the detector, a voltage is produced which is proportional to the x-ray energy. The number of strikes at each voltage is monitored to build a spectrum of x-ray energies and therefore elemental composition. A rough idea of composition is gained from the relative number of strikes, use of correction techniques allow a more accurate assessment. Elements with atomic number less than 5 are not detected by this method, which must be borne in mind when interpreting data.

CHAPTER 2

EXPERIMENTAL DETAILS

2 Experimental Details

In this chapter we review the experimental and practical aspects of the work undertaken to achieve the results presented in the main body of this work. Further experimental detail is presented in annex E pertaining to further work carried out which is discussed in annex F.

2.1 Materials

2.1.1 Electrolyte materials

Five separate sources of electrolyte were used in the work presented here. Each source was specified as fully stabilised, 8 mol% yttria stabilised zirconia with the exception of Keele ceramic, which was a 7.5 mol% YSZ. The sources were:

- Tioxide specialities
- Dynamic ceramic
- Keele University
- Toyo soda
- Daichi

The Toyo soda material was purchased as a sub-micron particle sized powder. This material was acquired for the sole purpose of replicating the Tioxide material, it was used in the preparation of plastic-ceramic.

The Tioxide and Keele ceramics were supplied as plastic / ceramic sheets, approximately 1.5 mm thick. These materials were an intimate mixture of fine zirconia powder, polyvinyl alcohol, and water. The Tioxide ceramic was used for virtually all amperometric sensor and all pump-gauge work described here. The Keele ceramic was used successfully to make sensors but the only results given here using it are the preliminary electrode tests, and only here due to the shortage of Tioxide ceramic. The Keele ceramic has a slightly greater flexibility and shrinkage upon firing but otherwise gives similar results to the Tioxide material.

The Dynamic Ceramic material was ordered as pre-sintered, closed end 8 mol% YSZ tubes of >97% density. These were delivered as 100 mm length, 9 mm OD, 5 mm ID tubes with one flat closed end of 4 mm thickness in two batches of 5 tubes as specified to fit the miniature furnace (Appendix C1.3.5). They were used for all potentiometric cell measurements reported. Density measurement and S.E.M. examination have been used

confirmed the density specification whilst Impedance spectroscopy and x-ray diffraction were used to look at conductivity and crystal structure.

An assessment of YSZ ceramic manufacturing techniques was performed by Taha et al [98]. Powders were prepared using sol-gel, hydrolysis and reaction of molten salts then assessed for surface area, agglomerate size, crystallite size, shrinkage and weight loss on sintering. In conclusion they found advantages in each process investigated the sol-gel process allowing low sintering temperatures whilst the molten salt route gave theoretical density ceramics.

2.1.2. Electrode materials

As previously stated, the electrode material and structure are critical to sensor operation. All devices under examination here were fabricated using metallic paste electrodes, however using painting as the deposition process there is little control over the quantities laid down. A thorough mixing of pastes was required prior to application as separation of components occurred over time. In addition electrode firing temperatures and times were suspected to have a large influence on electrode condition. The final variation is in electrode composition. Electrodes used were M4 and M6 cermets as described below and occasionally Pt metal paste. An electrode material investigation was also conducted comparing silver, gold, platinum and palladium electrodes. This work will be discussed in more detail later. Electrodes were also modified in certain cases by electroplating onto an existing cermet electrode. Previous workers prepared the cermets so details given here have been taken from notes and reports of these workers (A.Ioannou and J.Gopaul). Details of platinum inks were taken from ESL data sheets. Ceramic used in cermets was 8 M% YSZ powder from Daichi. These cermets were exclusively used in all tests but the electrode materials investigation.

The platinum ink used as the basis for electrode pastes was ESL 5542 from Electro-Science Laboratories. This ink, it was found, contained 68% wt platinum and 32% wt of solvents (ESL 401) that burned out completely upon firing to 1000°C.

The platinum cermet M4 was calculated to contain:

59.7% wt Pt 6.7% wt YSZ. 33.5% wt solvent

Upon firing this equates to:

89.8% wt Pt 10.1% wt YSZ.

This in turn gives values of:

71.6 % vol Pt 28.4% vol YSZ.

Table 2.1

The platinum cermet M6 was calculated to contain:

63.6%wt Pt 4.5%wt YSZ. 31.8%wt solvent

Upon firing this equates to:

93.4%wt Pt 6.6%wt YSZ.

This in turn gives values of :

93.7%vol Pt 6.3%vol YSZ.

Table 2.2

Further to these basic platinum cermets, a series of metal electrode pastes were prepared for the electrode materials investigation. These were platinum, gold and silver pastes ESL 5542, ESL 8880-H and ESL 9990 respectively, all procured from Electro-Science Laboratories. These were virtually pure metals with only trace impurities with the exception of the ESL 8880-H which had a minuscule amount of cadmium (as supplied) to aid adhesion. In addition a palladium paste was made from Aldritch Palladium powder mixed with ESL 401 solvent using the triple roll mill to give a consistency similar to those of the ESL pastes. Metal cermets, layers and mixes were prepared from combinations of these pastes and a 93% wt YSZ ceramic pastes as used for the platinum cermets above. Preparation of electrode material investigation mixes and cermets was performed by hand mixing similar volumes of the respective ESL pastes for electrode mixes and by mixing of approximately 80% to 20% metal to YSZ paste for cermets by volume. These resulted in very approximate 50%-50% metal mixes and 80%-20% metal-cermets, no great accuracy was attempted here as paste quantities were kept small for financial reasons and time restrictions prevented accurate metal volume calculations being attempted. The full implications of this have not been established

2.1.3 Test gases

Test gases used were prepared by mixing bottled gases and air using the Brooks mass flow valves. Air where used unmixed (all 21% oxygen gases unless otherwise stated) was taken straight from the air tap, through mass flow valves. In other cases, where indicated, gases were dried by passing through a column of anhydrous calcium chloride prior to use. The exceptions were concentration modulation tests where the gases were a mixture of bottled oxygen and nitrogen. For mixes exceeding 21% oxygen, gases were prepared by mixing bottled oxygen and nitrogen (BOC white spot). Gases containing H_2O were prepared by bubbling gas mixtures through distilled water columns at controlled temperature. Further preparation details of H_2O containing mixtures are given in Appendix E3.1. Gases containing CO_2 were prepared by mixing bottled CO_2 with O_2 / N_2 mixtures, again using the mass flow valves. Appendix C1.1.1 contains details of gas mixing equipment.

2.1.4 Wires

Wires for electrical connections to the sensors and within the sensors were of semi-annealed thermocouple grade platinum of diameter 100 μm. This wire was sourced from Englehard. 20 mm of this wire was used for each electrode connection with a further 500 mm of 200 μm diameter per connection, sealed into the test-rig. All wires used in hot zones were platinum to ensure that measured EMFs are due to sensor effects and not thermoelectric in nature. Wire for R type thermocouples were the platinum described above along with a similar specification platinum 13% rhodium wire, although wire diameter varied from 40 to 200 μm dependant upon application. Wire for K type thermocouples were 100 μm diameter as supplied by Lab Facilities, cut to length and spot-welded at the joint. In each case the appropriate compensation cable was used for connection from test-rig to monitoring device.

2.2 Sensor construction

2.2.1 Amperometric sensors

The technique of amperometric sensor assembly used in this research differs from the traditional technique described in section 1.2.5.3. The technique used was novel and approaches the same design from a different angle. It was based upon a material developed by ICI for the manufacture of solid oxide fuel cells. In fuel cell applications large, thin, flat sheets of zirconia are required for reacting fuel and air across an electrolyte membrane. This material contained plasticisers and binders to allow sheet formation and machining

prior to firing to obtain a dense sheet of sintered material. It was found that by application of a suitable solvent, the plastics could be dissolved allowing components to be stuck together with the application of minimal pressing forces. Alford et al [25] suggested that processing with polymers disperses agglomerates to enhance mechanical properties and ease forming at a lower cost.

This concept was developed further by Tioxide to give a material, soluble in water and using 8 mol% yttria fully stabilised rather than the 3 mol% yttria partially stabilised material.

This new material contained polyvinyl alcohol as its plastic and around 82.5% volume of ceramic. 82.5% is the shrinkage that was observed upon firing to achieve a material approaching fully density. Shrinkage tests were conducted by measuring and weighing samples before and after firing. Measurements were taken by photography through a microscope of the samples and of a calibrated graticule for comparison. Shrinkage was found to be very consistent. This materials manufacture is suspected to involve a large shearing force such that agglomerates are broken up and coated in plastic thus aiding the sintering process although an alternative route is to introduce a chemical dispersant. Care had to be taken in handling and storing the material as older samples left in the atmosphere were seen to dry out and loose the ductility that kept it machinable. The firing cycle used in plastic burnout and ceramic sintering is given in the following ramp:

Ramp °C/min.	Temperature °C	Dwell time min.	Stage purpose
2	150	10	Drying
2	400	10	Polymer burnout
2	700	10	Ramp rate adjustment
1	1450	60	Full sintering
-1	0	End	Cooling

Table 2.3

Xie et al [99] investigated the advantages of microwave sintering of 8 mol% yttria stabilised zirconias. A 2.45 GHz microwave source using a 5 kW power supply and a 0.78×10^{-2} m wavelength with a resonant cavity was used to realise a density of 96% at 1300°C. Results were compared with conventional sintering and showed higher densities for sintering temperatures between 900 and 1400°C. At higher temperatures,

improvements were negligible. For both microwave and conventional firing, a high green density and the elimination of agglomerates were important.

Using the plastic-ceramic material described above, the sensor assembly procedure becomes far simpler:

1. Discs and rings of plastic-ceramic were cut from the sheet using simple steel punch and die tools.
2. Pt wires were sandwiched between two rings and a disc with the application of a small amount of water to assist adhesion in the order ring, wire, disc, wire, ring
3. Electrodes of Pt / YSZ cermet were applied by painting onto the electrolyte making contact to the wires.
4. Sandwiching a metallic wire former between the above components and remaining disc, again with a little moisture created a diffusion barrier.
5. The whole structure was now pressed using a force of 200 N/mm^2 to ensure a gas tight seal using either a purpose made clamp or pneumatic press.
6. The wire former was then withdrawn to leave a well-defined cylindrical pore.
7. The structure was finally fired using the slow ramp given above such that organic solvents and binders were burned out and full sintering occurs reducing porosity to a value close to zero.

The first amperometric sensors made were simple two electrode devices. These consisted of a single pump cell, internal cavity and a diffusion barrier created by the use of a 200 μm wire former. Upon firing the resultant barrier had a diameter of 165 μm and a length of 1650 μm.

For measuring oxygen levels in the ppm region it was necessary to increase diffusion hole S/L (Cross section area to Length) ratio to allow sufficient gaseous diffusion. Large diffusion barriers were created in two electrode amperometric sensors by drilling the green ceramic using miniature HSS drill bits. Sensors were constructed using drills of 0.7, 1.0, 1.5, 1.6, 1.8 and 2.0 mm diameters to created pores through the 0.52 mm thick green discs. Upon firing, a reduction of 17.5% was recorded in the linear dimensions, resulting in S/L ratios of 0.61, 1.24, 2.80, 3.18, 4.03 and 4.97 mm.

2.2.2 Pump-gauge

Pump-gauge devices were made in the same way as the four electrode amperometric sensors, but omitting the diffusion barrier step. There was a fear that since the internal volume was sealed, pressure would build up inside the device upon firing, especially as electrode and electrolyte solvents burned off. This pressure developed inside the device would be capable of pore creation or seal disruption as it was released. This problem appears not to have occurred, presumably due to the structure remaining porous until sintering occurred, at which point the solvents had long burnt out and only compressive pressures would be experienced as cooling occurs. Pressure gradients could be avoided by connection of the two platinum leads, thus allowing oxygen ion flow driven by the pressure gradient. This, however, was found to be unnecessary.

2.2.3 Half cell preparation

In order to assess the performance of the various electrode configurations and electrode / electrolyte impedance characteristics, it was necessary to eliminate the effects of diffusion barriers. This was done by the fabrication of half sensors. These cells comprised a single electrolyte disc with two rings to hold platinum wires and give a reproducible electrode area. Half-cells were made in the same manner as amperometric sensors but omitting steps 3, 4 and 6. Electrodes were applied, either prior to firing the ceramic or to the fired ceramic then cured by re-firing at a lower temperature of 700°C dependent upon the examination requirements.

2.2.4 Potentiometric cells

The green ceramic was an excellent material for making amperometric and pump-gauge devices. Attempts, however, to seal a disc of green ceramic to alumina tubes, to fabricate potentiometric sensors, all failed. Higuchi et al [100] fabricated sensors by hot pressing of green zirconia sheets to form a planar potentiometric sensor. The response of the sensor was found to be influenced by mounting direction but this minimised by careful design of protective cover. Advantages were realised in terms of reduction in cost and complexity with easy connection and fast response. Whilst a similar device would be manufacturable using the plastic-ceramic technique. This geometry however, does not easily lend itself to the analyses under development in this research. In order to fabricate sensors for potentiometric measurements it was decided to buy in closed end tubes from a commercial supplier. The tubes were made to specification: a flat closed end of outside diameter 9mm and inside diameter of 5 mm fabricated from 8 mol% YSZ, sintered to a density of no less

than 95%. These tubes were designed to fit the miniature furnace, that would allow the short gas feed paths necessary for step change and concentration modulation experiments whilst maintaining an easily interchangeable sensor. A sample cut from one of these tubes indicated a density of >99%. The supplier was Dynamic Ceramic. Tube wall thickness was determined by manufacturing requirements but also gave the possibility of examining the effects of electrolyte thickness by shaving down the end.

2.3 Impedance analysis

Impedance analysis work was performed to gather information of the electrode/electrolyte This analysis used a Solartron SL1260 frequency response analyser, described in Appendix C1.2.1, which allows impedance measurement with good noise rejection, sampling over multiple cycles and the subtraction of test-rig impedances via nulling sweeps. The instrument was computer controlled with real time plotting of measured data that could be stored in data files for post-measurement analysis and data presentation. Despite the advanced instrumentation, for accurate data, care had to be taken in test-rig design to provide good electrical shielding from electrical noise and induction. In addition, optimum test parameters had to be selected. The values selected were derived from the literature where other workers have suggested the use of the largest possible frequency range. The range of 30 MHz to 10 mHz was used, taking the upper end to the instrument capabilities and a lower end, such that electrode degradation would not significantly distort the results within the test time that would not become excessive. A minimum of three cycles is required for assessment at each frequency to be measured. This meant that the lower frequencies had a large effect on test time with a logarithmic spacing between frequencies used. The signal amplitude was chosen such that the non-linearities in the non-ohmic behaviour would be minimised whilst maintaining a good signal to noise ratio, a value of 10 mV was used. Bauerle [50] used a frequency range of 100 kHz to DC with a 13 mV amplitude. A small amplitude was selected so that currents were kept small to avoid electrode damage or joule heating occurring. In this work, all of the tests were performed applying a 10 mV sinewave and measuring the resultant current. With the exception of bias effect tests, no bias voltage was applied to the waveforms. The systems were analysed using a range of operation temperatures in the impedance test-rig detailed above and using oxygen / nitrogen atmospheres obtained by mixing air with nitrogen gases mixed through the flow valves previously described.

2.3.1 Electrode assessment

One main draw back of the plastic / ceramic sensor assembly technique was that it involved applying the internal electrodes prior to sintering the ceramic. Therefore the electrodes were subjected to temperatures of 1450°C. Exposure to high temperatures was suspected to be detrimental to obtaining a good electrode microstructure with sintering and grain growth reducing the essential three phase boundary length, affecting both sensor response times and operation temperatures. In order to assess these effects, a series of electrodes were examined, M4 and M6 cermets as well as Pt metal electrodes fired at 1450 and 1000°C to simulate exterior and interior sensor electrodes. Details of M4 and M6 cermets were presented in Section 2.1.2.

For electrode samples fired at 1450°C, samples of green ceramic were cut from one single green ceramic sheet to identical sizes, platinum wires attached and electrodes of M4, M6 cermets ant Pt paste applied. Two rings of green ceramic were used with each sample to give structural support for wires and to define a reproducible electrode area. For electrode samples fired at 1000°C, the discs and wires were pre-sintered before the application of electrode pastes which were then cured at 1000°C for 1 hour. The samples were then analysed using impedance spectroscopy at temperatures of 400, 450, 500 and 550°C in air. Before commencing these tests, nulling files were created for each test temperature to correct for the impedance of test-leads and test-rig connections. These files were then used at the relevant temperatures throughout these experiments. In each test, the temperature was allowed to stabilise for one hour before commencing the tests. Final macroscopic electrode areas were calculated at 20 mm^2 per electrode. These may be converted to approximate microscopic TPB length with reference to relevant scanning electron micrographs (see section 5.7). Details of the samples are given in Table 2.4. Cells were marked on one side by indentations, applied before sintering, so that a trace of electrode modifications could be recorded.

Sensor	Ceramic	Marked electrode			Un-Marked electrode			Fired Mass	
Number	Mass	Mass	Mix	Temp	Mass	Mix	Temp	Ceramic	Complete
FRA-5	0.3054	1.5	Mix4	1450	1.5	Mix4	1450	-	0.2644
FRA-6	0.3056	2.5	Mix6	1450	1.8	Mix6	1450	-	0.2666
FRA-7	0.3123	2.0	Mix4	1000	2.0	Mix4	1000	0.2696	0.2714
FRA-8	0.3152	1.4	Mix6	1000	2.3	Mix6	1000	0.2719	0.2740
FRA-9	0.3196	1.5	Mix4	1450	1.1	Mix4	1000	0.2769	0.2774

FRA-10	0.3143	2.5	5542	1450	4.0	5542	1450	-	0.2754
FRA-11	0.3123	1.2	5542	1000	1.4	5542	1000	0.2665	0.2683

Ceramic mass is the mass of ceramic and wires before addition of electrode paste and subsequent firing

Table 2.4 Electrode application mass measurements

After the analysis at each temperature had been completed, additional electrode layers were applied to samples FRA6, FRA7 and FRA8. These additional electrode layers were added to observe the effect of electrode thickness on electrode impedance. These modified cells were re-designated FRA6T, FRA7T and FRA8T respectively. Unfortunately, the painting electrode deposition process does not lend itself to precise electrode thickness control, however, a rough indication was gained by weighing the samples before and after firing, and allowing for solvent burn-out. Table 2.4 gives a comparison of electrode masses recorded at each stage. Following analysis of these modified cells, cell FRA6T had a platinum coating applied by electroplating and re-designated FRA6P. Electro-plating was achieved by immersing the cell in hydrogen chloroplatinic acid and applying a 100 mA DC current between the electrode and a platinum wire sacrificial cathode for 5 minutes for each electrode in turn. The sample was then rinsed with distilled water and dried before re-testing. The plating current was realised through voltage control to the voltage-current converter, and measured using the ITT multimeter. A stop clock was used for manual timing control. The plating was undertaken at room temperature and pressure with no chemical additives to aid metal deposition. During the plating, electrode darkening was observed with gas bubbles given off from each electrode accompanied by the distinctive smell of chlorine. No colour change in the liquid electrolyte was observed.

2.3.2 Time dependency

During these tests it was noticed that if a sweep was repeated under identical conditions, the electrode resistance grew slightly. This was analysed by repeating a single sweep at 700°C in air, 9 times over a period of 4 hours for both 1450 and 1000°C fired M4 electrode samples. Sweep times were recorded automatically by the internal PC clock during data acquisition and written into the impedance data files. These tests were performed in the impedance test-rig using nulling files to allow to test-rig impedance. The samples used in these analyses were samples FRA5 and FRA7 as detailed above before electrode thickening.

2.3.3 Oxygen concentration

For each cell tested in the electrode assessment section 2.3.1, and for each temperature, an impedance analysis was carried out using 21, 10 and 2% oxygen concentrations. These tests were performed to assess the concentration dependence in the percentage oxygen range. The atmospheres were produced by mixing air and nitrogen using mass flow valves previously described, and were allowed to flush through the test-rig for 10 min prior to testing. Again, nulling files were used although the files were created in air and used for all concentrations, this was not expected to influence results. The impedance analysis used a 10 mV sinewave from 30 MHz to 10 mHz with no bias potential.

2.3.4 Bias effects

To help relate the impedance data to actual sensor performance, results were taken with applied bias' to investigate the impedance behaviour of the three polarisations as pump potentials increased. Sweeps were taken with bias voltages of between -1.2 and 1.2 V at a temperature of 550°C in air. The same sample (a complete sensor) was also evaluated using a current / voltage sweep under the same conditions. The impedance analysis used the same 10 mV sinewave and a frequency of 30 MHz to 100 mHz as previous tests and performed in the impedance test-rig. The 550°C Nulling file was used. The current / voltage sweep was also carried out in the impedance test-rig and performed using the LabView / DAQ system to give a potential sweep from 0 to 2V using 0.1V increments and a 30s stabilisation period. From impedance results, resistance contributions of grain, grain boundary and electrode interface phenomena could be compared with the total cell resistance deduced from the slope of the I / V curve.

2.3.5 Thick film sensor

To provide comparative information, an impedance analysis was carried out on a zirconia thick-film amperometric sensor (also developed within the university and kindly supplied by J.Gopaul). This sensor proved an interesting comparison as it used an electrolyte (8 mol% YSZ) layer of 40-50 μm thickness compared to almost 1000 μm thickness of the green sheet devices. The sensor had a similar electrode area employing similar platinum cermet electrodes. The electrodes differed in the deposition process and high temperature firing history. In addition the thick film sensor structure was supported upon a dense, 99.8% purity, alumina substrate. Further details concerning fabrication and characteristics are given in Gopaul et al [52, 101].

Impedance sweeps were taken in air at temperatures between 400 and 550°C in the impedance test-rig. The analysis parameters were a 30 MHz to 10 mHz frequency sweep, 10 mV sweep amplitude with no bias applied but using the appropriate nulling files.

To back-up these tests a series of current voltage sweeps were also employed. These were also performed in the impedance test-rig using the LabView / DAQ system to record current / voltage data for pump potentials of 0 to 3 V in 0.1 V steps. The experiments were performed at temperatures from 650 to 900°C in air passed through a column of $CaCl_2$ to remove moisture.

2.3.6 Firing temperature

In Appendix E1.1.6 current / voltage sweeps were used to examine the effects of sintering temperature on the performance of electrode / electrolyte / electrode cells. In this section we detail an experiment on the same cells performed using frequency response analysis. The final year undergraduate O.Pampam whose report can be consulted for further details performed this work. The cells, described in Appendix E1.1.6, were examined in the impedance test-rig using temperatures of 400 to 550°C in atmospheric air. Nulling files were generated for each temperature, prior to beginning the tests, and used throughout the testing. Test parameters were frequency range of 30 MHz to 0.1 Hz, 10 mV applied signal, no applied bias. The impedance sweeps were all performed in atmospheric air, with a temperature stabilisation time of >30 minutes. The relatively high minimum frequency employed was selected so as to keep testing times short so that a large number of analyses could be performed. This was at the expense of electrode performance data. The Z60W and ZPlot impedance software was used throughout to control and monitor the experiments

In addition to the frequency response work, density measurements, hardness measurements, measurements of volumetric change upon sintering were recorded along with a visual examination by scanning electron microscope (see section 2.7.2) details of SEM sample preparation are given in section 2.7.1. The SEM results are presented in Appendix F1.8. Density measurements were taken by Pyknometer bottle, using de-gassified, temperature controlled, distilled water. Hardness measurements were performed using a Vickers hardness tester with a 10 Kg load. Dimensional measurements employed both micrometer and using the S.E.M measurement facility. Steil et al [102] also used scanning electron microscopy to investigate the densification of YSZ with sintering

temperature using both polished and fractured edges for examinations. Sintering control was attempted by Dietz [86] to fabricate sensors with Knudsen diffusion characteristics. This attempt was met with some success by inclusion of alumina into the zirconia to inhibit sintering. The sensors produced showed a complex diffusion character in between that of Bulk and Knudsen mechanisms. For this reason the technique was not recommended.

2.3.7 Metals, cermets, layers and mixes

In order to gain an insight as to which electrode materials / combinations were worthy of further assessment using the various response rate techniques described, an extensive preliminary testing regime was employed. Impedance spectroscopy was selected as the most widely recognised and understood technique. It was decided that impedance spectroscopy would be performed on a variety of test samples carrying simple metal electrodes, cermet electrodes, intimate metal mixes and layered metal electrodes. The most appropriate electrodes could then be discerned and used in further testing.

The first step was to produce the electrode pastes from which the electrodes were to be formed. Electrode materials acquired included ESL 9990 silver paste, ESL 8880-H gold paste, ESL 5542 platinum paste, 8 mol% YSZ paste, ESL 401 vehicle, Aldritch silver powder and Aldritch palladium powder. From these starting materials a series of pastes were produced.

Simple metal electrode pastes of ESL 9990, 8880-H and 5542 were used as provided. Aldritch silver and palladium pastes were prepared by mixing with 401 vehicle to get pastes with consistency similar to the ESL pastes. Samples were prepared by weighing an amount of powder into the glass sample bottle adding solvent drop by drop until a suitable paste was formed. The produced pastes were then roll milled for five minutes using a triple roll mill.

Mixing similar volumes of ESL (platinum, silver and gold) and Aldritch (palladium) pastes, with smaller volumes of the YSZ paste (see section 2.1.2) gave the cermet pastes. The aim was to achieve pastes of 20% volume ceramic. In this manner, cermets of silver, gold, platinum and palladium of similar consistency were produced.

Samples of the simple metal pastes were also mixed together to produce binary metal mixes of approximate 50 / 50 by volume. Samples were produced of Ag/Au, Ag/Pt and Au/Pt.

For electrochemical tests, zirconia half-cells were prepared from the sheet of Keele plastic / ceramic with platinum connection wires to form well-defined electrolyte test cells. These were fired (without electrodes) at 1450°C using the previously defined ceramic-sintering ramp. Electrodes were then applied and cured at 850°C. The electrode curing temperature of 850°C was selected to allow a similar preparation for all electrodes whilst remaining short of the melting temperature of silver at 960°C.

In addition small samples were prepared from the ceramic cut-outs left after the production of the plastic / ceramic rings. These were also fired along side test cells at 1450°C to form small ceramic discs. These discs were used for density measurements (by Pyknometer) and for paste solvent content evaluation by measuring residual mass after firing. In addition these samples also provided suitable specimens for optical and scanning electron microscope examination (see Appendix F1.8).

Details of paste assessment are given in the Table 2.5. Electrode macroscopic area was measured at 12.6 mm^2. SEM Examination of these samples allowed an estimation of electrode TPB length to be achieved (see section 5.7).

ID	Paste	% Solid mass	% Solvent mass
P1	Old 5542 + solvent	54.55	45.45
P2	Old 8880 + solvent	78.57	21.43
P3	Aldritch Ag + solvent	69.23	30.77
P4	Aldritch Pd + solvent	40.74	59.26
P5	8880-H	89.83	10.17
P6	9990	78.16	21.84
P7	9990 + solvent	44.00	56.00
P8	8880 + solvent	75.00	25.00
P9	Pd + solvent	33.33	66.67
P7'	9990 + solvent	64.29	35.71
P8'	8880 + solvent	80.00	20.00
P7"	9990 + solvent	63.33	36.67
P8"	8880 + solvent	83.33	16.67

P9	9990 + solvent	75.00	25.00
P10	P8"cermet	85.96	14.04
P11	P9 cermet	67.06	32.94
P12	P4 cermet	78.69	21.31
P13	P1 cermet	60.61	39.39
P14	P1 + P6 + solvent	70.97	29.03
P15	P1 + P5 + solvent	78.13	21.88
P16	P5 + P6 + solvent	75.00	25.00

Table 2.5 Electrode paste measurements

Electrochemical cells were placed into the impedance test-rig where they were tested at temperatures from 400 to 600°C in air. The test regime employed 30 MHz to 10 mHz frequencies at 10 mV amplitude with no bias voltage. These experiments were carried out in the impedance test-rig, allowing a temperature stabilisation time of 1 hour. An atmospheric air test environment was used, reducing test complexity, temperatures were monitored by K and R type thermocouples to ±1°C. Impedance spectra were applied and monitored using the Frequency Response Analyser (SL1260) under computer control. Nulling files were not employed as these have negligible effect at the low frequencies this work was concerned with primarily. Whilst attention here focussed on the low frequency electrode polarisations, the high frequency polarisations were recorded as they added only a small amount to the total testing time. Results are reported in section 5.2.

2.3.8 Electrode material

Following the results of the preliminary electrode assessments, electrode combinations were selected for further analysis. The electrodes selected were the simple metals Au, Ag, Pd, Pt and binary mixes of Pt/Ag, Pt/Au and Au/Ag. These were applied as pastes (as described in section 2.3.7) using a small paintbrush to the inner and outer end faces of the potentiometric cells described in section 2.1.1. Internal electrode application was aided by the use of a long thin paintbrush with a plastic outer shield to prevent electrode application to the inner tube walls. Again electrodes were cured by firing for 10 minutes at 850°C. No additional preparations of electrolyte surfaces were undertaken prior to electrode application

The cells were then incorporated into the response rate rig in frequency response configuration (as described in Appendix C 1.3.5). Frequency response was performed using 30 MHz to 10 mHz frequencies with 10 mV amplitude to the cells at temperatures

from 400 to 600°C. For these tests both inner and outer electrodes were maintained in atmospheric air at atmospheric pressure. No bias voltages or nulling files were used. Again, impedance spectra were applied, monitored and recorded using the SL1260 under computer control. Macroscopic electrode areas were measured at 12.5 mm^2 and 50.2 mm^2 for measurement and reference electrodes respectively. Results are reported in section 5.3

2.3.9 Platinisation

Frequency response analysis was used to investigate the improvements in low temperature performance achieved when platinum cermet electrodes were electroplated. These were in addition to the experiments of amperometric sensors (Appendix E1.4.7) and performed as part of the electrode assessment (section 2.3.1). In this section we report the effects of sinusoidally electroplating a sensor half-cell, altering the plating current amplitude and application time.

The technique of electro-plating the electrodes of an amperometric sensor is discussed elsewhere (Appendix E1.4.7) and the results examined using current / voltage sweeps. Here we report frequency response analysis of the same device. The same device as used in the bias assessment (section 2.3.4) was employed, although those tests were performed prior to electroplating. In this experiment frequency response analysis was used to analyse sensor performance before and after the electro-plating took place. The analysis was carried out in the impedance test-rig at temperatures from 400 to 900°C in air. The sweep frequency used was again 30 MHz to 10 mHz with a 10 mV sinewave. No bias voltages were applied and nulling files were used. Impedance spectra were monitored, controlled and recorded using the SL1260 under computer control. Results are reported in section 5.1.

Following the electrode materials assessment in which various electrode materials were assessed using each of the response rate techniques reported in this work, a further test series was performed to investigate platinum metal, cermet and plated electrodes using the same procedures. This entailed removal of the platinum metal electrodes using carborundum paper. Then platinum cermet electrodes were applied in paste form and fired at 850°C for 10 minutes. The sensor was then analysed according to the same regime as for electrode materials detailed in section 2.3.8. This analysis was followed by assessment using step changes, pressure modulations, concentration modulations and current/voltage sweeps. The cermet electrodes were then electroplated using hydrogen chloroplatinic acid and a DC current of 40 mA for 10 minutes for each electrode. Following the plating, the

electrodes were rinsed with distilled water and dried before the tests being re-performed as before. Note that all of these platinum electrode tests used the same electrolyte cell.

2.3.10 Data analysis

Data files stored by the impedance ZPlot software includes information on measurement frequency, signal amplitude, applied bias, measurement time, real and complex impedance components (Z' and Z"), general diffusion (GD) and error status for each data point recorded. This data may be recalled, either by the ZView included graphing facility or, as a text file, into most computer software applications. The impedance graphing facility allows the data to be viewed as a number graphs, calculations to be made of the R and C components, semi-circle depression angles and allows simulation / fitting routines to be performed. In this work however, the technique was used as a simple comparative technique, so measurements of grain, grain boundary and electrode interface resistance were taken and analysed as Arrhenius diagrams. Resistances were obtained by semi-circle fitting to the complex impedance diagrams produced. Capacitive data were recorded in some of the tests, these values however did not vary greatly between tests and so were not of prime interest.

As previously mentioned the measurement is handled by a Windows based software package shown in (fig. 2.1) with on-line results display (fig. 2.2). This demonstrates the three graphical formats for data presentation Bode plot, 3d plot and complex plot. Complex plane plots are the most commonly used graphical format, providing an easily recognised (semi-circle) output. Bode plots are well suited to systems where several time constants are present as their logarithmic scales enable all data to be viewed on a single graph. The 3d plots (real impedance versus complex impedance versus frequency) allow identification of erroneous data points that may not be apparent in the 2d plotting techniques. In this work Complex plane plots were used primarily for data interpretation, with 3d plots for visual identification of erroneous data points. In addition, for comparison of several data sets of temperature, oxygen concentration, and electrode, grain and grain boundary components, the resistance values obtained from complex diagrams were plotted as Arrhenius diagrams (log R versus 1000/Tk). These generally give a straight-line plot over several orders of magnitude for thermally activated processes.

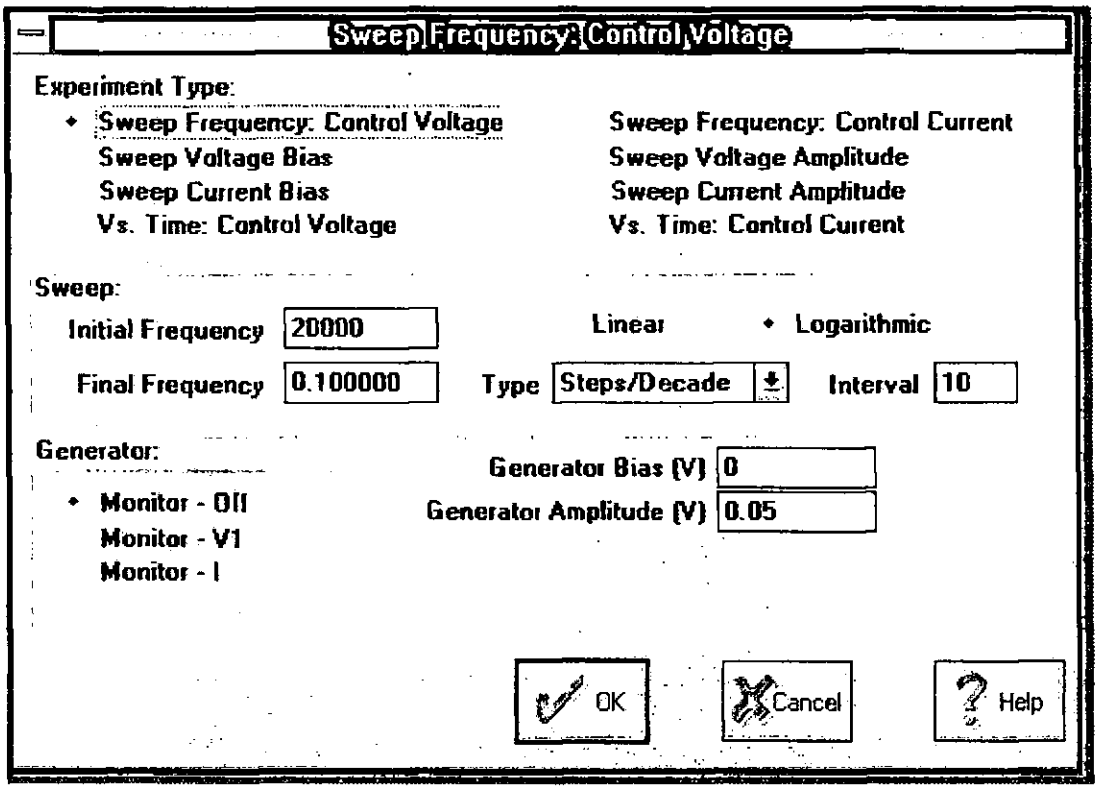

Figure 2.1 Windows based instrument control package

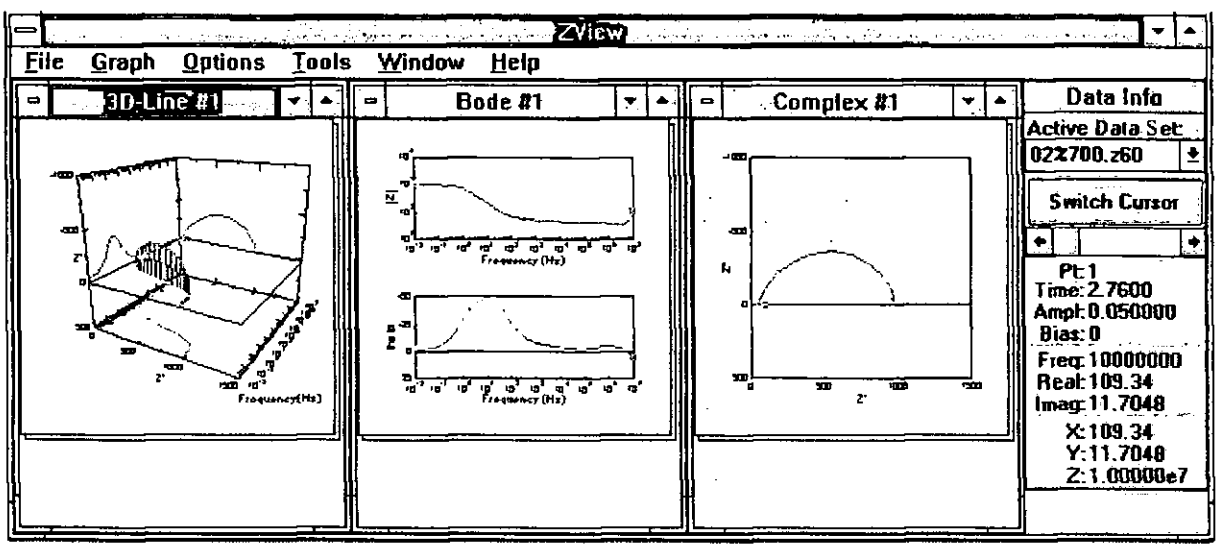

Figure 2.2 Windows based results display and analysis package

2.4 Step concentration technique

2.4.1 Rig verification

We now move on to describe the methods of operation and verification of the step-concentration response-rate analysis technique. Having assembled the miniature furnace test-rig in step change configuration, as described in Appendix C1.3.5, the next step was to evaluate test-rig performance. Control of the gas step was achieved by interfacing two fast acting solenoid valves to a PC running a purpose written LabView virtual instrument.

Measurement and recording of sensor response was taken care of by the same virtual instrument but with the sensor output amplified ×100 to give a high signal to noise ratio without exceeding the input range of the DAQ card. The amplification was achieved using a home-made solid-state electrical signal amplifier that had a sufficiently fast response and broad bandwidth to have no unwanted effects on the signals being amplified. Test-rig performance evaluation was undertaken by operating a potentiometric cell with platinum cermet electrodes at 700°C. The temperature was selected as response is known to be sufficiently rapid so that delays would be attributable to the test-rig apparatus rather than sensor response. The tests were performed by applying a concentration step and measuring corresponding the device response. Verification tests were performed examining the effects of flow rate and step size variation.

2.4.1.1 Flow variation

The effects of gas flow rate were examined by feeding a gas concentration step from 21 to 2% oxygen in nitrogen to the sensor at 700°C. Gas mixing and flow rate of both gas mixes were controlled by a set of four separate mass flow valves. By maintaining equal flow rates for both gas mixes any change in sensor output can be attributed to the gas concentration and not gas flow change, pressure change or electrode cooling effects. Thermal properties of oxygen and nitrogen are similar which helps to minimise the possible disturbances of changing gas compositions. Measurements were taken of gas steps for 10 s prior to the step, 15 s during the step and for 10 s after reversing the step. These timings were variables in the virtual instrument as was the rate of data collection. Gas flows rates of 20, 40, 60, 80 and 100 ml/min were examined. Gas sources were compressed air and bottled nitrogen, the reference electrode was maintained in atmospheric air at atmospheric pressure. In order to ensure computer timings, the solenoid valve voltage was computer controlled and recorded along with sensor EMF output.

2.4.1.2 Step amplitude

The next evaluation test was to vary the step size by variation of secondary gas concentration variation. Steps from 21% to 0-21% were used to observe the affects on the sensor again operated at 700°C with an atmospheric air reference. In these tests the flow rate for both gas mixtures was maintained at 100 ml/min following on from the results of flow rate variation. The procedure and measurements were otherwise identical to those for flow rate examination. In both step amplitude and flow rate variations, an offset was seen even where no partial pressure differences existed between measurement and reference

gases. This was traced to small temperature differentials between the measurement and referenee electrodes. The effects were greatly increased by the signal amplification (i.e. ×100) and were very difficult to eliminate, partially due to the small size of the furnaee hot zone, measured at 8 mm. The furnace hot-zone temperature profile was recorded by keeping the controlling thermoeouple stationary whilst reeording temperatures at discrete intervals along the furnaee length with a second thermocouple. The temperature differentials in all response rate tests were monitored by K type thermoeouples near each electrode and maintained to a differential of <1°C.

2.4.2 Technique evaluation

The actual response rate tests were performed using a 21% to 2% oxygen in nitrogen gas concentration step with flow rate set at 100 ml/min for both gas mixes and using an atmospheric air referenee. These tests were now repeated at temperatures varying from 600 to 400°C, where sensor response begins to slow. These tests used a dynamie ceramie YSZ sensor with platinum / YSZ, M4 cermet electrodes fired at 1000°C. Data were recorded for 500 s following the step both from 21 to 2% and 2 to 21% to check for step symmetry. Data points were recorded every 2 seconds to keep data time-scales eomparable this did, however, lead to insufficient data being eollected at lower temperatures. Solenoid valve controlling voltage was also recorded as a reference for each step. Measurements were recorded using the virtual instrument created for these tests.

2.4.3 Amperometric sensors

In addition to the experiments on potentiometrie sensors, the step ehange technique was applied to amperometric sensors. These tests could not be performed with sensors installed in the sensor test-rig as the gas volume of this was large enough to diminish the rapid ehange in gas eoncentrations generated. For this reason, tests were performed in the small sensor test cell detailed in section Appendix C1.3.6. Instrumentation involved the LabView / DAQ system to apply pump potentials as well as to monitor sensor currents, a 7150 multimeter was employed to monitor sensor temperature and a current controlled power supply used to maintain heater eurrents.

Prior to carrying out the step change experiments, the sensor was characterised, both in the large sensor test-rig and small test-eell to ensure that true readings were being taken and to determine suitable testing parameters. Small-eell testing was performed using temperatures from 450 to 700°C, 21 to 2.5% oxygen and pump potentials of 0 to 2 V.

Results were compared with similar data acquired from the same sensor in the large sensor test-rig. These results are reported in section 4.2.3.

The amperometric sensor response rate test arrangement involved connecting the solenoid valves directly to the small test cell to minimise gas volumes involved. Solenoid valves were switched by hand to allow the fastest possible data collection rates. Gas concentration steps were of air to 13% oxygen, both flowing at 100 ml/min through mass flow valves. Current / voltage characterisation indicated that the sensor would work in the selected region of 21 to 13% oxygen only at temperatures above 550°C. A constant pump potential of 1.2 V was used to maintain operation in the limiting current region. Separate tests were employed for both positive and negative going steps, with limiting currents recorded for 50 s following the change, acquired at 100 ms intervals for each temperature and in each direction. Results of these tests are reported in section 4.2.3.

A series of tests were performed into controlling factors of the test-rig set-up. Factors examined were: test chamber volume, applied pump voltage, length of gas feed pipe, step direction, step magnitude, gas feed flow rate and sensor temperature. As these tests involved such a large number of variables, a set of standard settings were employed for each and experiments altered one of these at a time. In these experiments the solenoid valves were automatically switched to obtain a good comparison between tests. Switching was performed 2 s after the start of the data recording. In these experiments, the sensor pump potentials were set at 1.2 V and controlled using purpose written Virtual Instruments that also recorded pump currents. The variables examined are detailed below with standards indicated by bold typeface:

Chamber volume	30, **24**	mm^3
Applied pump voltage	1.0, **1.2**, 1.6, 2.0	V
Feed pipe length	**25**, 50, 100, 200, 400	mm
Step direction	**High to Low**, Low to High	$\%O_2$
Temperature	550, **600**, 650, 700	°C
Step magnitude	From 21 to 5, 10, **13**, 15	$\%O_2$
Gas flow rate	25, 50, **100**, 150	ml/min

Table 2.6

The variation in gas feed pipe length was achieved by insertion of a length of flexible plastic gas tube (Tygon 3640) which was sequentially cut to shorter lengths for each experiment. This had dual effects of increasing effective test-chamber volume and of increasing gas leakage into/out of the system. Sensor temperature control was realised through DC current control to the two thick-film heaters on either side of the sensor. Temperatures were recorded via 7150 Multimeter and displayed as temperatures on the controlling PC monitor. Gas step sizes were controlled by adjustment of ratio of nitrogen and oxygen gas flow rates via the mass flow valve controller. Gas flow rates were controlled by the same method but keeping set ratios whilst altering flow rates of both gases. Results and discussion of these analyses can be found in section 4.2.3.

2.4.4 Electrode materials

The concentration step technique was utilised alongside other techniques in the study of electrode materials. This formed part of the test series detailed in section 2.3.8, investigating the effects of electrode material on sensor response rates. These used the same potentiometric cells as previous tests with simple metal and binary mixed metal electrodes. The experimental set-up was as detailed above with a few modifications. Firstly a concentration step was generated, switching between 25 and 17% oxygen. Rather than 21-2% used previously. This level was used to bring the step change into line with concentration modulation experiments in terms of magnitude whilst also generating the step either side of the reference gas concentration. By stepping either side of the reference, non linearities in the system were minimised, keeping generated EMFs small and reducing errors by keeping the measurement and reference gases of similar composition. The use of gases exceeding 21% oxygen necessitated using bottled oxygen and nitrogen in place of air and nitrogen, this had the added benefit of reducing atmospheric contaminants such as CO_2 and H_2O. Another alteration to the system previously described (section 2.4.2) was the manual switching of solenoid valves. This change was implicated to reduce system complexity and increase data sampling rates, but at the expense of the ease of data analysis. This alteration involved a simplification of measurement software, the virtual instrument could be simplified by removing the complex valve switching to improve measurement speed. Cells examined in these analyses included: the simple metals Au, Ag, Pd, Pt and the binary metal mixes of Pt/Ag, Pt/Au and Au/Ag. These cells were tested between 400 and 600°C, going from high to low and low to high gas concentrations at a total flow rate of 100 ml/min. Data were recorded until a stabilisation in readings was

attained with data timings dependent upon test-runs to get approximately 500 points before stabilisation. Results of these tests are presented along with discussion in section 5.4.

2.4.5 Platinisation

Continuing the technique evaluation work of section 2.4.2, The cell used had its platinum cermet electrodes electroplated to assess the difference that this would make to the cell response rate. The plating is described in section 2.5.9 (the same potentiometric cell was used for both of these analyses). The experiments were identical to those carried out in section 2.4.2, using the same 21 to 2% step but at temperatures of 250 to 600°C. In addition, to ensure correct operation at low temperature, the steps were performed from 21 to 15, 10, 5, 2, 1 and 0% oxygen These were all performed at a temperature of 400°C to ensure that response rates were not concentration dependent and that the Nernst equation was still obeyed. After these conformation tests, the electro-plated electrodes were annealed in an attempt to destroy the improvements in cell response achieved. This was performed by firing the cell at 1000°C for 10 minutes then repeating the concentration steps for temperatures between 400 and 700°C. The results of these may be found in section 5.1.

In addition to the electrode materials assessments described in section 2.4.4, the platinum electrode sample was re-examined with its electrodes replaced with platinum cermet electrodes and then again after these were electroplated with platinum. This was to provide comparative information for the metal / cermet / electro-plating for each response technique under similar conditions. Electrode applications are detailed in section 2.3.9. The step concentration experiments were performed as with the electrode materials experiments detailed in section 2.4.4. Results of these tests may be found in section 5.1.

2.4.6 Data analysis

In the first set of step change experiments, using the 21 to 2% oxygen step, The data recorded were analysed automatically by spreadsheet. A macro was written which automatically normalised the data, removing any residual offset caused by small temperature differentials and returning the time at which data reached a value 70% of Nernst voltage. This procedure had a number of problems, stemming from a certain degree of noise in the data the realisation of voltages greater than Nernst predictions (particularly at low temperature) and stable voltages not being attained within the sampling period. In these cases the data were sorted by hand to eliminate noisy data and estimate a final EMF.

For the electrode materials investigation the above analysis was not rigorous enough, as well as taking a lot of data sifting time. The technique was improved, using an alternative spreadsheet macro to aid analysis rather than complete it. This macro took an average value for initial and final stabilised EMFs to check agreement with Nernst potentials. These were then used to normalise the data to give a step from 0 to 1. This removed any small offsets obtained and allowed easy comparison between various data sets. Next the data was put through a five point moving average to reduce noise. Finally the times were recorded by hand for the EMFs to reach 10, 20, 30, 40, 50, 60, 70, 80 and 90% of the final - initial values. These could then be plotted versus percentage reading for each temperature for each electrode to give a simple output for comparison. Data for various electrode performances were compared using Arrhenius type diagrams, plotting log (s) versus 1000/Tk. Results and discussions are presented in section 3.2.

2.5 Concentration modulation technique

2.5.1 Rig verification

The next response rate method to be developed was that of Concentration Modulation. This technique combined the principles of step change in gas concentration with those of frequency response analysis. Thus a sinusoidal modulation of gas concentration was applied over a range of frequencies and temperatures, to a range of sensor cells. Again the first stage of testing the new technique was verification, tests of flow valve modulation parameters were assessed. This was simply achieved by applying various sinusoid signals to the flow valve controller whilst monitoring the return flow valve position signal (see section 3.3). At this stage the gas flows were not fed to an active sensor. For each parameter: frequency, modulation amplitude, oxygen offset and valve model, performance was investigated individually to determine the limitation reached in each case. Modulation frequency was varied from 2 to 0.2 Hz, modulation amplitude varied from 1 to 20% of valve opening, Offset was varied from 5% to 80% of valve opening, and valve types of type E and type Tr were examined. Results from sensors using flow valves have previously shown good linearity in previous sensor tests as well as a number of calibrations provided they were not operated at openings below of a few percent. This has given a good confidence in their output and capabilities. In this verification sinewaves were applied to the flow valve controller and valve output signal recorded using a purpose written virtual instrument which allowed the desired parameter to be typed in and real time output displayed on-screen and stored as a CSV file. In addition, computer output waves were

double checked using the oscilloscope to ensure that the DAQ system was operating correctly. As with step change verification, the effects of a number of variables had to be assessed. This was again realised by comparing the effects of altering one variable at a time at a time whilst keeping others at standard settings. Standard settings were; Frequency = 0.4Hz , Modulation amplitude = 4%, Oxygen bias = 21%, Valve type = E.

Flow rates were maintained around 100 ml/min. Results of these verifications may be found in section 3.3.

2.5.3 Technique evaluation

The measurement described above and analysis techniques described below were used to assess the performance of platinum cermet electrode potentiometric sensors over a range of temperatures and at a series of modulation frequencies. The gas modulation apparatus was connected to the response rate-rig, set-up in the concentration modulation configuration (Appendix C1.3.5). This entailed the use of two 100 ml/min mass flow valves fed from bottled sources of oxygen and nitrogen. The sensor was operated at temperatures of 500 to 800°C using modulations of 0.16 to 0.016 Hz, sinusoidally modulating ±4% oxygen around 21% using an air reference. The modulated valve was a type E controlling the flow of bottled oxygen whilst nitrogen gas flow rate was a constant 79.1 ml/min through a type Tr valve. The LabView Virtual Instrument was used to store 200 data points for each test at a sample rate of up to 20 Hz dependent upon modulation frequency. Modulations were left to stabilise before commencing data storage. Results are presented in section 3.3 by plotting the phase difference between gas modulation and sensor response and sensor output EMF amplitude against frequency and temperature parameters.

2.5.2 Analysis procedures

The next verification tests were for data analysis procedures. Recorded data in the tests detailed above includes valve controller input signal, flow valve output signal, sensor EMF and time base. Data analysis was performed by importing data produced into a spreadsheet and plotting, along side a calculated sinewave, against time to give matching sine traces. The calculated sinewave was based upon the time base of the actual data, and could be adjusted for phase, amplitude, offset and frequency to match the measured data parameters. Data were also plotted against the calculated sine wave to give a Lissajous figure. A Lissajous figure allows accurate comparisons of phase between calculated and

measured signals. If the signals are in phase, and frequencies match the resultant plot is an inclined line at 45°. An ellipse would be produced if a phase difference were present, a circle is obtained if the phase difference equals 90° and a line of -45° gradient if it were 180° phase difference. Amplitudes and offsets are shown as intercept and gradient variations respectively. Frequency differences result in complex patterns rather than simple lines and ellipse'. Using these two plots, values were obtained for the parameters that most closely described the sinusoidal gas input as well as values for the sensor pseudo-sinewave output. These values could then be plotted to indicate the alteration in trends of the describing parameters with change in electrode activity.

2.5.4 Amperometric sensors

The concentration modulation technique was also applied to an amperometric sensor. This was operated in the small sensor test-cell described in section Appendix C1.3.6 and section 2.4.3. Gases were fed directly into the small sensor test-cell to minimise test-chamber volumes and test apparatus delays. Flow valves used were again two 100ml/min valves fed by bottled oxygen and nitrogen sources. The oxygen flow rate was the modulated source, using an E type valve, nitrogen was fed at a constant rate through a Tr type valve. The sensor was operated at temperatures from 550 to 700°C using a modulation of ±4% around 21% oxygen at frequencies 0.016 to 0.16 Hz. Particular care was taken in slow temperature ramping to ensure that the sensor was not subjected to thermal shocks. A modified version of the concentration modulation virtual instrument was used to apply a pump potential of 1.2 V, maintain flow valve modulations and measured sensor current. Sensor temperature was monitored by R type thermocouple and 7150 multimeter with thick film heaters powered by DC power supply. The sensor used was that used in step change tests (section 2.4.3), and current / voltage curves (Appendix E 1.1). These previous tests indicated that the sensor could be operated in this region giving complete data if a pump potential of 1.1 V was exceeded. Sensor limiting current was analysed using the data analysis technique of potentiometric cells, using Lissajous figures to determine input and output modulation parameters. Results of these examinations are presented in section 4.2.4.

2.5.5 Electrode materials

The concentration modulation technique was also applied to potentiometric cells with various electrode single metals and binary mixes. These cells have previously been described in section 2.1.2 and used in the electrode assessments of sections 2.3.7, 2.3.8 and 2.4.4. Modulations of 21% ±4% oxygen were applied to each electrode cell at frequencies

of 0.32 to 0.039 Hz, and temperatures ranging from 400 to 600°C. Gases were mixed by a steady flow of bottled nitrogen at 100 ml/min Tr type valve whilst bottled oxygen was modulated through an E type flow valve. These tests were performed in the response rate test-rig in the concentration modulation configuration. Sensor output was amplified ×100 to increase the signal to noise ratio and data was recorded using the purpose written virtual instrument. Modulation analysis was carried out using the Lissajous diagram and sinewave comparison techniques detailed in section 2.5.2. Comparisons of electrode materials phase lags and amplitudes were compared over the range of temperatures and frequencies examined. Electrodes examined were Pt, Ag, Au, Pd, Pt/Ag, Pt/Au and Ag/Au on 8 mol% YSZ potentiometric tubes. Results and discussion are presented in section 5.5.

2.5.6 Platinisation

Concentration modulation analyses were also used in the analysis of improvements attained by electroplating the platinum cermet electrodes of a potentiometric cell. The cell used for technique evaluation had electrodes subject to electroplating using hydrogen chloroplatinic acid electrolyte and a platinum wire cathode using a 30 mA sinusoidal current for 10 minutes on each electrode. Sinusoidal currents were generated using a function generator coupled to the voltage to current converter. Following the electroplating, the electrodes were washed and dried before the analysis was re-performed. Concentration modulations were applied using 21%, ±4% oxygen gas modulations at 0.16 to 0.016 Hz at temperatures from 400 to 600°C. Instrumentation used were the LabView / DAQ, virtual instrumentation and analysis carried out as detailed in section 2.5.2, in the response-rate test-rig in the concentration modulation configuration. Results of these tests are reported in section 5.1.

In addition to the electrode materials assessments described in section 2.5.5, the metal platinum electrode sample was re-examined with its electrodes replaced with platinum cermet electrodes and then again after these were electroplated with platinum. This was to provide comparative information for the metal / cermet / electro-plating for each response technique under similar conditions. Electrode applications are detailed in section 2.3.9. The step concentration experiments were performed as with the electrode materials experiments detailed in section 2.5.5. Results of these experiments are reported in section 5.1.

2.6 Pressure modulation technique

The final sensor response rate technique employed was that of Pressure Modulation. The pressure modulation technique involves sending sinusoidal pressure waves to the measuring electrode and measuring the ability of the sensor to track the modulations. This technique is closely related to that of Concentration Modulation, but the partial pressures are changed by a barometric pressure change rather than altering the relevant concentration levels. The pressure modulations were produced by a DC electric motor connected to a cylinder / piston arrangement through a gearbox, cam, and connecting rod. The component parts to this rig were manufactured in the University workshops and designed using AutoCAD solid modelling software by the author. Details of fabricated parts are described in Appendix C1.3.5. The solid model diagram of the fully assembled test-rig is given in Appendix C figure C19. Two gearboxes were used to provide a wider range of frequencies than achievable by controlling motor voltage alone. The pressure waves were then sent through an expansion chamber containing a flexible membrane. This had the dual function of reducing the pressure wave magnitude and preventing contaminants, e.g. oil, from affecting cell output by separation of "dirty" and "clean" atmospheres by the membrane. The test and reference atmospheres in these experiments were atmospheric air, although a simple modification of shut off valves would enable the use of alternative atmospheres. In the case of potentiometric cells, the pressure wave was then passed into the response-rate test-rig (in pressure modulation configuration) through the inside of the sensor to the electrode face. Pressure wave magnitude could be controlled, either by alteration of the cam position, or volume changes in the expansion chamber. The membrane was cut from a thin plastic sheet and sealed by compression between viton o-rings and expansion chamber face. The whole gas system was sealed but pressure could easily be released by disconnecting feed pipes.

2.6.1 Rig verification

The response rate rig in pressure modulation configuration was used for further assessment of sensor response rates. This rig (described in Appendix C1.3.5) was connected to the Tektronic oscilloscope for data capture. The dual oscilloscope channels were used for recording sensor EMF and the output of the magnetic pickup. Whilst this instrument gave good measurement capabilities, it did not lend itself to detailed rig verification. To overcome this the oscilloscope was replaced with the LabView / DAQ system (for test-rig verification only) running a modified version of the concentration modulation virtual instrument. This allowed sensor output capture and detailed analysis. The pressure

modulation apparatus was connected to the response rate test-rig (in pressure modulation configuration) by reinforced flexible plastic tubing (Tygon) and jubilee clips.

The rig verification was performed using a potentiometric cell with platinum cermet electrodes. This was operated at 700°C (where response can be considered fast) with an air reference. Tests were performed using various modulation amplitudes, modulation frequencies and also using steady state pressure steps to quantify pressure leakage. In all cases, sensor output was amplified by 100× to obtain a good signal to noise ratio.

Gearbox cams had various connection positions from which the magnitude of modulations could be controlled. These positions gave piston movements of 10 to 100 mm in 10 mm increments and were similar for both gearboxes. Gearbox positions of 10 to 50 mm movements were assessed but large amplitudes gave noticeable deviation from sinusoidal output and so not used. For these tests a motor voltage of 4 V was used, and as with all pressure modulation tests reported, the modulation medium was atmospheric air. These movements gave a theoretical pressure change of ±0.2 bar.

To alter the attained modulation frequency, either the motor voltage could be altered or the gearbox interchanged. For these tests the 1:72 gearbox was used with motor voltages of 2 to 10 volts. The amplitude was maintained at 10 mm movement (position 1), again at 700°C using an air reference. This was able to return a frequency range of 0.04 to 3.3 Hz, with a small range of overlap between the two gearboxes.

To assess the pressure leakage from the rig, sensor output was monitored whilst the cam position was quickly rotated from minimum to maximum position, resulting in a pressure step using the 10 mm cam position. Sensor output was then observed over a time of almost 6 minutes. Although this technique was rather crude, leakages sufficient to have significantly effected modulations would have clearly shown up. The sensor was operated at 700°C where the response can be considered negligible for the time period assessed. Results of these verifications are reported in section 3.4.

In order to calculate the magnitude of pressure modulations, volumes of both the test rig and swept volume were required. These were taken by a dimensional measurement of each test-rig component. From these readings we are able to calculate the size of pressure modulations achieved at room temperature and to compare these with measurements taken

from the rig at operating temperature. A quantification could then be achieved of the effects of test-rig temperature and performance. It is recognised that, at this stage, we have not taken the effects of gas thermal expansion/contraction into account.

Using the test-rig volumes calculated above along with the Nernst and ideal gas equations we are able to mathematically model the modulation process and expected results. This was then compared with actual measurement data both by overlaying sine wave traces and using Lissajous figures.

An assessment of the temperature effects on pressure modulation amplitude was performed by applying a 0.3 Hz, 10 mm amplitude modulation to the sensor operated at 600 to 800°C under these conditions, sensor response should be fast compared to the modulation so effects may be attributed to the test-rig. The results were compared to expected sinewaves calculated using the test-rig dimensions and Nernst equation. Disagreement between sensor outputs at the various temperatures would indicate unanticipated temperature effects on the modulations produced. Results of these comparisons are reported and discussed in section 4.1.4.

2.6.2 Analysis procedures

For actual technique application, the Virtual Instrumentation was replaced with the oscilloscope. Although the waveform was now no longer recorded, it did enable measurements to be taken with much greater ease. Measurements of sensor output and gearbox cam position were displayed on the oscilloscope screen and, from these, measurements directly taken of sensor output amplitude, modulation frequency and time delay from cam maximum displacement to sensor output maximum. From modulation frequency and time delay, the phase difference could be deduced.

Measurements were performed upon a potentiometric sensor with platinum cermet electrodes, operated over a range of temperatures from 500 to 800°C using frequencies of 0.116 to 3.254 Hz. Realising this frequency range entailed use of both high and low ratio gearboxes with motor voltages from 2 to 10 V DC. The modulation amplitude was maintained at a cam movement of 10 mm. This results in a theoretical pressure modulation of –0.0381 to +0.413 bar around atmospheric pressure. Data were analysed by plotting sensor output amplitude and phase lag against modulation frequency and temperature. The results of these experiments are given in section 4.1.4.

2.6.3 Amperometric sensors

Pressure modulations were also applied to an amperometric sensor. The sensor (again the device used for amperometric step, concentration modulation and characterisation work) was placed in the small test chamber (Appendix C1.3.6) to which the pressure modulation apparatus was connected, including expansion chamber. The sensor output was recorded using a modified version of the concentration modulation Virtual Instrument with temperature being maintained using DC power supply with thick film heaters and monitored using 7150 multimeter and R type thermocouple. The sensor was operated at temperatures from 550 to 750°C with a pump potential, supplied through the Virtual Instrument, of 1.2 V selected according to previous tests (section 2.4.3). Modulations were applied using both high and low ratio gearboxes with motor voltages of 2 to 10 V to obtain frequencies of 0.395 to 3.254 Hz. Gearbox cam position 1 was used to give a 10 mm cylinder sweep. The data stored included time base and pump current was both displayed and written to data file. Test-rig modulation position was not recorded as the Virtual Instrument sample speed could not reliably detect the transducer pulses produced at these frequencies. Unfortunately this meant that no phase lag data were recorded. Modulation frequency was determined using the oscilloscope to monitor the position transducer signal. Before recording sensor waveforms, a period of oscillation was allowed so that readings could stabilise (generally a few seconds was adequate). Sensor temperature was monitored independently using a PC controlled multi-meter, and no temperature changes were noticeable upon initiating modulations. Results of these experiments and discussion are presented in section 4.2.5.

2.6.4 Electrode materials

The effects of electrode material on sensor response rate were examined using the pressure modulation technique. The evaluation was performed using the test cells detailed in section 2.4. These were 8 mol% YSZ potentiometric cells with simple metal electrode and binary metal mix electrodes of Pt, Ag, Au, Pd, Pt/Ag, Pt/Au, Ag/Au. These experiments were again carried out in the sensor response rig (in pressure modulation configuration) using both high and low ratio gearboxes to obtain as wide a frequency range as possible. The gearbox cam was set on position 1 to get a 10 mm cylinder sweep and motor voltages of 2 to 10 V DC were used to generate frequencies of 0.04 to 3.3 Hz. Temperatures of 400 to 700°C were examined for each sensor where suitable at each frequency. Measurements were taken using the Tektronics oscilloscope, waveforms were not recorded. Sensor EMFs

were amplified ×100 to get a good signal to noise ratio. Measurements of sensor output amplitude, modulation frequency and test-rig to sensor delay time were recorded. Upon initiating a new reading, the system was allowed to modulate until a stable response was obtained. This rarely took longer than a few minutes. Both reference and modulated atmospheres were air. In between sweeps, pressure was vented and the cam returned to a central position to initiate each new sweep with zero pressure differential between measurement and reference electrodes. Results and discussion are presented in section 5.6.

2.6.5 Platinisation

In addition to the electrode materials assessments described in section 2.6.4, the platinum metal electrode sample was re-examined with its electrodes replaced with platinum cermet electrodes and then again after re-examination these were electroplated with platinum. This was to provide comparative information for the metal, cermet and electro-plated electrodes for each response technique under similar conditions. Electrode applications are detailed in section 2.3.9. The pressure modulation experiments were performed in an identical manner to the electrode materials experiments detailed in section 2.6.4. Results from these analyses are reported and discussed in section 5.1.

2.7 Scanning electron microscopy

2.7.1 Materials investigation

In section 2.3, electrode / electrolyte samples were prepared for burn-out analyses. These were also used to get a visual image of the systems under test in the preceding techniques using both optical and scanning electron microscopy. The samples were fractured to give two parts, one of which was used for electrode face examination, the other for electrode and electrolyte edge examination. The samples were adhered in suitable orientation to an S.E.M. stub using a conductive carbon based cement. After drying, the samples (and stubs) were then given a sputter coating of gold. This was necessary to ensure that the sample faces were conductive and so would not electro-statically charge up upon electron scanning to the detriment of image quality (see section 1.2.7). The gold coating applied was of the order of a few angstroms and so would not be visible to the microscope. Sputtering was performed at 5 kV for 3 minutes under a vacuum of <0.1 torr (all 8 samples were sputtered together). The samples were then marked using a series of scratches on the stubs, for identification, before placing into the S.E.M. chamber and evacuating. Before taking the micrographs, all of the samples were closely examined so that a good idea of a suitable scale for micrographs could be attained that would allow direct comparison whilst

still revealing any interesting features. Scales of ×743 and ×2000 were selected for electrode faces and edges respectively. Micrographs were then taken, ensuring that micrographs were representative of the entire sample. In some cases slightly blurred micrographs were obtained. This was latter identified as a poor selection of resolution and working distance settings. Unfortunately time and financial pressures prevented these from being repeated. In any case the desired microstructure images are visible if not perfectly clear. Energy Dispersive X-ray spectrometry analyses were attempted upon a few of the samples but no intelligible results were attained through insufficient working knowledge of the system. Micrography, discussions of the interpretation and further analysis are given in section 5.7.

2.7.2 Firing temperature

In addition to the electrode microstructure analysis, an S.E.M. examination of plastic / ceramic samples fired at various temperatures was performed. This work was carried out by undergraduate project student O.Pampam (other aspects of this work are reported in Appendix E1.6 and section 2.3.6). Samples that had been fired at temperatures from 1150 to 1550°C were examined. Furnace ramps used in this work are shown in figure 2.3. Again these samples were fractured but in this case, only the fracture edge was examined in detail. The samples were adhered to S.E.M. stubs and sputtered with gold for 1.5 minutes at 5 kV under a vacuum of <0.1 torr, four samples at a time. Again the stubs were marked before loading into the test-chamber for identification. All samples were examined prior to recording micrographs so that a suitable scale could be selected for consistent and directly comparable results. A magnification of ×6230 was selected and all samples examined prior to micrography to ensure a representative image was taken. Micrographs and discussion of this work appears in Appendix F1.7 & F1.8.

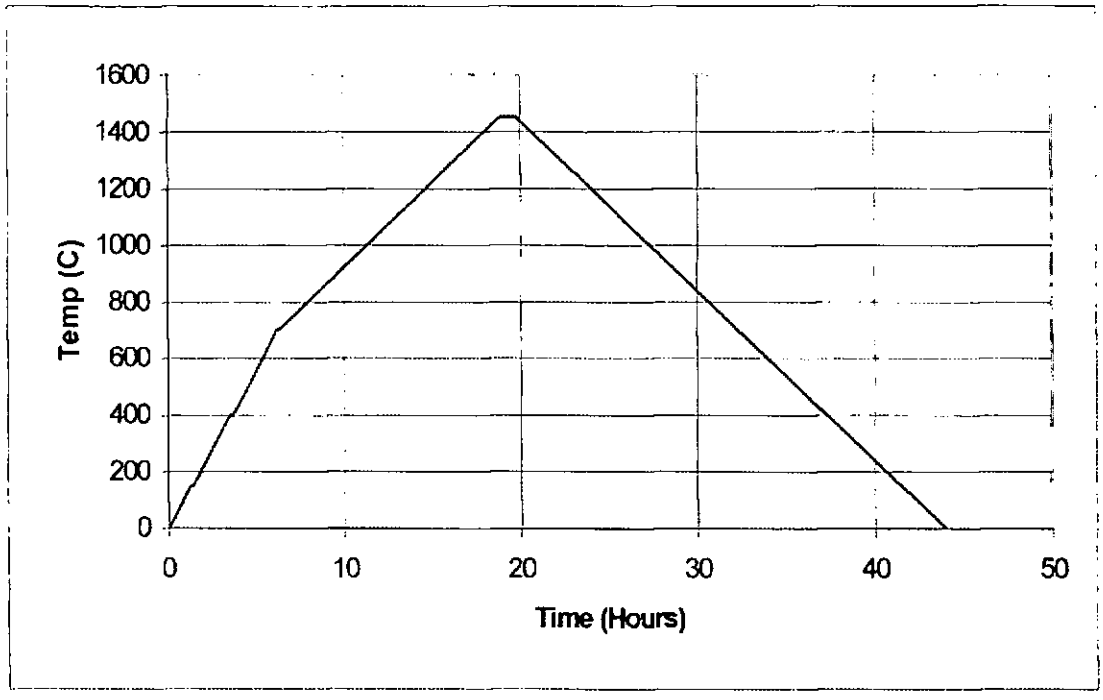

Figure 2.3 Sintering temperature experiment furnace ramp rates

2.7.3 Miscellaneous micrographs

Other undergraduate projects, G.Salami and Z.Tural, under my supervision also yielded scanning electron micrographs relevant to this research. The micrographs were of samples of plastic / ceramic created within our laboratories from a mix of Zirconia and PVA powders. These were fired at 1450°C with samples prepared as for firing temperature work and taken under similar magnification. The second set of micrographs were of the high temperature glass used to seal pump-gauges in Appendix E2.4. Sputtering and preparation of these samples was identical to that described above. These micrographs and a discussion of their implications are given in Appendix F1.9.

In summary, in this section we have reviewed practical aspects of the work presented. Preparation of materials, sensors, and test rigs. Details of tests carried out for each of the response rate techniques have been presented encompassing both verification of the technique and its application to sensor systems.

CHAPTER 3

RESPONSE RATE MEASUREMENT TECHNIQUE DEVELOPMENT

RESULTS & DISCUSSION

3 Response rate technique development

In this section we report the development of the four response rate assessment techniques of impedance spectroscopy, step gas concentration, concentration modulation and pressure modulation. Factors influencing performance and those introducing limitations to each technique are explored such that the techniques may be used with confidence in chapter 5 in the analysis of the simple platinum cermet electrodes and in chapter 6 to compare and contrast a variety of nobel metal electrode materials. Experimental details of these response rate measuring techniques are given in chapter 2.

3.1 Impedance analysis

The technique of impedance analysis was carried out using a commercial frequency response analyser (Solartron SL1260). This instrument had been recently calibrated, and, as a highly developed, widely accepted electrochemical measurement technique, required little in the way of verification before use. To aid understanding and familiarity of device function, the instrument output was viewed using a digital storage oscilloscope. In addition, one verification test that was carried out was impedance analysis of known RC electrical circuits, analysed primarily to gain familiarity with the instrument and ensure correct operation. Figure 3.1 shows the results obtained from analysis of an RC circuit containing a 10 kΩ resistor in parallel with a 22 μf capacitor. The results are displayed as 3d and complex plane plots indicating, as anticipated, a semi-circle arc of 10 kΩ diameter and with a maximum impedance at a frequency of $f=\pi RC/2=0.69$ Hz. Also depicted is a Bode plot for the same data. Bode plots are dual plots of log impedance versus log frequency and phase angle versus log frequency which allow comparison of data over several orders of magnitude. Bode plots are interpreted as a pure resistance is represented by a horizontal line of 0° phase angle, a pure capacitance is represented by a straight line of −1 gradient and phase angle of -90°. Between straight lines exists a transition zone known as a corner, the frequency of which represent the semi-circular region of complex plane plots. Identification of frequency values on complex plane plots is usually in the form of markers which leads to an overcrowded diagram. In general the phase angle vs. frequency graph is more sensitive than the impedance vs. frequency graph. Bode plots are not however widely employed as they are not instantly understandable or easy to interpret accurately.

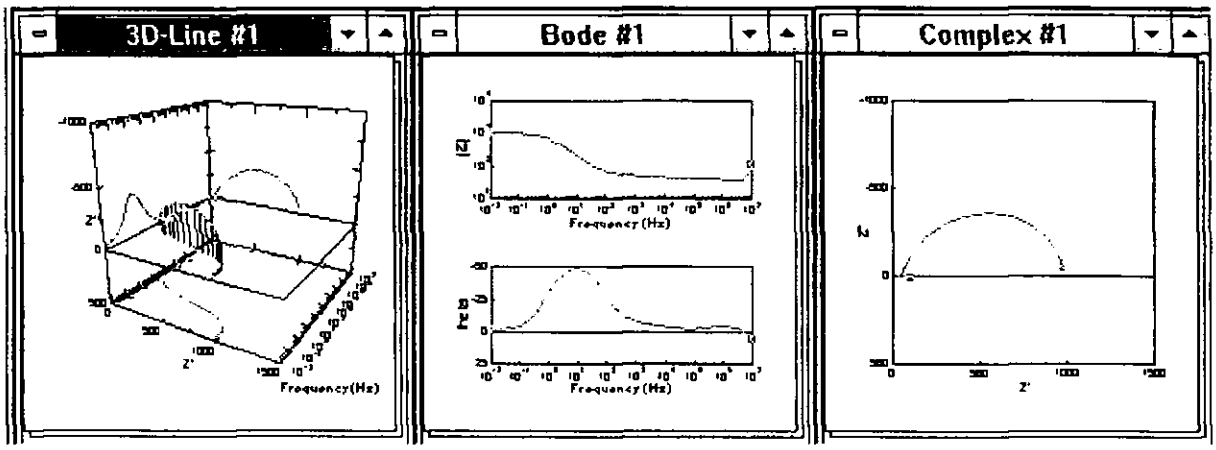

Figure 3.1 Bode, 3d and complex plane impedance plots

Individual impedance sweeps are usually depicted as complex plane plots as these are easily recognised and interpreted. Arrhenius diagrams are commonly employed. These diagrams plot the log of component resistance against inverse of temperature in Kelvin.

$$k = A \exp(-Ea/RT) \qquad \text{Equation 3.1}$$

$$\ln(k) = \ln(A) - E_a/RT \qquad \text{Equation 3.2}$$

Plotting ln(k) versus 1/T we get a linear plot with gradient of E_a/R and intercept of ln(A) where k is the rate constant (in this case the component impedance), A is the impedance at infinite temperature, E_a is the activation energy and R and T have their usual meanings. Activation energy calculated in this way has units of $kJmol^{-1}$. Activation energies are often quoted in electron volts (eV) which should more correctly be referred to as $eVmol^{-1}$. The correlation between the two is the charge on an electron multiplied by Avagadro's constant such that $1\ eVmol^{-1} = 96.5\ kJmol^{-1}$.

Figure 3.2 shows some complex plane plots taken from a real electrode / electrolyte / electrode cell over a range of temperatures. The two plots are of the same data showing all three polarisation arcs but are displayed on two different scales to show the scaling problems encountered with complex plane plots. From these plots it can be seen that imperfect semi-circles are often obtained with greater deviations usually arising at the higher and lower frequencies where we are limited on one hand by the limits of the instrument capabilities and the other by the long times required to reiterate readings. Noisy apparently random data are also occasionally seen in the intermediate data.

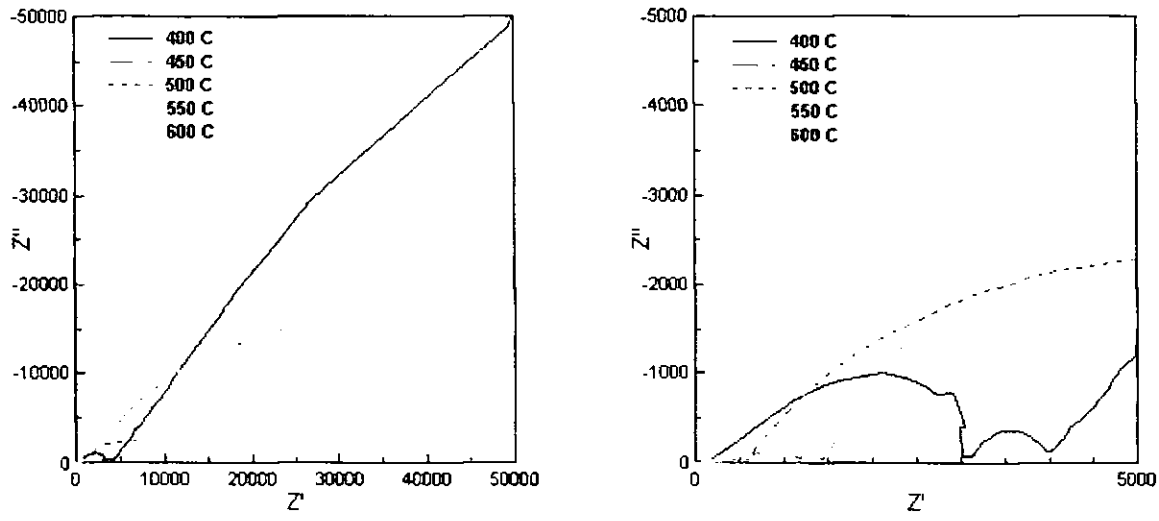

Figure 3.2 Complex plane plot of a real cell

3.1.1 Measurement optimisation

The impedance measurement instrument and software does allow some scope for improving the quality of data obtained. Optimisation features include:

- Nulling files

  By recording test lead impedance both open circuit and closed circuit, the impedance introduced through test leads can be subtracted from that measured from the cell. Use of this technique was found to remarkably improve measurements at the higher frequency end of the spectrum.

- Integration

  The software allowed repeated measurement at each measurement frequency in order to improve accuracy. Limits on measurement time and cycle number could be imposed so that lower frequency integration did not take excessive time. Also a certain amount of intelligence was built in to allow the machine to terminate integration if sufficient accuracy had been achieved, again reducing measurement time. This feature did show substantial improvements in data noise rejection when used.

- Noise rejection

  The instrument is marketed as having excellent noise rejection capability.

- Screening

  Instrument test leads were BNC shielded cables, test-rig cables were also screened and a non-inductively wound furnace was used to limit electro-magnetic pickup. Use of a non-shielded system dramatically deteriorated the measurement quality.

- Measurement techniques

  The instrument had the capability to perform a variety of different measurements by measuring/controlling current and voltage whilst sweeping frequency, DC bias, signal amplitude or over time. All measurements reported here used a controlled voltage and measured current whilst sweeping frequency. A few experiments were attempted using controlled current and measured voltage but no significant improvement/deterioration was noticed.

- Batch measurement

  The system was capable of running a series of pre-programmed experiments with no supervision and controlled timings. This feature was not employed due to the requirement to re-set temperature/gas controlling equipment and review data produced before proceeding.

3.1.2 Electrode assessment

Figure 3.3 shows Arrhenius type plots for the electrode interfacc resistance data obtained for a variety of platinum cermet electrodes over a range of temperatures. The first point to note is that we obtained very similar gradients for each sensor in each of the Arrhenius plots. This is to be expected since similar materials were used in each device. We also, however, see differences in the intercepts for each sensor in each plot. This is also to be expected in the electrode interface plot as each electrode firing / cermet was expected to give a different electrode interface microstructure. The difference in intercept was approximately three orders of magnitude between the best and worst electrodes. The trends in electrode improvement are not immediately clear, but if we tabulate the results in order of electrode resistance we do see that the higher firing temperatures are generally worse than the lower temperature electrodes. The electrode paste (M4 and M6) appear to be fairly even but generally out-perform the simple metal electrode. The electro-plated sensor however shows a clear advantage over the high temperature fired electrodes, a fact backed up from other all other tests of comparison. See also the SEM results obtained for high and low temperature fired cermet electrodes (section.5.7).

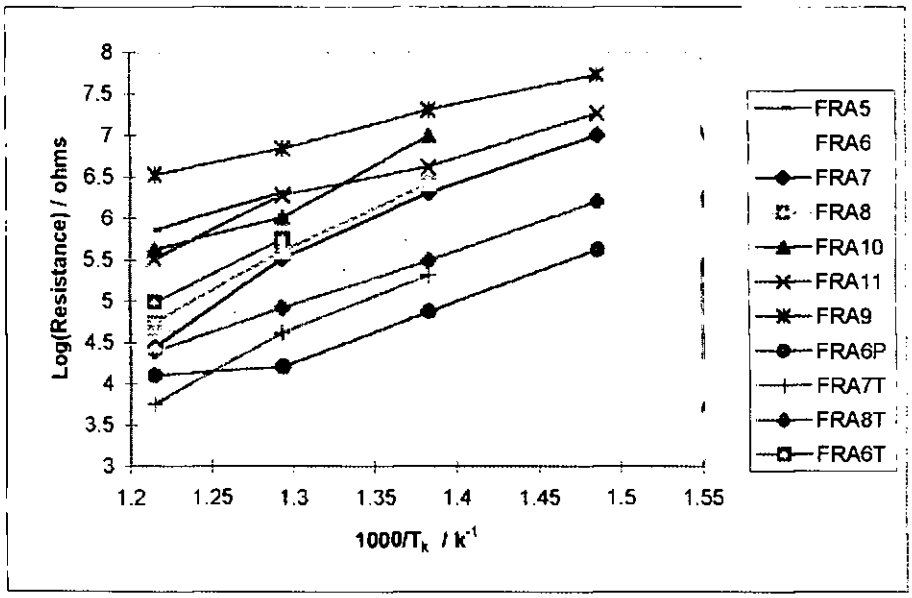

Figure 3.3 Arrhenius plot of electrode interface resistance for each electrode variation samples

Sensor	Marked electrode		Un-Marked electrode		Component resistance		
Number	Mix	Temp	Mix	Temp	Grain	Boundary	Electrode
FRA-9	Mix4	1450	Mix4	1000	1	1	1
FRA-5	Mix4	1450	Mix4	1450	2	2	2
FRA-10	5542	1450	5542	1450	8	7	3
FRA-11	5542	1000	5542	1000	9	10	4
FRA-6T	Mix6	1450	Mix6	1450	6*	4*	5
FRA-8	Mix6	1000	Mix6	1000	7	8	6
FRA-7	Mix4	1000	Mix4	1000	3	3	7
FRA-6	Mix6	1450	Mix6	1450	5*	6*	8
FRA-8T	Mix6	1000	Mix6	1000	10	9	9
FRA-7T	Mix4	1000	Mix4	1000	4*	5*	10
FRA-6P	Plated	0	Plated	0	11	11	11

Component resistance market as lowest is highest resistance, * resistances are very similar

Table 3.1

Figures 3.4 and 3.5 show respectively, Arrhenius plots for the electrolyte grain and grain boundary component resistances. These show a very good correlation between slopes for each specimen but there does exist a large spread in terms of intercepts. This was not expected since all specimens had been cut to the same size and shape, from the same

material and had had comparable high temperature histories. Despite these precautions, there existed a difference of some two orders of magnitude between the best and worst electrolyte impedances. Some light was shed on the cause of this difference by examining the change in electrolyte properties upon thickening of the electrode layers. This was expected to have negligible effect on the electrolyte properties, but in some cases did. This leads us to suspect that these did not have complete contact across the entire electrode face. In preparation, electrode layers were kept deliberately thin in an attempt to avoid gas diffusion limitation in the electrode layer. Calculations since show this would not be a significant factor in these measurements (see Appendix F1.6). Intricate electrode variations would not be expected to affect the electrolyte polarisations to this extent. No conclusive relationships has been drawn between electrode and electrolyte impedances, although grain interior and boundary impedances were approximately equal for each sample tested. This suggests that electrolyte purity in the samples used has been sufficiently controlled for it not to be of immediate concern. In all cases of cell impedance examined, cell resistance has shown to be dominated by electrode/electrolyte interface impedance, with the exception of bias potential application where electrode impedances have shown to be reduced whilst electrolyte impedances remain constant.

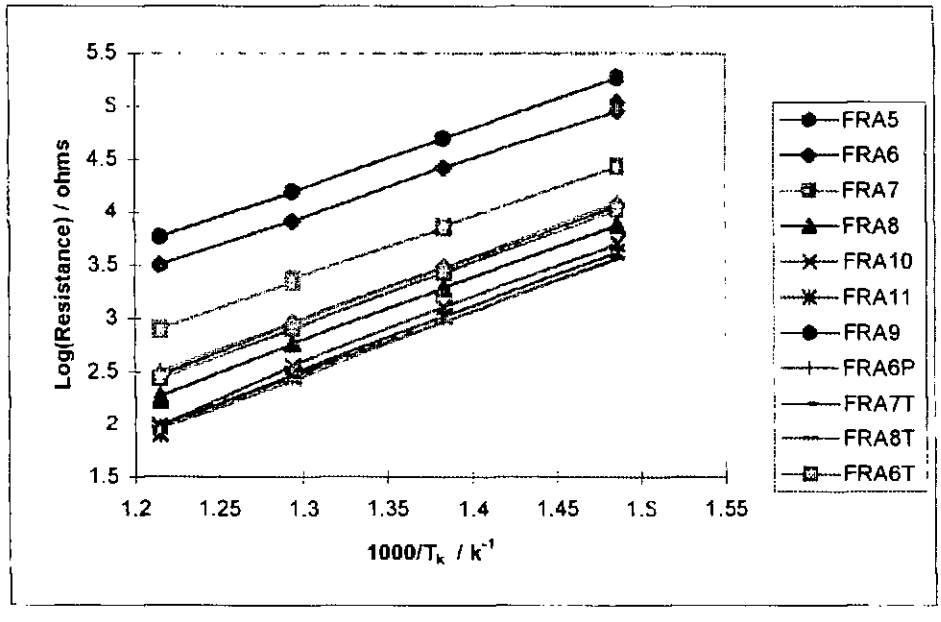

Figure 3.4 Arrhenius plot of electrolyte grain resistance
for each electrode variation samples

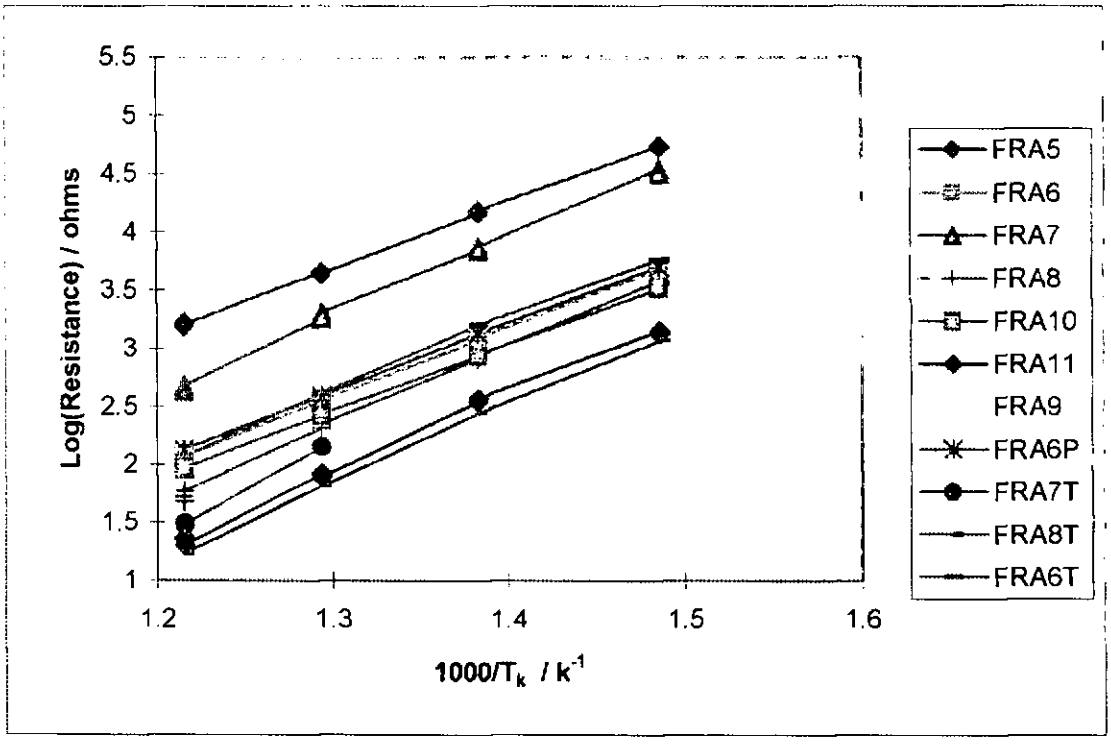

Figure 3.5 Arrhenius plot of electrolyte grain boundary resistance for each electrode variation samples

3.1.3 Sensor Cell Ageing

Repeated measurement of the same cell under constant conditions, intended to demonstrate technique reproducibility, showed (fig. 3.6) a slow but steady increase in electrode resistance over time at this elevated temperature. It should be noted that in the time scale of the figure, the time zero refers to the time from the initiation of the first test and not to the exposure time of electrode to high temperatures. After considering and eliminating effects due to temperature, pressure and gas composition variation, the effect was attributed to cell ageing phenomenon. Badwal et al [36] compared the performance of platinum electrodes before and after firing at 900°C using SEM and impedance spectroscopy. They saw that electrode deterioration by sintering and grain growth reduced the three phase boundary length and increased the electrode impedance.

The rate of increase observed in this work amounted to approximately 3% resistance per hour for both high and low temperature sintered electrode (1450 & 1000°C) samples. No long term stability tests have been attempted. Whilst these results do indicate a decrease in activation introduced by high firing temperatures, in the long term it would not be surprising to see higher temperature fired electrodes stabilising before those fired at lower temperatures. Also it could be anticipated that cermets would be less prone to ageing than

metals due to the structural stability introduced by the ceramic. Although no further deterioration tests have been performed, it is expected that at lower temperatures, the rate of deterioration would be significantly lower. This area remains open as an interesting area for further research.

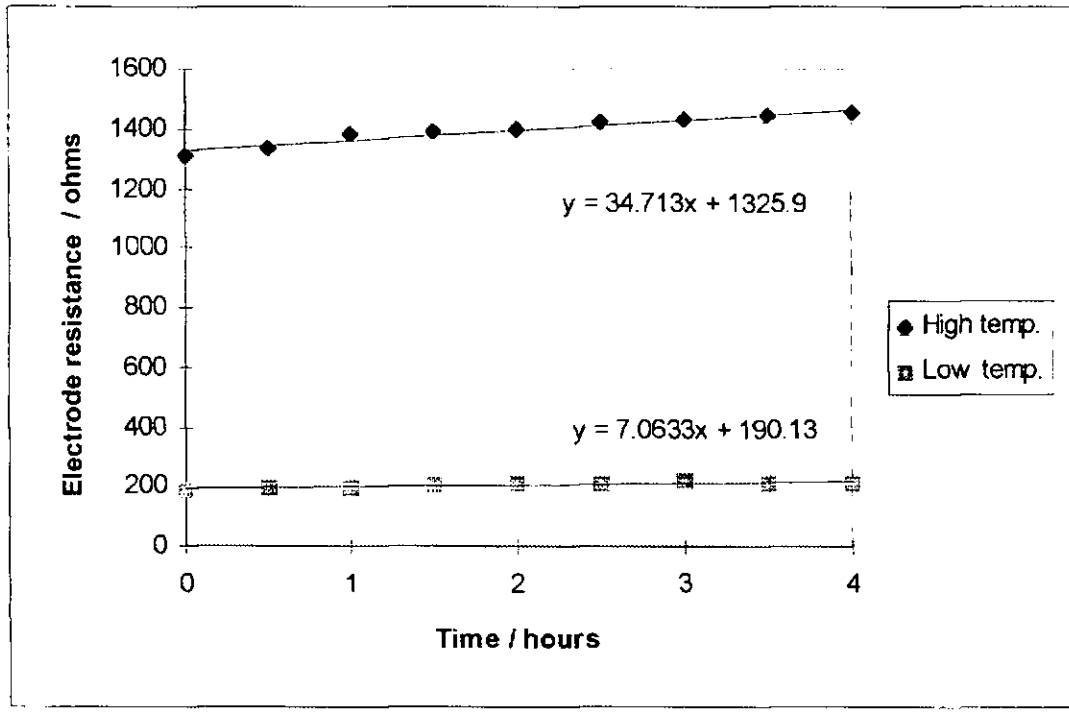

Figure 3.6 Time dependent characteristic of high and low temperature fired electrodes

Young [49] researched the use of commercial potentiometric zirconia sensors used in exhaust gases for A:F control. Aged sensors showed reduced performance, to remedy this their electrodes were removed and replaced with fresh electrodes. This gave a complete return of original performance and led to the conclusion that ageing is a function of electrode sintering, grain growth and de-bonding. Whilst electrode removal and replacement may not be easily achieved with amperometric type sensors, the work utilising AC current electrode electro-plating of four electrode sensors does allow this possibility. This work also shows that sensor ageing is more electrode than electrolyte related. Krafthefer et al [103] analysed zirconia potentiometric cells using SEM and conductivity measurements. Their work indicated that better adhered electrodes showed a lower susceptibility to ageing as SEM showed with electrodes that had been artificially aged, the porosity of platinum increased. He also found however that sensors with smaller zirconia ceramic grain size showed less susceptibility to ageing. Kleitz et al [104] demonstrated ageing in YSZ with the effect of decreasing conductivity especially at higher temperatures.

They suggested that ageing can be seen as a gradual enhancement of a conductivity blocking effect caused by impurities segregating at grain boundaries. Grain ageing was also observed with rate dependent upon atmosphere and grain size.

Cell ageing would have several effects on sensor performance depending on the cell type used. In amperometric cells, ageing would reveal itself as an increased resistance to oxygen pumping, thus requiring a higher pump potential to realise the limiting current condition. This would result in a lowering of the upper measurement limit at lower temperatures. In potentiometric sensors, ageing would result in a slower realisation of equilibration and therefore the reduction in sensor response times.

3.1.4 Oxygen concentration

A further assessment using impedance spectroscopy concerned the influence of oxygen concentration on the impedance of each cell. Oxygen concentration, as expected, had no apparent effect on either of the electrolyte impedances in the limiting concentration range (21-2%) analysed. Reducing oxygen concentration was however expected to increase electrode interface impedance as oxygen availability reduced. At oxygen partial pressures less than 0.1 atm, Adler et al [42] found that gas diffusion resistance could become significant. The results in this work (fig. 3.7) indicated this was not the case, actually showing reduced resistance at lower oxygen concentrations, for all samples at a temperature of 550°C, similar results were obtained at other temperatures. This effect was compounded by the ageing phenomenon mentioned above, since lower concentrations were investigated after the higher concentrations thus, the effect may be actually slightly larger than indicated. A review of literature revealed that a similar result was also seen by Verkerk et al [105]. Verkerk used a combination of DC polarisation and AC impedance to measure electrode resistance over a range of oxygen partial pressure. They found a minimum cell impedance was reached at oxygen pressures of 10^{-1} to 10^{-2} atm. Electrodes they investigated were sputtered platinum fired at 1200 to 1400°C onto zirconia, ceria and bismuth oxide electrolytes. The minima was attributed to a switch in mass transport limitation mechanism from anodic to cathodic dominated. The minima was seen for YSZ and ceria electrolytes but not for Be_2O_3 for which electrode resistance was much lower. Again, no further work has as yet been undertaken by the author, however the construction of low oxygen concentration apparatus may give the opportunity for further analysis of this phenomenon. These effects help to explain the apparent increase in conductivity seen in

sensor current / voltage curves as oxygen levels decrease at 600°C and 0 to 500 mV (Appendix F fig F2).

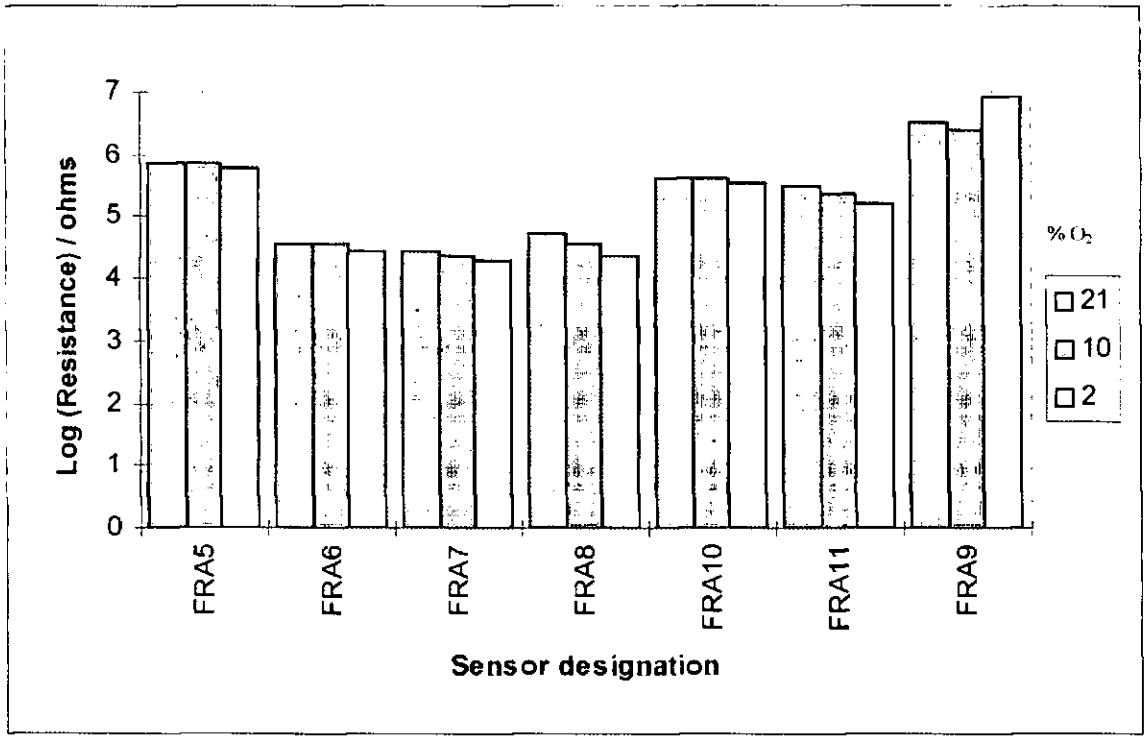

Figure 3.7 Oxygen concentration effect on electrode interface resistance

3.1.5 Electrode curing temperature

The electrode curing temperature effects on electrolyte performance has been assessed in Appendix F1.7 by current / voltage sweeps and Appendix F1.8 by SEM analysis. Here we give results of impedance analysis on the same samples. This work was carried out by the final year undergraduate O.Pampam. Since this work was aimed at investigating electrolyte impedance, to save time, low frequency electrode data were not recorded under this author's advice. With hindsight this is a disappointing omission as this data would have provided a valuable insight for the work studied here. Low frequency data would have given a good idea of the effect of curing temperature on electrode performance as electrodes were fired along with the electrolyte. The results that were obtained were analysed by plotting Arrhenius type diagrams and comparing the slopes and intercepts of these for grain and grain boundary resistances. Kleitz et al [104] investigated grain boundary impedance by altering porosity and purity to find that conductivity and porosity were proportional. Figure 3.8 shows Arrhenius plots for these two parameters plotted for each sintering temperature. The Arrhenius plots have similar slopes but show intercepts increasing with decreasing sintering temperature.

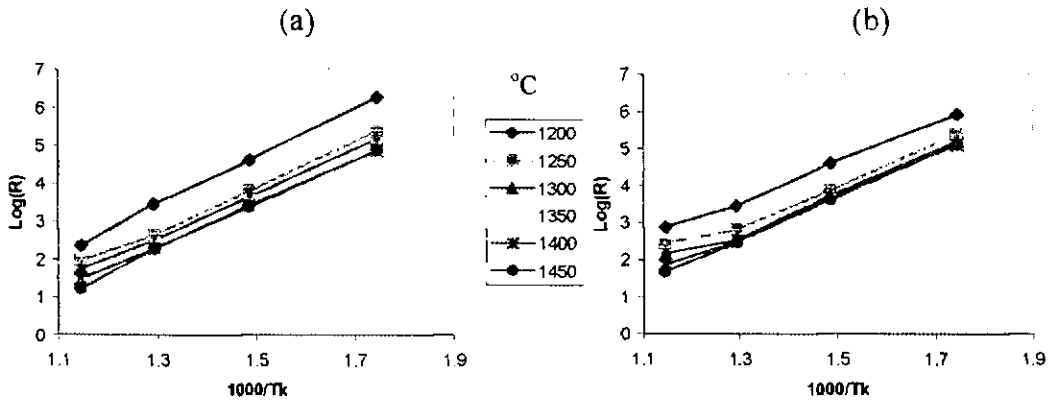

Figure 3.8 Sintering temperature effects on electrolyte (a) grain boundary and (b) grain interior impedance.

These results were backed up with hardness, shrinkage, density and scanning electron microscopy shown in figure 3.8c. This figure shows factored values to allow direct comparison of trends. The scanning electron micrographs are presented in Appendix F1.7. The results also show a significant improvement in densification with sintering temperature to approximately 1300°C for each electrolyte parameter after which densification improvement reduces. These improvements can be envisaged as due to better contact between grains. Herring's law shows that sintering rate is inversely proportional to the grain size Alford et al [25].

$$\frac{t_2}{t_1} = \left(\frac{r_2}{r_1}\right)^n$$

Equation 3.3

where t_1 and t_2 are the times to sinter spherical powders of radii r_1 and r_2. The exponent n is sintering mechanism dependent varying between 1 and 4. The driving force for sintering is surface free energy reduction. Finer powders sinter at lower temperatures, being less energy intensive.

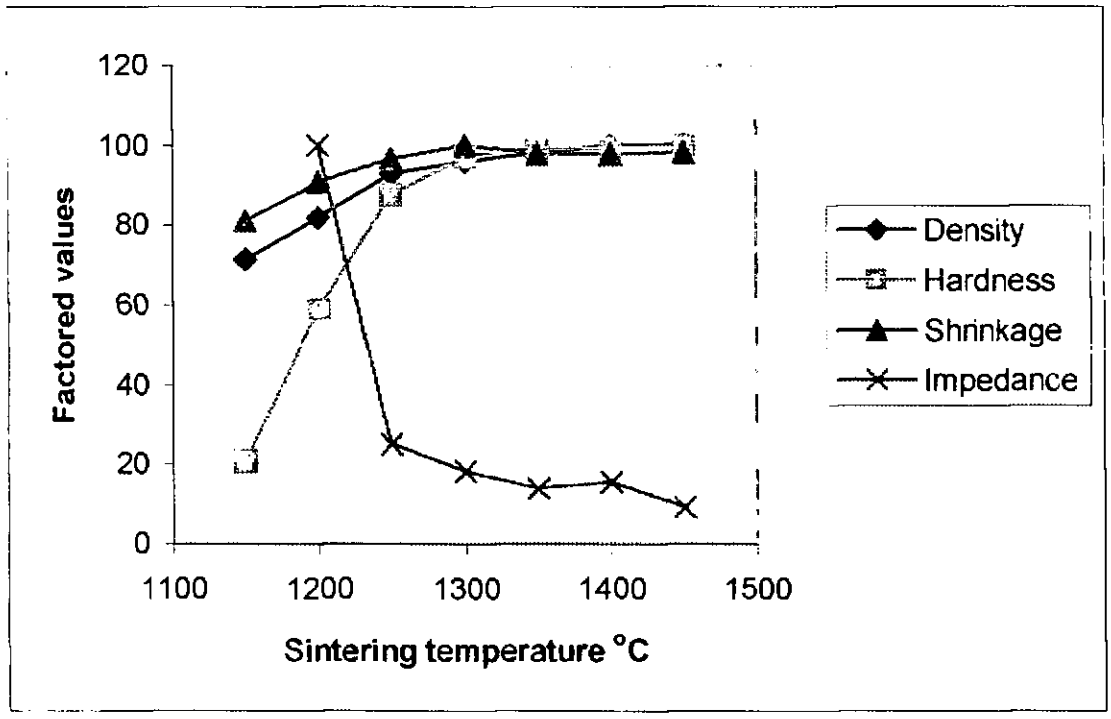

Figure 3.8c Sintering temperature effects on electrolyte properties.

Similar work was undertaken by Steil et al [102] who used impedance spectroscopy, physical measurements and scanning electron microscopy to examine at the densification of 8 mol% YSZ under varying sintering cycles. Steil et al used a Tosoh zirconia powder, isostatically pressed to 400 MPa before sintering with ramp rates of 2 °/min to the desired temperature which was maintained for 2 hours. Ceramic densification was achieved for temperatures of 1000 to 1300°C whilst grain growth occurred at temperatures from 1350 to 1700°C. Small pore sizes gave rise to a clear separation of electrolyte semicircles. Depression angle and blocking processes increased markedly for sintering at grain growth temperatures.

3.2 Step concentration technique

3.2.1 Flow variation

We now turn our attention to the assessment of the step concentration response time measurement technique. Figure 3.9 shows the results of flow rate variation tests. We see that in each case there is an initial time lag where the step change has to travel from the solenoid valves, down the carrier tube, to the sensor measuring electrode. This lag is seen to be equally flow rate dependent in both the increasing and decreasing concentration step directions. Figure 3.11 shows plot of estimated time lag versus that measured from figure 3.10. The estimated time lag was the result of considering the gas volume between flow

valves and sensor measuring electrode (≈1200 mm^3) and the flow rate of the gas. The resultant plot reveals a well fitting straight line with zero intercept, allowing a good confidence that this is the dominant factor in this initial lag.

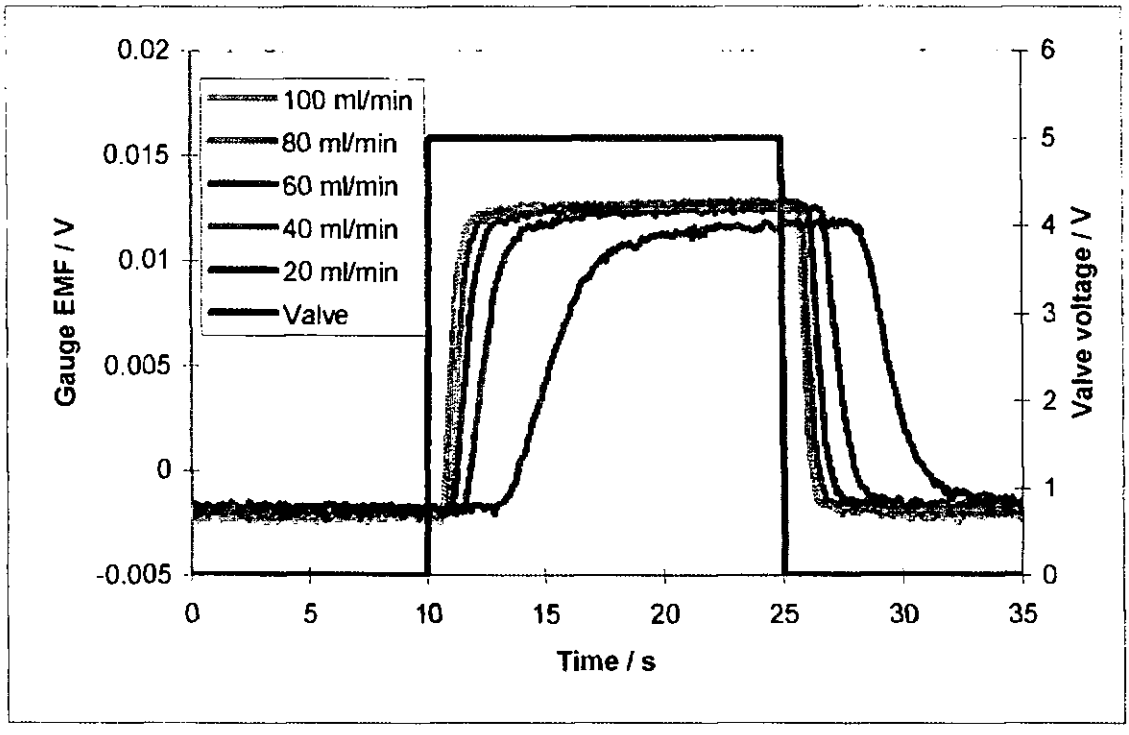

Figure 3.9 Step gas change response with flow rate variation

We also observe that the rate of initial sensor response was also affected by flow rate. Indeed at 20 ml/min the full change is seen not to be completed during the 15 s step as the peak EMF was substantially lower than that at other flow rates. This could be attributed to a 'blunting' of the step change wave front by gas diffusion. As the gas travels by bulk flow down the carrier tube, gas at the step front will diffuse, both ahead of and lag the true gas front, resulting in a dilution of the gas change front, the slower the gas flow, the greater the time this diffusion has to occur, thus giving a longer time for the gas change to be completed. A second effect is that of lamellar flow in which gas travels faster at the centre of the tube than that the walls, effectively smearing the gas step. Anderson & Graves [106] investigated the effects of step changes on potentiometric oxygen sensors using gases with different diffusion rates. These showed a significant variation in response rates in relation to diffusion coefficient. The diffusion coefficient of a gas describes the amount of gas that will pass through a unit area per unit time. The diffusion coefficients for oxygen in air at atmospheric pressure are 0.20 and 1.65 cm^2s^{-1} at temperatures of 20 and 700°C respectively. These however would indicate that gas front diffusion rates are negligible.

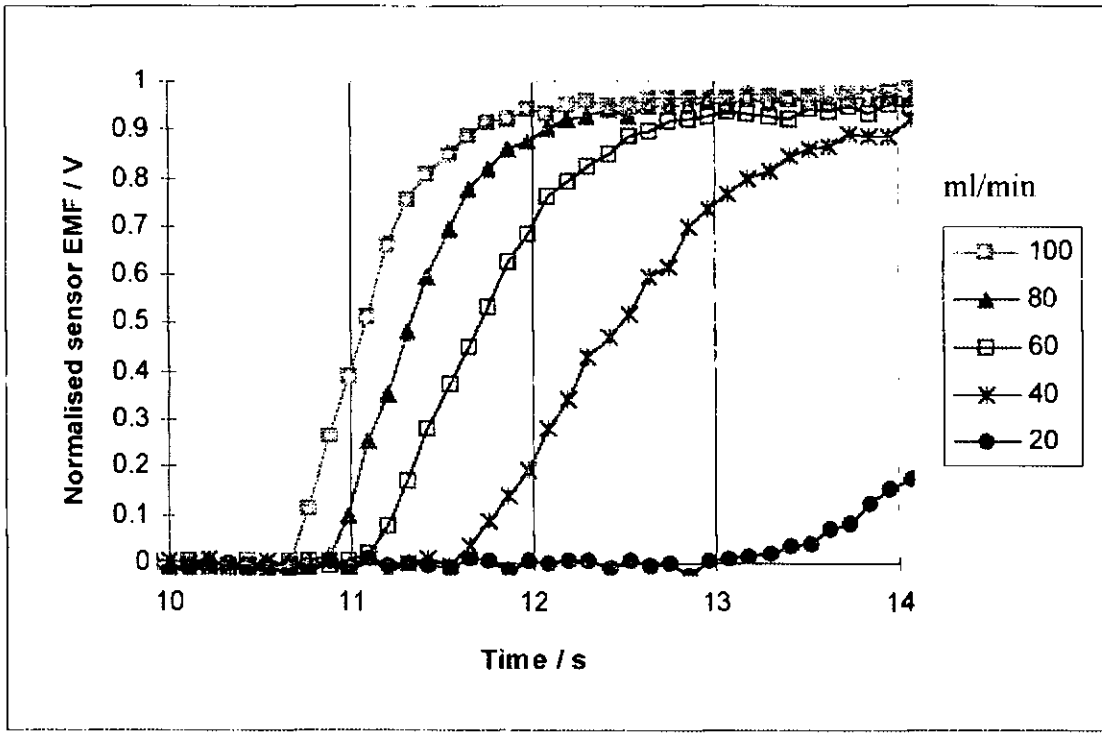

Figure 3.10 Enlarged step change response with flow rate variation

A second effect is that of laminar flow of gas in the carrier tube. Laminar type of flow is that in which the gas travels smoothly in contrast to turbulent flow, in which the fluid undergoes irregular fluctuations and mixing. In laminar flow, the velocity, pressure, and other flow properties at each point in the fluid remain constant. Laminar flow over a horizontal surface may be thought of as consisting of thin parallel layers. The fluid in contact with the horizontal surface is stationary, but all the other layers slide over each other. Laminar flow is common only in cases in which the flow channel is relatively small, the fluid is moving slowly, and its viscosity is relatively high or near solid boundaries, where the flow is often laminar, especially in a thin layer just adjacent to the surface. The result of this flow is again a blurring of the gas front arrival the measuring electrode and that the change will take a finite time to be completed. Although this laminar blurring effect would increase with gas velocity, the rate of gas front arrival at the measuring electrode will be greater and therefore contribute a less prominent effect than at lower velocities. Also, at higher gas velocities, the flow would tend towards turbulent. It is the effects of these flow mechanisms that is thought to be responsible for reducing initial sensor rates of change.

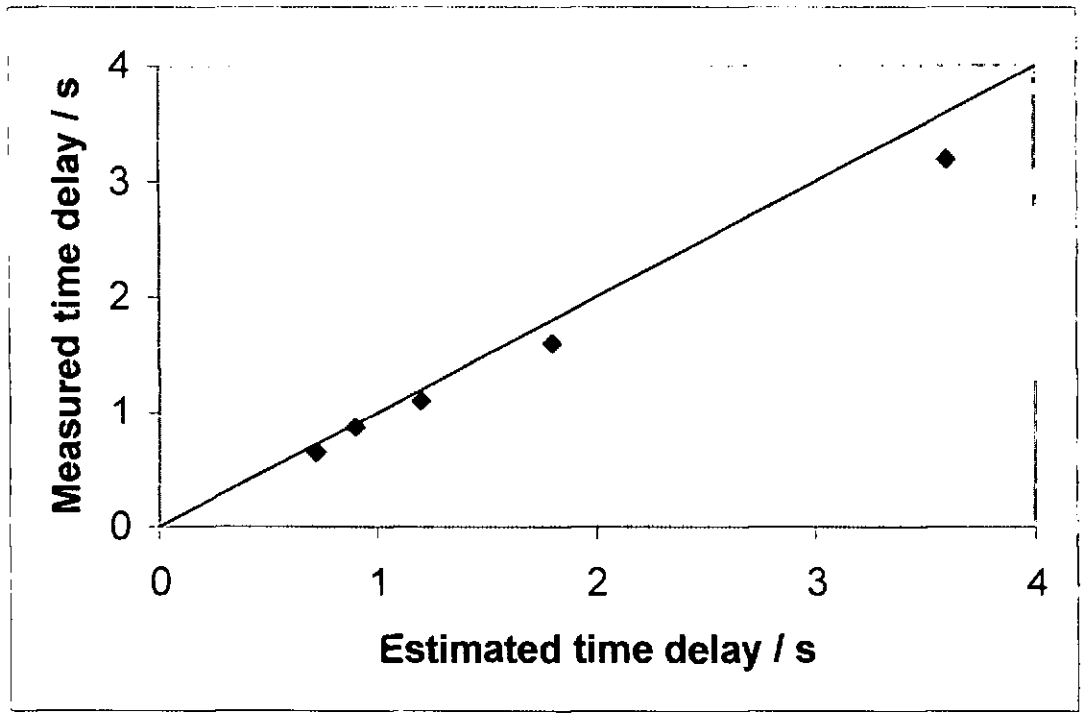

Figure 3.11 Estimated versus measured gas step delays

The final feature of these results is the negative offset of gauge EMF. This offset has been attributed to temperature effects. Fouletier et al [66] found that spurious EMFs using a zirconia tube as a pump-gauge. These spurious EMFs were traced to small electrode temperature differences resulting from gas flows. The offset EMFs found in this work were also traced to temperature differentials across the measuring and reference electrodes. Temperature differentials exist due to gas flows cooling the measuring electrode along with differing heat drains from the non-symmetrical test-rig set-up. These differentials are very difficult to eliminate whilst maintaining a high gas flow rate to keep the gas front sharp whilst maintaining an easily interchangeable sensor. Kocache et al [67] utilised a symmetrical zirconia cell to equalise heat drain and keep temperature differentials low. Similar cells however would have been prohibitively expensive to have made in the small quantities required in this work and would have been detrimental to ease of electrode removal/replacement. Solutions that were employed to combat electrode heat differentials included heating the incoming gas flow and positioning the sensor to one side of the furnace hot-zone. Sensor positioning can compensate for electrode temperature differentials by negating non-symmetrical heat drain by using non-symmetrical heat application. A limited degree of incoming gas heating is achieved by flowing used, heated gas down the outside of the carrier gas tube. This however appears to have had little affect as the offset would have been affected by gas flow rates. This is not seen to any significant extent. The problem was best tackled by keeping the offset at a fairly constant level then

subtracting this offset from the results prior to analysis. Anderson & Graves [106] found that step response EMFs were asymmetric with step direction but that the calculated oxygen pressures were symmetrical. A similar analysis was performed with the data gathered here with the oxygen concentrations calculated showing a greater symmetry than the raw voltage data. The symmetry, or lack of it, clearly derives from the logarithmic term in the Nernst equation. The degree of symmetry obtained for the lowest flow rate of 20ml/min is obviously affected by the fact that the gas concentrations did not stabilise before the step change had completed.

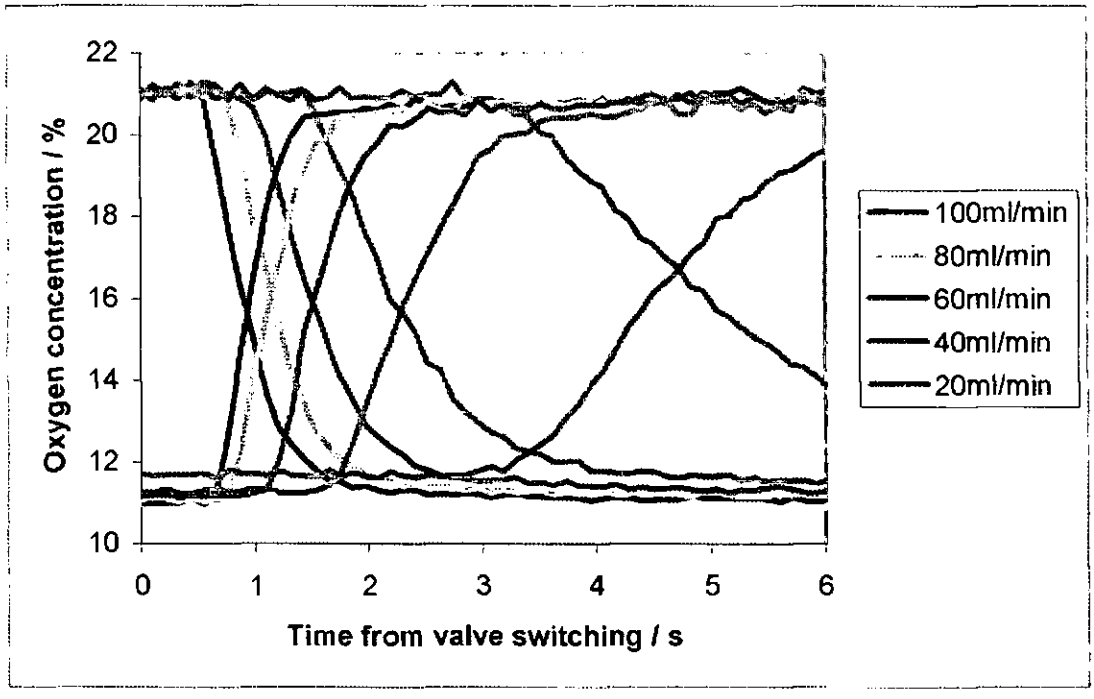

Figure 3.12 Step symmetry with oxygen concentration

3.2.2 Step amplitude

Figure 3.13 shows the results of tests exploring variation of gas step amplitude. Figure 3.14 depicts the same data normalised and indexed to show comparative trends. In these tests, clearly the initial time lag, rate of increase and sensor offset are virtually constant, with the only variations arising in time for the complete step to be realised and the magnitude of the resultant EMF. The constant initial lag and initial sensor response also indicate that gas front blunting and gas transit times are present but only marginally affected by gas composition. An important result is the step from 21% to 21% which effectively maintains a constant concentration to check for undesired effects of switching the gas supply source. This step shows no change in sensor EMF demonstrating that there is no effect of changing

the valve that the gas is flowing through, there is no change in offset and no difference in partial pressure in the two gas streams.

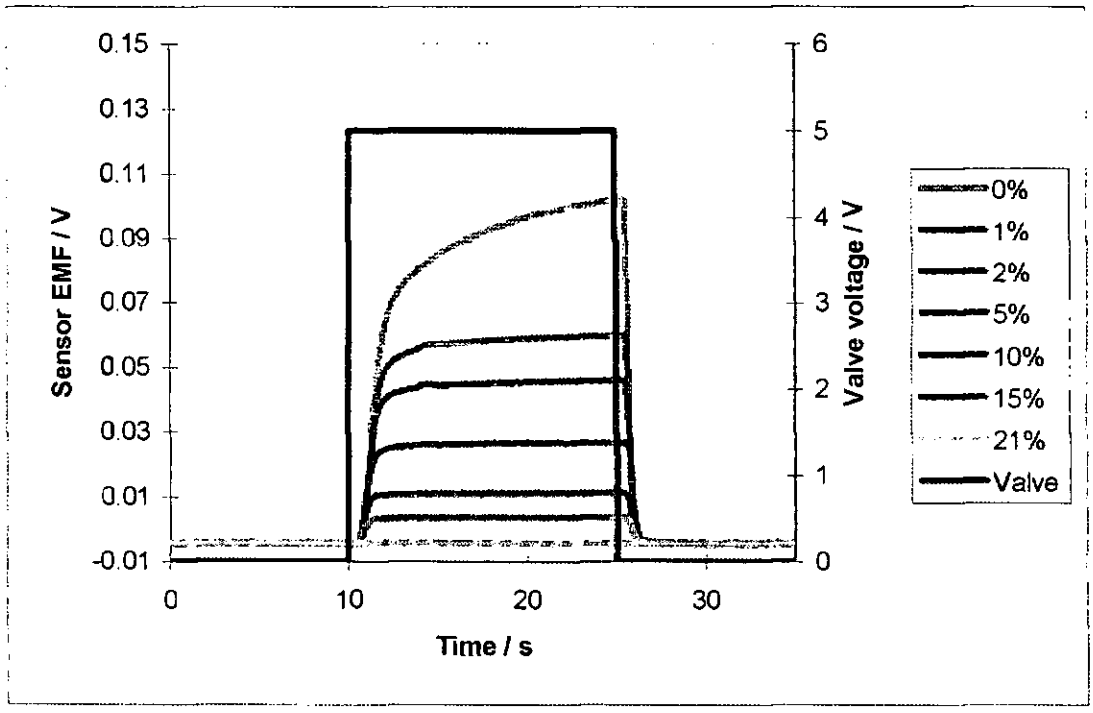

Figure 3.13 Step change response with step amplitude variation

These tests also showed that the step technique could be used for steps from 21% to as low as 1% without difficulty. Since a larger step provides a greater differential and better results resolution a step of 21 - 2% was chosen for further works to be based upon. Although this was later changed to 21% ±4% to allow direct comparison to other work. The change from 21 - 0% oxygen demonstrates a significantly slower response than that for other concentrations. This is due to the requirement to flush all of the oxygen from the cell to obtain a true reading. When stepping to a moderate oxygen concentration, this residual oxygen makes little difference resulting in negligible deviation from true readings. In the normalised data, a significant amount of noise is seen in the lower amplitude steps. This is due to the amplification of signal required for normalisation of these data.

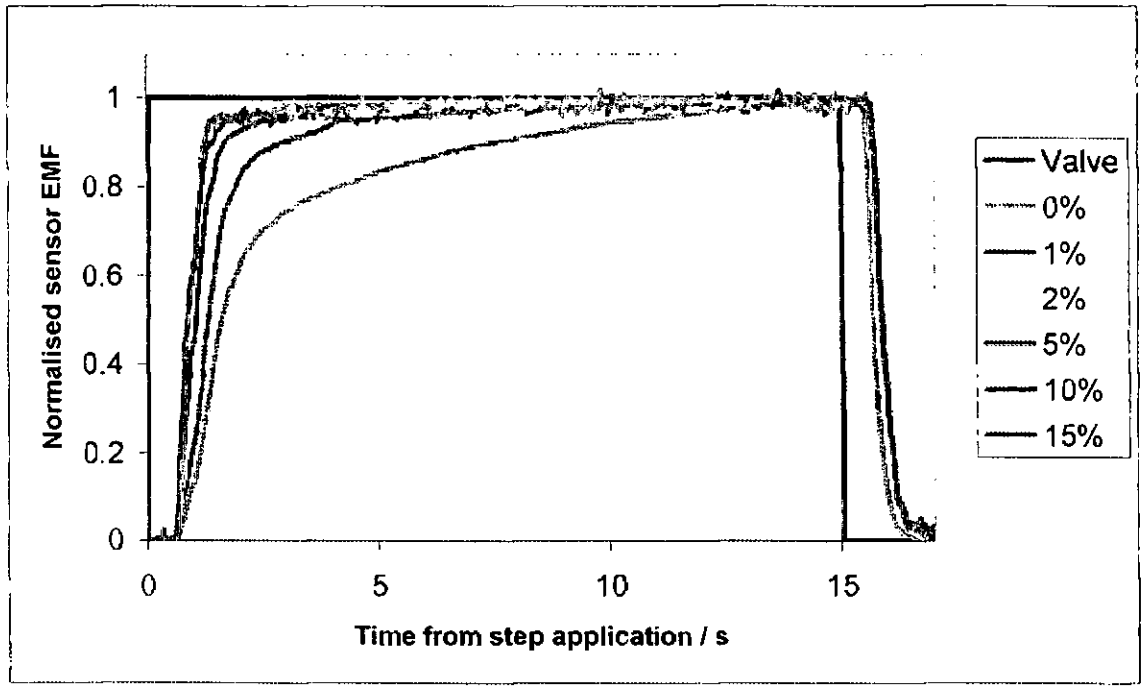

Figure 3.14 Normalised step change response with amplitude variation

3.3 Concentration modulation technique

In this section we discuss the results of verification of the concentration modulation technique. Figures 3.15 to 3.18 show the results of flow valve modulation experiments carried out to investigate the capabilities of the computerised mass flow valves. The diagram shows the effects of operating the valves beyond their capabilities in areas of frequency, amplitude, offset and valve type. These are compared with traces for a valve operated under acceptable conditions.

3.3.1 Frequency effects

If we attempt to use too high a frequency (>0.3 Hz) we see that the sinewave becomes deformed towards a saw tooth type wave and the amplitude of modulation is also reduced. Distortion occurs as the valves are unable to keep track with the input modulation, whilst amplitude reduced as the input wave reversed before valve maxima were reached. These problems were encountered, dependent upon amplitude, if a maximum frequency was exceeded. The valve output voltage was proportional to percentage of valve maximum flow where 5 V = 100%, 0V = 0%. Since the flow valve used here was a 100 ml/min valve we see that a 21 ml/min average with a ±4 ml/min sine modulation was recorded. An interesting portion of the measured sweep is the first couple of seconds. In this region we see that the valve took a little time to settle into a regular pattern. Since the same would be

true of the measured sensor output, care was taken to initiate each subsequent modulation from the average valve opening value at mid sweep.

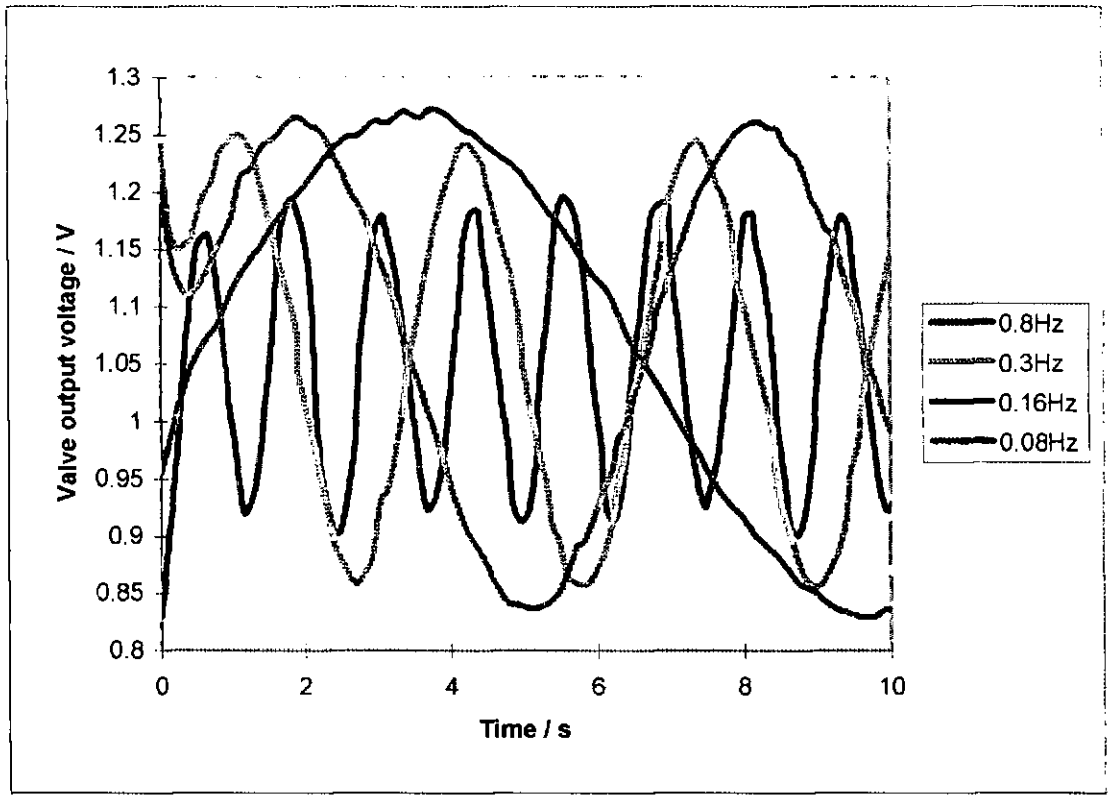

Figure 3.15 Flow valve modulation with frequency variation

Figure 3.16 shows the function of valve opening amplitude as a percentage versus frequency for the above data. This clearly shows the trend of decreasing modulation amplitude with modulation frequency. The zero frequency point is taken as the anticipated input modulation which experience shows has been obtained for non-modulated valve control. This figure shows that care must be exercised not to use modulation frequencies above those that the valve is capable of maintaining. This diagram does however provide a correction plot that may be employed for use at higher frequencies. We see that a decrease in valve amplitude becomes significant at frequencies greater than 0.2 Hz thus setting a ceiling for reliable measurements.

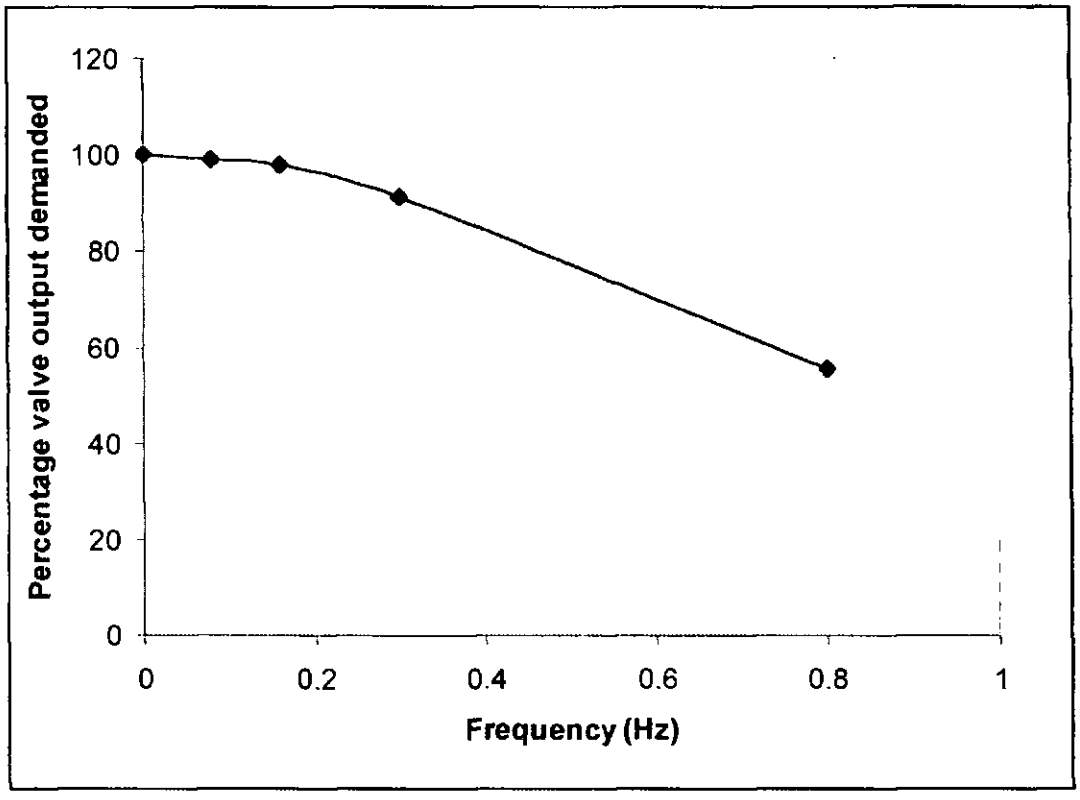

Figure 3.16 Flow valve amplitude with frequency variation

3.3.2 Amplitude effects

Figure 3.17 shows the effect of increasing modulation amplitude on the valve output. Provided limits of 5% and 95% valve opening were not passed, amplitude did not disturb the modulation provided modulations were performed at sufficiently low frequencies. For higher modulation amplitudes, a lower allowable maximum operation frequency was necessary before distortion became apparent. Distortion was found, irrespective of frequency, at the higher and lower ends of the valve openings <5% or >95% as the valves tended to stick either fully open or shut in these instances. Again, an initial operating period of a couple of seconds is seen for the valve to settle into a consistent modulation.

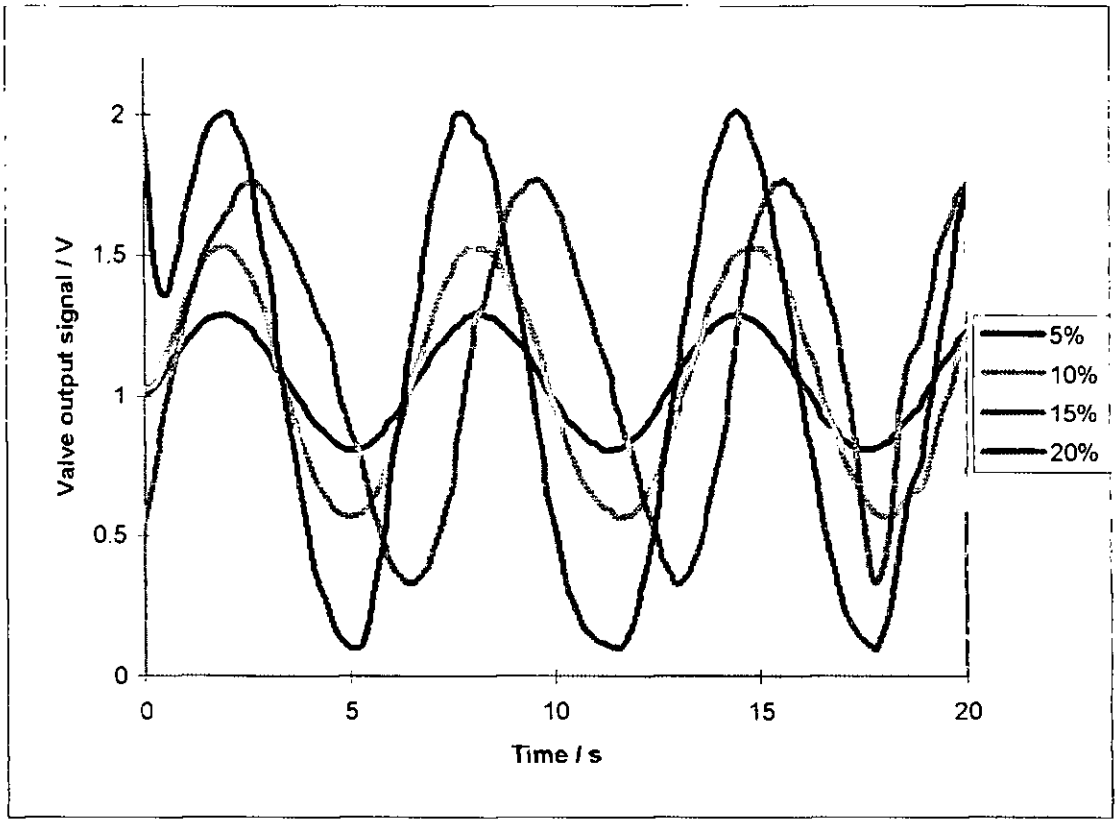

Figure 3.17 Flow valve modulation with amplitude variation

3.3.3 Valve opening offset

The offset, or mean oxygen concentration, also had no affect on dynamic valve performance provided very high and very low valve openings were not reached. Figure 3.18 shows the valve operated over a range of offsets with constant frequency and amplitude. This evaluation showed that if openings of >95% or <5% were attempted, the valve would stick at fully open, or fully shut, until these limits were no longer exceeded. These have the effect of rectifying the modulation, and were encountered if offset and amplitude levels were unsuitable. These effects were independent of frequency and valve type.

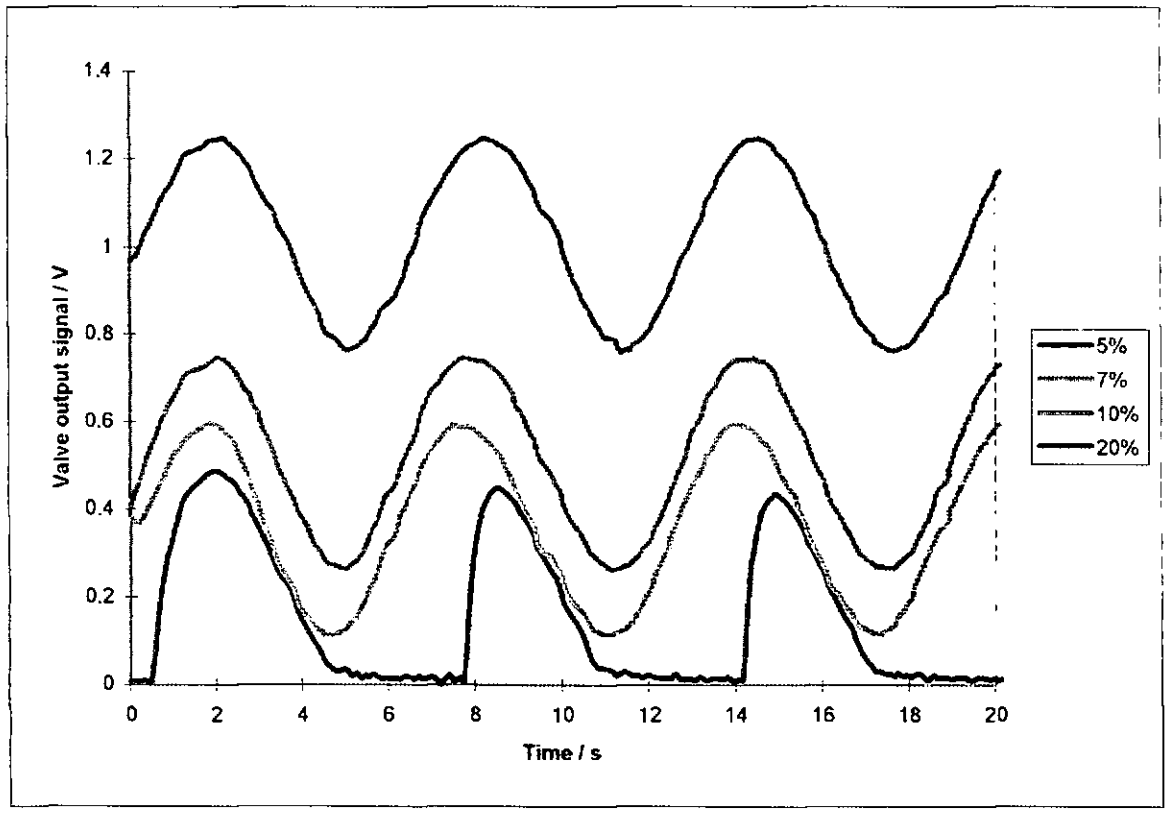

Figure 3.18 Flow valve modulation with offset variation

3.3.4 Flow valve type

Finally we examined two types of flow valves (designated type E and type Tr) from the same manufacturer (Brooks See C1.1.1). Comparison tests showed that the E type had significantly better response characteristics, especially when reducing flow rates were demanded. The resulting output sinusoids show unaffected increasing output but an extended reducing output giving a skewed modulation for the Tr type valve. This skewing occurs for both valves but occurs with type Tr valves at frequencies where E type valves operate without problem. This has led to the use of the 100 ml/min E type valve for oxygen modulation, with the 100 ml/min Tr type valve is used constant for nitrogen flows.

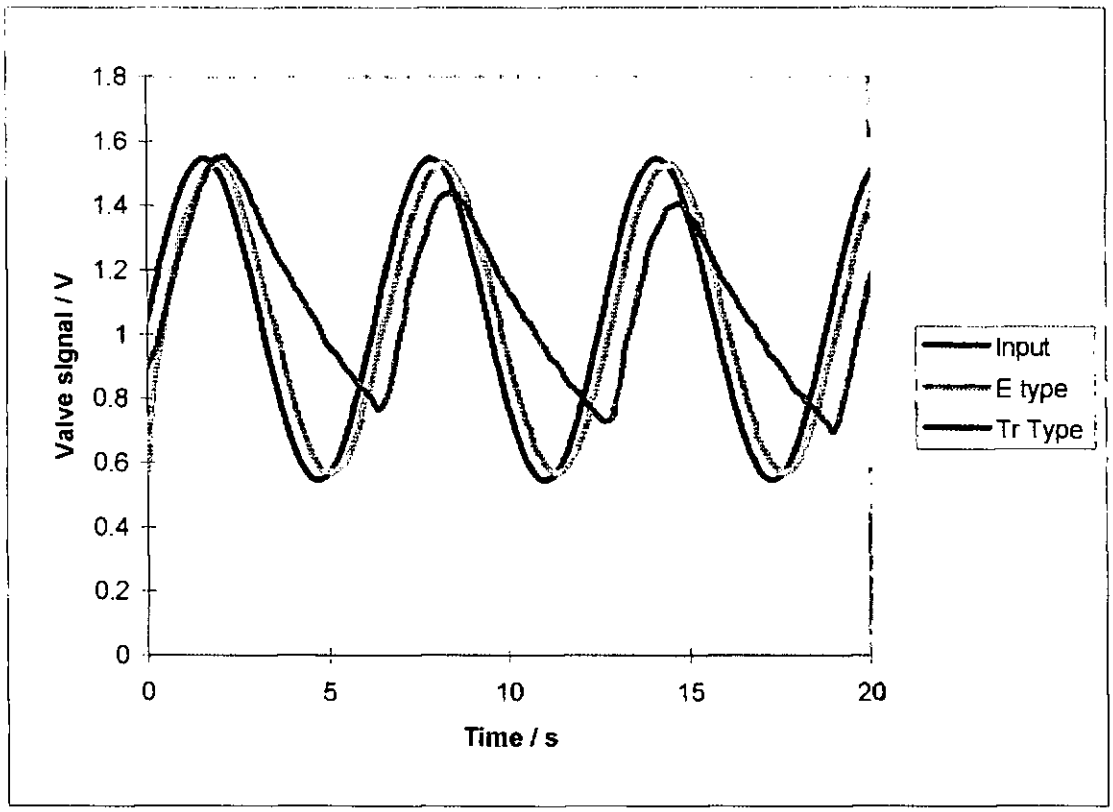

Figure 3.19 Flow valve modulation with variation in valve type

From these tests it was clear that the E type flow valve could be satisfactorily operated using a 4% oxygen gas modulation around 21% at a frequency of 0.2 Hz and lower. This was taken as the standard for testing of gas sensors. One other point to note is that modulations take a finite time to settle to a constant pattern. This manifests itself in the tests as the need to modulate, for 5 cycles or so, to be sure that results are stable.

A further problem anticipated was that of modulating gas flow rates. Whereas step concentration tests used a constant flow rate, switching gas composition, these tests involved the variation of both composition and flow rate. To ensure that flow variation was not a significant disturbance to the sensor output, a modulating flow valve was operated using air whilst a constant flow valve also flowed air. Thus a modulated flow rate of constant composition was generated and fed to a sensor operated at 700°C where response was know to be fast. Flow rate variation had the potential to affect results by either cooling electrodes or by introducing a small pressure fluctuation. This experiment showed no effect on sensor output provided flow variations were not very high or fast (>50 ml/min or >1 Hz). Had this problem occurred, it could have been minimised by modulating both oxygen and nitrogen flows but would have added to rig complexity and demanded two E-type flow valves for modulation matching.

3.3.5 Analysis procedures

The analysis of pressure modulation procedures reported in section 2.5.2 are demonstrated here for typical results of a typical modulation. The resultant plots show valve input/output and sensor response signals versus time (fig. 3.21) and a Lissajous figure for valve input signal vs. idealised sensor output (fig. 3.22). The idealised sensor output was obtained by matching a calculated sine wave in terms of offset, amplitude, frequency and phase to the measured sensor EMF. It is recognised that a sinusoidal concentration modulation does not give a truly sinusoidal modulation in output EMF due to the logarithmic factor in the Nernst equation, a point shown by figure 3.20. This figure shows theoretical EMF for sinusoidal concentration modulations around 21% oxygen at 800°C with varying amplitude. It is seen, through visual assessment, that below a 5% modulation, an approximation to sinusoidal can be made but these deviations become significant at higher amplitude modulations. The modulations used in this work are 4% modulations to retain the sinusoidal approximation whilst giving a good signal to noise ratio.

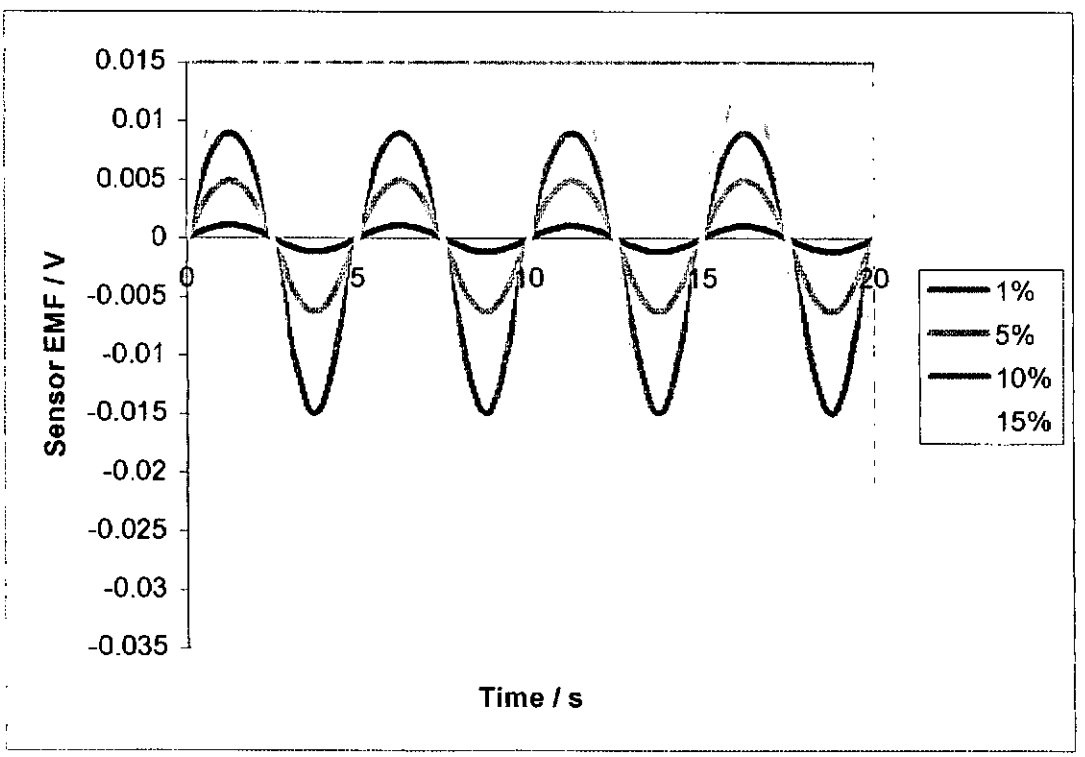

Figure 3.20 Deviation from sinusoid at high amplitude modulations

Figures 3.21 & 3.22 show a small phase difference in valve input / output resulting from the finite time required for physical changes in valve response to be realised. This delay is small and relatively constant for varying modulation frequencies and is sensor temperature

independent so is not examined further in this work. We also see that there is an almost negligible delay between valve output to sensor response. This was originally assumed to be attributable to the gas modulations taking little time to travel between the flow valve and sensor electrodes. In fact as we show later it appears that the flow valve output indication actually lags behind gas output. This delay may therefore be due to a attempt at noise reduction by long sampling times in the flow valve control equipment.

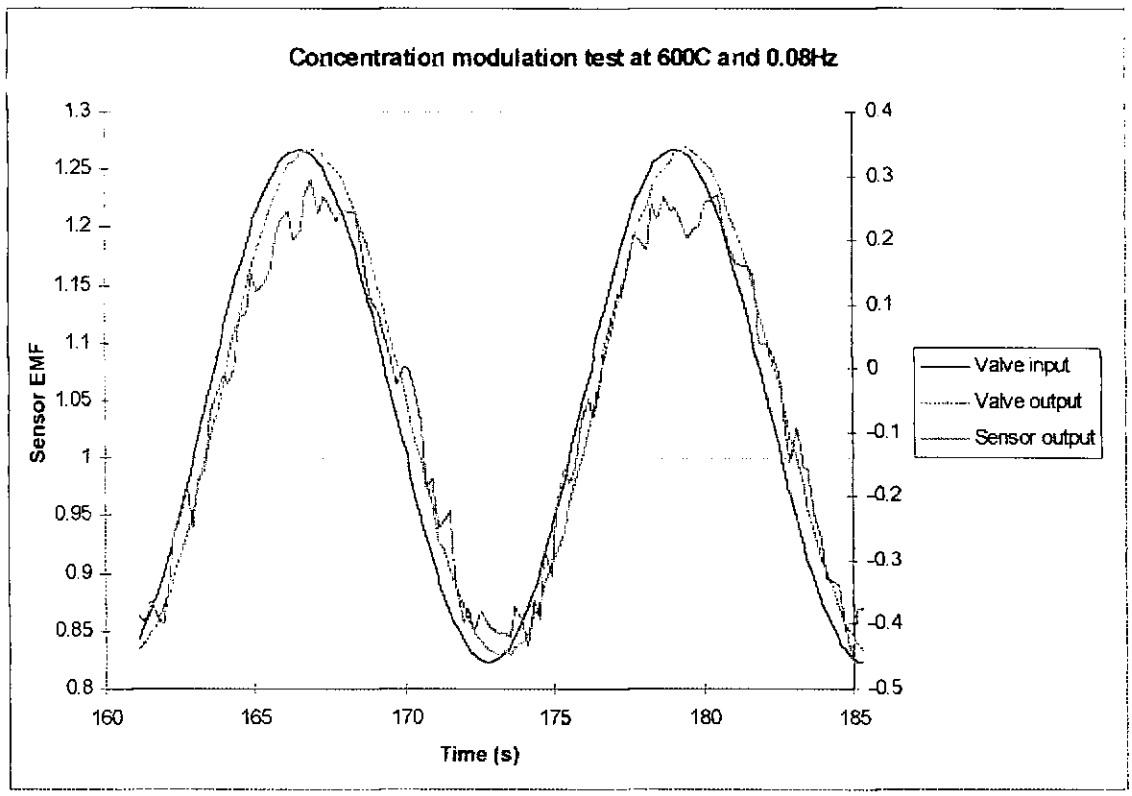

Figure 3.21 Input sinewave, flow valve output and sensor output signals

The Lissajous figure (Figure 3.22) demonstrates a gradient of unity, indieating an equal amplitude in flow valve input and output signals, with a center at 1.05 giving the mean value of the oscillation equating to a modulation around 21% oxygen with the flow valves used. We also see the phase shift discussed above revealed as an ellipse as opposed to a straight line which would be obtained if signals were in phase. Theoretically, a measurement of the phase difference can be obtained by comparing the ellipse maximum and minimum diameters (max/min = 1 = 90°, max/min = ∞ = 0° phase difference). In practice, considering the possibility of frequency mismatch and noise, it was considered easier and more reliable to compare phases of matched sine waves.

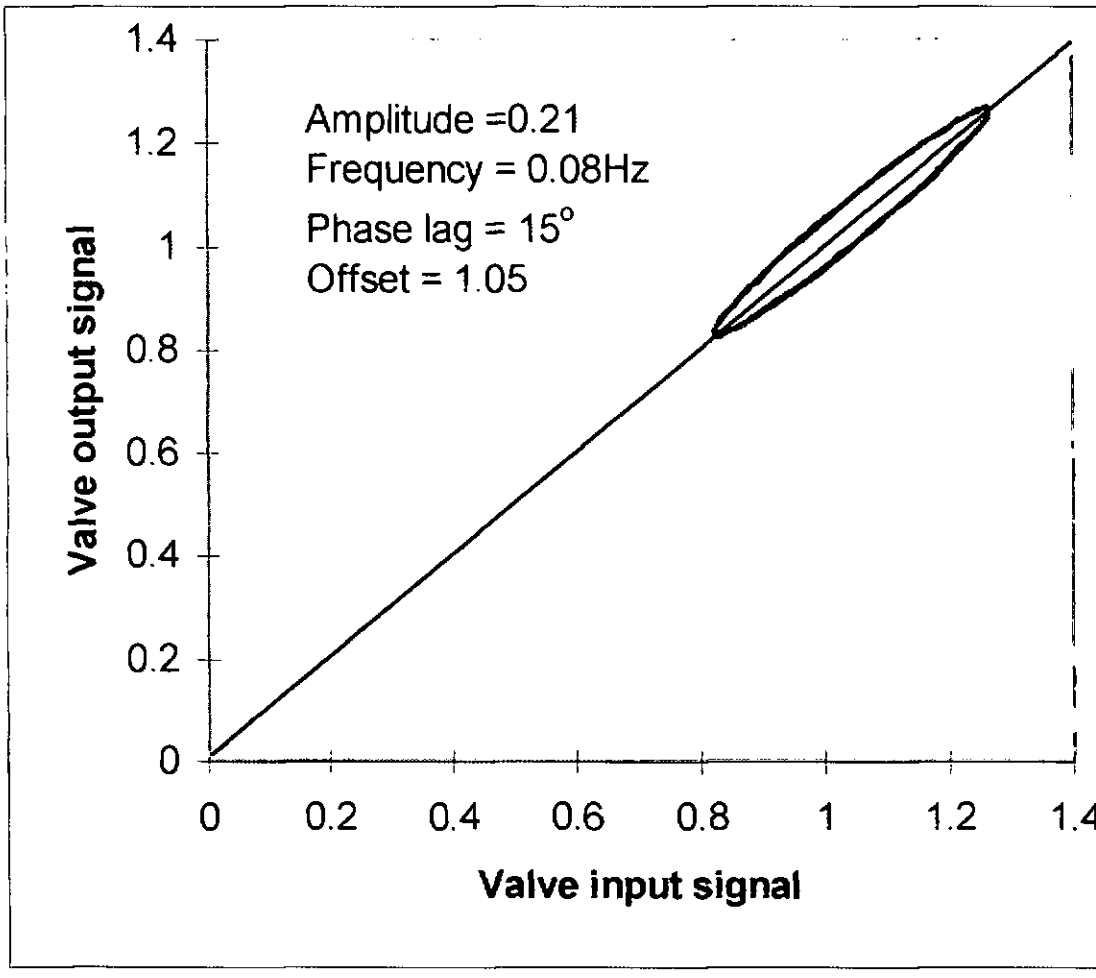

Figure 3.22 Mis-match in measured and calculated signal phases

3.4 Pressure modulation technique

The technique of pressure modulation is similar in many respects to that of concentration and as far as the sensor output is concerned, both sinusoidally vary the oxygen partial pressure and so are very closely related. The main differences arise from practical aspects of modulation realisation, leading to different practical problems as discussed in this section, and the mechanical difference of bulk gas flows rather than concentration flows involved in the modulation reaching the measurement electrode.

3.4.1 Mathematical model

A mathematical model has been developed for predicting and comparing modulation EMFs derived from pressure modulation tests. The model assumes the sensor obeys the Nernst equation, ideal gas law for isothermal pressure / volume changes and a sinusoidal change in piston displacement. Factors not included are:

- Non-Nernstian EMFs encountered at low temperatures.

  At temperatures where non-Nernstian EMFs were encountered, response rates were sufficiently low not to affect the measurements taken in this work. Non-nernstian EMFs from sensors at low temperature have been reported [21] Fouletier et al and [36] Badwal et al.

- Electrode temperature differentials.

  Electrode temperature differentials have been discussed in relation to concentration modulation work, the same principles are applicable in pressure modulation work with similar results and consequences. This has been encountered by Kocache et al [67]

- Temperatures generated during pressure modulations.

  It is recognised that the ideal gas law for isothermal pressure changes does not hold perfectly for the rapid modulations under examination here, however temperature / pressure changes are expected to be small compared to the sensor operating temperature and modulation pressures produced.

- Pressure generated through heating / cooling of test atmosphere gases.

  As a volume of gas is passed from a cool region to a hot region, the gas will naturally expand and since the volume is not changed to compensate, and additional pressure increase will arise. The reverse is true for hot gases entering a cool area. These effects would cancel out over a number of cycles but would also lead to a skewed sine pressure modulation being produced.

- Non-linearities in the pressure generating cycle.

  Non-linearities were visually observed at lower frequencies and higher pressure modulation amplitudes, where the motor / gearbox combination lacked the power and momentum to ensure sinusoidal modulations. In order to reduce this effect, low frequencies / high amplitudes were avoided as far practicable.

- Gas leakage.

  Leakage of gas pressure from the closed modulation system would have also introduced irregularities into the system. However, no significant gas leakage was observed from the system under steady state conditions over a suitable time period (several minutes).

- Test-rig expansion.

  The relatively low pressures and use of suitable materials means that expansion of the test-rig volume under pressure would have been negligible in comparison to the measured test-rig volume.

- Instantaneous sensor response

  Sensor response at this stage is taken as instantaneous, a situation approximated at higher sensor temperatures.

The starting equations for the mathematical model were:

$$EMF = \frac{RT}{4F} \ln \frac{P'}{P''} \qquad \text{Equation 3.4}$$

The Nernst equation

$$\frac{P_1}{V_1} = \frac{P_2}{V_2} \qquad \text{Equation 3.5}$$

Ideal gas equation for an isothermal volume change

$$Y = Offset + Amplitude \times Sin(Time \times Frequency + Phase) \qquad \text{Equation 3.6}$$

Describing a sine wave of given offset, amplitude, frequency and phase

Assuming we have the same oxygen concentrations on either side of the cell, the device measures the barometric pressure component of the partial pressures P'=P_1 and P"=P_2. P_1 is taken as the reference (atmospheric) pressure and assuming isothermal behaviour P_2 can be described as a function of P_1 and the change in volume from equation 3.5.

$$P_2 = \frac{P_1 \times V_1}{V_2} \qquad \text{Equation 3.7}$$

$$EMF = \frac{RT}{4F} \ln \frac{P_1 V_2}{P_1 V_1} \qquad \text{Equation 3.8}$$

P_1 cancels out and the EMF is seen to be dependent upon the volumes V_1 and V_2. V_1 is the volume of the test-rig where atmospheric pressure is obtained (V_{rig} taken as the sweep mid-

point) and V_2 is the volume of the test-rig at any specific moment. A sinusoidally oscillating piston varies the volume and hence the pressure. We can equate for this bringing in the equation for the volume modulation where:- r, l, t, f and p are the piston radius, sweep length, time, frequency and phase respectively from equation 3.6.

$$EMF = \frac{RT}{4F}\ln\left(\frac{V_{rig} + (\pi r^2 l \sin(tf + p))}{V_{rig}}\right) \qquad \text{Equation 3.9}$$

Alternatively it is also possible to work backwards from the EMF to calculate the actual pressures using the modified version of the Nernst equation (see equation 3.10). In the mathematical model we can also include the factor of 100 used for the amplification of signals used to give a better signal to noise ratio.

$$P_2 = P_1 \exp(-4FE / RT) \qquad \text{Equation 3.10}$$

Dimension measurement of the pressure modulation test-rig has revealed a midpoint volume of 122.2 cm^3 with maximum and minimum volumes achieved upon modulation of 127.0 and 117.4 cm^3 respectively. These equate (using equation 3.8) to pressure changes of +0.0406 and –0.0375 atm respectively giving a total pressure change of 0.781 atm. These figures relate to the modulations operated with the minimum modulation amplitude as dictated by gearbox cam positions. Pressure calculations take the assumptions given at the start of this subsection.

A result of this model is shown below (figure 3.23) which depicts the anticipated sensor output compared to a sinusoidal pressure modulation input. At piston sweep lengths (higher modulation amplitudes), the model predicts a similar deviation from sinusoidal output to that given in figure 3.20 for concentration modulation work. Figure 3.24 shows the calculated pseudo sine of the resultant sensor output with sweep length. According to the model prediction, this deviation remains small within the range of 0 to 20 mm sweep used in this work.

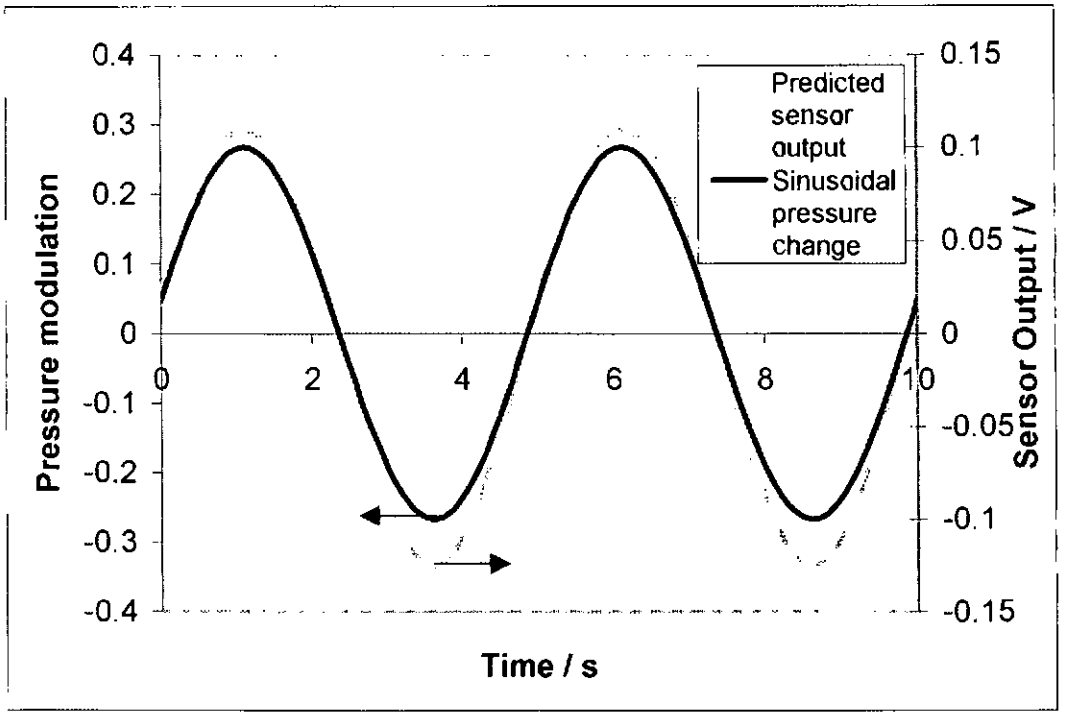

Figure 3.23 Predictions of the mathematical model

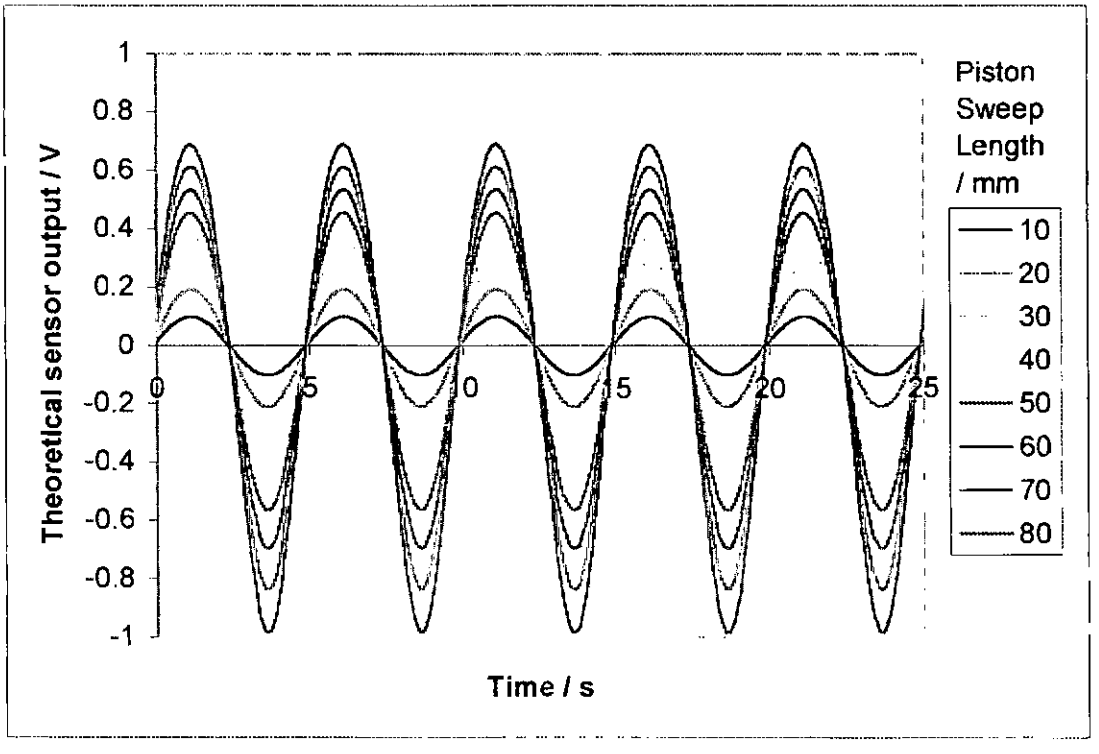

Figure 3.24 Modelled sensor output with piston sweep length

In summary, the pressure modulation mathematical modelling has been used to assess the predicted output from the pressure modulation rig such that excessive deviations from the expected sensor output could be identified and quantified. This has enabled measurements

to be taken at an amplitude where significant perturbation is achieved without too great an effect from the logarithmic nature of the Nernst equation.

3.4.2 Rig verification

Pressure modulation rig verification tests have been conducted by comparing measured sensor outputs with the mathematical model detailed above. These test measurements were conducted by varying test parameters to find which parameters had a non-negligible effect on sensor response. In addition, tests were conducted at temperatures where sensor response was known to be fast in relation to the input frequency.

The first verification test performed was to verify that a pre-determined frequency could be attained by adjusting the potential applied to the motor with each gearbox utilised. Figure 3.25 shows the results of these tests. We see that linear plots were obtained with a slope of 0.3505 and 0.103 Hz/V for the low and high ratio gearboxes respectively, indicating a linear relation between applied voltage and attained frequency. Least squares line fitting to these trends gave R^2 values of 0.9994 and 0.9999 for low and high ratio gearboxes respectively. The method of motor voltage control of desired frequency was deemed acceptable for the developmental work carried out here. We also see non-zero intercepts for each gearbox. These intercepts are due to an initial motor potential required to overcome sticking friction within the apparatus. This indicates that a motor potential of approximately 0.97 and 0.87 V is required to initiate motion for the low and high ratio gearboxes respectively. Again, these initial start-up potentials were reproducible and so did not prevent this manner of frequency control. For more accurate work, a rotational velocity transducer and closed loop monitoring / control system would be desirable.

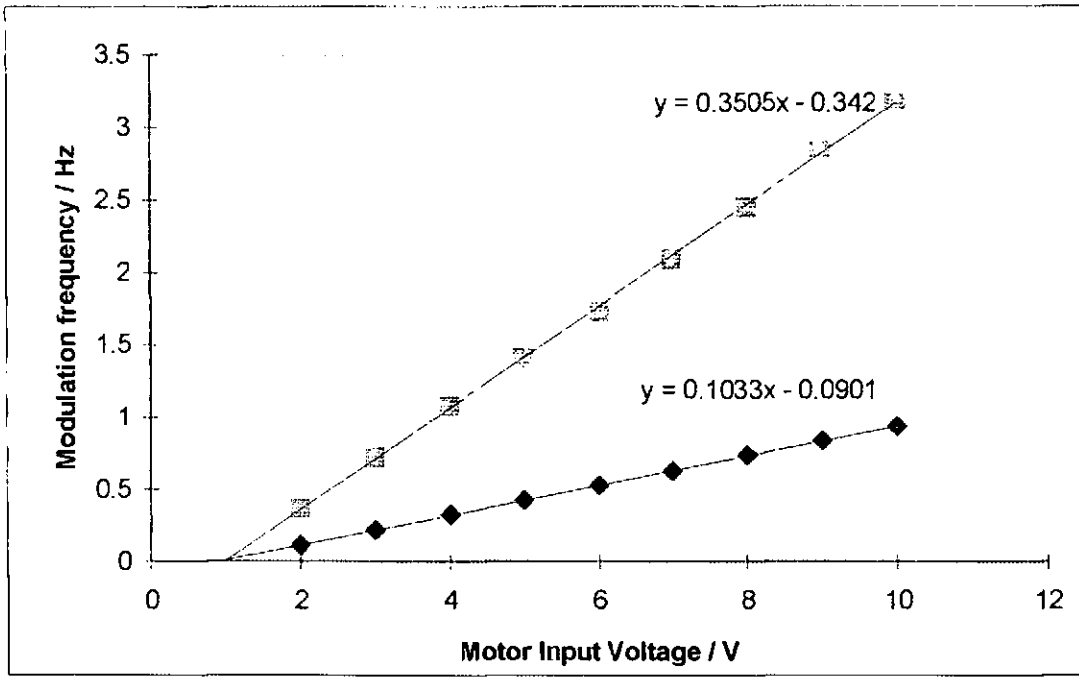

Figure 3.25 Modulation frequency vs. motor voltage

The next test set performed investigated pressures produced by modulations as the gearbox cam position was altered to provide various modulation amplitudes. The results are shown in figure 3.2.6. This chart shows measured sensor voltage amplitude readings along with values calculated from dimensional test-rig analysis in conjunction with equation 3.9. These results show that attained and expected pressures do not match with a higher amplitude realised than expected from theoretical considerations. Possible sources for this disagreement have been explored as reported below in order of assumed influence:

- Temperature modulation of the sensor

  This would also have been detected by the thermocouple and one would expect the sensor amplitude to drop output as pressure increases and increase as pressure drops due to heat exchanges whereas the opposite has been observed here.

- Incorrect calculation of test-rig volume

  An over-estimation of test rig volume could account for the discrepancy seen, however this would require a test rig volume of 103.3 cm^3 rather than the 120.3 cm^3 measured. Considering the individual component volumes used for this assessment there are no obviously incorrect volumes and the resultant of a series of volume over estimations unlikely considering the approximate 15% difference.

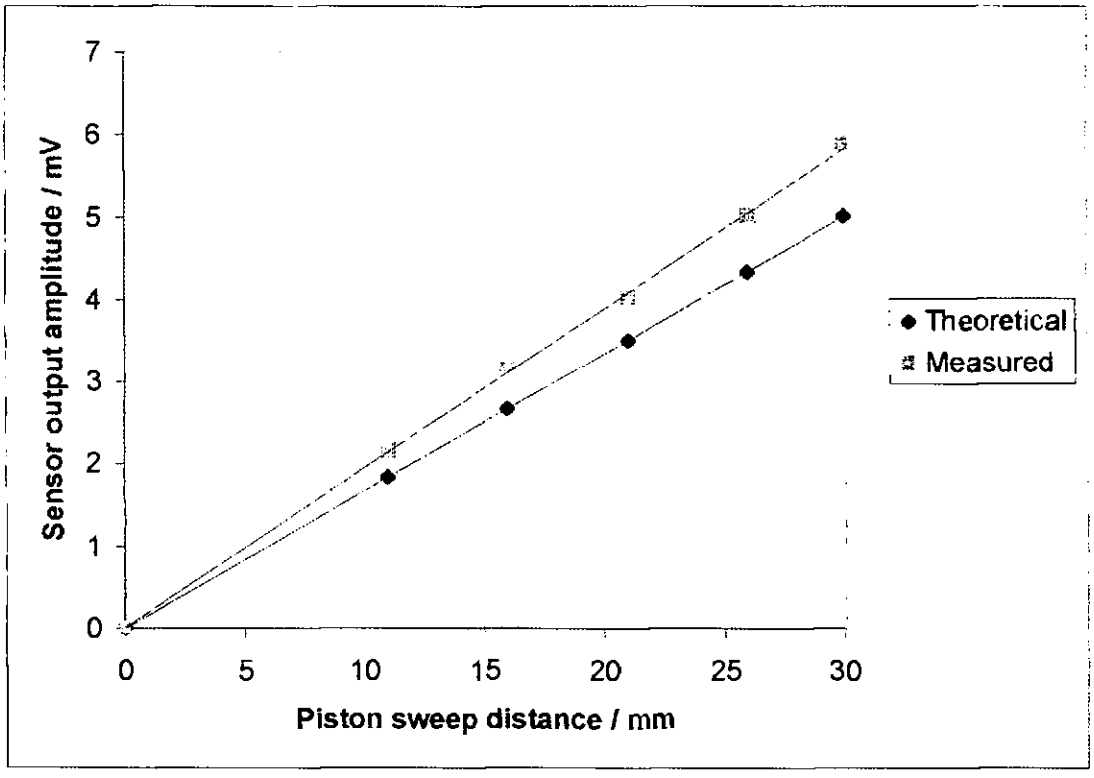

Figure 3.26 Sensor output vs. Piston modulation amplitude

- Gas leakage into/out of the system

  Again gas leakage would tend to reduce rather than increase the realised modulations. However, for reference, an analysis of leakage rates was carried out.

- Modulation of oxygen concentration

  There is no obvious way in which the modulation of barometric pressure could influence the oxygen concentration measured at the measuring electrode. This is dismissed as a cause of error.

The factor of gas leakage from the system was investigated by measuring pressure decay over time using the output of the sensor as a pressure measurement. The results showed a slow rate of leakage estimated at around 10 μbar per second at maximum pressure attained at the 10 mm gearbox position. This translates to a loss 0.025% of pressure reading per second and appeared to he virtually linear over the five minutes of leakage time examined. Whilst it is realised that the leakage would not have been linear over greater time scales, the modulations investigated here were of the order of seconds and so gas leakage can be assumed as zero. With these modulations being centred around atmospheric pressure, during modulations, total leakage averages out to zero so length of test-time is not significant.

- Gases experiencing expansion/contraction through heating/cooling as passed into furnace hot/cool-zone

  A modulation of local gas temperature with pressure modulation through flow of gas between cold and hot regions would give a pressure amplitude greater than that calculated. This was not detected by a modulation in thermocouple temperature but this may have been too slow to respond sufficiently to become apparent. In the absence of a better explanation, this is deemed the most likely cause. Direct pressure measurement using a pressure transducer would provide allowance of these effects. In preference, the modulation amplitudes were reproducible and so were not deemed to have influenced the application of this technique for response rate measurement.

3.5 Summary

Using frequency response analysis techniques, little difference was measured between M4 and M6 cermets but both cermet electrodes gave superior performance with lower electrode impedance than platinum metal electrodes. The electrode firing temperature did influence the electrode impedance but the effects were not sufficient to necessitate avoidance of electrode exposure to high temperatures. Electrode deposition by painting of pastes has shown to be lacking in terms of providing a reproducible cell impedance. The effects of oxygen concentration on electrode impedance are not obvious and require specific investigation for the results to be fully understood. Electrode microstructures do show a degradation with time with an initial rate of ≈3% / hour at 700°C. This is thought to occur through electrode sintering. Plastic-ceramic electrolyte properties were influenced by sintering temperature, particularly for temperatures <1300°C. Electrical and mechanical properties were similarly affected.

The step change test apparatus has been shown adequate for measurements of potentiometric sensor response rates at low temperature where the response is slow. The rig has not been optimised for extremely quick step changes but rather has been designed to give an easily interchange electrolyte cell to allow comparisons of various electrodes. The test-rig has limitations in terms of small electrode temperature differentials but these are not sufficient to have warranted re-design.

This work has clearly demonstrated the technique of concentration modulation and has led to the development of an integrated system for carrying out such experiments. The test-rig

has been characterised to give confidence in its operation and to find the limits at which it fails to operate satisfactorily. This technique has not previously appeared in the literature, probably due to the imagined degree of complexity and analysis compared to that of step change methods. In actual fact these problems have proved less challenging than expected, indeed the set-up is simpler than that employed for the step changes. This is chiefly due to the flexibility of equipment used and the benefits of virtual instrumentation. Data analysis requires a similar degree of processing once the results have been obtained. Further modifications envisaged, may take care of this automatically. The test-rig as described previously (para 2.5) is similar to the step change rig with complexity removed as the solenoid valves and interfacing are replaced by direct interfacing of computer to flow valve controller.

Test-rig verification experiments have highlighted the limits to concentration modulation parameters obtainable with the current set-up. These have shown that the system may be used with confidence provided that these limits are not exceeded. The question of valve output indication lag behind actual valve output has not been fully explained, however in using the input waveform for comparison, any delays here can be grouped with gas feed rate delays and regarded as an inherent delay in the system and subtracted from the overall phase lags measured. These lags have been shown to be consistent and not alter significantly over modulation frequency or sensor operation temperature.

An obvious enhancement is to include the frequency response analyser for generating modulations and analysing data produced. This should provide far greater accuracy due to its noise rejection and analysis capabilities over a great number of oscillations. The inclusion of the frequency response analyser would also allow far lower frequencies to be examined with greater ease due to the manner of data analysis that rules out manual / spreadsheet analysis. There also exists the possibility of increasing the upper frequency limits. Small improvements in this area are possible by using a smaller valve modulation amplitude but for significant improvements the gas valve used needs to be upgraded or substituted. A suitable system may perhaps be developed around a flowing inert gas being dosed with oxygen using a solid electrolyte oxygen pump. The main problem with this system would be attaining sufficient ionic current through the electrolyte to maintain a reasonable amplitude and gas flow rate.

A mathematical model has been developed to describe basic expected response of pressure modulation analysis. This model incorporates geometric test-rig dimensions, ideal gas laws and sensor output equations. Results from this mathematical model agree to a limited extent with initial test-results to enable model short comings to be revealed. There does exist a difference between calculated and measured modulation amplitudes, however this is not thought to be crucial to application of the technique. Pressure leakage from the system has been shown to be negligible for the frequency ranges utilised. Further improvements for this technique would include, a general improvement in rig build standard, use of a more powerful motor, incorporation of a pressure transducer and feed back system for improved frequency control. An additional improvement would result from automation of the data acquisition and analysis technique.

CHAPTER 4

TECHNIQUE APPLICATION TO A Pt/YSZ SYSTEM

RESULTS & DISCUSSION

4 Technique application to Pt/YSZ system

In this chapter we report the results of applying the response rate measurement techniques to oxygen measurement cells of Pt/YSZ. Techniques are applied to cells of both potentiometric and amperometric types in order to assess both sensor performance and technique application.

4.1 Potentiometric cells

4.1.1 Impedance spectroscopy

Impedance analysis was used to examine the potentiometric sensors employing zirconia tubes purchased from Dynamic Ceramic specifically for response rate investigations. These tubes had a pair of M4 platinum cermet electrodes applied to the end faces and were fired at 1000°C for 1 hour. The impedance sweeps were performed using temperatures from 400 to 600°C and using oxygen concentrations of 21, 5 and 0.5%. The results (fig. 4.1) showed electrolyte properties towards the lower end of those obtained from green sheet samples (see section 3.1.2) In figure 4.1 solid lines depict limits found for electrode impedance in section 3.1.2, dashed lines depict the electrolyte limits found. The result was a slightly surprising as the electrolyte was significantly thicker in these sensors, at around 3mm, compared to 0.5mm for a typical fired green specimen yet electrolyte impedance was generally lower. As with plastic-ceramic sheet samples, similar impedance was measured for both electrolyte grain and grain boundary impedances and therefore electrolyte purity is thought to have been similar for each electrolyte type. Electrolyte density measurements also gave similar results with >97% theoretical densities. Electrodes were also of comparable composition and condition to those used in plastic ceramic work but were slightly larger. This geometric electrode area difference accounts for the comparatively low impedance of these dynamic ceramic cells with similar ratio of electrode / electrolyte impedance maintained. There does exist a degree of curvature to the electrode impedance plot. The origin of this curvature lies in the degree of extrapolation required to obtain readings within a reasonable time frame at these temperatures. Even with several hours of measurement time, only a small proportion of the semi-circle arc may be obtained thus substantial errors can be obtained. Significantly lengthening test time could have produced more accurate data.

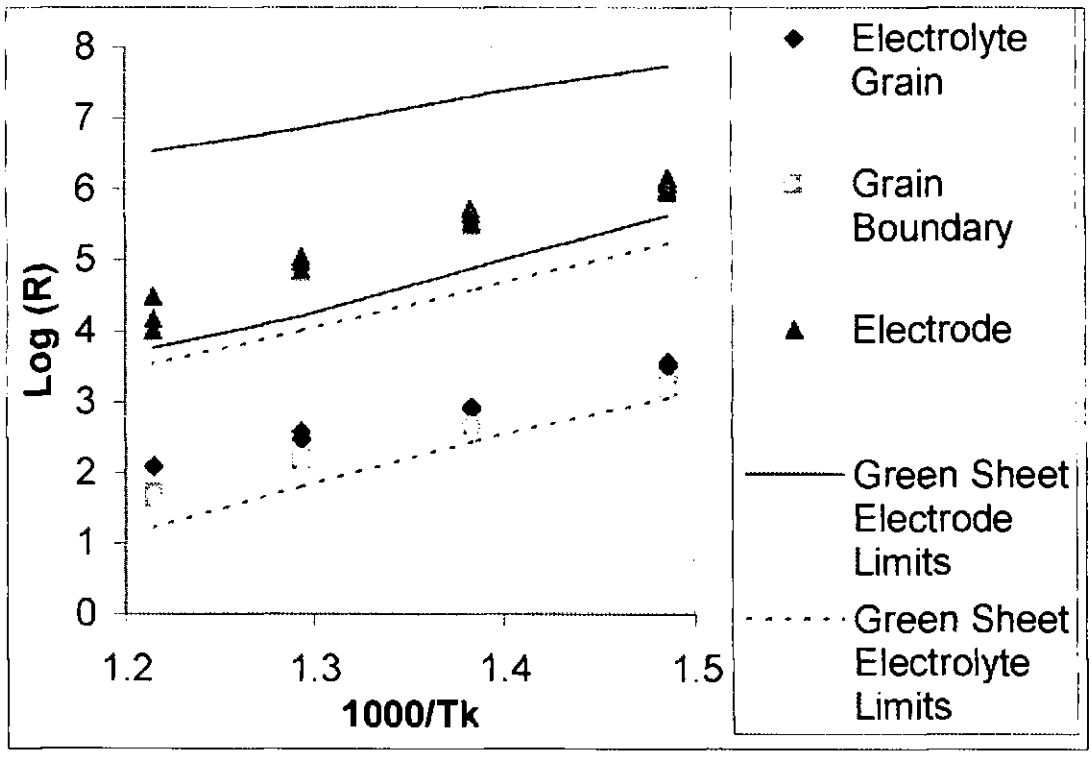

Figure 4.1 Arrhenius plot for potentiometric sensor, showing electrolyte and electrode components

In addition to component resistance, impedance spectroscopy also allows measurement of component capacitance to be measured. Figure 4.2 shows an Arrhenius plot of measured cell capacitance taken along with the above resistance data. The capacitance shows a steady decrease with temperature. The significance of capacitance in terms of sensor response rates is that an electrical circuit is established with an effective time constant given by the RC electrical time constant T = RC.

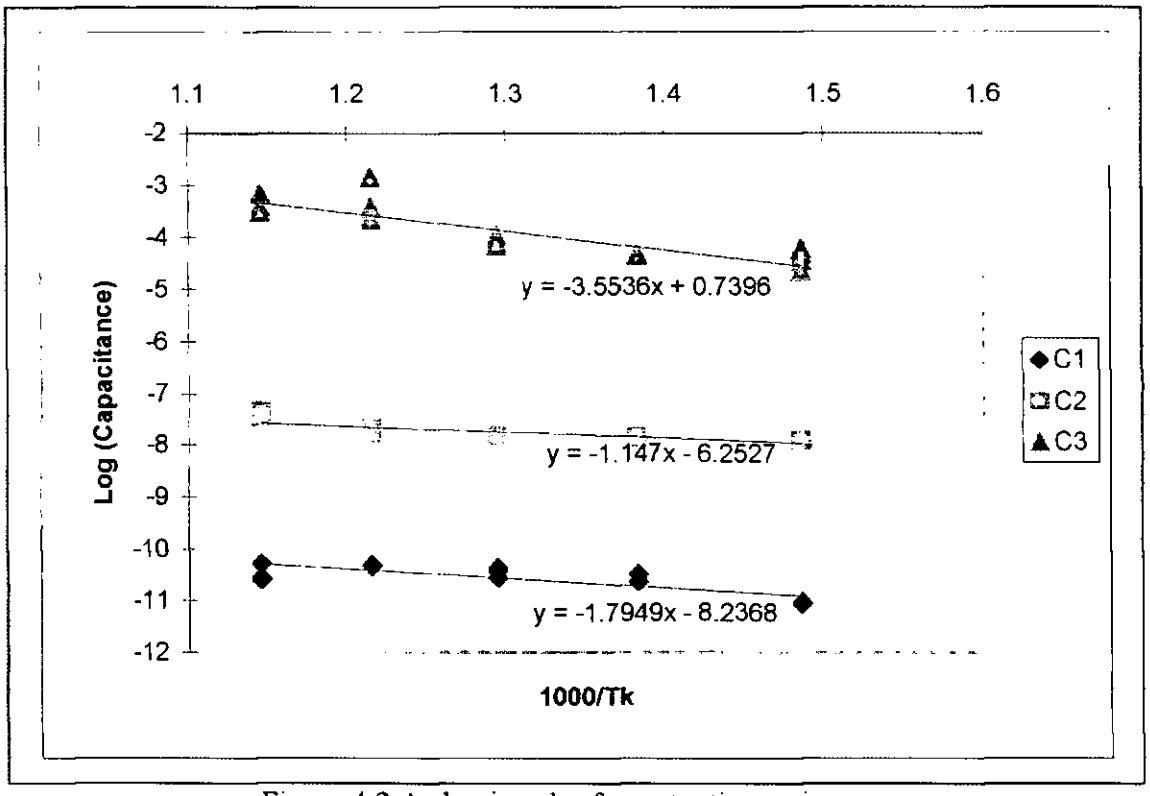

Figure 4.2 Arrhenius plot for potentiometric sensor,
showing electrolyte and electrode capacitance components

Using the electrical time constant along with the data for variation in resistance and capacitance with temperature from figures 4.1 and 4.2, we are able to calculate the time constants for the individual components in the system. These are depicted in figure 4.3 over a relevant temperature range. From this figure, three things are immediately apparent: Firstly the dominant time mechanism is clearly that related to electrode impedance, a fact widely reported by other workers for potentiometric type devices. Secondly a rapid drop in time constant for tens of seconds at 400°C to tenths of seconds at 800°C for the dominant mechanism was recorded. Again this is a widely reported phenomenon. Finally the time constant attributable to the electrolyte grain impedance has a significantly lower time constant than does that of the grain boundary. The root of this is due to the lower capacitance since they have very similar resistive values. It is of course this difference in capacitance that gives the separation of impedance semi-circles. The implication of this is that electrolytes with large grains and therefore fewer grain boundaries would give faster response. The benefit of increased grain size would need to be assessed against the reduction in grain boundaries and overall it is still the electrode response which dominates.

The conversion of impedance data to time constant data is useful in this work as it allows direct comparison of the results obtained through impedance analysis to that obtained by the other measurement techniques employed.

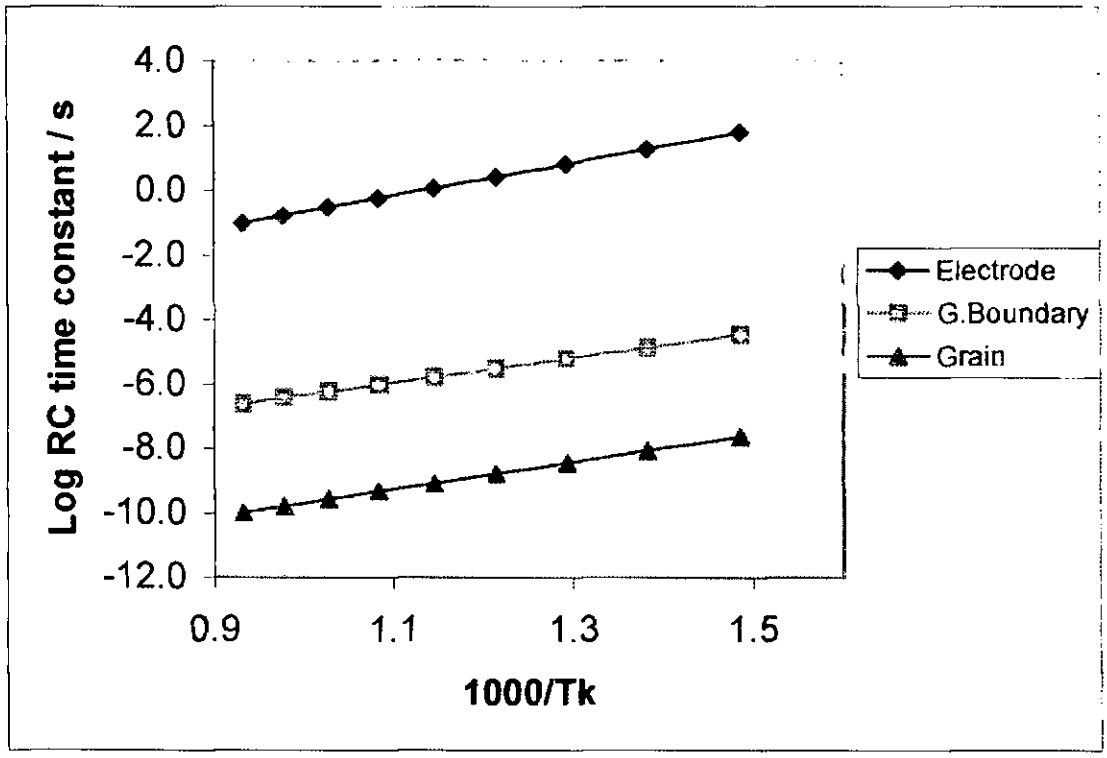

Figure 4.3 Calculated time constants for potentiometric sensors using impedance analysis results.

Figure 4.4 presents the impedance data recorded as part of the electrode study from section 3.1.2. This figure shows the data only for the electroplated sample both before and after the electroplating process (open markers before, solid markers after). This clearly shows the improvement achieved in the electrode impedance alone with no change in electrolyte results. This is an important result as it gives a high degree of confidence in the results as the technique is shown to be repeatable and gives directly comparable evidence of the electrode performance enhancement. In terms of operation temperature enhancement, the electro-plated electrode has a similar impedance to that of the cermet electrode which is some 100°C lower in temperature. This data is reproduced here to allow comparison of electro-plating improvements measured by impedance methods to similar improvements recorded using the alternative techniques.

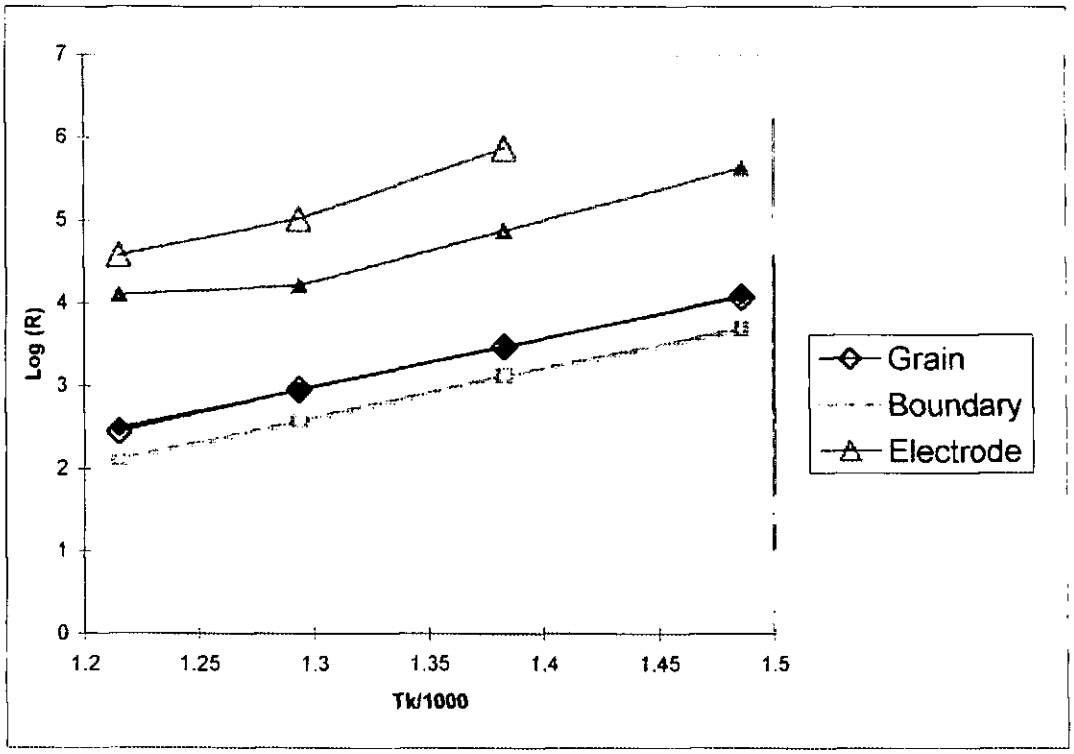

Figure 4.4 Arrhenius plots of impedance data for cermet (open markers) and electroplated (solid markers) samples from plastic ceramic.

Another useful manipulation of this impedance data is the conversion back to the phase angle and magnitude data originally recorded by the frequency response analyser. This is plotted in Bode plot format in figure 4.5 below. Presentation of data in this manner allows easy comparison with data recorded using alternative techniques for similar devices. This also gives a good idea of the data trends to be expected over the frequency ranges recorded. In figure 4.6 this data is reduced to the frequency ranges 0 to 5Hz employed by this work for the alternative response rate measurement techniques. In addition the scales are changed to linear scales to provide a clearer indication of changes in this region.

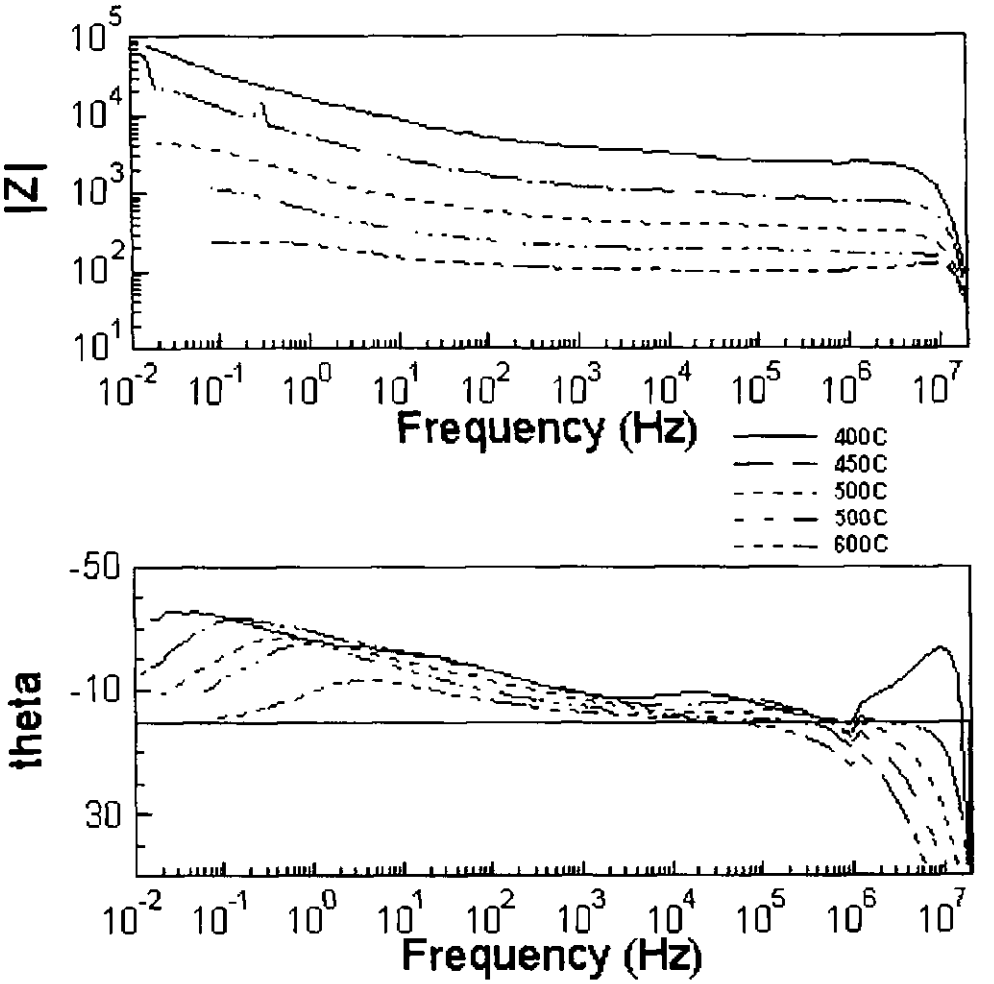

Figure 4.5 Bode plot of magnitude and phase angle recorded by impedance spectroscopy for the cermet electrode sensor at 400 to 600°C

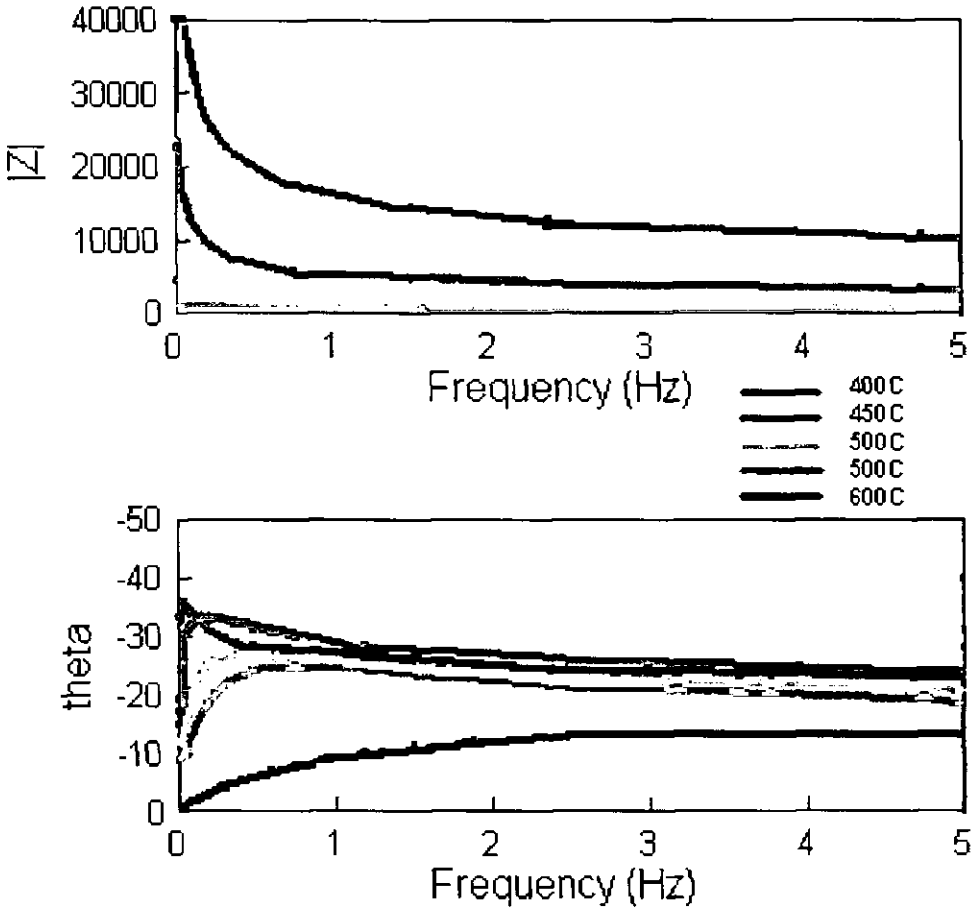

Figure 4.6 Bode plot of magnitude and phase angle over limited frequency range for the cermet electrode sensor at 400 to 600°C

4.1.2 Step change technique evaluation

Figure 4.7 shows the response of a platinum cermet electrode potentiometric device using a concentration step change. The figure shows a complete scan time of 500 s triggered a few seconds before step was applied. The data have been normalised by addition of an offset (identified earlier as caused by small electrode temperature differentials) but the data are not indexed to final peak or Nernst EMFs. The results depicted at 450 and 475°C show a low frequency oscillation, the origin of which has not been conclusively established, this oscillation was not found in subsequent runs and so was probably attributable to induction pickup from other electronic equipment. These tests have demonstrated very clearly the increase in sensor response rate with decrease in temperature. The higher temperature steps show that test-rig delays are negligible when working at the lower temperature response of interest in this research. At temperatures below 475°C the gas steps begin to increase with increasing temperature. This is again

attributed to electrode temperature differentials, which, at low temperatures have been reported to produce non-Nernstian behaviour in these cells [71]. The full magnitude of these non-Nernstian EMFs is not revealed as the step is reversed before the full sensor output is realised, however approximate graph extrapolation estimates have returned values of 80 to 100 mV at 425°C and 50 to 70 mV at 475°C. As a significantly higher output was seen at 425°C than at both 400 and 475°C, it is believed that this is not an easily reproducible effect in terms of maximum EMF.

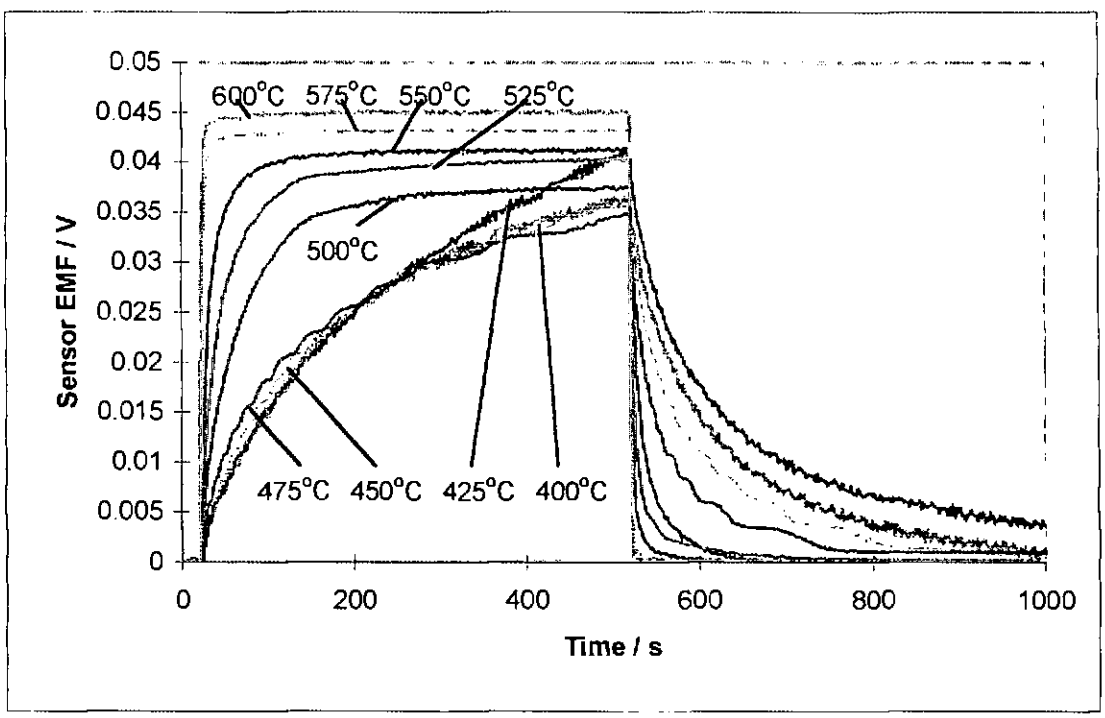

Figure 4.7 Step change response with sensor temperature variation (not indexed)

The results for these tests are further analysed in figure 4.8 where we compare peak EMF to the calculated Nernst EMF as well as response times to 70% of peak and Nernst EMFs. In this figure open markers indicate Nernstian EMFs whilst closed markers indicate peak EMFs. We see agreement between peak and Nernstian values at high temperature but significant deviations occurring at lower temperatures where EMFs higher than those predicted by Nernst are attained. This deviation is also translated onto the response times, affecting sensor readings at lower temperatures. Assessment of the time taken to reach both 70% of peak EMF and 70% of Nernst EMF, shows times taken to reach 70% of Nernst EMF begin to drop at low temperatures. This indicates that for low temperatures, errors in response rate measurement can arise where deviations from Nernst law are seen. Such deviations have been reported in the literature [37] and attributed to small temperature differentials at low temperature. Although these deviations do affect the data,

the general trend in results is very clear. Okamoto et al [71] found non-Nernstian EMFs attributable to CO adsorption onto Pt sites at similar temperatures. No CO presence would be expected during these tests so this mechanism is disregarded.

Also included in figure 4.8 are data recorded for different electrode deposition techniques. Electrodes employed were the M4 platinum cermet electrodes for which the basic data is shown in figure 4.7, as well as cermet electrodes enhanced by electro-deposition of platinum and enhanced electrodes annealed by high temperature exposure. In general response rates rose with decreasing temperature but significant improvements were realised where the electroplating technique was employed. Whilst high temperature exposure shows a definite reduction in response rate for electro-deposited electrodes, a clear advantage over cermet electrodes was maintained. Translating the improvement into temperature reductions by a simple read across the temperature scale, we see that the electro-plated sensor out-performed the cermet electrode sensor by almost 100°C. A similar improvement was also seen in impedance spectroscopy work (see section 4.1.1). Electroplating improvements include both the lower temperature to which the Nernst EMF was obeyed and reduction in response times. These improvements are diminished upon annealing but still retain an advantage over simple cermet electrodes. This improvement may result from an enhancement of electrode distribution or the presence of additional metal as in this case the plating used DC using a sacrificial platinum wire.

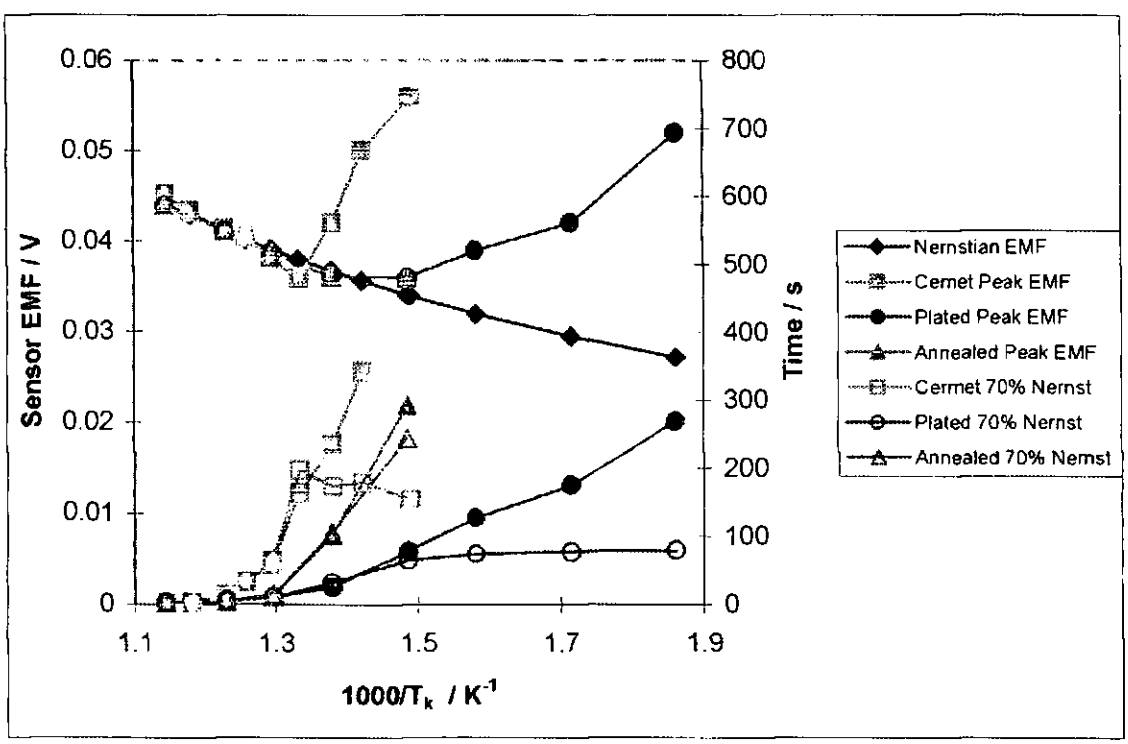

Figure 4.8 Arrhenius plot of step change response times and EMFs

$$Pt^{IV}Cl_6^{2-} + 4e^- \leftrightarrows Pt + 6Cl^- \qquad \text{Equation 4.1}$$

Platinum deposition rates can be simply calculated using Faraday's law, given the atomic mass, number of electrons required and the density of platinum. We see that the mass of deposition is given by Atomic weight / number of electrons / Farad which returns a value of 0.505 μg/mA.s. This equates to a volume, taking the density (of 21.45 g/cm^3) into account, of 2.36×10^{-5} mm^3 / mA.s. Again, taking into account the macroscopic electrode area covered we can calculate an electrode thickness produced by deposition. Taking a typical macroscopic electrode area of 12.5 mm^2 we find a depth of 1.88 nm/mA.s. The plating current and time used in this work were approximately 3 mA for 1 minute which gives a plating thickness of 0.34 μm. No independent checks of plating thickness were made however this does sound a reasonable figure and one that suggests that the improvement is restricted to surface area phenomena. Electro-deposition of platinum is often accompanied with a characteristic change in sensor electrode appearance from grey to black and a change in sacrificial platinum wire electrode from silver to black when using AC currents. The black appearance is a well known form of platinum "platinum black" which has such an intricate surface structure that light is not reflected directly from it. It does not indicate the presence of a platinum compound.

4.1.3 Concentration modulation technique application

The concentration modulation technique was applied to a simple platinum cermet and to an electroplated potentiometric cell. The calculated and characteristic measured sensor EMF traces are shown (fig. 4.9) for a 0.08 Hz modulation at 600°C. The sinusoidal nature is seen along with a certain amount of noise which does cause problems in data analysis, especially at lower temperatures. The range of results are shown as comparisons of amplitude (fig. 4.10) and phase (fig. 4.11) variations over temperature, electrode and frequency variations. Theoretical analysis showed (section 3.4.1) that a pseudo sine wave rather than a real sine wave could be expected, however, figure 4.9 presents measured data alongside a true sine wave, confirming that modulation amplitude is sufficiently small such that deviations from a sinusoid was negligible.

We do see a small offset in the resultant modulation with the average reading lying at about –0.6 mV. The offset is attributed to the same small electrode temperature differentials as seen in step response technique investigation. Note also that in these

analyses, the maximum frequency used of 0.16 Hz is below that at which flow valve response lag became substantial (see figure 4.16).

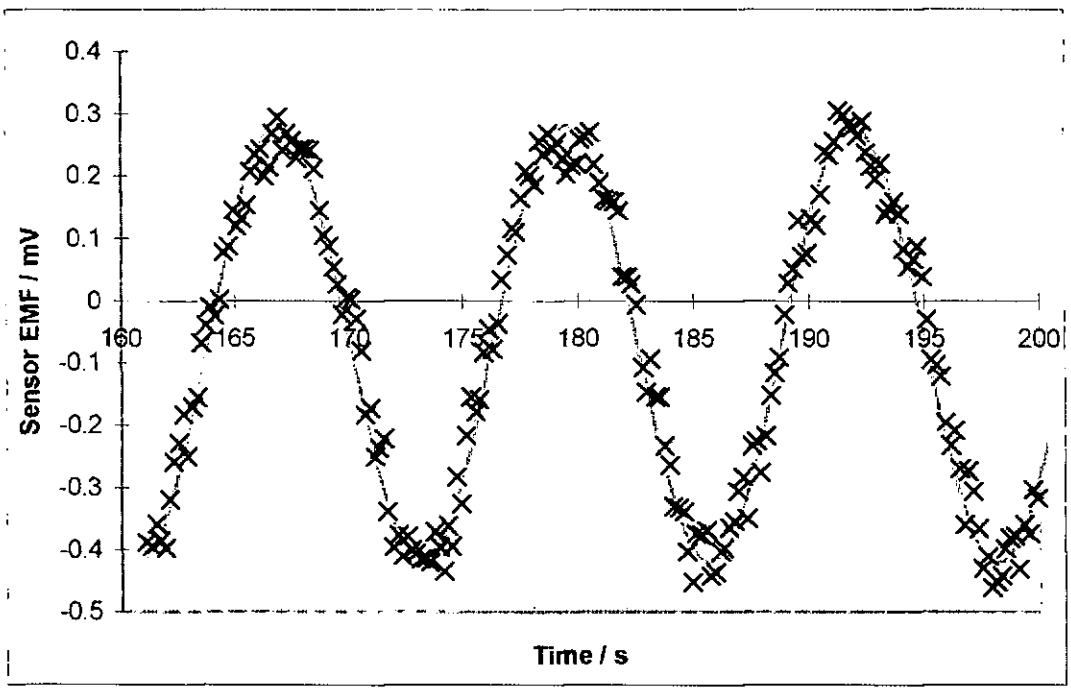

Figure 4.9 Sensor output signal and calculated sine wave

Graphs of results from these experiments show two sets of results for each frequency / temperature regime. These results sets are of the cermet electrode sensor and those for a sensor using electroplating at high sinusoidal current. In using sinusoidal currents there is no net gain or loss of platinum from the electrodes, just a re-organisation as metal is lifted from the sintered electrode structure and re-deposited in the finely divided form platinum black.

The sensor amplitude variations (fig. 4.10) are shown to be unaffected by modulation frequency by the sensor achieving Nernst amplitudes at higher temperatures, therefore the modulations are solely due to ideal sensor response. Deviations from Nernst amplitudes at lower temperatures can be visualised as the sensor not reaching Nernst EMFs before the modulation pulls the EMF back down. Therefore the slower the sensor response, the lower the modulation amplitude recorded. On the graph this is seen as a drop from Nernst voltage (also displayed) at lower temperatures, whilst a good agreement is attained at higher temperatures. As expected this drop is smaller at lower frequencies for each temperature. Such results demonstrated very little benefit from the electroplating procedure when a low sinusoidal plating current (5 mA) was used, with only a slight

improvement in characteristics (not shown). The high plating current (30 mA) electroplated sensor however, shows a significant improvement of the order of that seen in step and impedance analyses >100°C. These two attempts were both conducted using an alternating current for 10 minutes with a platinum wire secondary electrode.

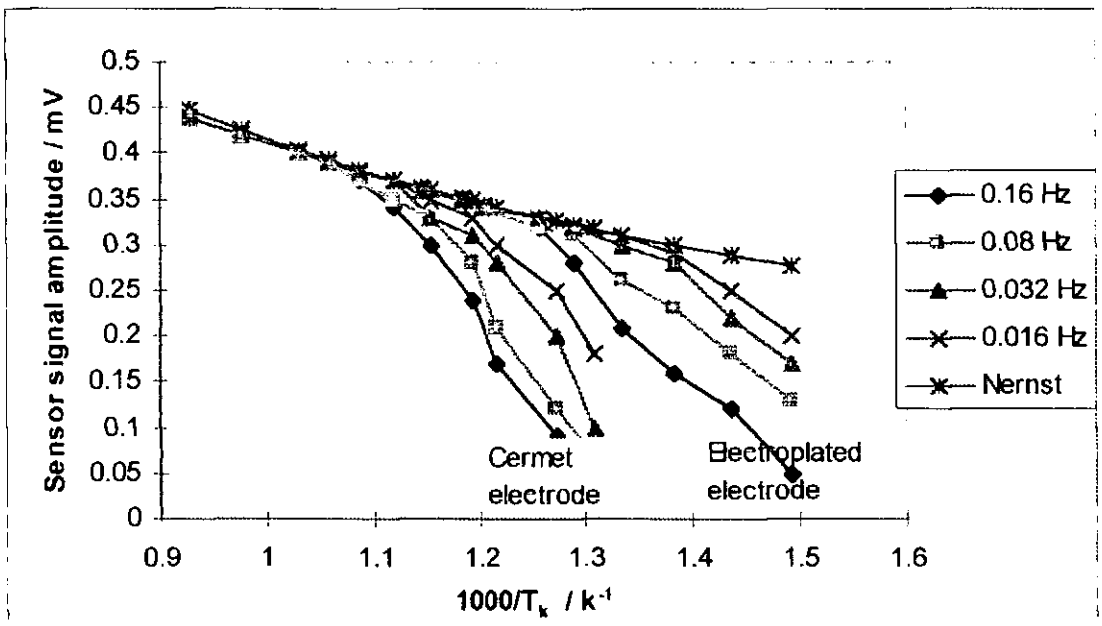

Figure 4.10 Sensor sinewave amplitude with temperature variation for cermet and electroplated sensors.

Similar results are also observed with concentration modulation phase angle measurements (figure 4.11). At higher temperatures where response was fast, phase angle remained zero as the sensor easily kept track of the modulations. As temperatures reduced, phase angle increased as a slower response gave a larger response time lag. Again only a small improvement was gained by electroplating using the small (5 mA) current but this improvement became significant when a higher plating (30 mA) current was used.

Interestingly, the zero phase angle (with reference to the flow valve output signal) was not expected at high temperature. Taking carrier tube dimensions and gas flow rate into account, to estimate time for the gas at the set flow rate to travel to the measurement electrode, a phase lag of almost 20° is expected assuming the sensor has an immediate response. This effect was also observed where the input, output and sensor waves were recorded, oscilloscope style, using a data acquisition package, indeed we do see the same on an actual oscilloscope. This shows that the effect is not due to data acquisition timing

delays but reflected some unexpected system phenomenon. Causes of this phenomenon have been considered and include:

- Gas diffusion resulting in the gas change arriving at the measuring electrode ahead of the bulk gas flow, this was ruled out as no significant diffusion effects were observed in the similar set-up for step changes.

- Gas flow cooling effects resulting in an EMF change prior to gas front arrival. This was eliminated by investigations using modulations with no concentration change. No electrode cooling effects were apparent until amplitudes were far greater than those used here.

- Phase lag being masked by data acquisition channel record timings. This was checked by feeding the same signal to each DAQ channel, the results showed no processor lag whilst the DAQ timing was controlled and even when not controlled the effect was vary small.

- The possibility of sensor lag actually being 340° behind valve modulations. This possibility was investigated by halting the modulation mid cycle, the sensor EMF halted along with the valve modulation, not the next cycle on.

- The only remaining explanation is that the flow valve output signal actually lagged the actual output. No specific experiments were conducted to confirm or negate this explanation.

Also, interestingly, there was no increase in sensor output amplitude at lower temperatures as seen in figure 4.7, step change tests, in fact a reduction in sinusoidal amplitude was observed, presumably the Non-Nernstian increased EMFs do not have time to develop above expected Nernstian EMF levels.

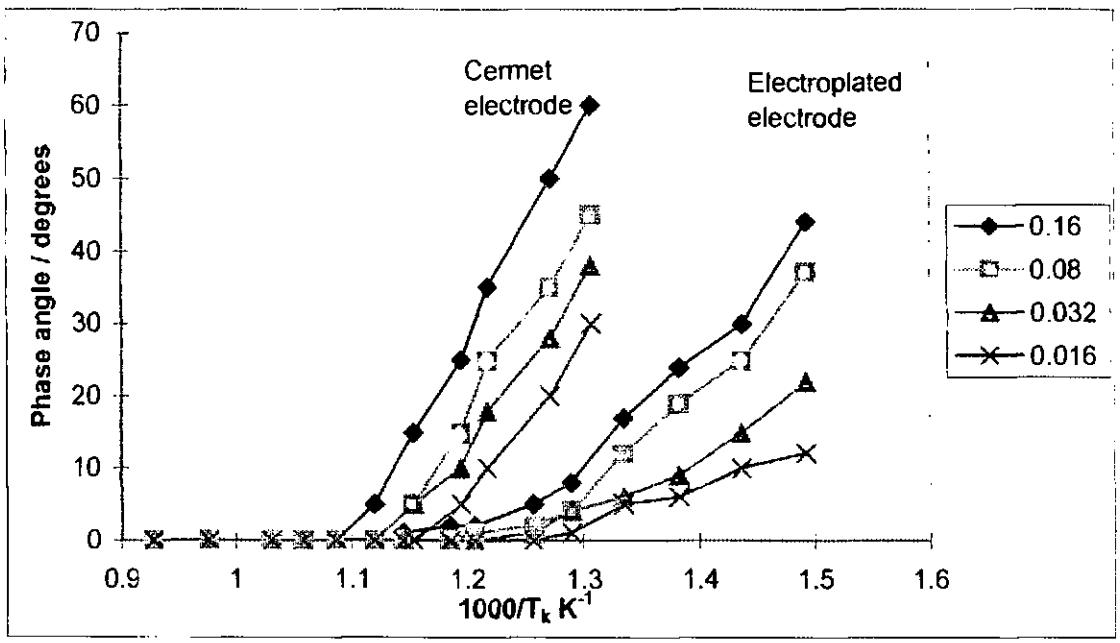

Figure 4.11 Sensor sinewave phase angle with temperature variation for cermet and electroplated sensors.

4.1.4 Pressure modulation technique evaluation

The pressure modulation technique was also used in the assessment of the simple platinum cermet electrode potentiometric cells. Figure 4.12 shows the effect of reducing sensor temperature on the pressure amplitude measured at various frequencies. The clear trend is for the measured pressure amplitude to drop away as sensor response rates are exceeded. Thus at high temperatures we see a virtually constant pressure amplitude maintained whilst, at temperatures below 650°C the actual pressures were not realised even at the lowest frequencies used.

The first point of interest was the apparent increase in pressure with frequency seen at high temperatures. Possible causes for this feature have been identified as:

- Significant pressure loss through gas leakage at low frequencies
  This has been ruled out by assessment of steady state gas leakage rates from this system which have shown to be negligible at the frequencies dealt with here.

- An initial expansion of gases as tests were initiated through heating by the furnace
  This has been ruled out as the effect proved to be independent of test order

- An expansion of gases through heating by the non-isothermal pressure development

The observed pressure increase from this effect is of the order of 5 to 10% which would require a temperature increase of about 5 to 10% or 40 to 80°C at the highest temperature assuming a constant average volume.

- A resonant frequency of the sensor system having been encountered
  The effect occurred at temperatures where response was expected to be fast in comparison to these frequencies and was effective over a wide range of temperatures over a small frequency range so it is not thought to be a sensor effect

- An increase in sensor temperature over testing time
  There was no indication of temperature rise from the thermocouples and again the effect was not influenced by test frequency order so this is not thought to be responsible

A second point of interest is the difference seen upon switching gearboxes. Here we see results recorded using the different gearboxes displaying results out of line with each other, especially at 600°C. These have been identified as due to small differences in cam positioning between the two gearboxes being exaggerated at 600°C where the sensor was very sensitive to pressure modulations in this frequency range.

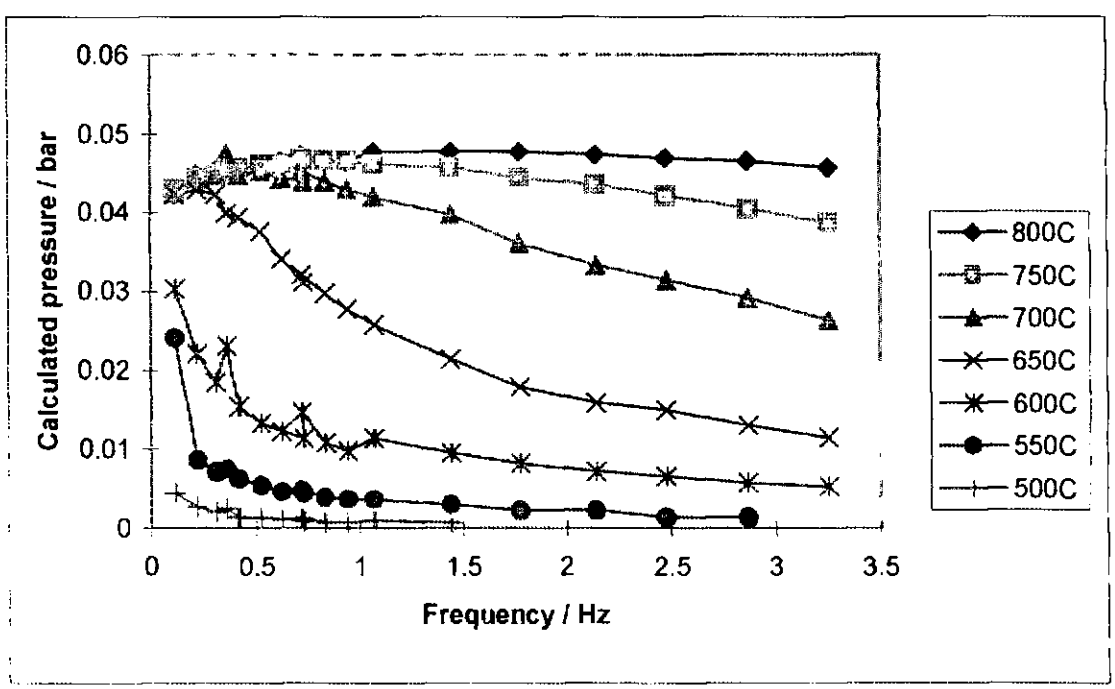

Figure 4.12 Pressure vs. modulation frequency, calculated from Equation 3.10

Figure 4.13 shows the effects of modulation frequency upon phase lag measurements taken over a range of temperatures. These results demonstrate virtually no phase lag being experienced at high temperature and low frequency, but an increasing lag with reduced temperature and increased frequency. A virtually constant delay would be expected between piston position and instantaneous sensor response due to gas pressure transit from piston to sensor. Given the speed of sound at ambient of roughly 330 m/s, this equates to a gas transit time lag of around 1 ms which would give a 1° phase lag at the highest frequency considered here. At higher temperatures the speed of sound increases so the phase lag would drop.

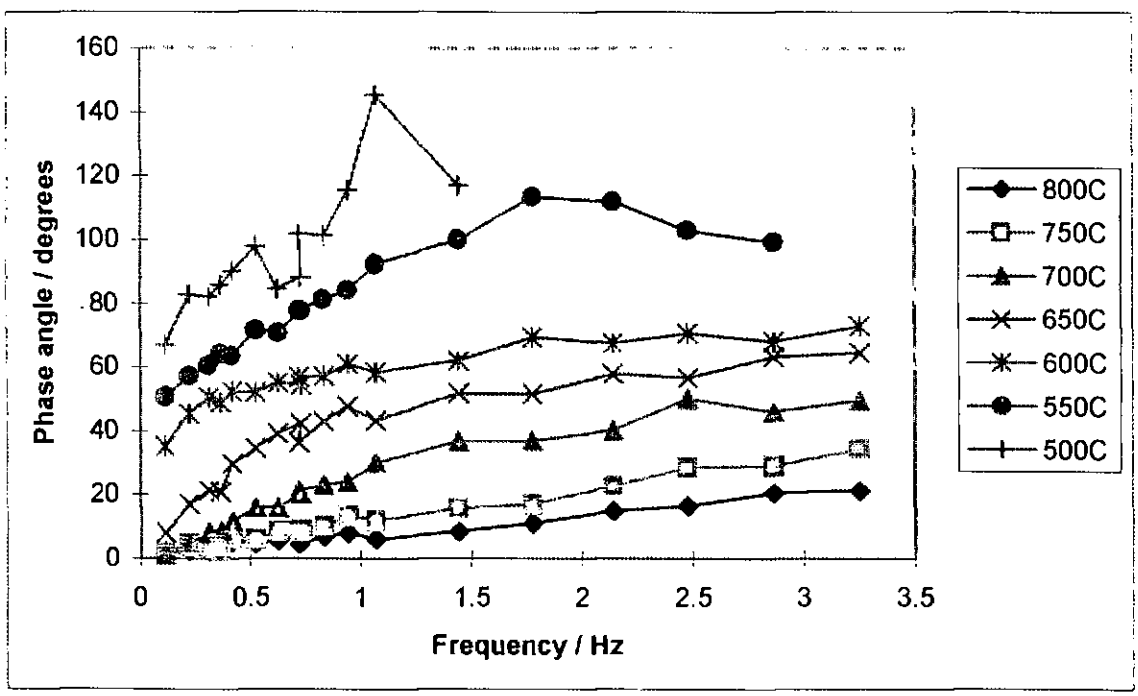

Figure 4.13 Phase lag vs. pressure modulation frequency

Comparing figures 4.12 and 4.13 (which are effectively amplitude and phase angle vs. frequency graphs for pressure modulation) to figure 4.6 (amplitude and phase angle vs. frequency graphs for impedance spectroscopy), we see similar trends between the two techniques but a lack of direct correlation. In both cases amplitude dropped rapidly with increasing frequency for intermediate to low temperature however at high temperature the pressure modulation remained more or less constant. This is because a system limit was reached for pressure modulation as the sensor read the true oxygen partial pressure. In the case of impedance spectroscopy, improved response will always lead to higher currents for the applied voltage.

Graphs of phase angle show a similar trend to one another but there is no direct correlation of temperature/frequency/phase angle. This is possibly because the two techniques took measurements from similar but individual electrode/electrolyte systems.

4.2 Amperometric cells

In addition to potentiometric sensors of platinum/zirconia, these same response rate investigation techniques have been used in conjunction with the amperometric type devices under development during this work. Here we report the application and results of these investigations with the aim of clarifying both sensor and technique performance and applicability.

4.2.1 Thick film sensor impedance

The first of these applications was that of impedance spectroscopy to compare the performance of thick film to plastic / ceramic sheet devices. The results showed the thick film device had a very small electrolyte impedance due to its reduced thickness (approximately 20 μm), the care taken to eliminate contaminants and inspite of the relatively high electrolyte porosity.

The relation of electrolyte thickness to cell impedances was studied by Kenjo & Nakagawa [107]. They examined the Au/YSZ system using DC current pulse examination and found that extrapolation to zero thickness gave a residual impedance. They suggested that this was due to electrode contact in discrete spots of the electrolyte surface. No comparison with this has been performed here as only two material thicknesses have been examined which used slightly different electrode areas.

The electrode performance of the thick film sensors however shows (figure 4.14) a higher impedance than the cermet electrodes used in green sheet cells. This has been attributed to exposure to repeated high temperature firing, necessary for fabrication. A similar cermet paste was used for the thick film electrode to that used for green sheet devices. Repeated high temperature exposure would tend to cause platinum evaporation and a dense, highly sintered structure. Despite this, one could envisage a low temperature device utilising the advantages of thick film electrolytes with electroplated electrodes thus combining the advantages of the best of each component. Work on these thick film devices has been reported [51]. One problem they encountered was a cracking of electrolyte membranes due to the difference in expansion coefficients of the ceramic and supporting substrate.

However this problem was circumvented by De Souza et al [108] who reported a thin film fuel cell device using a 9 μm thick YSZ electrolyte on a nickel cermet supporting electrode. This electrolyte layer showed high density with no sign of cracking and deposition was achieved using a reportedly inexpensive technique. The key was to develop a substrate with a shrinkage profile matched to the zirconia such that it placed the electrolyte under compression during sintering.

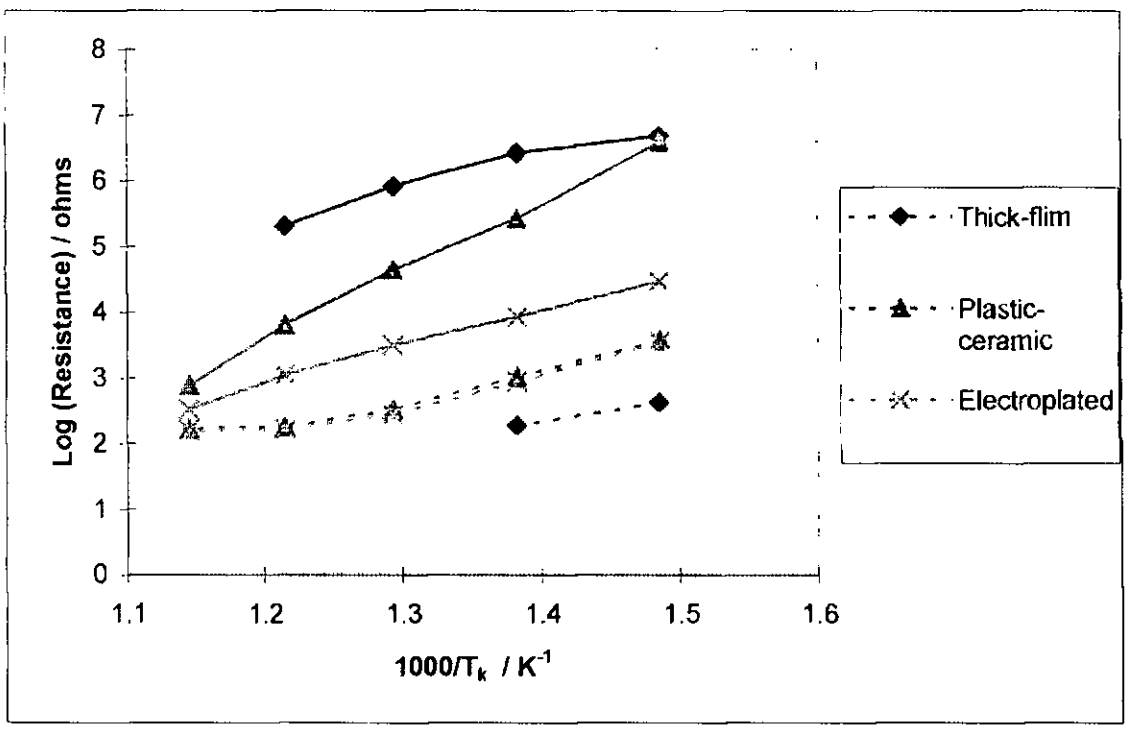

Figure 4.14 Arrhenius plot comparison of impedance data for thick film sensor, cermet electrode plastic-ceramic sample and electroplated electrode plastic-ceramic sample. Solid lines are electrode impedance, dasbed are electrolyte

Figure 4.14 also shows electrolyte and electrode impedances for a device both before and after the electro-plating procedure, demonstrating that the electrolyte properties were virtually unaffected by the process but that there was a substantial improvement in electrode impedance. The improvement is of the order of 100°C when translated into temperature effects, which is in approximate agreement with other platinisation work investigated.

4.2.2 Amperometric sensor impedance bias effects

In addition to straightforward comparisons, impedance spectroscopy was used to analyse the effect of applied bias on the individual electrode / electrolyte components to better

understand what occurs when pump voltage is applied to amperometric cells. The results were then compared to a current / voltage sweep taken for the same sample. The results of these tests show (fig. 4.15):

- An initial large electrode resistance at low temperature due to slow electrode kinetics.
- Electrolyte impedances appeared virtually unaffected by bias voltage, and only became significant as electrode impedance dropped.
- Slow electrode kinetics were overcome by 0.5 V bias and electrolyte resistances became dominant.
- The I/V sweep showed that at these bias, and at this temperature, we did not obtain the limiting plateau region until a bias of 1.5 V.
- By taking the gradient of the I/V sweep (fig. 4.15) we obtained a close match with impedance results; an increased resistance is predicted as limiting conditions are incurred. Presumably this resistance would be shown as a Warburg impedance (45° gradient due to diffusional effects) on a complex impedance plot.

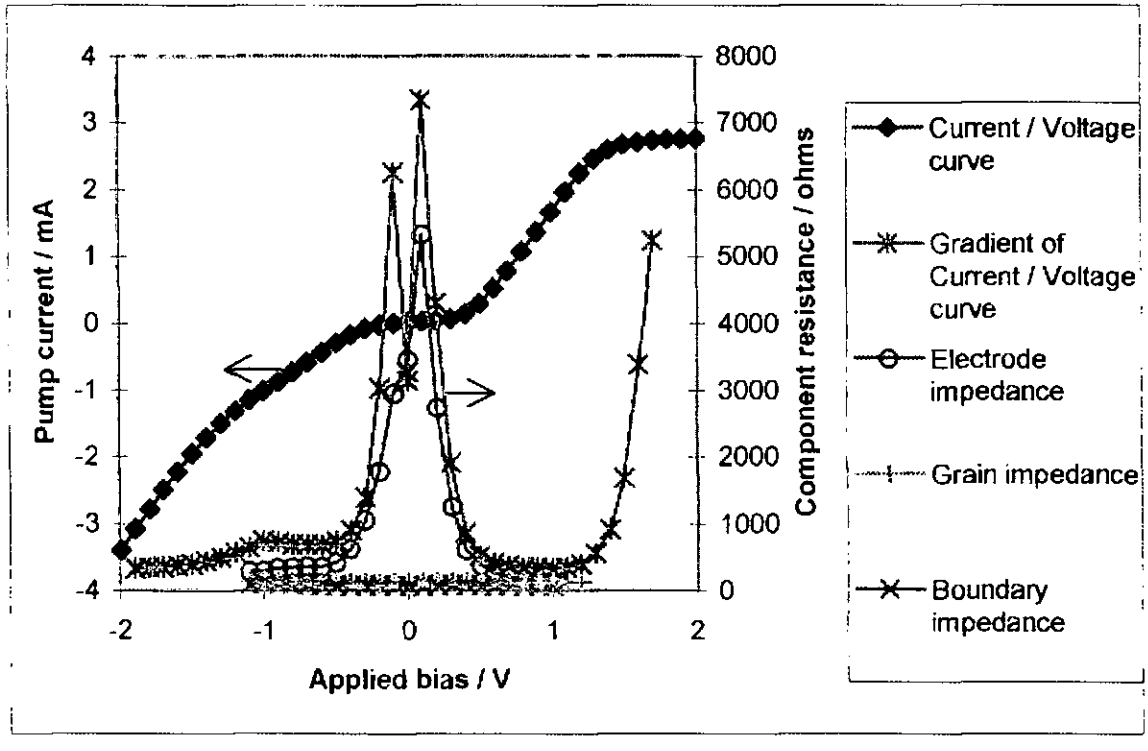

Figure 4.15 Current / voltage sweep and impedance bias sweep

of a complete sensor and Comparison of AC impedance data and DC resistance calculated from I/V sweep for a complete sensor

These results showed that the electrode impedance is very sensitive in the low bias voltage region at low temperatures, but that at higher bias the ohmic I/R slope was equally due to electrolyte properties. Low temperature sensor improvements can now be targeted at electrode interfaces to reduce the initially slow kinetics, and at the electrolyte for improvements thereafter. The use of smaller diffusion barriers would also give improvements by raising the maximum permissible impedance for current limiting conditions to be realised.

Whelan & Borbidge [59] produced a conventional potentiometric sensor which operated at 250°C with a response time of just 3 minutes. This was achieved by the application of a short duration bias voltage which was reported as increasing electrode activity through the electric field strength forcing reactions to proceed at a faster than normal rate.

4.2.3 Amperometric sensor step change

In this section we report the application and characterisation of step gas concentrations to amperometric cells.

4.2.3.1 Sensor characterisation

The first step was to fully characterise the sensor used within the small test-chamber required for this work, both to evaluate its operation limits and compare with results obtained in the main sensor test-rig (see Appendices C1.3.1 and C1.3.6). The current voltage curves obtained are shown in figure 4.16 and are in good agreement with experiments performed in the sensor test-rig. These tests show typical characteristics with operation in air at temperatures of 550°C and above in air. Plots of current limits (figure 4.17) demonstrate linear characteristics and also give temperature coefficient data displaying an α temperature coefficient of 1.69 (see Appendix F1.2). These results suggest operation of the sensor at temperatures of 550°C and above, with a pump potential of 1.2V. As reported (Appendix F figure F2) at a temperature of 600°C, at low pump potentials we see greater currents being drawn at low oxygen concentrations than at higher concentrations.

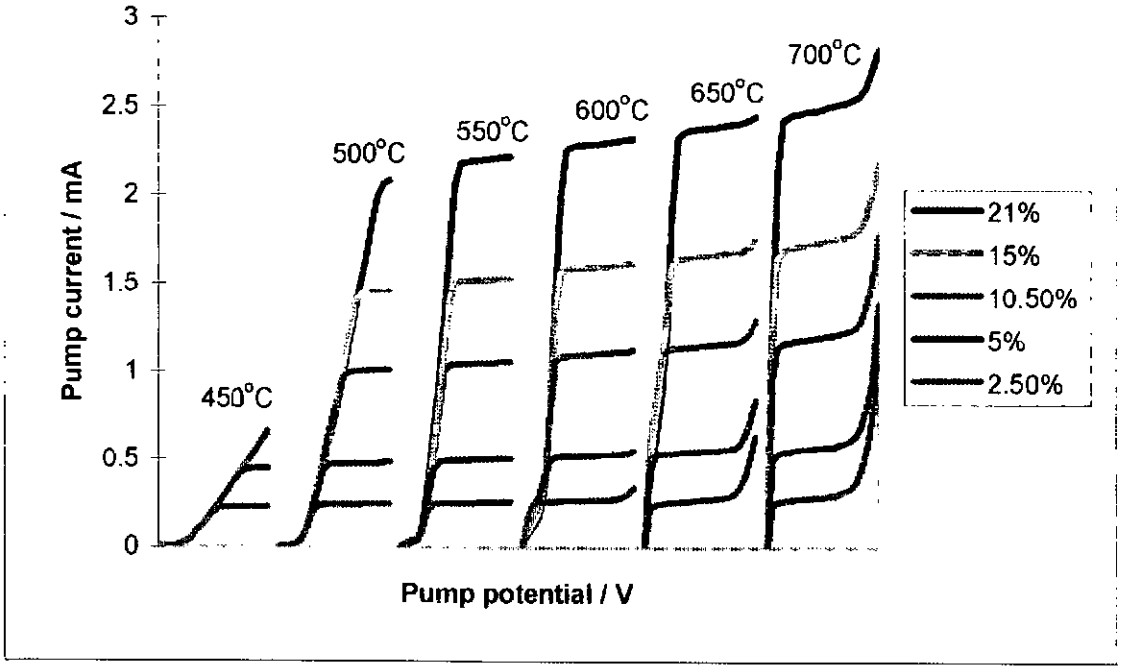

Figure 4.16 Stand alone amperometric sensor current / voltage curves

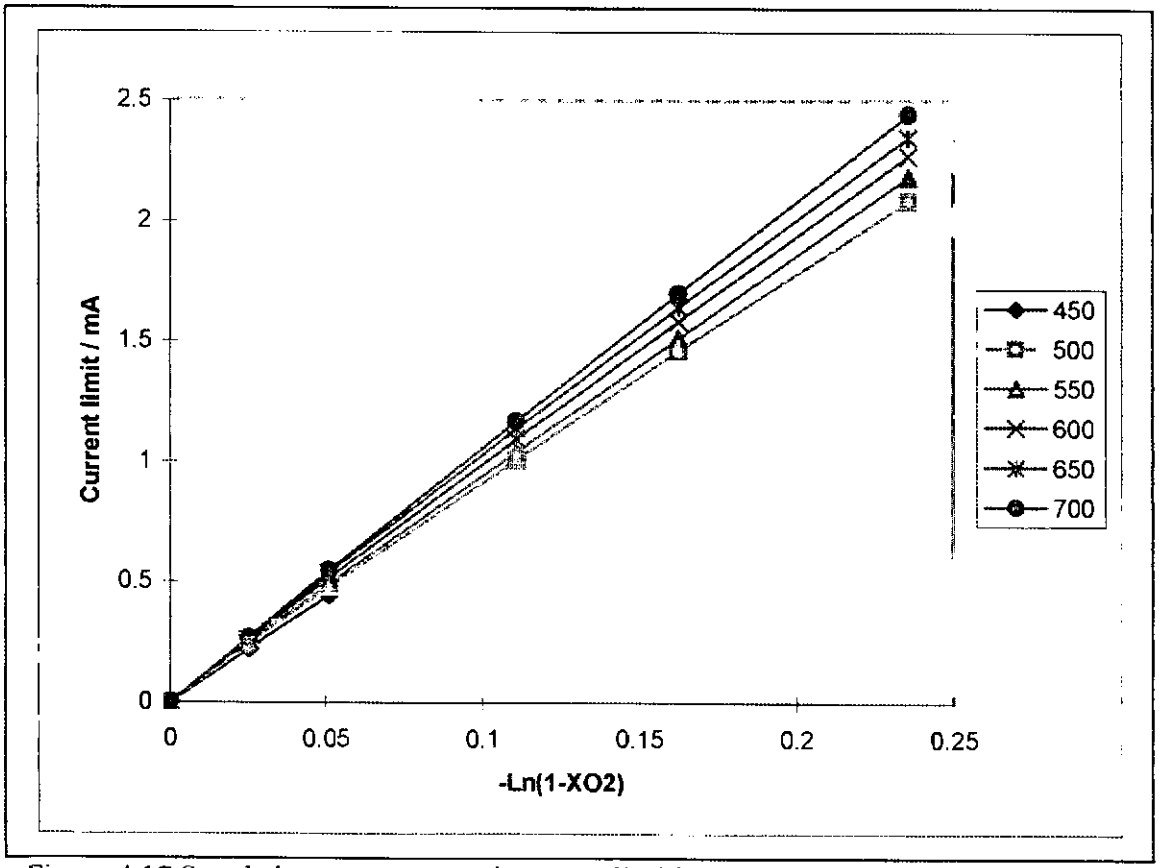

Figure 4.17 Stand alone amperometric sensor limiting current characteristics taken from current plateaux levels

4.2.3.2 Operation temperature

Gas steps were applied to the amperometric sensor (figure 4.18) at different operation temperatures and the sensor displayed virtually no temperature dependence across the 550 to 700°C range examined (once converted to oxygen concentrations). This is a surprising result as both electrolyte and electrode properties have been clearly demonstrated to be highly temperature dependent. The explanation must be that at these temperatures, amperometric sensor response rates are not influenced by electrode/electrolyte properties but on geometrical and gas diffusion factors. Maskell [4], working from data derived from Crank [109], calculated theoretical current-time characteristics and predicted a 90% response to a step change of 12ms for a 2mm length diffusion barrier. Since the responses measured here are of the order of seconds, the S/L ratio is not expected to be response rate limiting for these amperometric sensors. We are left with internal sensor dimensions and gas diffusion behaviour as response rate limiting factors.

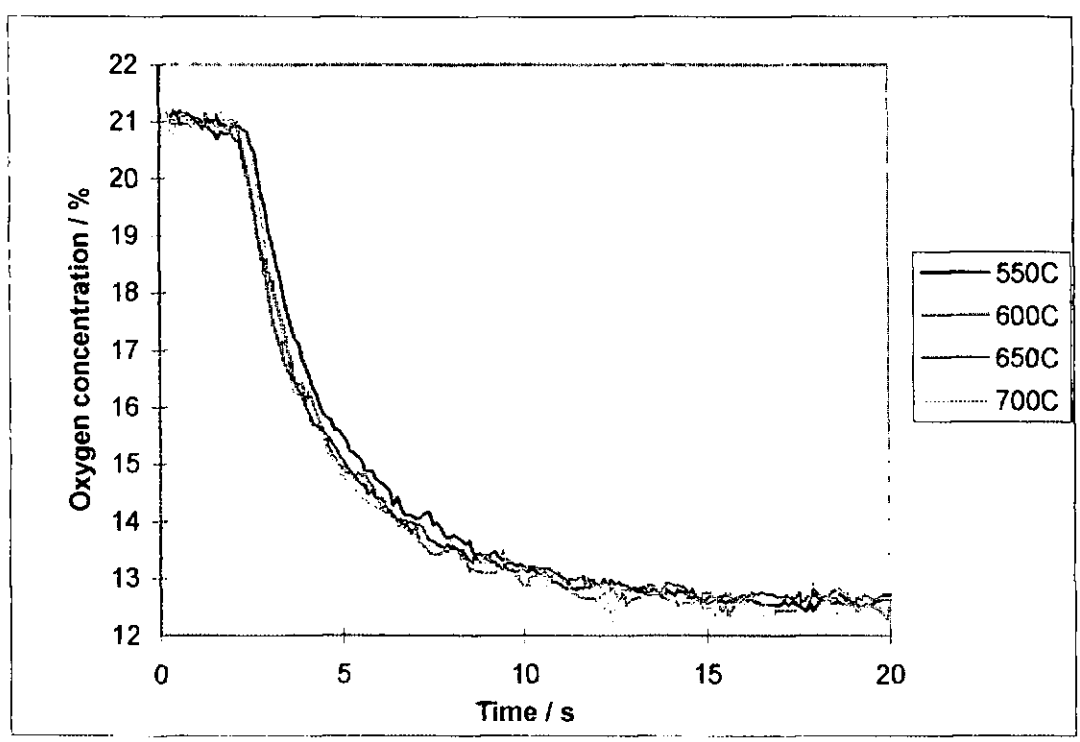

Figure 4.18 Concentration step using amperometric sensors with variation in operation temperature

4.2.3.3 Pump Voltage

Tests were also performed at various pump potentials at 600°C (figure 4.19). The sensor response rate showed no real pump potential dependence whilst potentials were sufficient to attain the limiting currents. This is in agreement with the operating temperature work,

again indicating that the pumping characteristics are not a dominant factor in amperometric sensor response in these tests.

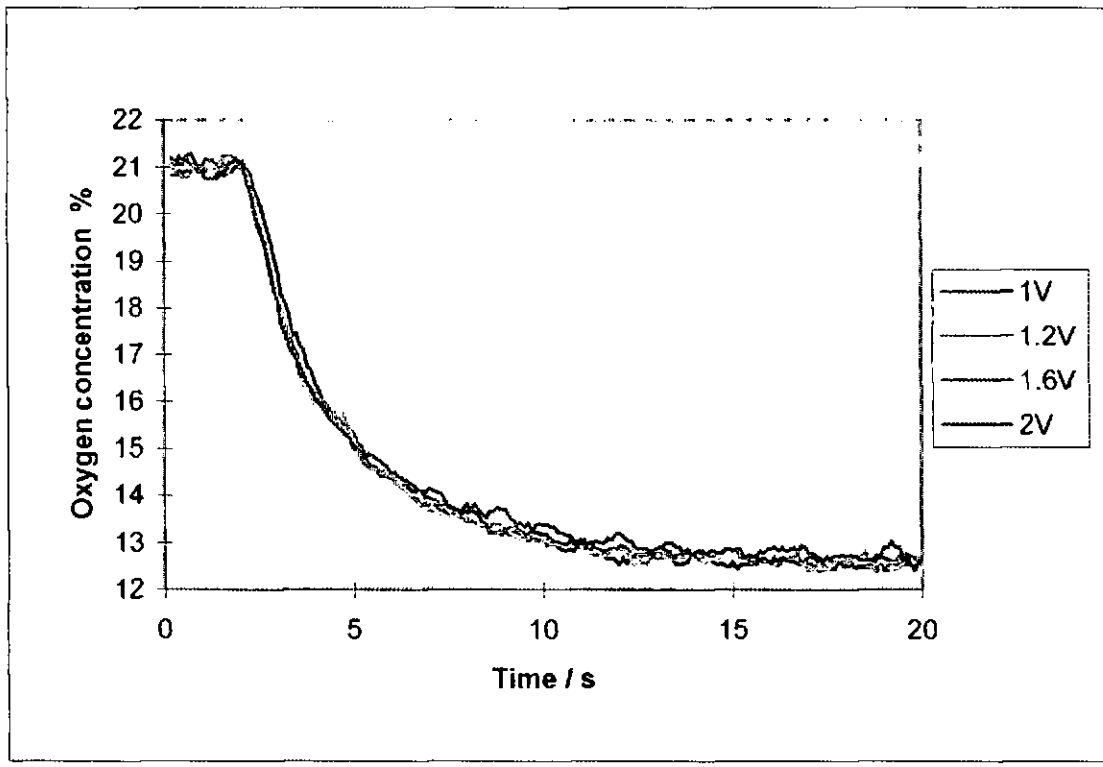

Figure 4.19 Concentration step using an amperometric sensor with pump voltage

4.2.3.4 Step amplitude

Figure 4.20 shows sensor response to concentration steps with varying step amplitude. Here we see that sensor output is sensitive to step amplitude, if however we index the step outputs to represent fraction of final output current then we see complete agreement. Given this agreement we surmise that for oxygen levels (at least of this order), the sensor response times are independent upon oxygen concentration. This result could be expected since we have seen little variation in electrode / electrolyte impedances with oxygen concentration. Also diffusion coefficients for oxygen and nitrogen are similar (Annex F table F7), so the changing gas composition would not experience significant diffusion rates alterations. Experiments using oxygen and helium may show such effects as the diffusion coefficient of helium is far higher than that of nitrogen. Such experiments have not been examined here due to time constraints.

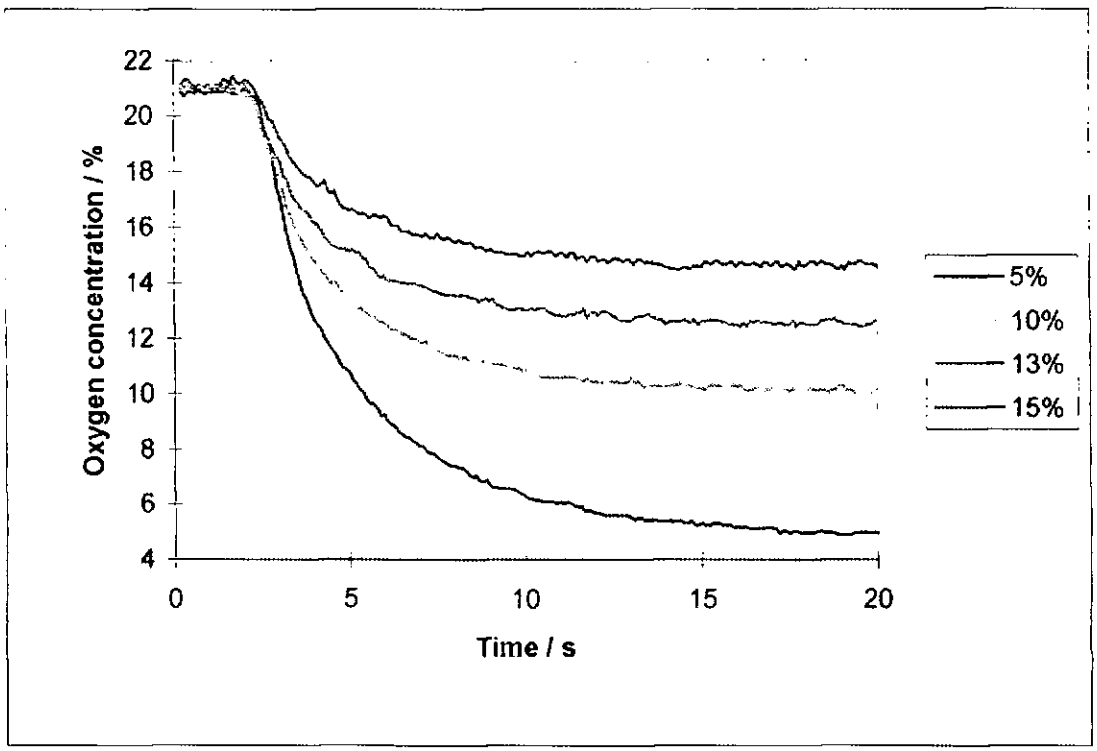

Figure 4.20 Concentration step with step amplitude

4.2.3.5 Step direction

The direction of gas change (high to low or low to high) was studied and showed identical response rates. Similar experiments with potentiometric devices have been shown to generate asymmetrical results unless converted to oxygen partial pressures. This is not the case with amperometric sensors which are linear devices.

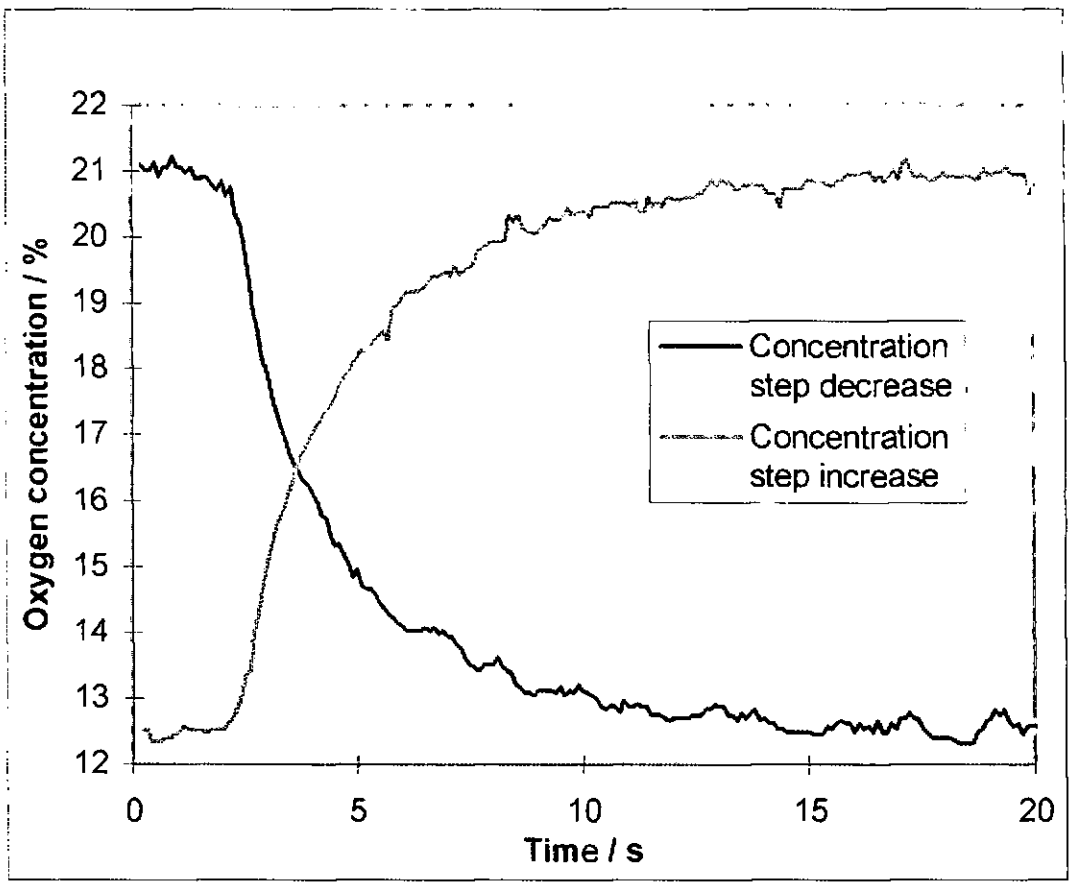

Figure 4.21 Concentration step with positive and negative going step direction

4.2.3.6 Tube length variation

Results thus far have failed to show up any dependence of response rate on test-parameters. This raises the possibility that the results are dependent upon the test-rig rather than the sensor. To investigate this figure 4.22 shows results of experiments using a variation of gas feed pipe length. This was expected to be the most influential test-rig parameter since the solenoid valves could operate in milliseconds and test-rig volumes had been kept small. Indeed the results do show an increasing time delay prior to initial sensor response for feed-pipe tube lengths of 25 to 400 mm. This is explained by the time taken by the gas front to travel from the valves to the sensor chamber. Calculation of this time delay and inclusion of this time into the results by a time offset brings the results back into line. Close examination of this does reveal that, for longer pipe lengths, the change occurs slightly earlier than expected and displays a slightly extended step. This is accounted for by forward and backward diffusion of the gas front thus blurring the gas step arrival. The effects are however small and do not give basis for concern about the 25 mm feed-pipe length used throughout these tests.

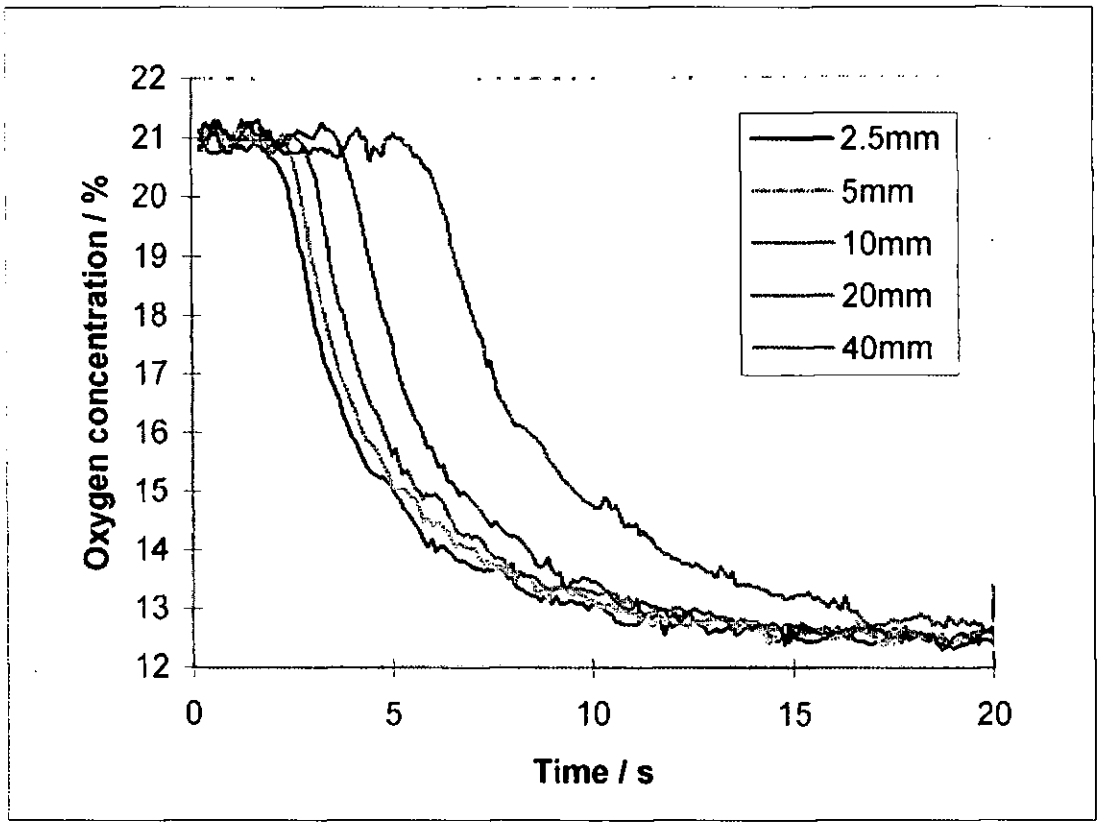

Figure 4.22 Concentration step with tube length variation

4.2.3.7 Chamber volume

Having discounted the feed-pipe, attention was focused on the test chamber volume. This had already been minimised as far as practicable to prevent significant influence so a larger chamber volume was employed to see if this had a large effect on response rate. The free volumes of the two test chambers used were 24 and 30 mm^3. The results showed no such effect for the initial, rapid step (21 to 15%) but did lag slightly behind over the last 2% change. This was a relatively small lag and is not sufficiently large to rule out noise. Generally the two runs did not differ on the scale to suggest that the test-chamber volume had been a significant factor in these tests.

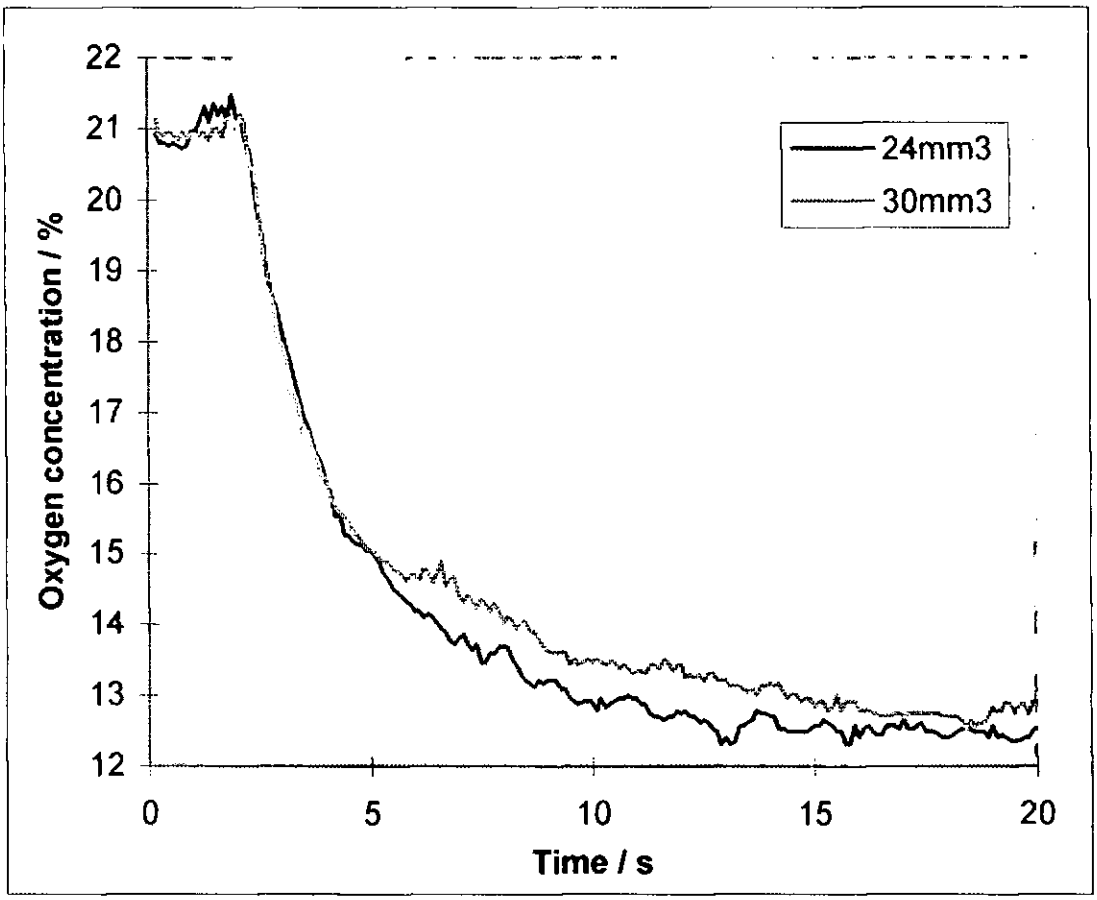

Figure 4.23 Concentration step with chamber volume

4.2.3.8 Flow rate variation

Finally the gas flow rate was varied from 150 ml/min to 25 ml/min, the results are presented in figure 4.24. Here we do observe a significant dependence of response time, both in terms of an initial delay and throughout the entire gas step. Whilst we would expect a significant lag at the lower flow rates it was suspected that the gas step transmission to the sensor may not have been a dominant factor at higher flow rates. These results suggest that the response rate measured was a function of the rate of gas step arrival at the sensor diffusion pore. If so, this indicates that measurements were dependent upon test-rig response rather than sensor response.

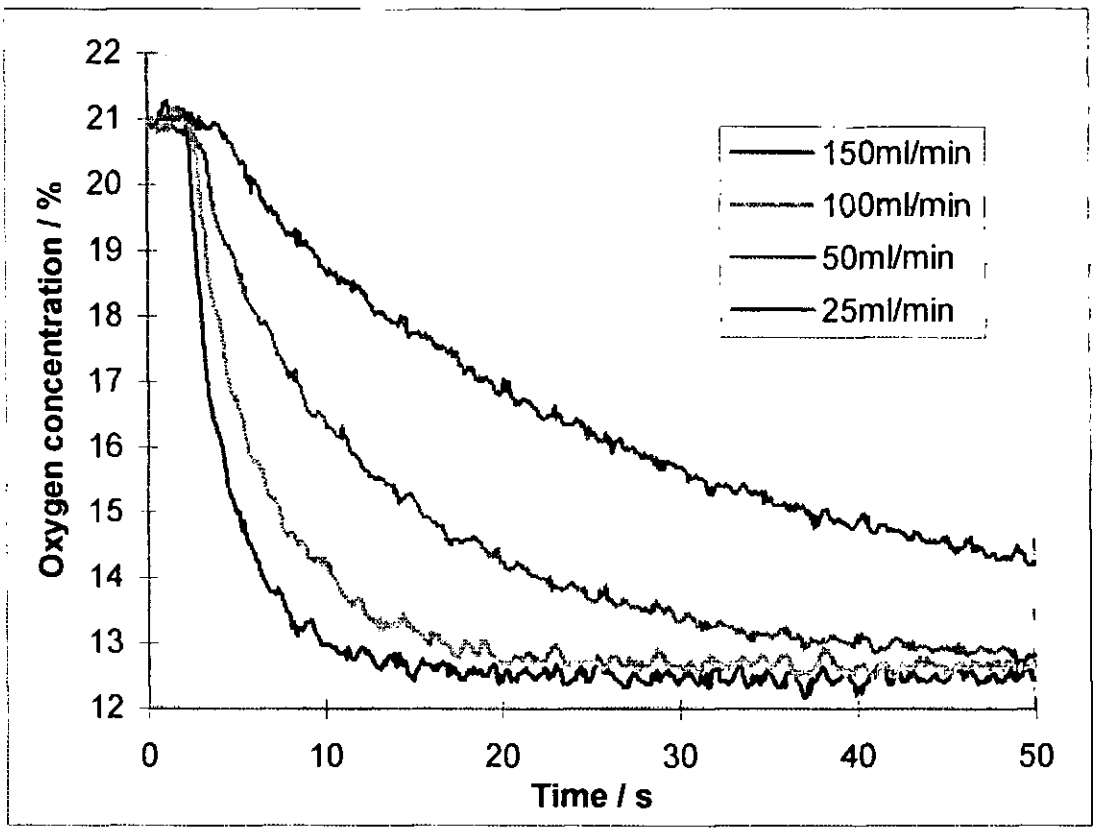

Figure 4.24 Concentration step with flow rate variation

Figure 4.25 plots the inverse of gas flow rate against response time for the given percentage oxygen concentration drops. This shows that there is a small residual response time, of approximately 1 second, upon extrapolation to infinite flow rate which shows the sensor response time however the data are not sufficiently accurate to give a precise indication.

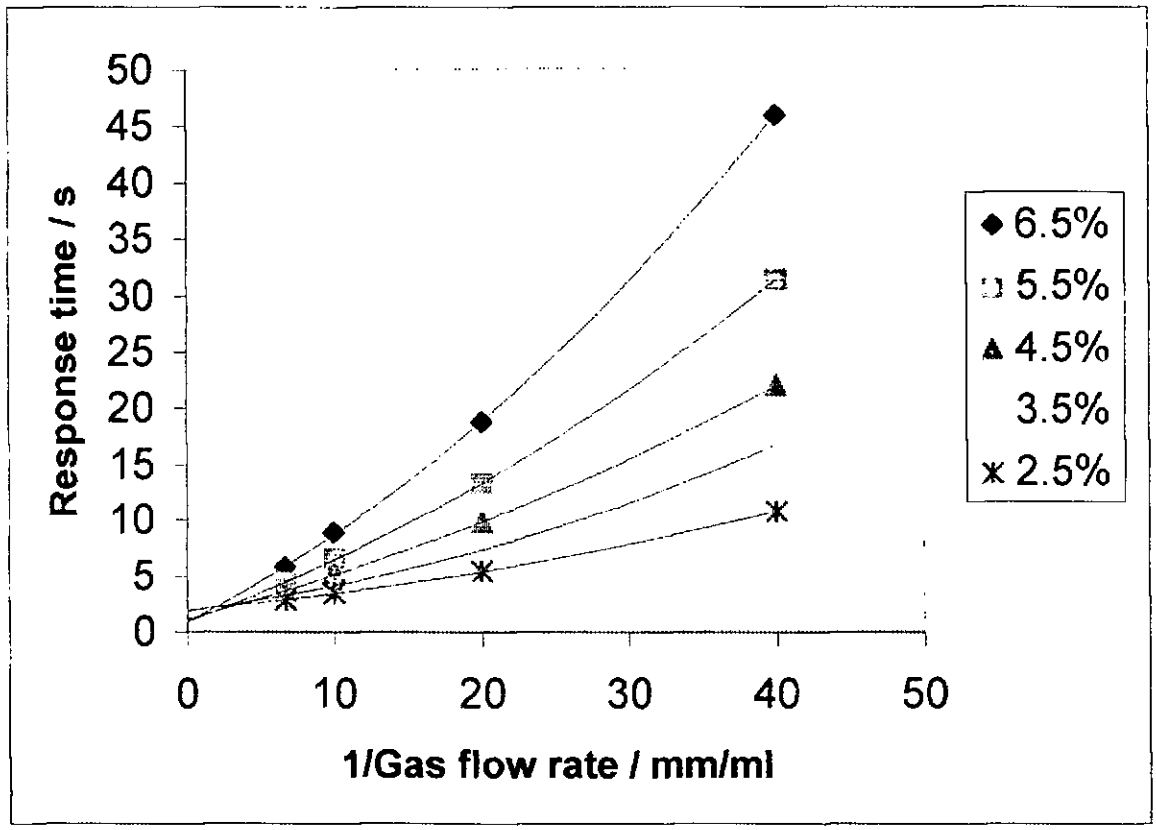

Figure 4.25 Concentration step with flow rate variation

Whilst slightly disappointing we have shown that the sensor operates rapidly over the whole operation range and is not significantly affected by operation temperature in the range tested. It is also thought that the working electrode was operating at a sufficiently high voltage (above 1 V) which causes it to respond kinetically very rapidly independent of temperature.

In conclusion, the sensor response above 550°C is rapid but operation at lower temperatures is prevented by electrolyte and electrode resistances preventing the necessary diffusion limiting condition being realised. Further tests using lower maximum oxygen concentration would have allowed lower temperature investigation. A 2.5 to 5% oxygen step would have allowed operation down to 450°C whilst maintaining the limiting condition; this was not completed due to sensor failure. This gas step reduction would also allow lower pump potentials to be utilised. There is plenty of scope in this work for further investigation, altering sensor parameters test rig improvement and results interpretation.

4.2.4 Amperometric sensor concentration modulation

In this section we report results of concentration modulations applied to an amperometric sensor. Figure 4.26 shows the input / output waveforms, again showing a small lag

between flow valve input and output signals, with a larger delay to the sinusoidal sensor output. Again, modulation experiments (not shown) using air in both valves demonstrated that modulations were attributable to concentration variation and not to accompanying flow or pressure variations. The sensor output displays an appreciable amount of noise which is attributed to the method of data acquisition used employing a high degree of signal amplification. Note also the true sinusoidal nature of the sensor output obtained, as unlike their potentiometric counter parts, amperometric sensors give a linear output.

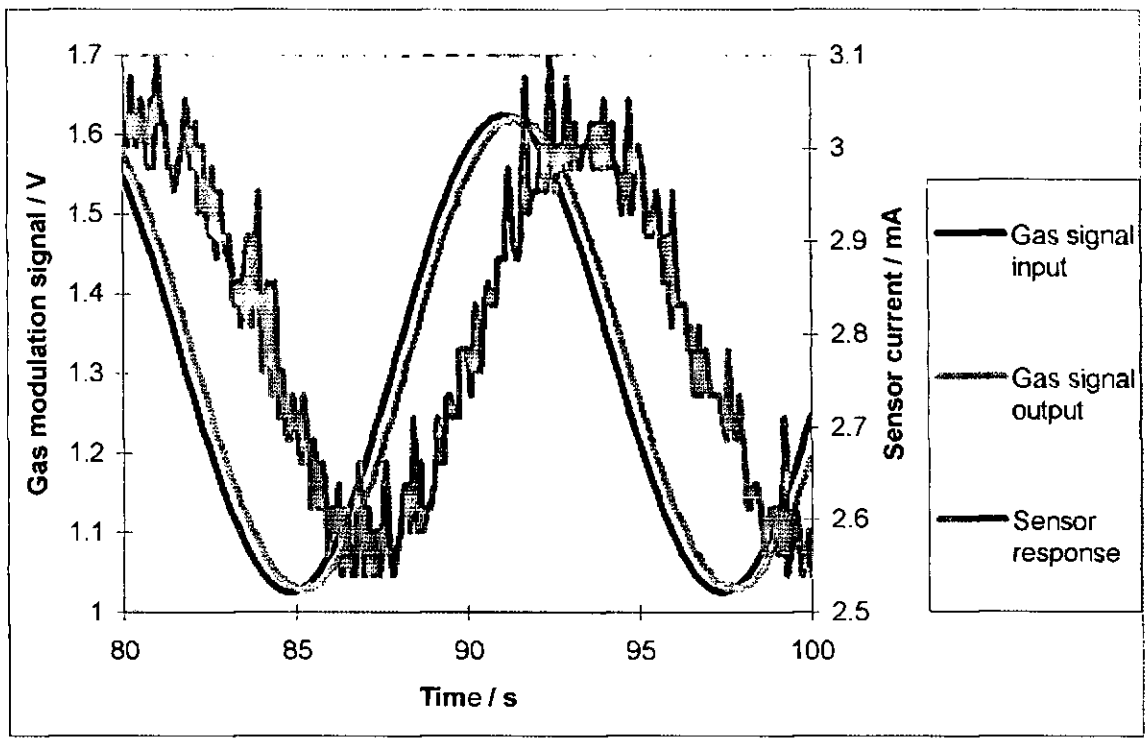

Figure 4.26 Concentration modulation of an amperometric sensor

Figure 4.27 shows measured sensor amplitude and phase of response with frequency variation for concentration modulation experiments. These results show a non-linear drop in amplitude and phase lag with increasing frequency. Unfortunately this device broke before further testing could be performed. Tests repeated at a constant 0.08Hz between 550 and 700°C showed no obvious temperature / response rate dependence, in line with the conclusion that the system is volume / flow rate dependent and partially as these sensors have not demonstrated any significant temperature dependence.

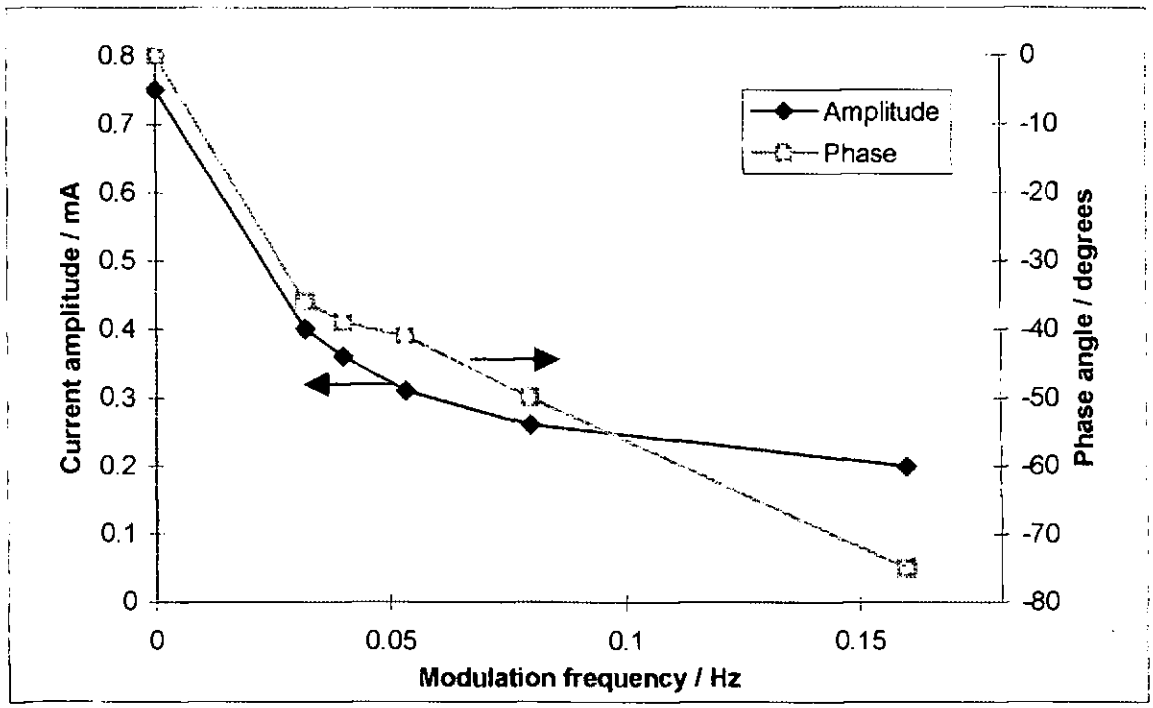

Figure 4.27 Concentration modulation results with frequency variation

These tests indicate that the modulation frequency required for reliable analysis of amperometric sensors systems is significantly lower than that used here pointing towards a relatively slow response times for the complete sensor system (including gas feed tubes, gas chambers, heaters, insulation etc.). The sensors would probably require faster modulation frequency but the influence of the test set-up would need to be dramatically reduced to obtain sensible sensor response data. Further work would be required (possibly in linking the FRA to the flow valves) in order to get a realistic frequency range for an accurate assessment.

4.2.5 Amperometric sensor pressure modulation

According to the accepted equations describing amperometric sensor output, the limiting current is independent of barometric pressure whilst bulk diffusion is the dominating mechanism. These equations however refer to sensor in steady state conditions. It is therefore not surprising to see the assumptions breaking down when relatively fast pressure modulations are applied. Dietz [86] recognised that amperometric sensors operated in the bulk diffusion region were unaffected by barometric pressure but pressure changes would produce un-quantified temporary current changes.

Figure 4.28 shows the effect of such pressure modulations on the output of limiting current with temperature variation, clearly the sensors were responding to the input modulations

with a sinusoidal type response. This response may be seen as an increased and decreased rate of inward gas diffusion when the external pressures are greater than the internal and vice versa respectively. The graph shows that there was little change in modulation amplitude with temperature at this single intermediate frequency. There was however an increase in the average current, which can be attributed to the temperature coefficient of these sensors in line with those of figure 4.17 (limiting current characteristics). The other notable feature of this plot is that a sinusoidal nature of the waveforms begins to break down at the lowest temperature. Whilst similar effects may be expected due to a slowing of sensor response rate, this effect was traced to current limiting by electrolyte ohmic resistance rather than diffusional characteristics. As the temperature dropped, so the cell resistance increased such that a reduced current was drawn at a specific voltage. Finally there does exist a phase difference in the plots; this is due to the manner of data collection and not necessarily to sensor response delays. Data were captured by manually triggering rather than automatically during modulation.

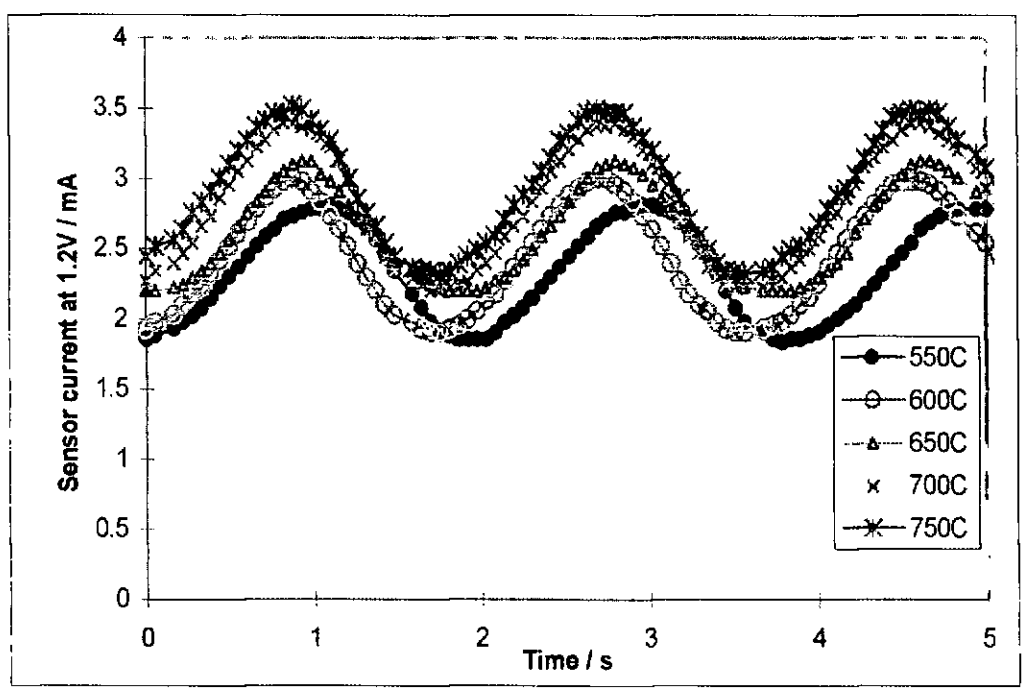

Figure 4.28 Current vs. time graphs

Figure 4.29 shows the minimum and maximum limits of current oscillations attained from pressure modulations. The general trend is very apparent. As opposed to potentiometric sensor pressure modulation results, where amplitude decreases with frequency, here we see amplitude increasing with frequency. This may be explained by the fact that amperometric sensor current modulations arise from pressure differentials between sensor internal and

external atmospheres. The diffusion pore would tend to equalise these pressure differentials but was less capable of doing so at higher frequencies. Thus a higher frequency gave a greater pressure differential and, therefore, a higher current amplitude. At lower temperatures this trend was not maintained. This may be explained in part by the electrolyte ohmic resistance at low temperatures giving an upper limit on the current that may be drawn. In fact using the current / voltage curves obtained for this device (figure 4.16) a prediction of these ohmic current limits can be made. A close match is obtained by I/V extrapolation to 1.2 V, assuming no diffusion limitation to the upper limits of the lower temperature modulation current. This factor is probably influential for the upper modulation limits, and for the 550°C curve which also finds a limit. This phenomenon cannot be used to explain the effects seen on the lower modulation limits where the minimum currents cease to drop and even increase with frequency. We are therefore led to believe that there are some response rate effects having an effect at these high frequencies and low temperatures. Such effects were not apparent in concentration modulation evaluations as the modulations there were all below 0.5 Hz where these effects were not measured. In pressure modulation experiments we consider sensor behaviour rather than test-rig limitations as the pressures were transmitted at the speed of sound rather than gas flow and therefore would be little influenced by gas transit distance. Chamber volume would have been influential only upon the magnitude of the pressure modulation produced.

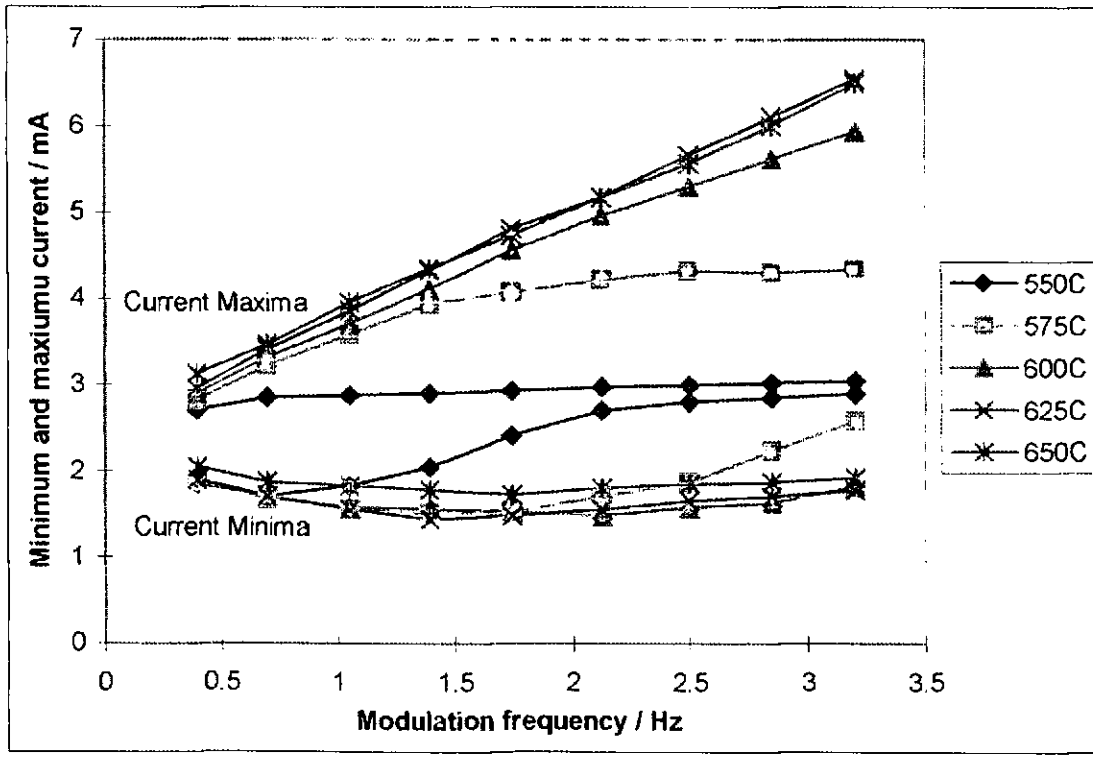

Figure 4.29 Modulation limits vs. frequency

The above results were extended by reducing the lower frequency range and extending the upper temperature to provide the data shown in figure 4.30. The peak to peak modulation amplitude is plotted against the modulation frequency and shows a virtually constant, linear relation between frequency and amplitude for slow modulations at higher temperatures. As the frequency was raised, the sensor was no longer able to draw the necessary upper current limit whilst at the same time the lower current limit increased resulting in an overall decrease in current amplitude. These effects are important for amperometric sensors operating in oscillating pressure systems such as vehicle exhausts and pulsed combustors.

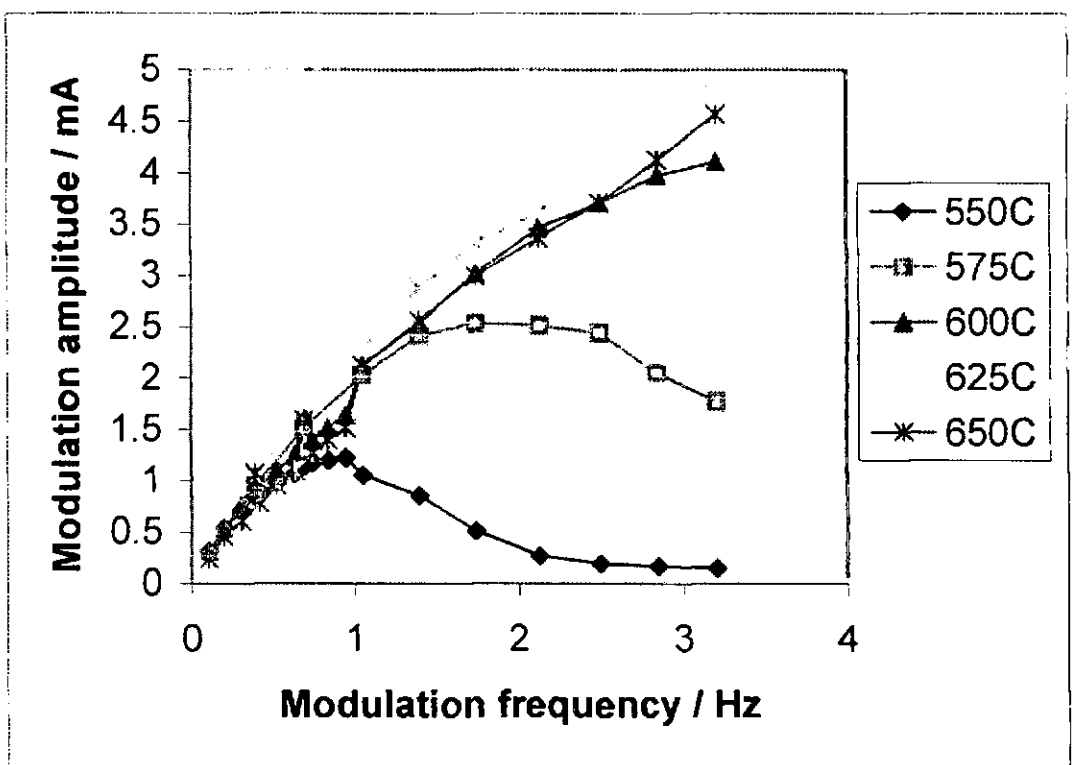

Figure 4.30 Modulation amplitude vs. frequency

Analysing the effects of temperature on the current modulation amplitude by re-plotting this data, figure 4.31 shows how the effect of reducing temperature is translated into modulation effects. These results indicate that a constant level of modulation amplitude can be expected, provided operation temperature is sufficient. The level of this amplitude is frequency dependent, and assuming that it relates to the pressure differential across the sensor, is expected to be affected by diffusion barrier dimensions. At temperatures insufficient for this constant amplitude, a reducing amplitude was measured as the effects of frequency reverse.

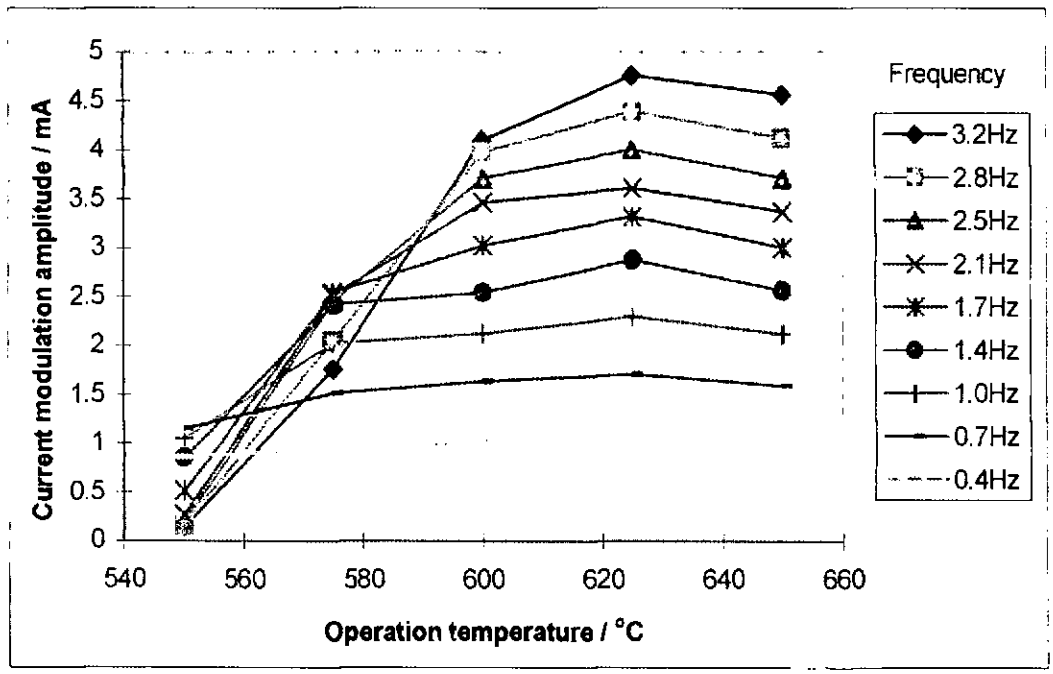

Figure 4.31 Modulation amplitude vs. temperature

No data was recorded for the phase lags seen in pressure modulated amperometric systems as the data acquisition system used did not have sufficient measuring frequency to reliably detect the single point pickup used for the modulation system output.

4.3 Summary

4.3.1 Impedance

Using impedance spectroscopy a clear resolution of three polarisations with the high frequency electrolyte impedances better resolved at low temperatures has been shown with low frequency electrode impedance better resolved at higher temperatures. The electrode impedances were approximately two orders of magnitude greater than those measured for either electrolyte impedance, with grain boundary impedances generally slightly smaller than those for grain interiors. The Dynamic Ceramic material appeared to be a slightly better conductor than the Tioxide material with impedances for a thicker electrolyte giving grain and grain boundary results similar to those recorded for the best Tioxide samples. The examination of the thick film electrolyte showed a particularly low electrolyte impedance but relatively poor electrode performance. This was attributed to the much thinner electrolyte layer along with repeated firing of the inner electrode at high temperatures. The combination of cell resistance and capacitance measurements was used to show the effect of temperature on cell time constant which gave similar graphs to those

developed with step change techniques. Electro-deposition of platinum resulted in significant reduction in electrode impedance with the same order of improvements seen with concentration modulations and step change analyses. The plating process showed no effects on electrolyte impedance. Impedance data were also converted into phase lag and amplitude type graphs which aided the comparison between concentration/pressure modulation and impedance techniques.

Plastic-ceramic cells were examined using frequency response analysis with bias application to mimic pump overvoltages. This indicated that there was a dramatic reduction in electrode impedance with bias application as the high overvoltage overcomes kinetic limitations. This explains the significance of electrolyte impedance on pump cells. Whilst this is not a particularly surprising result, it is of significant importance. It indicates that improved electrolytes will allow a reduced operation temperature in amperometric cells. It also shows that whilst electro-platinisation of gauge cell electrodes is advantageous, the effects would be less significant for pump cell electrodes. It is possible to use a positive feedback to increase the applied voltage dependent on the current drawn. Such a technique may be useful in overcoming the limitations of electrolyte conductivity at low temperature.

4.3.2 Step changes

A simple Pt cermet/YSZ potentiometric cell was used in the assessment of the step gas concentration change technique. A rapid drop in response rate was observed as operation temperatures reduced. In addition to longer response times, non-Nernstian EMFs are measured at low temperatures below 475°C for the simple cermet electrode cell. By electroplating the electrodes using a 3 mA DC current applied for 1 minutes, electrode performance was significantly improved. Electroplating deposition is calculated at 2.02 mg $A^{-1} s^{-1}$, a deposition of approximately 1.35 μm thickness. Annealing the improved electrode by re-firing for 10 minutes at 1000°C did give a reduction in performance but some advantage was retained.

Steps gas concentration changes were also applied to amperometric sensors but these did not show temperature dependence. Extensive investigation indicated that the recorded response times were not due to electrolyte or electrode characteristics but other factors such geometrical dimensions of the test-chamber, sensor internal cavity or diffusion barrier. This has shown that response of the entire system is of the order of seconds over

the range of parameters examined. The immediate problem is the inability to ionically pump hard enough at low temperature and until this problem is overcome we can only surmise at improvements. A large diameter diffusion barrier with a small internal cavity would be beneficial and, for this to work at reduced temperature, electrolyte impedance needs reducing. Perhaps more important than sensor dimensions is sensor mounting and gas feeding. This is supported by the work of Saji et al [10] who made an amperometric sensor with a spinel porous layer to control gas diffusion and minimise internal volume. They recorded response rates of 200 mS to a step change in air/fuel ratio at 720°C.

4.3.3 Concentration modulations

The simple Pt cermet/YSZ system was used to evaluate the concentration modulation technique. During concentration modulation experiments, a reduction in output from the calculated Nernst EMF at low temperatures was attributed to reducing response rates. A second effect observed was that of increase in phase angle between valve output signal and sensor output. Closer observation showed that valve output signal appeared to lag actual valve throughput. Electrode improvement through application of low amplitude (5 mA) sinusoidal plating currents gave only a slight performance increase. Re-application using higher sinusoidal currents (30 mA) gave significant improvements of the order measured using impedance and step change assessments.

Concentration modulations applied to the amperometric sensor indicated slow system response such that at the lowest frequency employed, the full expected amplitude was not realised. System response did not show temperature dependence and therefore as with step change assessments the response measured was a function of test-rig or sensor barrier/internal cavity dimensions, electrode/electrolyte response.

4.3.4 Pressure modulations

The pressure modulation technique was applied to the simple Pt cermet/YSZ operated over a range of temperatures. Reduced sensor response rates had the effect of lowering sensor EMF amplitude and increasing phase angle as seen using concentration modulations. At higher temperatures where response could be considered fast, an amplitude independent of frequency was observed. At temperatures below 650°C stable amplitudes were not recorded, even at the lowest frequencies. Where sensor response was faster than the modulation frequency, a stable phase angle was realised. This related to a 50 mS time delay that was attributed to gas transit times from piston to sensor electrode.

One, as yet, unexplained phenomenon was an initial increase in amplitude with frequency. In addition a small amplitude difference was observed under identical conditions when gearboxes are interchanged. These were evident when sensor response was most sensitive and were attributed to small test rig dimensional differences. Similar trends were observed for sensors using impedance and pressure modulations of similar frequeney.

Application of the technique to amperometric sensors showed a response to pressure changes but no dependenee to constant pressure levels. This was attributed to oxygen transfer through the diffusion barrier where pressure differentials existed, thus sensor output amplitude actually increased with frequency. Sensor current amplitudes were temperature sensitive but this was due to oxygen diffusion exceeding cell conductivity at lower temperatures. For temperature/frequency ranges where sensor response was considered fast, a linear relation between modulation frequency and sensor amplitude was observed. Using smaller modulations alongside a variation in sensor geometric dimensions would provide further scope for assessment of amperometric sensor response using this technique.

In summary, in this chapter we have introduced initial results and investigations into the response rate measuring techniques of frequency response, step changes, concentration modulations and pressure modulations applied to PT/YSZ sensors. Results have been presented for amperometric and potentiometric sensors.

CHAPTER 5

ELECTRODE MATERIALS INVESTIGATION

RESULTS & DISCUSSION

5 Electrode materials investigation

Having developed the various techniques of response rate analysis and used a simple ZrO_2/Pt cermet to compare and contrast these techniques, In this chapter we use these techniques along side Scanning Electron Microscopy in the analysis of a variety of electrode materials and structures.

5.1 Platinum electro-deposition

In chapter 5 platinum electro-deposition was explored as a method of improving electrode performance and used to demonstrate that, with all other parameters being constant, the developed techniques could detect an improved sensor response rate. In chapter 5 however, each technique used a similar but separate cermet / plated electrode for comparison. In this chapter, in order to get a good set of data for comparison of simple metal, cermet and electro-deposited platinum electrodes, a single potentiometric cell was examined using impedance spectroscopy, step gas concentration change, concentration modulation and pressure modulation techniques with each electrode configuration in turn. The results of these examinations are compared in the sections below.

5.1.1 Current / voltage analysis

Taking the slope of current / voltage curves for the electrode / electrolyte cells allows a measurement of cell resistance to be obtained. These have been shown in previous work to be electrode-dependent at low applied voltage and electrolyte-dependent at higher applied voltage. In fig 5.1, the slope is taken at 50 mV which can be regarded as low voltage and therefore dominated by the electrode resistance component. The results infer a reduced resistance for the cell when electroplated, followed by the pure metal electrode then cermet electrode. Similar resistance increase with temperature is observed across the range with an advantage of approximately 50 to 75°C maintained by the electroplated over the cermet electrode. When plotted versus 1/T (not shown), the three electrodes return straight lines of similar gradient indicating that activation energies for all three electrodes are similar. This is not unexpected as the material in all three is platinum, the only change being the electrode microstructure. It is surprising to see the plain metal electrode returning a better performance than the cermet.

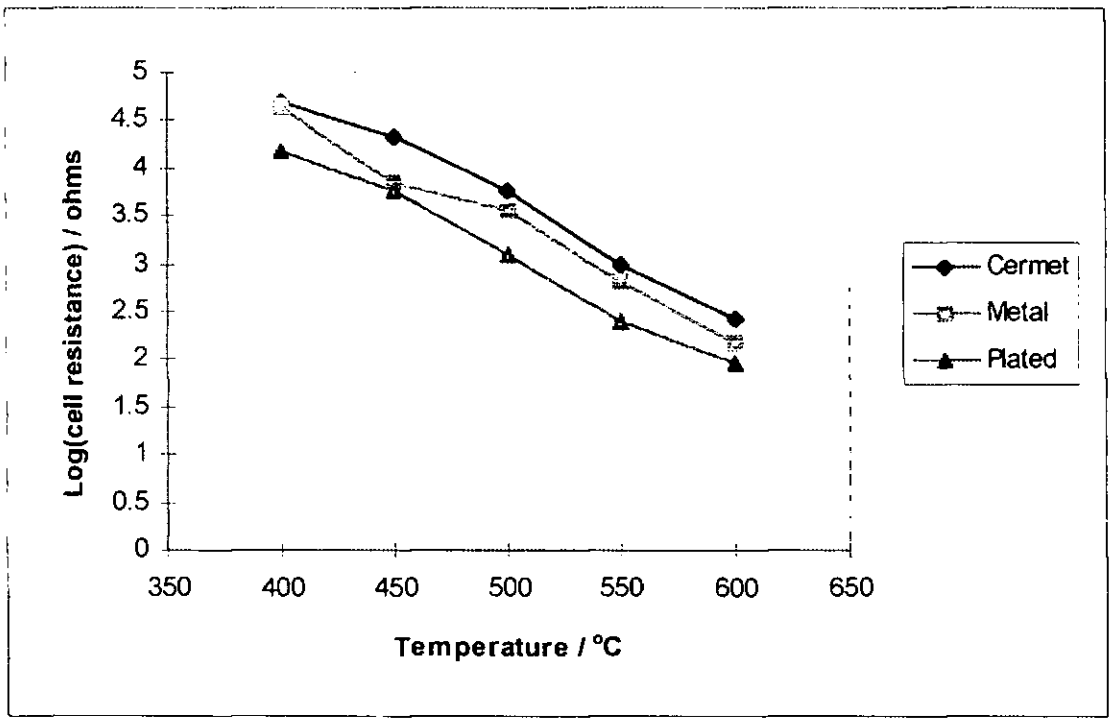

Figure 5.1 Platinum electrode cell resistances from current / voltage curves at 50 mV

5.1.2 Impedance

The results of frequency response analysis of the three systems are reported in figure 5.2 which shows electrode impedances for each electrode type and figure 5.3 which shows electrolyte impedances. We see a small improvement in electrode performance when the cermet is used in place of the simple metal electrode but a marked improvement when the cermet is electroplated. This maintains the trend seen in current/voltage analysis but with a greater separation for the cermet electrode with a temperature improvement of >100°C. The improvement measured in the electroplated specimen is seen as deriving from improved three phase boundary length achieved with finely deposited platinum. The fine deposition was reinforced hy the black coloration of electrodes after platinisation, a well known phenomenon occurring when platinum is of a finely divided form. Somewhat surprising in the results obtained is the change in slope that occurred with platinisation, indicating a change in electrode activation energy. The activation energy is expected to remain constant for an electrode irrespective of its microstructure or macroscopic area. Electrolyte impedances showed no such alterations in activation energy. Grain and grain boundary impedances do however show a small improvement going from metal to cermet electrodes and again when electroplated. These are thought to have occurred by improved electrode surface coverage allowing a slightly greater electrolyte area to be utilised. Comparing the cell resistances obtained by impedance and current / voltage methods we do obtain approximate agreement for cermet and metal electrodes. The resistances of

electroplated samples however appear to be an order of magnitude higher in current/voltage assessment. This is at least partially attributable to incomplete separation of electrode from electrolyte impedances for the current / voltage assessment exacerbated by the low electrode impedances obtained.

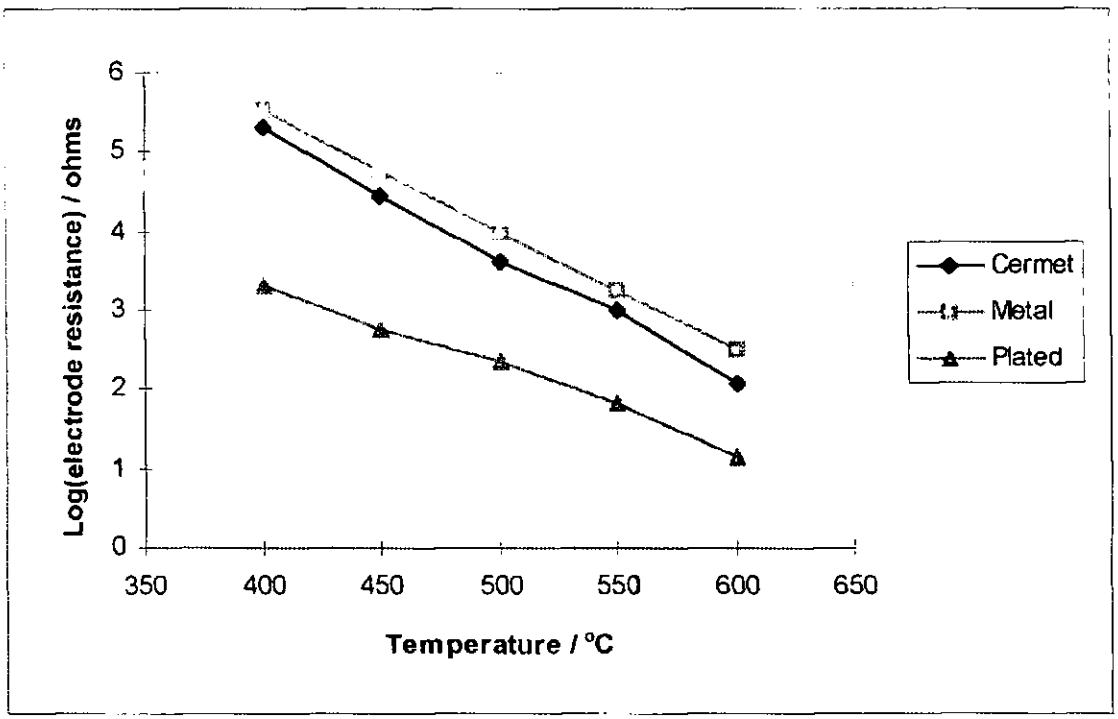

Figure 5.2 Platinum electrode cell frequency response analysis.

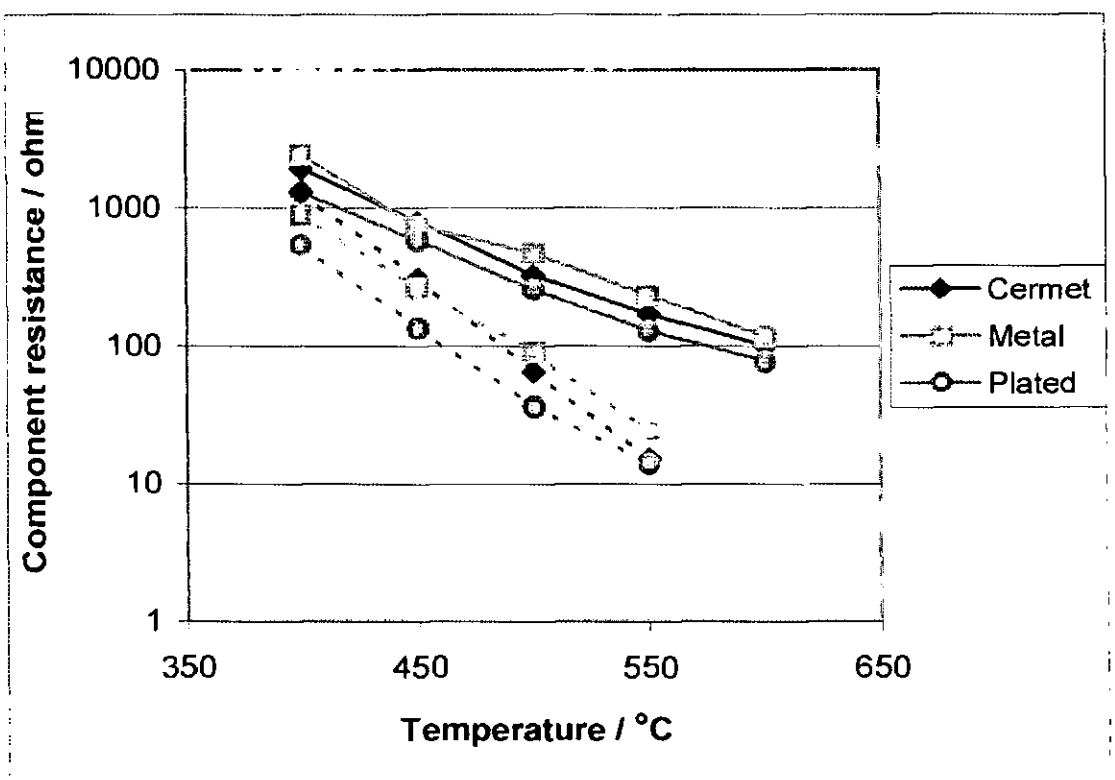

Figure 5.3 Platinum electrolyte cell frequency response analysis.

Dashed lines indicate grain boundary impedance, solid lines are grain impedances

By combining the measured cell resistances with the measured capacitances obtained by impedance analysis, we are able to obtain the electrode time constants for each electrode structure (fig 5.4). Time constants are seen to follow the pattern of cell resistances since the cell capacitances are influenced to a lesser extent. The trend of similar time constants for cermet and metal electrodes is maintained with a large reduction in time constant reproduced for the electroplated structure. The inference from this analysis is that sensors with plated electrodes will respond approximately two orders of magnitude faster than those of cermet or metal electrodes.

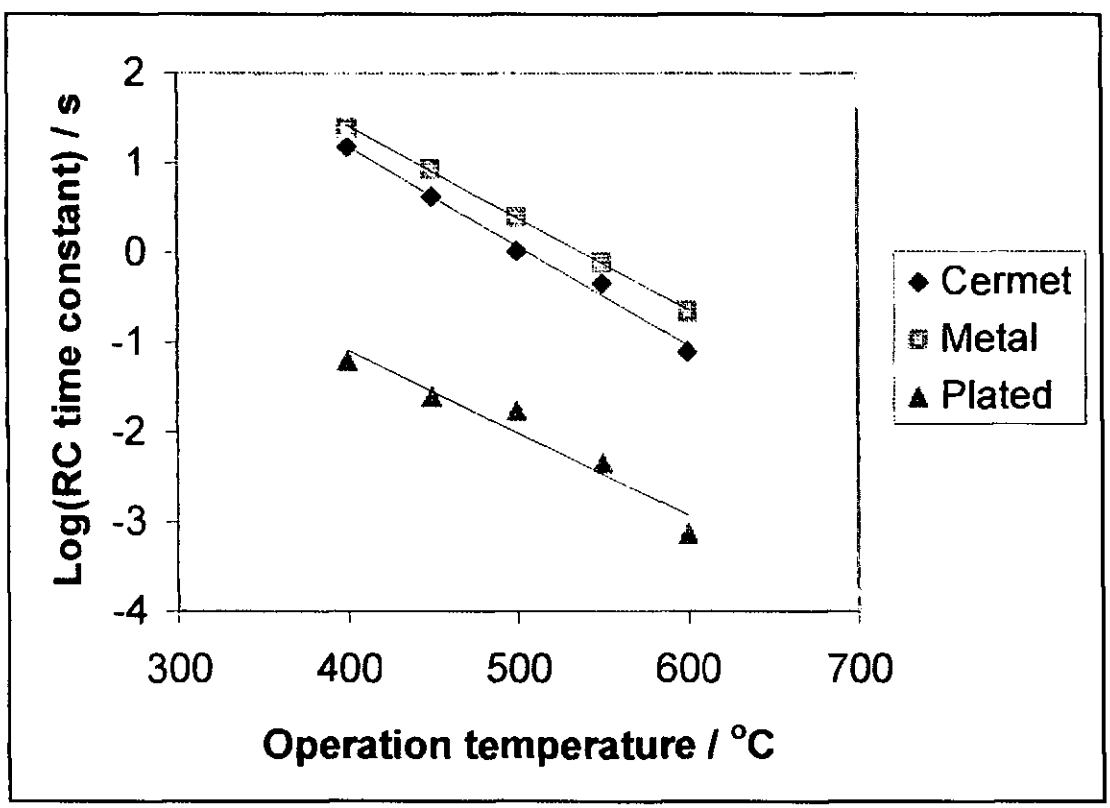

Figure 5.4 Platinum electrode cell RC time constants

5.1.3 Step technique

Results for the step change technique of each electrode type are reported below in figure 5.5. These show similar response rates for platinum metal and cermet electrodes but a significant improvement where electroplated platinum electrodes were used. These results are comparable with those for frequency response analysis of these samples with up to 1 order of magnitude faster responses. The degree of improvement obtained by electroplating is, however, less at higher temperatures. This is consistent with the change in activation energy derived by frequency response analysis. Comparing these response

times with the time constants derived from the frequency response work we obtain the same trend of similar metal and cermet performance but faster response with electroplated electrodes. Step changes return slower responses overall, in addition they measure to 50% response times (i.e. the time taken for the system to register 50% of the final stabilised reading) whereas time constants should reflect theoretically 100% response times. In partial explanation the time constants show only electrode response, steps include electrolyte response which would add to the response but not by the amount shown. The inclusion of electrolyte response also partly explains the merging of response times at higher temperatures as electrode impedance dramatically decreases. Data is insufficient in the electrolyte frequency range to provide conclusive evidence; however, electrolyte time constants are estimated to be in the region of 10^{-6} to 10^{-5} seconds for these temperature ranges and therefore much faster than electrode component response rates. There does however remain an element of disagreement between these two techniques which has as yet not been identified.

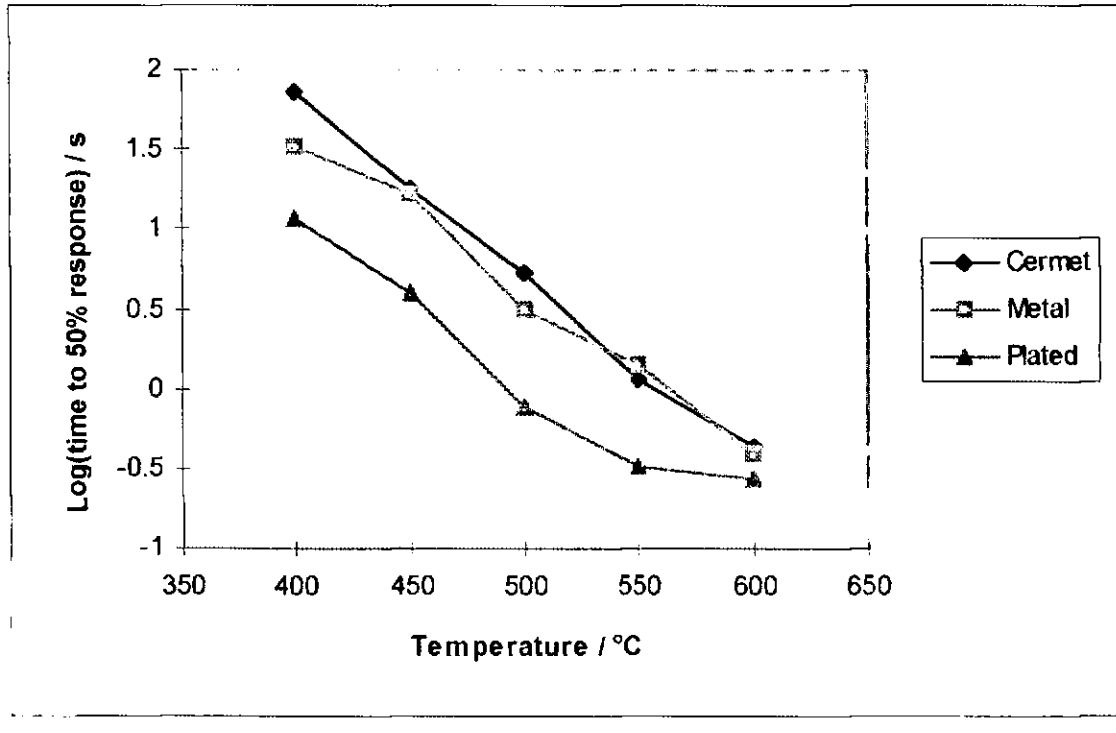

Figure 5.5 Platinum electrode cell step response results at 50%

5.1.4 Concentration modulation technique

The results of concentration modulation examination of the various platinum electrodes conducted at 0.3Hz are presented in figure 5.6. The platinum metal, cermet and electroplated electrode samples gave pseudo-sinusoidal output amplitudes which were converted using the Nernst equation to yield percentage oxygen modulation amplitudes

which were plotted versus temperature. The results show similar performances for the metal and plated electrodes with a slower response from the cermet electrode. In comparison with the above I/V, impedance and step response analyses we do not obtain the anticipated agreement, with the difference between plated and metal electrodes marginal and even points indicating superior performance from the metal electrode. As with the step change technique, the plated electrode appears to lose its performance advantage at higher temperatures. The comparatively poor cermet electrode performance is in agreement with the trend established by I/V analysis but contrary to that of impedance and step change analyses.

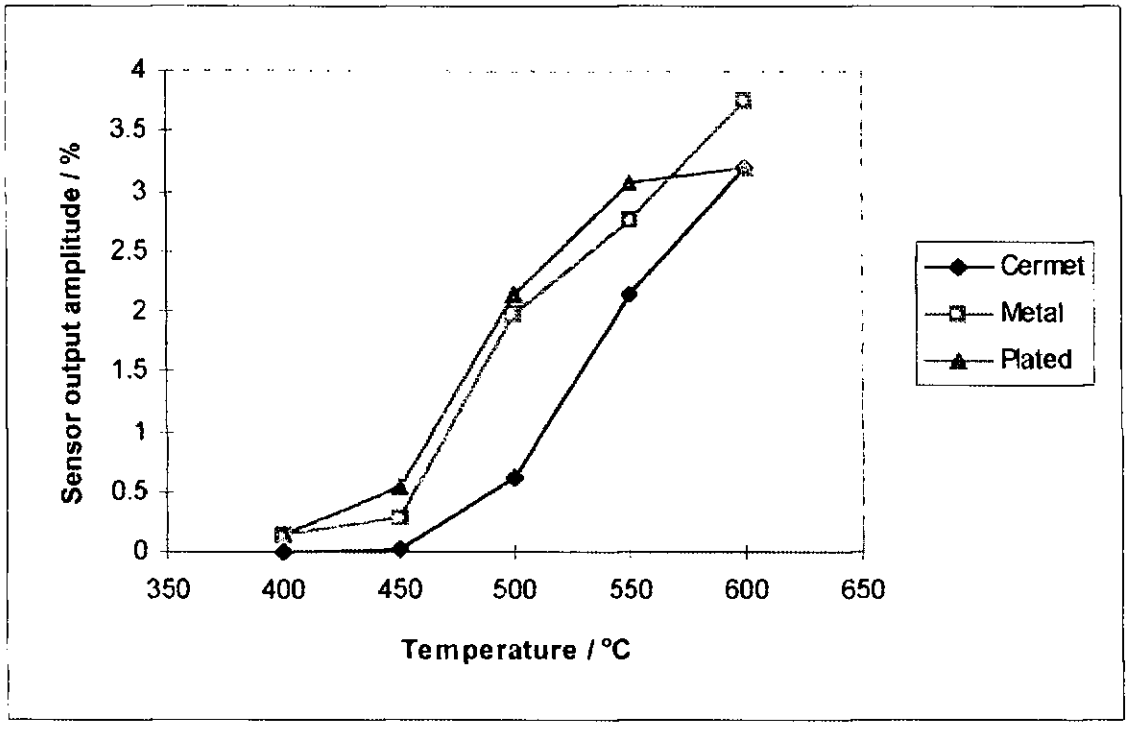

Figure 5.6 Platinum electrode cell concentration modulation results at 0.3 Hz

The amplitude and phase lag information for the electroplated electrode are depicted in figures 5.7 and 5.8 respectively and show the trends of decreasing amplitude and increasing phase lag as modulation frequency increases. The amplitude measured at low frequency represents the input modulation level, coinciding with a low phase lag as response approaches/exceeds modulation frequency.

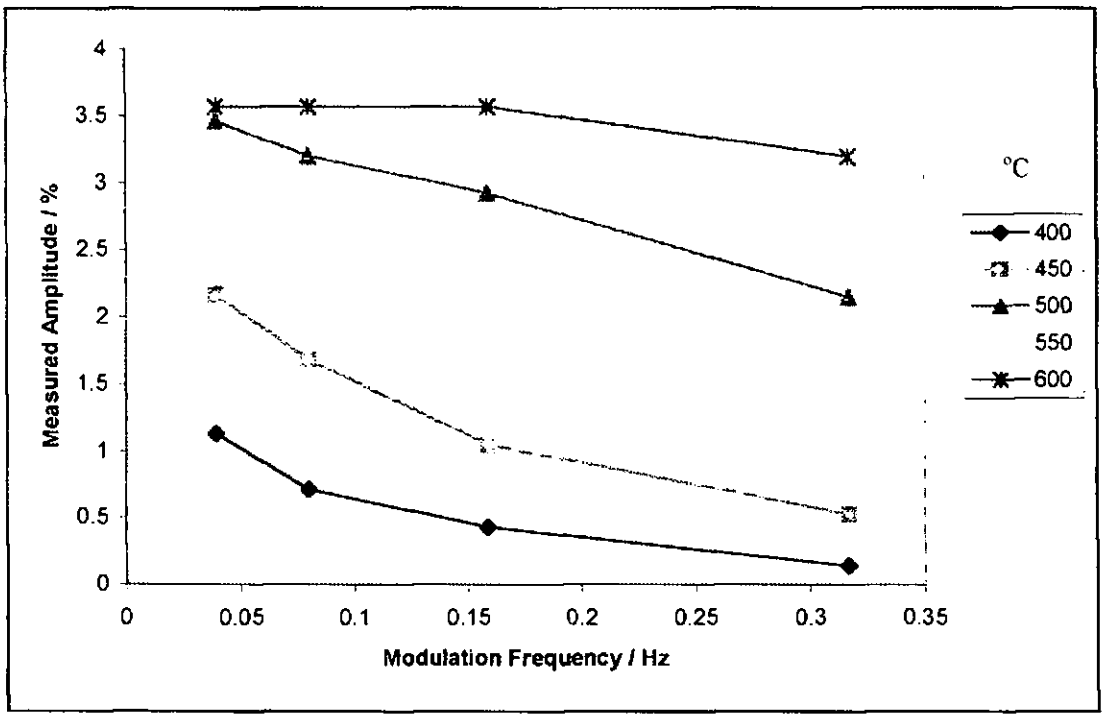

Figure 5.7 Platinum electrode cell concentration modulation results at 0.3 Hz

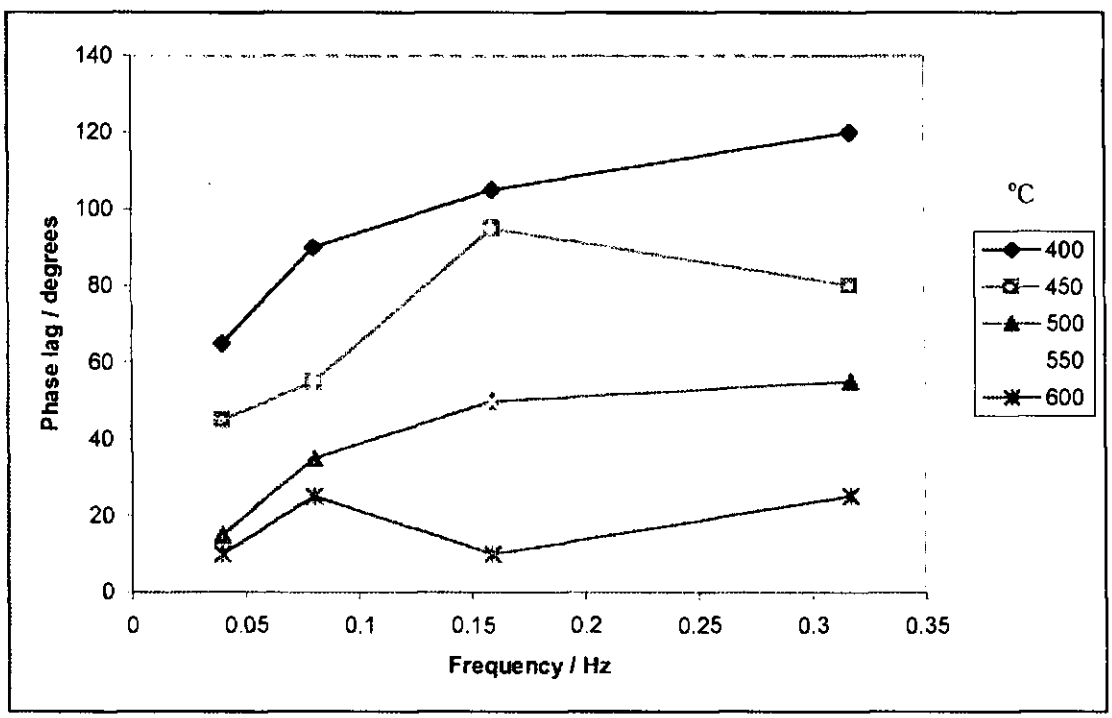

Figure 5.8 Platinum electrode cell concentration modulation results at 0.3 Hz

By fitting a logarithmic curve to the data shown at each temperature depicted in figure 5.7 and equating this with the constant amplitude displayed at higher temperatures, we can obtain an estimation of frequency at which the modulation amplitude matches the response of the electrode / electrolyte system at that temperature and therefore obtain a response rate at each temperature.

$$P = k \ln(f) + c$$

where P is the maximum amplitude, k and c are response rate related constants and f is the matching frequency. Implementation of this analysis reveals the time constants plotted in figure 5.9. Whilst this returns a graph generally as per expectations, the results indicate a far slower overall response than similar measurements using step and impedance measurement techniques which suggested worst case response rates of <100s for response at 400°C albeit response times to 50% response for step measurements and for only electrode response for impedance measurements (see figures 5.4 & 5.5).

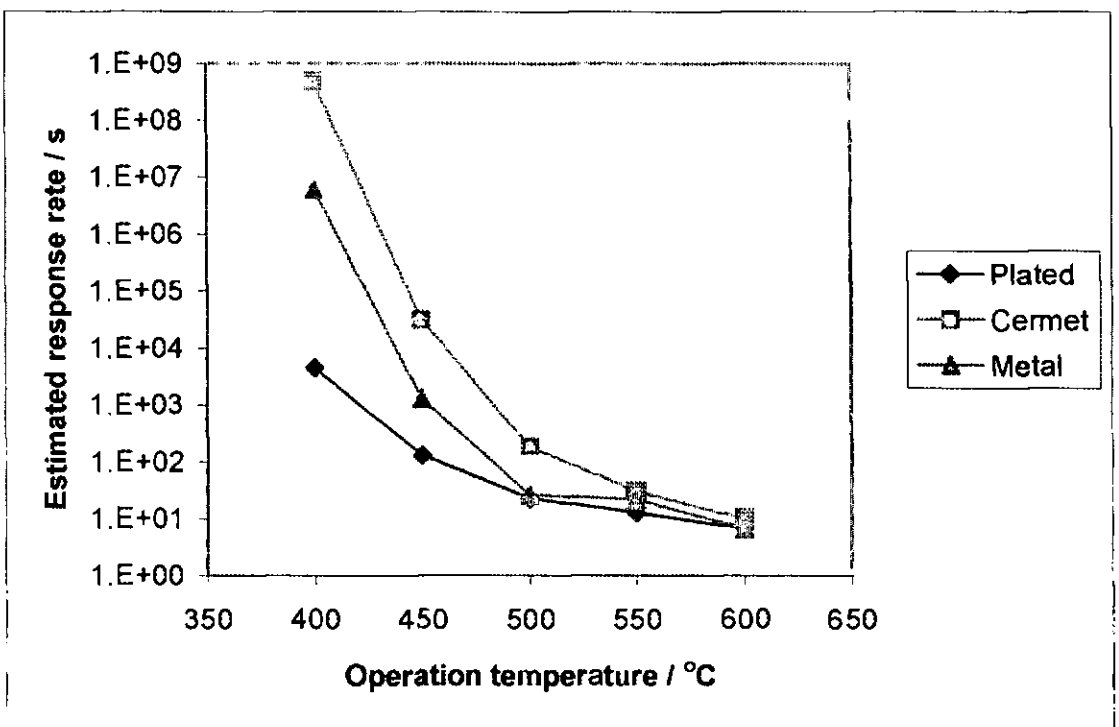

Figure 5.9 Estimated response rates from extrapolation to amplitude maximum

5.1.5 Pressure modulation technique

Figure 5.10 shows results of pressure modulations also performed at 0.3 Hz over a range of temperatures using metal, cermet and electroplated electrodes in turn. These results show similar performance realised by metal and cermet electrodes but a marked improvement in response of the electroplated electrodes. These results closely mimic those of concentration modulations but with the large separation between cermet/metal and plated electrode responses. This trend is in accordance with results of step and impedance techniques.

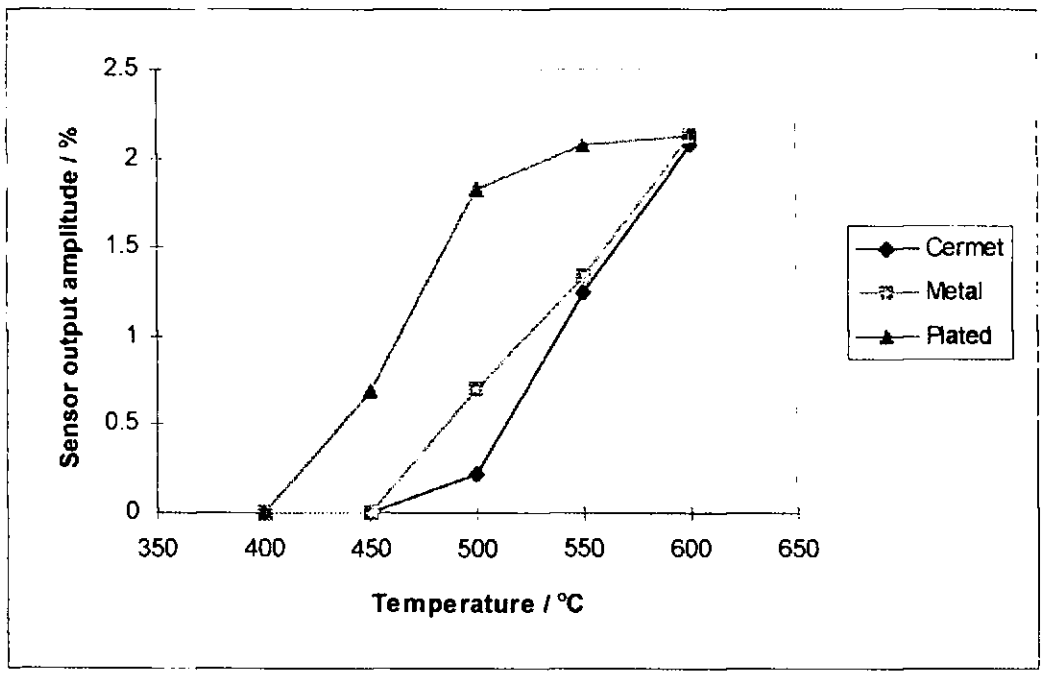

Figure 5.10 Platinum electrode cell pressure modulation results at 0.3 Hz

Figure 5.11 shows the measured modulation amplitude plotted against frequency for cermet and plated electrode cells (joined markers indicate cermet). As with figure 5.7, a point is reached at which cell response exceeds modulation frequency and amplitude reaches the limit dictated by maximum pressure developed within the system. For slower responses, the sensor amplitude is governed by sensor response.

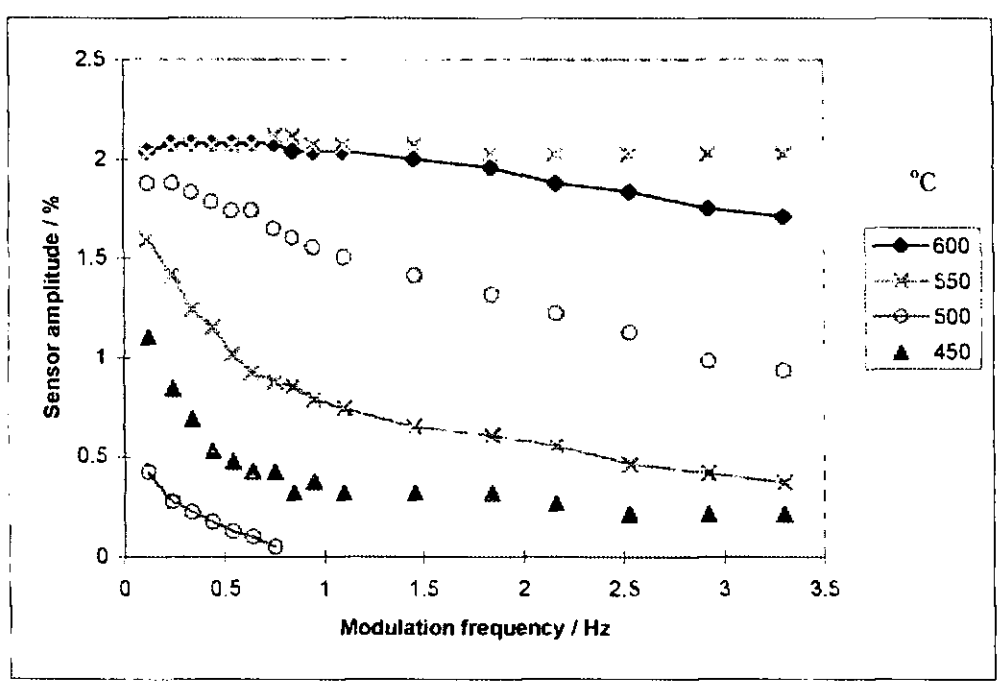

Figure 5.11 Platinum electrodc cell pressure modulation amplitudes. Joined markers are Cermet results, Un-joined markers indicate electroplated electrode results

As with figure 5.9, an estimation of the frequeney at which sensor response matches the limiting amplitude ean be extrapolated; sueh an estimation has been performed to obtain figure 5.12. These results give eomparable results to those from eoneentration modulation analyses but are somewhat slower than impedanee or step ehange work would suggest. Unfortunately, the limited frequency range over whieh this teehnique was useful meant that eaeh eell eould only be assessed over a limited temperature range.

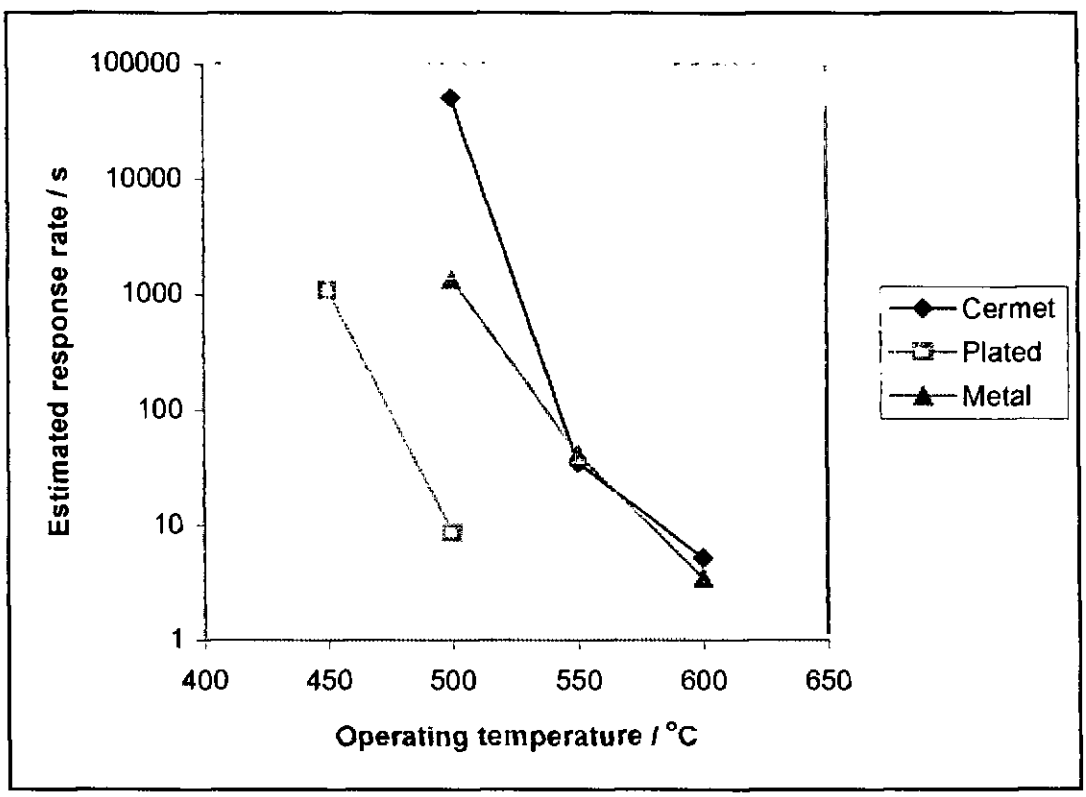

Figure 5.12 Platinum eleetrode eell estimated responses

5.2 Half cell impedance assessment

Prior to experimentation with various electrode materials using the developed experimental techniques, small samples were fabrieated to get a feel for electrode preparation and to reduce the number of variables worthy of examination. These initial eleetrode samples were assessed using frequeney response analysis to eharaeterise the electrode properties of eells for eombinations of platinum, silver, gold and palladium metals, eermets, mixes and layers.

5.2.1 Base metals

Figure 5.13 gives the results in Arrhenius plot format for a straightforward comparison of the simple base metals. To get an idea of the reproducibility, several samples were examined for some electrodes. The results show a fair degree of scatter which may be attributed to the inability of painting of pastes to give an entirely reproducible electrode. From this initial analysis however it is seen that silver electrodes consistently give the best results, palladium give the worst whilst gold and platinum give intermediate results of similar performance.

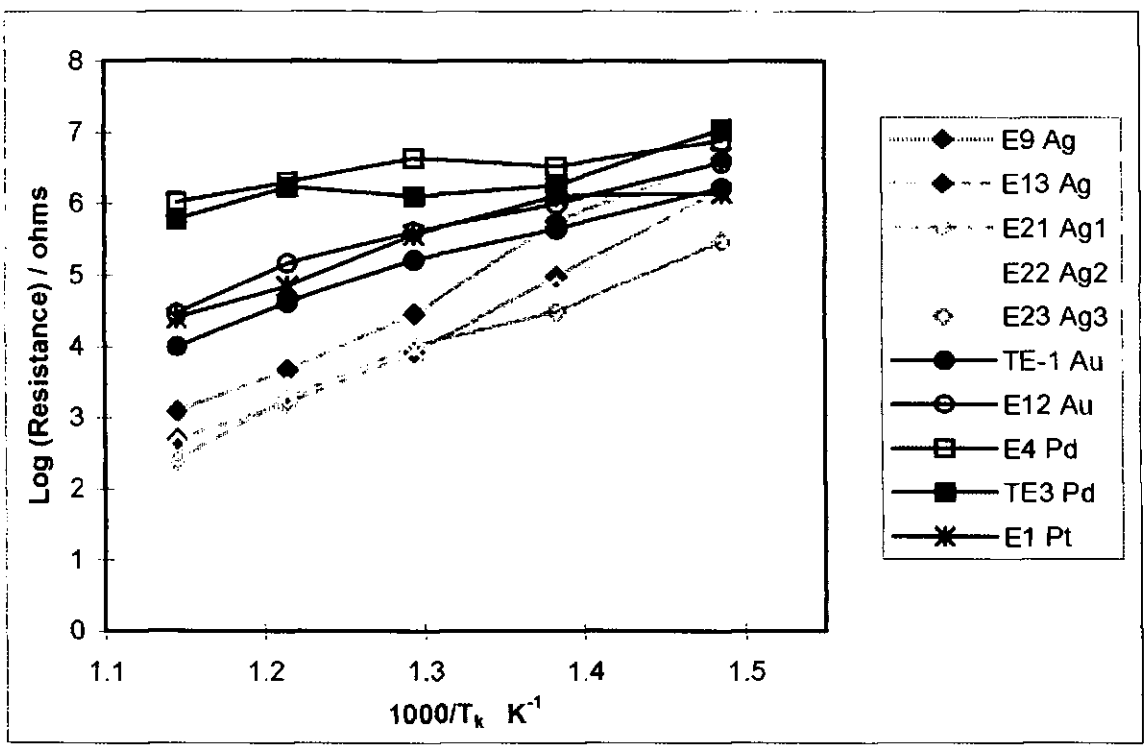

Figure 5.13 Arrhenius plot for base metals

5.2.2 Cermets

Figure 5.14 shows Arrhenius plot slopes and impedance data at 500°C for cermet electrodes with simple metal electrode averages for comparison. Data is not presented for palladium as the electrode did not adequately adhere to the electrolyte. This may be due to the use of the base powder and insufficient mixing or inappropriate sintering. The results do not give any clear trends in improvement. This is probably due to inadequate preparation techniques. Precautions of clean preparation and thorough mixing were adhered to but no detailed investigation into the resultant microstructure was completed. These tests have demonstrated that without extensive electrode preparation there is no clear benefit in the use of cermets, so the extra preparation time and variables involved

ruled out using cermets for extended investigation in this work. The previous electrode assessment indicated that platinum cermets often gave benefits over simple metal electrodes; the variability in performance seen here highlights the requirement for careful preparation. Such work has been carried out for platinum cermets used in other tests by previous workers [2, 96, 101].

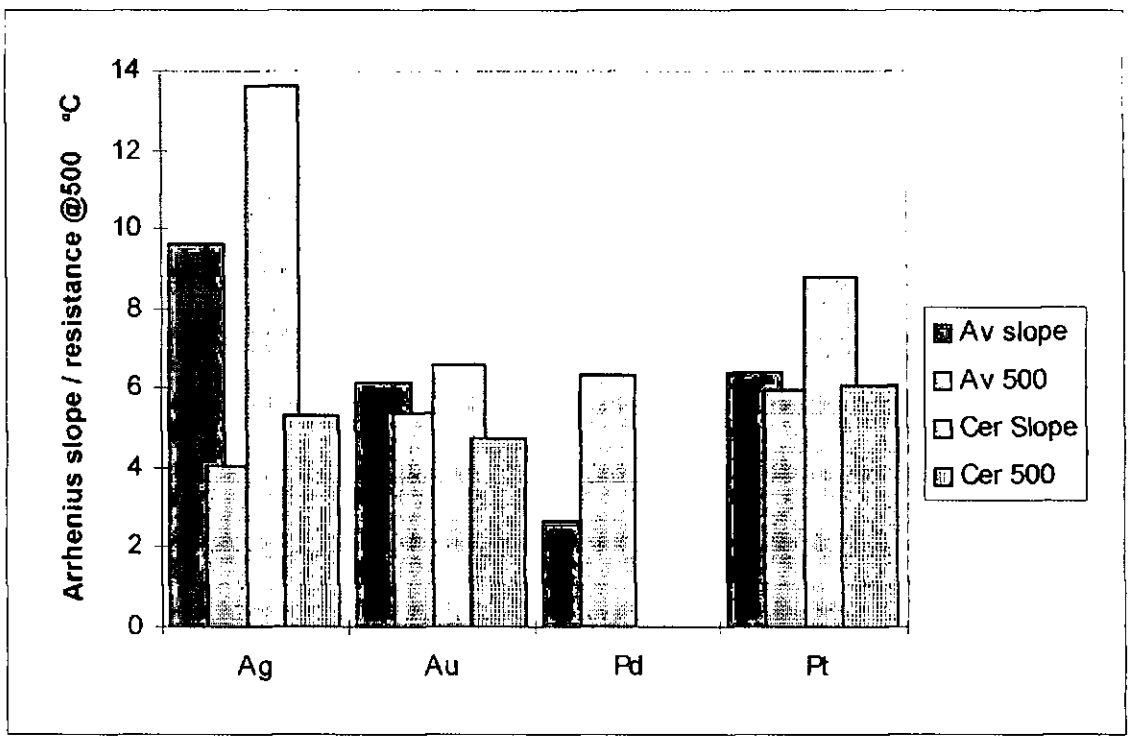

Figure 5.14 Bar chart of metal / cermet Arrhenius parameters

5.2.3 Binary mixes

Figure 5.15 shows Arrhenius plot parameters obtained for binary metal mixes, along with simple metals for comparison. Palladium electrodes mixes were not examined as there was insufficient of the powder to allow sufficiently accurate preparation. Again there were no dramatic results as a consequence of combining metals, with impedances obtained of the same order as those of the constituent pastes being achieved. The accuracy of preparation through lack of specific investigation prevented a more detailed examination; the purpose of the tests were to show up any areas of significant interest and therefore this work has shown, as expected that no simple yet significant improvements are realised for binary mixes. These mixes were however used in the extended electrode examination as no other, more interesting, results were obtained.

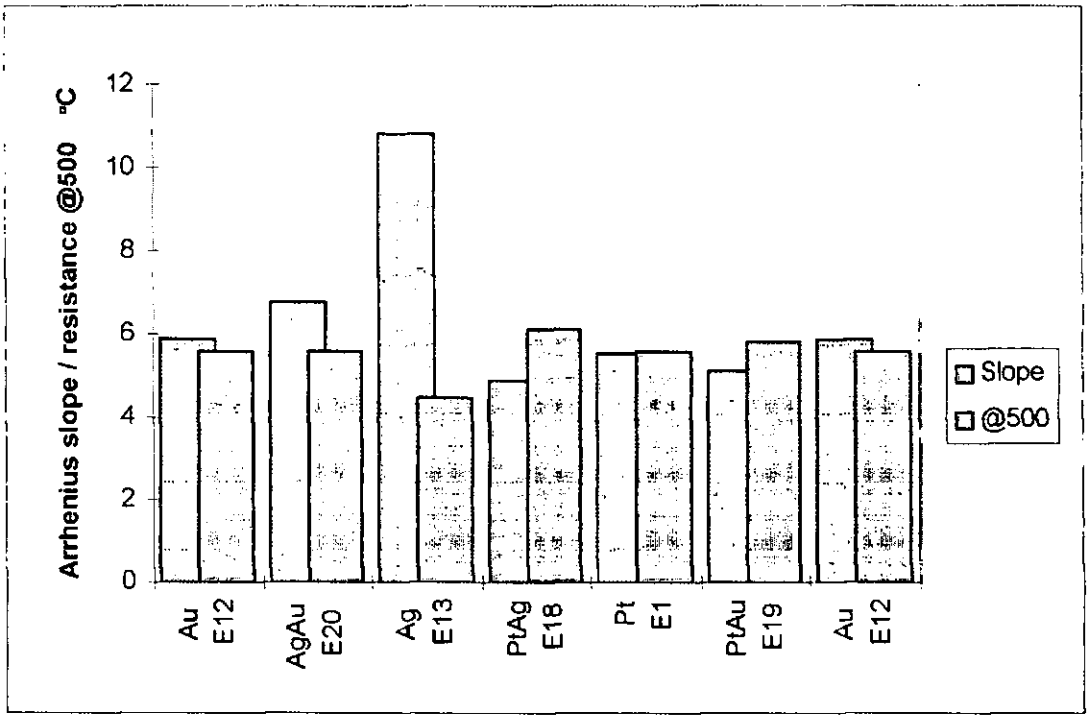

Figure 5.15 Bar chart of mixed metal electrode Arrhenius parameters

5.2.4 Layered electrodes

Figure 5.16 gives Arrhenius plot parameters for layered metal electrodes. The plots give two sets of parameters for each sample, the first is for the impedance data of the initial layer, followed by data for the layered electrode to give direct comparison of any improvements realised. With this direct comparison we can be more specific as to the results obtained as deposition plays less of a role. The results show electrode improvements when silver is applied as the second layer. This may be surprising if it is envisaged that the silver forms a solid blocking layer (see section 5.7.2) over the existing electrode but may be explained as the silver passing through the initial layer and giving direct contact to the electrolyte. This may be the case as the silver approaches its melting temperature at the electrode curing temperatures used. A platinum second layer appears to worsen electrode performance. This may be due to the blocking effect as the additional platinum may reduce gas diffusion rates. Gold applied to silver had little effect on electrode performance at 500°C but did have the effect of improving higher temperature performance, worsening low temperature performance thus giving a change in slope. The change in slope for silver on platinum was purely an improvement in lower temperature performance. In general, the changes were not dramatic enough to warrant further investigation and therefore layered electrodes were not included in the further assessment or investigation.

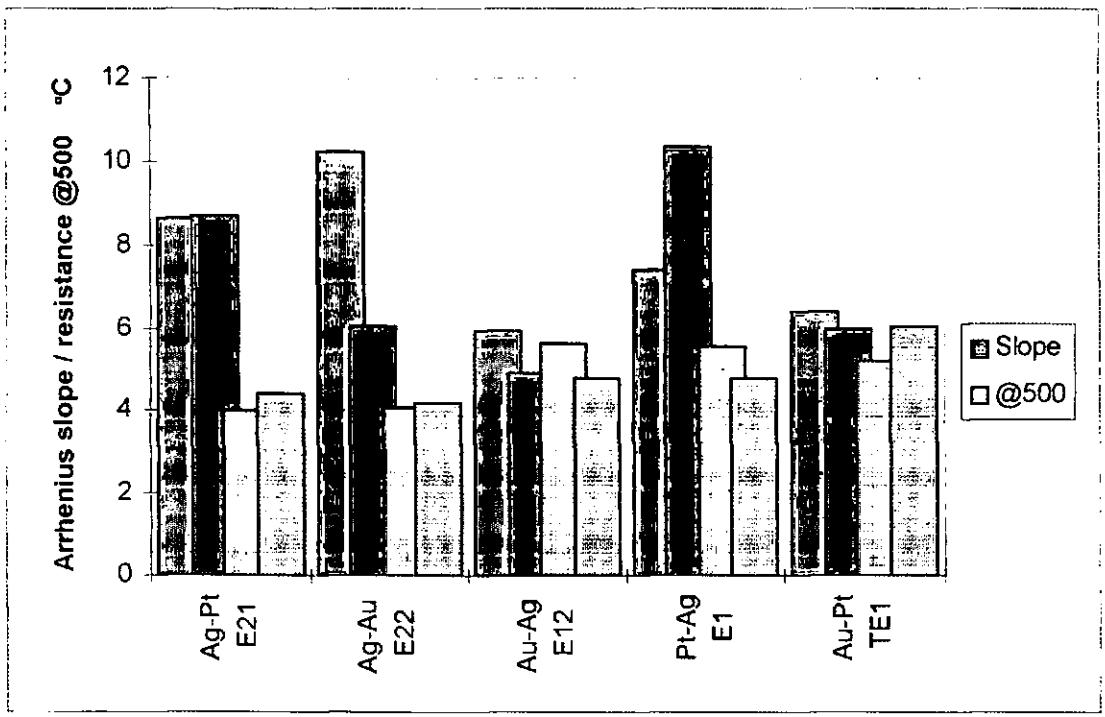

Figure 5.16 Bar chart of layered electrode Arrhenius parameters

5.2.5 Electrolyte findings

Whilst the above examination was primarily used to assess electrode performance, data were recorded for electrolyte impedance. The results are given in figure 5.17. The interesting point of this data lies in the apparently two sets of results, separated by ordering by electrolyte impedance at 500°C. The cause of this is suspected to be that the electrolyte samples used were fired in two batches. These batches were cut from the same sheet of plastic-ceramic to similar dimensions and fired at the same ramp rate. During the firing of the first batch however the furnace thermocouple broke at 1450°C resulting in the shutdown of the furnace and hence a faster decreasing temperature ramp rate. Upon visual inspection the samples visually appeared unaffected by this and so were used indiscriminately along with the second batch electrolyte samples. The separation of cell impedance into its separate components by frequency response analysis enables us to assume that this has had negligible effect on the electrode results but does give an insight into the necessity for electrolyte firing cycles to be closely controlled.

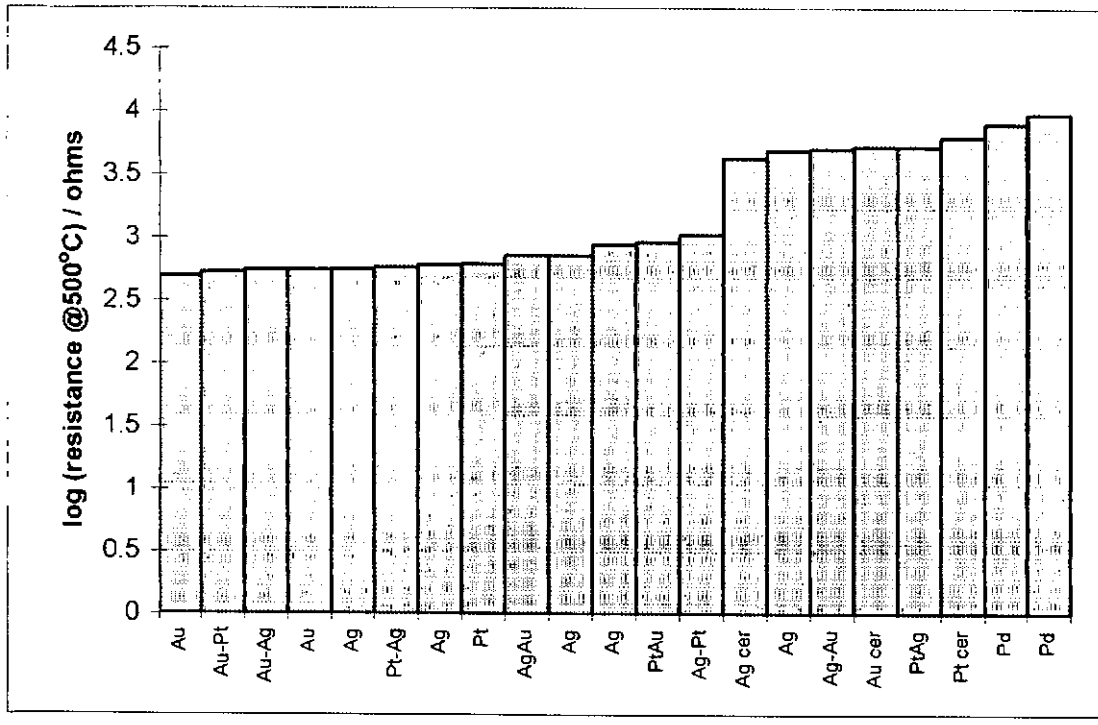

Figure 5.17 Bar chart of electrolyte impedance

5.2.6 Electrode selection

From the work presented in this section, a selection of electrode materials was chosen for extended assessment by application to potentiometric cells. The choice was based primarily on simplicity as there were no remarkable findings as a result of layered or cermet electrodes. The selection made was of primary metals of silver, gold, platinum, palladium along with gold/platinum, gold/silver and silver/platinum as binary metal mixes of approximate 50% / 50% by volume.

5.3 Impedance analysis

Figure 5.18 shows potentiometric test cell impedances as measured for cells employing the selected electrode materials, each at 500°C in air. These results are in agreement with the initial electrode test results above. Simple silver electrodes again provide the lowest electrode impedance, with the highest given by palladium. Platinum, gold, gold/platinum and gold/silver electrodes gave very similar results. Platinum/silver mix electrodes also give lower resistances. The other interesting result seen is that of the electrolyte impedances of the silver electrode sample. Whilst the other electrolytes tend to follow the trend laid by the electrode, suggesting that small electrolyte impedance changes depend upon electrode coverage. The silver sample electrolyte shows increased electrolyte impedances where one might expect the least. This factor becomes more understandable

when contemplated in combination with the electrode edge on micrographs in Appendix F1.8. These micrographs show an apparent phase change, attributed to contact with the metal layer. No similar effect was found in initial electrode assessment samples, this may possibly be explained as the initial electrode assessment used 7.5 mol% YSZ and so was already on the PSZ/FSZ limit whereas potentiometric cells used 8 mol% FSZ.

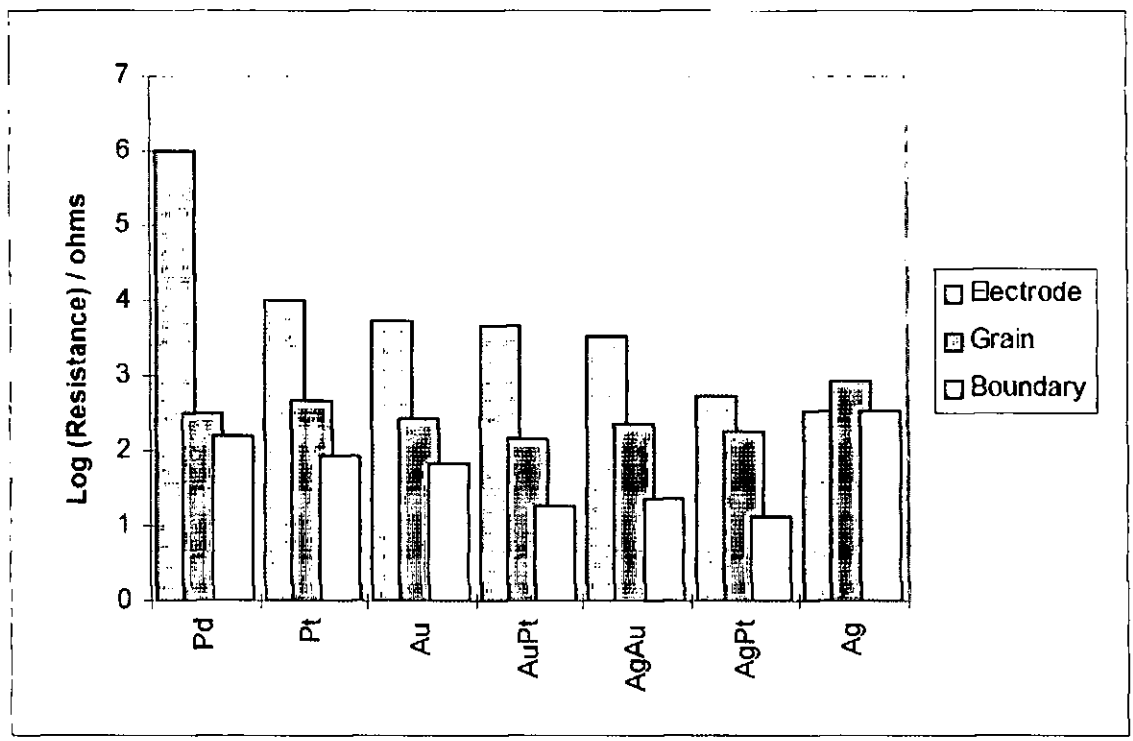

Figure 5.18 Bar chart of cell impedances at 500°C

Circle fitting to the semi-circular complex plane impedance plots, allows the facility of component capacitance measurement. Such measurements were taken for each component of each electrode cell to allow a comparison between materials. Figure 5.19 shows the comparison of the three components for all of the samples tested and clearly shows marked component capacitance separation. Grain and boundary capacitances are expectedly similar for the various cells but the similarity in capacitance for electrodes is also notable. The two electrode capacitances that do not fit the remainder of the group are those of gold and palladium metal electrodes and may be indicative of poor adherence of the electrode to the electrolyte (see SEM analysis).

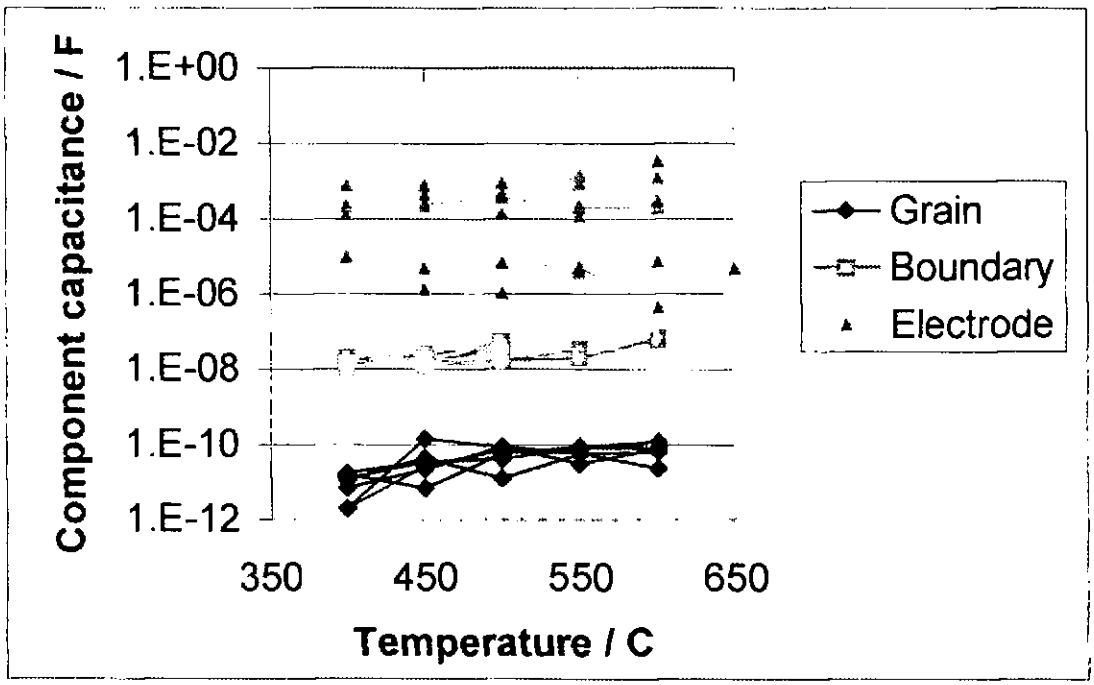

Figure 5.19 Measured cell component capacitances

Combining component resistance and capacitance measurements, we are able to calculate an RC time constant for each cell. These are depicted in figure 5.20 which again shows the three clearly distinguished components for each cell. The electrode component is obviously the dominant, response rate controlling factor (Note: no bias potential is present) with electrolyte grain and boundary components four and six orders of magnitude less influential respectively.

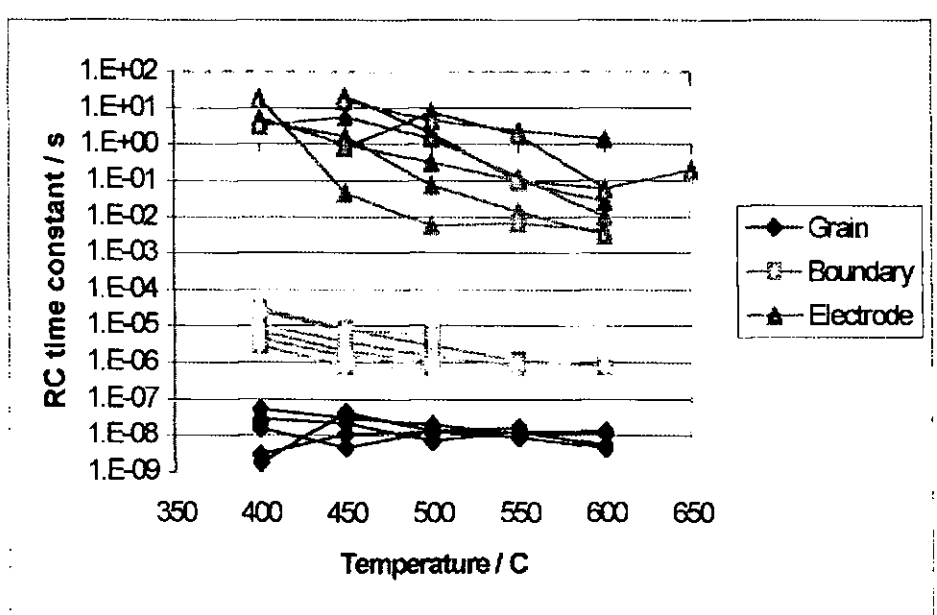

Figure 5.20 Calculated component RC time constants

Figure 5.21 focuses on the RC time constant of the electrode components, identifying each. The effect is to give a particularly unclear picture of cell response times with much overlapping and no single trend with temperature. The notably fast and slow responding electrodes of silver and palladium do not mark themselves out as exceptional in this analysis. This is attributable to palladium having a high resistance multiplied by a low capacitance compared to silver's low resistance multiplied by its average capacitance effectively cancelling out the differenees between them. Platinum metal, cermet and plated electrodes all gave reasonably linear and clear response to such tests, and even in this experiment, the platinum maintains a fairly linear relationship. It would appear that comparison of RC time constants derived from impedance data is not an effeetive way to compare cell response rates of differing electrodes material.

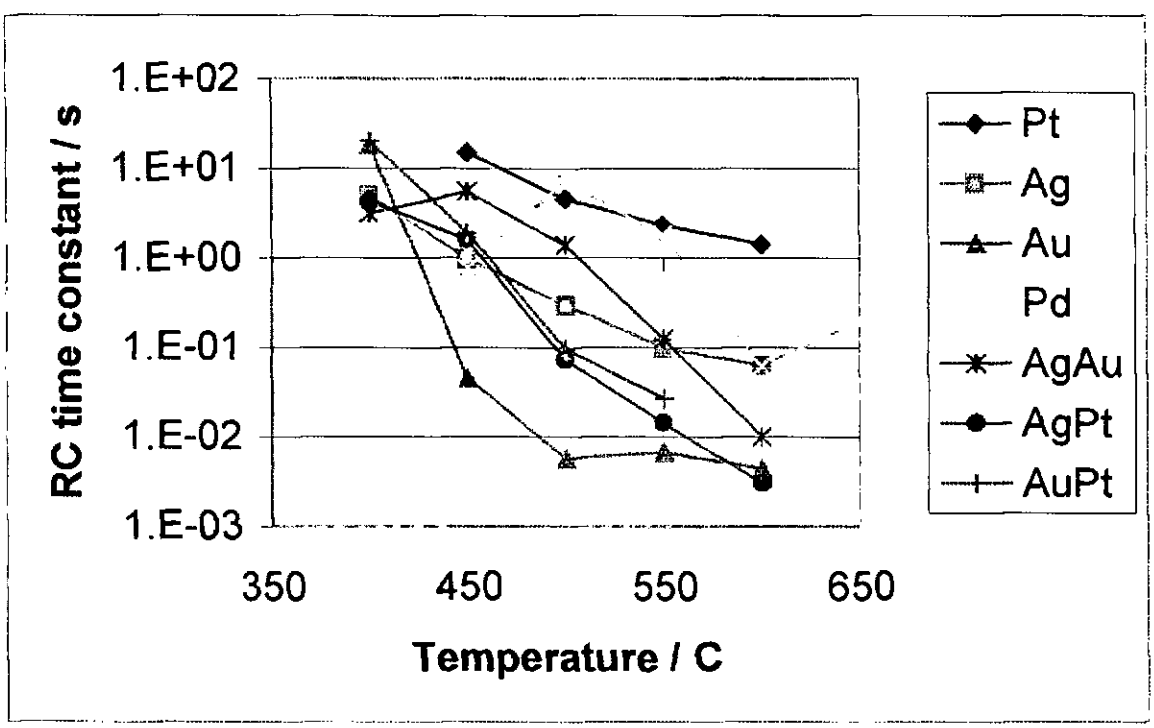

Figure 5.21 Electrode RC time constants calculated from individual R and C values obtained by frequency response analysis

5.4 Step change analysis

Figure 5.22 shows the results of step concentration tests carried out at 500°C for each of the electrode samples. These results show a clear spread of response rates, with silver giving the best performance and palladium giving the worst. Electrode performance in order are: silver, gold, silver / gold, silver / platinum, platinum, gold / platinum then palladium. On this logarithmic scale, these results are virtually linear and, at this

temperature, fairly evenly spaced. Included in the chart for comparison are the response plots for platinum cermet and electro-deposited electrodes, showing the appreciable spread of electrode performance attributable to deposition technique rather than material.

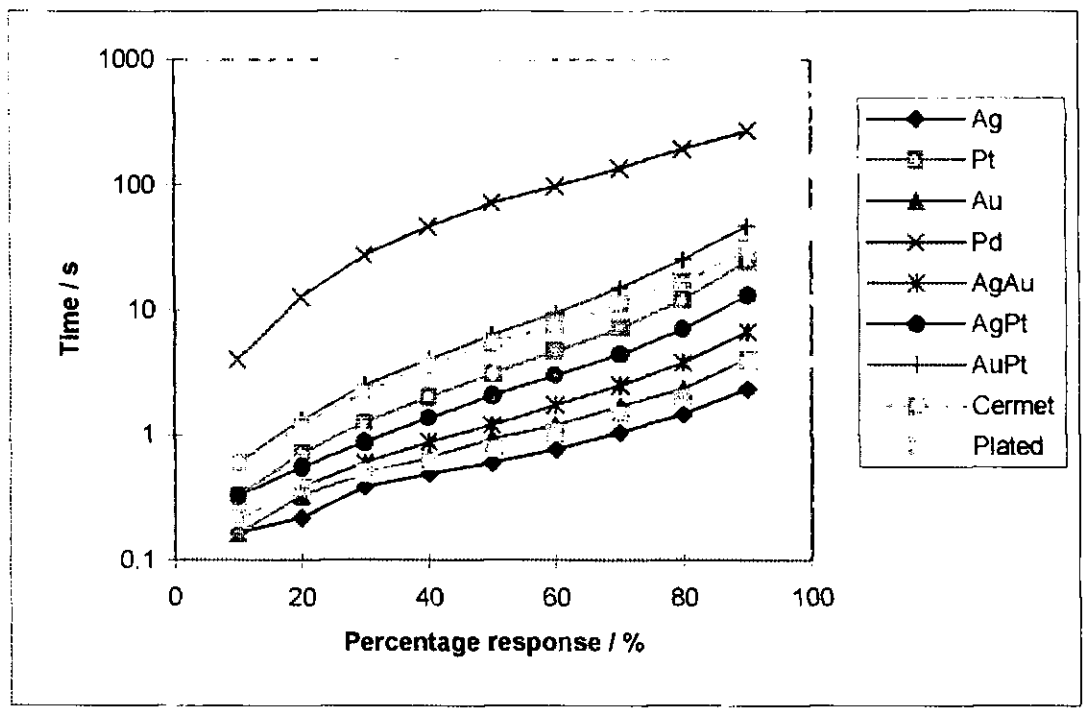

Figure 5.22 Step concentration test results at 500°C

Figure 5.23 shows step results over the range of temperatures at 90% of total response. Over these temperatures, the performance order is not rigidly retained. These results agree with the frequency response work in the best and worst cases, the rest of the data fall in-between but do not follow the same order. This, in part is explicable by the close correlation between the frequency response data (resistance readings). Comparing the Arrhenius plots for both step and frequency response data, there are similarities but these are not sufficiently congruent to enable a definite correlation. Trends and comparisons of this plot are far clearer than the equivalent impedance RC time constant comparison with a more direct link of results to the desired information and resulting in a more clear and understandable output. The advantage of frequency response of separating out electrolyte and electrode parameters becomes redundant following the conclusion that electrolyte impedance has a negligible effect where no bias potential is applied.

Winnubst et al [3] used step changes in oxygen concentration to measure the response rates of platinum and gold on various ZrO_2 and Bi_2O_3 electrolytes. They found that gold gave considerably better performance compared to platinum on a YSZ electrolyte. A similar

performance enhancement of gold over platinum was seen in this work. Their results were presented as operational temperatures at which a specified repose rate could be attained. The dissimilar manner of presentation of their results makes diffieult a direct comparison between their results and those presented here. They do however appear to give response rates of a very similar magnitude, although superficially their results do indicate slightly faster responses than those recorded here. Activation energies of 216 and 199 kJ/mol were reported for gold electrode and platinum electrode sensors respectively.

Kobayashi et al [26] measured response rates of aged zirconia sensors utilising platinum paste electrodes. Response times of several seconds were recorded for both young and aged sensors operated at 700°C. Their results show a slightly slower response than the sensors used in this work. This also indicates that ageing would not have been a significant factor in the results presented here.

Fouletier et al [37] used step pressure changes to examine response rates of platinum and silver electrodes on zirconia potentiometric devices. They also found a marked improvement of silver over platinum. Their silver electrodes displayed a similar performanee at higher temperatures to those presented here but were significantly better at low temperatures. The performance of their platinum electrodes was significantly worse across the entire temperature range. Activation energies of 0.6 and 1.0 eV were reported for silver electrode and platinum electrode sensors respeetively.

Results presented by Doughty et al [110] for platinum electrodes on a zirconia sensor showed markedly worse performance than those presented here. The response rates of their sensors were not significantly affected by electrolyte thickness. An activation energy of 150 kJ/mol was reported.

Anderson & Graves [106] measured the response rate of a zirconia sensors utilising platinum paste electrodes. This sensor gave a response time of 1 second, operated at 600°C, showing a slightly faster response than the platinum electrode sensors used in this work.

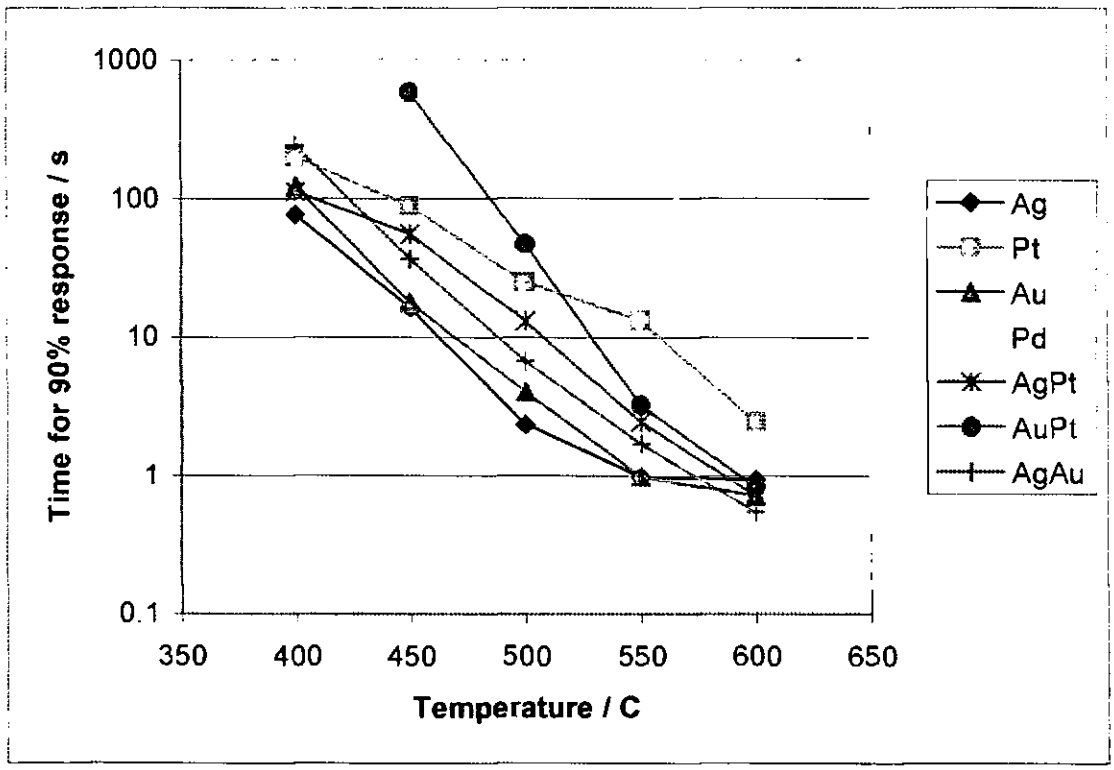

Figure 5.23 Step concentration test results

(time measured at 90% of maximum sensor output)

5.5 Concentration modulation analysis

Concentration modulations were applied to the potentiometric cells with various electrode materials the results of which are presented here. The results were analysed by comparing the output waveforms to calculated waveforms from which amplitude, phase, frequency and offset were recorded. The amplitudes were then converted to oxygen concentrations using the Nernst equation.

Figure 5.24 shows the sensor indication of gas modulation for each electrode over the range of frequencies examined at 500°C. From these results we can predict in each case a convergence on a 4% modulation at zero frequency with the exception of the palladium electrode which shows no significant response across all frequencies. This convergence and agreement with the imposed modulation indicates that the system is operating correctly. In comparing the outputs of the various cells we see that the best is the silver / gold binary mix, followed by silver, platinum, silver / platinum, gold, gold / platinum then palladium in that order. The surprise result here is the performance of the silver / gold electrode which has not shown particularly good results in other response rate techniques employed. This may be a result of alloying of silver which can give surprising results.

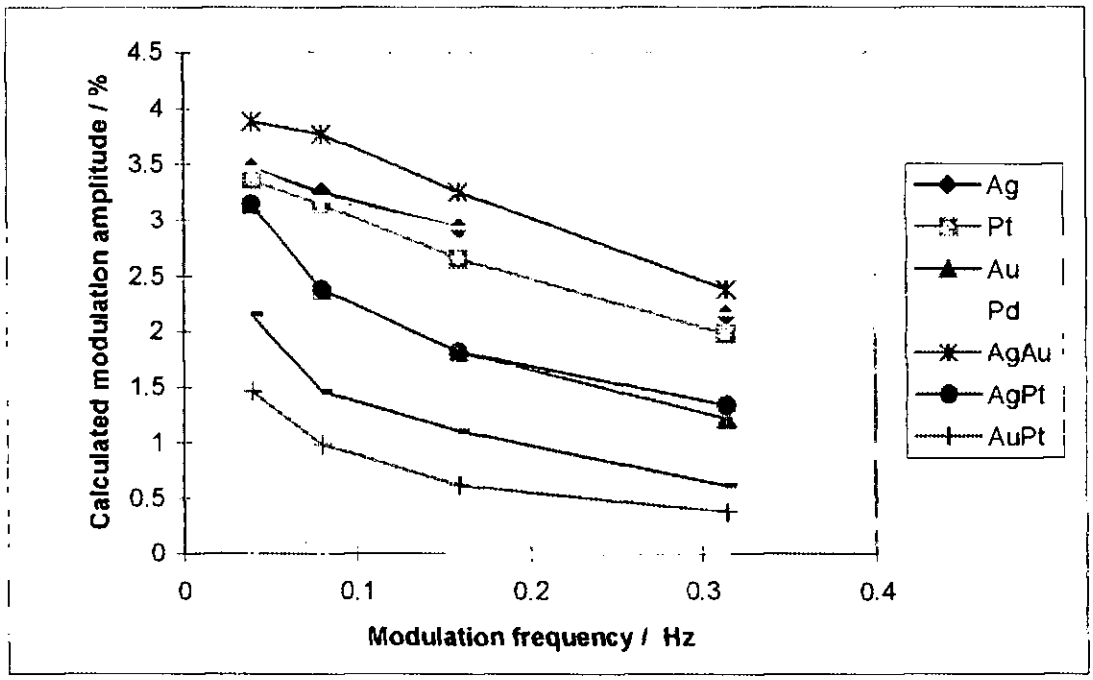

Figure 5.24 Sensor EMF amplitude vs. frequency for various electrodes

Figure 5.25 shows the sensor amplitude dependence upon temperature at a frequency of 0.08 Hz. These results follow the order of performance suggested by frequency variation and again indicate a convergence of amplitude at 4% as temperature is increased. Whilst the overall trends of increasing output amplitude with temperature are obvious, the plot is untidy with lines crossing one another indicating varying electrode activity order over various temperature regimes. The use of smaller temperature steps could be expected to help resolve these trends which have also been seen with step and impedance techniques but with dissimilar electrode performance order.

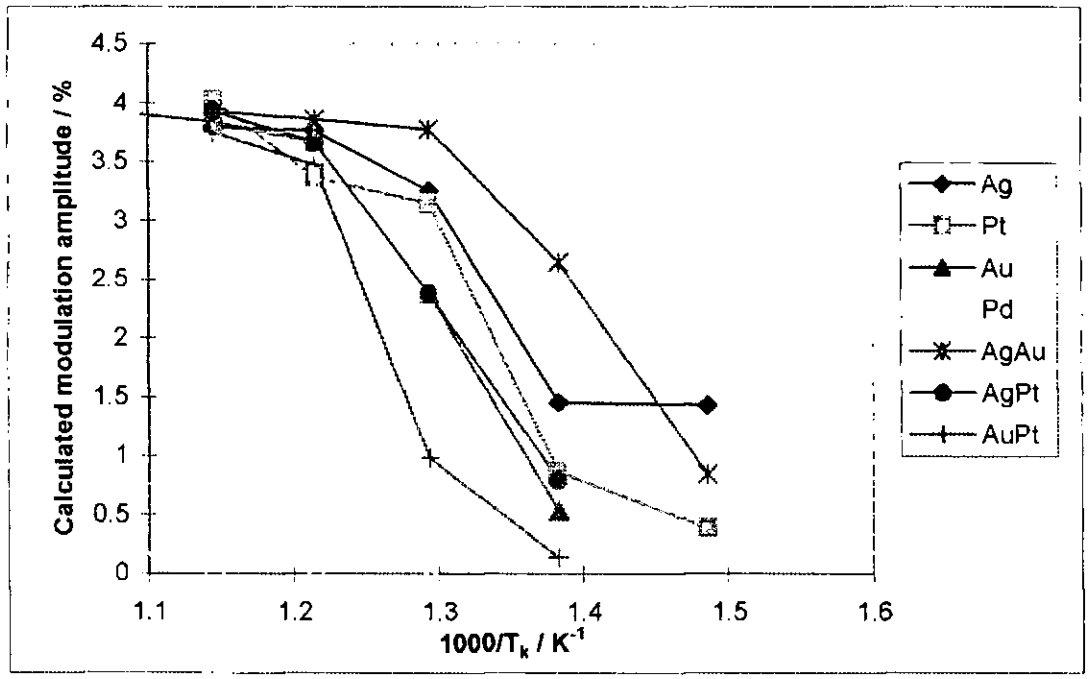

Figure 5.25 Sensor EMF amplitude vs. temperature for various electrodes

Figure 5.26 shows the frequency dependence of phase lag of the sensor output behind the gas valve modulation input waveform. Input waveform rather than output waveform was selected as previous experiments indicated that the valve output may lag a small degree behind the actual gas output and whilst this effect may be small and constant, it was decided better to use the input wave as a base. The results show a definite increase in phase lag at lower temperature with a similar trend for each electrode material with the exception of palladium which did not perform sufficiently well to base any conclusions on. The results also show that the better performing electrodes, as determined by amplitude comparison, showed lower phase angle. All traces showed a tendency to converge upon a low phase difference at low frequency; however the data are insufficient to indicate whether this is a zero value with any certainty.

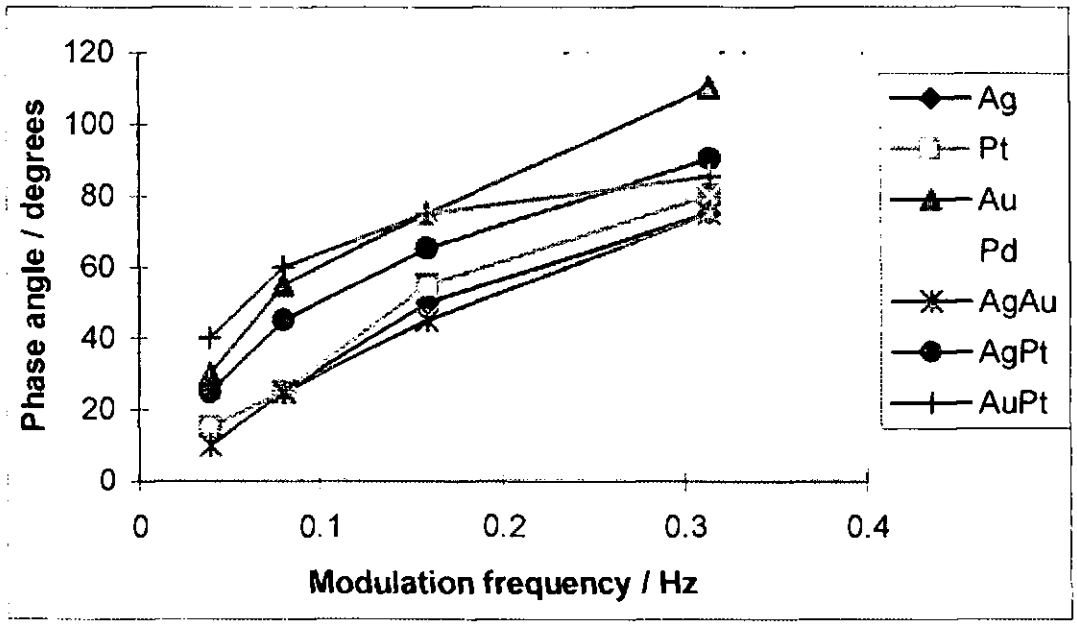

Figure 5.26 Sensor phase lag vs. frequency for various electrodes

Figure 5.27 shows the phase lag dependence upon temperature. Again, as with the amplitude vs. temperature plot, there exists a degree of performance cross-over but the underlying trend is clear. This underlying trend indicates a reduction in phase lag with increasing temperature and a convergence towards a low phase lag at higher temperature. The broad electrode performance order observed throughout these tests is again observed with the best performance achieved by the silver/gold binary mix and worst by palladium.

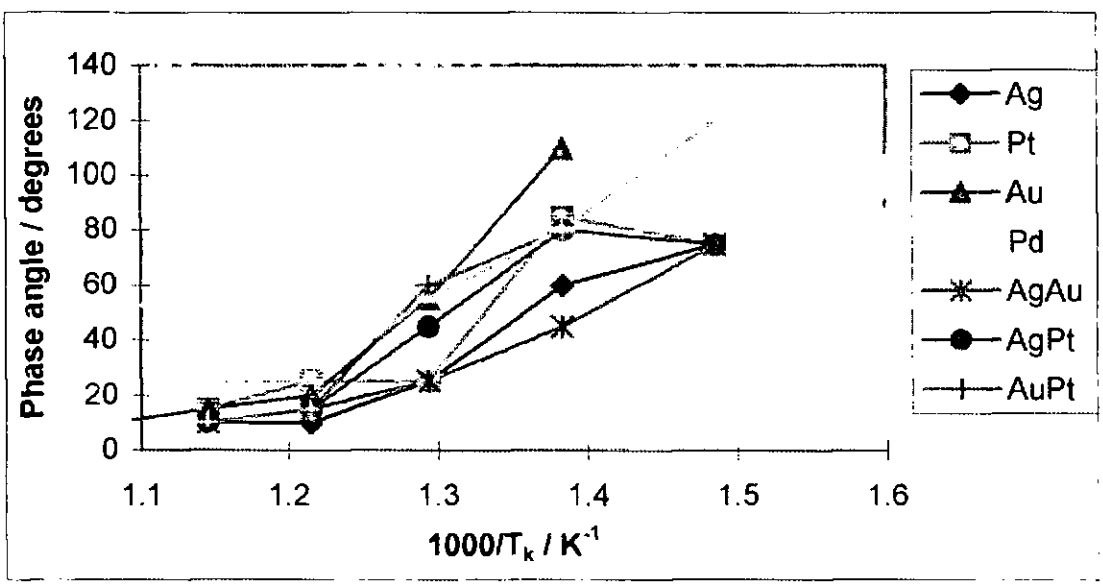

Figure 5.27 Sensor phase lag vs. temperature for various electrodes

5.6 Pressure modulation analysis

In this section we present results for pressure modulation analyses carried out upon potentiometric cells with various electrode materials. Figure 5.28 shows a comparison of results obtained from these various cells at 550°C for the range of modulation frequencies examined. From these plots we get an order of electrode performance of silver/gold, silver, silver/platinum, gold/platinum, platinum, gold, palladium in descending order of performance. As with previous examination of these electrode materials, the majority of electrodes give an intermediate performance with little difference between them and some interchange of order. The best and worst electrodes are clearly distinguished, although these experiments do place the silver/gold mix above that of silver as did the concentration modulation experiments. The general trend of results give a clearly understandable pattern with decreasing modulation amplitude recorded at higher frequencies as the sensors are unable to keep track of modulations. An amplitude limiting situation is seen at lower frequencies as the sensors are able to record the full pressure swing applied by the modulation apparatus. The drop in amplitudes are more pronounced with decreasing electrode activity as expected. The gold electrode sample appears to have undergone a rapid decrease in performance at frequencies above 1 Hz; this appears at the frequency where gearboxes were interchanged and so is probably an experimental artefact of this process. One other point to note is that (for at least the silver / gold electrode) we again obtain a small initial increase in amplitude with frequency. This may again be attributed to the factors previously suggested for this effect.

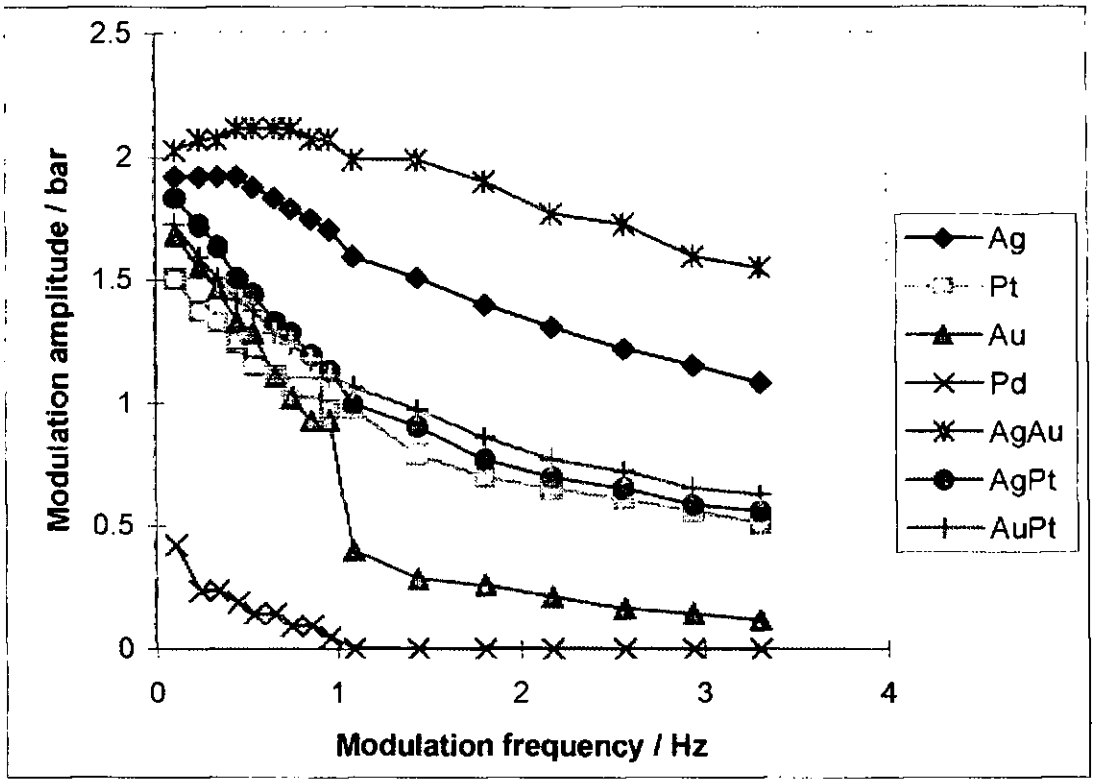

Figure 5.28 Modulation amplitude vs. modulation frequency for various electrodes

Figure 5.29 shows the effects of temperature, on modulation amplitude, taken at a modulation frequency of 0.5 Hz. These show that a constant modulation amplitude is attained at higher temperatures as for lower frequencies, this being of the same order as that predicted from dimensional analysis of the test-rig. As the temperature is decreased we see that sensor response drops and amplitude falls away from this constant value. These demonstrate that the order of electrode performance is effectively retained over the range of temperatures investigated.

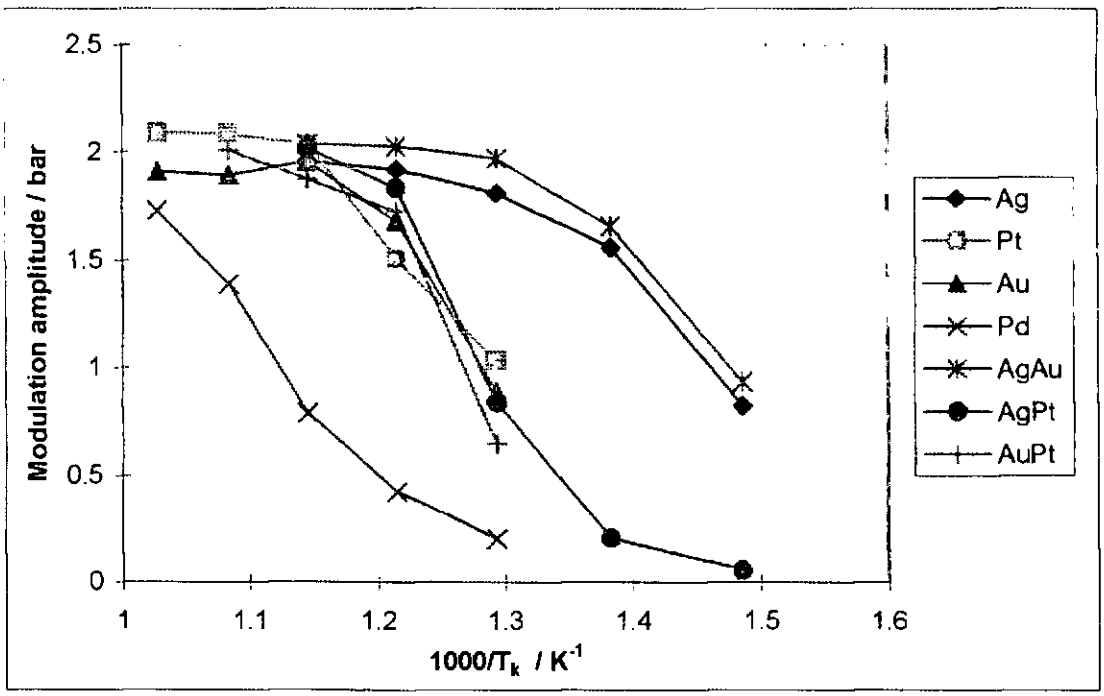

Figure 5.29 Modulation amplitude vs. temperature for various electrodes

The effects of phase angle between the cam position and sensor output was also observed with frequency. The results of these measurements are presented in figure 5.30. Again these are fairly noisy data, indicating that there exists a fair degree of potential for test and measurement improvement. The trends show through this noise fairly well. The trend is for increasing phase angle with frequency and decreasing electrode activity. The point to note is that phase angle decreases towards zero at zero frequency demonstrating that inherent phase delays due to pressure wave transit are small as expected.

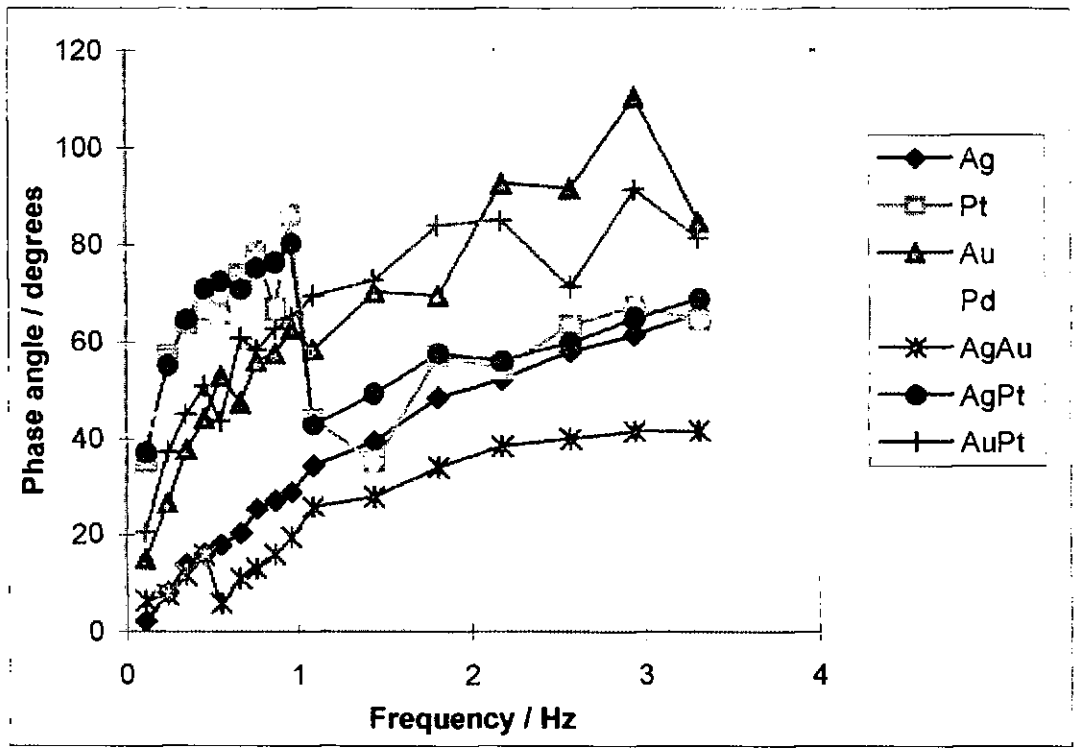

Figure 5.30 Modulation phase angle vs. modulation frequency for various electrodes

Finally figure 5.31 demonstrates the temperature dependence of phase angle for the various electrode materials. Phase angle decreases with increasing temperature and electrodc activity. Phase angle assessment of clectrodc performance order does agrec with that of amplitude assessment for pressure modulations and a fair correlation with results from concentration modulations.

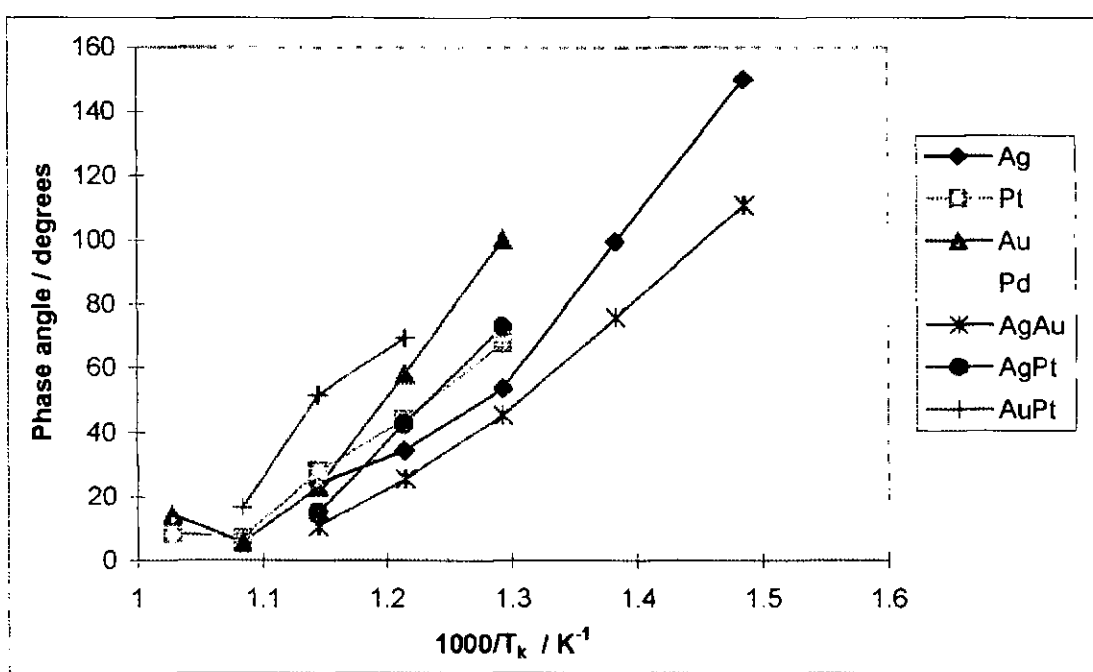

Figure 5.31 Modulation phase angle vs. temperature for various electrodes

Similar experiments were performed by Dubbe et al [54 & 111]. They used a pressure modulation technique to examine Au/Na_2CO_3 and Pt/CeO_2 sensors. By utilising a much smaller pressure perturbation through a loud speaker, a far greater measurement range was analysed. Whilst they also noted significant phase angle changes between 0.5 to 3 Hz similar to those presented for Ag and Ag/Pt electrodes, the correlation at higher and lower frequencies is not good and the method of application/measurement is probably sufficient to disregard any closer comparison.

5.7 Scanning electron microscopy

In this section we show the results of the scanning electron microscopy of the various electrode structures which were examined using the response rate techniques. The resultant micrographs have all been obtained using similar magnification of ×750 for electrode faces and ×2000 for electrode fracture edges. This ensures that electrode structure micrographs are directly comparable. Images were selected as representative of each electrode area. The accepted theory for superior electrode performance dictates that electrode structure should be an open and porous structure to allow the gaseous oxygen to diffuse through. The metal layer should allow electronic conduction across the electrolyte surface but not provide a barrier to hamper gas diffusion rates. The layer of metal at the electrolyte interface should be finely divided to give a long three phase boundary as this is the only active region. Scanning electron micrographs let us examine these electrode features and therefore aid our understanding of the processes involved.

5.7.1 Platinum

The face of the platinum electrode appears fairly porous with an open structure and a finely divided form, giving a good platform for comparison of alternative electrodes. We do see scope for improvement in structure here however as there appears to be a significant proportion of the electrolyte face without electrode coverage. Electrode continuity looks to be acceptable as a route may be traced between virtually all the electrode surface. Verkerk et al [105] used platinum sputtered electrodes for his examination of electrolytes, a scanning electron micrograph of which shows similar porosity to that displayed by this platinum paste electrode.

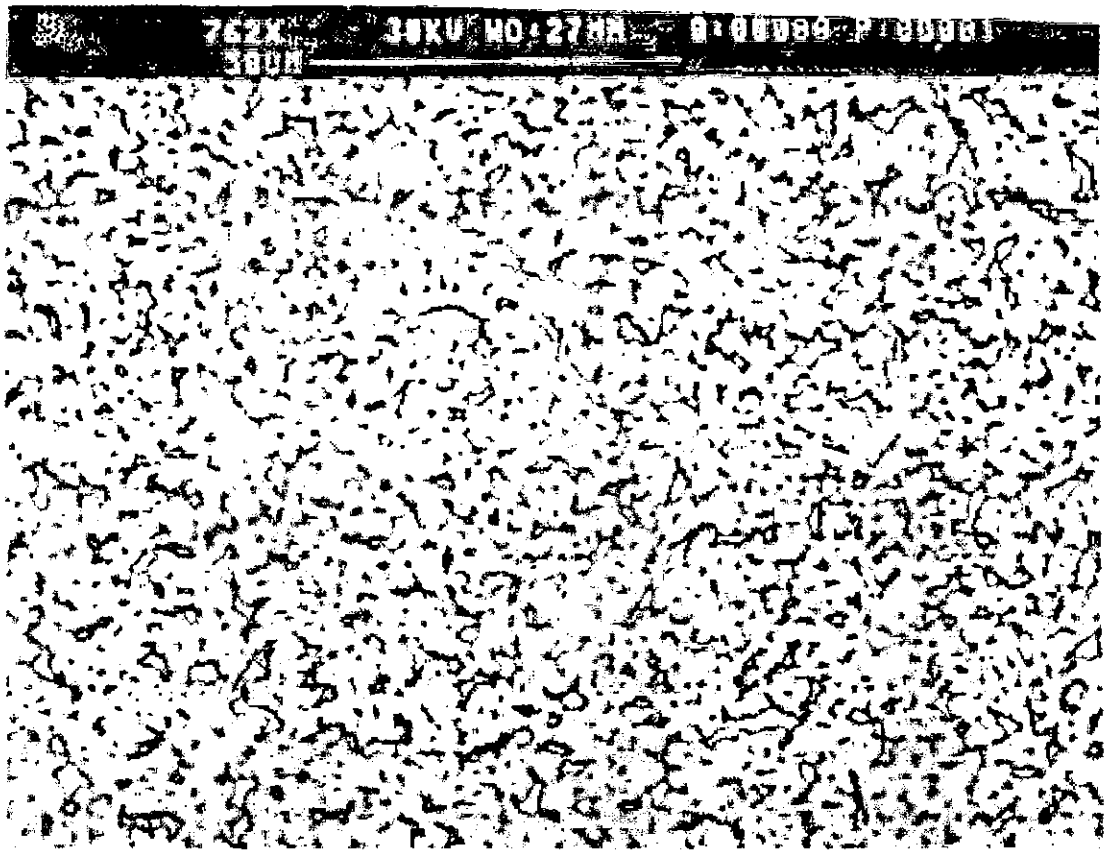

Figure 5.32 Platinum electrode face

The platinum fracture edge (figure 5.33) shows a thick but openly porous structure. Whilst the electrode thickness is a little overly thick, this does not look like it would significantly impede gaseous diffusion and would give some mechanical integrity to the structure. The electrode is seen to be sitting on a sharp edge of the zirconia with an apparently good adhesion. The electrolyte shows a very dense form with no significant porosity or cracking. There does however appear to be a little of what appears to be a second electrolyte phase at the electrode / electrolyte interface. This second phase is only a few μm thick but is at the surface layer, crucial to the electrolyte interface conductivity. This may explain the rather disappointing results of the platinum electrode's performance in comparison to those of the alternatives examined. The second phase is suspected to be a tetragonal or monoclinic zirconia phase which may have resulted from yttria diffusing from the ceramic into the electrode. This is worthy of further investigation and may require the use of a higher yttria content ceramic to overcome. The platinum electrode thickness is measured at approximately 20 μm with the second phase at 5 μm and based on an electrolyte, approximately 1000 μm thick.

Figure 5.33 Platinum electrode edge

5.7.2 Silver

The silver electrode face provides a stark comparison with that of platinum. The micrograph shows a virtually fully dense structure with a clear crystalline form. This results from the melting temperature of silver being far lower than platinum and so would have been closer to melting at the 850°C firing temperature used for each electrode. From the microstructure it is very surprising that the electrode worked at all, but may be due to a very high oxygen diffusion through the solid metal phase. The upside of the dense metal is a good electronic connection and almost complete electrolyte coverage which helps explain the excellent electrode performance, assuming a high diffusion of oxygen in silver. Wang & Nowick [47] used scanning electron micrographs to examine foil electrodes of silver and platinum. In both cases they saw a fine porosity. A high magnification study of this electrode was attempted to the limits of the microscope used but no finer porosity was evident.

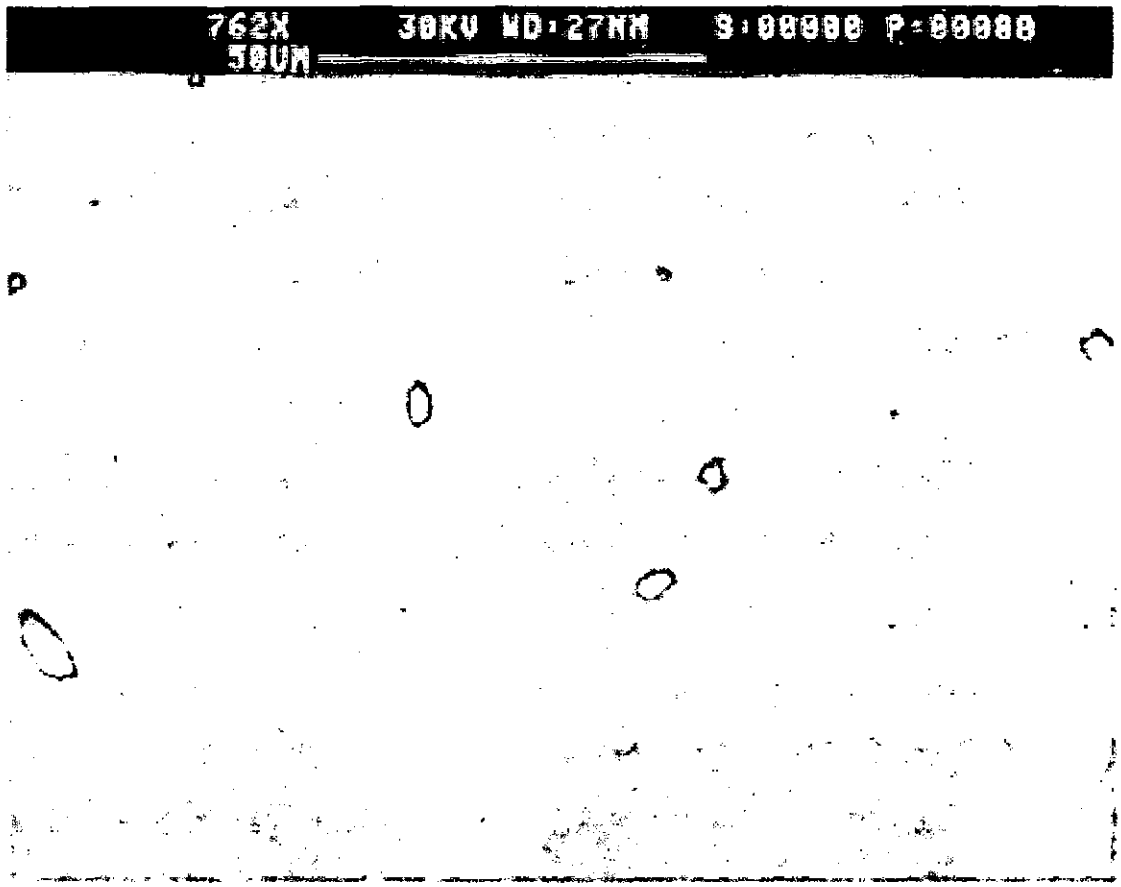

Figure 5.34 Silver electrode face

The silver electrode fracture edge (figure 5.35) shows a very thin dense layer resting upon a very thick layer of apparent second phase zirconia (similar but much thicker than that seen with platinum) this rests on a solid layer of first phase zirconia which extends to the opposite sample face. The degree of second phase zirconia here is very surprising, extending almost 35 μm into the electrolyte, compared to the electrode thickness of just 4μm. It should be noted that the electrodes were applied to a pre-sintered electrolyte, not co-sintered with the electrolyte. If this is due to yttria being adsorbed into the electrode layer we effectively have a silver/yttria electrode which may go some way to explain the apparently high oxygen diffusion rates seen with a dense electrode. Again this is worthy of further investigation. Examination of a second silver fracture edge from a second sample confirmed these apparent findings. No second phase was seen during examination of a second gold electrode fracture edge. Steil et al [145], in examining the densification of YSZ using SEM and impedance spectroscopy, used silver and platinum electrodes and noted that silver would diffuse deeply into porous samples altering electrode geometry and so these samples were not used for electrolyte conductivity comparisons. The electrolyte samples investigated here were highly dense electrolytes with electrodes applied only after fully sintering the ceramic, so silver ingress into the electrolyte is not thought likely.

Mishra & Agarwal [107] compared silver and gold electrodes on SnO_2 sensors for measuring H_2 or CO. They found that at temperatures of 300 to 400°C silver was very mobile such that doping of the SnO_2 was unnecessary. Again the high mobility of silver would not be expected to affect the electrolyte to the extent seen here once the eleetrolyte is fully sintered.

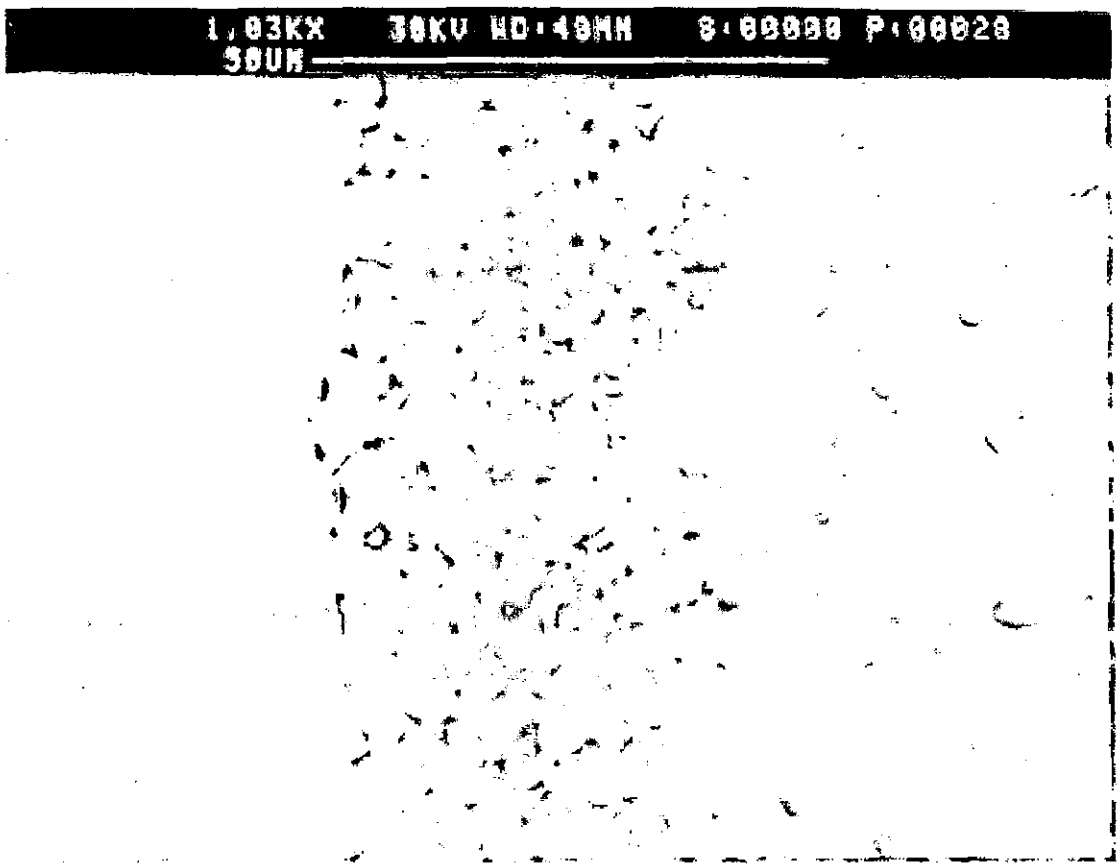

Figure 5.35 Silver electrode edge

5.7.3 Gold

The face of the gold electrode (figure 5.36) lies between that of silver and platinum with a greater degree of porosity than the silver but significantly more dense than the platinum. There does not appear to be any significant crystallinity but clearly the metal grains have started to grow (gold melts at 1063°C compared with 961°C for silver, 1769°C for platinum and 1552°C for palladium). Again electronic conductivity of this electrode would not be a problem but gaseous diffusion would have been severely hampered by the electrode density.

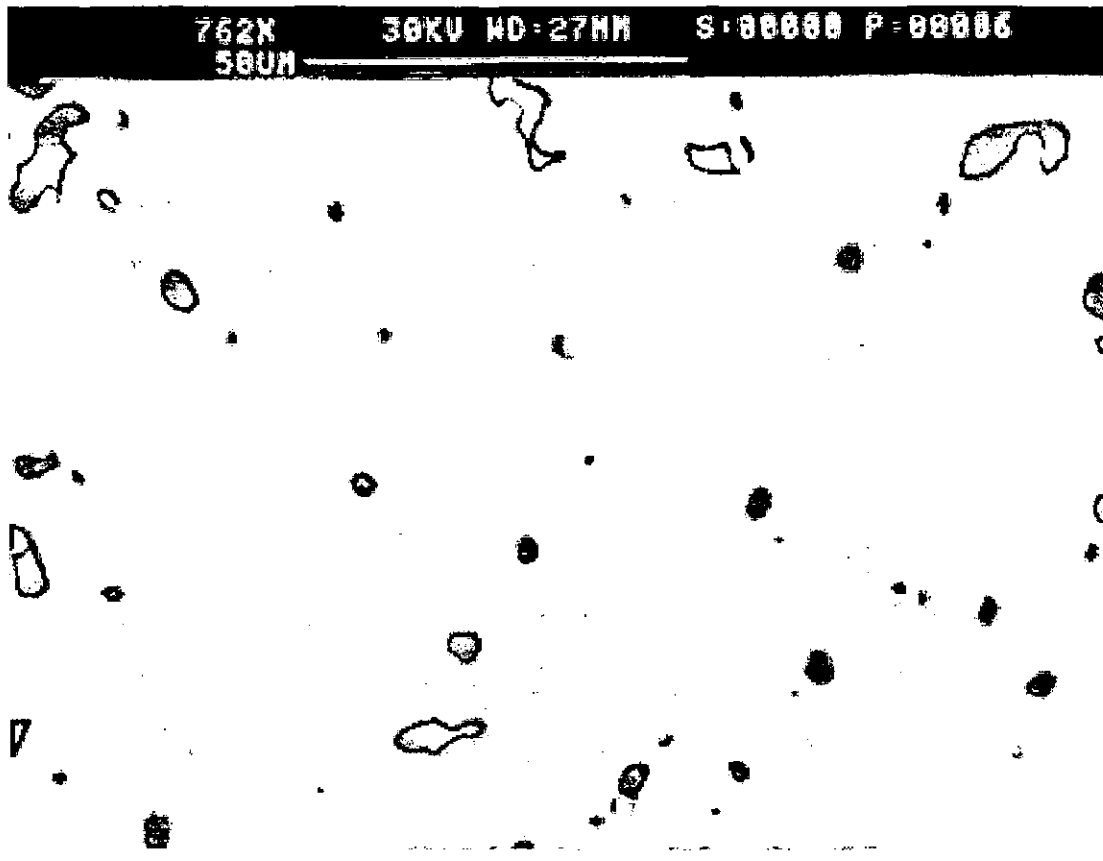

Figure 5.36 Gold electrode face

The fracture edge (figure 5.37) shows again a thin layer of solid metal resting on a sharp single phase zirconia electrolyte. There is no indication of any second phase and the zirconia does appear fully dense. The electrode thickness here is just 4 μm but electrode adhesion to the electrolyte does not look as good as that of platinum or silver. This micrograph again reveals the non-porous nature apparent in the electrode face. These electrode microstructures do go some way to explain the fairly poor electrode performance and inconsistent nature of response tests employing gold electrodes seen in this work.

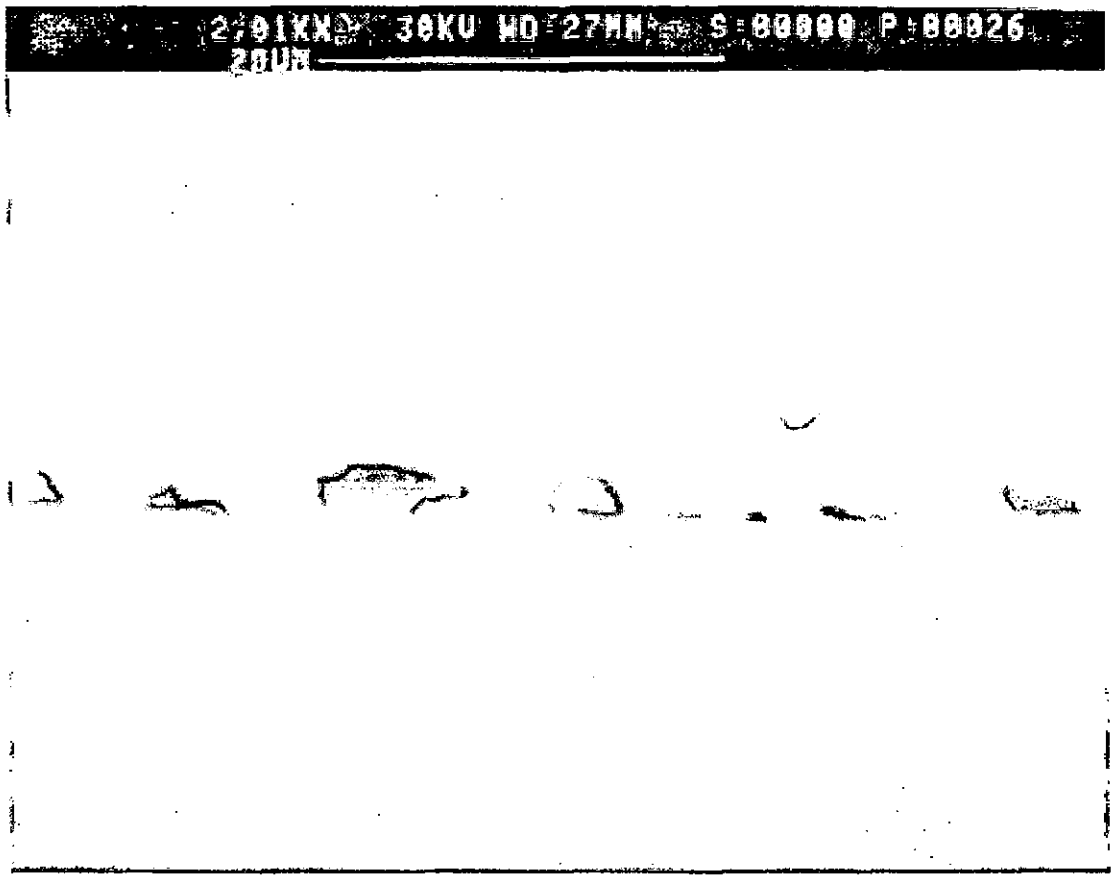

Figure 5.37 Gold electrode edge

5.7.4 Palladium

The palladium face micrograph (figure 5.37) displays a similar open and porous structure to that of platinum (reflecting the high melting point). The face appears more granular than that of platinum but this may be attributable to the paste manufacture as this paste was made in-house from a powder rather than prepared commercially. The granular nature may point towards a poor electronic continuity with perhaps some surface oxidation of the particles hindering conductivity.

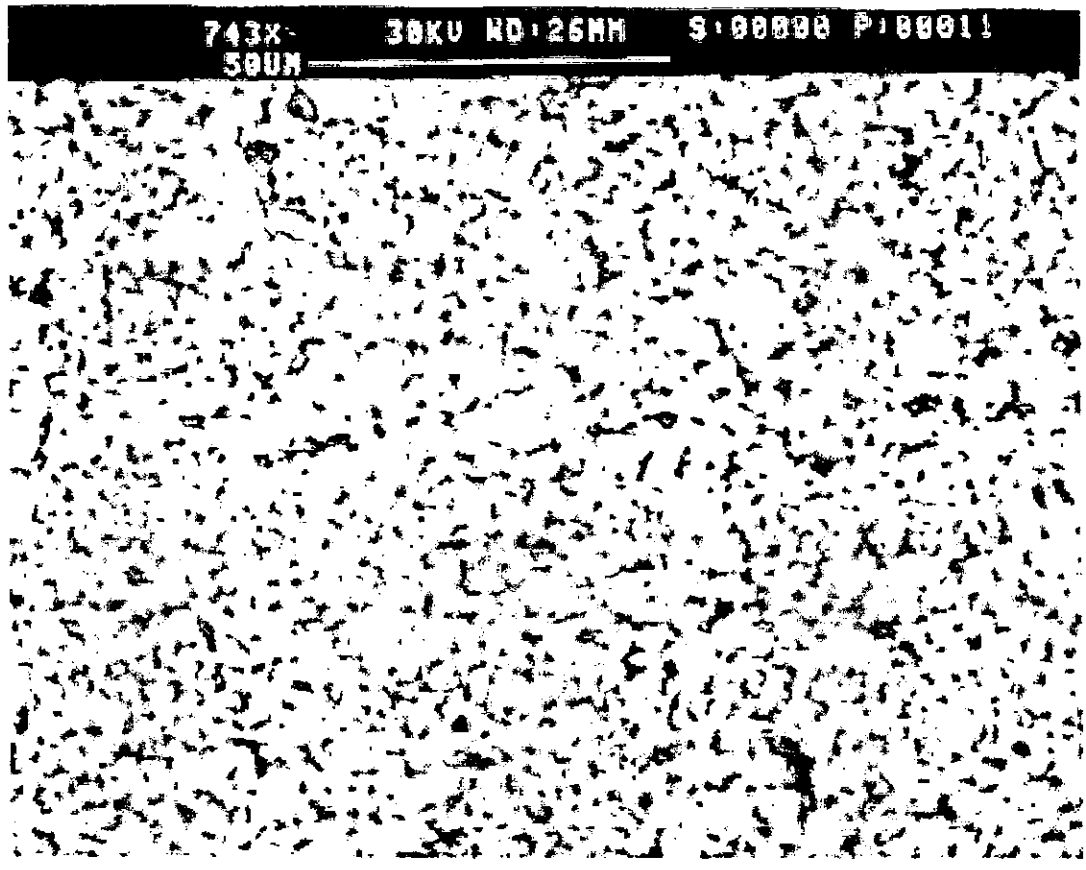

Figure 5.38 Palladium electrode face

The fracture edge (figure 5.39) shows a reasonably thick electrode layer at 10 μm with an open porous structure. Considering its microstructure, it is surprising that it makes such a poor electrode. This may be attributable to its susceptibility to oxidation. Another possibility is its adhesion to the electrolyte, the micrograph shows this to some extent with fairly little of the fracture edge still supporting the electrode layer which flaked off when fractured. This may again be due to metal oxidation during firing. No second phase electrolyte is apparent with palladium electrodes.

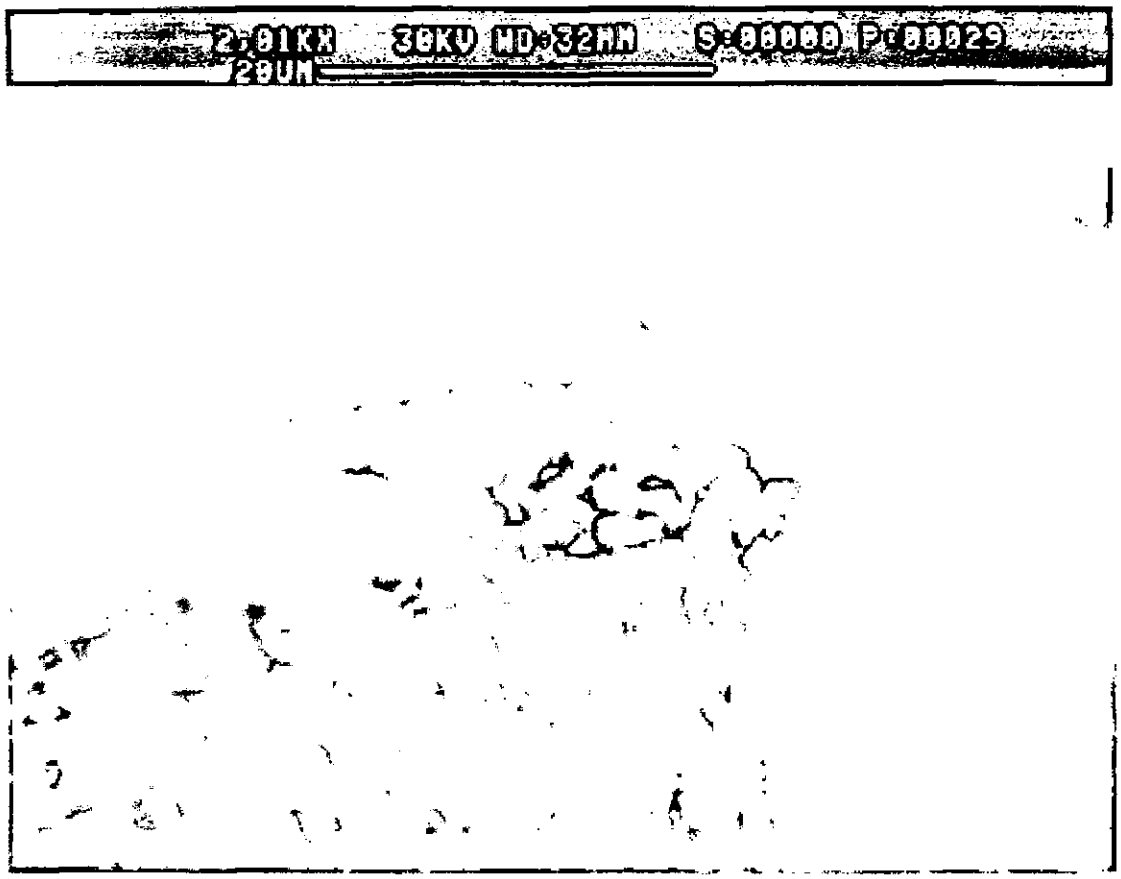

Figure 5.39 Palladium electrode edge

5.7.5 Silver/Gold

Figure 5.40 shows the surface microstructure of the silver/gold binary mix electrode with an appearance in between that of silver and gold, more crystalline than gold but more open than silver. Electronic conduction across the electrode would not be a problem but this electrode does demonstrate the lowest surface coverage of the electrode with very large pores. It did however, form a particularly good electrode. This may again attributed to oxygen diffusion through the silver metal. The fracture edge was not recorded, however, examination of the electrolyte did not indicate any evidence of second phase despite the silver content.

Figure 5.40 Silver/gold electrode face

5.7.6 Silver/Platinum

The silver/platinum microstructure is far more similar to platinum than silver, and may be envisaged as a sliver coating the platinum's rigid structure. Whilst this electrode's performance was fairly good, it is somewhat surprising that an extremely good electrode is not obtained by combining the Pt structure with Ag / O_2 diffusion properties. Electronic conductivity may not have been as good as that of other electrodes due to the high porosity, no surface oxidation is anticipated to the inertness of material components. Again the fracture edge was not examined although we could expect some second phase to be present.

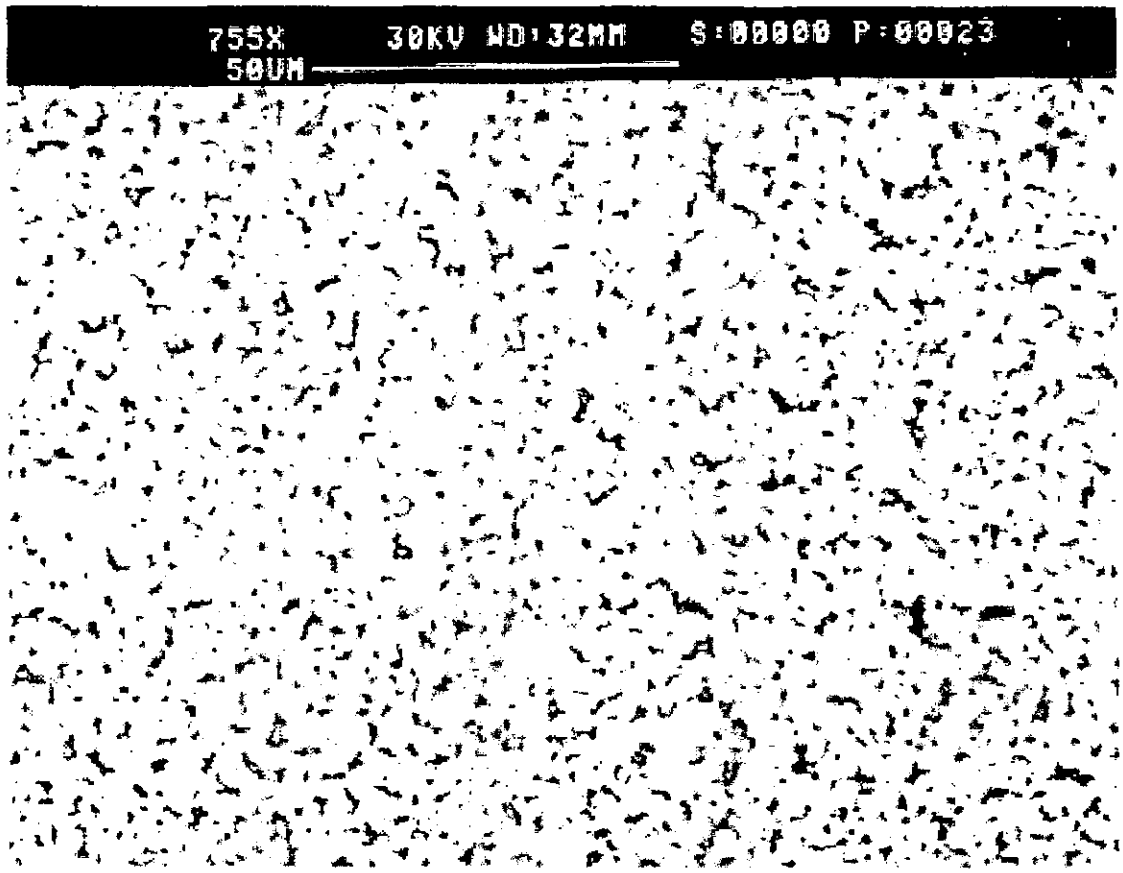

Figure 5.41 Silver/platinum electrode face

5.7.7 Gold/Platinum

For the gold/platinum electrode (figure 5.42), again we see that the open Pt structure is retained, though less open than Ag/Pt, Despite this encouraging microstructure, this again did not translate into a particularly good electrode. Electronic conductivity should not have been a problem as the electrode is coherent and has good electrolyte coverage. It is possible that with this electrode and the silver/platinum electrodes, the gold and silver have formed a second layer underneath the platinum and may explain the rather unremarkable electrode performance obtained.

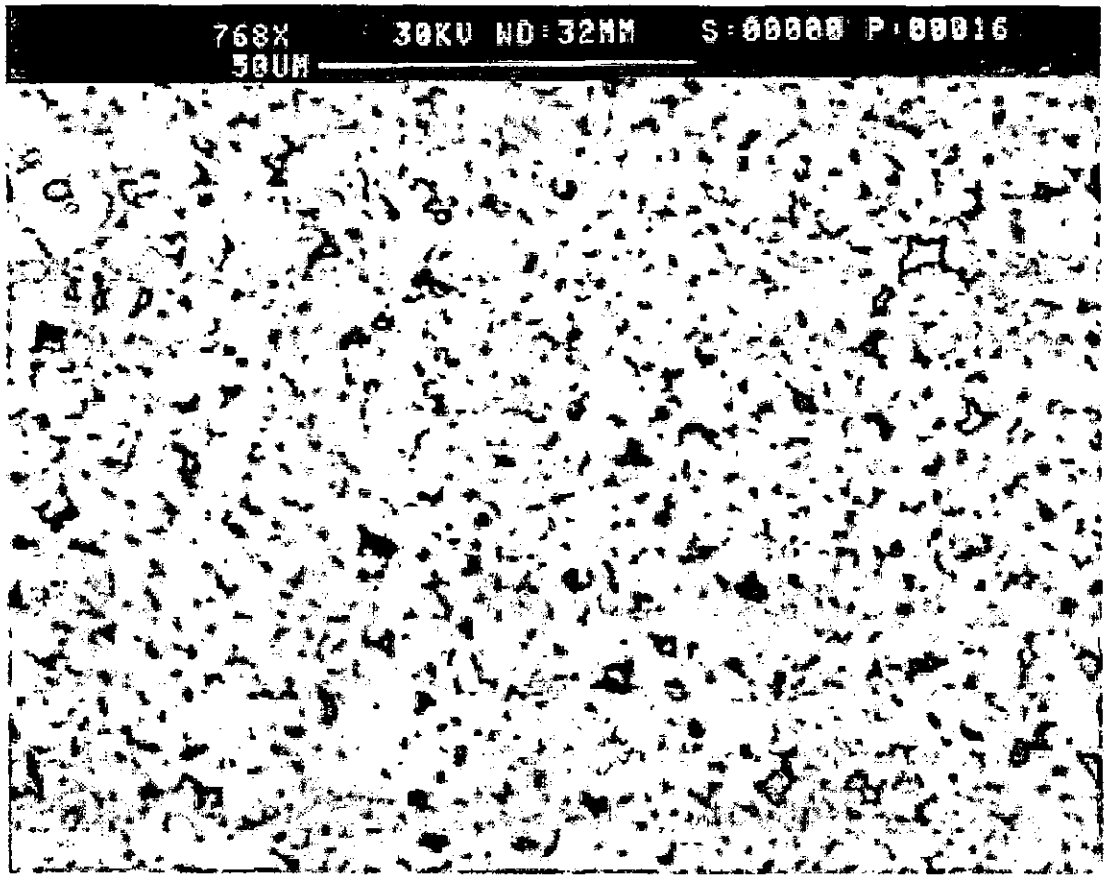

Figure 5.42 Gold/platinum electrode face

5.7.8 Platinum Cermets

The cermets assessed (figure 5.43 & 6.44) were identical Pt cermets but fired at 1000 and 1450°C respectively to compare the effects of firing on microstructure. Firing effects on electrode performance have previously shown to be small but not insignificant and this is reflected in the microstructure. Whereas with simple Pt metal electrodes, high temperature firing (1450°C) were resulted in a metal film, with the cermets the structure is retained by the ceramic so the effect is reduced. Some sintering and closing of the structure were apparent but these were not excessive.

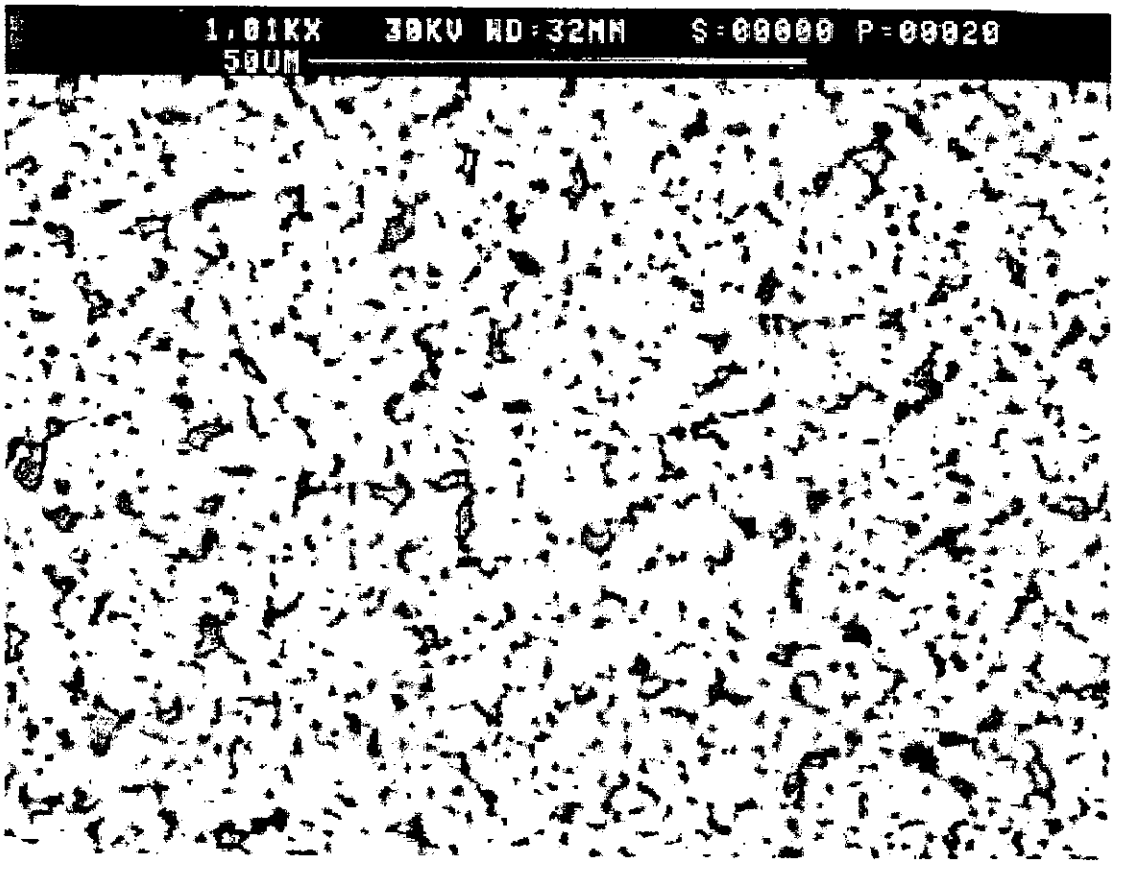

Figure 5.43 Platinum cermet electrode face fired at 1000°C

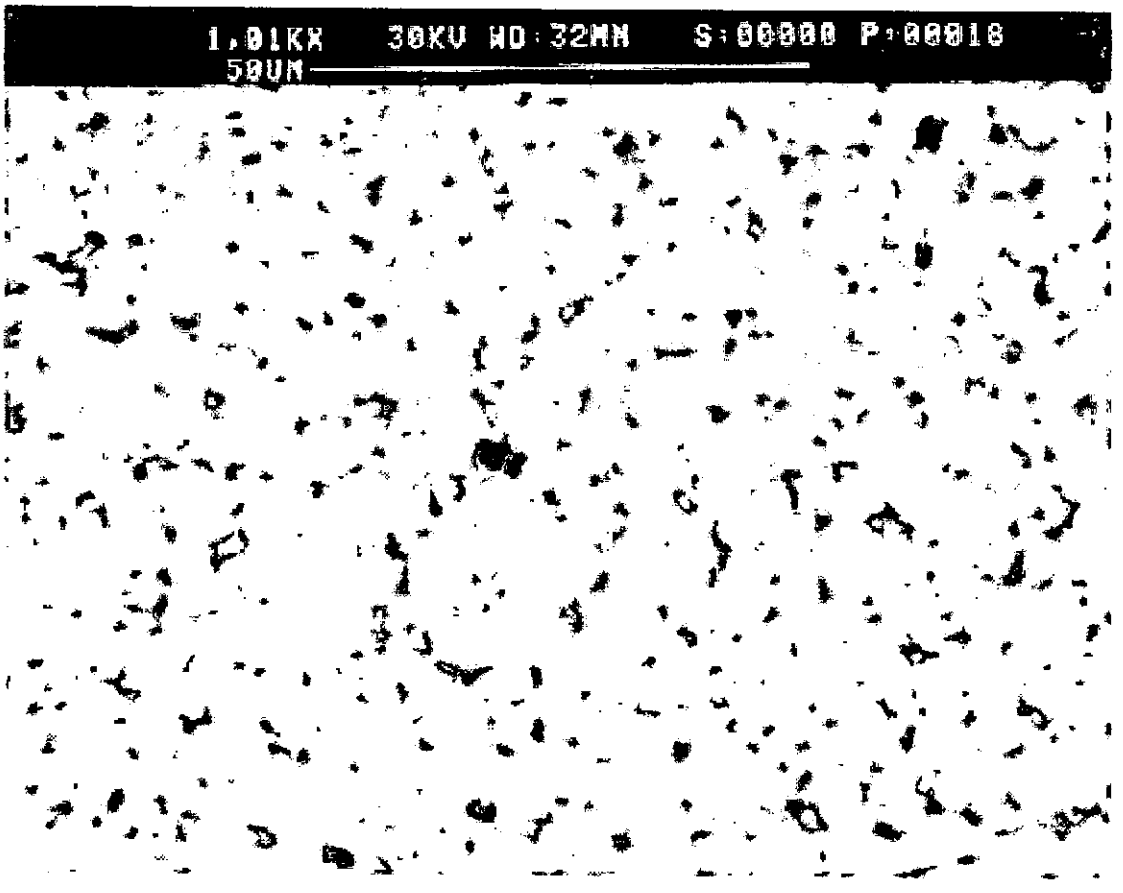

Figure 5.44 Platinum electrode face fired at 1450°C

From the electrode face micrographs (figures 5.32, 5.34, 5.36, 5.38, 5.40, 5.41, 5.42, 5.43 and 5.44), an estimation of apparent three phase boundary lengths is permissible. This was achieved by electronically magnifying a scanned image of each micrograph and measuring the apparent outline length of each electrode over a small representative area. This length was then taken as an approximation of three phase boundary length over a known electrode area. The results of this estimation are presented in figure 5.45, which is in agreement with visual assessment of the porosity of the electrodes. This assessment would appear to show an inverse relation between boundary length and electrode activity, indicating that whilst the electrode porosity may be an important factor, the electrode performance is dependent on much more than this alone. Estimated boundary lengths using this manner are only resolved to the resolution of the micrographs, a significantly finer porosity may be present but not apparent.

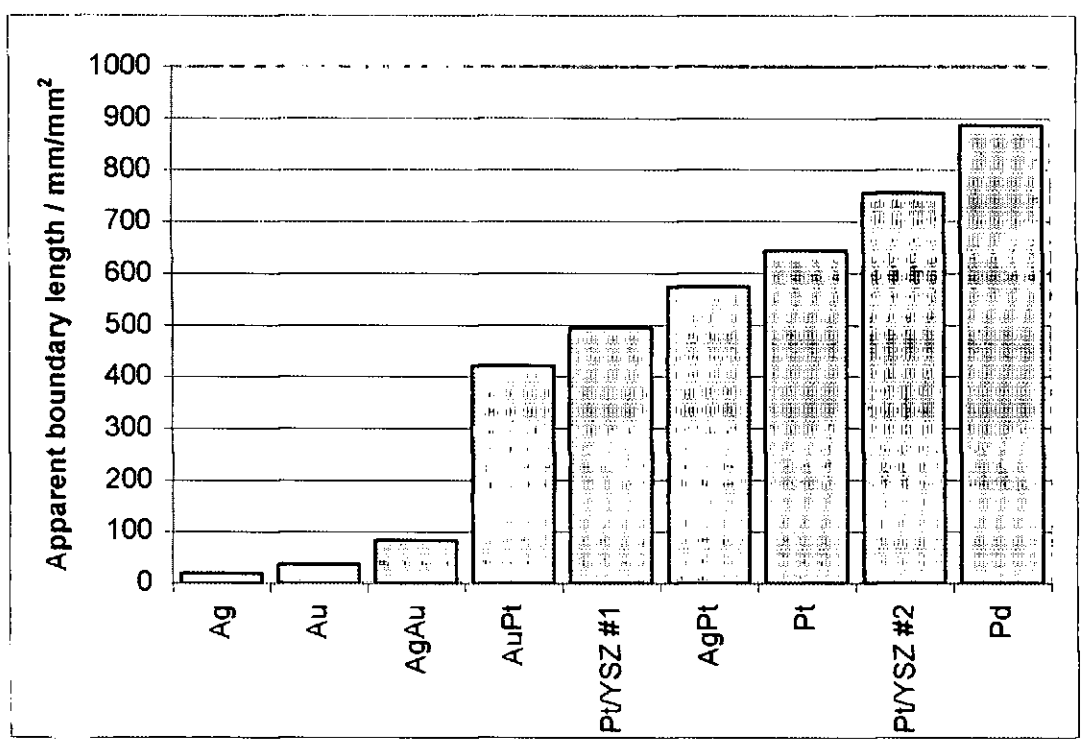

Figure 5.45 Estimation of apparent three phase boundary length

Pt/YSZ #1 is a cermet electrode sintered at 1450°C,

Pt/YSZ #2 is a cermet electrode sintered at 1000°C

5.8 Summary

The effects of the nature of electrodes have been examined by the analysis of platinum metal paste, cermet paste and electro-deposited electrodes on the response rates of a sensor. Response rates were examined using impedance, step concentration, concentration

modulation, and pressure modulation techniques. Results of each examination technique consistently showed superior performance of electro-deposited over metal or cermet electrodes. Impedance results also indicated a reduction in activation energy for electro-deposited over platinum metal or cermet electrodes. Various electro-plating routines showed electrode improvements using both direct and alternating currents but that currents below 10mA did not reliably improve electrode performance. The electroplating procedure is worthy of further examination with platinum cermet electrode / electrolyte cells providing a good basis for study with frequency response techniques. Electro-deposition yields similar improvements to those achieved with silver but the use of silver has shown detrimental effects on electrolyte impedance unlike electro-deposition of platinum. The longevity of electrodes of both Ag and plated Pt is open to question, indeed, Tedmon et al [113] showed that whilst non-porous silver is usable due to its high oxygen solubility, it is vulnerable to volatilisation which limits its life. Similar doubts over platinisation have been raised by Feltham & Spiro [56].

An initial electrode material investigation was performed using single electrode / electrolyte / electrode cells investigated using frequency response analysis. This initial assessment showed a scatter in electrode performance of similar samples, attributed to the method of electrode application, Improvements in this area are certainly possible. Arrhenius plot slopes indicated fairly consistent activation energies for each electrode material. Examination of cermets, mixes and layered electrodes showed no significant advantage over simple single metals in impedance measurements. Other factors, such as life, cost, inertness were not investigated. In this assessment silver stood out as a particularly good electrode, Pt and Au as intermediate and Pd as particularly poor. By refining and tailoring the deposition process for each electrode, the comparative electrode performance may be significantly altered. A substantial difference in electrolyte impedance was found and traced to the firing of samples in two separate batches. During firing of one of these batches a furnace failure occurred. The electrode impedance results were not influenced by this as they were applied after the sintering of the electrolyte and as impedance spectroscopy separates out the individual components. Electrolyte impedance did appear to be influenced by electrode impedance. This effect was probably due to improved surface area at the electrode / electrolyte interface. The exception was for Ag electrodes where a significant electrolyte deterioration was found.

The simple metal electrodes of Ag, Au, Pt and Pd and binary mixes of Ag, Au and Pt were applied to potentiometric cells for examination using each of the response rate investigation methods. Comparisons of RC time constants obtained by impedance and step change techniques did not provide an effective measure for comparing electrode performance although each technique did give a general agreement of electrode performance order with silver particularly good and palladium particularly poor. Other electrodes gave similar performances and resolution between these did not give a definitive ordering. The Ag/Au mix indicated superior performance to silver in concentration and pressure modulation experiments but not so in impedance or step change studies. Silver formed electrodes with good performance but appeared to have detrimental effects on electrolyte impedance, effects backed up by SEM examination. A certain degree of correlation could be obtained between impedance and step change techniques and again between pressure modulation and concentration modulation techniques but the modulation techniques indicated a significantly slower response than the other methods. This may indicate that the response rate dominant mechanism changes dependent upon the manner in which it is measured.

Each of the electrode materials and combinations was analysed by scanning electron microscopy, investigating electrode faces and fracture edges. SEM proved a valuable tool in the assessment of solid state electrochemical cells by providing clear evidence of microstructural characteristics of the samples investigated using other methods. Factors examined using the SEM technique include porosity, electrode thickness, electrode adhesion to the electrolyte, electrode coherence, electrolyte coverage and electrolyte second phases. The SEM analysis revealed electrode porosity as palladium, silver/platinum, gold/platinum, platinum, silver/gold, gold, silver in order of decreasing porosity. This order is contrary to that expected from the response rate evaluations performed and leads us to the conclusion that response rate does not depend on porosity alone. Poor microstructure of Ag may he a sign that significant further improvement is possible with this material.

The investigation showed a second electrolyte phase occurring in the presence of both platinum and silver although in silver the effect was substantially larger. This secondary phase is thought (although not proven) to arise from electrode adsorption of the yttria content of the ceramic. Yttria absorption may be influential in the high oxygen diffusion

rates found in silver and would also account for the higher impedance of the supporting electrolyte. This theory has yet to be conclusively verified.

Platinum used in binary mix electrodes appears to form a supporting structure that may allow a greater porosity in mixed electrodes incorporating lower melting temperature electrodes. The use of cermets provides a similar supporting structure capable of withstanding high temperatures with little degradation of the electrode microstructure or characteristics. However, whilst microstructure improvements were seen under SEM examination there was no correlating improvement in electrode performance. Details of SEM examination findings are presented in the table below.

Electrode Material	Electrode Coverage	Thickness μm	TPB mm/mm^2	Comments
Pt	Good	20.4	644	Slight 2nd electrolyte phase evident
Ag	Excellent	4.9	19	Large 2nd electrolyte phase evident and highly crystalline structure
Au	Good	5.5	37	Poor adhesion to electrolyte
Pd	Good	7.1	887	Poor adhesion and granular appearance
Pt/Ag	Good	-	574	Possibly formed double layer electrode
Pt/Au	Good	-	420	Possibly formed double layer electrode
Ag/Au	Poor	-	84	Slight crystallinity
Cermet (1000°C)	Good	-	756	Similar to Pt metal electrode
Cermet (1450°C)	Good	-	495	Obviously deteriorated porosity due to higher firing temperatures

SEM evaluation summary

CHAPTER 6

CONCLUSIONS

6 Conclusions

6.1 Review statement of purpose

The aim of this research was to explore avenues for the development of sensors that could work at reduced operating temperatures whilst retaining an acceptable response time. The first step in this task was to prepare and characterise sensors over a range of conditions so that the effects of low temperature performance could be quantified. Having identified the undesirable effects, suspected controlling factors were identified and evaluated. This was realised by employment of established techniques and by the development of novel techniques that allowed investigations into these governing factors. Four response rate examining techniques have been employed, namely, impedance spectroscopy, step gas changes, concentration modulations and pressure modulations. These have been used alongside electrochemical analyses and scanning electron microscopy. These techniques have been utilised in the analysis of alternative electrodes and have led to the identification of problems and solutions associated with improved performance.

6.2 Plastic-ceramic

Not only has this work explored four methods of response rate measurement, but it has incorporated the development of novel sensor fabrication methods. The sensors employed a new, low cost and flexible construction technique with the potential of improvements in terms of cost / performance over existing commercial sensors. These advantages come elimination of complex machining and laser cutting techniques. The use of plastic-ceramic results in a great flexibility in device fabrication, completely eliminating the requirement of high cost manufacturing techniques to fabricate a reliable and potentially reproducible device. The negative side of this technique is a slight deterioration of the internal electrode through high temperature exposure. This work was presented at the Sensor and Actuators VIII conference by Maskell & Page [87].

6.3 Amperometric sensors

These sensors manufactured using novel techniques have been extensively characterised. Reproducibility, sensitivity, leakage mechanisms and temperature characteristics have been examined. Sensors showed good reproducibility (considering hand fabrication), linear characteristics to oxygen partial pressure, with flat limiting plateaux and no obvious sensitivity to external influences. Sensors have been fabricated to suit the range of partial pressures to be measured. Oxygen concentration measurements have been made from 26

ppm (0.0026%) to 600,000 ppm (60%) oxygen and linear characteristics demonstrated. Amperometric sensors did not show the reduction in response rate observed in potentiometric cells at low temperature but did show a reduction in measurement range. This reduction in range has been identified, originating from electrolyte resistance which may be avoided by using smaller diffusion holes or overcome by using thinner or higher conductivity electrolytes.

6.4 Pump-gauges

Pump-gauge devices were fabricated using the plastic-ceramic technique to demonstrate that a high integrity seal could be achieved and to investigate the leakage mechanisms in comparison with the gold seal devices of other workers. Results of these investigations indicated that physical gas leakage was not a dominating leakage mechanism and thus plastic-ceramic seals were effective. Leakage rates observed were higher than those reported for gold-seal devices and the cause was traced to an electrochemical leakage mechanism. This was a surprising result considering the comparative gold seal and platinum lead geometry, but has been attributed to the catalytic nature of the platinum connection leads. This examination also confirmed improvements in electrolyte and electrode performance over gold-seal devices. Measurements taken during electrode response rate analysis showed no significant additional reactivity for platinum over gold bringing this conclusion into question.

6.5 H_2O-CO_2

The effects of reducible gas species on amperometric sensors have been previously demonstrated by Usui et al [89, 91, 90] and Takahashi et al [73]. During the course of this work, an unreported effect upon gauge EMF was observed. This was further examined and proved these devices to be very sensitive to low concentrations of reducible species. This work was written up as a research paper proposing the basis for a combined oxygen sensor / reducible species detector. The sensors were shown to be more sensitive to water than to carbon dioxide in this respect, which has been attributed to the lower dissociation potentials required for water. This work has been published Maskell & Page [87].

6.6 Frequency response analysis

Frequency response analysis was used as an established method of solid electrolyte component examination. It was used to evaluate the performance of both amperometric

and potentiometric sensor components under a variety of conditions. The analysis showed that whilst exposure to elevated temperatures was detrimental to electrode performance the effect was not excessive and was reduced by the use of cermets which outperformed simple metal electrodes in this respect. The technique showed a significant time-dependent nature to electrode impedance, a factor worthy of further investigation. Oxygen concentration had an unexpected effect on electrode impedance which according to literature could be attributed to anodic rather than cathodic impedance domination. The use of bias voltages allowed a direct correlation of component resistances in amperometric cells to measured current/voltage curves. This demonstrates that although high under zero current conditions, electrode impedance dropped rapidly upon bias application to give electrolyte domination of amperometric cell resistances. The examination of a thick film sensor revealed the advantages of using a thin electrolyte layer but that performance of these devices was severely hampered by poor electrode performance. Frequency response examination of electrolyte sintering temperatures gave a good correlation of mechanical and electrical properties showing that sintering had been achieved using temperatures as low as 1350°C but that improvements were seen with temperatures as high as 1550°C. The technique was used to evaluate electrode material composition on electrode performance and showed an electrode performance in decreasing order of silver, silver/gold, silver/platinum, gold/platinum, gold, platinum, palladium. In addition we saw that platinum cermet electrodes could be further improved by electro-deposition, through the finely deposited microstructure obtained.

6.7 Step concentration changes

Step gas concentration changes were used as a direct and established method of measuring response rates in gas sensors. A test-rig was assembled and characterised with sensors operated at high temperature where response is known to be fast. Lowering the operation temperature revealed logarithmically increasing response times in potentiometric cells but little change in amperometric sensors response. Geometric sensor factors are shown to be responsible for amperometric sensor response but with the response measurements taken being essentially controlled by test chamber dimensions. Amperometric sensor tests did show that response times of a few seconds were obtained irrespective of temperature for operation above 550°C. At lower temperatures, the sensors ceased to operate over the full test range of oxygen concentrations but no indication of slowing response was evident. Potentiometric sensor response measured using the step technique with various electrodes showed that improvements of the order of 100°C could be obtained by electro-deposition

of platinum onto platinum cermet electrodes. In addition we obtained a decreasing order of performance of silver, gold, silver/gold, silver/platinum, platinum, gold/platinum, palladium at 500°C but accompanied by a variation in order with temperature.

6.8 Concentration modulations

A novel response rate assessment technique developed was that of concentration modulations. Gas compositions were sinusoidally modulated using computer controlled mass flow valves, the output of which proved reliable and stable provided certain parameters were not exceeded. Concentration modulations applied to amperometric sensors again showed no temperature dependence but the response rates measured have been attributed to test cell dimensions rather than intrinsic sensor parameters. Modulations applied to potentiometric cells showed a distinct temperature dependence with measured sensor amplitude decreasing and phase angle increasing with reduced temperature. Again this technique was used to evaluate the improvements gained by electro-deposition of platinum and agreed with the step and frequency response analyses of a temperature improvement of some 100°C over platinum cermet electrodes. Electrode materials were assessed using the concentration modulation technique and gave a decreasing performance order of silver/gold, silver, platinum, silver/platinum, gold, gold/platinum, palladium. The results of this analysis did not, however, give a direct correlation to those of impedance or step change analysis techniques indicating a substantially slower response for all electrodes.

6.9 Pressure modulations

Pressure modulations were employed as a second novel response rate analysis technique. Modulations were derived from a DC motor driven piston/cylinder arrangement that allowed modulations of 0.1 to 3 Hz to be realised. Amperometric sensors showed a response to these modulations attributed to gas flows in the diffusion barrier. These did show a temperature dependence at high frequency but this was due to sensors attempting to draw currents beyond their electrolyte resistance capabilities. Modulations were also applied to potentiometric cells; these demonstrated a similar performance drop-off to that seen in concentration modulations. Electrode materials were assessed using the concentration modulation technique and gave a decreasing performance order of silver/gold, silver, silver/platinum, gold/platinum, gold, platinum, palladium. Again, the results of this analysis did not however give a direct correlation to those of impedance or

step change analysis techniques indicating a response more in line with those of concentration modulation.

6.10 Scanning electron microscopy

Scanning electron micrographs were taken in order to provide some additional information of the systems examined throughout this work. These, it was hoped, would help us to understand the response rate information by giving a visual picture of electrode porosity, integrity, adhesion and electrolyte condition. Whilst this analysis did provide the information required, the results did not give the straight-forward correlation hoped for. Instead, we find that there is no single direct correlation between microstructure and sensor response rate (see table 6.1). The best performing electrode revealed an apparently solid, thin, dense microstructure whilst the worst gave the open, porous and finely divided microstructure anticipated from a fast responding electrode. Whilst slightly disappointing, this has enabled the anticipated theory to be challenged as the microstructure does not give a direct correlation to electrode performance.

Greater success was achieved by this technique in evaluating the electrical and mechanical performance of the electrolyte systems. A direct correlation between electrolyte porosity with electrolyte impedance, mechanical properties and sintering temperature was found. Further we have seen an unexpected electrolyte transformation, possibly the result of yttria absorption by silver and to a lesser extent platinum electrodes.

6.11 Technique comparison

One objective of this work was to relate the response rate techniques developed in the course of this work mathematically to one another. This task has not been realised and is hampered slightly by the small degree of overlap between frequencies examined by all techniques. The poor overall degree of correlation between the various techniques, each applied to a single set of electrode samples indicates that the dominant mechanism may vary according to the method by which it is measured. In an attempt to maintain consistency, driving amplitudes, operation temperatures and electrode / electrolyte cells have been kept consistent. The frequency range examined by each of the techniques is diagrammatically represented in figure 6.1. The steady state techniques of current / voltage measurement and concentration step measurements are depicted with frequencies represented by the inverse of sampling frequency used.

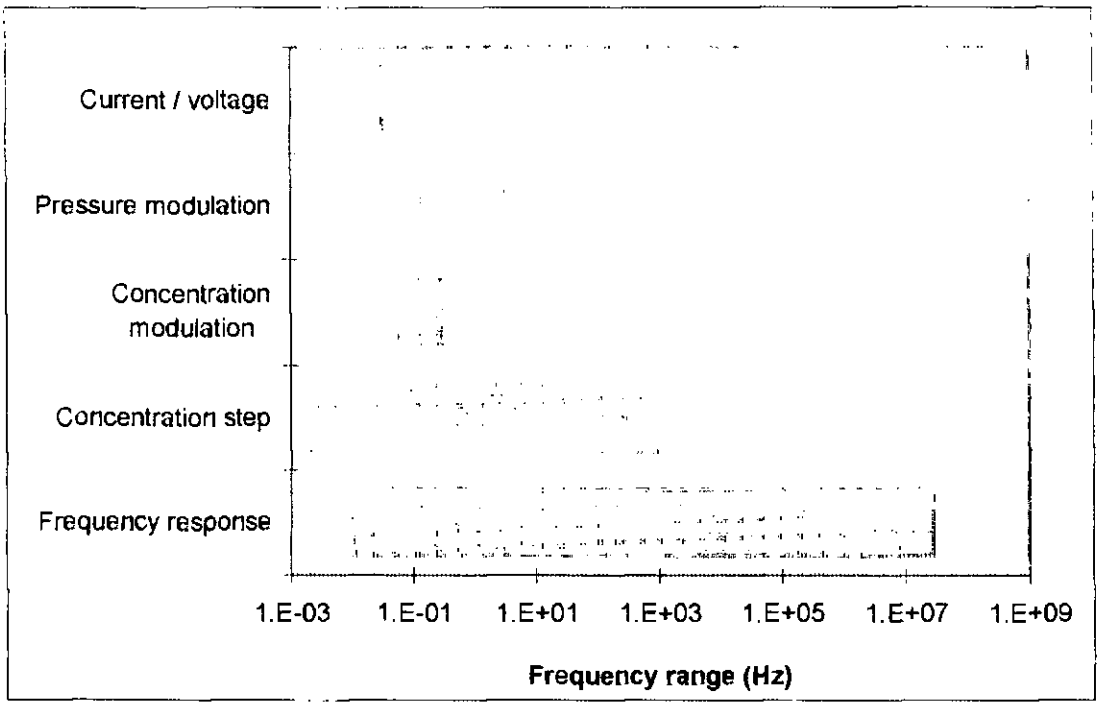

Figure 6.1 Response technique frequency comparison

6.12 Materials investigation

A materials comparison was performed using each of the above mentioned analysis techniques to determine sensor response of the potentiometric cells. Despite promising results from each individual test, these did not tie together over the temperature ranges examined to give a clear order of electrode performance. This may have been partially due to the use of electrodes with insufficient difference in performance for the techniques to reliably separate. This is also possibly partly due to the different frequency ranges and measurement techniques employed emphasising different mechanisms. Details of potential technique enhancements are provided in para. 6.14. In particular this could provide an insight into the apparent improvement of the Ag/Au system seen in pressure and concentration modulation experiments. The Table below sets out the performance order obtained from each technique, ranked into order of aggregate performance. This is contrasted against scanning electron microscopy using a visual assessment of expected electrode performance. This clearly shows that visual examination of electrode structure is not sufficient to estimate electrode performance. Figure 6.2 represents the data graphically in a star diagram .

Electrode	FRA	Step	C.Mod	P.Mod	I/V	Total		SEM
Ag	1	1	2	2	1	7		7
Ag/Au	3	3	1	1	2	10		5
Ag/Pt	2	4	4	3	3	16		2
Au	5	2	5	5	6	23		6
Pt	6	5	3	6	4	24		4
Au/Pt	4	6	6	4	5	25		3
Pd	7	7	7	7	7	35		1

Table 6.1

Low number indicates good performance

Note: This is a qualitative not a quantitative comparison.

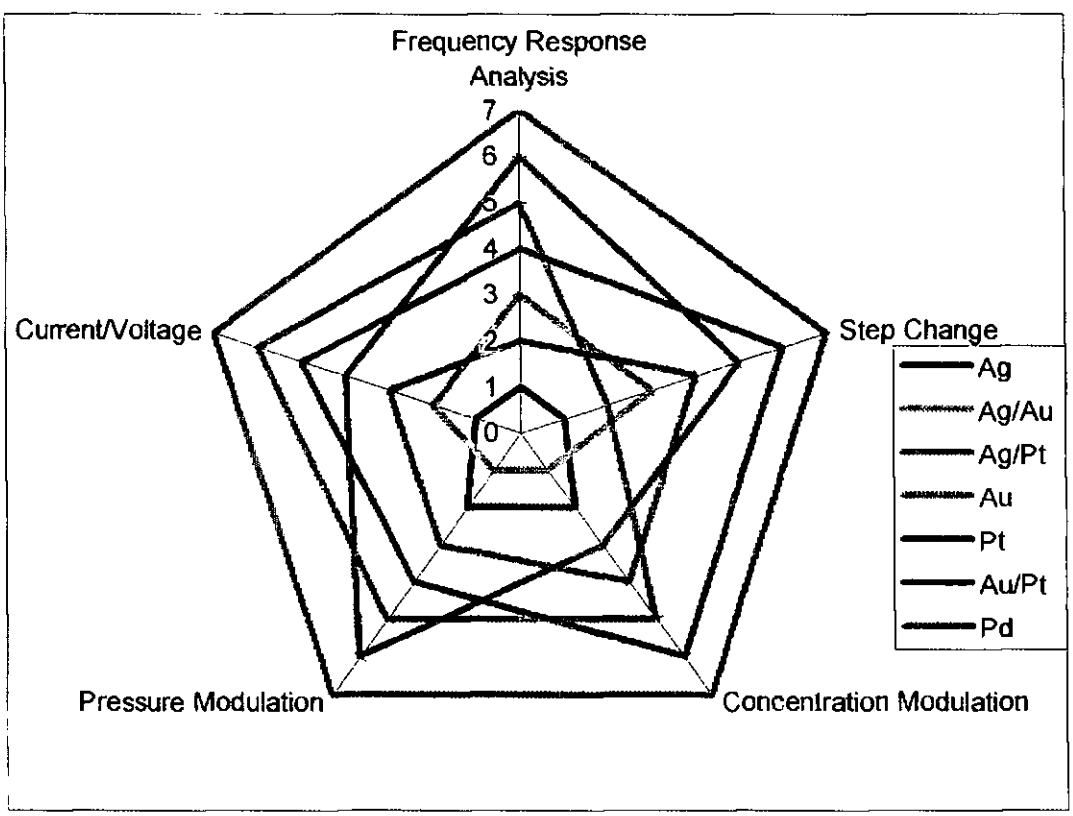

Figure 6.2 Electrode performance comparison

6.13 Platinisation

This research has clearly shown that improvements in sensor performance may be realised through electro-deposition of platinum onto platinum cermet electrodes. There exist two possible theories for these improvements. The first is the addition of metal to increase the metal to ceramic ratio. Previous workers however spent time in developing the cermet to find the optimum metal/ceramic ratio, so this is unlikely. The second theory is that the deposition occurs in a finely divided form that increases three phase boundary length. This

is supported by the finding that deposition by a sinusoidal current can provide similar improvements given sufficient amplitude / time. The basis of this reasoning is that there is no overall increase in electrode material and since there is no reason to expect a chemical change, the improvement must be in the physical re-distribution of the electrode. Scanning electron micrographs suggest that this method may not be suitable for gold or silver electrodes which do not appear to be hindered by electrode microstructure. A method for electroplating the inner electrodes of an amperometric sensor has also been demonstrated. Whilst this showed the technique was feasible, it failed to give the expected improvement in performance; results of tests of amperometric sensor response rates however showed that the real world sensor response would depend more upon sensor installation and that electrolyte impedance became the dominating factor once sufficient bias voltage was applied.

Platinisation of a cermet electrode cell (potentiometric) was performed and results compared to those of the initial cermet electrode and a platinum metal electrode using the same electrolyte sensor base. These three electrodes were examined using frequency response analysis, current voltage sweeps, step concentration changes, concentration modulations and pressure modulations. In each case the plated electrode showed superior performance to the metal or cermet electrodes which gave similar performances.

6.14 Recommendations

Solid state electrolyte sensors applications are currently hampered by high operation temperature requirements. In this work we have examined the effects of reducing operation temperatures in order to identify the associated problems, the aim being to propose causes and investigate how these problems may be avoided or overcome. In this section we make recommendations for the measurement and realisation of low temperature sensor operation.

The first point to be made is that of sensor type. There currently exists a plethora of oxygen sensing methods and techniques. Of these, most are capable of operation at room temperature, for specific applications, these alternatives should considered if elevated operation temperatures are not desirable. Of course solid electrolyte sensors are better suited to certain applications where operation above several hundred degrees celsius is required; it is these that this research is aimed towards.

We have shown that amperometric and potentiometric sensors suffer from different problems as operation temperatures are reduced (ref figure 4.8 & 4.29). Whilst potentiometric devices showed extended response times and increasing measurement errors, amperometric devices revealed a reduction in upper detection limit with no apparent effect on accuracy or response time. In both devices however the problems may be alleviated by attention to reducing electrode and electrolyte impedance although the former is more important in potentiometric, and the latter more so in amperometric devices

Electrodes investigated during this work have included combinations of platinum, silver, gold and palladium as simple metals, binary mixes, cermets, and layers. Most of these demonstrated unremarkable (neither significantly slower nor significantly faster) performance in comparison to the platinum paste electrodes most commonly used in this type of research. Electrodes that did stand out included the palladium metal electrode which was noted for its poor performance and should be avoided unless significantly enhancing fabrication methods are developed. Silver electrodes and silver/gold mix gave significantly better electrodes with lower impedance and faster response. However relatively low melting temperatures may be a fabrication obstacle in certain applications. Also silver electrodes did show signs of altering the supporting electrolyte although this has not been conclusively proven. The best performance however was displayed by electro-deposited platinum onto a platinum cermet base. This proved to be a flexible and easily achievable enhancement that is recommended. Improvement longevity has not been established by this work and has been questioned by other workers.

Electrolytes used in this work were all fully stabilised yttria stabilised zirconia. Although no alternative electrolytes have been examined here, we have demonstrated through indirect measurement that electrolytes can have a significant effect on sensor performance at low temperature. We have also shown that increasing the sintering temperature gives an improvement in electrolyte performance as does decreasing electrolyte thickness. In addition to improved electrical properties, a thinner electrolyte will reduce the power required for heating but at the expense of robustness and increasing the likelihood of failure through thermal shock. Alternative electrolytes have appeared in the literature and are worthy of further examination.

In addition to sensor materials, improvements are possible through improved design. In amperometric devices this may be realised by reduction of the S/L ratio and internal cavity dimensions whilst using a thinner electrolyte membrane on the pump. Another area of better low temperature operation could be to increase the macroscopic area of the electrodes. The use of plastic/ceramic materials has shown distinct advantages over conventional amperometric assembly techniques with the only apparent disadvantage coming through higher electrochemical leakage rates. These may be overcome by use at lower temperatures or by replacing the catalytic platinum wires with palladium which showed poor performance as electrodes. Oxidation of palladium may however detract from any advantage realised.

Potentiometric sensors may be optimised in terms of design by using short gas flow paths and high electrode areas; however these are more bulky than amperometric sensors partly due to the requirement for a piped reference gas. In order to keep measurements accurate, a fine temperature (±1°C) control is necessary. Actual heating power requirements may be higher than those of amperometric devices due to sensor size. Heat losses need to be minimised and devices miniaturised if power requirements are critical.

A large part of this work has been dedicated to evaluating techniques for response rate assessment of solid electrolyte gas sensors. Techniques evaluated have included frequency response analysis, step concentration changes, concentration modulations, pressure modulations and scanning electron microscopy. Firstly we have shown that scanning electron microscopy cannot alone give any indication of electrode response behaviour when comparing differing materials. It has however shed light onto mechanisms involved by allowing visual examination of microscopic structure. The other techniques have all shown an ability to give quantitative response data, although little correlation between techniques has been possible.

By far the easiest in terms of application, accuracy and results interpretation was frequency response analysis. This however is only so due to the level of development that has gone into developing this as a commercial system. This is reflected in the purchase price in excess of £20,000 for the analyser alone. The main benefit of this technique is the ability to resolve cell impedances into grain, grain boundary and electrode components.

The concentration step analysis is perhaps the simplest in terms of concept and interpretation and with further development in terms of automated results analysis, would form a highly useful technique. This is reflected in the literature with widespread adoption as a direct response rate measurement technique.

The techniques of concentration and pressure modulation both suffer from lack of development in terms of application and interpretation. One main drawback with both is the limited range of frequencies achieved in the systems developed here. The concentration modulation technique has scope for much lower frequencies by development of improved data recording and analysis equipment and would benefit significantly from automated analysis. The upper frequency limit in this system is set by the flow valve performance limits; even so attention here could not be expected to see improvements much greater than one order of magnitude in frequency. Pressure modulation frequency limits are determined by the mechanical nature of modulation generation. Further development could see improvements at each end of the frequency ranges. This technique would also benefit from a refined and automated data analysis system to ease the effort in understanding the results obtained from such experiments.

6.15 Future publications

One important product of scientific research is the generation of research publications leading to the dissemination of knowledge and experience, this section briefly lists the findings of this work that may be worthy of consideration for publication or have been already accepted.

- Solid electrolyte sensors fabricated using plastic-ceramic techniques

  This work has already been published by Maskell & Page [87].
- H_2O and CO_2 detection using solid electrolyte sensors

  This work has already been published by Maskell & Page [147].
- Analysis of gas diffusion mechanisms using split electrode sensors

  One novel aspect of this work is the introduction and utilisation of split gauge electrodes. Whilst this has little practical benefit in commercial terms, this does allow a more thorough understanding of the mechanisms at work in such cells.
- Solid electrolyte sensors review

There is scope within the currently available literature for an up to date review of solid electrolyte sensors with attention to recent advances in terms of implementation.

- Investigation of electrode material on performance of zirconia electrolyte sensors

  One main area of this work is the back to back comparison of electrode materials. This study has provided a detail study of the effects of electrode material on sensor performance, including the observed and unexpected influence of the silver electrode on the electrolyte microstructure.

- Techniques for gas sensor response rate measurement

  A second main area presented in this study is the introduction and development of pressure and concentration modulation techniques. A paper outlining the development and implementation of these techniques and their contrast with frequency response and step response techniques would be of value.

- Enhancement of sensor electrode performance by platinum electro-deposition

  Little appears in the available literature concerning the improvement in response rates that may be obtained through electro-deposition of platinum. This study has provided conclusive evidence that significant improvements may be obtained in this manner.

- Non-linear performance of amperometric sensors in high oxygen concentrations

  The effects of deviations from linearity of amperometric sensors has been reported in the available literature but this has not previously been mathematically justified. This study has led to the identification of the controlling factors and demonstrated that these non-linearities can be eliminated.

- Characterisation of amperometric sensors operated at ppm levels of oxygen

  No reports have been found pertaining to measurements of very low oxygen concentrations using amperometric sensors. This study has undertaken such measurements and the resulting sensors have been fully characterised.

- Sintering temperature effects on electrical and mechanical properties of plastic-ceramic materials

  One interesting and practically useful aspect of this study has been the comprehensive study of electrolyte electrical and mechanical properties and their dependence upon sintering temperature.

6.16 Further work

As with the majority of research, this work has raised as many questions as answers. The questions deemed worthy of further investigation are listed here.

6.16.1 Amperometric sensors

Response rate measurements on amperometric sensors showed no dependence upon operation temperature. This is contrary to expectations since both electrode and electrolyte electrical parameters are significantly temperature dependent. This has been attributed to be due to operation limits being encountered before response rate limitations. This could be examined by construction and analysis of sensors with varying diffusion barrier and internal cavity dimensions.

The sensors developed in this work, operate well in laboratory conditions. There also exists a market capacity for cheap reliable sensors that these devices could satisfy. However if this is to be realised then work will required towards commercialisation. There is such currently such capacity in the market for sensors to be incorporated into domestic heating systems. Significant fuel savings and associated environmental benefits are available for exploitation using a sufficiently developed sensor. This should entail the following considerations:

- Reproducibility.
- Design optimisation.
- Size and cost reduction.
- Long term stability and reliability.
- In- house manufacture of plastic-ceramic.
- Integrated sensor heating.
- Thermal insulation and packaging.

Sensors with split internal electrodes showed that oxygen concentration varies across the internal electrode area. There is scope for mathematically modelling this effect both for academic interest and in the study of gas diffusion at elevated temperatures.

Impedance analysis of a thick film amperometric zirconia sensor showed that these devices suffered from very high electrode impedance whilst the electrolyte impedance was low. In comparison, electro-deposition of platinum showed that significant improvements could be realised in electrode impedance without detrimental effects to the electrolyte. Therefore there exists the possibility in developing a very low temperature device by combining the two processes of thick film deposition of the electrolyte along side electro-deposition of the electrode.

Investigation into the operation of sensors in dirty environments encountered in actual applications. This would enable sensors to be built more ruggedly as well as give a greater indication of anticipate failure modes. This requirement is suspected as numerous mechanical failures were observed during the course of this study.

6.16.2 Pump-gauges

Limitations were seen in electrode response evaluations using concentration and pressure modulation techniques due to the limited frequency ranges. Using pump-gauges it should be possible to generate modulating pressures or concentrations by applying sinusoidal currents to the pumps of fully sealed or leaky pump gauges. This would enable a wide range of frequencies to be attained and analysis performed.

Sensor gauges were shown to give a large second gauge step in the presence of water or carbon dioxide. This work could be built upon by the analysis of other reducible or reducing gas species and combinations of these.

6.16.3 Analysis techniques

Current / voltage curves were matched to bias variation in impedance analyses to show that electrode impedance diminishes as voltages are applied. This was only achieved over a limited temperature / bias potential / oxygen range. Increasing the measurement range may prove informative to help clarify the processes of leakage, non-linearity at high / low concentrations and temperatures. The outcome may be a thorough identification of the controlling factors leading to the enhancement of sensor design.

The impedance analyses used in this work only represents a fraction of the capabilities of the frequency response analyser. In particular, there are a number of operation modes e.g. modulating current and measuring voltage, batch measurement, and parameter measurement over time that could be put to use in sensor analysis.

There exist a number of possibilities for improving the step concentration technique particularly in the area of automated data capture and analysis. Benefits would also arise from further signal noise reduction and, for higher temperature assessment, use of absolute pressure steps or a reduction in gas transit path.

The concentration modulation technique has large scope for improvement and refinement, particularly by automated analysis that would enable far lower frequencies to be analysed. This would significantly decrease data analysis time and effort but would not take much system re-design. Also a reduction in signal noise would benefit both measurement accuracy and ease interpretation

As with the above technique improvements, the pressure modulation technique would benefit from noise reduction, automated data collection and analysis but also perhaps from a re-think in terms of operating principle. Potential system improvements may come in the form of using a loud speaker arrangement as used by Dubbe et al [45 & 111] or in the form of an electrochemical pumping technique. The current system is a little crude for very accurate measurements. Incorporation of a pressure or linear displacement transducer would allow electronic phase comparison of sensor output and actual input cycle.

Scanning electron microscopy proved to be a very useful tool for the evaluation of electrode and electrolyte microstructures, insights into sensor performance were gained, especially concerning the mirco-structure of the silver electrode and its apparent influence on the electrolyte substrate. In particular a further investigation into electrode sintering would be valuable in attempting to optimise electrode preparation techniques for each material. In addition an examination by Energy Dispersive X-ray Spectrometry that is an SEM add-on could prove informative in determination of the apparent phase transition seen with silver electrodes as this would enable the comparative proportions of Yttria content to be measured and

identified / eliminated as the cause for the measured electrolyte impedance increase.

6.16.4 Electrodes

Significant amount of time was spent in preparing and assessing various electrode preparations, however the number of variables mean that much more work could be undertaken in this area. A list, in order of estimated reducing importance, of electrode preparation variables includes:

- Electrode material
- Method of deposition
- Adhesion of electrode to electrolyte
- Electrode poisoning
- Porosity of electrode layer
- Effect of glass contamination of electrodes
- Firing temperature and ramp rate
- Electrode reproducibility
- Thickness of electrode layer
- Electrode mixes, cermets, layers
- Electrolyte surface preparation
- Electrode degradation over time

6.16.5 Electrolytes

Whilst electrode preparation is important and has more variables than the electrolyte preparation, electrolyte preparation should not be overlooked and is by no means straightforward. Key parameters include:

- Dopant level
- Mechanical integrity
- Electrical (electronic and ionic) properties
- Longevity
- Reproducibility
- Contamination
- Surface preparation
- Degradation over time

- Thermal shock resistance
- Electrolyte reduction in low oxygen atmospheres or at high potentials

An possible examination that has not been fully conducted in this work is to measure electrolyte conductivity per unit thickness and area. This is fairly straightforward and although it has also been conducted by other workers, it does provide a good base line from which further work may be conducted in looking into electrolyte conductivity improvements.

An ongoing student project has been experimentation concerning producing the green ceramic in-house. This will hopefully lead to a greater control and composition flexibility of the final material. This is a goal that is being steadily approached and a reasonable degree of success obtained. Successful completion of this project will greatly increase the scope of further work possible with these devices. Examples include: the use of alternative electrolytes, fabrication of devices with non-conducting exterior for direct heater attachment, significant material cost reductions, and a far greater control of electrolyte purity and thickness.

It has been suggested that, by using a gadolinia doped ceria electrolyte, a higher ionic conduction can be realised for a similar electrolyte thickness. Of course this is not a panacea as this electrolyte has a higher electronic conductivity and lower mechanical strength. These detrimental effects may be reduced by lower operation temperatures and improved sensor design but some evaluation would be required to get an idea of the advantages / disadvantages.

6.17 Implications and applications

Amperometric sensors currently commercially available are excessively expensive for widespread inclusion for domestic applications, as indicated by their current absence from such systems. It is a conclusion of this work that the use of plastic ceramic manufacturing techniques could allow substantial cost reductions that would open up the large domestic appliance sector. Further cost reductions are possible by the development of thick film sensors due to suitability for mass production and reduced materials usage. Thick film devices are still at early development stages whereas plastic-ceramic devices could be market ready in a shorter time-scale. These devices do not appear to suffer the lengthy response rates of potentiometric devices operated at lower temperature, although the upper

limit of concentration measurement diminishes. In addition they are more suited to portable devices as no reference gases are required and reduced size lessens heating requirements.

Work on the effects of reducible gas species on gauge output of a four electrode amperometric sensor have shown that these devices may be used in the detection of low levels of such species. Whilst there currently exist fully developed and more sensitive sensors for such detection, these devices may be beneficial as an additional capability as a combined oxygen/reducible species sensor.

The developed response rate techniques of step concentration, concentration modulation and pressure modulation analyses have not matched the fully developed impedance spectroscopy as an analysis tool. As a non frequency dependent technique, step concentration change can not separate out electrode and electrolyte components but does provide real response rate information. The pressure and concentration modulation techniques combine these principles and with further development could be used as additional tools in the analysis of gas sensor systems. The benefits of such systems are not yet apparent.

Of the electrode materials investigated, significant low temperature response rate improvements were realised over current platinum cermet electrodes by the use of silver or electro-deposited platinum. These two alternatives may be used to reduce operation temperatures in potentiometric devices although further research of measurement accuracy and life expectancy requires investigation. Whilst these electrodes may be incorporated into amperometric sensors, these devices did not display the same critical dependency on electrode performance as potentiometric devices. Exposure to the high sintering temperatures used in plastic-ceramic devices may negate the advantages of these alternative electrode materials so methods of application after sintering need development.

APPENDIX C

EXPERIMENTAL EQUIPMENT

$$\Delta p = \left[\left(\frac{V}{\gamma v P_o} \right)^2 + \left(\frac{\tau}{2\pi R v} \right)^2 \right]^{-1/2} \qquad \text{Equation B14}$$

$$\phi = \tan^{-1} \left(\frac{\tau \gamma P_o}{2\pi R V} \right) \qquad \text{Equation B15}$$

where Δp, V, γ, v, P_o, τ, R, ϕ are measured pressure amplitude, volume, ratio of specific heats, pressure pulsation amplitude, atmospheric pressure, periodic time, a resistance related parameter and phase angle respectively.

oscilloscope. Similar systems have appeared in the literature for use in the analysis of medical aspirators, and along side impedance spectroscopy for solid electrolyte systems. Dubbe et al [45] proposed the pressure modulation technique and used it along side impedance spectroscopy to investigate the Pt / CeO_2 system, and to derive a detailed model describing electrode kinetics. The technique used a 1mbar pressure sinusoidal modulation introduced to one side of a potentiometric cell. The other side was exposed to a constant reference atmosphere and sensor output EMF was monitored. The system was used along side impedance spectroscopy with the EMF amplitude and frequency recorded. Actual pressure waves were recorded by a cold wire microprobe. A number of resonances were seen at high frequencies, whose frequency and amplitude changed with both oxygen partial pressure and temperature. Frequencies ranged from 0.1 to 500 Hz. They concluded that three phase, electrode / electrolyte / gas, boundaries do play an important role in the performance of porous electrodes and that impedance spectroscopy and pressure modulation spectroscopy allow detailed models to describe electrode kinetics. In another paper [111] Dubbe et al used the pressure modulation technique, again in combination with impedance spectroscopy, to examine the response of the Au / $NaCO_3$ system. They found the pressure modulation system to be more reproducible than the impedance methods and showed that additional information can be gained employing this technique dependent upon the system under investigation. Reproducibility, measured by repeating experiments, was especially poor for impedance spectroscopy where CO_2 levels were altered. This non-reproducibility was attributed to the corrosion of the gold / carbonate interface by current application. Whilst these systems were similar in concept to the technique developed here, they used a much smaller oscillation amplitude at much higher frequencies. These were realised using an audio speaker for modulation generation. This made their system more suitable for investigating the higher temperature performance or electrolyte examination where response is sufficiently fast and would have been little use for electrode investigation below 600°C. Dubbe et al [143] again used the pressure modulation system to assess the response of a carbon dioxide potentiometric cell consisting of silver electrodes on a Na_2CO_3 / $BaCO_3$ electrolyte. The Ag / (Na, Ba)CO_3 was poorly characterised by impedance methods compared to the Au / (Na, Ba)CO_3 system due to the high diffusivity of Ag, however use of pressure modulation enabled the identification of determining processes.

Vaughan & Brown [144] described a pressure modulation technique, covering practical and data analysis problems. This system was developed for measuring volume and leakage rates in medical respirators but proposed as a technique applicable to other vessels. Modulations were applied by DC motor via a gearbox and piston / cylinder arrangement in a similar manner to that employed in this work. Pressure pulsations were monitored by digital manometer and DAQ system. It was deemed essential that modulation and DAQ frequency were not similar to avoid measurement errors. The system was likened to AC impedance measurement but relating volume and leakage to capacitance and resistance. "In AC theory the voltage ins normally described in relation to the current, the two being in phase when current flows through a resistance and $\pi/2$ out of phase when the current flows into and out of a capacitance. With airflow it is easier to relate the pressure to the volume of air (which is analogous to the electric charge) since this is easily measurable. The pressure is, therefore, in phase with volume so far as the capacitance is concerned and $\pi/2$ ahead when a resistance is considered." Whilst the apparatus described was similar to the technique developed in this work, it was applied to the monitoring of aspirator leakage in breathing systems, a very different application. Relating the pressure and leakage to resistance and capacitance in AC theory they derive expressions:

Much less work has been reported on response rates in amperometric and pump-gauge devices. Benammar & Maskell [80] demonstrated a response time of 65 mS to a step concentration gas change using solenoid valves to switch the gas flow into the test chamber. The device tested was a pump-gauge operated in the AC mode at 800°C. Here again the electrochemical response was probably substantially faster and the response of the test-rig was influential. The step was measured from 10 to 90% of initial to final response. Whilst step pressure experiments generally allow faster response times to be measured, amperometric devices are sensitive only to pressure changes, not absolute values so measured response would be complex. Saji et al [10] measured response of an amperometric zirconia sensor with a porous diffusion layer at 720°C to within 200mS. Usui et al [92] researched response rates of amperometric sensors using a step change in oxygen concentration. Response rates of 3 to 21 s for 90% response was seen for a 0 to 95% oxygen step at an unspecified temperature.

B1.6 Concentration modulation

No references have been found in the literature regarding the concentration modulation techniques of measuring response rates. The most relevant literature pertains to sinusoidal modulations in pump-gauge devices [74, 78]. In these works sinusoidal concentrations are obtained at the potentiometric gauge cell by pseudo sinusoidal currents applied to the pump. Differences between this and their work arise through the method of applying the modulation. These papers covered work with both fully sealed and leaky devices. In the fully sealed work internal pressures as well as concentrations would have been produced whereas with the work with leaky devices, pressures would have been dissipated.

Vitzethum et al [84] proposed the use of a computer controlled zireonia pump to attain adjustment of oxygen partial pressure by adding or removing oxygen from a flowing gas source. This system was used a 600 mm long tube of caleia stabilised zirconia to control the degree of oxygen introduced to gas streams to generate set gas mixtures. The system was linked to a DAQ system to enable computer control of gas mixtures produced. His system was not, but could easily be, adapted to provide an oscillating gas mixture as used here to analyse response rates. To utilise this technique modulation amplitudes would have to be small.

Since Faraday's constant is the charge required to liberate 1 mole of electrons and 4 electrons are required to liberate 1 mole of oxygen, 4F is the charge required to evolve 1 mole of gas. Since 1 mole of gas occupies 2.24×10^{4} ml at STP, the volume of gas at STP evolved by 1 amp for 1 second is $22.4\times10^{4}/4$ F = 0.058ml. or 58 mm^3 Using the ideal gas equation PV=nRT we find that at 700°C and standard pressure we get 0.207 ml^3 aS^{-1} of oxygen

Caneiro et al [83] used a zirconia electrolyte tube to introduce O_2 to CO or CO_2 streams, this system could also be utilised to form the basis of a concentration modulation test rig. The main advantage of using electrochemical-pumping techniques is that higher frequencies than possible with flow valve control methods are achievable.

B1.7 Pressure modulation

A further technique of pressure modulation has been developed for response rate measurement in this work. This technique has a close relation to the coneentration modulation technique described above. Sinusoidal modulations are achieved through mechanieal oscillation of barometric pressure at a single concentration rather than a modulation of concentration at a single pressure. Modulations are produced using an electrieal motor driven eam, with data collection and analysis carried out using an

rates of the electrolyte to adsorbed oxygen species and by the amount of oxygen species required to attain Nernstian EMFs. An empirical relation was found:

$$V_t - V_0 = V_\infty - V_0 \exp(-t/\tau)^{1/2} \qquad \text{Equation B12}$$

where V is the cell voltage at times 0, t and ∞, parameter τ follows an Arrhenius type law given by Fouletier et al [37]:

$$\tau = AP_m^{-1/2} \exp(E_{act}/RT) \qquad \text{Equation B13}$$

where A is a constant, E_{act} is the activation energy and P_m is the mean partial pressure. This equation was found to hold except for at the start of the change where diffusing and mixing of the step front were suspected.

Plots of $\log(T_r)$ versus $1000/T_k$ gave linear plots indicating activation energies of 199 $kJmol^{-1}$ and 216 $kJmol^{-1}$ were obtained for platinum and gold electrodes on 21 mol% YSZs respectively. Further comparisons were made by comparing temperatures required for 1 and 10 second response to be obtained. They concluded that Au had a positive influence on response rates, worthy of further investigation, whilst zirconia electrolytes gave faster response than bismuth oxide, at least at high temperatures. They also found that cubic zirconia was faster than monoclinic or a mixture of cubic / monoclinic. They suggest that for practicable sensors high temperature response rates are affected by aerodynamics rather than electrochemical response.

Kobayashi et al [26] used step change response rate tests to assess the effects of electrolyte on cell response. They found a very similar response at 700°C from PSZ and FSZs with response times at around 5 s. The limited amount of work on response times may indicate that the test-rig rather than sensors, especially at this relatively high temperature control these response times.

Inoue et al [38] used a step pressure change from P_{O2} from 10^5 to 10^3 Pa at 200°C to 370°C. They measured a 90% response time of below 1 minute at 300°C for $La_{0.6}Sr_{0.4}Co_{0.98}Ni_{0.02}O_3$ electrodes on a ceria electrolyte, rising to 12 minutes at 200°C.

Xiang & Sheng [39] reported a zirconia potentiometric sensor that gave Nernstian EMFs to temperatures as low as 200°C. The sensor incorporated electrodes of $Bi_3Ru_3O_{11}$-YSZ painted onto the electrolyte at a thickness of 100 μm. The electrolyte was an unremarkable 10 wt% YSZ at 1.5 mm thick so the electrode must have been very effective. Cell resistance was measured at 8.37 kΩ at 200°C with a response time to a step concentration change reported at 20.6 seconds. Step responses were produced between oxygen at air and $\pm 1.6 \times 10^3$ Pa. At 400°C response times were below 10 s. The response times did not significantly degrade over a period of 90 days. This cell resistance is very small in comparison to my measurements despite a similar electrolyte being used.

Whilst a rapid response for a sensor has been identified as an important factor, and electrochemical response rates as critical in this respect, it is the response of the sampling system can not be neglected. Kocache et al [67] reported a response to a step gas change of the Bendix analyser of seconds at 800°C. The electrochemical response at this temperature would be significantly quicker and is unlikely to be the controlling factor.

measurement errors were encountered at low oxygen pressures. They also found that the response depended on step direction with both electrode time lags longer for a decrease than for an increase in pressure, and that the operation temperature plays a very important role. They stated that electrode microstructure may play a role through hindering gas diffusion to the three phase boundaries. The dependence of response time on pressure was examined, keeping the initial : final pressure ratio constant, the results gave agreement to:

$$t_r = A(P_m)^{-1/2} \exp -\frac{E}{RT} \qquad \text{Equation B9}$$

where t_r is the response to 99% and P_m is the average pressure. This indicates that response times are proportional to the square root of average pressure. Extrapolating the data indicated that response time grew significantly as pressure was decreased. Activation energies for the electrodes of Ag = 0.6 eV and Pt = 1.0 eV are obtained from this work. A linear relation of log (response time) to $1/T_k$ was seen. Electrodes with mineral binders or glassy phases, which can develop oxygen, were identified as contributing to slow response and should be avoided.

Anderson & Graves [106] examined the response of an 8 mol% YSZ potentiometric sensor with Pt paste electrodes with an area of 0.25 cm^2 using a step change in gas concentration. Response times of approximately 1 s to step changes at 600°C were obtained. Gas steps analysed were O_2 / N_2, CO / N_2, H_2 / N_2, D_2 / N_2. The data was found to conform to the equation:

$$\phi_V(t) = \frac{(V_t - V_\infty)}{(V_0 - V_\infty)} \qquad \text{Equation B10}$$

Forward and reverse steps, however showed an asymmetry. This asymmetry was eliminated when the voltage data were converted to partial pressures.

$$\phi_C(t) = \frac{(P_{O2t} - P_{O2\infty})}{(P_{O20} - P_{O2\infty})} \qquad \text{Equation B11}$$

The response of the device to step gas changes was thought to depend upon both the shape of bulk gas composition front and internal electrochemical response of the sensor. They found that electrical response, by application of small current pulses, was much faster than composition response. Examination of reactive gases revealed a response dependent upon concentration. This work then extended to examine non-equilibrium gas mixtures. In this work a significantly different response was obtained as a sharp EMF step occurred as the sensor recorded the output at stoichiometry. Pre-equilibrating reactive gases via a secondary catalyst improved the response with higher EMFs obtained.

Winnubst et al [3] defined response rate as the time lag between a step change in bulk oxygen partial pressure and the final value of EMF registered by the sensor. They used the step change to measure response rates in ZrO_2 and Bi_2O_3 sensors with Pt and Au sputtered electrodes onto polished surfaces. Step changes were applied from 21 to 100% and back from 100 to 21% oxygen at atmospheric pressure. To eliminate gas step test-rig transit times, response from 10 to 90% of total response was used for time measurement. A direction dependence was found in output EMF but, as with the work of Anderson & Graves [106], this was shown to be eliminated when converting to oxygen partial pressures. They found that charge transfer from the electrode is determined by response

Gur et al [140] studied the Pt / scandia stabilised zirconia system using AC impedance. They used temperatures from 600 to 900°C with frequencies from 40 to 20 kHz. A change in electrode mechanism was seen at 700°C by a change in slope of the Arrhenius plot and attributed these to changes in electrode morphology.

Badwal & deBruin [141] examined Pd electrodes on ceramic electrolytes using frequency response analysis. Electrodes were sputtered at 1000 to 6000 angstroms thickness with a diameter of 10 mm. They saw a dual behaviour with that of a noble metal at high temperatures reverting to that of a reactive metal at low temperatures. The noble-reactive metal transition was accompanied by a large resistance increase. A change in electrolyte activation energy was also observed at 775°C from 61 $kJmol^{-1}$ at high temperatures to 107 $kJmol^{-1}$ at lower temperatures. Electrode activation energy was obtained at 84$kJmol^{-1}$ in air. In addition two electrode arcs were observed above 775°C. The transition temperature was oxygen concentration dependent moving from 736°C at 5% to 870°C in 100% oxygen. It was also affected by DC bias. A scanning electron micrograph showed an electrode coverage and porosity comparable to that of Pt metal electrode presented here (see section 5.7).

B1.5 Step changes

The step change technique is the most commonly used method of directly evaluating sensor response rates. This method is used as it is simple to set up, inexpensive and data requires only simple evaluation and analysis. In most evaluations the device under test is a potentiometric sensor and it is mainly the electrode upon which attention has been focused. The step change in most tests is applied only to the measuring electrode whilst the reference electrode atmosphere is maintained constant. The technique usually involves step changes in gas concentration by switching gas flow from one source of bottled gas or mixed gases to another.

Young [142] measured response rates in Bendix zirconia potentiometric sensors by using a step change in A:F ratio. A propane burner was used to produce the steps. Factors of step direction, distance from burner, A:F ratio, and presence of protective cover were investigated. Switching frequency and gas flow velocity had measurable influence on response times recorded. Temperatures were varied between 170 and 645°C using a variety of A:F ratio steps whilst temperature did show a definite influence, the response times for 50% response are 0.5 s at 170°C were seen dropping to 0.1 s at 645°C an activation energy of 2.7 $kcalmol^{-1}$ (11.3 $kJmol^{-1}$) were obtained. These remarkable response times and low activation energy are not explained.

Alternatively, for rapid step changes, a step change in barometric pressure is employed [37, 64, 110]. This method has the advantage that the pressure switch is very rapid allowing measurement of fast reacting systems. Doughty et al [110] examined potentiometric response rates of zirconia oxygen sensors using a step pressure change. They measured times for 10, 50 and 90% theoretical EMF. They investigated the response of partially and fully YSZ with Fe_2O_3 additions using platinum electrodes. They obtained an activation energy of 150 $kJmol^{-1}$ and found that Fe_2O_3 increased response times when included in the electrolyte but had beneficial effects when included at the electrode interface.

Fouletier et al [37, 64] measured sensor response by rapid partial evacuation to examine platinum and silver electrode response rates on zirconia electrolyte sensors. This work showed that platinum and silver electrodes followed the same laws at least for small pressure steps and that although silver gave faster response at low temperatures, large

electrolytes. They concluded that the diffusion path in the electrode is strongly influenced by the electrolyte. Rate limiting steps are diffusion processes at anode / cathode for high / low P_{O2} respectively. The diffusion processes occur on the electrode surface.

Isaacs & Olmer [138] compared various electrode materials as point electrodes on a yttria PSZ electrolyte using AC impedance and current / voltage measurements. Point electrodes were used so that the effects of electrode morphology were minimised. The size of contact point was corrected for by measurement of the electrolyte impedance. Electrodes were classified according to specific currents per unit circumference which gave a higher dependence than electrode impedance. Specific currents gave electrode kinetics in the order of Rh>Pd>Pt>Au and surface contaminants showed that electrode processes were rate controlling.

Kleitz et al [104] found that the lowest activation energies are obtained with solid porous silver electrodes with activation energies close to that of the electrolyte. They also suggested that insufficient electrode coverage could lead to marked deviations of results.

Ziehfreund et al [139] used impedance to study the effect of platinum impregnation of YSZ electrolytes. They found that impregnation lowered the electrolyte conductivity by blocking ion transport at grain boundaries. By evaporation of platinum containing YSZ to get a microporous thin film with high platinum dispersion, conductivity was improved over non impregnated YSZs.

Ageing of the Pt/YSZ system has been examined by Kleitz et al [104] who found a decreasing conductivity over time, especially at temperatures exceeding 800°C. Ageing was attributed to a gradual enhancement of the blocking effect. This was attributed as due to segregation of impurities at grain boundaries. This lead to expectations that larger grain size samples age less than smaller grain electrolytes and that ageing is purity dependent. A further complication is the phenomenon of semi-circle depression. In complex plane plots, the characteristic semi-circles are often depressed below the x axis, a phenomenon not well understood. Kleitz et al [104] studied semi-circle depression which is small for electrolyte polarisations but may reach 45° for electrodes. Depression is usually attributed to a statistical distribution of relaxation frequencies or an elementary jump of an ion due to local energy storage effects associated with slow relaxation of the polarisation. Semi-circle depression can also give errors in calculated capacitance values. The depression is often represented in equivalent circuits by a constant phase element CPE. The analysis presented here does not extend to this phenomenon. In their analysis they reported that a second high frequency electrode semi-circle is often observed but it is relatively small for zirconia, especially with high yttria content. It is easily detectable for lower yttria content zirconias, ceria or thoria electrolytes. Overlapping semicircles is also a problem for ceria and thoria samples.

Kaneko et al [41] investigated the behaviour of Pd and Rh electrodes on YSZ using impedance spectroscopy over a range of temperatures and oxygen partial pressures. Oxygen atmospheres of 1 to 10^{-5} atm and temperatures from 580 to 900°C were examined. A two stage impedance result suggested a change from metal to oxide as oxygen was raised through 10^{-1} to 10^{-2} atm or temperatures of 650 to 700°C for Pd or 850 to 900°C for Rh. Changes observed were not reversible thus resulting in hysteresis. Steps were seen in electrode and electrolyte impedance but electrolyte changes were small. Electrode activation energies were 15 and 190 kJ/mol for Pd and 50 and 380 kJ/mol for Rh for the oxide and metal respectively.

They also showed that double layer capacitance was temperature dependent but P_{O2} and potential independent and suggested that AC impedances are dominated by faradaic capacitances. Using chronoamperometry they found a double layer capacitance of 0.2 and 1.3 μcm^{-2} at 555 and 695°C respectively and insensitive to oxygen partial pressure and electrode potential.

Bauerle's electrode interface resistance was seen to be very sensitive to variables with temperature proving a strong influence to reveal that it is a thermally activated process with an activation energy of 2 - 2.5 eV. Oxygen also had a strong effect above 600°C with an increase in oxygen giving a reduction in electrode resistance but no effect below 400°C, on the electrode capacitance or on the electrolyte resistance or capacitance values. The electrolyte resistances showed similar temperature dependence to the electrode suggesting similar mechanisms. The activation energy for electrolyte resistance changed slightly with temperature to give values from 1.1 to 0.9 eV. Bauerle postulated that the electrode resistance involves 5 steps:

1. Flow of oxygen into the pores of the platinum electrode.

2. Adsorption of molecular oxygen on the pore walls in the electrode.

3. Surface diffusion of oxygen molecules to electrode-electrolyte interface.

4. Dissociation of oxygen molecules.

5. Electron transfer reaction at the interface.

Of these the steps 4 and 5 appeared to be critical.

However, whilst AC impedance is useful for separating electrode and electrolyte components, it cannot resolve or distinguish between electrode mechanisms [42]. Bauerle [50] found that his platinum electrodes could be improved by passing a high current (1 Acm^{-2}) at elevated temperature (800°C) to improve porosity. The use of symmetrical electrodes and small AC current with no bias allowed electrode parameters to be $R=1/2R_1$ and $C = 2C_1$. A difference in electrode size, structure or bias was postulated to lead to distorted semi-circles.

Braunstein et al [137] derived an analytical formula to approximate the resistance of a cylindrical sample with non-symmetrical circular electrodes.

$$R = l/\sigma \ln(S_o^2/S_aS_b)/(2S_o-S_a-S_b) \qquad \text{Equation B8}$$

where l, σ, S_o, S_a, S_b are electrolyte thickness, specific conductivity, electrolyte cross section and the electrode cross sections.

Since Bauerle's work, AC impedance methods have been highly developed and widely employed to study a variety of solid electrolyte systems.

Verkerk et al [105] examined platinum electrodes on ZrO_2, Bi_2O_3 and CeO_2 electrolytes with variation in temperature (770 - 1050°C) and oxygen partial pressure (10^{-5} to 1 atm) using DC polarisation. Electrode polarisation was found to be electrolyte dependent. A bend in Arrhenius plot was seen at 960°K and was P_{O2} dependent. Verkerk et al [136] also used impedance spectroscopy to study platinum electrode kinetics on the various

Maruyama et al [132] used YSZ and Na_2CO_3 / $Na_3Zr_2Si_2PO_{12}$ (NASICON) potentiometric sensors as a two sensor system to identify CO and CO_2 components which were unaffected by the presence of H_2.

Brailsford et al [133] examined the behaviour of a potentiometric sensor in a multi-component gas mixtures containing O_2, H_2, H_2O, CO, CO_2, and N_2 and developed a model to predict the response.

B1.4 Impedance

Bauerle [50] was the first to employ this technique in evaluating solid electrolyte systems in 1969. He used the technique to study 9 mol% YSZ bars and wafers (for geometry variation) with Pt electrodes (sputtered and paste) over a range of temperatures from 400 to 800°C and oxygen partial pressures from 1.5×10^{-5} to 1 atm. Electrolyte specimens were commercial grade, prepared using standard procedures and prepared under high purity conditions with geometry of 1×3×4 mm or 1×1×12 mm. He observed the three polarisations on a complex plane plot and attributed these to the electrode double layer, grain boundary impurities and an ohmic electrolyte resistance phenomena. A high temperature dependence was observed for all three polarisations. Impedance phenomena were identified by varying factors such as cell geometry, oxygen concentration, electrolyte purity and electrode microstructure. The system was likened to an electrical RC circuit with R and C components for each polarisation. The intercepts of each semicircle relating to the resistance magnitude whilst capacitance values were obtained from the frequencies at semicircle maximums. Since it is possible to fit a variety of RC circuits to any impedance spectra, consideration of the likely mechanisms is required if the technique is to be used for more than a simple comparison of systems. The circuit proposed by Bauerle is shown in figure B1.

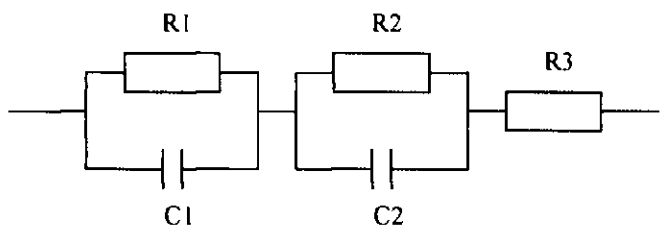

Figure B1 Bauerle's equivalent circuit.

The electrode capacitances were of the order 30 – 80 $\mu F/cm^2$ and showed only a weak dependence on variables. A theoretical maximum capacitance of 190 $\mu F/cm^2$ was calculated and only exceeded with non-porous platinum paste electrodes. Grain boundary capacitance was of the order 0.028 to 0.015 $\mu F/cm^2$, temperature independent, but affected by electrolyte purity. The grain boundary polarisation were eliminated by careful preparation to achieve a pure electrolyte whilst silica and calcia were found in the grain boundaries of less pure specimens and given as the root of grain boundary impedance. Aoki et al [134] investigated the effect of silica on the grain boundary impedance of calcia stabilised zirconia. They found that bulk conductivity was unaffected by grain size but grain boundary impedance decreased with grain size.

Robertson & Michaels [135] conducted a review and analysis of Pt / YSZ double layer capacitances. Double layer capacitances were found in the literature [50, 136, 3] to be between 60 and 350 μcm^{-2}. They calculated that attributing the entire capacitance to double layer implied an impossibly small layer thickness <3 angstroms. They suggested that a more reasonable thickness of 0.63 angstroms to give a maximum of 14.1 μcm^{-2}.

$$I_{L2} = -4FD_{O2\text{-}H2O\text{-}X}SP/RTL\ (1+X_{H2O}/2X_{O2})\ \ln(1-X_{O2}) \qquad \text{Equation B4}$$

They also found that the gas diffusion coefficient changed due to the presence of hydrogen from the decomposition. H_2 has a diffusion coefficient over 3 times greater than that of oxygen in nitrogen. The effect of carrier gas on diffusion is also significant, especially with helium, which gave far higher limiting currents due to faster diffusion of oxygen and resulting in a non-linear output at high humidities. Usui et al [89] further investigated the operation of amperometric sensors in humid air atmospheres. As humidity increased the primary limiting current was seen to gradually change from values predicted using $D_{(O2\text{-}N2)}$ to $D_{(Air\text{-}H2O)}$ (0.181 to 0.256 at S.T.P. respectively with similar temperature coefficients [130]). They also compared a calculated H_2O decomposition voltage with that recorded at which the second current plateau was indicated, and found agreement. The decomposition potential of water $E^o(T)$ was related to the standard Gibbs free energy change $\Delta G^o(T)$.

$$\Delta G^o(T) = -nFE^o(T) \qquad \text{Equation B5}$$

$$\Delta G^o(T) = -247.657 + 0.05502T\ (kJmol^{-1}) \qquad \text{Equation B6}$$

where n, F and T are the number of electrons involved in the decomposition (2 in this case), Faraday's constant and the temperature in Kelvin. This gave a value of 1.091 V at 400°C which agreed with the onset of the second plateau at 1.2 V. Calculation for the value at 800°C using this formula shows a drop to 0.976 V.

For the CO_2 to CO reduction the Gibbs free energy is given [21] by:

$$\Delta G^o(T) = -283.328 + 0.8753T\ (kJmol^{-1}) \qquad \text{Equation B7}$$

This shows values of 1.163 V at 400°C and 0.981 V at 800°C. The CO_2 reduction therefore requires higher potentials below just over 800°C but lower potentials at higher temperatures.

Olmer et al [131] used a YSZ cell for water vapour reduction. YSZ surfaces were doped with ceria and electrodes of Ni, Pt, and Au were also examined. A decrease in potential required for reduction was found when using CeO_2 doped electrolytes. The reduction was made easier by the electronic conduction of the ceria allowing an enlargement for the reaction zone. Water reduction catalytic activity on pure YSZ were in the order Au > Pt > Ni, the reverse of the order seen in oxygen reduction.

Logothetis et al [81] reviewed the operation and application of solid state electrochemical cells. In this work they mentioned the use of a four electrode amperometric sensor, both with and without external reference gas for the analysis of H_2O in oxygen / nitrogen gases. They stated that "With reducible species present a second current plateau may be realised accompanied by the gauge abruptly increasing to large values." Although the principle of utilising an integral gauge was hinted at, no results were presented or analysis performed.

Yamazoe & Miura [16] in their review of environmental gas sensing pointed out that, whilst CO_2 is a harmless gas, it does contribute to the greenhouse effect and is useful for monitoring combustion and biological related activities and therefore detection is very useful.

B1.3 H_2O/CO_2

Dietz et al [12], in first proposing amperometric sensors, made reference to the fact that the presence of moisture in testing gases may affect results if a sufficiently high pump potential were employed. They made no specific measurements suggesting that for oxygen measurements, potentials exceeding 1 V should be avoided to prevent reduction of other gas species.

Takahashi et al [73] investigated the influence of reducible and reducing gases such as CO_2, CO, H_2O, H_2 and C_4H_{10} on porous layer amperometric sensors. The initial current plateau, in the range 0.3 to 0.8 V, attained was shown to be proportional to oxygen concentration, but also to reduce in proportion to an increase in reducing gases where used. This was attributed to reactions lowering the free oxygen available in the sample gases. H_2O and CO_2 on the other hand were seen to result in a second limiting plateau in the range 1 to 2 V. Whilst the initial plateau was dependent only upon oxygen partial pressure, the second was found to be proportional to the concentration of the H_2O / CO_2 component, with an offset given by the oxygen concentration.

Usui et al [89, 90, 91] used Fujikura 2 electrode amperometric zirconia sensors, with single diffusion pores, for the measurement of humidity in oxygen containing gas mixtures. They gave a detailed analysis of behaviour based upon these experiments which utilised a variety of inert carrier gases to assess diffusional behaviour, along with a range of oxygen concentrations and humidity levels. Usui et al [90] measured humidity levels in nitrogen at atmospheric temperatures above 100°C. Atmospheric temperatures showed no influence over the range of gas temperatures 100 to 160°C with the sensor operated at 450°C. In the absence of oxygen, sensors gave a single current limit at elevated pump potentials and a linear output corresponding to H_2O concentration. Usui et al [91] demonstrated a sensor operated in humid oxygen / nitrogen atmospheres over a range of temperatures (400 to 500°C), gas contents (10 to 50% H_2O, 0 to 41% oxygen) and carrier gases (N_2, Ar, Ne, He). They observed the primary and secondary current limits with linearity for both oxygen and water contents respectively. With oxygen reduction in an inert atmosphere we find the limiting current is given as:

$$I_{L(O2-X)} = -4FD_{O2-X}SP/RTL \ln(1-X_{O2}) \qquad \text{Equation B1}$$

note that at low oxygen concentrations (<20%) the term $\ln(1-X_{O2})$ approximates to X_{O2}. This term relates to a pressure gradient along the diffusion barrier length produced as oxygen pumped out of the internal cavity. With water reduction, 1 mole of H_2 was evolved as 1 mole of H_2O was reduced so there should be no change in internal barometric pressure or gas flow through the diffusion barrier as there is with oxygen reduction. As there is no pressure gradient with H_2O reduction this term does not appear. Other changes are that only 2 electrons per reduced molecule are required. and the diffusion coefficient refers to that of water rather than oxygen in the inert carrier gas. For water reduction in an inert atmosphere we find a limiting current given by:

$$I_{L(H2O-X)} = -2FD_{H2O-X}SP/RTL \, X_{H2O} \qquad \text{Equation B2}$$

Combining these we see that the two limiting plateaux may be calculated by:

$$I_{L1} = -4FD_{O2-H2O-X}SP/RTL \ln(1-X_{O2}) \qquad \text{Equation B3}$$

with Pt electrodes and gold seals. Electrolytes studied included partially stabilised, fully stabilised, single crystal zirconias. Partially stabilised zirconias had polished or abraded surfaces for electrode deposition. Three separate leakage mechanisms of physical leakage, semipermeability and electrochemical leakage were identified as previously discussed (section 1.2.5.2.6).

Mathematical analysis of the leakage mechanism allowed identification of the electrode rate constants and for the electrolyte resistance to be deduced from leakage rates and the temperature and P_{O2} dependence. Physical leakage $\propto P_1-P_2$ Semipermeable leakage $\propto P_1^{1/4}-P_2^{1/4}$. Leakage rates did not show the $\propto P_1-P_2$ and so physical leakage was ruled out. The $\propto P_1^{1/4}-P_2^{1/4}$ was observed to a certain extent but semipermeability was ruled out after further testing.

Three electrochemical-pumping analyses were used:

1. Coulometric pumping
   Apply a known current for a set time to remove oxygen from the internal cavity, then before the cavity is fully depleted, reverse the current direction to pump in for the same time. The pumping operation should remove and replace identical quantities of oxygen and, in the absence of significant leakage, therefore give a symmetrical gauge EMF vs. time graph. Plotting internal oxygen partial pressure versus time should give a linear plot with identical but reversed slope for each pumping direction. Any significant leakage would reveal itself as a non-linearity.

2. Recovery tests
   Apply a small constant EMF to the pump cell to remove oxygen from the internal cavity. When the gauge EMF stabilises, hold the pump open circuit and record the gauge EMF over time. As oxygen leaks back into the device, the EMF drops and leakage rates are recorded.

3. Steady state tests
   In this analysis a small constant current is applied to the pump to remove oxygen from the cavity. As oxygen is removed, the gauge EMF will rise until the leakage current equals the applied current and a steady state attained. The applied current is then equal to the leakage current at the partial pressure differential indicated by the gauge.

By applying either of the second two tests over a range of temperatures and external oxygen concentrations, data is acquired which can be used to identify leakage rates and dominant mechanisms. In their work Kaneko et al found leakage rates increasing with temperature and external oxygen concentration in a manner indicating electrochemical leakage via the metal-ceramic seal. Type of zirconia electrolyte made little difference but sensors with electrodes on abraded electrolytes showed significantly higher leakage than those on polished electrolytes. This indicated that internal electrode activity was an important factor.

In conclusion they determined that since electrolyte resistance was low compared to electrode resistances, leakage rates were controlled by electrode kinetics. The external resistance was only 3× greater than the internal electrode, surprising as the TPBs involved were that of a porous platinum electrode and a small length represented by the gold seal / electrolyte contact. This result suggested that the combination of gold and platinum had formed an alloy affecting the electrode performance. This result lead to the feeling that Au, especially in contact with Pt may form a good electrode material.

Lee et al [126] constructed amperometric sensors with porous diffusion barriers by sintering of alumina and zirconia mixtures with or without a dense cap. Porosity was controlled by the proportion of alumina to zirconia used in the barrier and examined by SEM. The dense cap had benefits of both further restricting gas diffusion and preventing sensors bending due to thermal expansion mismatches. Sensors were reported as reproducible with uncertainties of 18% for the better devices. Density of the cap was increased by zirconia addition along with grain size. Limiting currents were proportional to oxygen concentration only below 40%, dependent upon device configuration.

Ioannou & Maskell [51] demonstrated the concept of a thick film amperometric sensor using a thick film partially stabilised zirconia membrane on an alumina substrate with platinum / zirconia cermet electrodes. Devices showed positive or negative temperature coefficients dependent upon electrolyte sintering temperature. Work on these devices was continued by Gopaul et al [52, 101] who used a fully stabilised zirconia material. They showed that a temperature coefficient of $T^{3.1}$ was attributable to the expansion and contraction of cracks in the electrolyte due to thermal expansion mismatch between electrolyte and substrate. Investigations were performed over a range of temperature and barometric pressures.

Liaw & Weppner [127] constructed an amperometric sensor using TZP discs joined using a glass seal with platinum paste electrodes applied onto a diamond-polished surface. The sensors were analysed by impedance spectroscopy and current / voltage curves. The sensors gave limiting currents in air down to 300°C after which the upper detection limits were reduced. Both electrolyte impedances (grain and grain boundary) gave activation energies of 0.94 eV. They concluded that the diffusion limits of practical sensors were dependent on electrolyte thickness and diffusion barrier configuration. They suggested that a thick film electrolyte with an ionic conducting diffusion barrier could be used for lower temperature operation and miniaturisation.

Logothetis & Hetrick [128] reviewed zirconia oxygen sensors based on pumping. They concluded that amperometric sensors have the advantage of linear output, high sensitivity and weak temperature dependence. For amperometric sensors with good electrodes, response rates depend upon the diffusion barrier characteristics and sensor structure. It is desirable to operate amperometric sensors at small pump potentials as complete oxygen depletion at the cathode can limit device performance.

Copcutt & Maskell [129] used a zirconia 4 electrode amperometric sensor to measure SO_2 and NO in O_2 / N_2 atmospheres. The device was created using sintered ceramic discs adhered with a glass seal, a laser drilled diffusion hole and platinum electrodes. This did not prove to be a straightforward exercise with problems of electrochemical leakage and electrode corrosion preventing reliable measurement. The sensors failed to determine NO levels.

B1.2 Pump-gauge

Much of the literature concerning pump-gauges has been previously mentioned in discussing the operation modes (see section 1.2.5.2). The work done in this study however is not concerned with oxygen measurement or operation mode but closely follows that of Kaneko et al, [61]. Kaneko et al, used electrochemical pumping analysis to research leakage rates and identify leakage mechanisms in gold seal pump-gauges. The work presented in this report uses similar techniques to compare the leakage mechanisms seen in their gold seal devices with those of the novel plastic / ceramic sensors developed here. In their work a number of devices were fabricated using a range of zirconia electrolytes

B1. Literature review

B1.1 Amperometric

The diffusion controlled limiting current zirconia amperometric sensor was first proposed in 1982 by Dietz [86]. He pointed out that a significant restriction to gas diffusion was required to achieve diffusion limiting since the diffusion of oxygen in air is 60,000 times faster than that in water, previous diffusion controlled sensors operated with aqueous electrolytes. He realised these restrictions by inclusion of a carbon track which was burnt out on firing or by a laser drilled pore. In addition, he suggested the response times of amperometric sensors are proportional to L^2 therefore the S/L ratio is critical to sensor operation. The sensor body was of 7.5 mol% YSZ assembled using a glass seal and platinum / YSZ cermet thick film electrodes. By varying the diffusion pore dimensions he realised both bulk and mixed bulk / Knudsen diffusion mechanisms but suggested that knudsen diffusion sensors gave a complex behaviour that complicated analysis. Knudsen and surface diffusion are not considered in this work as they involve diffusion barriers many times smaller than obtained with these devices.

Usui & Asada [88] examined amperometric sensors using an 8mol% YSZ electrolyte to find factors affecting the operating temperature. The device worked well at temperatures below 500°C with a limiting current obtained at 330°C in 40% oxygen. The output did show a dependence on carrier gas through diffusion coefficient variations. Electrolyte thickness variation of 0.16 to 1.69mm was examined and showed that temperature did influence the operation temperature limit by 100°C over this range. The main factor governing operation temperature was found to be the diffusion barrier dimensions.

Usui et al [92] further investigated their amperometric sensors varying oxygen concentration, temperature, carrier gas, pressure, S/L ratio. They also investigated response time and stability. Their sensor employed a glass seal to join a disc with a 30 μm diameter ×1mm length barrier to a 0.15 mm thick 8 mol% YSZ electrolyte, using platinum electrodes. Bulk to Knudsen diffusion transition was evident as barometric pressure was reduced below 0.4 atm but pure bulk for 0.4 to 5 atm. Sensor stability showed less that 2% variation in limiting currents over 650 days operation.

Usui et al [89] used an amperometric device with a porous diffusion barrier as a sensor. They found that this resulted in mixed Knudsen / bulk diffusion. Mixed diffusion proved difficult to evaluate since the different mechanisms have different dependencies on pressure, temperature and gas composition. Response times were measured at 3-21 s. They found that a small area to length ratio for the diffusion barrier is required for efficient control of limiting currents.

Maskell [4] indicated that physical deterioration of the diffusion pore can occur due to dust or electrolyte structural changes.

Usui et al [125] attempted to use a porous electrode as a diffusion barrier in an amperometric sensor. To help aid gas diffusion restriction, a non-porous alumina disc was added to restrict diffusion to the electrode edges. Limiting currents were not parallel to abscissa but linearity to oxygen concentration was found at a set pump potential. Analysis showed that two regions of diffusion caused the non-parallel limits with an outer interface region that oxygen could easily reach virtually unrestricted and a second inner interface region which could only be reached by diffusion through the tortuous and cramped electrode structure.

APPENDIX B

LITERATURE REVIEW

temperature sensor using neither potentiometric or diffusion limiting processes. The sensor used an actively operated zirconia, three-electrode sensor with a strong relation between current and oxygen mole fraction at selected potentials. Sensor operation was in a cyclic voltammetric regime between -0.625 and +0.325 V. Since the current was not diffusion dependent it was unaffected by gas flow and proved to be a reliable indication of oxygen concentration.

Solid-electrolyte potentiometric oxygen sensors employing zirconia have been commercially available since 1965. Solid electrolyte amperometric sensors were proposed by Heyne [77] in 1973 and are currently commercially available from Fujikura. Present amperometric sensors can be made as small as 1.7×1.75×0.3 mm by thick film constructions. Typically these sensors are operated at temperatures exceeding 500°C. As well as the most common oxygen sensing applications, zirconia has also been utilised for other sensing purposes. Usui et al [93] used an amperometric zirconia sensor as a N_2O sensor. N_2O can be detected as it decomposes to N_2 and O_2 above 300°C and therefore will dilute oxygen atmospheres or add oxygen to nitrogen atmospheres to allow a calculation of its presence provided the carrier stream is known. Usui et al [94] used an amperometric gas sensor to measure hydrogen in H_2/N_2 atmospheres. They achieved this by reversing the electrode connections (internal anode) and found a limiting current proportional to H_2 concentration. The mechanism was suggested to be either a reaction with oxygen ions in the electrolyte or by a diffusion of hydrogen ions (protons) through the electrolyte. This device would require the absence of oxygen to provide a meaningful output. Lu et al [123] showed that using ZnO electrodes on a zirconia potentiometric sensor a good selectivity for hydrogen could be obtained. This device had a fast response, good reproducibility and stability. Madou & Kinoshita [124] used zirconia sensors for pH measurement in aqueous solutions at room temperature. Thin oxide films on zirconium gave a response to pH close to Nernstian behaviour.

concentrations below 500ppm but are also oxygen dependent although so long as combustibles are not present in high concentrations (>5%), air is adequately rich in oxygen. Disadvantages include high power consumption due to the need for elevated temperatures for operation and poisoning of the catalyst can be a problem with exposure to lead or phosphorous vapours and silicones. The use of filters can prevent contamination but also restrict measurement range. The relatively high costs compared to semiconductor sensors have limited employment of these devices. They also require periodic re-calibration due to ageing effects.

A1.12 Solid electrolyte

Nernst & Bose [118, 119] performed the first work on solid electrolytes 100 years ago in 1889. They discovered high ionic conduction and low electronic conduction in yttria stabilised zirconia and put this to use in the "Nernst Glower". Work has proceeded since then, especially over the last 40 years, to identify mechanisms, achieve improvements, and in finding new applications. Much technology for solid electrolyte sensors has its origins in the development of fuel cells. Fuel cells are devices that use oxygen ion conduction to react fuel and oxygen through a dense membrane with no flame. These devices are highly efficient, producing usable heat and electricity from the reaction. A planar design of fuel cell is depicted in figure A1.2 however similar tubular designs are under investigation. Solid electrolyte devices operate by conduction of ions (usually oxygen) through the solid structure and operate in potentiometric (potential measuring) or amperometric (current measuring) modes. Ion conductors include ZrO_2, Bi_2O_3, CeO_2, β alumina, polypyrrole and NASICON. Miura et al [120] proposed a solid state amperometric sensor for NO_2 made from NASICON electrolyte with a porous $NaNO_2$ layer and gold electrodes.

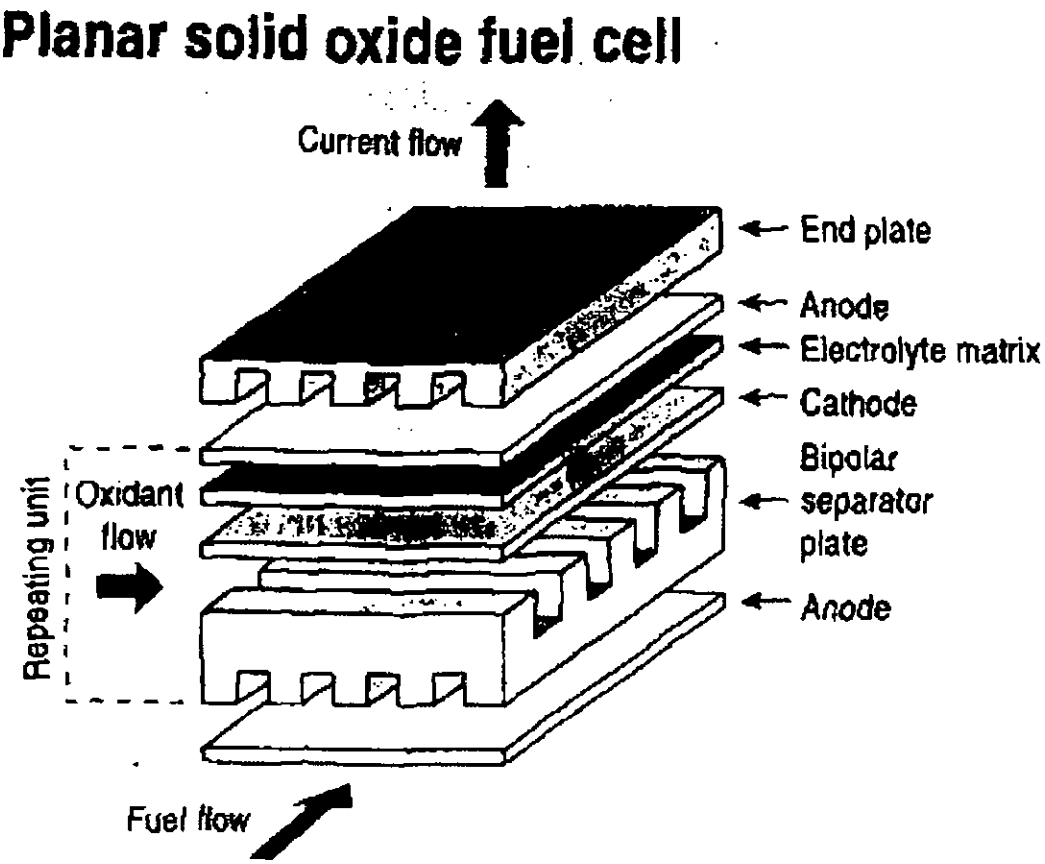

Figure A1.2 Planar solid oxide fuel cells Kilner [121].

Whilst most detailed devices in the literature focus on potentiometric, amperometric or pump-gauge (combination) devices, Makovos & Liu [122] gave details of a zirconia high

limited dynamic range and the high cost of detection and analysis components. They may also be employed to detect ions in solution.

A1.8 Gas sensitive transistors

These devices operate as gas sensitive semi-conductor transistors. The conduction between a source and drain is affected by a charge or potential on a gate electrode. This charge or potential arises from gases adsorbed onto or absorbed into the gate electrode material. Selection of gate electrode materials affects the degree of selectivity and sensitivity of the device.

A1.9 SAW / BAW sensors

Surface acoustic wave and bulk acoustic wave (SAW / BAW) sensors monitor changes in a periodic deformation induced in a material. Deformation is affected by the mass of material adsorbed onto the material surface and by environmental conditions. Quartz crystal micro-balances work on a similar principle. The sensor material is usually a piezoelectric crystal with a gas selective polymer film cover. An input signal is fed to the crystal to cause an acoustic wave whose frequency, amplitude and phase are monitored in the detector for induced changes. These devices are sensitive to temperature and humidity influences, which may be reduced by comparison with a device with no absorbent coating. Frequency measurement to high accuracy allows high sensitivity to be obtained, however selectivity is dependent upon the selectivity of coating applied to the device. These devices are small, easy to mount, easy to use and are suitable for miniaturisation with good potential for inclusion in sensor arrays (see below).

A1.10 Electronic noses

Many sensors are hampered by the problem of lack of specivity to one single gas component. This however can be turned to an advantage when an array of different sensors is monitored simultaneously. The result is a characteristic fingerprint for each analyate. Each sensor in the array exhibits an individual dependence on interaction with the sample and pattern recognition is used to identify the sample with comparison to a database. Similar odours will give similar patterns. These arrays are especially useful when characterising multi-component atmospheres such as aromas in the food and cosmetics industries. The trend toward more reliable, smaller and cheaper sensors with the improvements in microprocessor power and pattern recognition algorithms will further enhance the application of these instruments. It is crucial for the sample to be presented to the sensor array in a consistent way either by pumping sample headspace to the array or by inserting the array in the headspace. In addition consistent temperature, pressure and humidity are required for measurement reliability. Currently the numbers of sensors employed in arrays are kept small for ease of data interpretation and restrict complexity. The sensors employed in these instruments may include quartz crystal microbalances, metal oxide sensors, polymer sensors, optical and fibre optic instruments. One such instrument has been developed by Neotronics.

A1.11 Catalytic

Catalytic sensors (Pellistors) monitor the levels of flammable gases in air. They operate by passing a current through a wire imbedded in a catalytic coated porous ceramic to attain an elevated temperature. The presence of flammable gases will cause the temperature to increase as they burn off. The change in temperature maybe detected to indicate the presence of flammable gases. The wire may be used as both a heater and resistance thermometer. These devices may been seen as micro-calorimeters. Catalytic sensors are usually incapable of determining the composition of gases present but do give useful information on the combustibility of the mixture present (LEL). They are sensitive to

industrial use of humidity sensing is in the compensation humidity effects on other sensors. They are also employed in air-conditioning systems and in the control of industrial drying processes. Measurement methods include mechanical / gravimetric hygrometry, titrations, psychrometry, cooled mirror, optical, impedance sensors and electrochemical sensors. Details of these methods may be found in Moseley [115]. Electrochemical humidity sensors include alumina sensors, polymer film sensors, silicon oxide sensors and electrolytic sensors. Alumina sensors are based upon Pd electrodes separated by an Al_2O_3 membrane that acts as a capacitor, with humidity affecting the dielectric properties of the medium. Mulla et al [116] reported a humidity sensor using the resistive change that may be achieved using surface modified (sulphated) zirconia.

A1.4 Paramagnetic

A material is considered paramagnetic if the flux density of a toroid filled by the material is greater than that filled with a vacuum. When freely suspended in a uniform magnetic field, paramagnetic materials align themselves parallel to the field. Paramagnetic materials become magnetised in the same direction as the field and magnetic field lines are drawn as if attracted into the sample. Ferromagnetic material display paramagnetic behaviour but much more strongly. Oxygen is notable for its exceptionally strong paramagnetic behaviour. This effect is put to use in a number of analysers of various configurations. These include thermo-magnetic analysers, differential pressure analysers and automatic null balance analysers. A full description of these devices is given by Moseley et al [117]. Whilst these systems are precise and reliable they are bulky and expensive and do not find widespread employment as a result.

A1.5 Colourometric

These methods involve reacting the gaseous components to give a characteristic colour change whose intensity may then be measured to give an indication of concentrations. These instruments may be in the form of bubblers, detector tubes, diffusion based devices or as paper tapes.

A1.6 Infrared

An alternative gas analysis technique is infrared detection. Various gas components have characteristic adsorption wavelengths that may be measured to get an idea of gas composition. This method has the advantage that detection may be remote and is of high reliability and integrity with no degradation or poisoning problems. These analysers are inherently selective with the capability of detecting a wide range of gases, they are currently available as hand held devices making them handy portable instruments. Disadvantages however in the cost and size of detectors along with the degree of signal processing and analysis required do not make them suitable for widespread application. The development of these instruments has been aided by advances in lasers, filters, detectors and instrument engineering.

A1.7 Optical fibre

Optical fibre sensors were developed from advances in the optical communications industries. At certain wavelengths the interaction of a gaseous atmosphere with a polymer/dye will give a certain fluorescent intensity. A number of such polymer/dyes can be analysed over a range of wavelengths to provide analytical information. These devices have advantages of small size, flexibility, chemical and thermal stability, remote sensing (fibres may be kilometres long with negligible signal loss), they are insensitive to electrical interference, low weight and cost, have possibilities of distributed sensing and ongoing development from the telecommunications industries. Disadvantages are possible interference from ambient light, lengthy response times, long term stability problems,

A1 Alternative sensors

Whilst most gases are detectable using infrared or mass spectrometry analysers these are expensive and specialised instruments that are not suitable for the majority of applications. Hence the requirement of low cost, miniature analysers for use in well-characterised processes. There currently exists a wide range of sensing devices, which are sold in millions and, with a large research activity, the possibility for many further devices. Reviews of gas sensors have been published [5, 6, 12, 43, 114, 115].

A1.1 Semi-conducting

Semi-conducting oxide sensors operate by the influence of the gas on the surface oxygen stoichiometry, detected through a change in oxide resistance. By making sensors porous the surface area is greatly increased giving improved sensitivity. The resistance of these devices is highly temperature dependent, however a compensation of temperature effects can be made by comparison with a pellet of dense material. Sensors made from tin dioxide (Taguchi sensor) or zinc dioxide are the most common examples, although other materials may be used such as titanium dioxide, perovskites and metal phthalocyanines. Semi-conducting oxide sensors are usually used in air to warn of the presence of toxic or flammable gases. SnO_2 type sensors are oxygen dependent so have to be operated in known oxygen atmospheres. Generally, since gases detected are of low concentrations, the oxygen concentration in the bulk gas can be assumed to remain constant. In the case that this assumption is not valid, a solution was presented involving operating the SnO_2 sensor inside a zirconia pump-gauge [21]. Oxygen levels were controlled by pumping oxygen to create and monitor a known reference atmosphere. The combined device can then be used for CO, H_2 or CH_4 sensing.

Advantages of semi-conductor sensors include sensitivity, reversibility, low cost and ease of use whilst problems of reproducibility, stability and selectivity hamper sales. Quantitative measurements are not easily achieved with these devices. These limitations mean that these devices are best used in well-defined processes. The selectivity of semi-conductor sensors may be enhanced by the use of catalysts, control of porosity, use of dopants, coatings, particle size, by careful selection of operation temperature or by improved design. Whilst most organic materials are sensitive and selective they are poor conductors and not stable at elevated temperatures. Metal phthalocyanines are stable above 400°C and are semi-conducting. They react to gases with changes in electrical conductivity and may be used as surface acoustic wave sensors (see SAW / BAW sensors).

A1.2 Liquid electrolyte

Liquid electrolyte sensors operate through gases reacting at the electrodes to form ions in solution and subsequently generate a current or EMF. Amperometric devices have gas exposure limited by a diffusion barrier. They are currently available to measure oxygen, carbon monoxide, chlorine, nitrogen dioxide, hydrogen sulphide, ammonia, nitric oxide amongst other gases. Due to ambient temperature operation, they exhibit low power consumption. They also show the advantages of being compact, robust, reliable, they have no operational orientation, low cost and are suitable for high volume production. They are capable of measuring from 100% to ppm levels at temperatures of -50 to 55°C. They are however affected by humidity, may suffer from electrolyte evaporation and are not suitable for extreme miniaturisation. Improvements may be realised through the use of gel electrolytes.

A1.3 Humidity

Humidity is a significant component of the atmosphere that commonly causes problems in gas sensing and is also often required for sensing in its own right. Indeed the major

APPENDIX A

ALTERNATIVE SENSORS

[122] E.B.Makovos, C-C.Liu, Development of a solid electrolyte sensor for oxygen in hot gases, 1991, *Sensors and actuators B*, **3**, 15-22
[123] G.Lu, N.Miura, N.Yamazoe, High temperature hydrogen sensor based on stabilised zirconia and a metal oxide electrode, 1996, *Sensors and actuators B*, **35-36**, 130-135
[124] M.J.Madou, K.Kinoshita, Electrochemical measurements on metal oxide electrodes: Zirconium dioxide, 1984, *Electrochimica acta*, **29**, 411-417
[125] T.Usui, H.Hideo, K.Ishibashi, M.Nakazawa, Gas polarographic oxygen gas sensor using the pores of the platinum cathode as a gas diffusion barrier, *Journal of Applied Physics*, **29**, 1990, 606-610.
[126] J.H.Lee, H.Kim, B.K.Kim, Oxygen sensing characteristics of limiting current type sensors with microstructural and structural variations in diffusion barrier, 1996, *Materials letters*, **26**, 27-33
[127] B.Y.Liaw, W.Weppner, Low temperature limiting current oxygen sensors based on tetragonal zirconia polycrystals, 1991, *Journal of the electrochemical society*, **138**, 2478-2483
[128] E.M.Logothetis, R.E.Hetrick, High temperature oxygen sensors based on electrochemical oxygen pumping, 1986, *Fundamentals and applications of chemical sensors*, **309-8**, 136-154
[129] R.C.Copcutt, W.C.Maskell, A zirconia amperometric pump-gauge sensor operated in gases containing SO2 or NO2: Leakage and electrode overvoltage studies, 1994, *Solid state ionics*, **70/71**, 578-583
[130] R.C.Roberts, Molecular diffusion of gases, , *American handbook of physics*, , 2-249-2-252
[131] L.J.Olmer, J.C.Viguie, E.J.L.Schouler, An increase in the water vapor reduction rate by using an yttria stabilized zirconia electrolyte with ceria doped surface, 1982, *Solid state ionics*, **7**, 23-35
[132] T.Maruyama, X.Y.Ye, Y.Saito, Electromotive force of a CO-CO_2 sensor in a CO-CO_2-H_2-H_2O atmospheres and simultaneous determination of partial pressures of CO and CO_2, 1987, *Solid state ionics*, **24**, 281-287
[133] A.D.Brailsford, M.Yussouff, E.M.Logothetis, Theory of gas sensors: response of an electrochemical sensor to multi component gas mixtures, 1996, *Sensors and actuators B*, **34**, 407-411
[134] M.Aoki, Y.Chiang, I.Kosacki, L.Lee, H.Tuller, Y.Liu, Solute segregation and grain boundary impedance in high purity stabilized zirconia, 1996, *J Amer Ceram Soc*, **79/5**, 1169-1180
[135] N.L.Robertson, J.M.Michaels, Double layre capacitance of porous platinum electrodes in zirconia electrochemical cells, 1991, *J. Electrochem. soc*, **138**, 1494-1499
[136] M.J.Verkerk, A.J.Burggraaf, Oxygen transfer on substituted ZrO_2, Bi_2O_3 and CeO_2 electrolytes with Pt electrodes ii A-C impedance study, *Journal of the Electrochemical Society*, **130/1**, 1983, 78-84.
[137] D.Braunshtein, D.S.Tannhauser, I.Riess, Diffusiun limited charge transport at Pt electrodes on doped CeO_2, *Electrochemical Science and Technology*, **128**, 1981, 82-89.
[138] H.S.Isaacs, L.J.Olmer, Comparison of materials as oxygen catalytic electrodes on zirconia electrolyte, 1982, *Journal of the electrochemical society*, **129**, 436-443
[139] A.Ziehfreund, U.Simon, W.F.Maier, Oxygen ion conductivity of platinum impregnated stabilised zirconia in bulk and microporous materials, 1996, *Advanced materials*, **8-5**, 424
[140] T.M.Gur, I.D.Raistrick, R.A.Huggins, AC admittance measurements on stabilized zirconia with porous platinum electrodes, *Solid State Ionics*, **1**, 1980, 251-271.
[141] S.P.S.Badwal, H.J.DeBruin, Electrode kinetics at the palladium/ceramic oxide electrolyte interface, *Journal of the Electrochemical Society*, **129**, 1982, 1921-1928.
[142] C.T.Young, Experimental analysis of ZrO_2 oxygen sensor transient switching behavior, 1982, *Society of automotive engineers, SAE Paper 810380*, 1507-1519
[143] A.Dubbe, H.D.Weimhofer, Y.Sadaoka, Electrode kinetic study of silver ion doping effect in solid electrolyte potentiometric carbon dioxide gas sensors, 1997, *J electrochem soc*, **144/3**, 943-947
[144] N.P.Vaughan, R.C.Brown, A device for measurement of volume and leakage by pressure pulsation monitoring, 1994, *Measurement Science Technology*, **5**, 1-8.
[145] R.C.Copcutt, A.C.King, K.Kendall, Reaction-diffusion of fuel with air between planar solid oxide fuel cells stacked with ceramic felt, 1996, *Proc R Soc Lond.* **A**, 2639-2653
[146] T.Kenjo, Y.Horiuchi, S.Osawa, Determination of the rate constants of oxygen reduction in high temperature air electrodes on solid oxide electrolytes, 1990, *Journal of the electrochemical society*, **137**, 2423-2431
[147] W.C.Maskell, J.A.Page, Detection of water vapour or carbon dioxide using a zirconia pump-gauge sensor, 1998, *Sensors & Actuators B*, **57**, 99-107
[148] B.Omerod, July 1996, Chemistry & Industry, **6**, 182
[149] J.E.Anderson, Y.B.Graves, Steady-state characteristics of oxygen concentration cell sensors subjected to non-equilibrium gas mixtures, 1981, *Journal of the electrochemical society*, **128/2**, 294-300

[90] T.Usui, Y.Kurumiya, K.Ishibashi, M.Nakazawa, Gas polarographic humidity sensor usable above 100°c, *Journal of Applied Physics*, **28**, 1989, 2325-2326.

[91] T.Usui, Y.Kurumiya, K.Nuri, M.Nakazawa, Gas-polarographic multi-functional sensor: Oxygen-humidity sensor, *Sensors and Actuators*, **16**, 1988, 345-358.

[92] T.Usui, A.Asada, M.Nakazawa, H.Osanai, Gas polarographic oxygen sensor using an oxygen/zirconia electrolyte, 1989, *Electrochemical society*, **136,** 534-542

[93] T.Usui, A.Asada, K.Ishibashi, M.Nakazawa, N_2O gas sensing using a gas polarographic oxygen sensor, 1989, *Journal of applied physics*, **28,** 2046-2047

[94] T.Usui, A.Asada, M.Nakazawa, H.Osanai, Gas polarographic hydrogen sensor using a zirconia electrolyte, *Journal of Applied Physics*, **28**, 1989, 1654-1656.

[95] J.R.MacDonald, Impedance spectroscopy and its use in analysing the steady state AC response of solid and liquid electrolytes, *Journal of Electroanalytical chemistry*, **223**, 1987, 25-50.

[96] Southampton Electrochemistry Group, Instrumental Methods in Electrochemistry, AC Techniques, 1985, 251-283

[97] N.J.Evans, Electrochemical Impedance Spectroscopy, *Electrochemistry Newsletter*, **April**, 1996, 11-19.

[98] M.Taha, J.Palctto, Y.Jorand, G.Fantozzi, A.Samdi, M.Jebrouni, B.Durand, Compaction and sintering behavior of zirconia powders, 1995, *Journal of the European ceramic society*, **15,** 759-768

[99] Z.Xie, J.Li, Y.Huang, X.Kong, Microwave sintering behavior of ZrO_2-Y_2O_3 with agglomerate, 1996, *J Mater Sci Lett*, **15,** 1158-1160

[100] N.Higuchi, S.Mase, A.Iino, N.Kato, Heated zirconia exhaust gas oxygen sensor having a sheet shaped sensing element, 1985, *Sensors and actuators*, **618,** 93-99

[101] J.Gopaul, W.C.Maskell, K.E.Pitt, Planar oxygen sensor Part II: Knudsen diffusion in slots in a cracked zirconia film, 1988, *Not yet in publication*

[102] M.C.Steil, F.Thevenot, M.Kleitz, Densification of Yttria Stabilised Zirconia - Impedance spectroscopy analysis, 1997, *J Electrochem Soc*, **144/1,** 390-398

[103] B.Krafthefer, P.Bohrer, P.Moenkhaus, D.Zook, L.Pertl, U.Bonne, Life and performance of ZrO_2 based oxygen sensors, 1984, *Advances in ceramics*, **12,** 607-617

[104] M.Kleitz, H.Benard, E.Fernandez, E.Schouler, Impedance spectroscopy and electrical resistance measurements on stabilised zirconia, *Science and Technology of Zirconia*, **3**, 1981, 310-336.

[105] M.J.Verkerk, M.W.J.Hammink, A.J.Burggraaf, Oxygen transfer on substituted ZrO_2 Bi_2O_3 and CeO_2 electrolytes with platinum electrodes I. Electrode resistance by DC polarisation, *Electrochemical Science and Technology*, **130**, 1988, 70-83.

[106] J.E.Anderson, Y.B.Graves, The transient response of ZrO_2 oxygen sensors to step changes in gas composition, *Journal of Applied Electrochemistry*, **12/3**, 1982, 335-341.

[107] T.Kenjo, T.Nakagawa, Ohmic resistance of the electrode-electrolyte interface in Au/YSZ oxygen electrodes, 1996, *J Electrochem Soc*, **143-4,** L92

[108] S.deSouza, S.J.Visco, L.C.deJonghe, Reduced temperature solid oxide fuel cell based on YSZ thin film electrolyte, 1997, *J Electrochem soc*, **144/3,** L35

[109] J.Crank, The mathematics of diffusion, 1956, *Oxford: Oxford University Press*, 48

[110] G.R.Doughty, P.M.Fong, P.D.Pacey, Measurement of response times of zirconia gas sensors, *Extended Abstracts, The Electrochemical Society*, **90-1**, 1990, 1285.

[111] A.Dubbe, H.Weimhofer, W.Gopel, Combination of pressure modulation and impedance spectroscopy for study of electrode kinetics on solid electrolytes: The porous gold/solid sodium carbonate interface, *Journal of the Electrochemical Society*, **142**, 1995, 2757-2761.

[112] V.N.Mishra, R.P.Agarwal, Effect of electrode material on sensor response, 1994, *Sensors and actuators*, **22,** 121-125

[113] C.S.Tedmon, H.S.Spacil, S.P.Mitoff, High temperature zirconia electrolyte fuel cells, 1969, *J.Electrochem.Soc*, **116/9,** 1170-1175

[114] D.E.Williams, P.McGeehin, Solid state gas sensors and monitors, 1984, Electrochemistry (London, Royal Society of Chemistry), 246-289

[115] P.T.Moseley, Solid state gas sensors, 1997, *Measurement science and technology*, **8,** 223-237

[116] I.S.Mulla, S.D.Pradhan, K.Vijayamohanan, Humidity sensing behavior of surface modified zirconia, 1996, *Sensors and actuators A*, **57,** 217-221

[117] P.T.Moseley, J.O.W Norris, D.E.Williams, Techniques and mechanisms in gas sensing, Adam Hilger.

[118] W.Nernst, E.Bose, Zur theorie des Auerlichtes, 1900, *Phys. Zeils*, **26**, 289-291

[119] W.Nernst, (1989), *Phys. Chem.*, **4**, 117

[120] N.Miura, M.Iio, G.Lu, N.Yamazoe, Solid state amperometric NO_2 sensor using a sodium ion conductor, 1996, *Sensors and actuators B*, **35-36,** 124-129

[121] J.Kilner, S.Benson, J.Lane, D.Waller, Ceramic ion conducting membranes for oxygen separation, 1997, *Chemistry and industry*, 22, 907-911

[60] M.Benammar, W.C.Maskell, Measurement of oxygen partial pressure using miniature oxygen pump gauge operated in the potentiometric mode, *Solid state ionics*, **53-56**, 1992, 75-79.

[61] H.Kaneko, W.C.Maskell, B.C.H.Steele, Miniature oxygen pump-gauge I. Leakage considerations, *Solid state ionics*, **22**, 1987, 161-172.

[62] K.Suganuma, T.Okamoto, M.Koizumi, Method for preventing thermal mismatch effect in ceramic-metal joining, 1985, *J.Mater.Sci.Lett.* **4**, 648-650

[63] H.Q.Hao, Y.L.Wang, Z.H.Jin, X.T.Wang, Joining zirconia ceramic to stainless steel and itself using AgCuTi filler metal, *Journal of the American Ceramic Society*, **78**, 1995, 2157.

[64] M.Kleitz. J.Fouletier, Technological improvements and accuracy of potentiometric measurements with zirconia gauges, 1974, *Measurement of oxygen*, **26-27**, 103-123

[65] H.Taimatsu, H.Kaneko, F.Nakatani, Transient behavior of the electromotive force of an oxygen sensor induced by the temperature change, 1984, *Chemistry letters*, 389-392

[66] J.Fouletier, G.Vitter, M.Kleitz, Measurement and regulation of oxygen content in gases using solid electrolyte cells III Oxygen pump-gauge, *Journal of Applied Electrochemistry*, **5**, 1975, 111-120.

[67] R.M.A.Kocache, J.Swan, D.F.Holman, A miniature rugged and accurate solid electrolyte oxygen sensor, 1984, *Journal Phys.E.Sci.Instru*, **17**, 477-481

[68] H.Kaneko, H.Sato, H.Taimatsu, Preparation and electrochemical characteristics of a miniature zirconia oxygen sensor with a metal/metal oxide internal reference. , *Unpublished*, ,

[69] J.Fouletier, H.Seinera, M.Kleitz, Measurement and regulation of oxygen content in gases using solid electrolyte cells II Differential gauge, *Journal of Applied Electrochemistry*, **5**, 1975, 177-185.

[70] W.J.Flemming, Zirconia oxygen sensors: origins of non-ideal behavior, 1980, *Ceramic and science proceedings*, **1**, 272-280

[71] H.Okamoto, H.Obayashi, T.Kudo, Non-ideal EMF behaviour of zirconia oxygen sensors, *Solid State Ionics*, **3+4**, 1981, 453-456.

[72] H.Okamoto, H.Obayashi, T.Kudo, Carbon monoxide gas sensor made of stabilised zirconia, *Solid State Ionics*, **1**, 1980, 319-326.

[73] H.Takahashi, K.Saji, H.Kondo, T.Takeuchi, I.Igarashi, Influence of gas composition on the characteristics of limiting current type oxygen sensor, *Sensor Symposium*, **5**, 1985, 133-137.

[74] M.Benammar, W.C.Maskell, Operation of leaky zirconia pump gauge oxygen sensors in the ac mode: Experimental results, *Sensors and Actuators*, **12B**, 1993, 199-203.

[75] R.E.Hetrick, W.A.Fate, W.C.Vassell, Oscillatory mode oxygen sensor, *IEEE Transactions on Electronic Devices*, **29**, 1982, 129-132.

[76] M.Benammar, Techniques for measurement of oxygen and air to fuel ratio using zirconia sensors. A review, 1994, *Measurement science and technology*, **5**, 757-767

[77] L.Heyne, Some aspects of solid electrolytes, *Electrochimica Acta*, **15**,1970, 1251-1266.

[78] W.C.Maskell, H.Kaneko, B.C.H.Steele, Miniature oxygen pump gauge: III Application of a periodic current waveform, *Journal of Applied Electrochemistry*, **17/3**, 1987, 489-494.

[79] W.C.Maskell, H.Kaneko B.C.H.Steele, Miniature oxygen pump gauge: II Measurement of oxygen partial pressure, Proc. 2nd Int. Symp. Chemical sensors, Bordeaux, 7-10th July 1986

[80] M.Benammar, W.C.Maskell, A fast response oxygen sensor based upon a fully sealed zirconia pump gauge operated in the potentiometric mode, 1992, *Smart material structures*, **1**, 134-138

[81] E.M.Logothetis, J.H.Visser, R.E.Soltis, L.Rimai, Chemical and physical sensors based on oxygen pumping with solid-state electrochemical cells, *Sensors and Actuators B*, **9**, 1992, 183-189.

[82] M.Benammar, W.C.Maskell, A novel miniature zirconia gas sensor with pseudo-reference Part III: Simple implementation for the determination of air to fuel ratio, 1995, *Journal of applied electrochemistry*, **25**, 208-211

[83] A.Caneiro, M.Bonnat, J.Fouletier, Measurement and regulation of oxygen content in selected gases using solid electrolyte cells Accurate preparation of CO_2-CO and H_2O-H_2 mixtures, 1981, *Journal of applied electrochemistry*, **11**, 83-90

[84] F.Vizethum, G.Bauer, G.Tomandl, Computer controlled adjustment of oxygen partial pressure, *Advances in Ceramics*, **12**, 1984, 631-635.

[85] P.T.Whelan, W.E.Borbidge, Interpretation of the output signal from a zirconia oxygen sensor operating under applied current, 1988, *Journal of applied electrochemistry*, **18**, 188-195

[86] H.Dietz, Gas diffusion controlled solid electrolyte oxygen sensors, *Solid state ionics*, **6**, 1982, 175-183.

[87] W.C.Maskell, J.A.Page, Zirconia sensors constructed from a ceramic-plastic sheet material, *Sensors and their Applications*, **VIII**, 1997, 177-182.

[88] T.Usui, A.Asada, Operating temperature of a limiting current oxygen sensor using a zirconia electrolyte, *Advances in Ceramics*, **24**, 1988, 845-853.

[89] T.Usui, A.Asada, K.Ishibashi, M.Nakazawa, Humidity sensing characteristics in a wet air of a gas polarographic oxygen sensor using a zirconia electrolyte, *Journal of the Electrochemical Society*, **138**, 1991, 585-588.

[32] H.Takeuchi, Oxygen sensors, 1986, *Proceedings of the 2nd international meeting on chemical sensors*

[33] N.Yamazoe, J.Hisamoto, N.Miura, Potentiometric solid state oxygen sensor using lanthanum fluorite operative at room temperature, 1987, *Sensors and actuators*, **12**, 415-423

[34] R.A.Huggins, Ionically conducting solid state membranes, 1977, *Advances in electrochemistry*. **10**, 323-389

[35] U.Vohrer, H.D.Wiemhofer, W.Gopel, F.Schilling, J.Arndt, Mixed oxides for low temperature oxygen gas sensors: Phase characterization spectroscopic and electrical investigations of titania doped yttria stabilized zirconia, 1991, *Sensors and actuators B*, **4**, 411-416

[36] S.P.S.Badwal, M.J.Bannister, W.G.Garrett, Low temperature behaviour of Zirconia oxygen sensors, *Advances in Ceramics*, **12**, 1984, 598-606.

[37] J.Fouletier, H.Seinera, M.Kleitz, Measurement and regulation of oxygen content in gases using solid electrolyte cells I Discontinuous use of gauges, *Journal of Applied Electrochemistry*, **4**, 1974, 305-315.

[38] T.Inoue, N.Seki, K.Eguchi, H.Arai, Low temperature operation of solid electrolyte oxygen sensors using perovskite type oxide electrodes and cathodic reaction kinetics, *Journal of the Electrochemical Society*, **137**, 1990, 2523.

[39] X.L.Xiang, Z.Z.Sheng, A low temperature zirconia oxygen gauge based on new oxide composite electrodes, 1997, *Sensors and actuators B*, **37**, 175-177

[40] S.P.S.Badwal F.T.Ciacchi, Performance of zirconia membrane oxygen gas sensors at low temperatures with non stoichiometric oxide electrodes, 1986, *Journal of applied electrochemistry*, **16**, 28-40

[41] H.Kaneko, A.Nagai, H.Taimatsu, AC polarization of the YSZ/Rh and YSZ/Pd electrode systems, *Solid State Ionics*, **35**, 1989, 257-262.

[42] S.Adler J.Lane B.C.H.Steele, Electrode kinetics of porous mixed conducting oxygen electrodes, 1996, *J.Electrochem. Soc*, **143**, 3554

[43] D.M.Haaland, Non-catalytic electrodes for solid electrolyte oxygen sensors, *Journal of the Electrochemical Society*, **127**, 1980, 796-804.

[44] K.T-Y.Chen, H.M.Saltsburg, The behavior of the zirconia oxygen sensor during electrode catalyzed oxidation reactions, 1986, *Extended Abstracts, The Electrochemical Society*, **86-1**, 34946

[45] A.Dubbe, H.D.Weimhofer, K.D.Schrierbaum, W.Gopel, Kinetics of oxygen interaction with Pt/CeO_2 sensors: Application of a new pressure modulation spectroscopy, *Sensors and Actuators B*, **4**, 1991, 23-28.

[46] R.K.Usmen, E.M.Logothetis, M. Shelef, Measurement of Pt electrode surface area of automotive ZrO_2 oxygen sensors, 1995, *Sensors and actuators B*, **28**, 139-142

[47] D.Y.Wang, A.S.Nowick, Diffusion controlled polarization of Pt Ag and Au electrodes with doped ceria electrolyte, 1981, *Journal of the electrochemical society*, **128**, 55-63

[48] N.L.Robertson, J.N.Michaels, Oxygen exchange on platinum electrodes in zirconia cells: Location of electrochemical reaction sites, 1990, *J. Electrochem. soc*, **137**, 129-135

[49] C.T.Young, Static and dynamic properties of ZrO_2 oxygen system, 1983, *Progress in solid electrolytes*, **83-94**, 549-580

[50] J.E.Bauerle, Study of solid electrolyte polarization by a complex admittance method, *Journal of Physical and Chemical Solids*, **30**, 1969, 2657-2670.

[51] A.S.Ioannou, W.C.Maskell, Characterisation of amperometric zirconia oxygen sensors prepared using planar thick film technology, *Solid State Ionics*, **53**, 1992, 85-89

[52] J.Gopaul, W.C.Maskell, K.E.Pitt, Planar oxygen sensor Part I: Effect of crazing of a zirconia thick film on an alumina substrate, 1988, *Journal of applied electrochemistry*, **28**, 1-9

[53] K.Kinoshita, P.Stonehart, Preparation and characterization of highly dispersed electrocatalytic materials, 1977, *Modern aspects of electrochemistry Ed J O'M Bockris & B E Conway*, Plenum Press (New york), 182-267

[54] D.Weng, U.Landau, Direct electroplating on nonconductors, 1995, *Journal of the electrochemical society*, **142**, 2599-2604

[55] T.H.Etsell, S.N.Flengas, The determination of oxygen in gas mixtures by electromotive force measurements using solid oxide electrolytes, 1972, *Metallurgical transactions*, **3**, 27-36

[56] A.M.Feltham, M.Spiro, Platinized platinum electrodes, *Chemical Reviews*, **71/2**, 1971, 177-193.

[57] W.C.Maskell, B.C.H.Steele, Miniature amperometric oxygen pump-gauge, 1988, *Solid state ionics*, **28-30**, 1677-1681

[58] E.M.Logothetis, W.C.Vassell, R.E.Hetrick, W.J.Kaiser, A high sensitivity sensor for the measurement of combustible gas mixtues, 1986, *Sensors and actuators*, **9**, 363-372

[59] P.T.Whelan, W.E.Borbidge, Low temperature response of the reaction-bonded zirconia oxygen system, *Solid state ionics*, **9+10**, 1983, 1263-1272.

References

[1] W.C.Maskell, B.C.H.Steele, Solid state potentiometric oxygen gas sensors, *Journal of Applied Electrochemistry*, **16**, 1986, 475-489.

[2] A.S.Ioannou, W.C.Maskell, Factors influencing the response time of oxygen sensors, Presented at "Solid state Ionics for Sensors and Electrochromics",*Centro Ettore Majorana, Erice, Sicily*, **1-12** July 1992

[3] A.J.A.Winnubst, A.H.A.Scharenborg, A.J.Burggraaf, Response behaviour of oxygen sensing solid electrolytes, *Applied Electrochemistry*, **15/1**, 1985, 139-144.

[4] W.C.Maskell, Inorganic solid state chemically sensitive devices: electrochemical oxygen gas sensors, *Journal of Physical and Scientific Instruments*, **20**, 1987, 1156-1168.

[5] A.Jones, P.Moseley, B.Tofield, The chemistry of solid state gas sensors, 1987, *Chemistry in Britain*, **August**, 749-754

[6] T.A.Jones, Trends in the development of gas sensors, 1989, *Measurement and control*, **22**, 176-182

[7] W.J.Flemming, Physical principles governing non-ideal behavior of the zirconia oxygen sensor, 1977, *Journal of electrochemical society*, **124**, 21-27

[8] E.M. Logothetis, Air to fuel sensors based on oxygen pumping, 1987, *Ceram Eng Sci Proc*, **8,9-10**, 1058-1073

[9] J.Fouletier, Gas analysis with potentiometric sensors: a review, *Sensors and actuators*, **3**, 1983, 295-314.

[10] K.Saji, H.Takahashi, H.Kondo, T.Takeuchi, I.Igarashi, Limiting current type oxygen sensor, 1984, *Proceedings of the 4th sensor symposium*, , 147-151

[11] E.M.Logothetis, Automotive oxygen sensors, 1991, *Chemical sensor technology*, **3**, 89-104

[12] H.Dietz, W.Haecker, H.Jahnke, Electrochemical sensors for the analysis of gases, *Advances in Electrochemistry and Electrochemical Engineering*, **10**, 1977, 1-90.

[13] R.C.Copcutt, W.C.Maskell, CO/CO_2 electrochemistry on zirconia electrolyte with platinum electrodes in relation to amperometric oxygen sensors, 1992, *Solid state ionics*, **53-56**, 119-125

[14] G.Vitter, P.Foster, M.Lahlou, F.J.Gutierrez Monreal, Use of an oxygen mini-gauge for monitoring domestic and medium sized boilers, 1983, *Solid state ionics*, **9&10**, 1273-1276

[15] M.Benammar, W.C.Maskell, Simple implementation for the determination of air to fuel ratio, *Journal of Applied Electrochemistry*, **25**, 1995, 208-211.

[16] N.Yamazoe, N.Miura, Environmental gas sensing, 1994, *Sensors and actuators B*, **20**, *95-102*

[17] D.Janke, Oxygen sensing in iron and steel making, 1984, *Advances in ceramics*, **12**, 636-645

[18] A.S.Ioannou, W.C.Maskell, Influence of substrate composition on the sintering behavior of zirconia thick films, 1992, *J Mater Sci Lett*, **11**, 1623-1625

[19] A.J.A.Winnubst, K.Keizer, A.J.Burggraaf, Mechanical properties and fracture behavior of ZrO_2-Y_2O_3 ceramics, 1983, *Materials science*, **18**, 1958-1966

[20] S.P.Terblanche, Thermal expansion coefficients of yttria stabilized zirconias, 1989, *Applied crystallography*, **22**, 283-284

[21] J.Fouletier, E.Siebert, A.Caneiro, Accurate monitoring of low oxygen activity in gases with conventional oxygen gauges and pumps, *Advances in Ceramics*, **12**, 1984, 618.

[22] X.Guo, Y.Q.Sun, K.Cui, Darkening of zirconia: a problem arising from oxygen sensors in practice, 1996, *Sensors and actuators B*, **31**, 139-145

[23] D.M.Haaland, Internal reference solid electrolyte oxygen sensor, *Analytical Chemistry*, **49**, 1977, 1813-1817.

[24] P.Ramaswamy, D.C.Agrawal, Effect of sintering zirconia with calcia in very low partial pressure of oxygen, 1987, *Materials science*, **22**, 1243-1248

[25] N.Alford, K.Kendall, B.Clegg, T.Burton, Processing protocols give ceramics the edge, 1991, *Physics world*, **May**, 26-29

[26] K.Kobayashi, H.Kuwajima, T.Masaki, Phase change and mechanical properties of ZrO_2 - Y_2O_3 sold electrolyte after ageing, *Solid State Ionics*, **3/4**, 1981, 489-493.

[27] M.Kuwabara, T.Murakami, M.Ashizuka, Y.Kubota, T.Tsukidate, Electrical conductivity of yttria partially stabilized zirconia ceramics, *Journal of Material Science Letters*, **4**, 1985, 467-471.

[28] S.P.S.Badwal, M.V.Swain, ZrO_2-Y_2O_3: Electrical conductivity of some fully and partially stabilized single grains, *Journal of Material Science Letters*, **4**, 1985, 487-489.

[29] R.K.Slotwinski, N.Bonanos, E.P.Butler, Electrical properties of $MgO+Y_2O_3$ and $CaO+Y_2O_3$ partially stabilized zirconias, *Materials Science Letters*, **4**, 1985, 641-644.

[30] S.Ikeda, O.Sakurai, K.Uematsu, N.Mizutani, M.Kato, Electrical conductivity of YSZ single crystals, *Journal of Material Science*, **20**, 1985, 4593-4600.

[31] J.Fouletier, M.Henault, Doped ceria electrolyte in oxygen sensors, 1983, *Solid state ionics* **9+10**, 1277-1282

REFERENCES

C1 Equipment

C1.1 Apparatus

C1.1.1 Gas mixing

In order to provide a range of known test gases for testing of sensors, mixtures of compressed air, bottled 'oxygen-free' nitrogen and bottled oxygen were prepared using Brooks gas mixing equipment. The equipment included a range of mass flow control valves (type Tr and E) and a central control unit. They operate by controlling the flow of gas over a heated filament and calculating the flow by the rate of heat loss. The rate of heat loss was governed also by the thermodynamic properties of the gases used. The calibration chart included was used where required. The flow valves used ranged from 150 ml/min valves down to 5 ml/min maximum flow rate. These valves were controllable to 0.1% of their maximum throughput down to about 5% of their throughput. Gas input was through laboratory grade plastic tubing (Tygon 7440) using stainless steel Swagelok connectors. Plastic tubing was interference fitted to a short length of stainless steel tube using jubilee clips. For flow valve operation a gas input / output pressure differential of >200 mbar was required with a maximum input of 100 bar. Output pressure realised was sufficient to achieve the set flow rate provided the input differential was maintained. Control was given by a master control unit capable of controlling four valves separately, either by local control on the front panel, or by remote control (LabView) using 0-5 V signals.

In addition an array of fast acting Precision Dynamics miniature solenoid valves were employed to switch gas flows from gas inlet to exhaust. These were also either manually or remotely controlled via LabView. They featured 5 ms response, 1000 PSI pressure limit and maximum working temperature of 85°C, switching by 0-24 VDC input.

C1.1.2 Optical bench microscope

This was a small bench microscope of magnification ×20 used in the visual examination of sensor assembly.

C1.1.3 Time Electronics voltage source

This was a battery powered voltage supply, capable of generating microvolts up to 1 V. It was used as a voltage source in experiments before the DAQ card was obtained and as a microvolt source to control temperatures generated by non-adjustable furnace controllers

C1.1.4 Carbolite Rapid Heating furnace

These were electrically powered furnaces capable of reaching temperatures of 1600°C. They allow programmable temperature ramping and were used in ceramic sintering and electrode curing procedures. Programmable features allowed temperature ramp rates, set temperatures and dwell times for >10 cycles with automatic cold junction compensation. Firing chamber dimensions were of the order 150×150×300 mm, tiled with refractory furnace tiles and monitored by K type thermocouple.

C1.1.5 Home made operational amplifier circuits

Home made voltage-current and current-voltage converters were made using simple operational amplifier circuits to enable interfacing between the DAQ card and measurement system. These were found necessary to generate the currents required without suffering voltage drop across the input and to enable computerised current control. These circuits were based upon an op amp, similar in function to a 741 but with higher current range. These devices were contained in plastic circuit boxes with connection by push fit connectors. The circuits were powered by dual ±15V DC power supply. Circuit diagrams are given below.

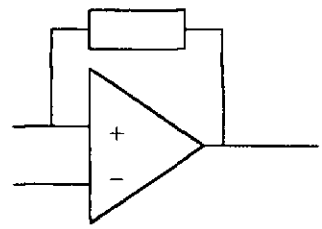

Figure C1 voltage to current converter.

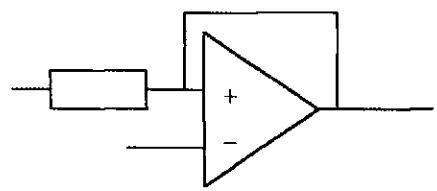

Figure C2 current to voltage converter.

C1.1.6 Thandar function generator

This was a signal generator capable of generating sine, square and saw tooth voltage waveforms used in the electro-plating of electrodes, as well as calibration and development work. This generator had a voltage range of 0-5 V with a frequency range of DC to 20 MHz.

C1.2 Instrumentation

C1.2.1 Frequency response analyser Model No. SL1260

Impedance analysis was carried out using a Solartron SL1260 Frequency Response Analyser. The Instrument had a frequency range of 32 MHz to 10 mHz, very good noise rejection and intelligent data collection to minimise measurement time. This instrument was capable of a number of different operation modes dependent upon the nature of test being undertaken. Signal amplitudes of up to 3 V or 60 mA could be sourced, with applications of DC biases up to 100 mA or 50 V. The instrument allowed programming directly from the front panel, however a computer interface was also provided and allowed far simpler operation. Details of controlling software are presented in C1.5.3.

C1.2.2 Solartron multimeters Model No. 7150

Three of these multimeters were used, mainly as DC ammeters and voltmeters although they also had resistance and AC measurement capabilities. They had the benefit of IEEE 4.88 interface, which allowed control and interrogation via computer using home written software (see section C1.5.1). This enabled their use for rapid and repetitive readings, especially useful for monitoring temperatures, allowing automatic cold junction compensation, temperature linearisation and on screen real time data plotting. They were used extensively through out this work. Measurement resolutions were dictated by signal magnitude but ranges extended from μV to 30 V, μA to 2 A and inter-measurement times were controllable from 100 μS to 400 mS

C1.2.3 ITT multimeter Model No. MX545

This was a further multimeter of use due to its low current resolution, it did not have the IEEE 4.88 capability limiting its use to manual readings. It was used infrequently where

sub-microampere current had to be measured. This meter had a range of 5 V to 1 mV and 2 A to 10 nA.

C1.2.4 Hand-held multimeters

These handy, versatile multimeters lacked the resolution and range of the bench meters but were used extensively for their continuity and resistance measurements. Ranges were 1 mV to 5 V, 1 mA to 2 A, 0.1 to 200 MΩ.

C1.2.5 Tektronics oscilloscope Model No. 2211

This was a 20 MHz digital storage oscilloscope, used frequently to check waveforms and as a development tool. It was only used in reported results for the pressure modulation readings. This scope had a range of 20 mHz to 20 MHz and 0 to 5 V. Waveforms could be dumped to a plotter for hard copy but had no other I/O capability.

C1.3 Test rigs

C1.3.1 Sensor rig

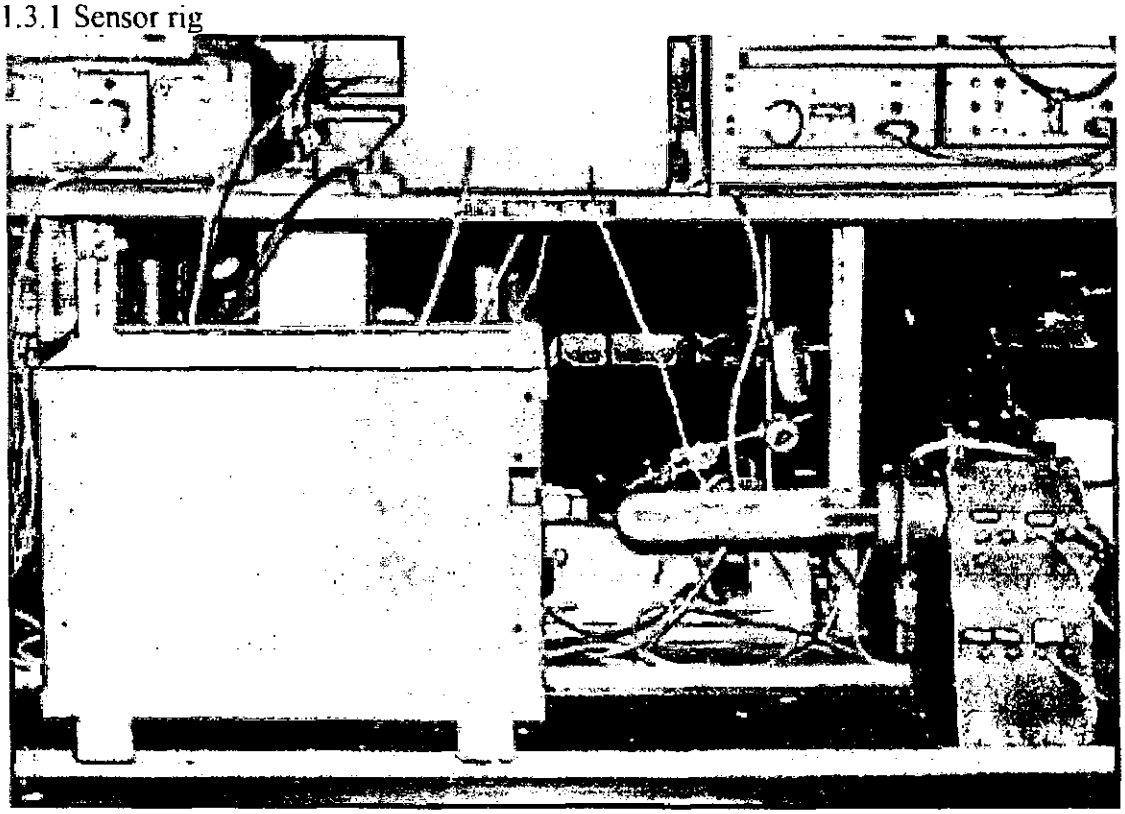

Figure C3 Sensor test-rig

The sensor test-rig comprised a furnace, 75 mm diameter, 450 mm length of Nichrome wire, spirally wound around a hollow ceramic core. It was coated in furnace cement, to hold the wire in place, and ceramic fibre, for thermal and electrical insulation, and contained in a ceramic fibre board box (250×250×400 mm). The furnace was powered by mains electricity, controlled by a Eurotherm temperature controller through which a stable temperature could be obtained to 1°C. Ramp rates and dwell times were not programmable. A silica glass chamber fitted snugly inside this furnace, containing the test atmosphere, sensor, connection wires and thermocouples. This chamber was closed at one end, with the other end sealed by viton o-ring, onto a water-cooled end plate. The end plate allowed access to the chamber and held multi-bore alumina tubes for support and insulation of Pt connection wires, K and R type thermocouples. The end plate was water cooled by a constantly fed water jacket from a cool reservoir via a peristaltic pump. Gases were fed into and out of the rig through single bore alumina tubes. The gases exited the test-rig through an oil-filled bubbler and were fed in by the mass flow valves discussed

above. Gas feeds to the flow valves originated from a compressed air supply or bottled gases with the possibility of drying using a $CaCl_2$ column after mixing. Alumina tubes were sealed to the brass endplate by brass collets and viton o-rings and sealed, where wires exit, using epoxy resin. Resin and o-ring seals were heat protected by the water-cooled endplate whilst the sensor and thermocouples were placed in the hot zone of the furnace. Platinum connection wires terminated on copper connection terminals held at room temperature on the test-rig supporting structure. This allowed easy and varied connection to instrumentation including the LabPC+ DAQ card, voltmeters, oscilloscope, frequency response analyser etc.

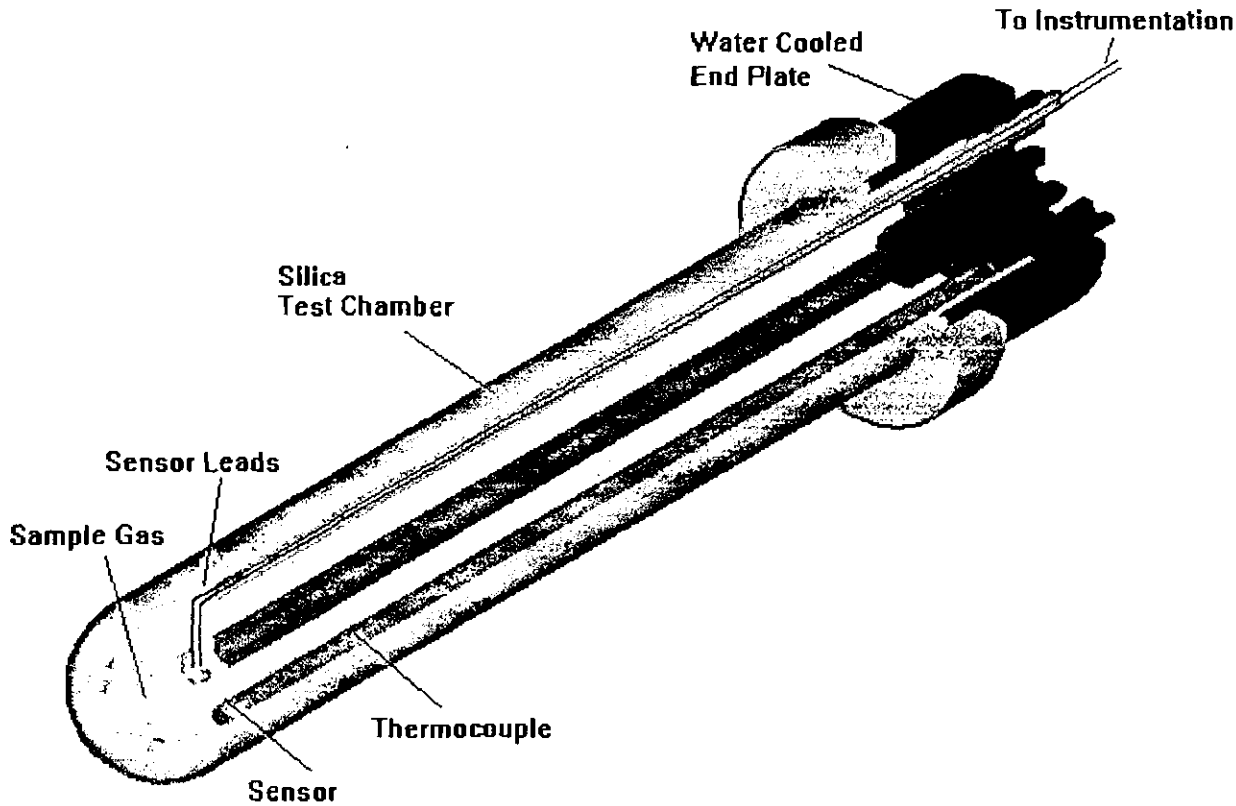

Figure C4 Sensor test-rig

C1.3.2 Humidity rig

For humidity testing, modifications were made to the gas input of the sensor test-rig. Whereas previously, the gases were fed directly into the test-rig after mixing by the flow valves, the mixed gases were passed through three columns of distilled water. The gas was broken up by fine grade sintered-glass frit gas distribution tubes to fine bubbles for complete saturation. In order to remove water droplet spray from the gases before entering the test-rig, it was then passed through a forth column containing ceramic fibre. To ensure that humidity did not condense out prior to entering the test-rig, tubes after the droplet removal column were heated by Nichrome wire using a DC electrical power supply. In this manner a tube temperature of approximately 90°C was maintained. To control the humidity entering the test rig, the water and drying columns were immersed in a temperature controlled water bath, which in turn, was well insulated and constantly stirred. Temperature control was provided by an electrical immersion heater and stabilised by cooling through constantly running tap water through a copper coil. The actual bath temperature was monitored by K type thermocouple and mercury-glass thermometer.

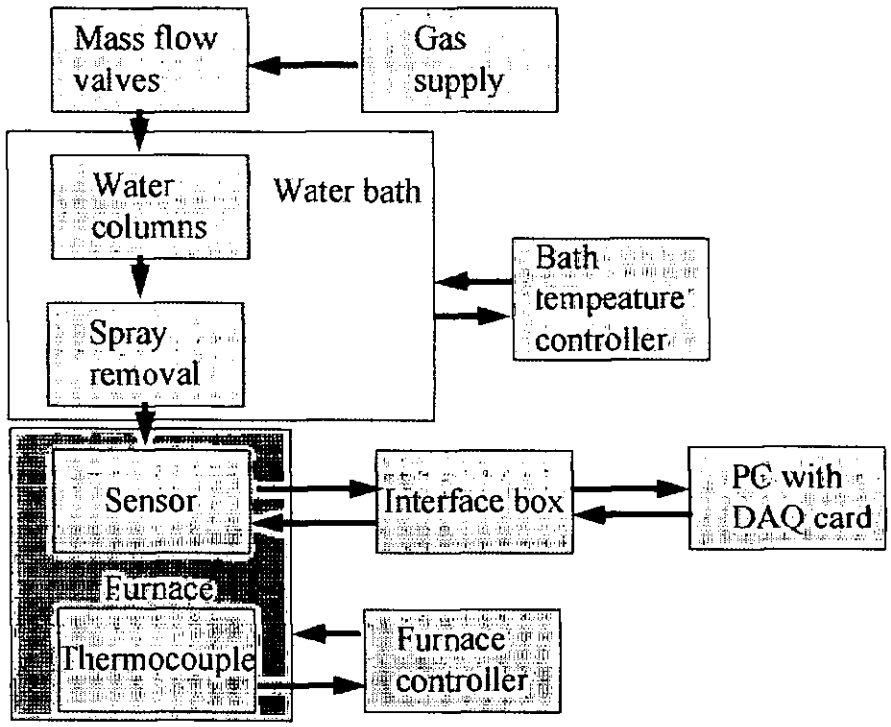

Figure C5 Humidity control apparatus

C1.3.3 CO_2 rig

For CO_2 tests, the sensor test-rig as described above was used but with the inclusion of a column of $CaCl_2$ to enable moisture removal and with gases mixed from oxygen, nitrogen and CO_2 bottled sources using the mixing equipment described above.

C1.3.4 Impedance rig

The impedance test-rig was a second adapted sensor test-rig. It was modified by the use of a non-inductingly wound furnace along with electrically shielded connection wires. Co-axial cables were used between BNC connection terminals and the Frequency Response Analyser. Again gases were mixed prior to entering the test-rig, with the possibility of drying or humidifying, and exited through an oil-filled bubbler. Atmospheric air was used as test atmosphere unless otherwise stated. Care was taken to keep test-leads short, and not to use high frequency electronics whilst testing. In addition, nulling sweeps were taken at each temperature at which tests were performed. Nulling files and procedures are described in section C1.5.3.

C1.3.5 Response rate rig

The response rate test-rig was based around a smaller furnace measuring 10mm diameter ×150mm length. This furnace was also wire wound and mains electrically powered with supply and controller made in-house. This furnace is referred to in this work as the miniature furnace. The furnace controller was designed to maintain a constant 700°C, therefore to attain higher and lower temperatures, an adjustable potential was applied to the thermocouple EMF. This fooled the electronics into maintaining alternative temperatures. The additional EMF was sourced from the Time Electronics voltage source. The furnace was contained in a metal casing with ceramic fibre and air gap for insulation. The potentiometric sensors used were designed to fit snugly inside this furnace, and were of sufficient length to exit the furnace and cool before connection to gas input equipment, sealed with viton o-rings. The connections were shielded from the furnace heat by several thin metal plates that provided excellent heat dissipation. Gases were fed directly through the inside of the sensor to the inner electrode, along with platinum connection wire and K

type thermocouple, through a multi-bore alumina tube. The gases exited the sensor passing back down the outside of the alumina tube and exited through an oil-filled bubbler. The sensor holder provided gas feed-paths, mounting of alumina tubes and the sensor. The sensor holder was made in-house from brass, machined to requirements with separate brass tube silver soldered on as a gas exit tube. Reference connection wires and the thermocouple was spring loaded to maintain physical contact. The exterior electrode was maintained in the furnace hot-zone in atmospheric air as a reference. Its temperature was also monitored by a second K type thermocouple to detect temperature differentials between interior and exterior electrodes. The second thermocouple was also used for furnace control. Temperatures were tracked for stability and equilibration by 7150 multimeters. In turn, a 286PC monitored these multimeters using an IEEE 4.88 interface card running in-house software. This software could compensate for cold junction temperature and also provide a graphical display of furnace temperature.

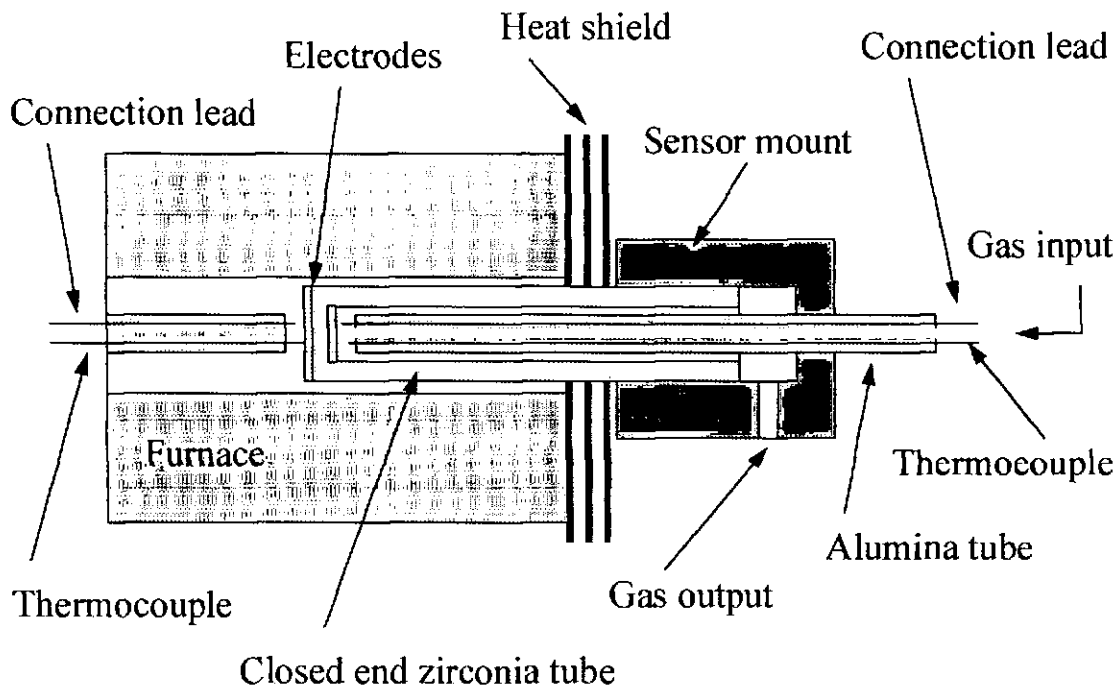

Figure C6 Response rate rig

The response rate rig was adapted slightly for connection as concentration step, concentration modulation, pressure modulation, impedance analysis and current / voltage tests as detailed below.

C1.3.5.1Concentration step configuration

In the concentration step configuration gases were mixed by mass flow valves from compressed air or bottled gases and switched using Precision Dynamics fast acting solenoid valves. The solenoid valves were interfaced through a high power op-amp circuit (see section C1.1.5) to LabPC+ DAQ card, and powered by a dual power supply. In this way gases could be switched at set timings whilst temperatures were independently monitored. Sensor EMF was also continuously monitored via the LabView / LabPC+ system, prior to and after gas switching, in order to induce and monitor the step change in internal gas concentration. The sensor output was amplified ×100 prior to monitoring to maintain a high signal to noise ratio. Data were stored automatically using internal timing to ensure consistency of data collection and timing. In order to attain a fast change between applied gas switch signal and gas arrival at the sensor electrode, gas volumes were kept as small as practicable, whilst maintaining an easily interchangeable sensor.

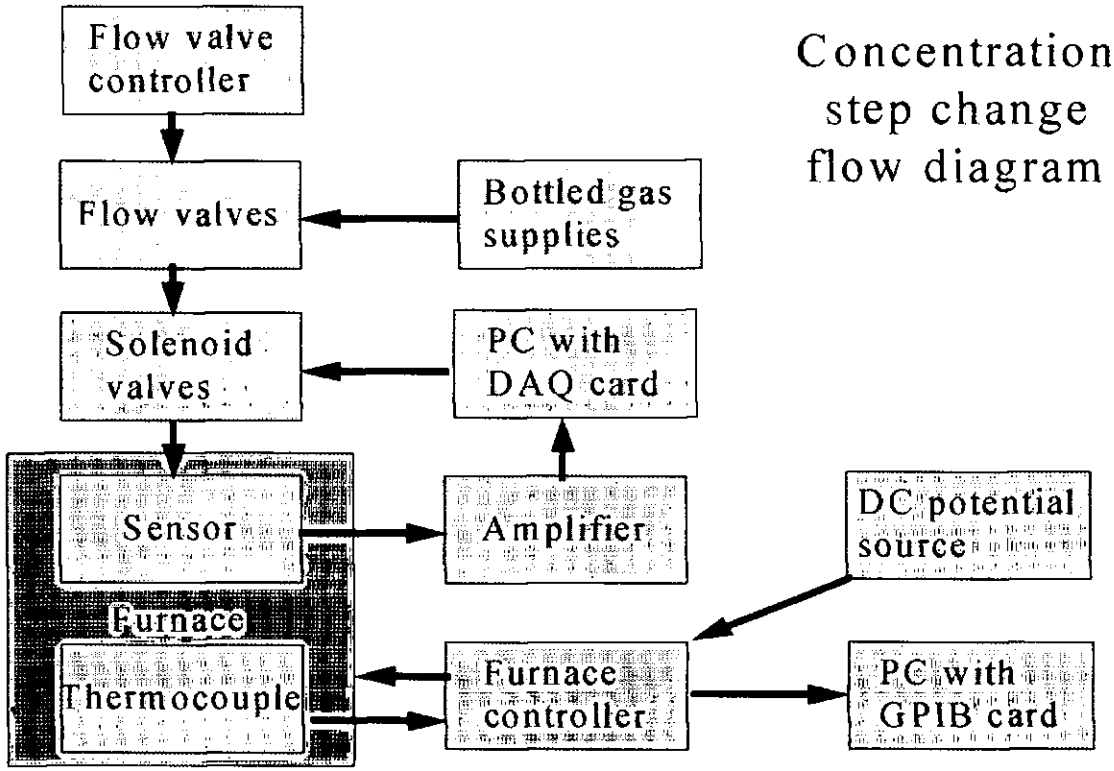

Figure C7 Concentration step configuration

C1.3.5.2 Concentration modulation configuration

Only slight modifications were required to adapt the step change rig into a concentration modulation rig. The major changes were to software and gas control equipment. The furnace, sensor, temperature control and gas exit components remained unchanged. The solenoid valves were removed and flow valves repositioned to feed directly into the sensor. Gas modulations were achieved via direct computer interface to the mass flow valve's control unit. The control unit could set mass flow openings remotely by the application of 0-5 V input signals (0 V =0%, 5 V = 100%) and, in addition, the unit provided a return signal to indicate actual valve opening (again 0 V = 0%, 5 V = 100%). So by applying a sinusoidal potential to the mass flow controller we could achieve a sinusoidal gas flow and monitor its progress. By mixing a sinusoidal gas flow with a constant gas flow we achieved a sinusoidal concentration modulation. Again the reference electrode was held in atmospheric air and electrode temperature differentials were monitored.

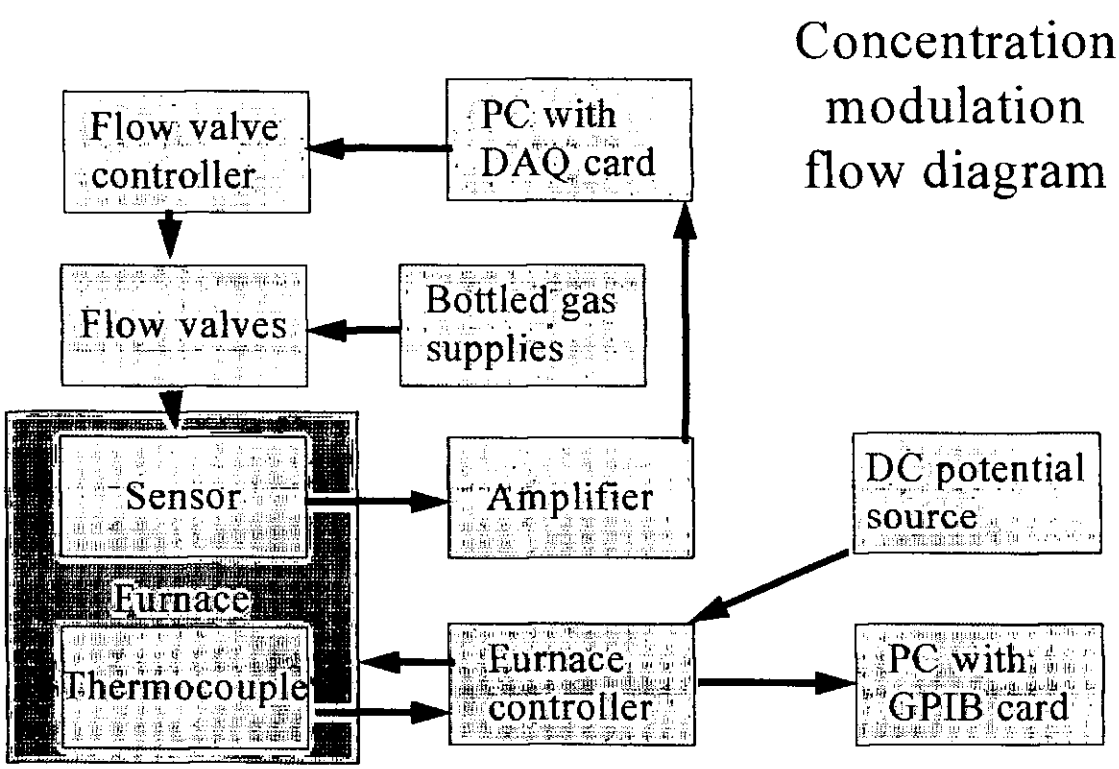

Figure C8 Concentration modulation configuration

C1.3.5.3 Frequency response configuration

Again the rig needed little alteration for use as a frequency response rig. The connection wires were already as shielded as practicable, so the frequency response analyser just replaced the computer interface, amplification was also removed. In addition the gas feed apparatus and bubbler were removed so tests were performed in air at atmospheric pressure. Temperatures were monitored and controlled as before.

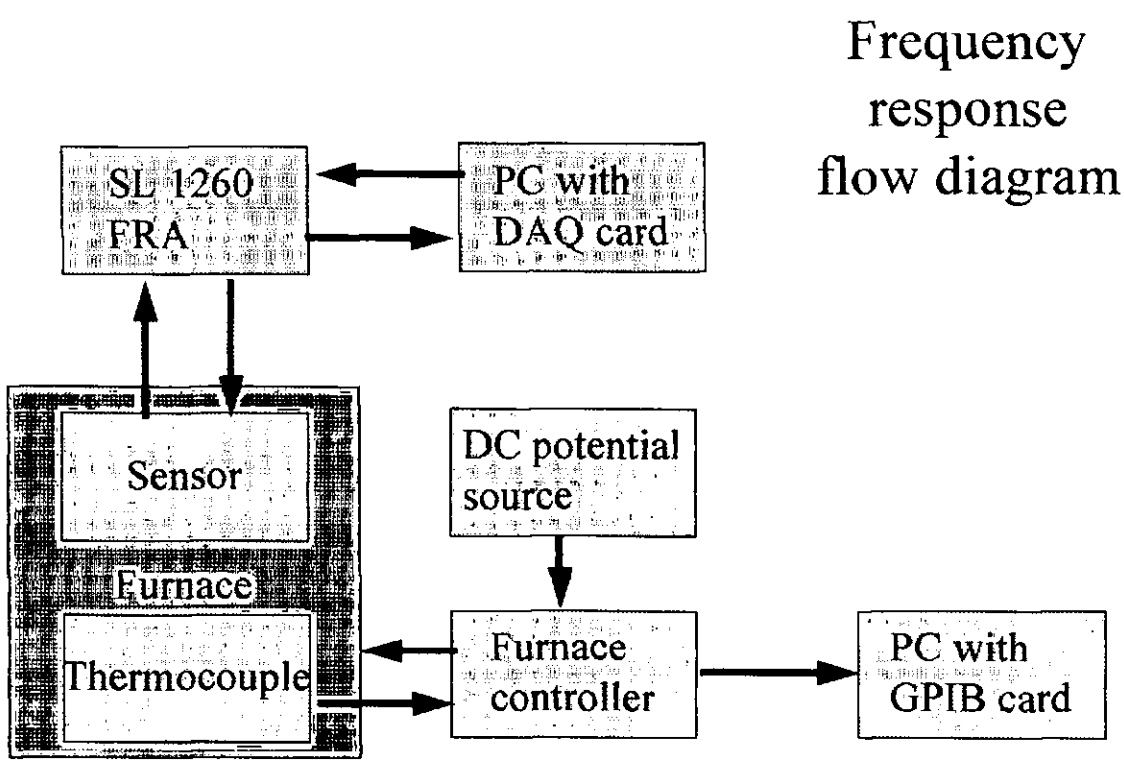

Figure C9 Frequency response configuration

C1.3.5.4 Pressure modulation configuration

The final configuration of the response rate rig was as a pressure modulation rig. For this the gas-input lines were closed off and the bubbler replaced with the pressure modulation apparatus to give a closed system. Sensor output was again amplified but fed to the oscilloscope for measurement and analysis rather than to the computer. The oscilloscope was used as the frequencies involved were at the detection limits of the computer sampling required to capture sufficient data per cycle.

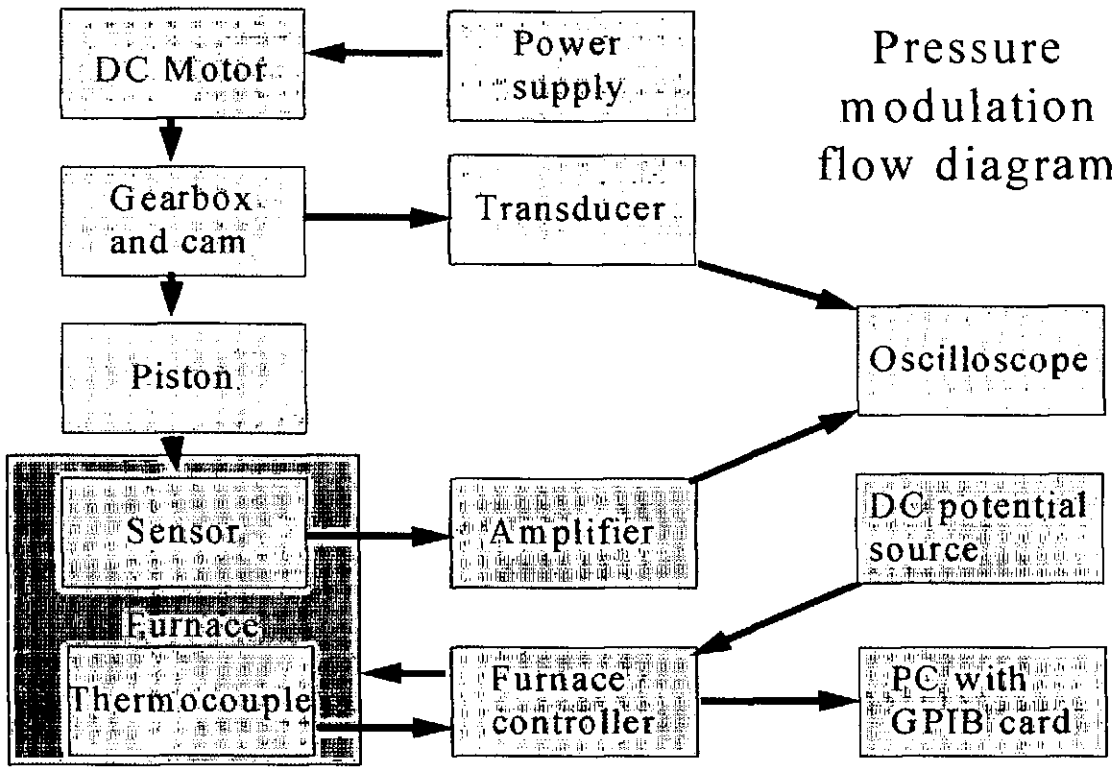

Figure C10 Pressure modulation configuration

C1.3.5.5 Pressure modulation rig construction

The pressure modulation equipment consisted of a cylinder and piston arrangement made in the university workshop. A 3D CAD model of the apparatus is shown in figure C11 with a connection flow diagram in figure C10. Components of the pressure modulation rig were fabricated from mild steel and aluminium, using common workshop machine tools, lathes, milling machines, drills and hand tooling. The only precision machining involved was the reaming and polishing of the cylinder internal surfaces to minimise piston o-ring wear. Bought in components included DC motor and gearbox, viton o-rings, roller bearings, magnetic pick-up and Swagelok connectors. Manufactured parts included gearbox cam, connecting rods, piston, cylinder, expansion chamber and supporting mounts. This assembly was connected to the miniature furnace test-rig and sealed using viton o-rings. Modulations were produced through a cam, linked to a DC motor and gearbox arrangement whose position was determined through magnetic pickups. The motor was powered by a DC power supply.

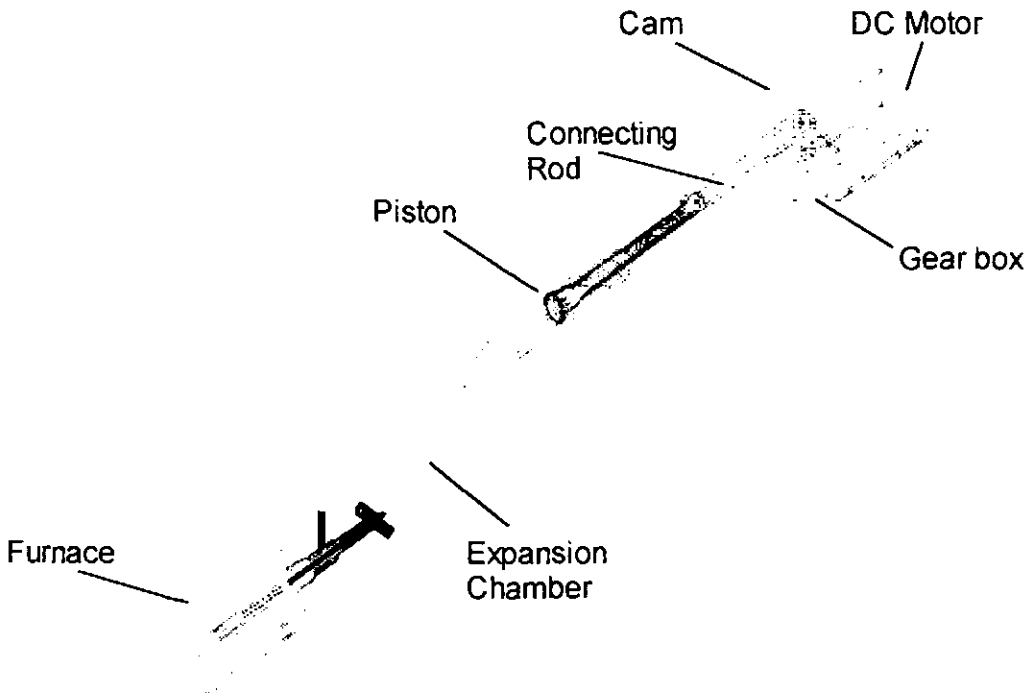

Figure C11 Pressure modulation 3D CAD model

C1.3.6 Small sensor test cell

For the response rate tests to be performed upon amperometric sensors it was necessary to obtain a small sealed volume to house a sensor with integral heaters to which various gases and pressures could be presented. The design of this cell followed that of previous workers but, miniaturised further to keep the test cell volume as small as practicable. The cell was made from brass to fit the sensor holders (again of previous design) closely but without shorting the electrical connections. Gas feed paths were kept small whilst allowing easy connection to concentration step, concentration modulation and pressure modulation apparatus. The sensors were heated using the thick film printed heaters of previous workers, powered by DC power supply. Temperature was monitored by a 40 µm R type thermocouple linked to the computer controlled Solartron 7150 multimeters. Sensor output was monitored and controlled by LabView DAQ system. Frequency response work and current voltage tests of amperometric sensors were mainly performed in the sensor test-rig (see section C1.3.1). This chamber was fabricated from a short length of brass tubing with a small brass plate silver soldered to the top. Gas feeds were through hollowed brass bars again silver soldered to the main body. For fitting to the sensor assembly, the bottom of the chamber was threaded to match the thread on the PTFE and brass sensor mounting of previous workers design. This cell had internal dimensions of approximately 15 mm diameter and 20mm height. A schematic of this cell is shown in figure C12.

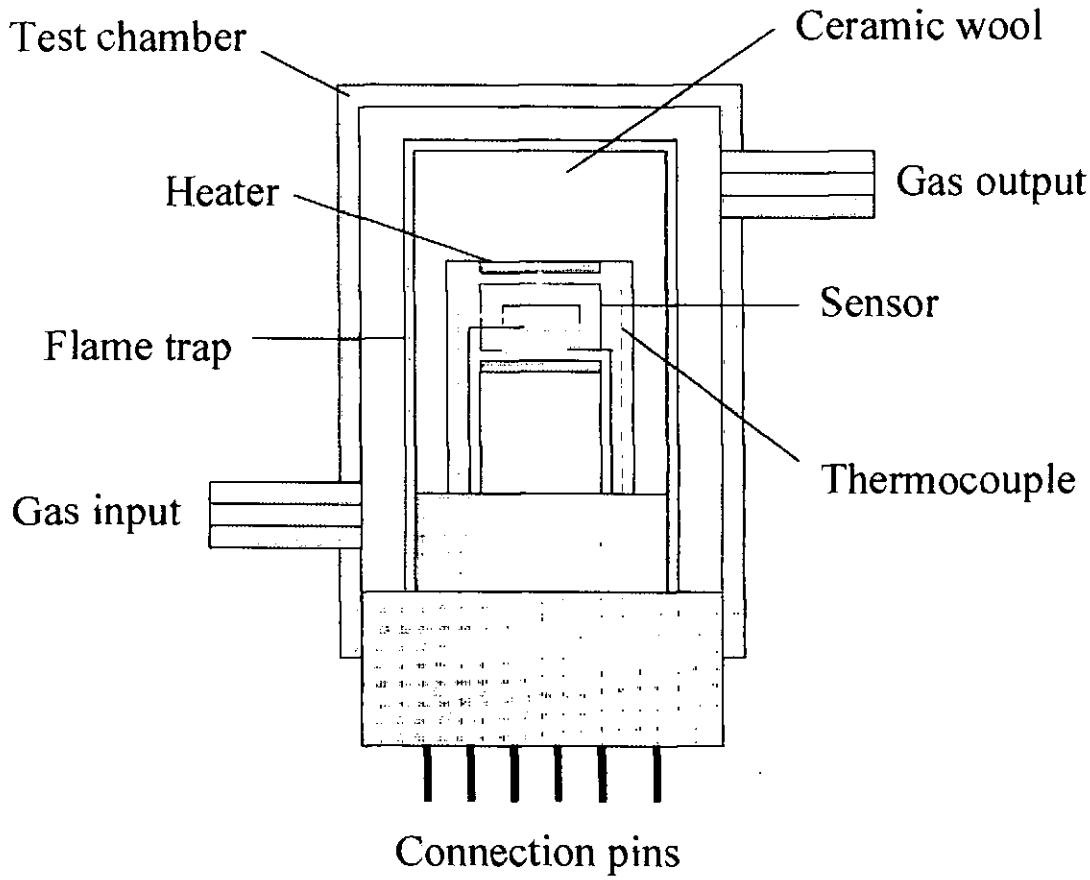

Figure C12 Small sensor test cell

C1.4 Data acquisition

C1.4.1 LabView

The majority of electrochemical tests and experiments carried out in this research have been performed with the use of a computer controlled data acquisition package. The package used was comprised of a 486PC with 66Mhz clock speed, using a National Instruments Lab PC+ DAQ card with connector block in conjunction with the National Instruments LabView DAQ software. This system provided a powerful, easy to use and extremely flexible test and measurement tool. The system features were:

- 83.3KHz sample rate
- 12 bit ADCs
- 8 single ended analogue input voltage channels
- 2 single ended analogue output voltage channels
- 24 TTL digital input/output channels configured as 3×8 bit channels
- 3 16 bit counter timer channels

The single ended analogue inputs could be jumper configured as 4 differential input channels and have ±5 V or 0 – 10 V ranges, again jumper configurable. Analogue channels are provided by 16 bit ADC and DACs to give a resolution of 150 μV. This DAQ card is controlled by the LabView software detailed below in section C1.5.2.

C1.4.2 Data logging

Prior to the acquisition of the LabView system, and for systems where LabView was deemed unsuitable, a separate data logging system was developed. This system utilised up to three Solartron 7150 multimeters and an IEEE4.88.2 GPIB card with either 286, 386 or 486 PC. This system is only capable of instrument measurement and control, as it requires IEEE compatible devices.

C1.5 Software

C1.5.1 QuickBasic programs

The control of 7150 multimeters was achieved by software written using Microsoft QuickBasic programming language. This is a text based programming system that lacks the power and performance of more advanced languages, but was easy to learn and understand and more than capable for the required use here. By sending simple control commands to the IEEE bus, each instrument could be set up and interrogated automatically with data written to file. This allowed acquisition of data far quicker than possible by hand and in easier to use formats than by oscilloscope.

A typical use was temperature monitoring, where data was required at one point per second over a period of several hours. Temperature linearisation and cold junction compensation were also programmed in. LabView lacks the outright accuracy required for small voltage measurements, recording by hand too slow, prone to recording errors and ties the operator to a lengthy period of tedious measurement. Oscilloscopes could not store data of this quantity at such long intervals and are then limited to a paper hardcopy. Chart recorders would do the job but do not lend themselves to data analysis.

C1.5.2 Virtual Instruments

LabView programs (known as virtual instruments) are not written codes as used by most other programming languages, instead LabView has its own unique graphical programming system. Each program has two different components, the 'front panel' and the 'block diagram'. The 'front panel' is the user interface, displayed on the screen it contains virtual switches, dialogue boxes and graphs (selected from on-screen menus) that allow user interaction and results display. The 'block diagram' contains the programming structure with various components (analogous to subroutines) 'wired' together to indicate the path of data flow. In this way a graphical flow diagram type program is developed which may contain deeply imbedded code. This can then provide a powerful program with a relatively simple appearance.

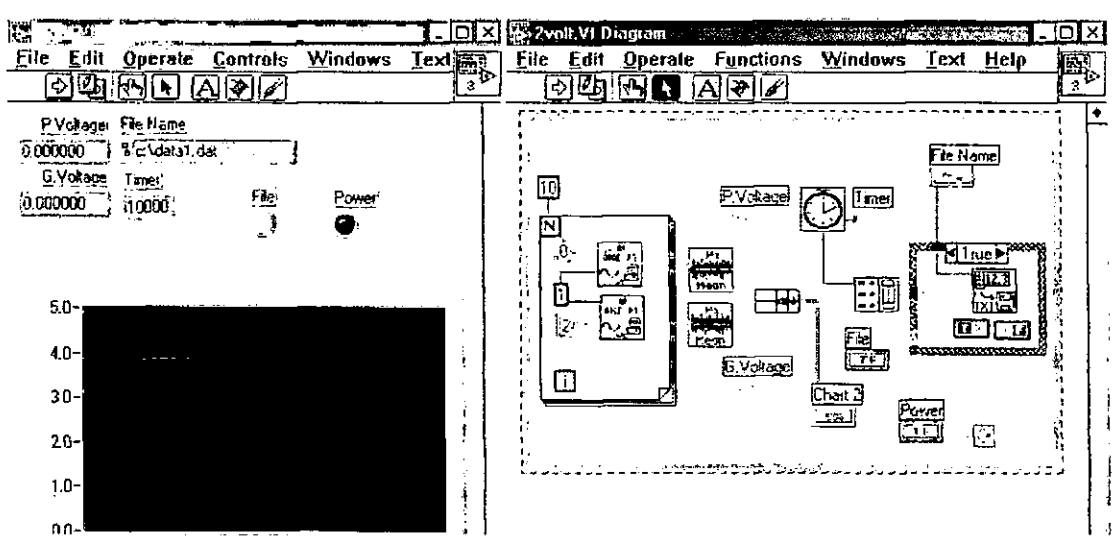

Figure C13 Simple LabView Front Panel and Block Diagram

C1.5.3 Impedance software

The Frequency Response Analyser used could be computer controlled using an IEEE 488.2 interface to a 486 PC running a windows based Z60W software. This commercially available software gave automatic real time data plotting with powerful analysis and simulation capabilities. Data could be displayed in a wide variety of formats, allowing easy transfer between applications. The software also included simple curve fitting, as well as powerful equivalent circuit fitting and simulation routines. It also allowed a series of tests to be performed using a batch program with variable timing for repetitive tests to be performed automatically. The use of this software greatly improved the ease of instrument use, measurement reliability and speed.

APPENDIX D

PROGRAMMING CODE

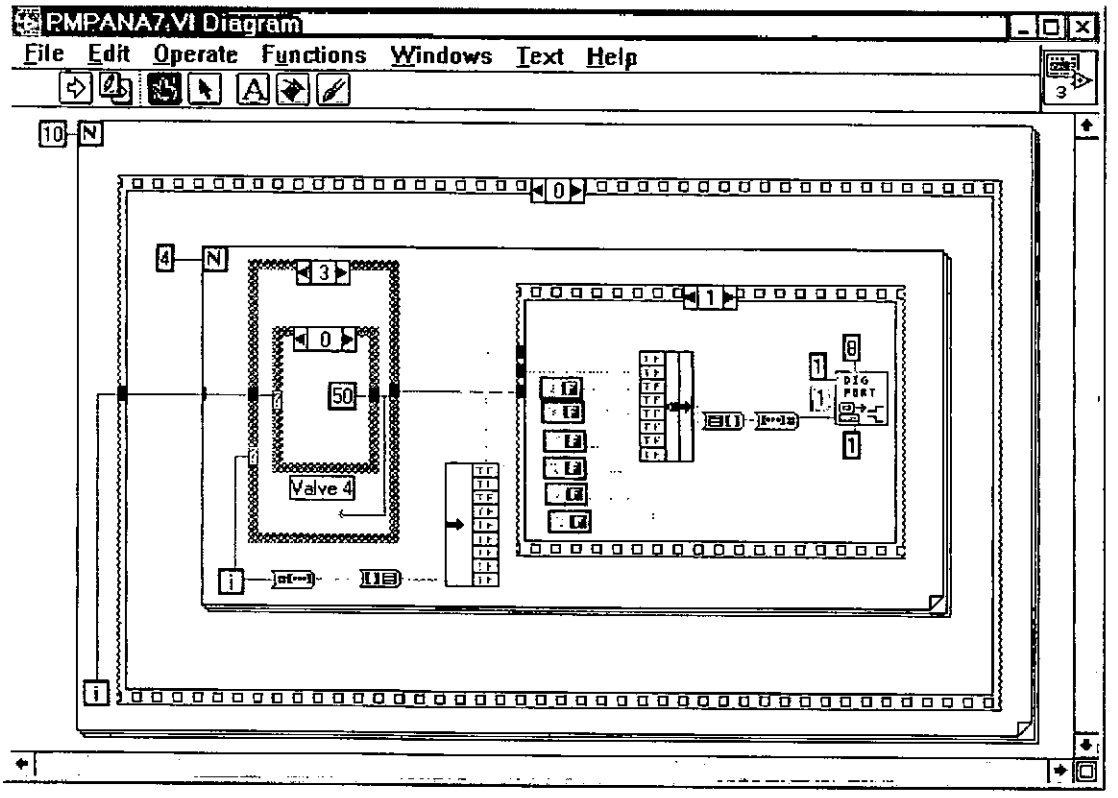
PMPANA7.VI Diagram
File Edit Operate Functions Windows Text Help
Valve 4
50
DIG PORT

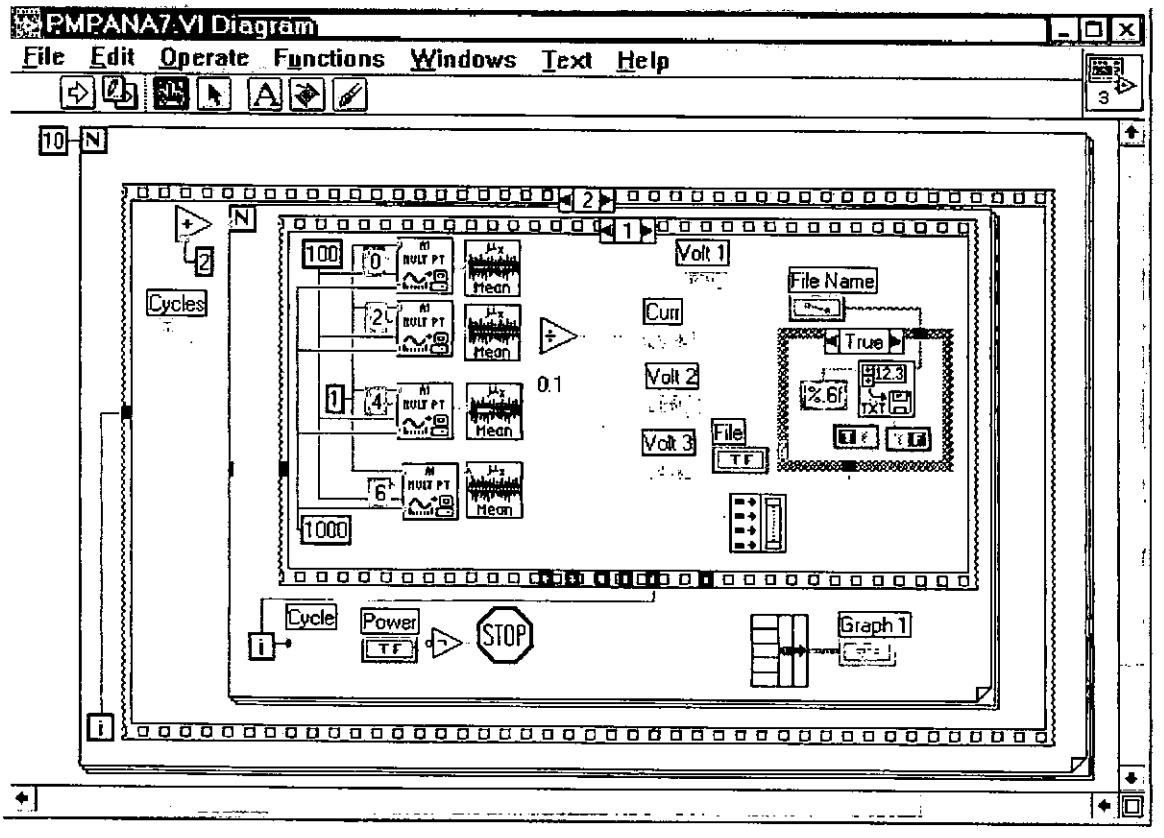
PMPANA7.VI Diagram
File Edit Operate Functions Windows Text Help
Cycles
Volt 1
Curr
Volt 2
Volt 3
File Name
True
File
0.1
Cycle
Power
STOP
Graph 1
Mean

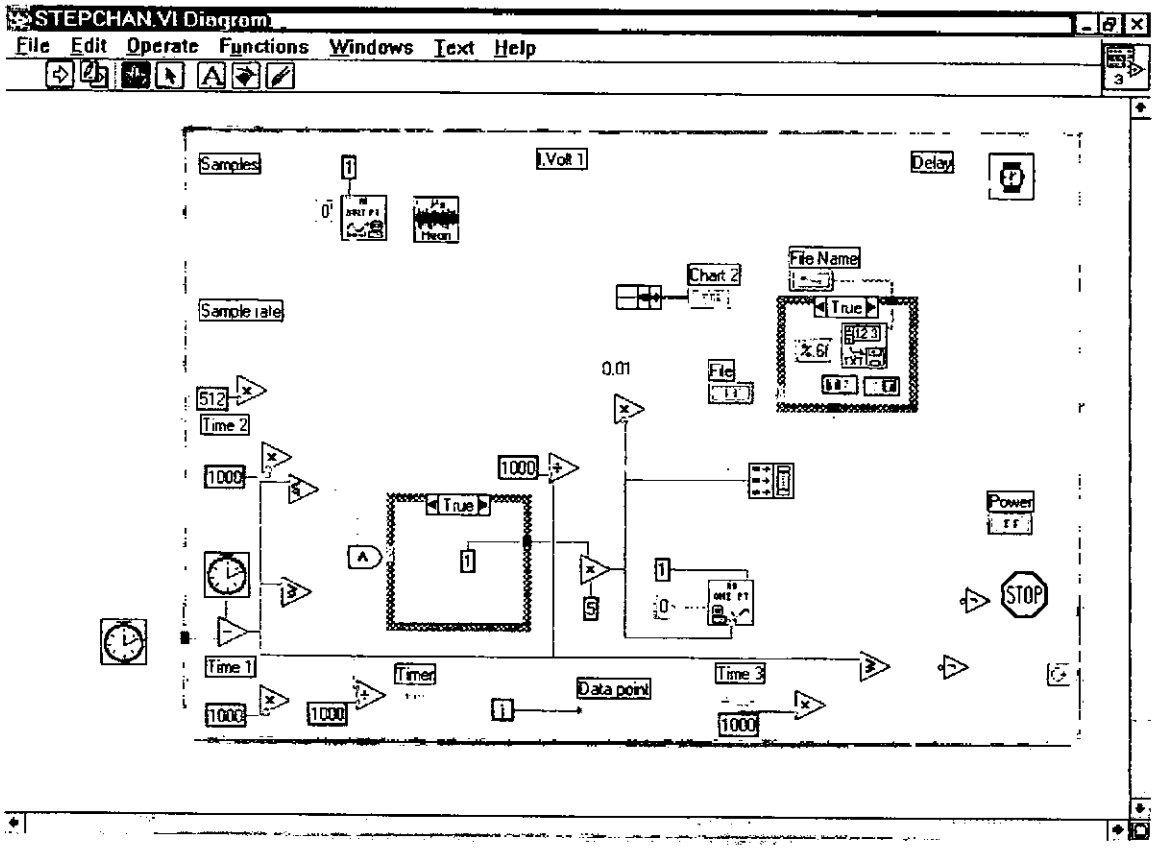
STEPCHAN.VI Diagram
File Edit Operate Functions Windows Text Help
Samples
Volt 1
Delay
Chart 2
File Name
Sample rate
True
0.01
File
512
Time 2
1000
True
Power
STOP
Time 1
Timer
Data point
Time 3

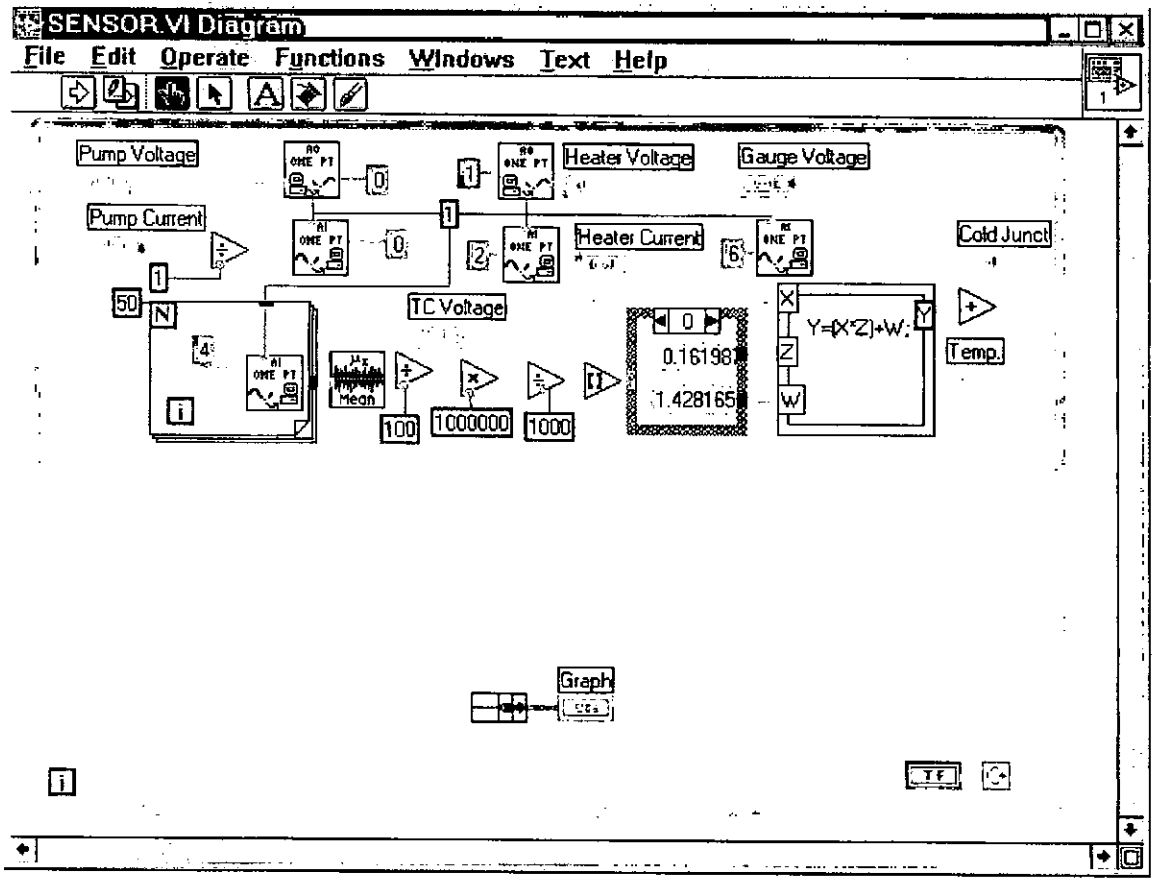
SENSOR.VI Diagram
File Edit Operate Functions Windows Text Help
Pump Voltage
Heater Voltage
Gauge Voltage
Pump Current
Heater Current
Cold Junct
TC Voltage
Mean
0.161987
1.428165
Y=(X*Z)+W:
Temp.
Graph
100
1000000
1000
50

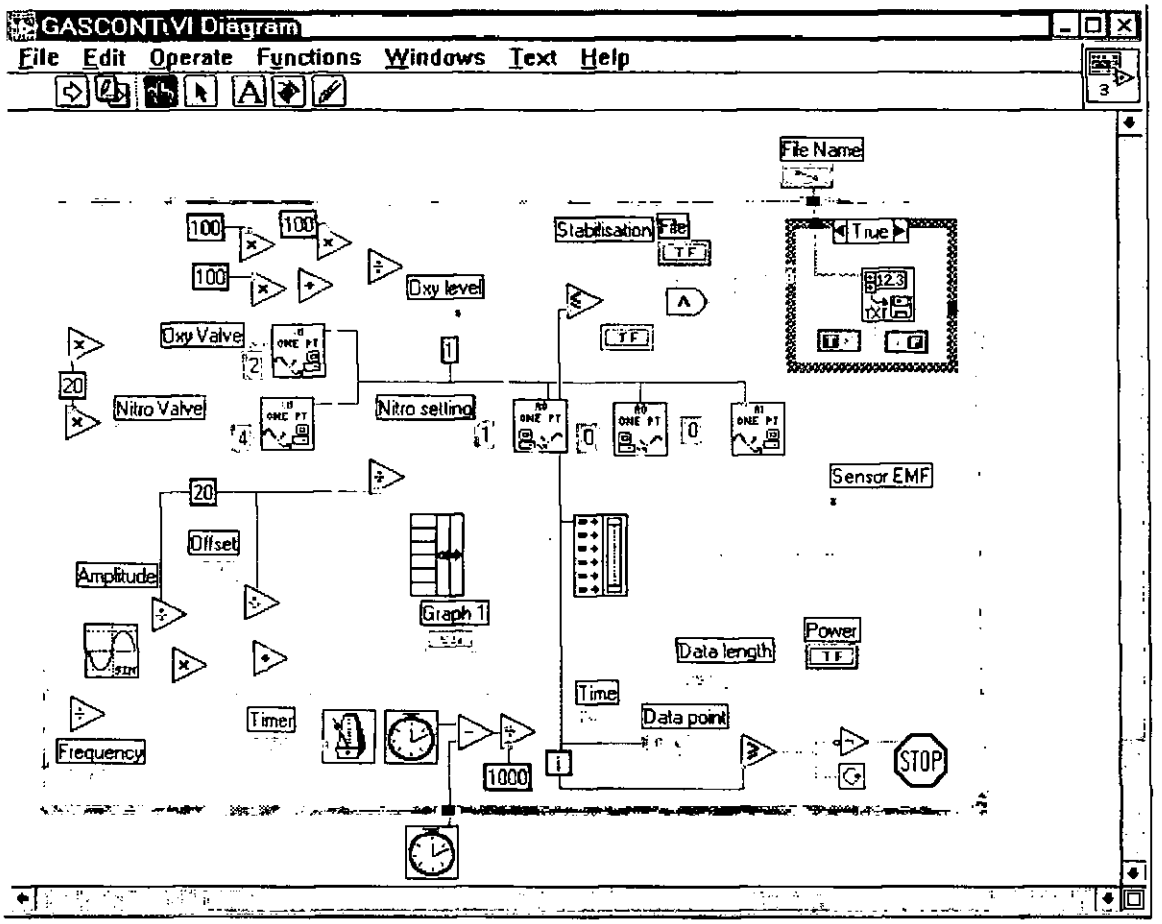
GASCONT.VI Diagram
File Edit Operate Functions Windows Text Help
File Name
Stabilisation
File
True
Oxy level
Oxy Valve
Nitro Valve
Nitro setting
Sensor EMF
Offset
Amplitude
Graph 1
Power
Data length
Time
Data point
Timer
Frequency
STOP

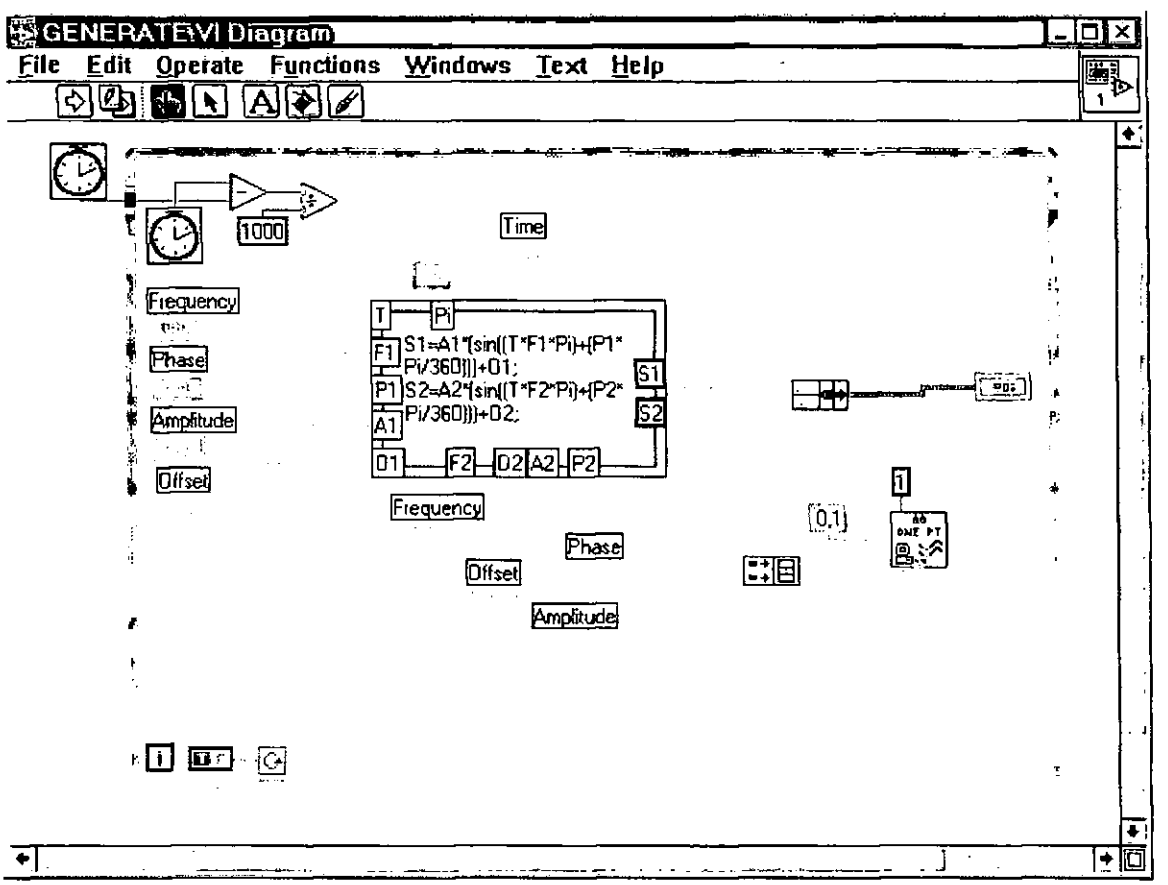
GENERATE.VI Diagram
File Edit Operate Functions Windows Text Help
Time
Frequency
Phase
Amplitude
Offset
S1=A1*(sin((T*F1*Pi)+(P1*
Pi/360)))+01;
S2=A2*(sin((T*F2*Pi)+(P2*
Pi/360)))+02;

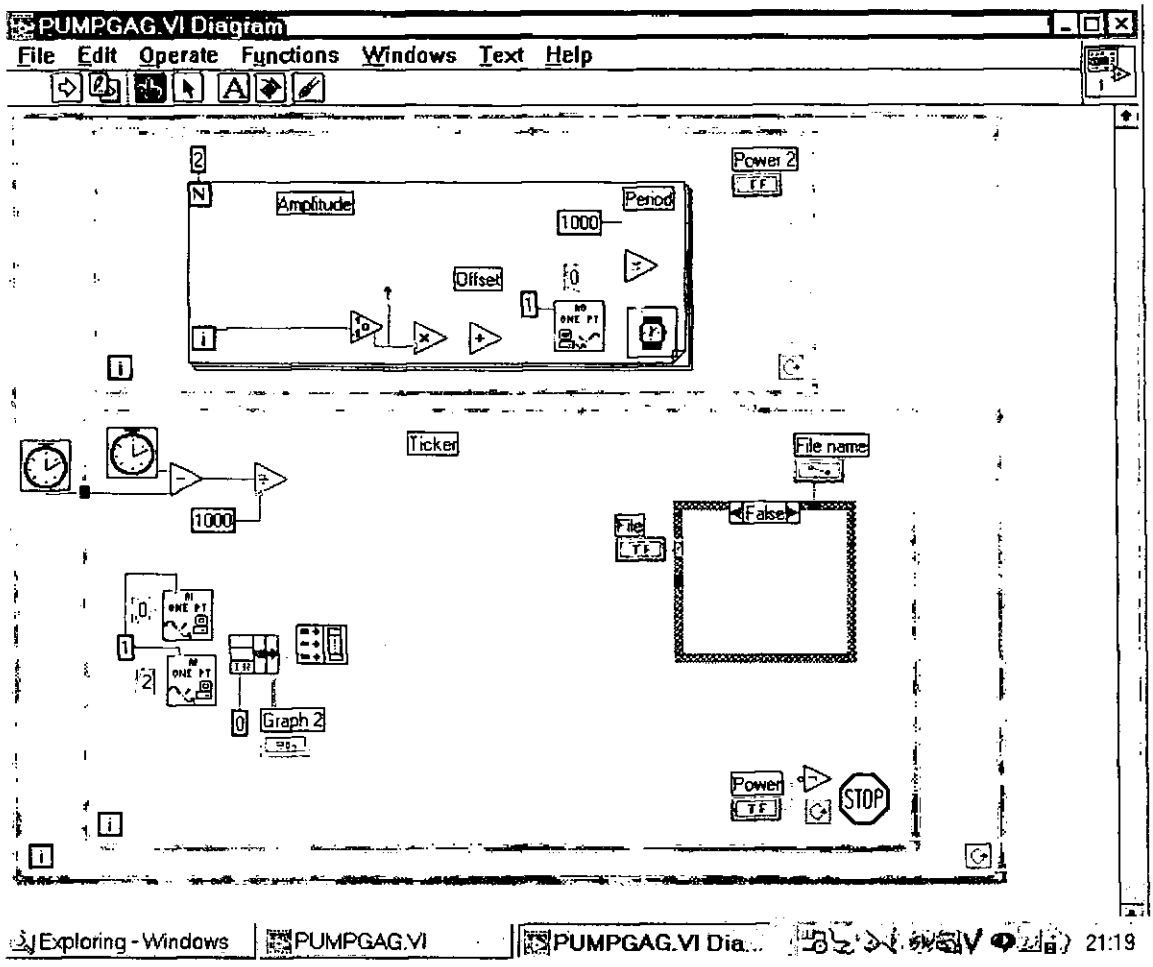
PUMPGAG.VI Diagram
File Edit Operate Functions Windows Text Help
Power 2
Amplitude
Period
1000
Offset
Ticker
File name
False
File
Graph 2
Power
STOP
Exploring - Windows
PUMPGAG.VI
PUMPGAG.VI Dia...
21:19

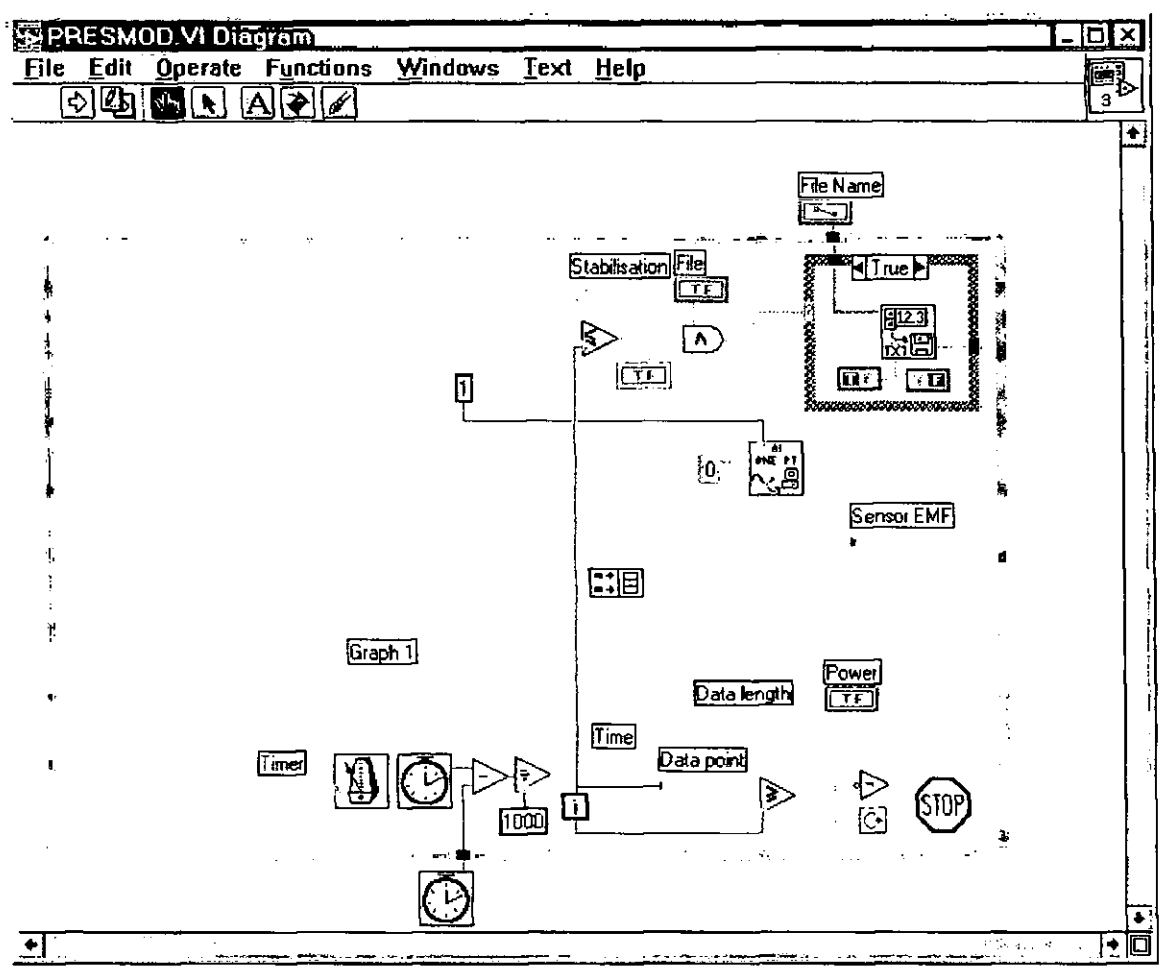
PRESMOD.VI Diagram
File Edit Operate Functions Windows Text Help
File Name
Stabilisation
File
True
Sensor EMF
Graph 1
Data length
Power
Time
Timer
Data point
1000
STOP

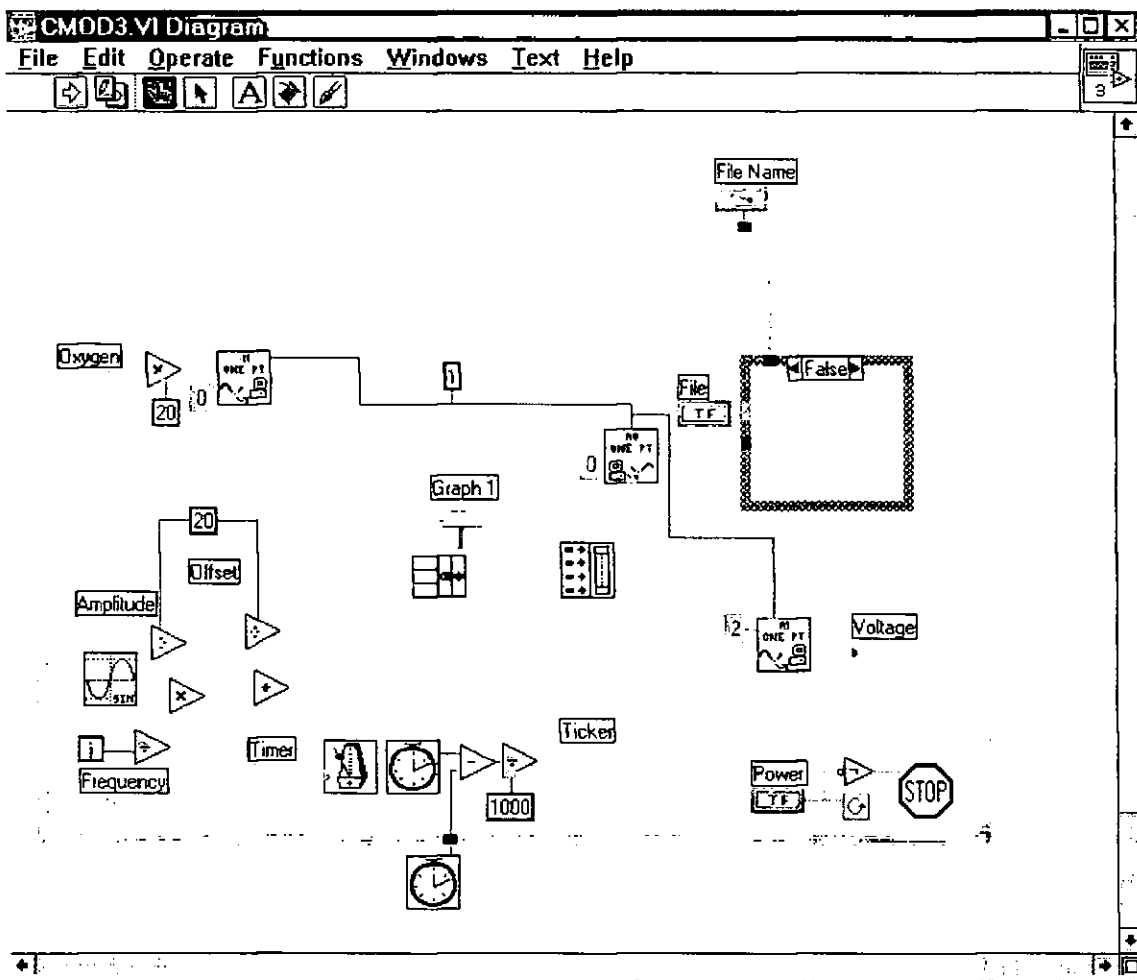
CMOD3.VI Diagram
File Edit Operate Functions Windows Text Help
File Name
Oxygen
20
0
1
File
TF
False
0
Graph 1
20
Offset
Amplitude
2
Voltage
Ticker
Timer
Frequency
1000
Power
TF
STOP

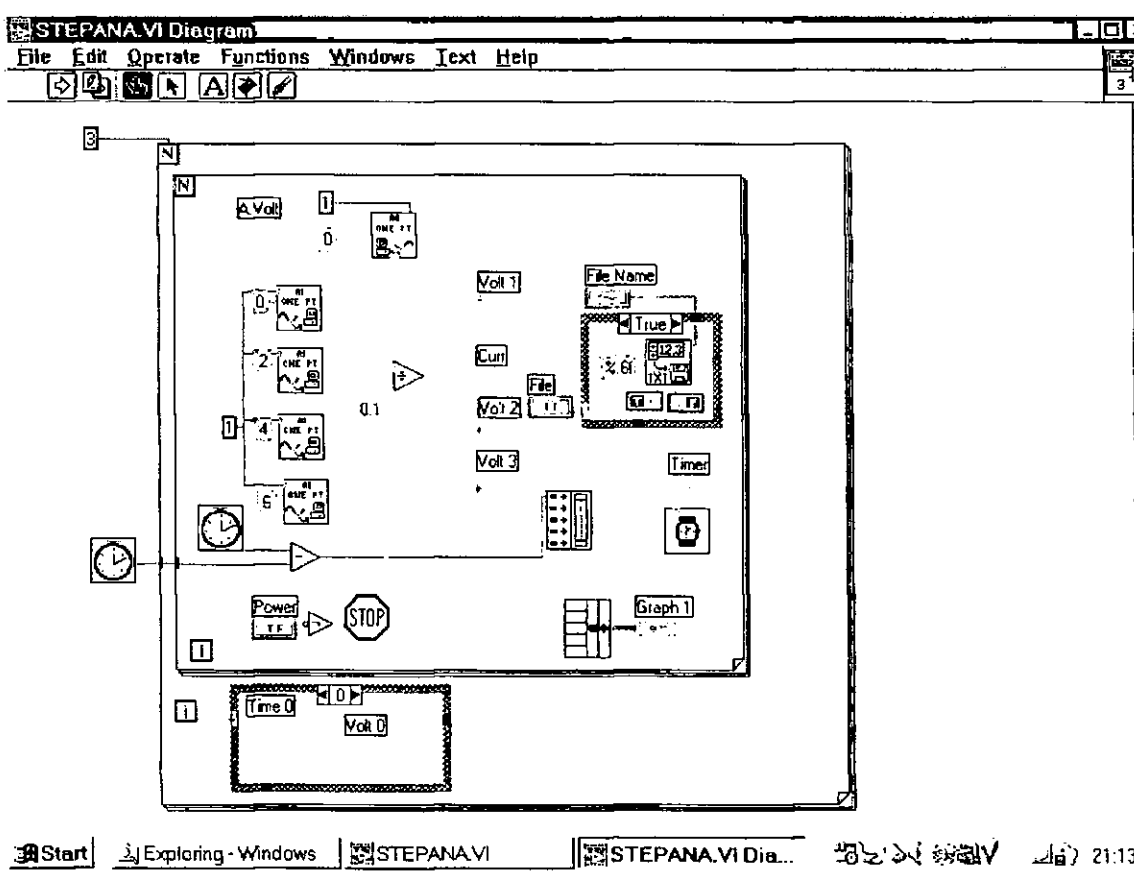
STEPANA.VI Diagram
File Edit Operate Functions Windows Text Help
3
N
A Volt
1
0
Volt 1
File Name
True
Curr
File
0.1
Volt 2
Volt 3
Timer
Power
TF
STOP
Graph 1
Time 0
0
Volt 0
Start
Exploring - Windows
STEPANA.VI
STEPANA.VI Dia...
21:13

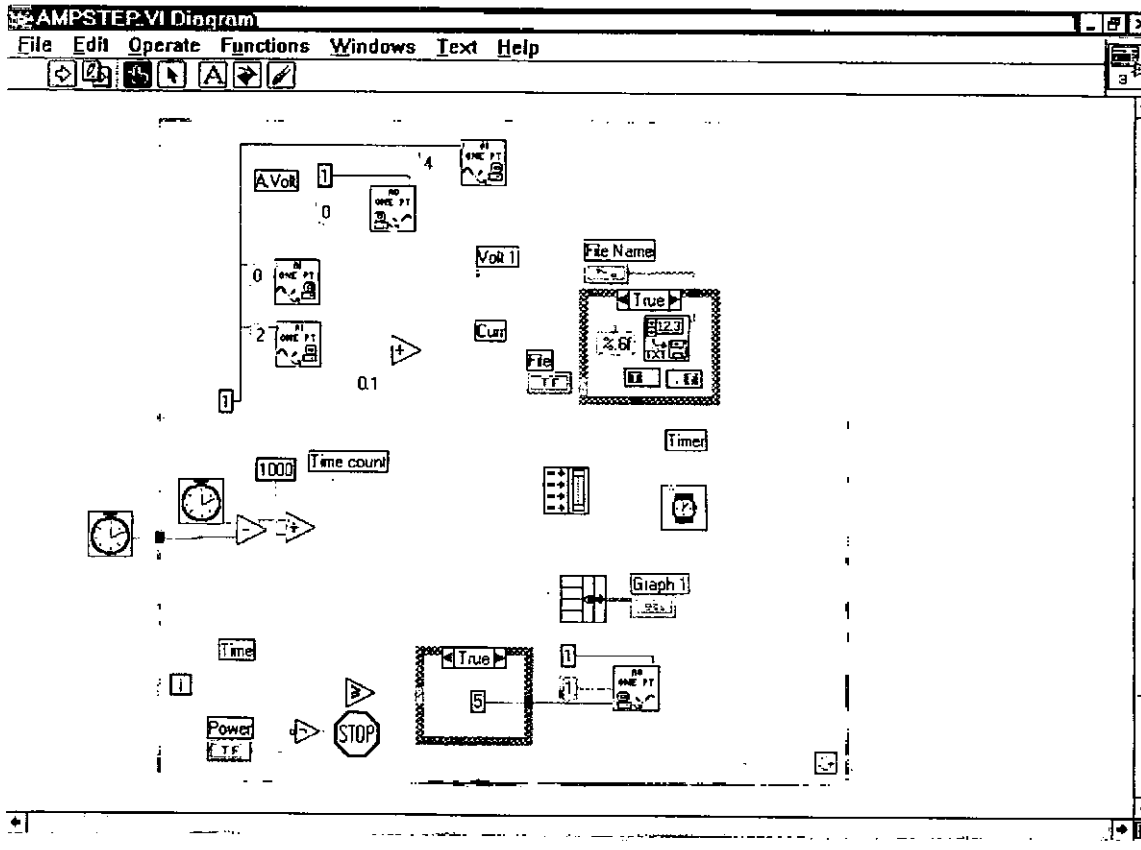
AMPSTEP.VI Diagram
File Edit Operate Functions Windows Text Help
A.Volt
Volt 1
File Name
True
Curr
File
0.1
Timer
1000
Time count
Graph 1
Time
True
Power
STOP

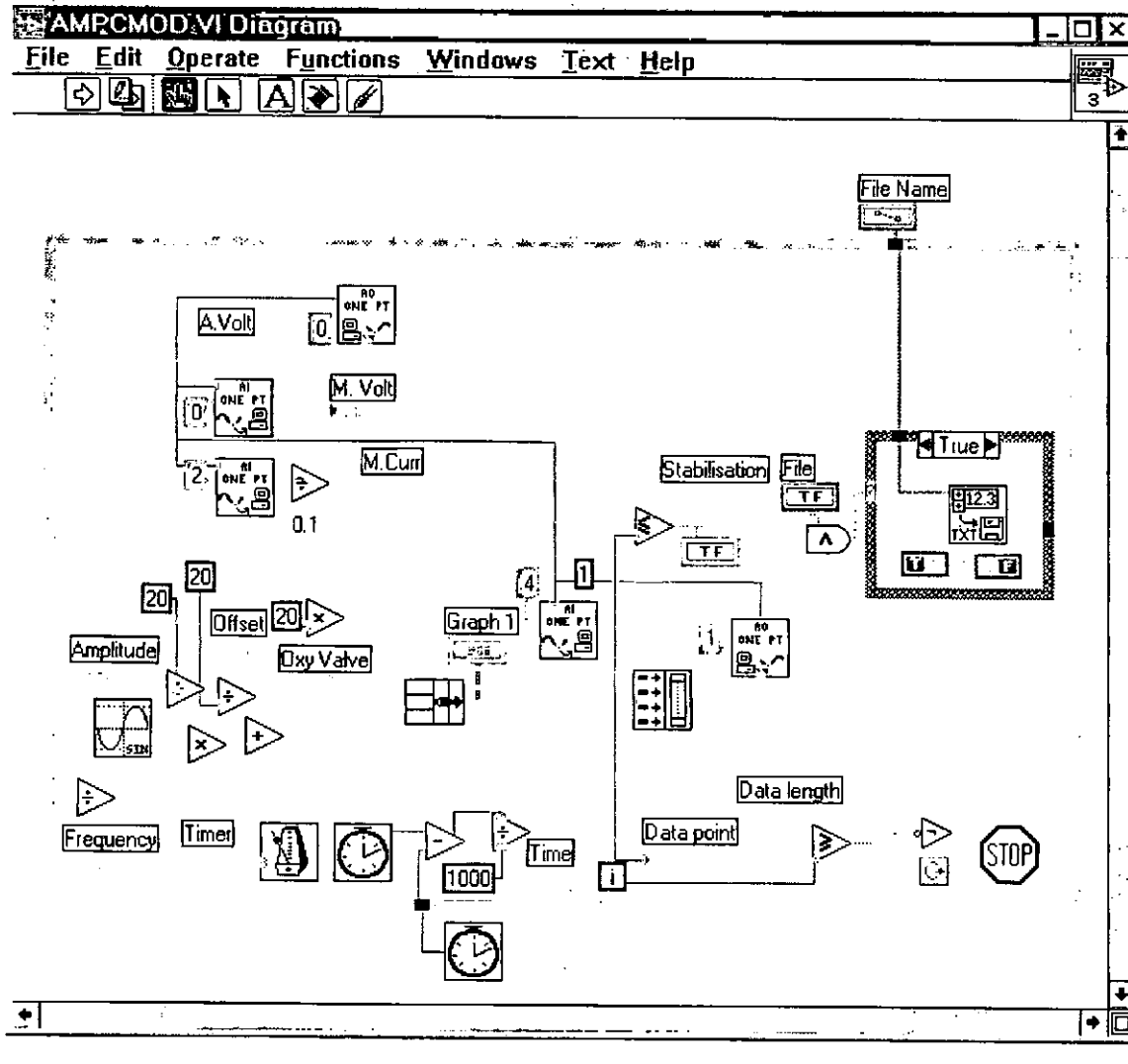
AMPCMOD.VI Diagram
File Edit Operate Functions Windows Text Help
File Name
A.Volt
M. Volt
M.Curr
0.1
Stabilisation
File
True
Offset
Amplitude
Oxy Valve
Graph 1
Frequency
Timer
Time
1000
Data length
Data point
STOP

```
DECLARE SUB Men2 ()
DECLARE SUB plot ()
DECLARE SUB Box (boxhor, boxver, boxht, boxwd, boxword$)
DECLARE SUB Check ()
DECLARE SUB Ibclr (BYVAL BD%)
DECLARE SUB Ibfind (BDNAME$, BD%)
DECLARE SUB Ibrd (BYVAL BD%, RD$)
DECLARE SUB Ibwrt (BYVAL BD%, WRT$)
DECLARE SUB Menu ()
DECLARE SUB ReadDVM ()
DECLARE SUB Pblock (D$)

' GPIB Function Declarations
DECLARE FUNCTION Ilwrt% (BYVAL BD%, Rd1$, Rd2$, WRT$, BYVAL CNT&)
' 488.2 Declarations
' COMMON SHARED /NISTATBLK/ IBSTA%, IBERR%, IBCNT%, IBCNTL&

COMMON SHARED Max1, Max2, Filnam$, Ans, Num, Col1, Col2, Col3, Rd1$, Rd2$
COMMON SHARED Pnt(), Read1$(), Read2$(), Dptinn$(), DVM1%, DVM2%, Rest
COMMON SHARED Tol1, Tol2, V1(), V2(), Inst, Xmax

REDIM Pnt(3000)
REDIM Read1$(3000)
REDIM Read2$(3000)
REDIM Option$(10)
REDIM V1(10)
REDIM V2(10)

CLS
Ans = 1
Num = 9
Col1 = 7
Col2 = 0
Col3 = 14

CLS
INPUT " Enter number of instruments ", Inst
IF Inst <> 2 THEN Inst = 1
CALL Ibfind("Dev1", DVM1%)
IF Inst = 2 THEN CALL Ibfind("Dev2", DVM2%)
CALL Ibclr(DVM1%)
IF Inst = 2 THEN CALL Ibclr(DVM2%)

CALL Men2

CALL Ibwrt(DVM1%, "NOT1D0")
IF Inst = 2 THEN CALL Ibwrt(DVM2%, "NOT1D0")

CALL plot
CALL ReadDVM

PRINT " Return to Default Settings"
    INPUT " Confirm You wish to RESET Device 1 (Y/n) ", conf$
    IF UCASE$(conf$) <> "N" THEN CALL Ibwrt(DVM1%, "A")
IF Inst = 2 THEN INPUT "Confirm You wish to RESET Device 2 (Y/n) ", conf$
IF Inst = 2 THEN IF UCASE$(conf$) <> "N" THEN CALL Ibwrt(DVM2%, "A")


END


SUB Box (boxhor, boxver, boxht, boxwd, boxword$)

'***** Write boxed word
LOCATE boxver + 1, boxhor + 1
```

```
'***** Draw top of box
LOCATE boxver, boxhor
PRINT CHR$(201);
FOR Z = 1 TO boxwd
PRINT CHR$(205);
NEXT Z
PRINT CHR$(187)
'***** Draw box sides
FOR Z = 1 TO boxht
  LOCATE boxver + Z, boxhor
  PRINT CHR$(186);
  LOCATE boxver + Z, boxhor + boxwd + 1
  PRINT CHR$(186)
NEXT Z
'***** Draw bottom of box
LOCATE boxver + Z, boxhor
PRINT CHR$(200);
FOR Z = 1 TO boxwd
  PRINT CHR$(205);
NEXT Z
PRINT CHR$(188);

END SUB

SUB Check
PRINT "GPIB0 INITIAL SETTINGS"
PRINT "PRIMARY ADDRESS                    0"
PRINT "SECONDARY ADDRESS                  NONE"
PRINT "TIMEOUT SETTING                    10SEC"
PRINT "TERMINATE READ ON EOS              NO"
PRINT "SET EOI WITH EOS ON WRITES         NO"
PRINT "TYPE OF COMPARE ON EOS             7-BIT"
PRINT "EOS BYTE                           00h"
PRINT "SEND EOI AT END OF WRITE           YES"
PRINT "SYSTEM CONTROLLER                  YES"
PRINT "ASSERT REN WHEN SC                 NO"
PRINT "ENABLE AUTO SERIAL POLLING         YES"
PRINT "ENABLE CIC PROTOCOL                NO"
PRINT "BUS TIMING                         500nS"
PRINT "PARALLEL POLL DURATION             DEFAULT"
PRINT "USE THIS GPIB INTERFACE            YES"
PRINT "BOARD TYPE                         PCII"
PRINT "BASE I/O ADDRESS                   02B8H"
PRINT
INPUT "PRESS RETURN FOR MORE", dummy$
CLS
PRINT
PRINT "DEV1 INITIAL SETTINGS"
PRINT "PRIMARY ADDRESS                    1"
PRINT "SECONDARY ADDRESS                  NONE"
PRINT "TIMEOUT SETTING                    10SEC"
PRINT "SERIAL POLL TIMEOUT                1SEC"
PRINT "TERMINATE READ ON EOS              NO"
PRINT "SET EOI WITH EOS ON WRITES         NO"
PRINT "TYPE OF COMPARE ON EOS             7-BIT"
PRINT "EOS BYTE                           00h"
PRINT "SEND EOI AT END OF WRITE           YES"
PRINT "ENABLE REPEAT ADDRESSING           NO"
PRINT
INPUT "PRESS RETURN FOR MORE", dummy$

END SUB

SUB Men2

'************** Set screen
```

```
CLS
PRINT " Open GPIB Configuration"
    INPUT " Do you wish to examine the GPIB configuration ", Ans$
    IF UCASE$(Ans$) = "Y" THEN
      CALL Check
      SHELL "c:\gpib-pc\ibconf"
    END IF
CLS
    PRINT " Set Inter-Measurement Time"
    INPUT " Enter Time Between Measurements: ", Rest
CLS
    PRINT " Set Maximum Measurements  "
    INPUT " Maximum for Device 1 ", Max1
    IF Inst = 2 THEN INPUT " Maximum for Device 2 ", Max2
CLS
    PRINT "Set Limiting Tolerance: "
    INPUT " Enter Tolerance 1 ", Tol1
    IF Inst = 2 THEN INPUT " Enter Tolerance 2 ", Tol2
CLS
    PRINT " Set Measurement Mode       "
    PRINT " Mode Options"
    PRINT " 0.. V-DC"
    PRINT " 1.. V-AC"
    PRINT " 2.. kOhms"
    PRINT " 3.. I-DC"
    PRINT " 4.. I-AC"
    INPUT " Enter Mode Number for Device 1: ", mode1
    IF mode1 < 0 OR mode1 > 4 THEN mode1 = 0
    CALL Ibwrt(DVM1%, "M" + LTRIM$(STR$(mode1)))
    IF Inst = 2 THEN INPUT " Enter Mode Number for Device 2: ", mode2
    IF Inst = 2 THEN IF mode2 < 0 OR mode2 > 4 THEN mode2 = 0
    IF Inst = 2 THEN CALL Ibwrt(DVM2%, "M" + LTRIM$(STR$(mode2)))
CLS
    PRINT " Set Measurement Range      "
    PRINT " Range Options"
    PRINT
    PRINT "      Volt     Ohm        Amp"
    PRINT " 0.. ......Autorange......"
    PRINT " 1.. 0.2.....N/A.......N/A"
    PRINT " 2.. 2.......N/A.......N/A"
    PRINT " 3.. 20......20k.......N/A"
    PRINT " 4.. 200.....200k......N/A"
    PRINT " 5.. 2k......2M........2"
    PRINT " 6.. N/A.....20M.......N/A"
    INPUT " Enter Range Number: ", range1
    IF range1 < 0 OR range1 > 6 THEN range1 = 0
    CALL Ibwrt(DVM1%, "R" + LTRIM$(STR$(range1)))
    IF Inst = 2 THEN INPUT " Enter Range Number: ", range2
    IF Inst = 2 THEN IF range2 < 0 OR range2 > 6 THEN range2 = 0
    IF Inst = 2 THEN CALL Ibwrt(DVM2%, "R" + LTRIM$(STR$(range2)))
CLS
    PRINT " Set Output Filename:  "
    SHELL "dir c:\temp\*.csv /w"
    INPUT " Enter Filename: ", Filnam$
    Filnam$ = "c:\temp\" + UCASE$(Filnam$) + ".CSV"

END SUB

SUB plot

CLS
SCREEN 9
Xmax = 280
Ymax = 1
VIEW (40, 20)-(590, 300)
WINDOW (0, Ymax)-(Xmax, 0)
```

```
LINE (0, Ymax)-(Xmax, Ymax)
LINE (Xmax, Ymax)-(Xmax, 0)
LINE (Xmax, 0)-(0, 0)

FOR Z = 1 TO 11
  IF Inst = 2 THEN LOCATE Z * 2, 75
  IF Inst = 2 THEN COLOR (14), (0)
  IF Inst = 2 THEN PRINT USING "#.####"; Max2 - ((Z - 1) * Max2 / 10)
  LOCATE Z * 2, 1
  COLOR (15), (0)
  PRINT USING "#.####"; Max1 - ((Z - 1) * Max1 / 10)
NEXT Z

END SUB

SUB ReadDVM

OPEN Filnam$ FOR APPEND AS #1
Time1 = TIMER
STP$ = ""
WHILE STP$ = ""
  '*************** Get voltmeter response
  IF Rest > 0 THEN SLEEP Rest
  Rd1$ = SPACE$(17)
  IF Inst = 2 THEN Rd2$ = SPACE$(17)
  CALL Ibrd(DVM1%, Rd1$)
  IF Inst = 2 THEN CALL Ibrd(DVM2%, Rd2$)
  Time2 = TIMER
  Time3 = Time2 - Time1
  Y = (VAL(LEFT$(Rd1$, 9))) / Max1
  IF Inst = 2 THEN Z = VAL(LEFT$(Rd2$, 9)) / Max2
  X = X + 1
  LOCATE (1), (1)
  PRINT X
  LOCATE (1), (15)
  PRINT Rd1$
  IF Inst = 2 THEN LOCATE (1), (35)
  IF Inst = 2 THEN PRINT Rd2$
  IF X = Xmax THEN CALL plot: X = 0
  CIRCLE (X, Y), .001, 15
  IF Inst = 2 THEN CIRCLE (X, Z), .001, 14
  STP$ = INKEY$
  Res = Res + 1
  WRITE #1, Res, Time3, VAL(LEFT$(Rd1$, 9)), VAL(LEFT$(Rd2$, 9))

  Entry = Entry + 1
  V1(6) = VAL(Rd1$)
  V2(6) = VAL(Rd2$)
  FOR Z = 1 TO 5
    V1(Z) = V1(Z + 1)
    V2(Z) = V2(Z + 1)
  NEXT Z
  IF Entry > 4 THEN
    TMin1 = V1(1)
    TMax1 = V1(1)
    TMin2 = V2(1)
    TMax2 = V2(1)
    FOR Z = 1 TO 5
      IF V1(Z) < TMin1 THEN TMin1 = V1(Z)
      IF V1(Z) > TMax1 THEN TMax1 = V1(Z)
      IF V2(Z) > TMax2 THEN TMax2 = V2(Z)
      IF V2(Z) < TMin2 THEN TMin2 = V2(Z)
    NEXT Z
    IF TMax1 <= TMin1 + Tol1 THEN SOUND 500, 1
    IF Inst = 2 THEN IF TMax2 <= TMin2 + Tol2 THEN SOUND 5000, 1
```

```
DECLARE SUB Men2 ()
DECLARE SUB plot ()
DECLARE SUB Box (boxhor, boxver, boxht, boxwd, boxword$)
DECLARE SUB Ibclr (BYVAL BD%)
DECLARE SUB Ibfind (BDNAME$, BD%)
DECLARE SUB Ibrd (BYVAL BD%, RD$)
DECLARE SUB Ibwrt (BYVAL BD%, WRT$)
DECLARE SUB Menu ()
DECLARE SUB ReadDVM ()
DECLARE SUB Pblock (D$)

' GPIB Function Declarations
DECLARE FUNCTION Ilwrt% (BYVAL BD%, Rd1$, Rd2$, WRT$, BYVAL CNT&)
' 488.2 Declarations
' COMMON SHARED /NISTATBLK/ IBSTA%, IBERR%, IBCNT%, IBCNTL&

COMMON SHARED Max1, Max2, Filnam$, Ans, Num, Col1, Col2, Col3, Rd1$, Rd2$
COMMON SHARED Pnt(), Read1$(), Read2$(), Option$(), DVM1%, DVM2%, Rest
COMMON SHARED Tol1, Tol2, V1(), V2(), Inst, Xmax, Temp(), Volt(), CJT

REDIM Pnt(3000)
REDIM Read1$(3000)
REDIM Read2$(3000)
REDIM Option$(10)
REDIM V1(10)
REDIM V2(10)
REDIM Temp(1000)
REDIM Vnlt(1000)

CLS
Ans = 1
Num = 9
Col1 = 7
Col2 = 0
Cnl3 = 14

OPEN "c:\jay\ktype.csv" FOR INPUT AS #2
INPUT #2, title1, title2
FOR z = 1 TO 1000
  INPUT #2, Volt(z), Temp(z)
NEXT z

CLS
Inst = 1
CALL Ibfind("Dev1", DVM1%)
CALL Ibclr(DVM1%)

CALL Men2

CALL Ibwrt(DVM1%, "NOT1D0")

CALL plot
CALL ReadDVM
CALL Ibwrt(DVM1%, "A")
END


SUB Box (boxhor, boxver, boxht, boxwd, boxword$)

'***** Write boxed word
LOCATE boxver + 1, boxhor + 1
PRINT boxword$
'***** Draw top of box
LOCATE boxver, boxhor
PRINT CHR$(201);
```

```
PRINT CHR$(205);
NEXT z
PRINT CHR$(187)
'***** Draw box sides
FOR z = 1 TO boxht
  LOCATE boxver + z, boxhor
  PRINT CHR$(186);
  LOCATE boxver + z, boxhor + boxwd + 1
  PRINT CHR$(186)
NEXT z
'***** Draw bottom of box
LOCATE boxver + z, boxhor
PRINT CHR$(200);
FOR z = 1 TO boxwd
  PRINT CHR$(205);
NEXT z
PRINT CHR$(188);

END SUB

SUB Men2

'************** Set screen
COLOR Col1, Col2
CLS
    PRINT " Set Inter-Measurement Time"
    INPUT " Enter Time Between Measurements: ", Rest
    PRINT " Set Cold Junction Temperature"
    INPUT " Enter Cold Junction Temperature: ", CJT

    Max1 = 1000
    Tol1 = 1
    mode1 = 0
    range1 = 0

    CALL Ibwrt(DVM1%, "M" + LTRIM$(STR$(mode1)))
    CALL Ibwrt(DVM1%, "R" + LTRIM$(STR$(range1)))

    PRINT
    PRINT " Set Output Filename:  "
    SHELL "dir c:\temp\*.csv /w"
    INPUT " Enter Filename: ", Filnam$
    Filnam$ = "c:\temp\" + UCASE$(Filnam$) + ".CSV"

END SUB

SUB plot

CLS
SCREEN 9
Xmax = 280
ymax = 1
VIEW (40, 20)-(590, 300)
WINDOW (0, ymax)-(Xmax, 0)
LINE (0, 0)-(0, ymax)
LINE (0, ymax)-(Xmax, ymax)
LINE (Xmax, ymax)-(Xmax, 0)
LINE (Xmax, 0)-(0, 0)

FOR z = 1 TO 11
  LOCATE z * 2, 1
  COLOR (15), (0)
  PRINT USING "####": Max1 - ((z - 1) * Max1 / 10)
NEXT z

END SUB
```

APPENDIX E

AMPEROMETRIC SENSOR DEVELOPMENT EXPERIMENTAL

E1 Amperometric tests

E1.1 Two electrode sensors

Having fabricated a sensor as detailed in section 2.3.1, the next task was to test it and record its characteristics. The tests were performed within the large sensor test-rig as described in section C1.3.1. Two 7150 multimeters were used to record pump current and the applied voltage which was sourced from the time electronics voltage supply. Gases were prepared by mixing bottled nitrogen with compressed air using two 100 ml/min flow valves. At this stage no equipment was computer controlled. The temperature was ramped to 400°C whilst the gases were flushed through the test-rig. Upon temperature stabilisation, measured pump current and applied voltage readings were recorded. The pump potential was then ramped in 100 mV steps from 0 to 1 V allowing time for readings to stabilise and measurements to be taken between steps. On completion the gas mixture was altered and the readings repeated for gas concentrations from 21 to 3.5% oxygen. These readings were taken for temperatures from 400 to 800°C and plotted via spreadsheet to reveal current / voltage curves. These tests were repeated for several different sensors to find reproducibility. See figure E1 for schematic connection diagram

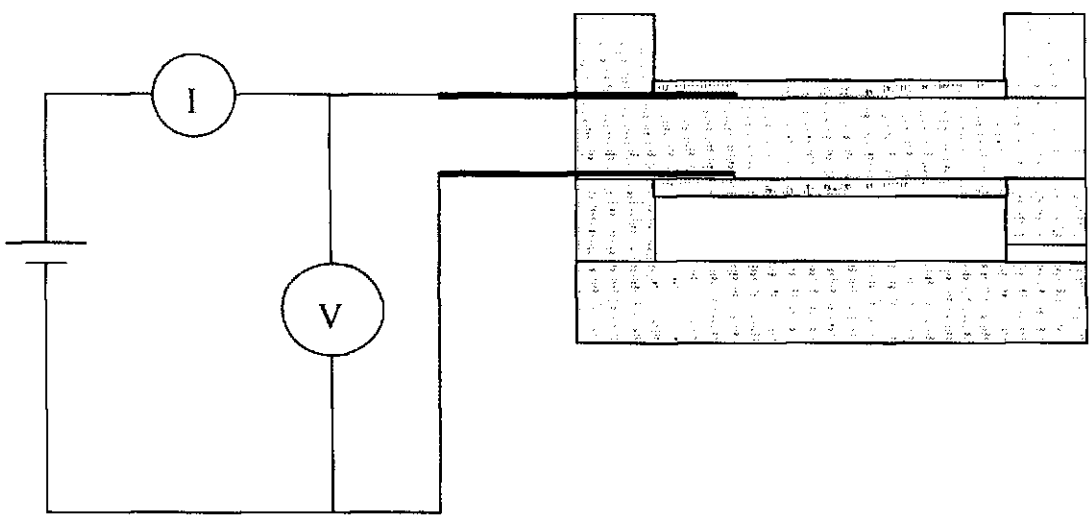

Figure E1 Amperometric sensor connection schematic

The purpose of these tests was several fold.

1. To see if sensors work

2. To check that theory were observed

3. To find the calculated S/L ratio and compare with dimensional measurements

4. To find the temperature coefficient and compare with theory / literature

5. To see at what temperature sensors cease to operate and how they begun to fail

6. To find the degree of reproducibility from sensor to sensor

E1.2 Four electrode sensors

Four electrode amperometric sensors were fabricated in the same manner as the two electrode devices but with the addition of an extra two electrodes to act as a potentiometric gauge. These were similar to pump-gauges as used by Hetrick et al [75] for measurements in exhaust systems in both rich and lean regions. In this work however they were operated as an amperometric sensors but with the benefit of additional information obtained from

the potentiometric cell. The devices were tested in a similar manner to the two electrode sensors but at one fixed temperature and using fewer gas concentrations. The main testing difference came from the use of LabView and DAQ card. This enabled computerised measurement and ramping. The virtual instrument developed included automated voltage sweeping with adjustable parameters to allow variation in the number of voltage steps, maximum applied voltage, two channels of voltage measurement and one of current measurement, whilst giving and on-screen display of results as recorded. Each data point recorded was an average of 1000 individual readings, sampled over a second and recorded to 6 decimal places. This feature greatly aided experimental diagnostics, reduced measurement time, gave enhanced repeatability and reproducibility and allowed results to be interpreted as they were taken. Results of pump voltage, pump current and gauge voltage were recorded. See figure E2 for schematic connection diagram. The purpose of these tests was to assess the degree of electrochemical leakage affecting results of these sensors.

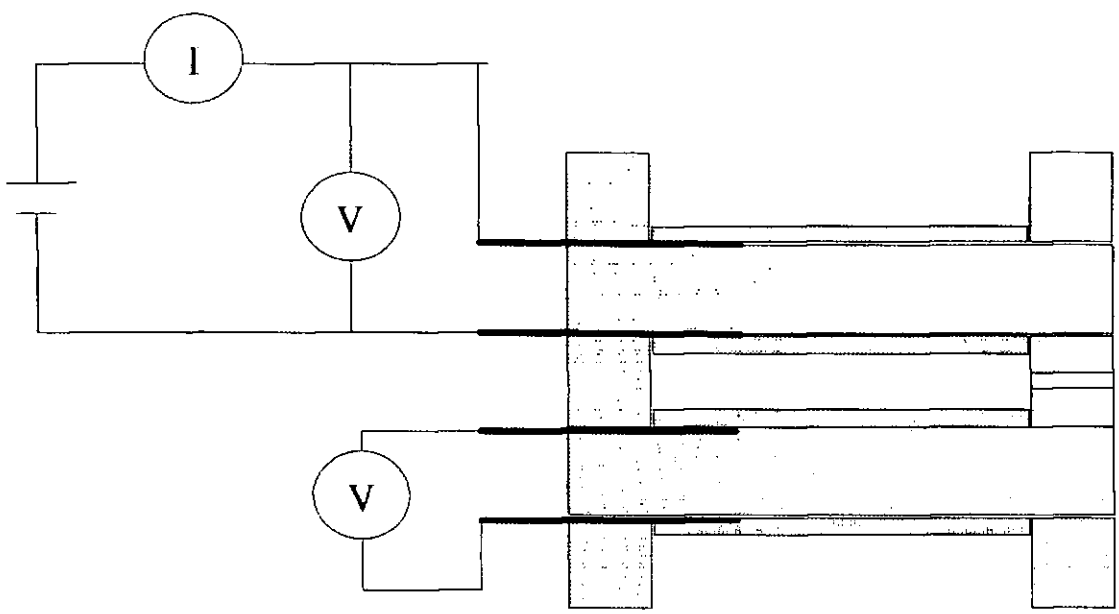

Figure E2 Four electrode amperometric sensor connection schematic.

E1.3 High oxygen concentrations

High oxygen concentration tests employed a similar method of testing to the four electrode tests. A four-electrode sensor was again used in the sensor test-rig with pump current, voltage and gauge voltage recorded using LabView and the DAQ system. The difference was in that the gases were derived from mixing bottled oxygen and bottled nitrogen through a pair of 100 ml/min flow valves. Results were recorded at 800°C using gases of 21 to 60% oxygen. The purpose of these tests was to examine sensor characteristics at the upper limit of oxygen concentration measurement. This was done with a view to developing the operation theory to allow for sensor operation at higher oxygen concentrations where typically a non-linearity has been observed. [57, 89].

E1.4 Split electrode sensors

Split electrode sensors were fabricated following the lines of the four electrode amperometric sensors. The distinction arises through incorporating a second wire to the gauge electrode and dividing this electrode into two separate components such that one half is close to the diffusion hole and the second, remote from it. Thus in the simplest form we have a five electrode sensor with one pump and two gauge cells. The testing regime was as that used for the four electrode sensors using the sensor test-rig and LabView (which was modified to give an additional gauge voltage measurement channel). Typical

parameters for these tests were 20 steps of 0.1 V per step with a 30s stabilisation between adjustment and measurement. Each point was again an average of 1000 individual measurements. The sensor was tested at 800°C using 21, 10, 5 and 1% oxygen. In the simple two-way split electrode device, each electrode had a width of approximately 1.5 mm with a 1 mm separation.

E1.5 Low oxygen ppm measurements

The low oxygen testing regime and test-rig were identical to that describe for standard sensors, except that gas flow valves were selected to give a very large nitrogen to air ratio. These ratios were obtained by using 2 off 100 ml/min flow valves to supply 100% nitrogen alongside a 5 ml/min flow valve supplying pure air. Each of these flow valves was controllable to give between 5 to 100% of its maximum flow. Using this method, oxygen concentrations of 10,000 to 260 ppm (0.01 to 0.0026%) were produced. Each of 6 sensors (see section F1.6) were tested using 0-1V pump potential and 800°C in the various atmospheres. In addition, the 0.7 mm diameter barrier sensor was tested at 700 and 900°C to get an idea of the temperature dependence. The testing set-up and procedure was otherwise identical to that reported for two electrode sensors although stabilisation times of minutes rather than seconds were necessary between adjustment and measurement. Tests were also performed of gas flushing times to ensure that a stable gas concentration had been achieved before commencing the tests. This was realised by monitoring sensor current immediately after re-setting the gas valves. A time of 5 minutes was found to be sufficient and a minimum of 10 minutes used. Further work carried out by a final year project student, extended this oxygen measurement range to 10 ppm and used a 0.5 mm diameter diffusion barrier. For this work a specifically adapted sensor test-rig was employed. Adaptations centred on ensuring excellent sealing to prevent contamination of the test atmosphere. Measures taken were the application of silicone sealant to the water-cooled endplate and the use of stainless steel and copper tubing in-place of plastic tubing previously employed. The second adaptation was that oxygen was introduced by electrochemical pumping oxygen from the external atmosphere into a stream of high purity nitrogen. This dosing was achieved using a zirconia tube arrangement similar to the miniature furnace previously described. By passing a current through this tube, a well-controlled volume of oxygen could be introduced to the nitrogen stream. For further details see Individual project report (D.Tzempelikos). This rig and sensor was also used to investigate the temperature dependence of large barrier, low oxygen sensors from 400 to 900°C. Canerio et al [83] used a similar system to add oxygen to a flow of CO or H_2 in order to prepare gases of known composition. Kilner et al [121] reviewed ceramic ion conductors for use as oxygen generators.

E1.6 Firing temperature

As part of a student project under my guidance, a range of half sensors were prepared from the Tioxide plastic / ceramic material and fired at temperatures between 1150 and 1550°C and analysed using Scanning Electron Microscopy and Impedance Spectroscopy. Results from this project led to the belief that current / voltage sweeps of these samples may prove informative. The half sensors were tested in the sensor test-rig in air at temperatures ranging from 450 to 550°C. The tests were carried out using the LabView / DAQ system to apply a 0 to 1 V sweep and measure resultant currents. The sample prepared at 1450°C was also tested over a range of oxygen concentrations (2 to 21% at 600°C) to investigate the influence of oxygen concentration on cell resistance. The student project used frequency response analysis to examine the same sensors, this work is outlined in section F1.6.

E1.7 Platinisation

In order to affect an improvement upon a previously characterised sensor, an attempt was made to electro-deposit a fresh layer of platinum onto a four-electrode amperometric sensor. For electro-plating of internal electrodes, it was necessary to fill the internal cavity with the liquid electrolyte (hydrogen chloroplatinic acid) through the 200 μm diffusion hole. Also a platinum anode was required within the structure. Immersing the sensor in the electrolyte and applying a vacuum to draw gas from the sensor solved these problems. Upon releasing the vacuum, electrolyte was pushed under atmospheric pressure into the cavity. This procedure was checked by visually observing gas bubbles exiting the sensor upon evacuation, and also by weighing the sensor before and after filling. The two masses confirmed that approximately 15 mm^3 (in agreement with internal cavity volume estimations of electrolyte) had entered the device. The problem of introducing an anode was resolved by using the two internal electrodes and a sinusoidal current such that metal was removed and deposited on each in turn. This results in no overall gain in metal on either electrode, but does re-organise the metal present (picking up sintered metal and laying back down as a fine deposit). The current applied was a 10 mA peak to peak sinewave applied with no bias at a frequency of 0.2 Hz for 10 minutes. A similar current was applied between the external electrodes to obtain a similar deposition for visual examination. The current of 10 mA was selected, as it was the highest current found not to evolve excessive gases that would drive electrolyte from the sensor. The frequency and time were selected solely as they were easily produced. The liquid electrolyte was then removed from the sensor by evacuating the device with the hole facing downward in a dry container. In this way, for gas to escape it had to push the liquid from the cell first. The cell was subsequently filled with water and the procedure repeated to dilute and flush the remaining acid from the sensor. Heating to 120°C for several hours then dried the cell.

The dried device was characterised in the sensor test-rig at temperature from 300 to 700°C in air using the LabView system to record pump voltage and currents, between 0 and 2 V. Results were compared with those for the same device prior to the electro-plating treatment. Frequency response analysis was also used to examine the same device (see section 2.7.9). These experiments had previously been attempted but failed, probably due to the use of excessive (150 mA DC) plating currents over stripping one electrode and evolving excessive gases. The failed sensor developed an internal short circuit between pump and gauge cells and indicated altered diffusion barrier characteristics.

E2 Pump-gauge tests

This series of tests followed those carried out by Kaneko et al [61] for their gold seal devices. In this work, devices were made as detailed in section 2.3.2 using the plastic / ceramic, incorporating no metal or glass sealing. All the tests detailed here were performed in the sensor test-rig with gases mixed from compressed air and bottled nitrogen. Instrumentation in all cases was 7150 multimeters, controlled and monitored by IEEE 4.88 interface.

E2.1 Current / voltage tests

The first leakage test performed was to supply a small constant voltage (100 mV) to the pump and monitor the current drawn over time. This was performed at 700°C in air using a single side of the cell. The gauge cell was left disconnected and open circuit to ensure that no additional leakage path was provided. Results of these tests are reported in section F2.1.

E2.2 Gas pumping technique

The second test involved applying a constant current, of 500 μA to pump oxygen out of the device for a period of 30 s before reversing the current for a further 30 s. This test thereby

pumped identical quantities of oxygen out of the internal cavity, then back in. These examinations were performed using a fully sealed pump-gauge device fabricated using the plastic ceramic technique without the use of an additional glass seal. Pumping was performed whilst monitoring the gauge EMF. Not only would leakage show as a non-symmetry of EMF traces but also as an offset in final EMF. These effects were not observed under the test conditions examined. These tests were repeated for the device at 700, 750, 800 and 850°C in air using the same pump current. Since the external partial pressure and temperature were known, the internal partial pressure could be calculated from the EMF using the Nernst equation. Instrumentation involved for this test included 7150 multimeters for the measurement of sensor currents and voltages with the current applied through a voltage to current converter and the Time Electronics voltage source. The multimeters were operated under computer control so timings were automated and data plotted on screen at real time. Results of this work are shown in section F2.2.

E2.3 Steady state tests

A further pump-gauge leakage test, more accurate than the two already described, involved the application of small constant currents to draw the oxygen from the device whilst the gauge EMF was monitored over time. This test was repeated for a series of pump currents (positive and negative) and a picture of leakage current versus partial pressure differential was gained. Applied currents of between 10 and –7 μA were used for temperatures between 700 and 850°C in air. Currents were applied using the home made voltage to current converter and Time Electronics voltage source. Measurements were repeated using 15, 10 and 6% oxygen gas concentrations. Again the instrumentation involved were computer controlled 7150 multimeters allowing real time data plotting. Results of this work are shown in section F2.3.

E2.4 Recovery tests

A final leakage test method was employed to double check the results of the steady state tests. These were dynamic recovery tests. In dynamic recovery tests the internal oxygen partial pressure was driven low by ionic pumping of oxygen, then currents were removed and the internal partial pressure monitored as oxygen leaked back in over time. They were performed by applying a large pump potential (900 mV which was insufficient to cause dissociation of H_2O or CO_2) to take the internal partial pressure to near zero. The potential was then removed and the pump electrodes left open circuit whilst the gauge EMF was monitored over time using a high impedance voltmeter. These tests were performed for temperatures of 700 to 850°C, and for oxygen concentrations of 21 to 6%. Again, the sensor used was a fully sealed pump-gauge without glass sealing, operated in the sensor test-rig. Gases were prepared from mass flow valve mixing of bottled nitrogen and compressed air.

Similar experiments have been performed by Kaneko et al [61], these showed that the dominant leakage mechanism was that of electrochemical leakage. To assess whether the same was true for plastic ceramic devices, the effects of electrochemical leakage were examined. This was investigated by the connection of the internal electrode to two 4mm^2 platinum cermet leakage electrodes applied to the outside of the sensor. Recovery tests were performed with one or both of these connected at temperatures of 700 to 850°C in air. Application of leakage electrodes was by painting followed by a firing at 1000°C for 10 minutes to cure the paste. Electrode connection wires were adhered to the electrodes during the curing process. Leakage electrodes were brought into play by short circuiting to internal electrode connection leads.

To reduce electrochemical leakage, recovery tests were also performed with areas of the sensor coated in glass paste and fired at 800°C for 10 minutes. This should have had the effect of eliminating leakage three phase boundaries and blocking physical leakage pores in the vacinity. The tests were performed from 700 to 800°C in air with the leakage electrodes disconnected. Glass was applied and tests performed firstly to just the area where the internal electrodes emerge to minimise electrochemical leakage, then to the whole of the outside ceramic where the ceramic discs join to seal physical leakage.

E3 H_2O / CO_2 sensing

E3.1 H_2O measurements

To investigate the effects of H_2O and CO_2 on sensor operation, measurements were taken from a split electrode sensor using the humidity test rig (see section C1.3.2 for details). A split electrode sensor was used as this device allowed measurements to be taken at points well within the sensor thus minimising disturbances (see section E1.4). The LabView / DAQ system was used for recording measurements of pump potential, pump current and the three gauge EMFs. The pump potential was ramped from 0 to 2 V using 0.1 V steps and a 60 s stabilisation time between step and measurement. Three variations of experiments were performed as described below.

- Oxygen variation tests were performed at 800°C in oxygen atmospheres of 21-2%. These gases were passed through water columns at 40°C before feeding the test-rig.

- Temperature variation tests used air passed through water at 40°C. Temperature was varied from 650 to 900°C in steps of 50°C.

- Humidity variation tests were performed at 800°C with air passed through the water column at temperatures from 25-57°C giving moisture contents from 21 to 2 mol%. In order to achieve 2 to 0.4 mol%, a humidified air stream was mixed with one dried by passing through a $CaCl_2$ column.

Gas molar contents of water were calculated by assuming 100% saturation of the gas stream to obtain moisture content in Kg/Kg from a psychrometric chart. Relating the relative atomic masses of air (21% oxygen in nitrogen) to that of water, enabled a conversion to mol%. In these tests CO_2 was present in the air in small amounts, however, as reported by Yamazoe & Miura [16], CO_2 can be removed from gas streams by washing with water. No specific CO_2 measurements were taken in this work

E3.2 CO_2 measurements

To compliment the experiments performed with H_2O, a similar set of experiments was undertaken using CO_2. The experimental set-up was simplified by the gaseous nature of CO_2, allowing bottled gas to be mixed directly with bottled oxygen and nitrogen using the mass flow valves. Oxygen and nitrogen gases were mixed to give 21% oxygen to which the CO_2 was added. Heated gas lines, spray removal and water bath were therefore redundant. The column of $CaCl_2$ was used as a precaution to remove atmospheric moisture from the test gases. Gases were mixed using various combinations of 150, 100, 75, 10 and 5 ml/min flow valves to attain maximum flow rates at the desired composition. The calibration data sheet accompanying the flow valves indicated that no conversion factor was required to allow for the thermodynamic properties of CO_2. The concentration of CO_2 obtained was calculated by dividing the flow rate of CO_2 by the combined flow rate of O_2, N_2 and CO_2 to give a reading of mol% CO_2. Data were again collected using the LabView / DAQ system to store pump potential, pump current and the three gauge EMFs from the same split electrode sensor as used for H_2O work. Results were recorded for pump potentials of 0 to

2.5 V using 0.1 V steps with a 60 s stabilisation time between adjustment and measurement of parameters.

In the first set of experiments the temperature of operation was set at 800°C and coneentrations of CO_2 were varied from 24 to 0.06%, leaving at least 30 min between re-setting gas mixtures and taking readings.

In a second set of experiments the gas concentration of 2.566% CO_2 was maintained for measurements at temperatures of 700, 750 and 800°C using the systems detailed above.

APPENDIX F

SENSOR EVALUATION

RESULTS & DISCUSSION

F1 Amperometric tests

F1.1 Plastic-ceramic fabrication

The plastic-ceramic technique of sensor fabrication was substantially simpler and therefore faster with accompanying cost savings compared to that of the gold or glass seal conventional methods. The resulting devices were robust with no mechanical seals to deteriorate or fracture since the entire device was fabricated from one material with no thermal expansion mismatches to contend with. The only disadvantage to this technique was that the interior electrodes had to be subjected to the high temperatures required for ceramic sintering. This does lead to a certain degree of electrode sintering, reducing the vital three phase boundary length with detrimental effects on low temperature performance. The plastic–ceramic fabrication technique has been demonstrated to produce well defined and characterised sensors [87]. A comparison of similar sensors produced via this method (fig. F1) indicates a degree of reproducibility that may be further improved by technique refinement.

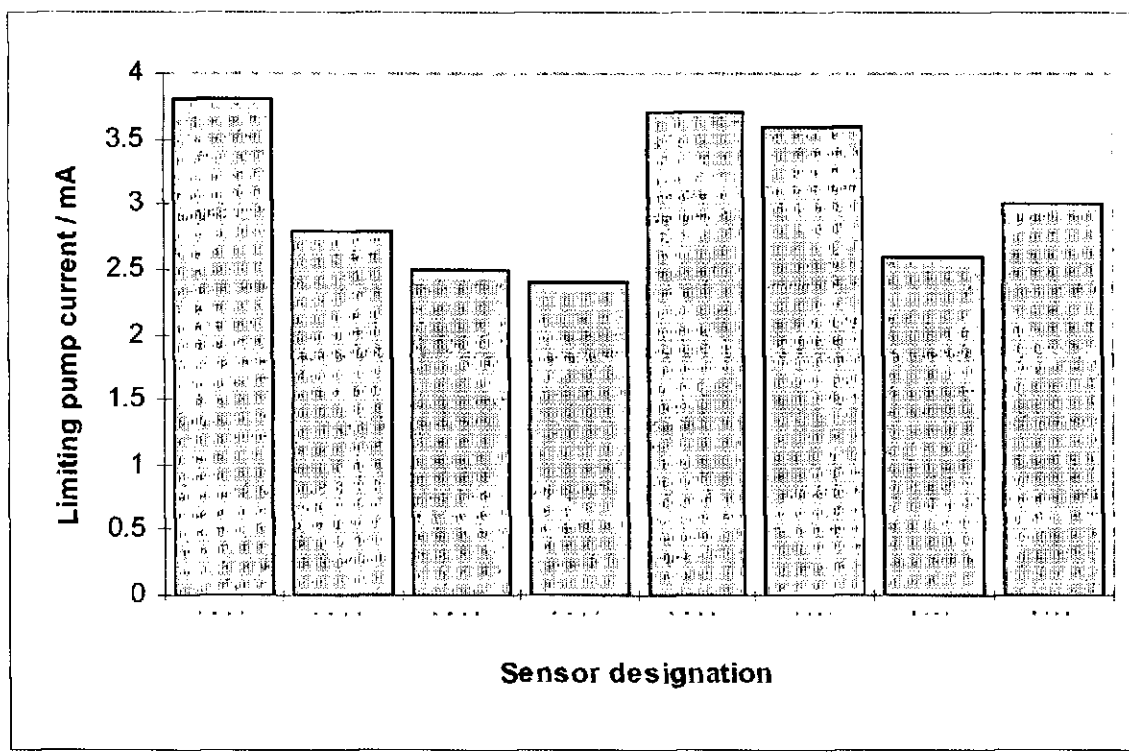

Figure F1 Sensor reproducibility chart

This chart shows the reproducibility of limiting current levels for separate sensors fabricated to similar geometrical dimensions. Although some sensors had four electrodes whilst others had two, this does not show any appreciable effect on the sensor output. The limiting current levels were measured at 800°C in air. The sensors used were made from various consignments of similar ceramic over a period of 3 years. Analysing these results we see a standard deviation σ on the limiting currents of $\sigma = 0.571$ on a sample mean of 3.05 however the sample size is too small and the fabrication too uncontrolled for this to give anything but an approximate idea of sensor reproducibility using this method. By careful control of fabrication conditions and procedures this standard deviation is likely to reduce significantly. No similar figures have appeared in the literature for similar studies on conventional amperometric zirconia sensors.

F1.2 Two electrode sensors

Figure F2 shows current / voltage curves for one single sensor operated between 450 and 800°C in atmospheres of 21 to 3.5% oxygen in nitrogen. These results gave a clear indication of sensor performance showing good characteristics with flat limiting current

plateaux attained to temperatures as low as 600°C. Below this temperature electrode kinetics began to slow with electrolyte impedance becoming too high for a diffusion limiting current situation to be obtained at 21% oxygen, at 3.5% however a limiting current plateau could be obtained as low as 500°C. Clearly the operation temperature can be lowered by increasing the restriction of gas diffusion placed by the diffusion barrier. With this sensor for example, at 450°C a current of 220 μA was obtained at a pump potential of 1 V. Theoretically a diffusion barrier with S/L ratio of 1×10^{-6}m would have allowed a detection limit of 21% oxygen at this temperature compared to 2×10^{-5} m used here. Employing a diffusion barrier with this order of diffusion barrier would bring this sensor into the same operating range as the Fujikura sensors which are suspected to utilise a laser drilled diffusion pore. Raising the pump potential would also have the effect of extending the measurement range at reduced temperature but with the danger of H_2O/CO_2 dissociation affecting the measurement.

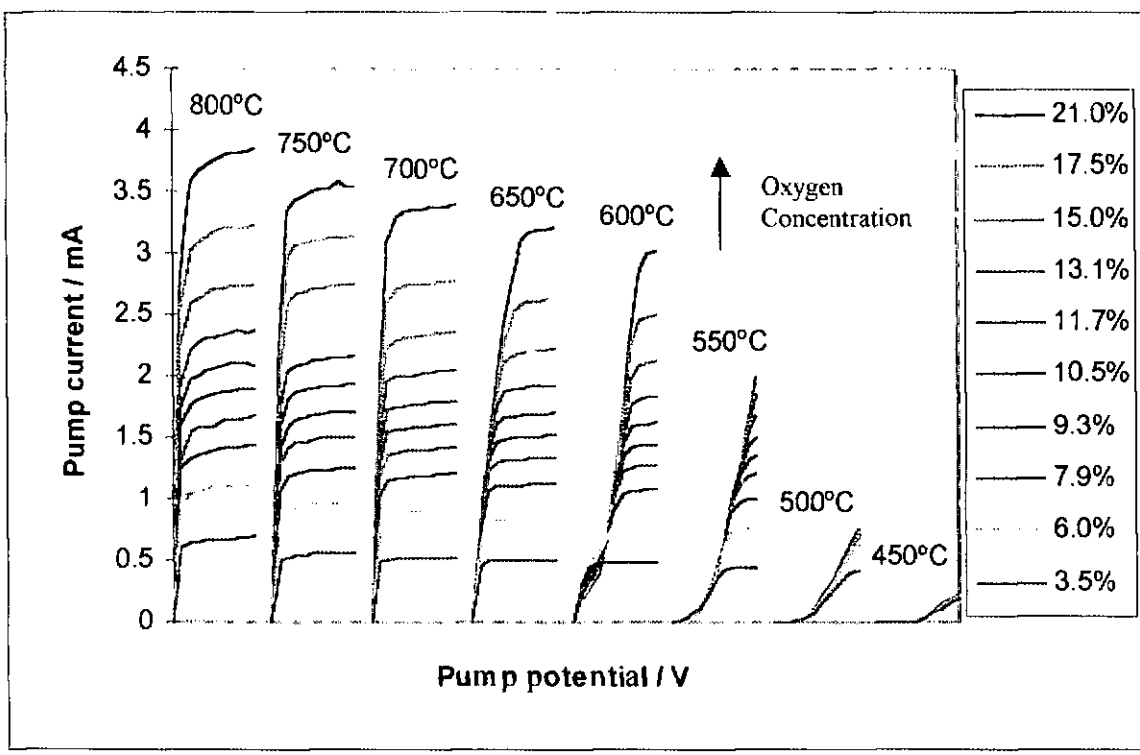

Figure F2 Temperature dependence of sensor current / voltage curves.

Usui [88] pointed out that by re-arranging Fick's law of diffusion we should see that the limiting current attained at a temperature is proportional to $-\ln(1-X_{O2})$. It should be noted that at low oxygen concentrations the logarithmic term linearises and $-\ln(1-X_{O2})$ approximates to X_{O2}. Using data from the above tests, we see that this theory held with practice where limiting currents were attained (fig. F3) This agreement is demonstrated by the straight line plot passing through the origin and with a gradient returning the value of 4FDP/RTL.

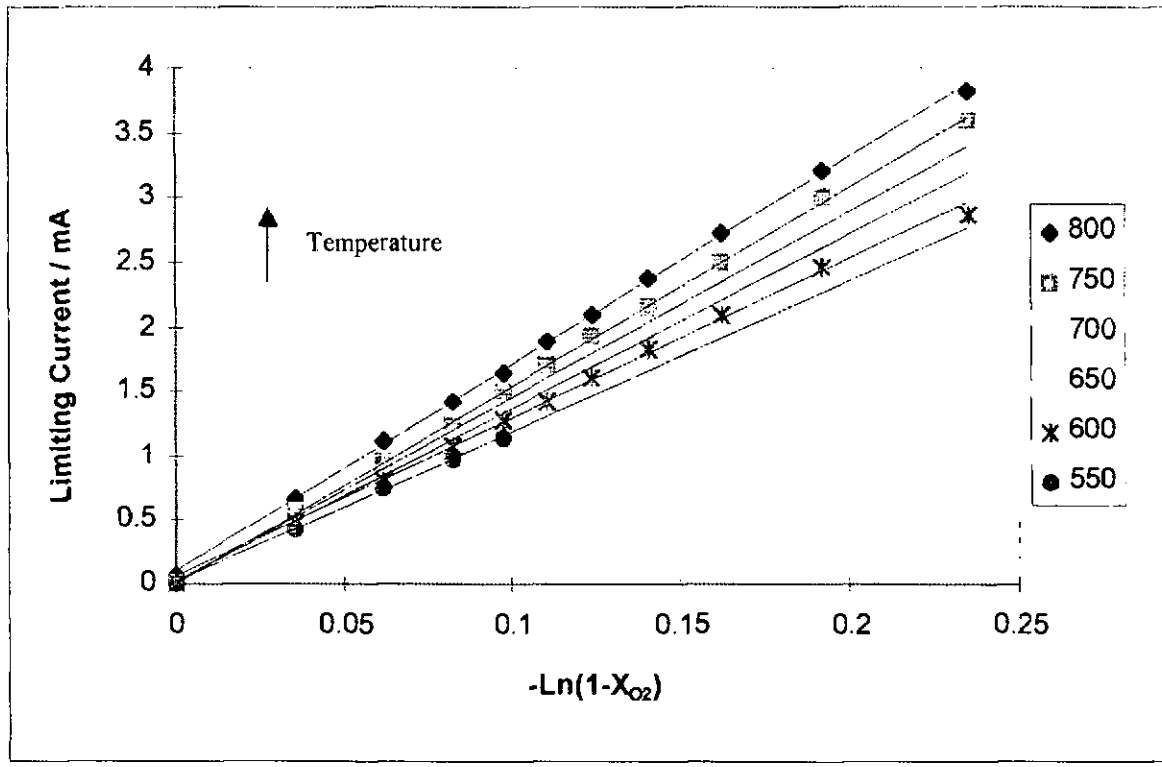

Figure F3 Limiting current characteristics

Amperometric type sensors are known not to be particularly sensitive to temperature, however the temperature dependence that does exist is determined by the temperature coefficient. The temperature coefficient of amperometric sensor operation is determined by both the T term in Fick's law and also by the temperature constant of the diffusion coefficient (α). A value for α has been obtained from literature [130] of 1.75. This value may also be measured directly from the temperature characteristics of the sensor. Usui & Asada [88] analysed the temperature dependence of amperometric zirconia sensors and found good agreement with theory with α=1.73. This was obtained by plotting log (I_{Lim}) versus log(T_k). Alternatively by plotting the log(slope of limiting current / oxygen concentration) versus log(Tk) we get a line of slope β where $\beta = \alpha - 1$. This is in effect the same plot as that of Usui et al but uses data acquired from all oxygen concentrations to obtain a more accurate figure. This plot is shown (fig. F4) and returns an α value of 2.25. The origin for the disagreement between the literature and this value has not yet been ascertained. Possible sources included physical leakage, electrochemical leakage, semi-permeability or ceramic thermal expansion.

The effects of thermal expansion were examined using the expansion coefficient developed by Terblanche's work [20] (see section 1.2.2.1) of 1.04×10^{-5} K^{-1}. Using this coefficient to calculate the change in dimensions of both diffusion barrier area and length we get a change in S/L from 1.919×10^{-5} at 800°C to 1.915×10^{-5} at 550°C. This change is insignificant in attempting to explain the apparent deviation in temperature coefficients.

The explanation of leakage effects has also been investigated in the work presented in section F2. This also failed to identify the cause of the deviation as leakage rates are shown to be small.

Deviations were also seen by other workers. Saji et al [10] found a value for β of 0.375 indicating that temperature dependence of the diffusion coefficient in a porous diffusion layer is smaller than that in bulk gas. Maskell & Steele [57] obtained a temperature

coefficient of $\beta = 0.95$ using a four electrode amperometric sensor with a laser drilled diffusion pore and gold seal.

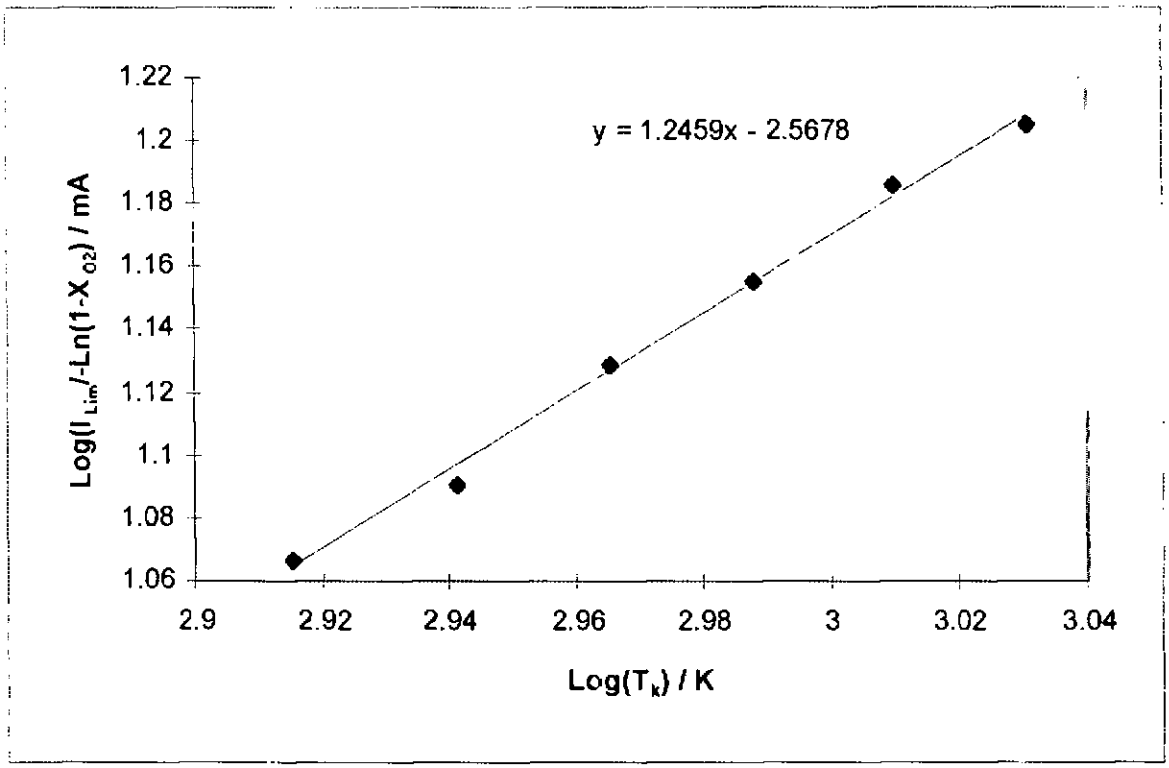

Figure F4 Temperature dependence of current limit

F1.3 Four electrode sensors

The use of double cell, four electrode amperometric sensors gives the benefit of combining amperometric and potentiometric cells in one device to aid the understanding of sensor operation. The output from such as sensor is shown in figure F5. This figure shows pump current and gauge EMF for a range of oxygen concentrations at 800°C. Both pump current and gauge voltage were seen to plateau upon applying a pump potential. The explanation of this is that as oxygen was pumped from the internal cavity of the device, the internal partial pressure dropped and was recorded as a Nernst potential using the gauge cell. As current limiting was achieved, so the partial pressure differential ceased rising and the gauge voltage also stabilised.

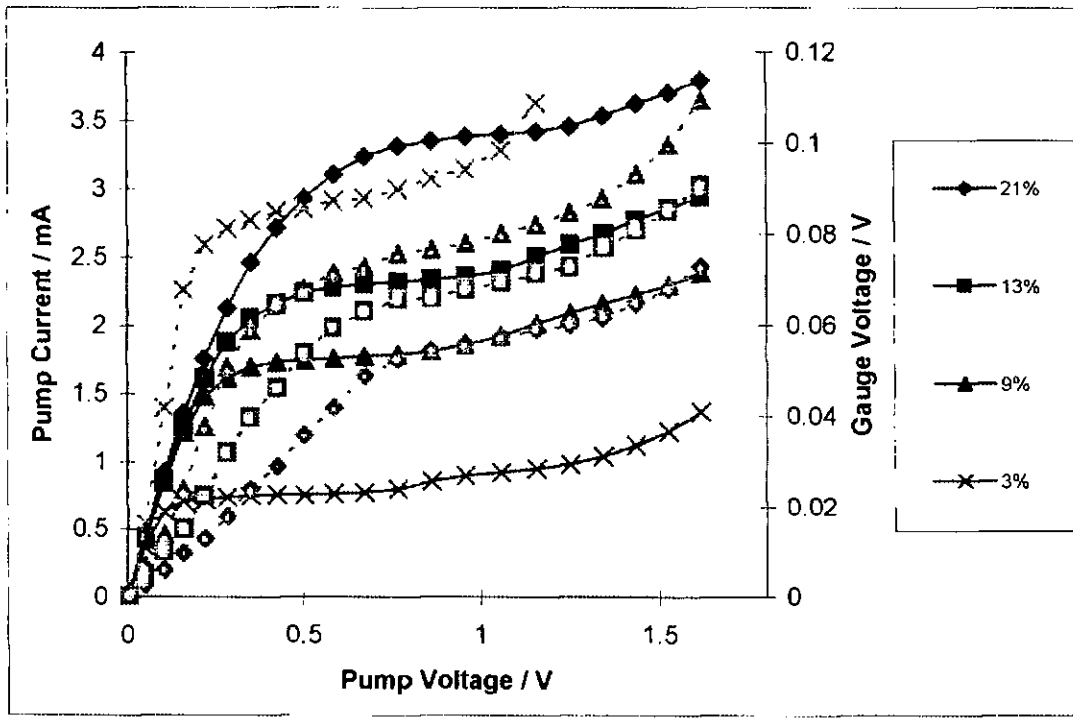

Figure F5 Characteristics of an amperometric sensor employing both pump and gauge cells (Pump current = solid lines, Gauge EMF = dashed lines))

These gauge EMFs allow us to calculate the average internal oxygen concentration within the sensor using the Nernst equation. This calculation using the equation in the form $P_1=P_2$ exp(-4FE/RT), where E is the gauge cell EMF. This data is shown in figure F6 and gives a good indication of the oxygen gradient across the diffusion barrier.

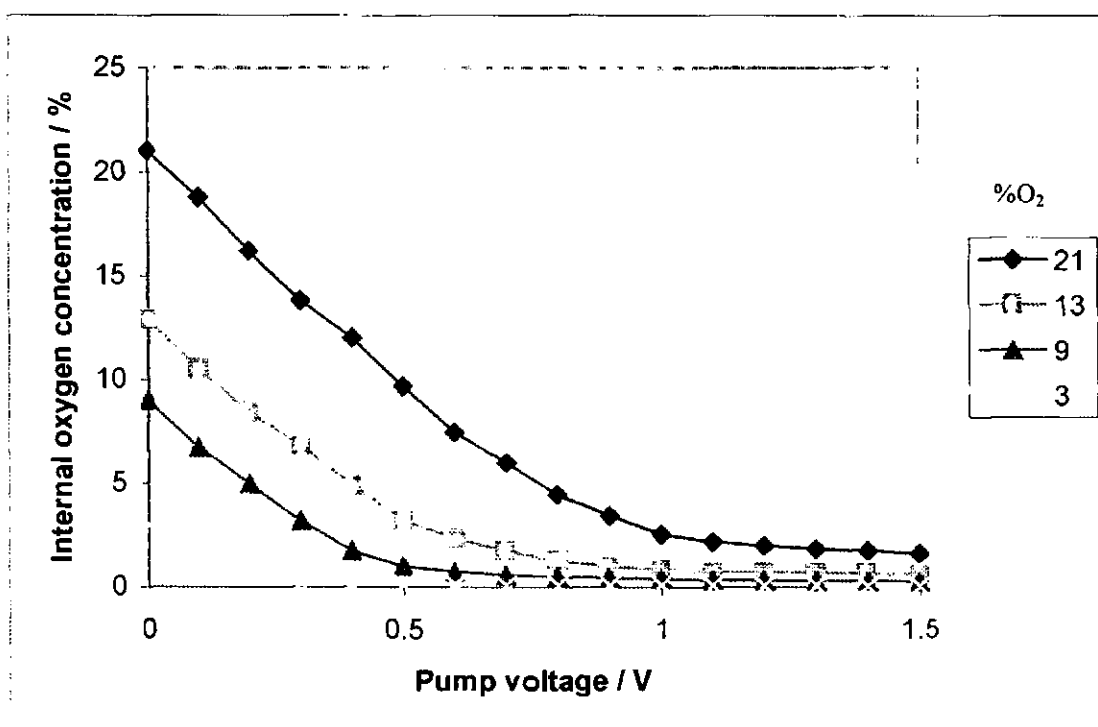

Figure F6 Calculated internal oxygen concentrations

Amperometric device limiting currents are subject to error as a result of electrochemical leakage. This error may be eliminated using the following technique:

By equating the limiting current equation derived from Fick's first law:

$$I_{lim} = 4FDSP/RTL \qquad \text{Equation F1}$$

with the expression Nernst equation we see that

$$I = -I_{lim} \times \exp(-4FE/RT) + I_{lim} \qquad \text{Equation F2}$$

If we now plot pump current against exp(-4FE/RT), we obtain a linear plot with an intercept and gradient indicating the true limiting current (fig. F7). This is achieved by extrapolating the rate of internal partial pressure reduction to zero thus using data from lower pump potentials where electrochemical leakage is less influential. This sensor can therefore provide more accurate information of the limiting current by separating physical leakage mechanisms from electrochemical leakage.

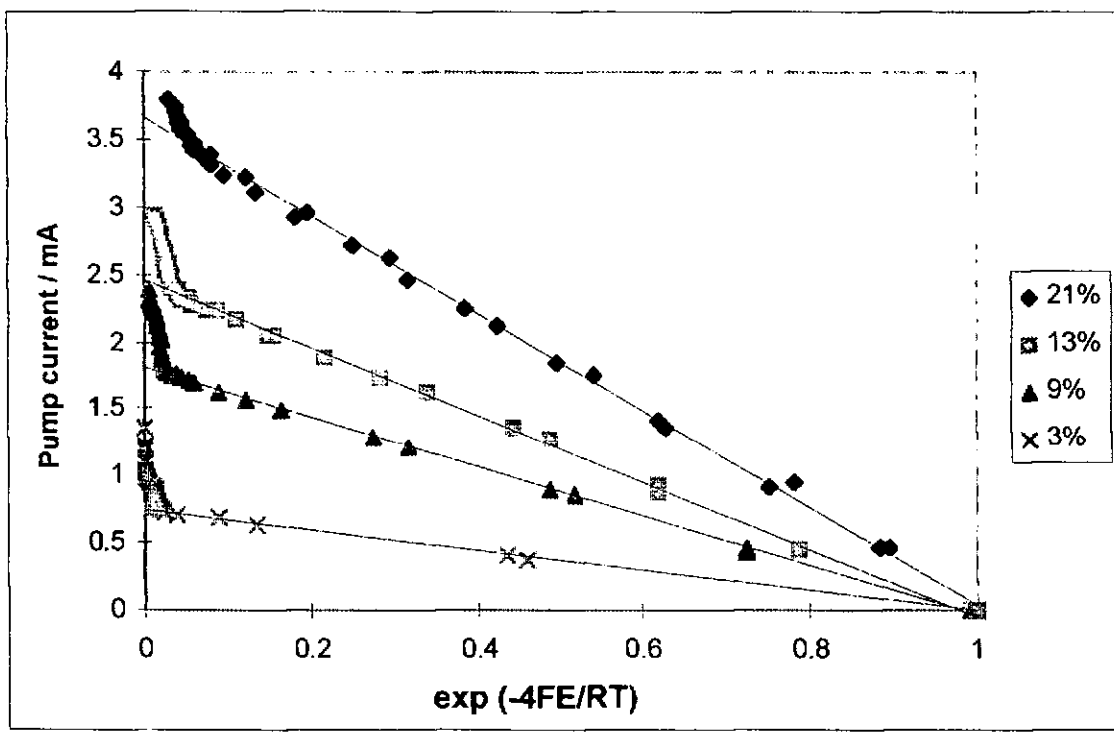

Figure F7 Exponential plot indicating electrochemical leakage

The benefits of this can be clearly seen if we overlay the results of the intercepts of this exponential plot with those of the limiting current taken at 1 V as in figure F8.

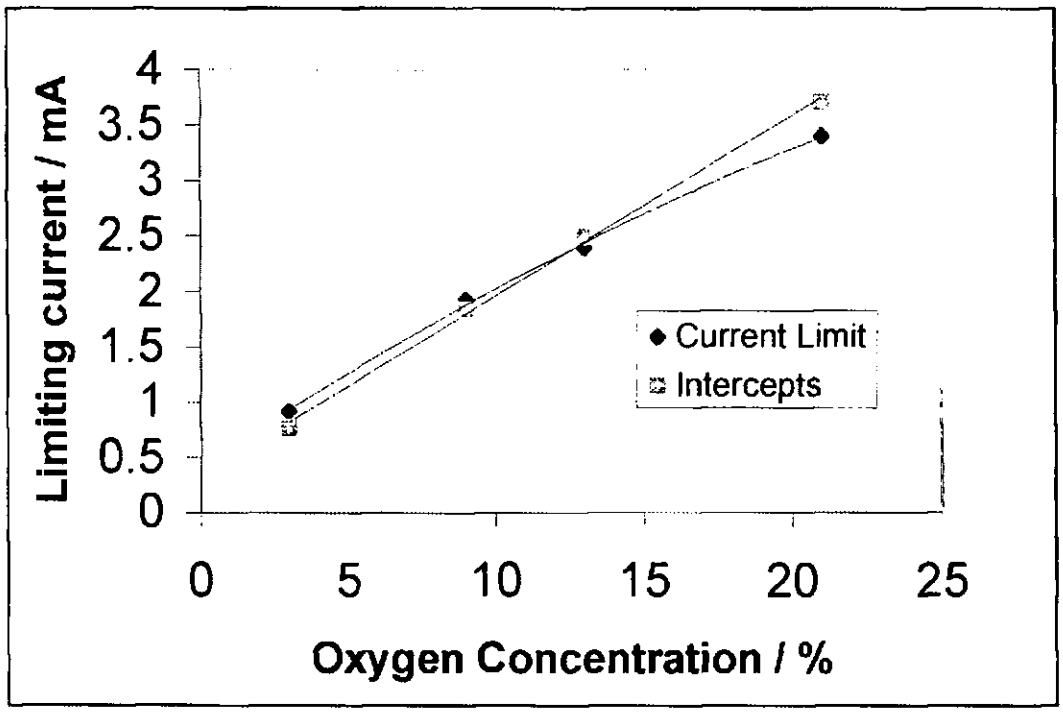

Figure F8 Overlaid results of limited current and exponential extrapolation plots.

In Figure F8 we see a deviation from linearity of the current limits, this is due to non-physical leakage mechanisms. This method has the additional advantage that the limiting current need not be attained for a measurement of oxygen level since the linear plot allows extrapolation. This may be exploited where electrolyte resistances prevent the diffusion limiting from being reached. Maskell & Steele [57] used an amperometric sensor with an additional pair of electrodes to obtain additional information for device characterisation. They used a plot of pump current versus exp(-4FE/RT) to eliminate non-physical leakage effects from the measurements. A substantial leakage was seen which resulted in limiting plateaux that were not flat. Their devices were fabricated from FSZ employing a gold seals and laser drilled diffusion pores with platinum sputtered or paste electrodes.

F1.4 High oxygen concentration measurement

The 4 electrode sensor proved particularly useful for deriving a limiting current where a large degree of non-physical leakage was present. At high oxygen partial pressures however, a large degree of curvature has been observed (fig. F9). Maskell & Steele [57] also reported a deviation from linear characteristics at high oxygen concentrations in a four electrode amperometric device. Dietz [86] created devices with small diffusion barriers by burning out a carbon track. These were able to obtain a limiting current up to 80% oxygen but lost proportionality above 40% oxygen. Usui et al [92] on the other hand, achieved sensor operation form 0 to 95% oxygen at 400°C using a two electrode amperometric sensor with no indication of deviation using a 30 μm diameter diffusion barrier and 1 mm length.

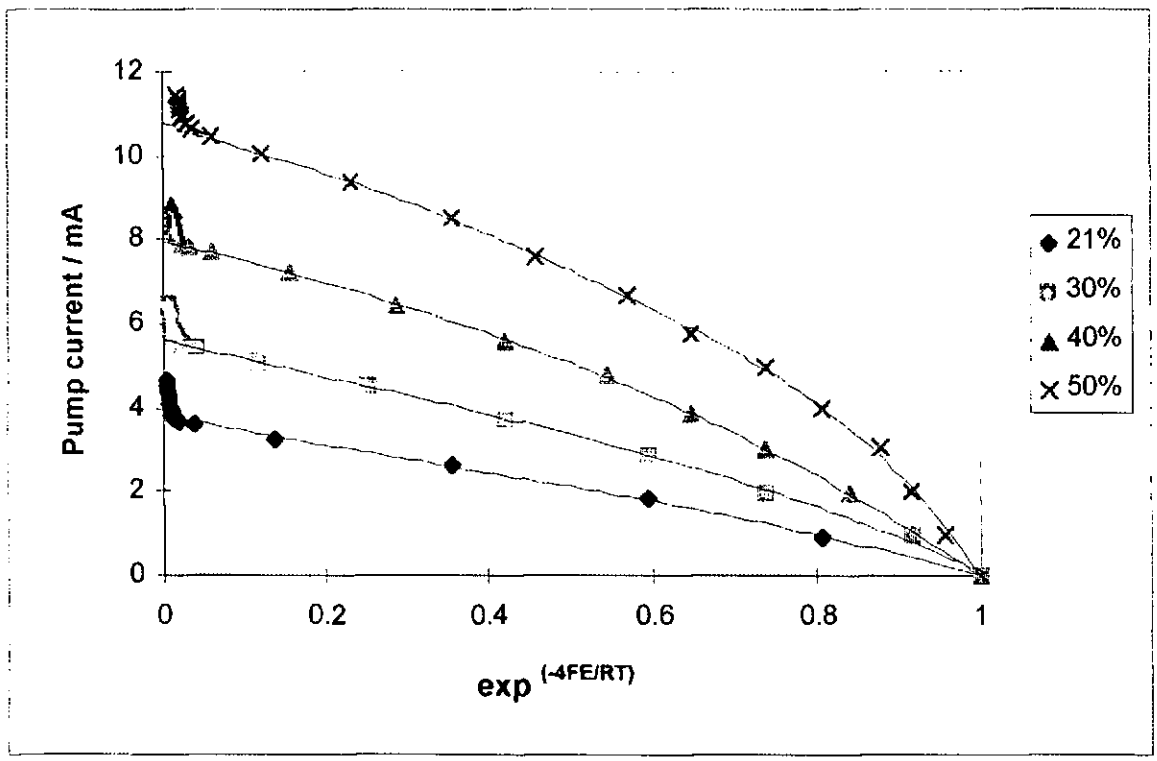

Figure F9 Exponential plot at high oxygen partial pressure

Assessing the assumptions made in developing these theories, the curvature was identified as deriving from the breakdown of these assumptions. The following work was carried out to develop a new theoretical expression that holds for four electrode sensors operated at high oxygen partial pressures.

For the new theory the starting point was taken from Usui et al [92], the equation for oxygen flux due to both diffusion due to partial pressure differences and gas flow due to the extraction of gas via pumping. It is assumed that barometric pressure gradient across the pore is negligibly small.

$$J_{O2} = -DA\frac{dc}{dx} + X_{O2}J_{O2} \qquad \text{Equation F3}$$

where J_{O2} is the oxygen diffusion flux, DA is the diffusion coefficient of the gas mixture, c is the molar oxygen concentration and x is the molar fraction of oxygen This equation is rearranged and the term c replaced according to the ideal gas equation where c = n/V = P/RT.

$$J_{O2}(1 - X_{O2}) = -\frac{DA}{RT}\frac{dP}{dx} \qquad \text{Equation F4}$$

J_{O2} is now replaced with I/4F according to Faraday's law, and integrated with respect to x between the limits of external and internal mole fractions.

$$\int \frac{IRTdx}{4FDAP} = -\int_{X1}^{X2} \frac{dX}{1 - X} \qquad \text{Equation F5}$$

This yields the following, however the constant can be seen to be zero by applying the zero current state : when I = 0 then X ≈ 0 (when the current flow is zero, there is effectively no

oxygen inside the sensor cavity) and therefore the constant = 0. dx is the diffusion length and is replaced by the barrier length.

$$\frac{IRTl}{4FDAP} = [\ln(1-X)]\frac{X2}{X1} + Const \qquad \text{Equation F6}$$

This may then be rearranged into the following form to give a general equation

$$I = \frac{4FDAP}{RTl}\ln(\frac{1-X_2}{1-X_1}) \qquad \text{Equation F7}$$

We now take the Nernst equation

$$E = \frac{4F}{RT}\ln(\frac{P_1}{P_2}) \qquad \text{Equation F8}$$

and rearrange and substitute $PX_n = P_n$ to obtain an expression for X_2

$$X_2 = X_1 \exp(-4FE/RT) \qquad \text{Equation F9}$$

then substitute this expression for X_2 in the general equation.

$$I = \frac{4FDAP}{RTL}\ln(\frac{1-X_1\exp(-4FE/RT)}{1-X_1}) \qquad \text{Equation F10}$$

This is then expanded into the form y=mx+c.

$$I = \frac{4FDAP}{RTL}[\ln(1-X_1\exp(-4FE/RT)) - \ln(1-X_1)] \qquad \text{Equation F11}$$

This shows that by plotting I vs. $-\ln(1-X_1 \exp -4FE/RT)$ we should get a straight line plot of gradient (4FDAP/RTL) and intercept of $((-4FDAP/RTL)(\ln(1-X_1))$ i.e. the limiting current

Below is the theory behind the original method for the low partial pressures. The equations were simplified in that the logarithmic term was be removed from the general equation which is valid only when X_1 is small.

$$X_1 \approx \ln(1-X_1) \qquad \text{Equation F12}$$
$$X_2 \approx \ln(1-X_2) \qquad \text{Equation F13}$$

$$I = \frac{4FDAP}{RTL}X_1 - X_2 \qquad \text{Equation F14}$$

The mole fractions and barometric pressure were then be combined to obtain partial pressures.

$$I = \frac{4FDA}{RTL}(p_1 - p_2) \qquad \text{Equation F15}$$

Next we use the Nernst equation to replace the unknown internal partial pressure with a term including gauge voltage

$$p_2 = p_1 \exp(-4FE/RT) \qquad \text{Equation F16}$$

$$I = \frac{4FDAP_1}{RTL}(1 - \exp(-4FE/RT)) \qquad \text{Equation F17}$$

The equation may then be expanded out into the form y=mx+c from which the accepted exponential graph is derived.

$$I = \frac{4FDAP_1}{RTL}(-\exp(-4FE/RT) + \frac{4FDAP_1}{RTL} \qquad \text{Equation F18}$$

These two theories were assessed by comparison of data obtained from a 4 electrode amperometric sensor at high oxygen partial pressures: 21%, 30%, 40%, 50% and 60% at 800°C. This data was examined using both theories and the resultant plots are given (figs. F9 & F10). These graphs show that the majority of curvature can be removed by utilising this new technique, and may be used even where partial pressures are too high for a limiting situation to be developed. This technique may have a possible use where operation temperatures are too low for a limiting current to be attained, yet, sufficient data are present for extrapolation to the limiting condition. An additional benefit of these analyses is that the higher pump potentials and therefore very low internal oxygen concentrations can be avoided which have been reported as detrimental to electrode and electrolyte ageing [21].

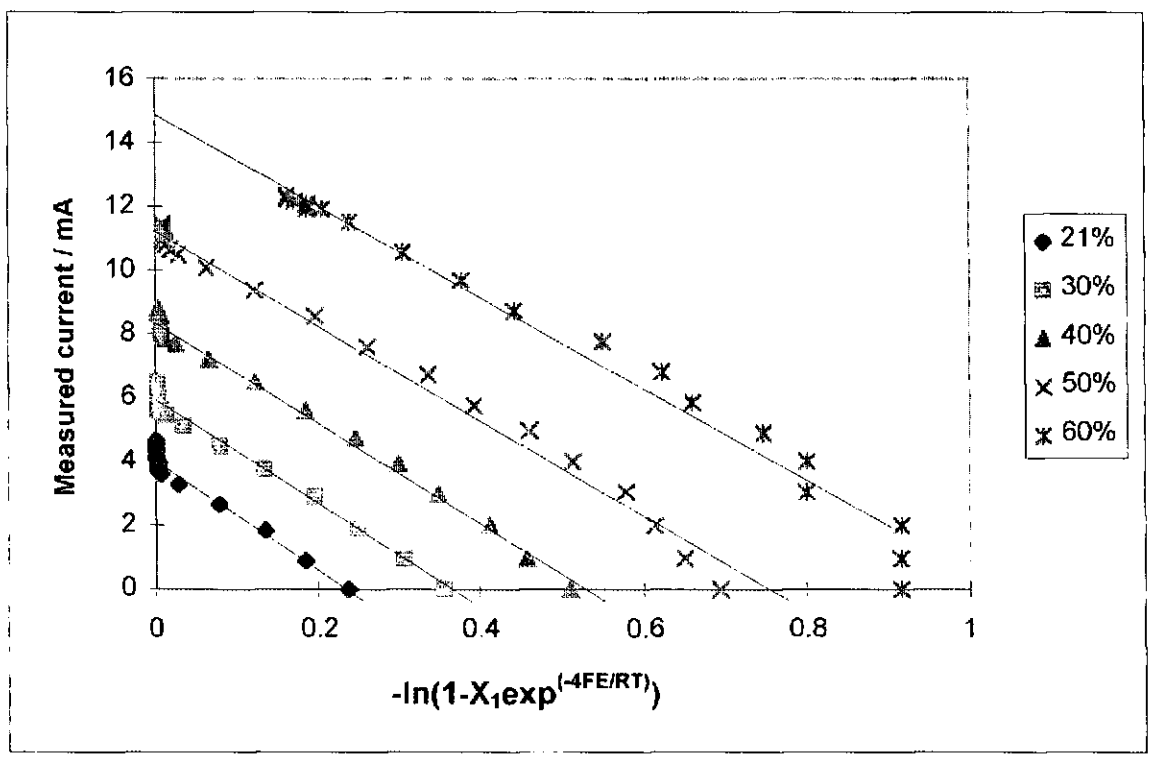

Figure F10 High partial pressure data plotted using new theory

Taking this analysis a stage further we see that the new theory returns similar slopes for each oxygen concentration. As stated these should return a value for -4FDAP/RTL. Since P here represents barometric pressure these should indeed be a constant for a constant temperature. The average slope of these lines is measured at 15.7 and compare very well to

a calculated value of this expression of 15.9. This good correlation helps to back up this new expression and gives added confidence in the method. A further test is to plot the values of the intercepts of this graph (the limiting currents returned) against the expression $-\ln(1-X_{O2})$ this again should reveal a straight line. The results of this plot are shown in figure F11. Again this gives a good straight line re-confirming the equations and returning a slope in agreement with that calculated above. The origin intercept is not quite zero showing a small positive offset. The data of this plot closely agrees with that obtained with the former method with the exception that a better linear fit is obtained at higher oxygen levels using the new theory. This appears to be a factor of the small remaining curvature on these graphs which do lead to a slight overestimation of limiting currents in each case.

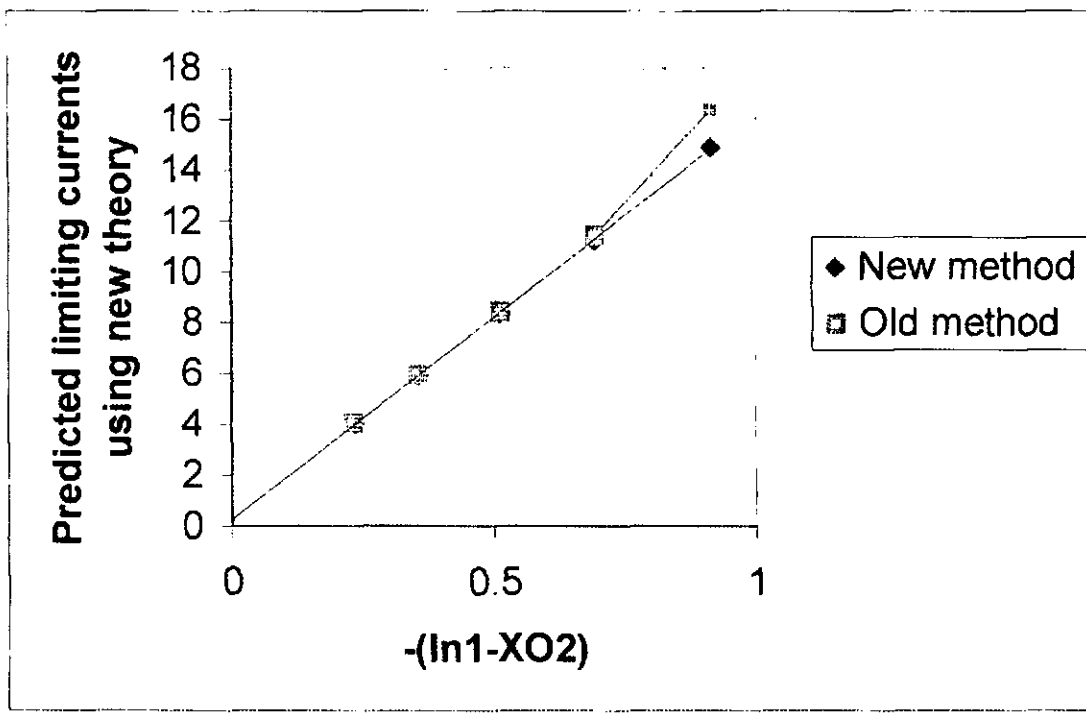

Figure F11 Predicted limiting currents versus $-\ln(1-X_{O2})$

F1.5 Split electrode sensor

The theory developed in section F1.4 went some way to explain the curvature obtained at high partial pressures. Whilst application of this theory did substantially improve linearity of plots, especially at higher oxygen concentrations, there was some degree of existing curvature. This was interpreted as a distribution of oxygen concentrations across the gauge cell resulting in a deviation from the idealised situation. To explore this idea split gauge sensors were developed and employed (section E1.4) with the intention of comparing internal oxygen concentrations near to the diffusion barrier to those remote from it. The results from such a sensor (fig. F12) supported this hypothesis, with the gauge near to the pore obtaining a far lower EMF than that of the further gauge. The graph shows results from a split electrode sensor operated in 10% oxygen at 800°C with the pump current drawn on the primary Y axis, the gauge EMFs on the secondary Y axis against pump potential on the X axis. The gauge EMFs shown are EMF1 = EMF of both gauges joined together, EMF2 = gauge furthest from the diffusion barrier, EMF3 = gauge nearest to the diffusion barrier. This clearly shows that the internal partial pressure decreased with increasing distance from the diffusion barrier. It would be possible in this manner to map out the partial pressure gradient using a multi-gauged device, in practice this is extremely difficult due to the device size.

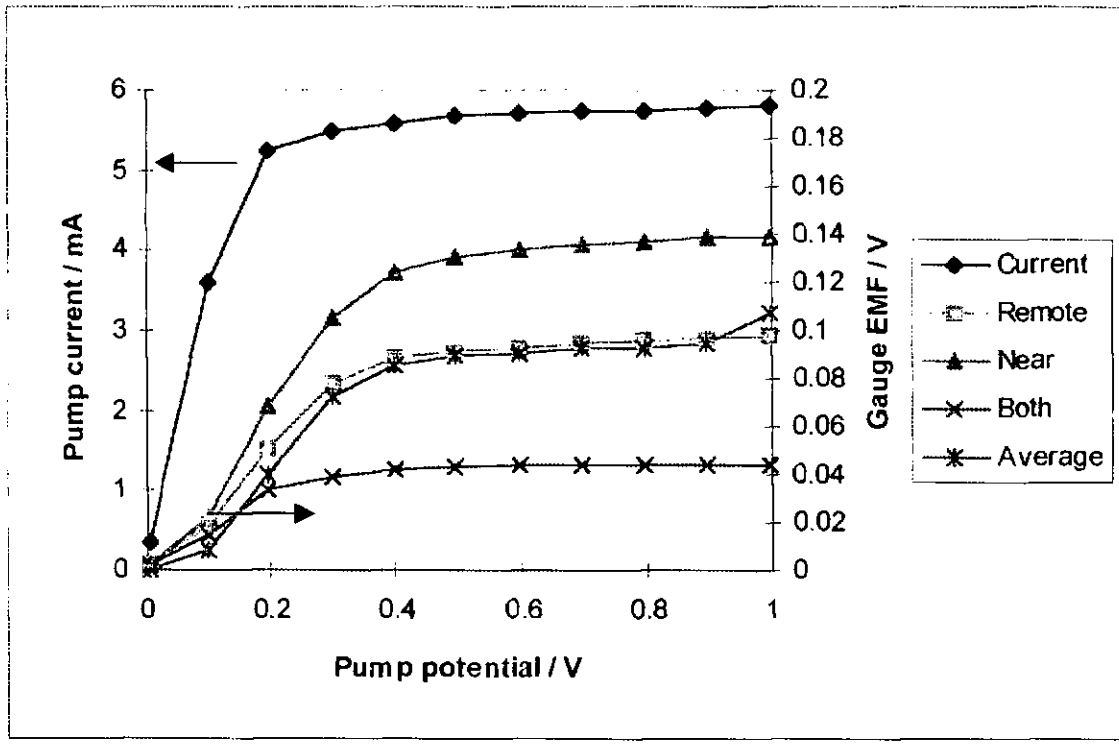

Figure F12 Gas distribution across the internal cavity investigated using a split electrode sensor.

An interpretation of these results is made by plotting the measured oxygen pressures at points along the sensor profile. The points are taken as approximate mid distances across the electrode active face and at points defined by the start and end of the diffusion barrier. The oxygen concentration at the external entrance of the diffusion barrier is assumed to be the same as that of the test atmosphere and the concentration just inside the sensor cavity to be a logarithmic extrapolation of the cavity oxygen decay profile. These are only approximate values as the sensor was not dismantled after testing for measurements to be taken and the accuracy involved does not warrant any detailed evaluation. This analysis however indicates that oxygen concentration along the diffusion barrier length is relatively constant but drops quickly inside the sensor across the cathodic electrode surface. This is an interesting result and perhaps worthy of further study employing a more intricate electrode array deposited using thick-film techniques to fully map out the electrode surface area. This may be followed by measurements involving high oxygen concentrations and the theory developed above for high oxygen concentrations.

The use of a multi-electrode gauge has not appeared in the literature to analyse oxygen gradients in a sensor. Copcutt et al [145] however, used a stack of solid oxide fuel cell discs to demonstrate the advantages of a ceramic felt packing. Fuel and air were fed to either side at the center of the SOFC discs and oxygen levels measured radially showing EMF drop with distance from the feed in point. The measurements showed a continually dropping oxygen gradient with a step where stoichiometric point was reached.

F1.6 Low oxygen ppm measurement

In many combustion systems, it is the oxygen levels in the exhaust that require monitoring. These oxygen levels are well below that encountered in atmospheric air. Maskell & Steele [1] reported that oxygen measurements at ppm levels can be very tricky using potentiometric sensors as the oxygen exchange current density is low and parasitic side reactions become determining. It is for this reason that this research includes an examination into the use of amperometric sensors in atmospheres containing 1% oxygen and less.

For measurement of oxygen levels at these lower concentrations, sensors with larger diffusion holes were employed. Details of fabrication and testing of these sensors have been presented in section E1.5. At the low oxygen concentrations employed, the current / voltage characteristics of each sensor gave typical amperometric sensor response with flat limiting current plateaux, the levels of which decrease linearly with partial pressure. The current / voltage curves for each large barrier sensor are shown in figure F13, demonstrating the limiting current plateaux for each sensor over a range of oxygen / nitrogen atmospheres. The sensors are identified by the diameter of diffusion hole (prior to sintering). Results of these tests have been backed up by those of project student (D.Tzempelikos) who repeated this work using similar sensors but with gas mixed using a purpose made dosing apparatus and an extended measurement range.

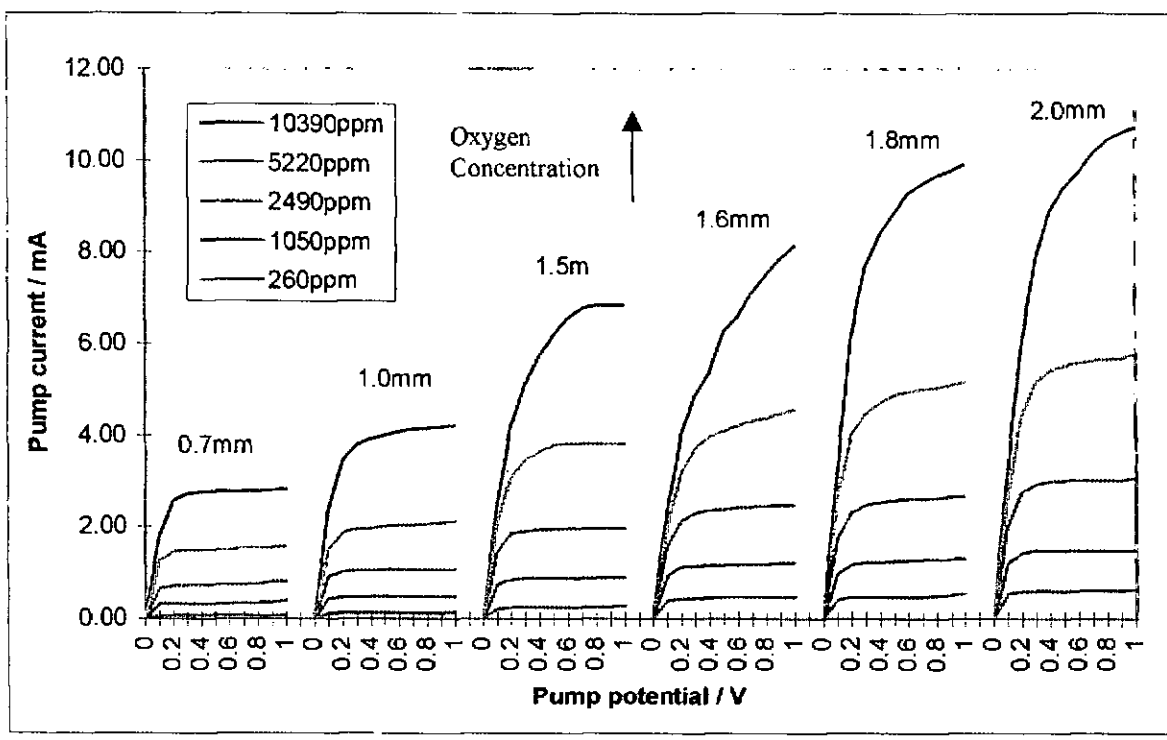

Figure F13 Current / voltage characteristics for sensors with large diameter diffusion barriers

As seen with the small barrier sensors, temperature has a relatively small effect on the oxygen concentration measurement, when compared with the dependence of potentiometric type devices. Limiting plateaux again increased with temperature due to the temperature effect on the diffusion coefficient, in conjunction with the temperature factor in Fick's law of diffusion. The temperature effect on diffusion coefficient has been determined (fig. F14) by calculating the slope of log(current limit / oxygen concentration) versus log (T_K) as previously proposed in section F1.2. This method returned a value of 2.06, comparing to 1.75 from literature and a value of 2.35 obtained for a small barrier sensor. Again the nature of this minor disagreement is unclear but as with previous work, non-physical leakage and thermal expansion of the diffusion pore can be ruled out. With these sensors, the magnitude of any other physical leakage sources would be small in comparison to that of the intentional diffusion holes due to their substantial S/L ratios ranging from 6×10^{-4} to 5×10^{-3} m.

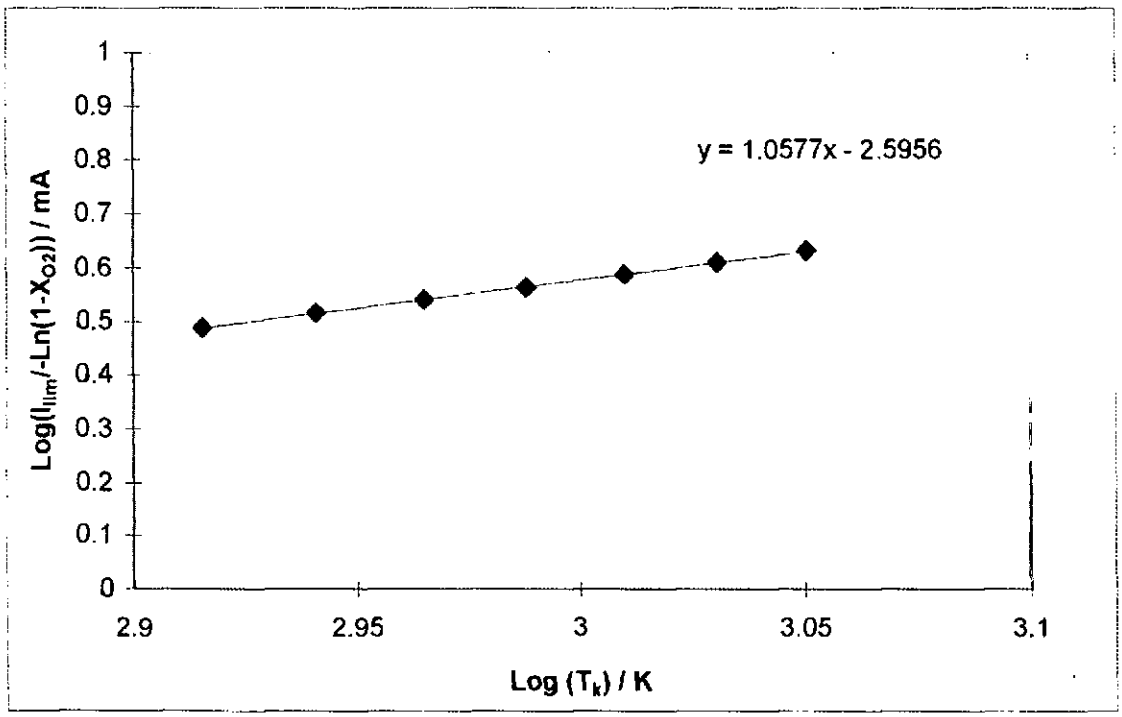

Figure F14 Temperature characteristic of large barrier sensors

A plot of limiting current versus oxygen concentration (fig. F15) shows linear characteristics for each of these devices. The intercepts of these plots indicate a small current was present at supposedly 0% oxygen. This current may have been partially due to electronic current arising through electrolyte semi-permeability, but following the results of D.Tzempelikos, seems more probably the result of a small oxygen leak into the test-rig. In his work he specifically investigated leakage rates through the plastic tubing and found that this could add tens of ppm of oxygen to a flowing nitrogen source. This would adequately explain the offset in my results that were obtained prior to this information.

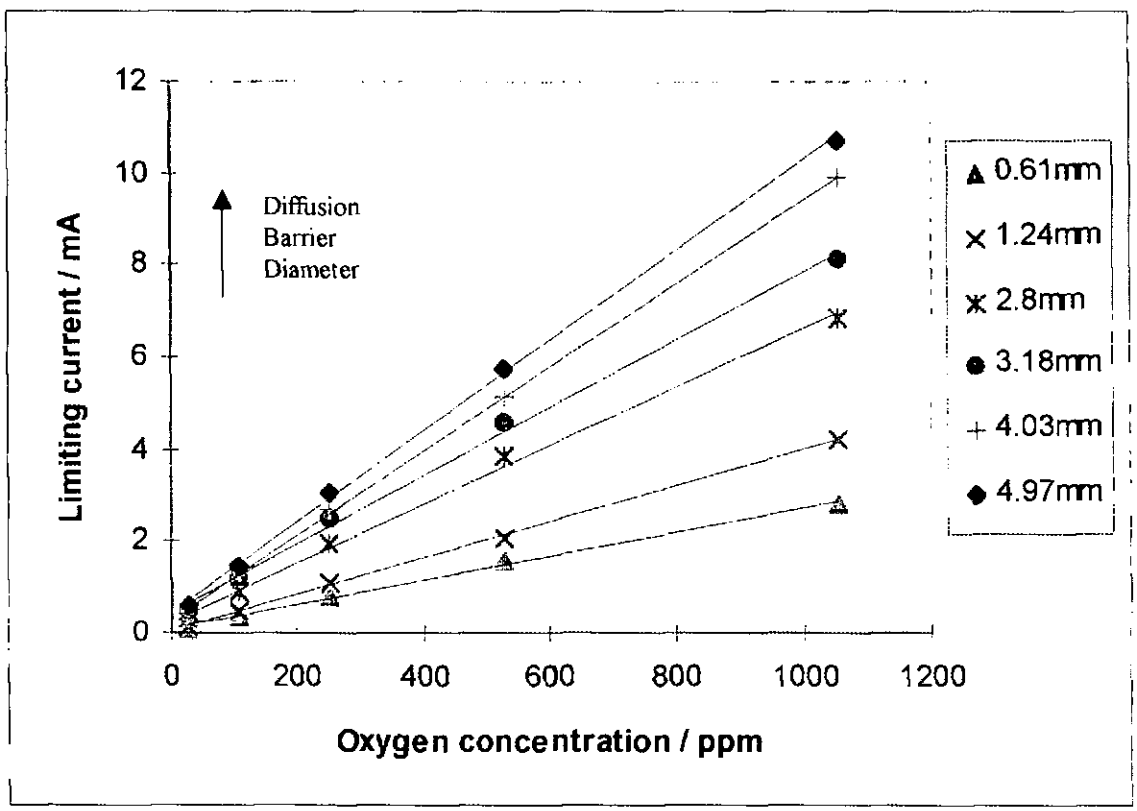

Figure F15 Limiting current characteristic with S/L ratio

The slopes of the lines from fig. F15 were plotted against the diffusion barrier S/L ratio (fig. F16), and should have, according to theory, given a slope of $4FD_0T_K^{\alpha-1}/RT_0^{\alpha}$. Taking F=96500, D_0=0.167, R = 8.134, α = 1.75, T_0 = 273 and T_K = 1073 we calculate a value of 2.25×10^{-3} A m^2 J^{-1} compared to a graph slope of 1.94×10^{-3} A m^2 J^{-1}. This is a small difference and implies that the diffusion rate calculations do hold for sensors with the large S/L ratios used in this work. The good agreement to a straight line also indicates that same mechanism is involved.

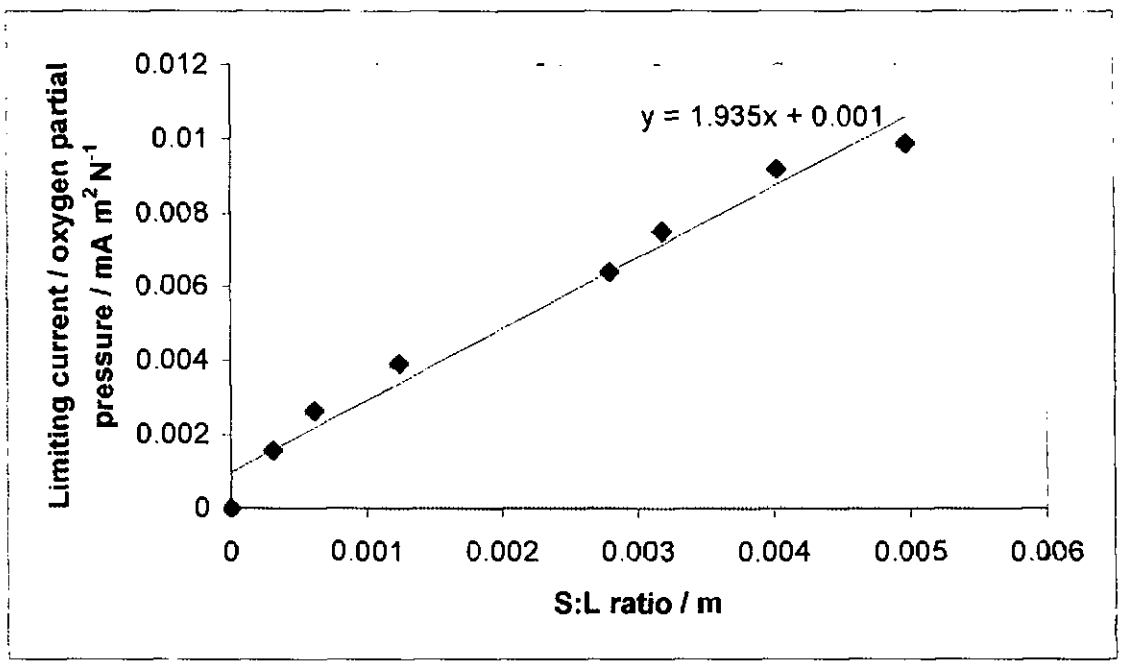

Figure F16 Limiting current slope versus S/L ratio

Another picture of this data is obtained by plotting the limiting current against barrier S/L ratio, at each concentration tested (fig. F17). Again a linear relationship is seen in agreement with theory. Although there does exists a certain degree of scatter around these lines, close examination shows, that for each S/L ratio, the scatter is in a similar position in relation to the trendline. This indicates that the scatter was due to diffusion pore tolerances and subsequent measurement rather than inaccuracies in limiting current measurement. S/L ratios were calculated from the drill size and ceramic shrinkage rather than actual pore measurement. Non-zero intercepts were again obtained. In fact by extrapolating the trend lines we get convergence at approximately S/L = -0.001 m. It is difficult to imagine how this could be accounted for. If on the other hand this was an effect of a leakage current through porosity or electrochemical leakage, a fully sealed device would display the same characteristic. This was seen not to be the case, a fully sealed device tested at 1% gave a current of only 0.2 mA at 1 V applied potential. Plotting the slopes from this chart against oxygen concentration, again returns a value for $4FD_0T_K^{\alpha-1}/RT_0^{\alpha}$ in agreement with the values obtained previously. This plot is shown in figure F18.

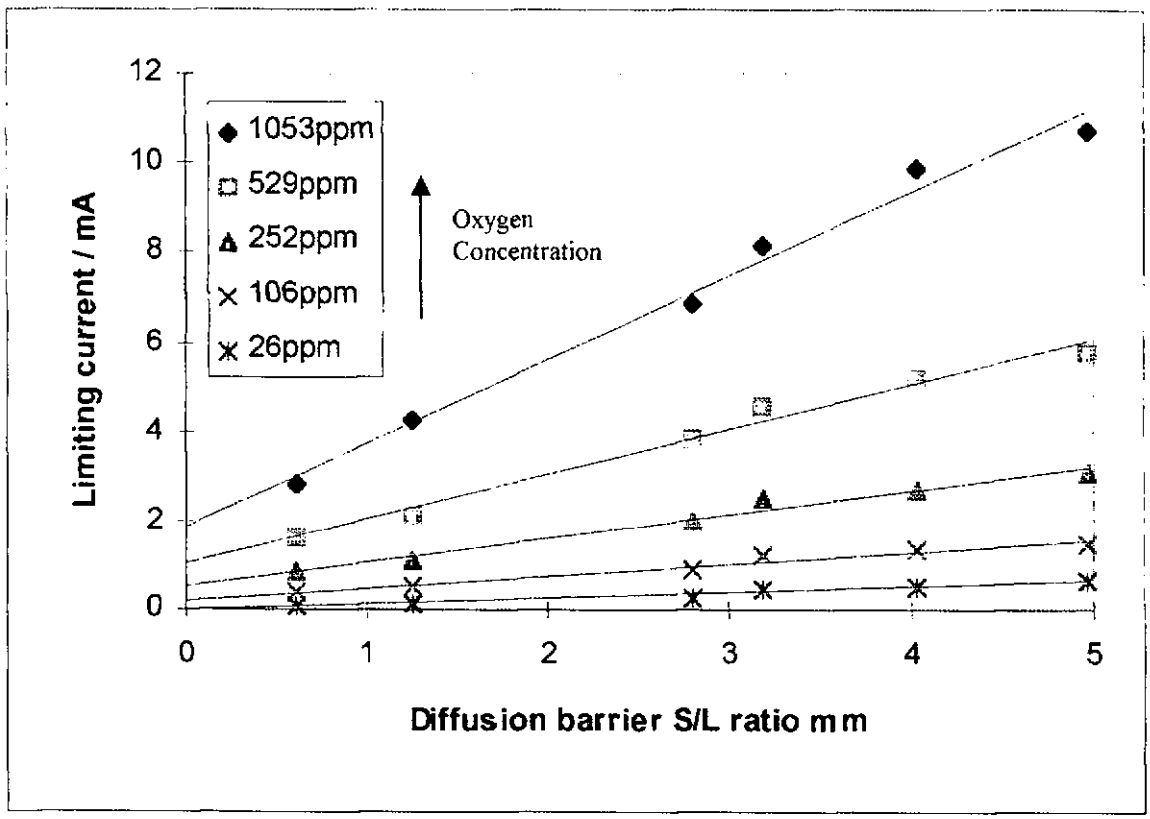

Figure F17 Limiting pump current versus S/L ratio plotted for each gas concentration

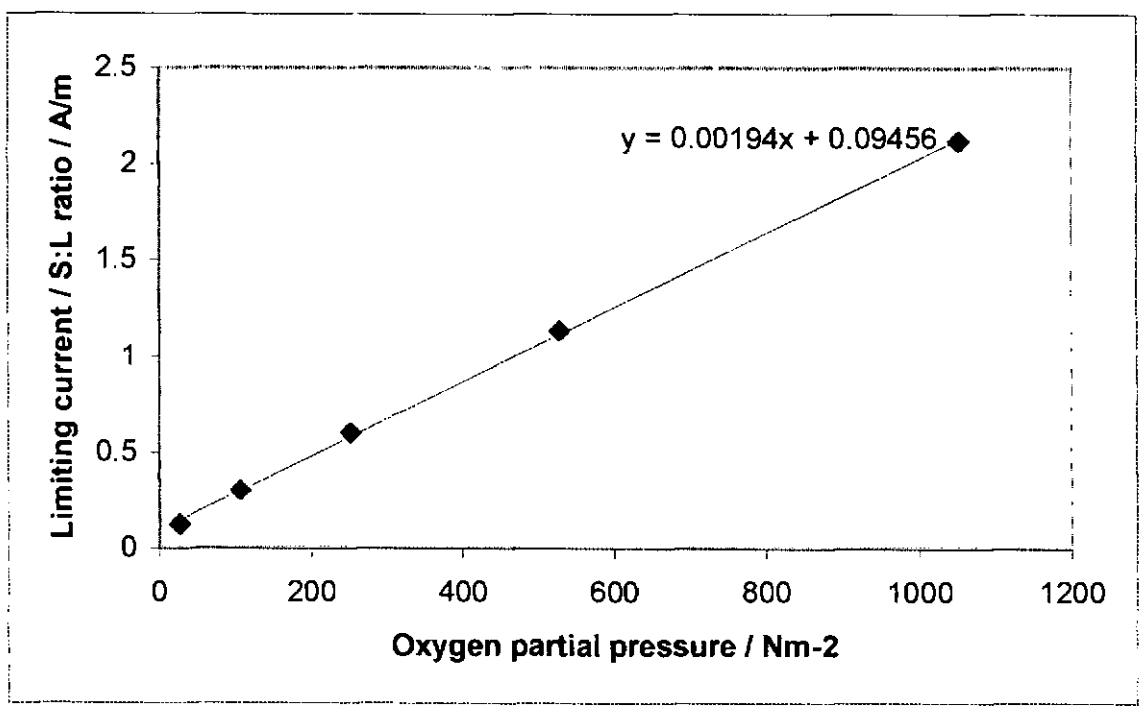

Figure F18 $I_{lim} \times L / S$ versus oxygen concentration

This does not point toward a large degree of porosity in the ceramic used in this work, scanning electron micrographs, density measurements and leakage examinations presented in later sections support this. Further evidence against this proposition is that a device made at the same time from the same ceramic but with no diffusion pore showed only a very small current (0.2 mA) at the highest oxygen concentration examined in this work.

In summary, this work has shown that sensors with large barriers can be easily assembled and used in the measurement of low oxygen concentrations. They have been shown to retain their linear characteristics with respect to oxygen concentration. However the behaviour of these sensors cannot be fully reconciled with Fick's first law of diffusion, the temperature coefficient needs further assessment as does the origins of non-zero intercepts for the plots.

To identify the areas of disagreement with the simple Fick's law of diffusion, this was rearranged to identify the plots necessary to return a straight line of limiting current versus temperature coefficient, oxygen concentration and S/L ratio.

$$I_{Lim} = \frac{4FD_0T_K^{\alpha-1}SP}{RT_o^{\alpha}L} \qquad \text{Equation F19}$$

Since F, D_0, R and T_0^{α} are constants:
$I_{Lim} \propto T_K^{\alpha-1}$ if S/L and P are constant
$I_{Lim} \propto P$ if $T_K^{\alpha-1}$ and S/L are constant
$I_{Lim} \propto S/L$ if $T_K^{\alpha-1}$ and P are constant

In accordance with the above, Figure F19 shows that S/L and P do remaining constant. Figure F20 shows that $T_K^{\alpha-1}$ and S/L do remaining constant. Figure F17 shows that $T_K^{\alpha-1}$ and P do remain constant for the data recorded as a set of linear plots is returned.

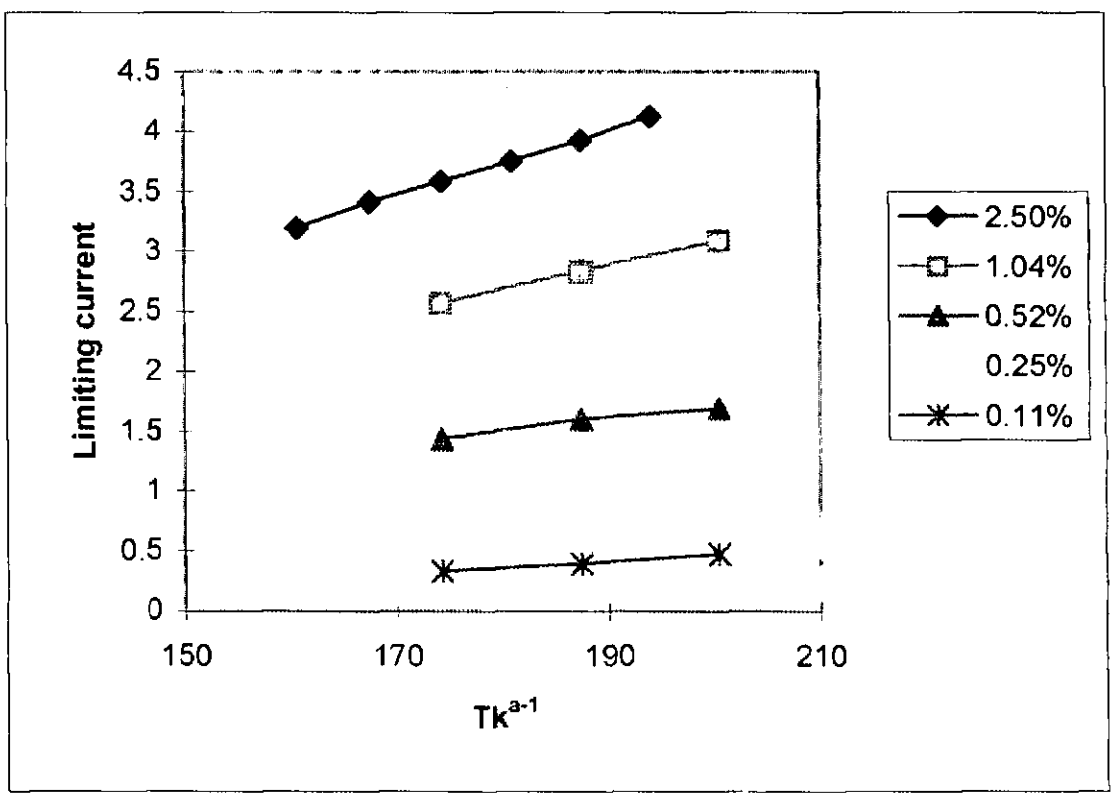

Figure F19 Limiting currents versus $T_K^{\alpha-1}$ with varying oxygen concentration

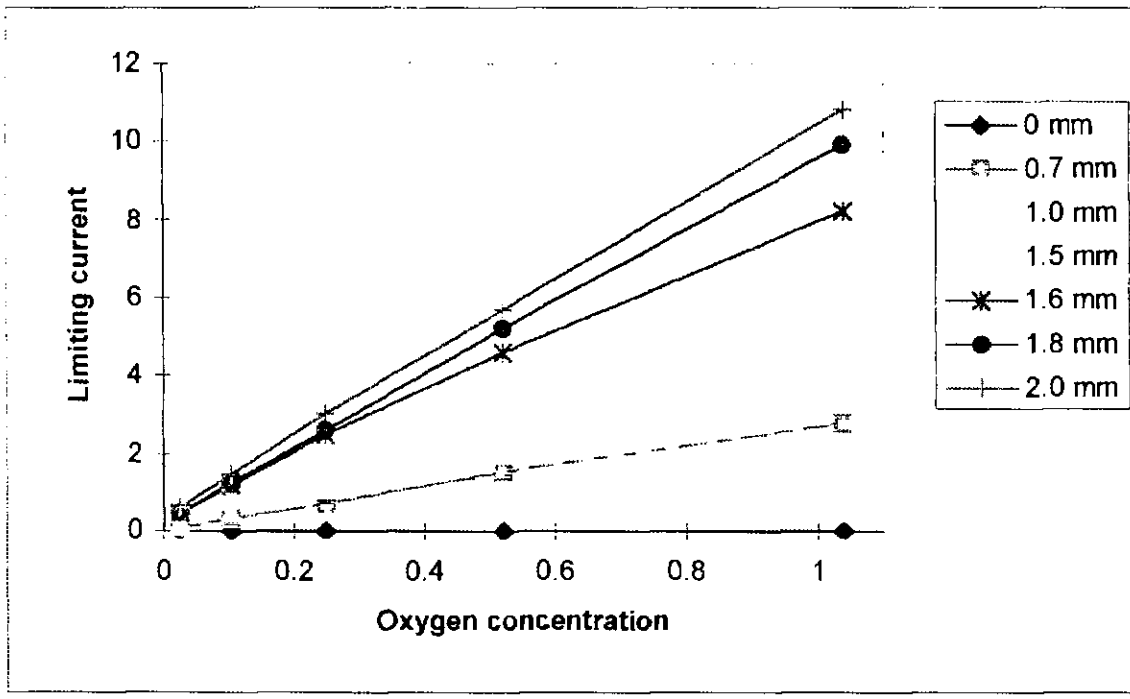

Figure F20 Limiting currents versus oxygen concentration

One possible origin of these discrepancies was the diffusion model used. The model used was based upon diffusion through a long, thin pore through which diffusion is assumed linear across both the length and area of the pore. With the short, wide diffusion pores used in this work, it could be imagined that this theory would not hold. It is envisaged that with a short, wide diffusion pore, the internal cavity may present itself as a second diffusion barrier that was essentially negligible when eonsidering long thin pores. An equation was derived to enable the cumulative effects of a series of diffusion barriers. This gives a calculation analogous to that of electrical capacitors in series.

We start with a general equation for the overall diffusion situation assuming that C is the external gas concentration, C_1 is the gas concentration at the junction of the two diffusion barriers and the final concentration after the second diffusion barrier is zero, S_1 is the cross-sectional area of the first barrier of length L_1 whilst S_2 and L_2 are the area and length of the second barrier. D is the gas diffusion coefficient. J is the gas diffusion flux.

$$J = -D\frac{dC}{dx} = -DS_1\frac{(C - C_1)}{L_1} = -DS_2\frac{(C_1 - 0)}{L_2} \qquad \text{Equation F20}$$

$$\frac{DS_1(C - C_1)}{L_1} = \frac{DS_2C_1}{L_2} \qquad \text{Equation F21}$$

The factor D cancels out and re-arranging we get:

$$\frac{S_1C}{L_1} = C_1\left(\frac{S_2}{L_2} + \frac{S_1}{L_1}\right) \qquad \text{Equation F22}$$

so C_1 may be expressed as:

$$C_1 = \frac{S_1}{L_1\left(\frac{S_2}{L_2} + \frac{S_1}{L_1}\right)}$$ Equation F23

Substituting C_1 into the equation:

$$J = \frac{-DS_2C_1}{L_2}$$ Equation F24

we get:

$$J = \frac{-DS_2}{L_2}\frac{S_1}{L_1\left(\frac{S_2}{L_2} + \frac{S_1}{L_1}\right)}$$ Equation F25

or

$$J = -D\frac{S_1S_2c}{L_1L_2\left(\frac{S_2}{L_2} + \frac{S_1}{L_1}\right)}$$ Equation F26

or

$$J = -D\frac{S_1S_2c}{S_2L_1 + S_1L_2}$$ Equation F27

or

$$J = \frac{-Dc}{\frac{L_1}{S_1} + \frac{L_2}{S_2}}$$ Equation F28

If the combination of L_1/S_1 and L_2/S_2 is equivalent to L/S then:

$$J = -DS\frac{c}{L} = -Dc\frac{S}{L}$$ Equation F29

or

$$J = \frac{-Dc}{\frac{L_1}{S_1} + \frac{L_2}{S_2}}$$ Equation F30

and so we see that

$$\frac{S}{L} = \frac{1}{\frac{L_1}{S_1} + \frac{L_2}{S_2}}$$ Equation F31

Using the equations developed above, the restriction caused by a third barrier was also incorporated. For this third barrier the scanning electron micrograph of an electrode structure (see section 5.7) was employed to estimate the barrier length at 2.2×10^{-5} m with an effective diameter of 3.93×10^{-6} m^2 by assuming an estimated porosity of 20% from visual assessment.

$$\frac{S}{L} = \frac{1}{\frac{L_1}{S_1} + \frac{L_2}{S_2} + \frac{L_3}{S_3}}$$ Equation F32

This did bring the results of figure F21 closer to a straight line but was still falls short of a total explanation.

M.Benammar in his PhD thesis reported on the effect of conical diffusion barriers and found that a tapered hole behaves as a straight hole with a constant cross-sectional radius given by the geometric mean of the maximum and minimum radii. It was thought that the sensor internal cavity may be acting as such a conical diffusion barrier. Using this, the examination was re-applied with this modified radius and although this again improved the results, they were still some way from returning a straight line.

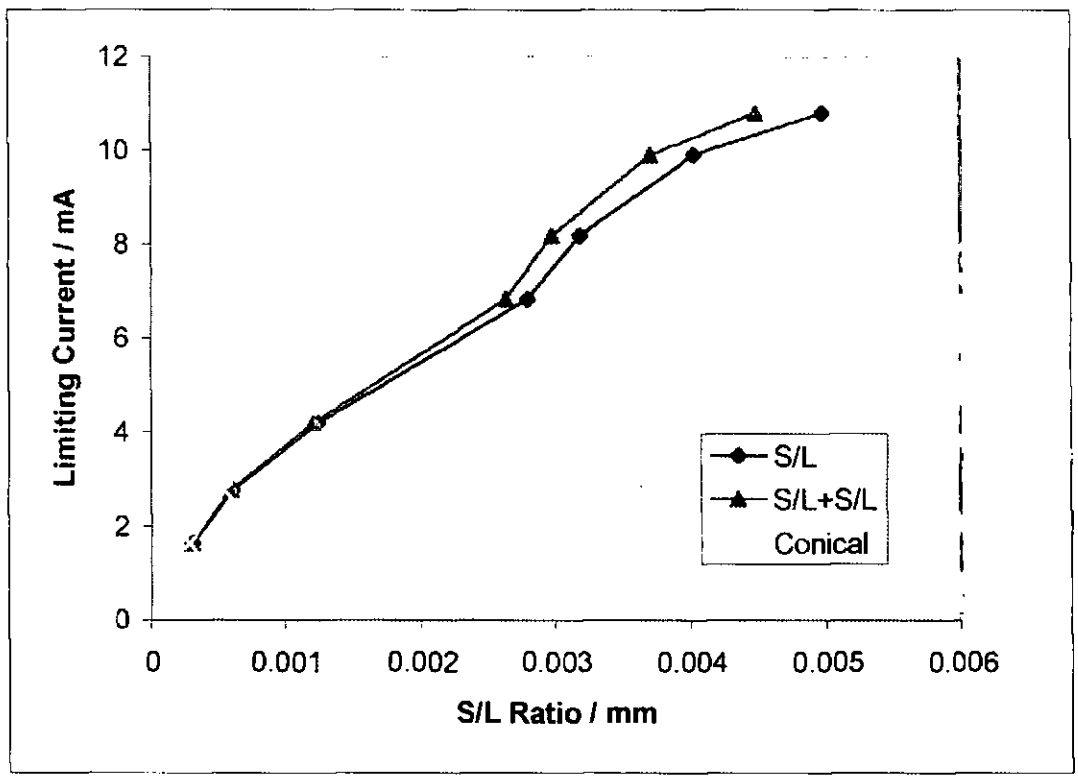

Figure F21 Limiting currents versus modified S/L ratio

At the higher oxygen concentrations, especially for the larger barrier sensors and particularly for the 1.6 mm diameter barrier, limiting currents may not have been fully realised, this is more significant when considering figure F8 where the true limiting currents are shown to be realised at the higher end of the plateau region. This probably accounts for the remaining deviation from a straight line.

F1.7 Firing temperature

The resistance dependence of pump cell upon sintering temperature was examined by performing current / voltage tests on half sensors. We are therefore looking at region 1&2 from figure 1.9, section 1.2.5.3.3. As there is no diffusion hole to create a diffusion limited current, regions 3&4 are not realised.

Figure F22 shows the current / voltage curves for cells prepared from plastic-ceramic and sintered at temperatures of 1150 to 1550°C. These tests were performed at 500°C in air and show an initial high resistance, due to slow electrode kinetics followed by an ohmic behaviour. Interestingly the electrode kinetics, appear to have similar effects for each sample despite the electrodes being subjected to the sintering temperatures in each case. We might expect the 1150°C fired sample to show improved electrode behaviour due to its

relatively non-sintered state. The lack of any significant degradation in electrode performance indicates that, contrary to expectations, these platinum cermet electrodes do not suffer particularly from high temperature exposure. Kenjo et al [146] investigated oxygen reduction in solid electrolyte cells with platinum electrodes using transient current/voltage and SEM analyses. They saw that whilst electrode grain size grew with sintering temperature, higher currents could be drawn indicating that higher sintering temperatures actually improved the electrode/electrolyte contact. In this work we do not see any evidence for improving electrode behaviour but this does give some confidence to say that electrode degradation caused by firing the electrodes alongside the electrolyte was not excessive. Indeed we may expect a slower deterioration in high temperature fired electrodes than those freshly deposited at a low temperature.

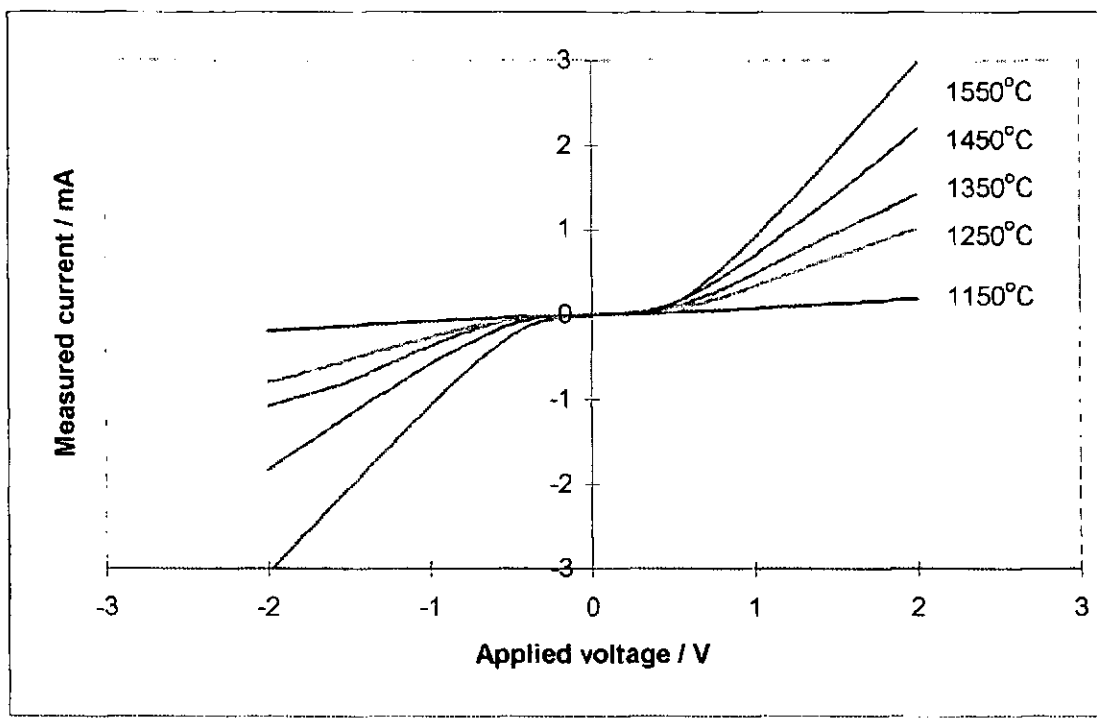

Figure F22 Current / voltage curves for half sensors with sintering temperature

Figure F23 shows cell the resistance obtained by calculating the slope of the current / voltage curves for each sample at temperatures of 450 to 550°C in air. These slopes were taken at 1V pump potential where electrode kinetics are sufficiently fast to have negligible effect so we are considering electrolyte bulk properties (backed up by bias variation work on impedance measurements)(see section 4.2.2). Plotting the resistances against sintering temperature we see the benefits of high firing temperatures on electrolyte properties. These results are in agreement with results taken from similar specimens using impedance spectroscopy to investigate electrolyte impedance (see section 3.1.5, figure 3.8). At sintering temperatures above 1450°C it appears that improvements are insufficient to warrant this high temperature as furnace element life is shortened and furnace expense increases significantly for high temperature capability.

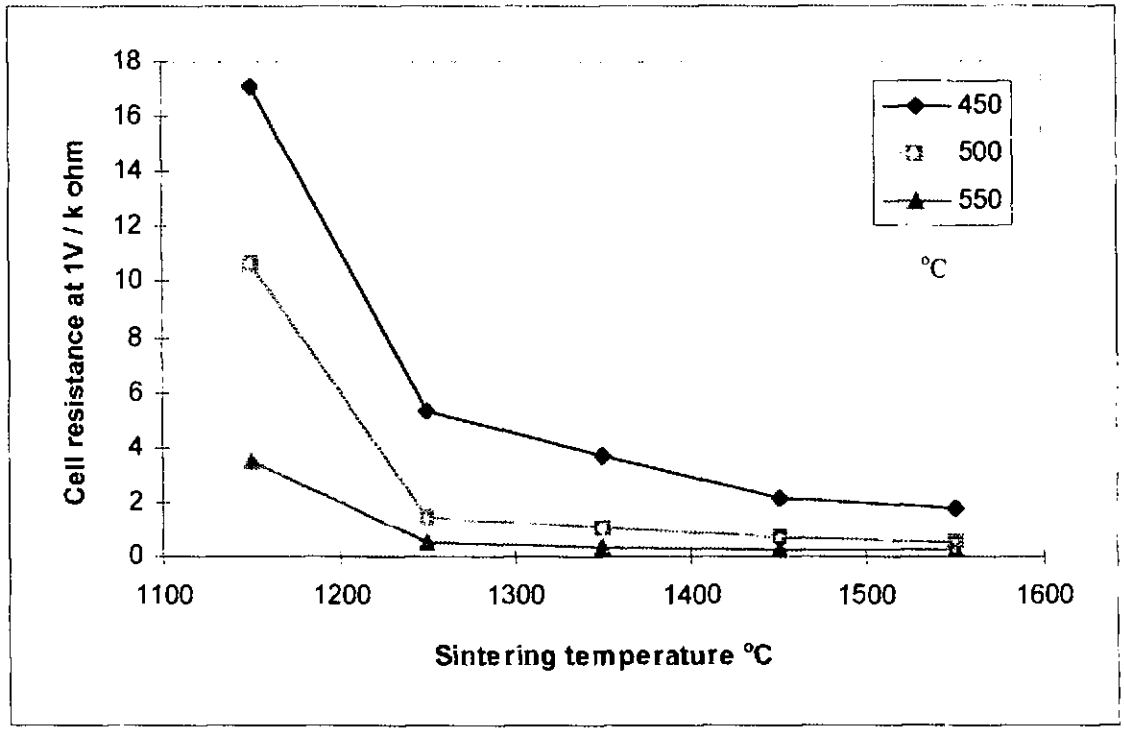

Figure F23 Sintering temperature versus cell resistance at 1 V pump potential

Figure F24 indicates the effect of oxygen concentration on cell resistance at 1V pump potential. These results were derived from a cell fired at 1450°C and tested at 500°C Here we cannot say whether effects are electrode or electrolyte dominated as impedance work has not been carried out with bias variation in low oxygen atmospheres although an impedance analysis into oxygen variation without bias application is presented in section 3.1.4. It may be expected that electrode domination does occur although the initial lag identified as slow electrode kinetics does not appear to be influenced in the current / voltage curves. Interestingly the cell resistance does start to increase substantially below 1% oxygen. This may go some way to explain the low oxygen concentration sensor performance.

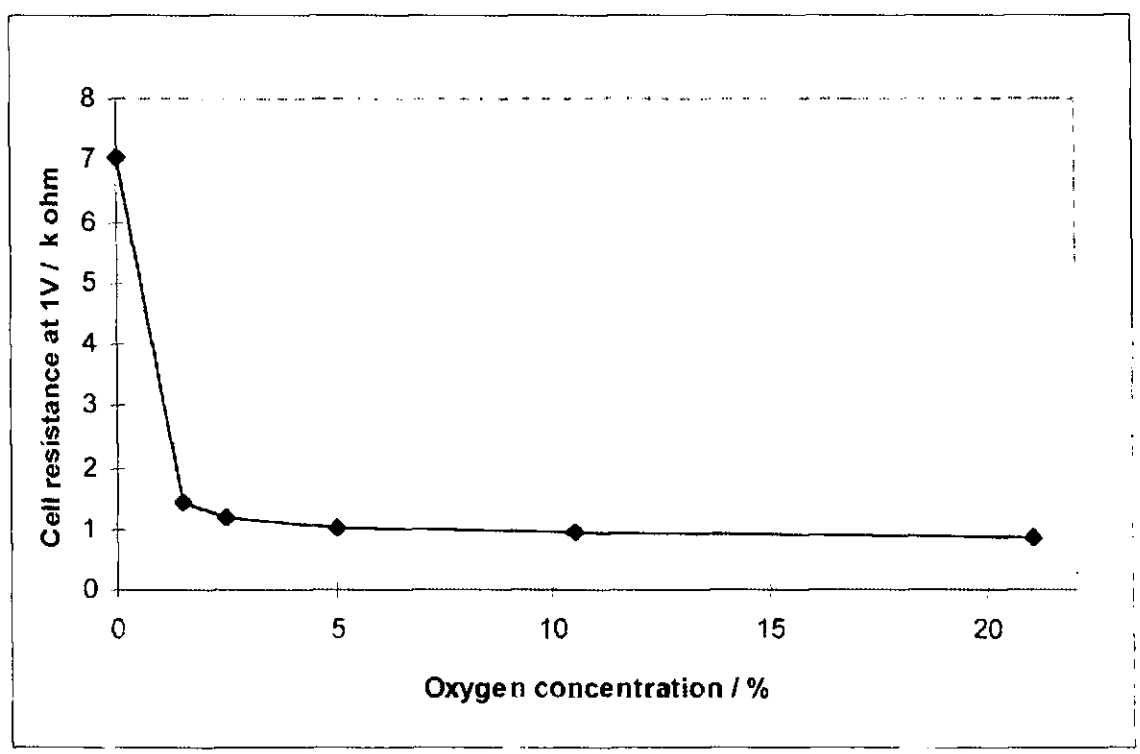

Figure F24 Cell resistance with oxygen concentration at 1V pump potential

F1.8 SEM Firing temperature

The effects of sintering temperature on plastic-ceramic zirconia specimens was examined by the project student O.Pampam. This included a scanning electron microscope study along with frequency response analysis and physical measurements reported (section 3.1.5). Here we present the results of the S.E.M. study. Figures F25 to F30 show micrographs of separate plastic-ceramic samples fired using similar firing cycles but with changes to the final sintering temperature. These temperatures ranged from 1150 to 1550°C and produced a clear visual indication of sintering stage that was well supported by density, shrinkage, hardness and conductivity measurements. The micrographs were taken at similar magnifications (×6230) to allow direct comparison and were representative of the specimen as a whole. The micrographs show a clear densification as temperature increased to give a dramatic densification from 1150 to 1350°C where after the density remained high and improvements were small.

The 1150°C sintered sample shows a powdery and loosely packed structure, clearly of low density and highly porous. Individual powder particles can be identified on close examination with approximate diameters of 0.1 to 0.2 μm. At this stage of firing, it is clear that little or no sintering or grain growth had occurred. The image quality of this micrograph is also poor. This is an additional attribute of the low density, as the same sputtering process was applied to this as to other samples but the image is clearly charging as excess electrons are not being conducted away. It would appear that the gold coating had been so thinly spread over the high surface area that good electrical continuity had not been achieved.

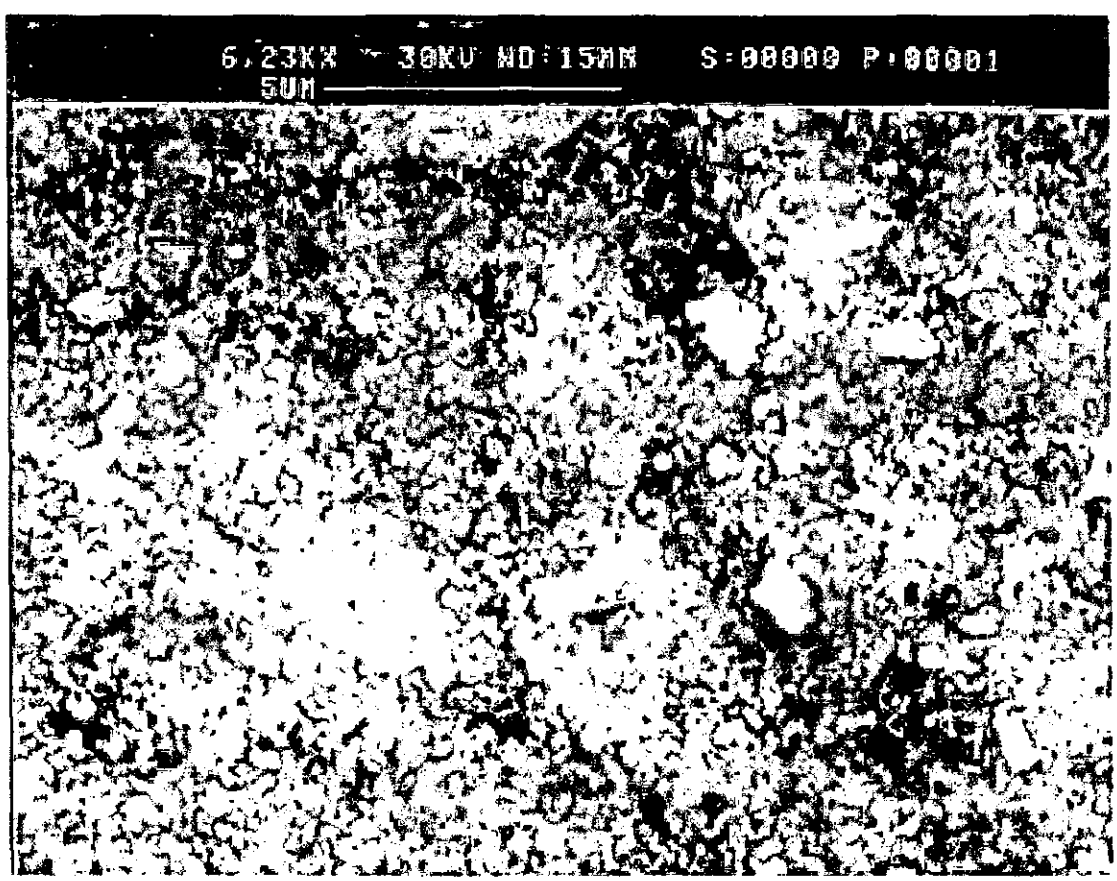

Figure F25 Tioxide plastic-ceramic fired at 1150°C

The 1200°C sintered sample shows a significant improvement over the sample fired at 1150°C however the sample still had a low density and loosely packed structure. Sintering

had started as the individual powder particles are no longer visible. A fair degree of sample charging is still present, again a testimony to the high surface area of this sample.

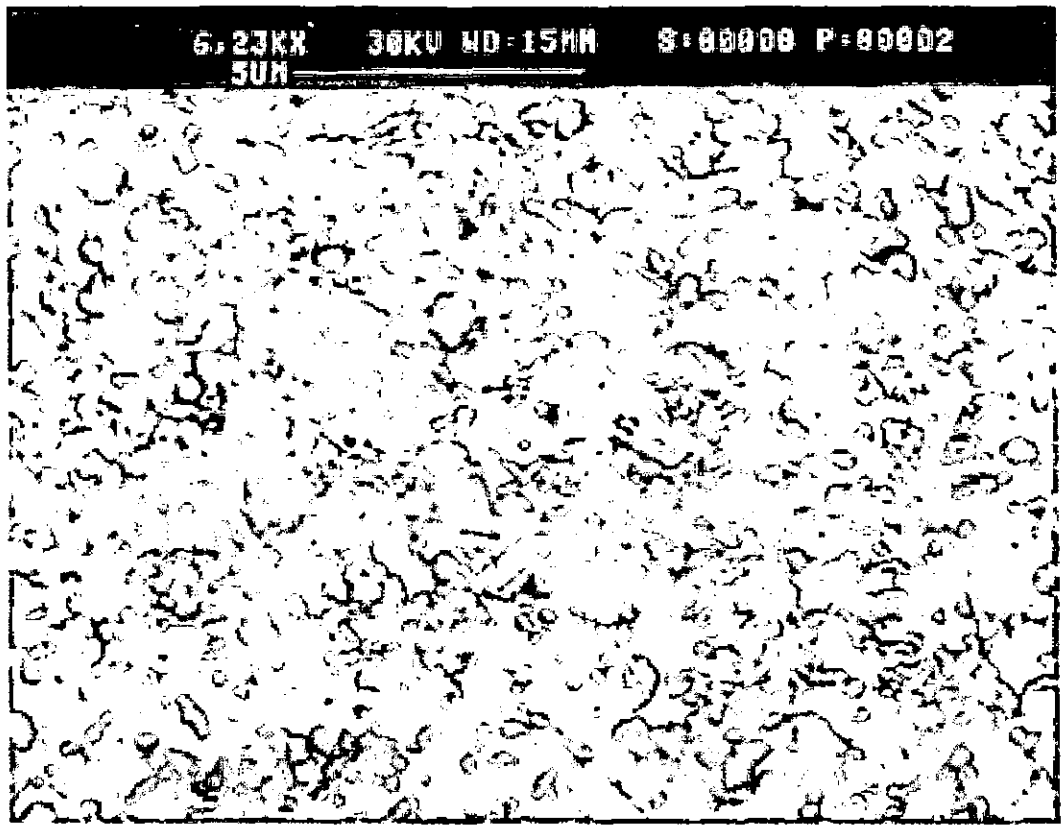

Figure F26 Tioxide plastic-ceramic fired at 1200°C

The 1250°C sintered sample shows a sample with very little open porosity, the sample is much denser with sintering virtually complete. There does remain a fairly high surface area, revealed by the slight charging and the sample does not have the full appearance of a single coherent body.

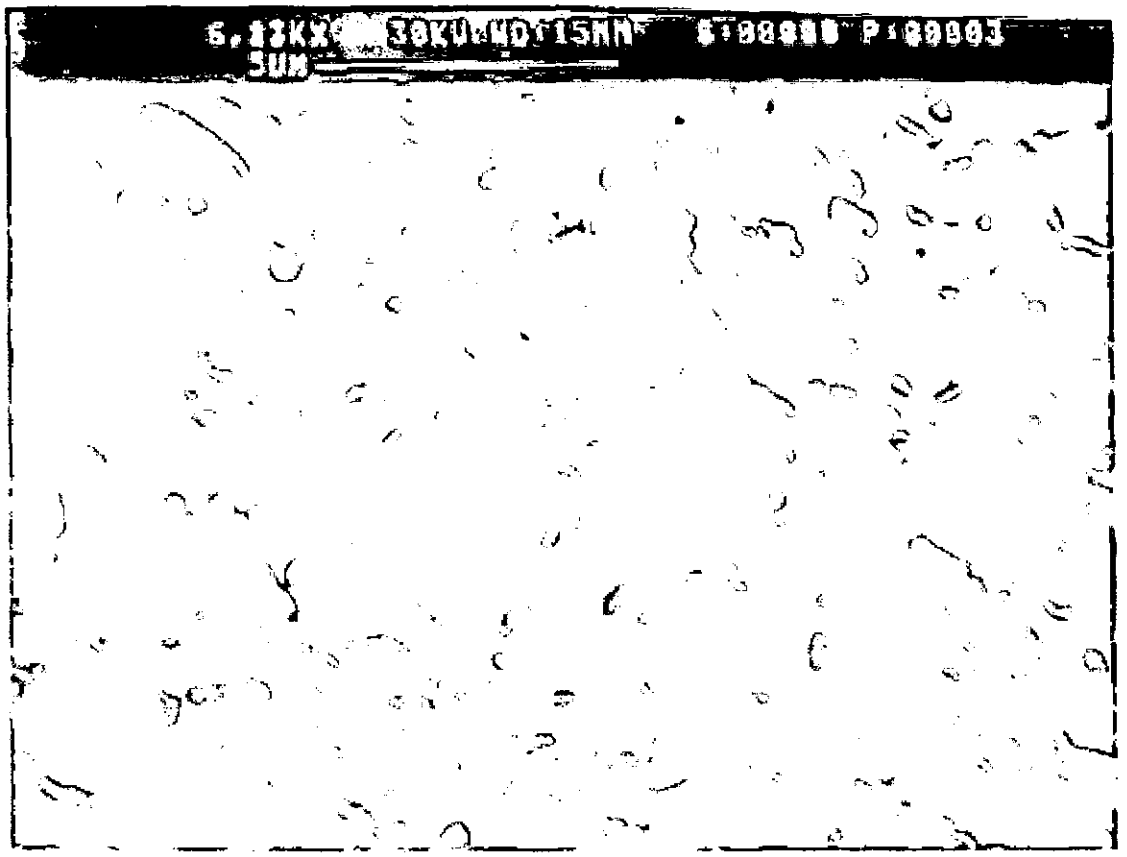

Figure F27 Tioxide plastic-ceramic fired at 1250°C

At 1350°C the sample shows a much improved fracture edge. The body now has a more glassy appearance with only a slight porosity that is almost certainly not open. The remaining pores have an average diameter of approximately 0.45 μm and cover an estimated 3% of the visible area.

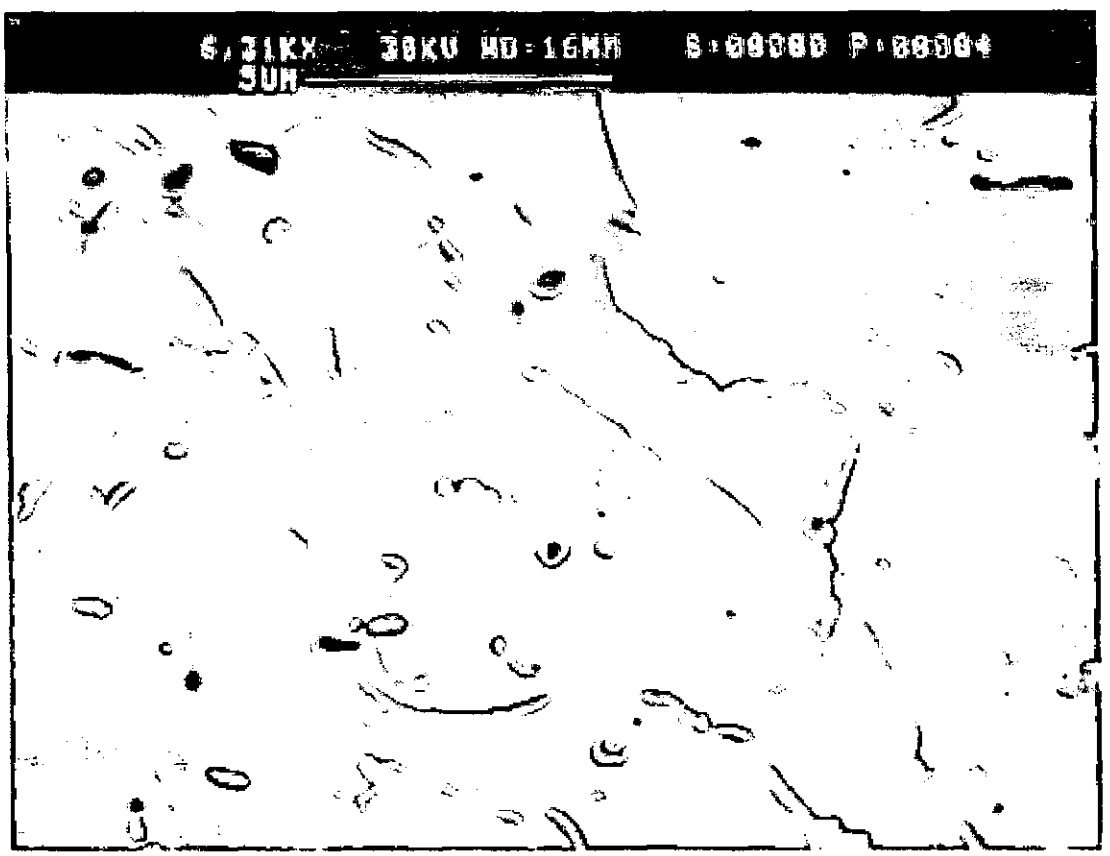

Figure F28 Tioxide plastic-ceramic fired at 1350°C

The 1450°C sintered sample shows a similar appearance to that of the 1350°C sample. The porosity appears very similar but made of fewer but slightly larger pores. The other change in appearance is that there appear to be fewer fracture edges, indicating a stronger material.

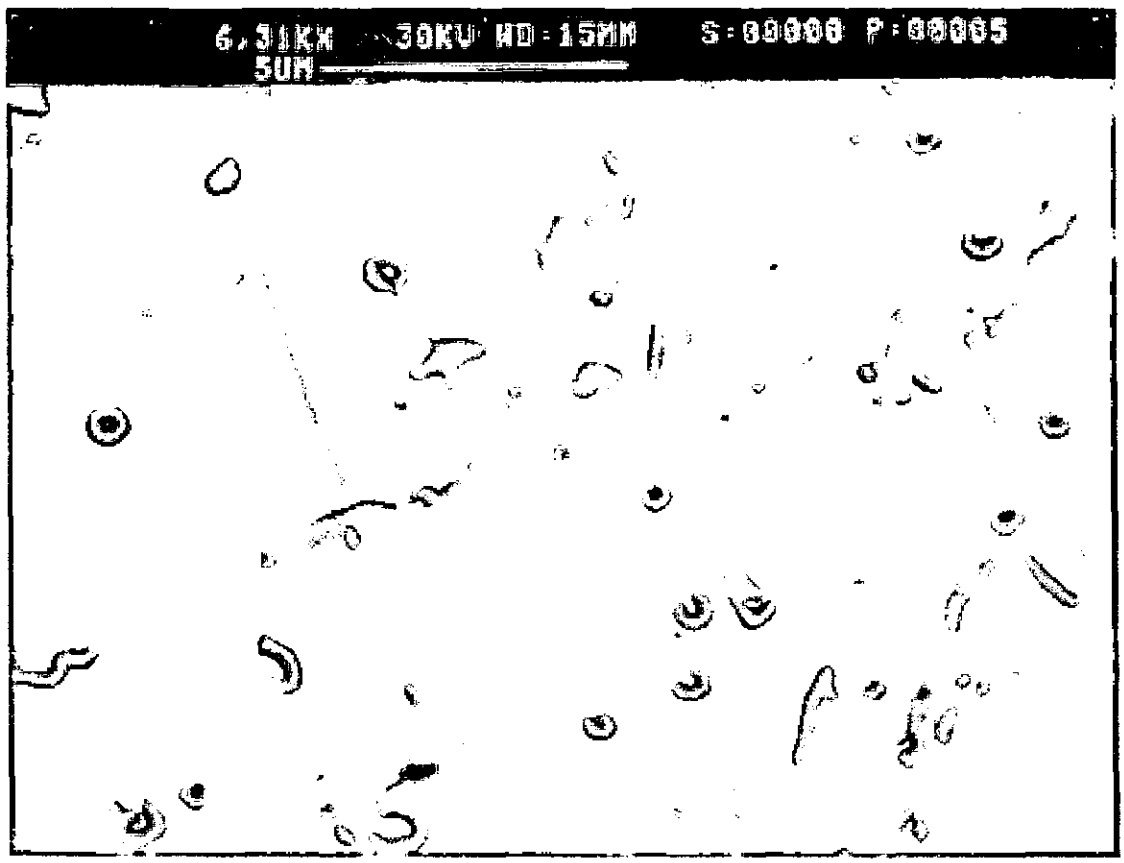

Figure F29 Tioxide plastic-ceramic fired at 1450°C

The 1550°C sintered sample again shows a highly dense, glassy surface to the fracture edge. Once more the pores appear to have grown in size but lessened in number. The remaining pores have an average diameter of approximately 0.6 μm and cover an estimated 2% of the visible area. Again fewer fracture edges are visible indicating a stronger still material.

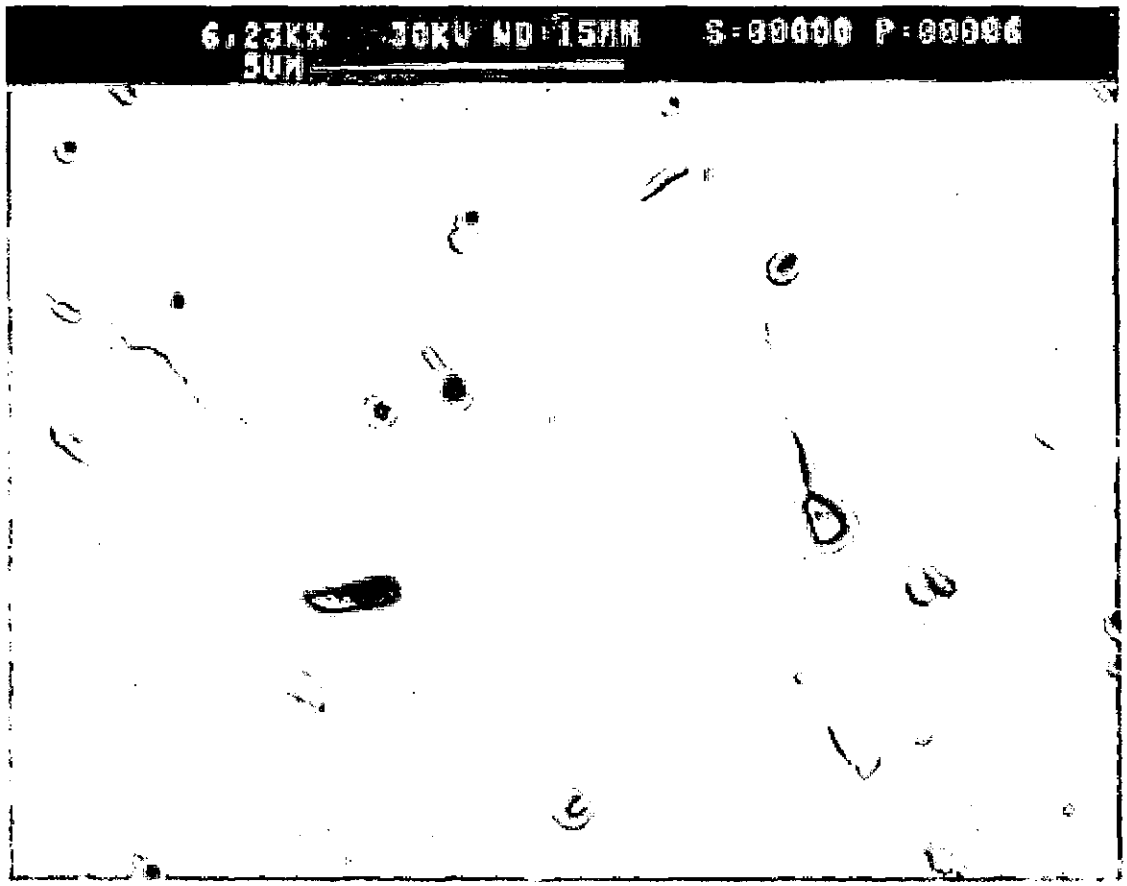

Figure F30 Tioxide plastic-ceramic fired at 1550°C

F1.9 SEM Green ceramic

Here we demonstrate that we have had success in another student project, this time by Z.Tural. This project researched in-house production of the plastic-ceramic zirconia sheets. By the end of the project the student had realised a flexible, easily worked material that utilised a water soluble plastic required for sensor manufacture. Along with hardness measurements, density measurements and frequency response analysis, the following micrographs were obtained. Comparing these micrographs with those obtained from the Tioxide material fired at similar temperature (1450°C we see that the in-house material has greater density despite the poor image quality. Whilst the images of the Tioxide ceramic were selected to be truly representative, in this case the solitary pore shown was specifically located to give some surface feature. This apparently high density image was backed up with the other measurements of density, hardness and frequency response analysis which showed similar performance to the fully sintered Tioxide material. Unfortunately this result was obtained in the last days of the project and so further analysis on reproducibility has not been performed.

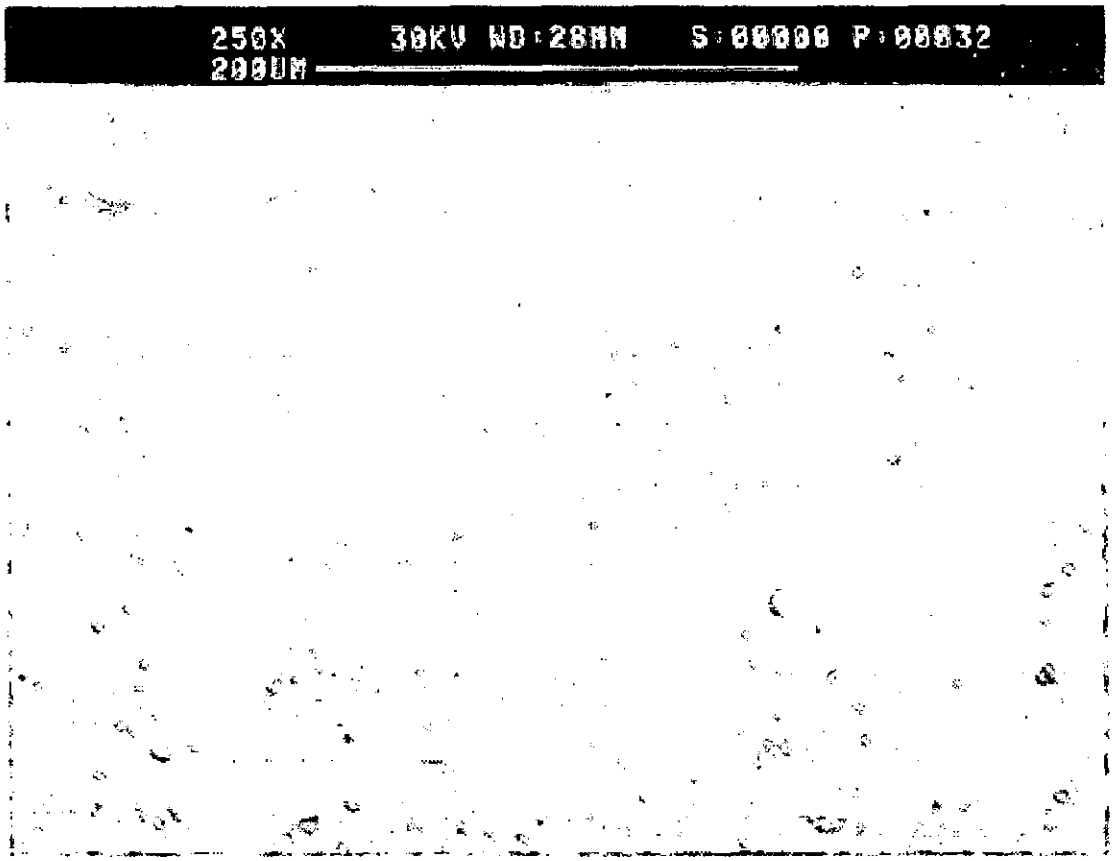

Figure F31 In-house plastic-ceramic fired at 1450°C low magnification

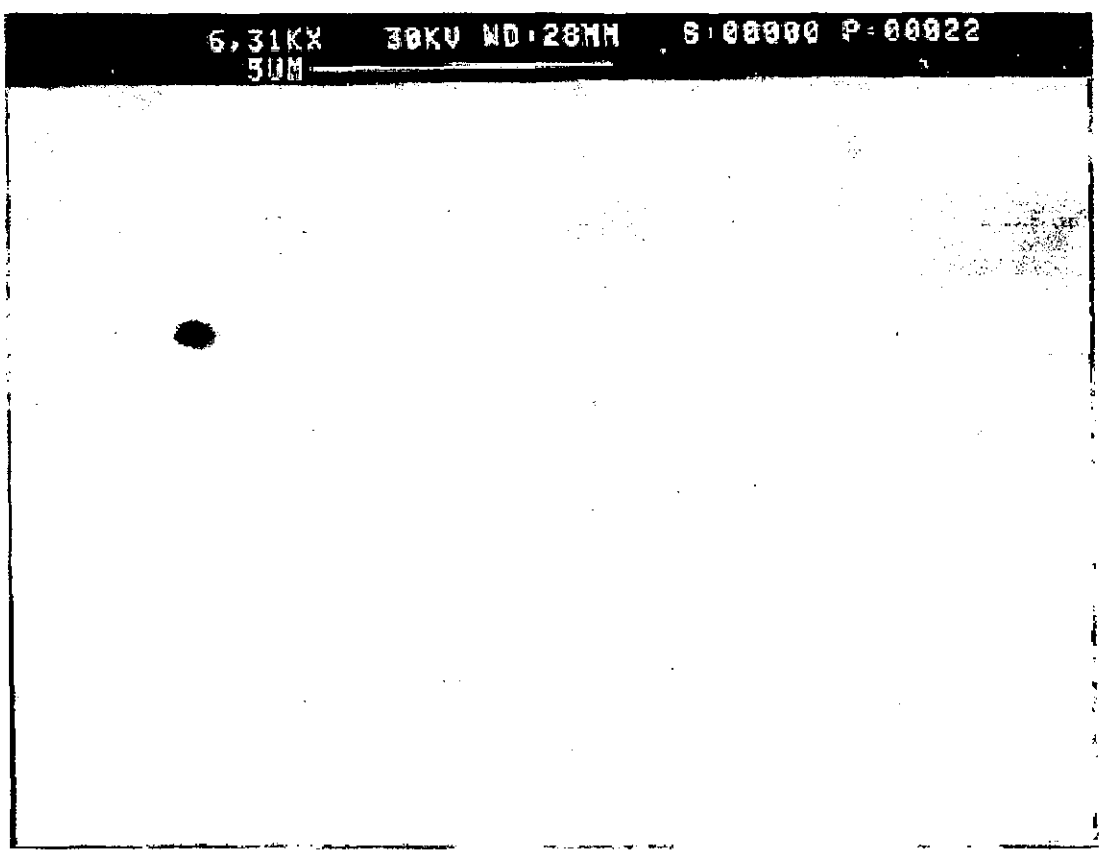

Figure F32 In-house plastic-ceramic fired at 1450°C high magnification

F1.10 Platinisation

In an attempt to realise and quantify an improvement in the low temperature performance of an amperometric device, electro-deposition of platinum was employed. The platinisation procedure was performed on a four electrode amperometric sensor to

establish whether this procedure could enhance the electrode performance. Figure F33 shows the current / voltage curves obtained before and after the electro-plating procedure (solid lines representing the sensor after deposition). This gave a disappointing result in that the improvement realised was not of the order seen in other platinisation experiments. There is a noticeable improvement with cell resistance having dropped and limiting currents attained at slightly lower pump potentials however the current plateaux have increased marginally (approximately 0.1 mA) indicating that some physical change had occurred affecting the gas diffusion path. The relatively small magnitude of this positive change could indicate some material blockage having been removed in the liquid electrolyte insertion / removal procedure or perhaps that some additional electrochemical leakage route had been created / enhanced. The electrode improvement may have been lessened by the small deposition currents used in order to minimise gaseous formation. Alternatively perhaps it was the gaseous formation that resulted in improvement of the electrode microstructure. At this stage the explanation is not clear but we have demonstrated that the platinisation of internal sensor electrodes is feasible and that electrode improvements are possible.

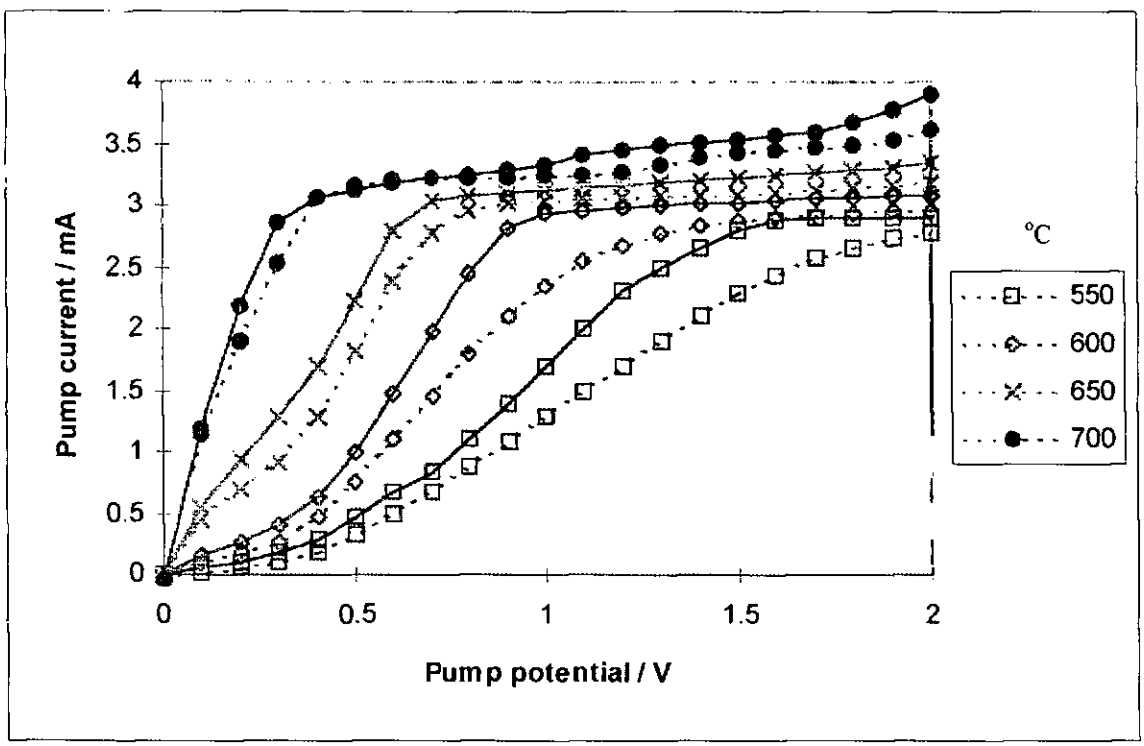

Figure F33 Amperometric sensor before and after platinum electro-deposition

In order to quantitatively compare the results before and after plating, we plot the I/V diagram slope differential of the two traces for each temperature to see the total cell resistance versus applied pump potential. The result of this analysis is given in figure F34. As expected, the highest resistances are seen at low temperatures and low pump potentials with the correspondingly greater reductions in cell resistance after electro-plating. The cell resistance improvements turn negative at higher pump potentials as a result of effective resistance imposed by diffusion limiting, which are reached sooner with the improved electrodes. Typically we are seeing a drop of a factor of 2 to 5 in cell resistance by electroplating. Whilst this is a fairly substantial decrease, an increase in temperature of only 20°C can have a similar effect.

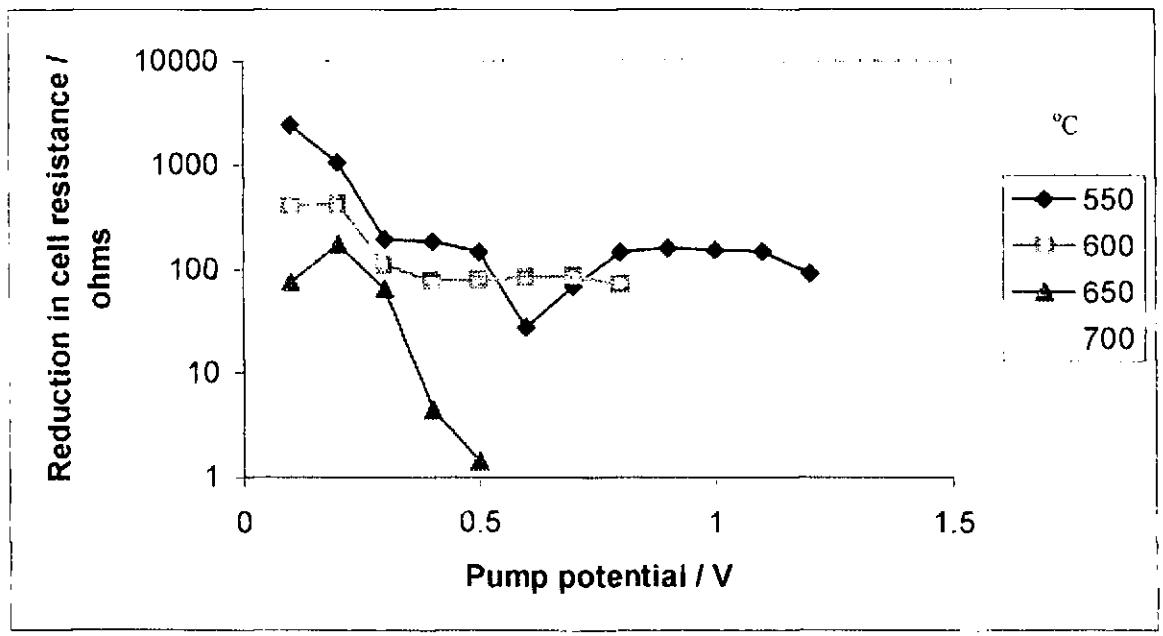

Figure F34 Post electro-deposit cell resistance improvementss

F2 Pump-gauge tests

With the application of the new sensor fabrication technique, one concern was that there may be a significant degree of unintended leakage into the system that would be detrimental to sensor operation. Leakage mechanisms had been previously examined by Kaneko et al [61] who investigated the leakage involved in fully sealed pump-gauges by electrochemical pumping analyses. A summary of the theory behind this work was presented in section B1.2. A similar schedule of testing was carried out to allow direct comparison to this work. In Kaneko's work, three pumping mechanisms were identified as physical leakage, semi-permeability and electrochemical leakage of which the electrochemical mechanism dominated.

For a physical leakage mechanism, a flux into the enclosed volume would be given by the equation:

$$J = K_1(P_1-P_2) \qquad \text{Equation F33}$$

from Fick's law, where J, P_1, P_2 and K_1 are the flux, external oxygen pressure, internal oxygen pressure and a diffusion related constant respectively.

For a semipermeability mechanism:

$$J = K_2(P_1^{1/4}-P_2^{1/4}) \qquad \text{Equation F34}$$

where K_2 is a proportionality factor for a given ceramic and a function of temperature.

With an electrochemical leakage mechanism an equation for the leakage current was derived as:

$$i_L = E / (R_L + k_1P_1^{-1/2} + k_2P_2^{-1/2}) \qquad \text{Equation F35}$$

where i_L, E, R_L k_1 and k_2 are the leakage current, EMF of the potentiometric gauge, electrolyte resistance and the two rate constants respectively.

From the above equations the data was plotted such that values for the constants k_1, k_2 and R_L could be obtained. The slope of $P_1^{-1/2}$ vs. dE/di_L gave a value for $k_1 + k_2$. The slopes of $P_2^{-1/2}$ vs. E/i_L gave a value for k_2 and the slope and intercept of $P_1^{-1/2}$ vs. $k_1P_1^{-1/2}+R_L$ (from the intercepts of the previous plots) gave k_1 and R_L respectively. From these it was determined that $k_1 = 4.0\ k\Omega\ atm^{1/2}$, $k_2 = 1.5\ k\Omega\ atm^{1/2}$ and $R_L = 0.5\ k\Omega$.

Tests performed included coulometric oxygen pumping, recovery tests and steady state leakage tests as detailed below.

The leakage current is given by the equation:

$$i_L = (16F^2VP_1/R^2T^2)\exp(-4FE/RT)(dE/dt). \qquad \text{Equation F36}$$

where F, V, R, T and E are Faraday's constant, the internal volume, molar gas constant, Temperature and Gauge EMF respectively.

Internal volume was calculated at 0.7 mm^3 using a gold seal to join pellets of partially stabilised, fully stabilised, polycrystalline and single crystal zirconia. Electrodes were of platinum paste fired at 600°C on polished surfaces.

Kaneko found that zirconia electrolyte type gave only little variation in leakage results. Leakage was controlled by electrode kinetics rather than electrolyte conductivity. Leakage rates were seen to be higher in abraded than on polished electrolytes suggesting that internal electrode activity was a factor. Contamination of platinum by gold was suspected to have altered the platinum characteristics. This was thought to be an indication that a mixed Pt/Au electrode may have a superior performance to a simple platinum one.

F2.1 Current / voltage tests

Figure F35 shows results from the current / voltage sweep of a fully sealed pump-gauge device. Upon application of the pump potential, a current was drawn which reduced with time until becoming negligible after approximately 55 seconds. This may be visualised as the slow oxygen evacuation of the fully sealed internal cavity. The current dropped away as oxygen became scarce, until oxygen in the chamber had been completely depleted and no further current could be drawn. Negligible currents were drawn after depletion had been realised, pointing towards low levels of leakage. This confirms the non-porous nature of the sintered green electrolyte, mechanical integrity of the ceramic-ceramic seals and the integrity of seals around wire connections. A calculation of internal cavity volume may be made using dimensional measurements and compared with a calculated amount of oxygen removed based upon Farady's Law: Integrating the curve to obtain the area underneath gives a measure of the volume of gas removed.

Area undemeath curve (I×t) by integration	=	15.75 mF
The charge to pump 1 mole of oxygen (4F)	=	38600 F
Quantity of oxygen pumped	=	4.08×10^{-8} mol
Volume of 1 mole at STP	=	2.24×10^{7} mm^3
Volume of 1 mole at 800°C	=	8.20×10^{7} mm^3
Volume of oxygen pumped	=	3.35 mm^3
Volume of air in internal cavity	=	15.94 mm^3
Internal cavity diameter	=	4.98 mm
Internal cavity depth	=	0.84 mm

Internal cavity volume = 16.36 mm^3

Table F1

This calculation shows an approximate agreement of the calculated internal cavity volume to that estimated using known green ceramic dimensions and shrinkage values.

In figure F35 we see a relatively slow rise in current upon application of the applied voltage. This is thought to have arisen due to the averaging routines of the 7150 multimeter used, true currents would be expected be realised fairly rapidly. The error caused by this would not significantly affect the results detailed above.

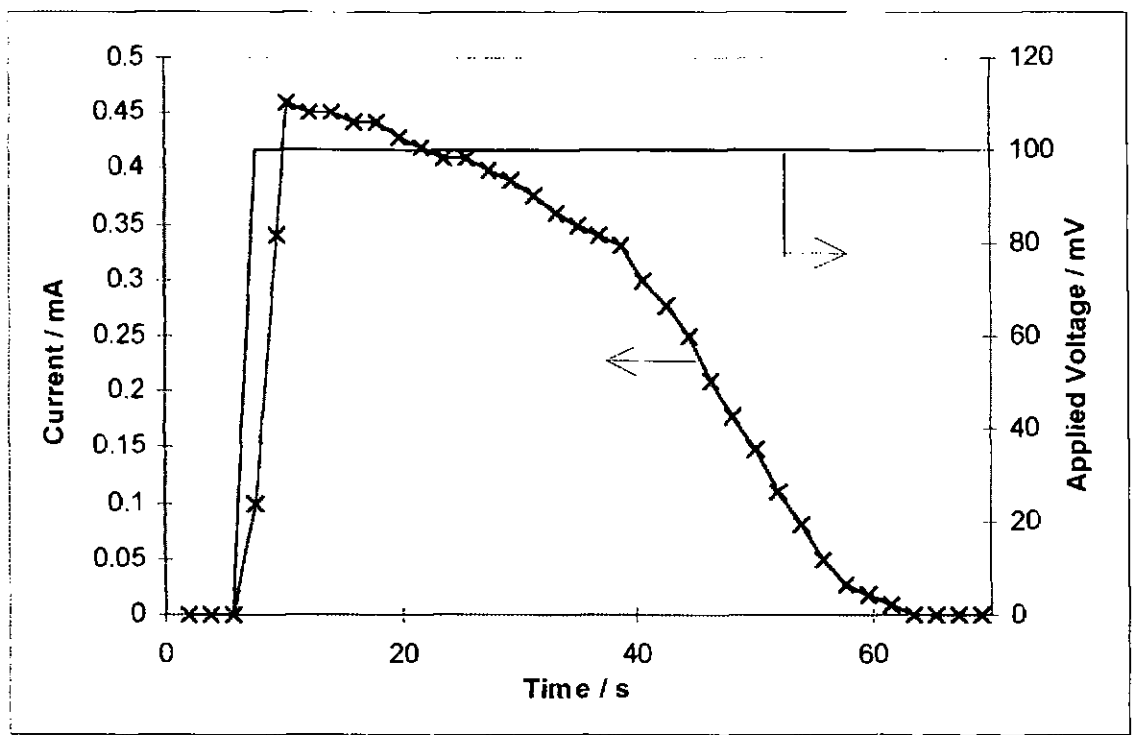

Figure F35 Oxygen depletion of a fully sealed internal cavity

F2.2 Coulometric pumping technique

The results of gas pumping tests are shown in figures F36 and F37. Figure F36 shows symmetry indicating low leakage levels. The current direction was switched manually in these tests, this accounts for the slight differences in peak current times. The gauge EMFs are seen to rise faster at higher temperatures as a constant pump current would have yielded an identical oxygen removal but faster pressure change due to thermodynamic gas expansion. There is also a temperature term in the gauge EMF which also has an effect.

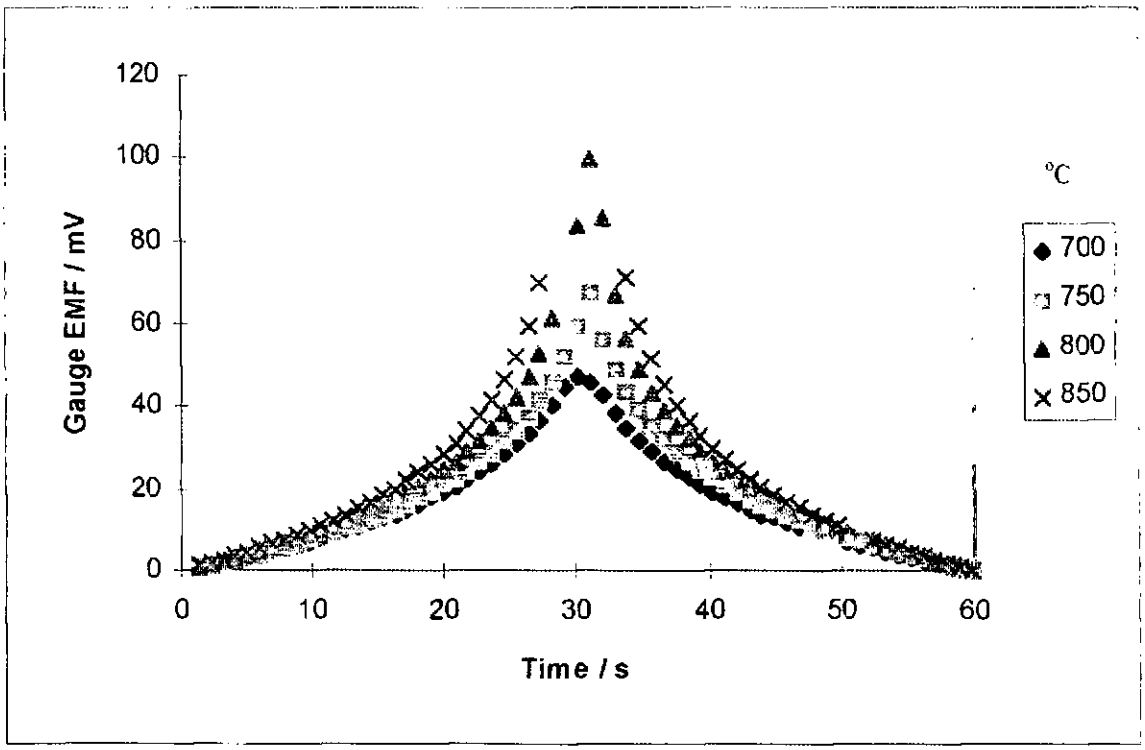

Figure F36 Positive and negative pumping test EMF

Combining the Ideal gas equation PV=nRT with Faraday's law I=nF allows us to derive an expression for the rate of pressure change.

$$P = \frac{-IRT}{4FV}t + X_{O2}P_0$$

Equation F37

so the rate of pressure change = -IRT/4FV.

Using the Nernst equation the EMFs from the above plot may be converted to internal partial pressure versus time plots, revealing the straight lines of (fig. F37). Again the rise in temperature is seen to give the faster pressure change. The linearity of these plots is a testament to low leakage rates as significant leakage would show as pressure change rates dropping at low internal pressures. Low leakage rates are also shown by identical initial and final internal partial pressures obtained.

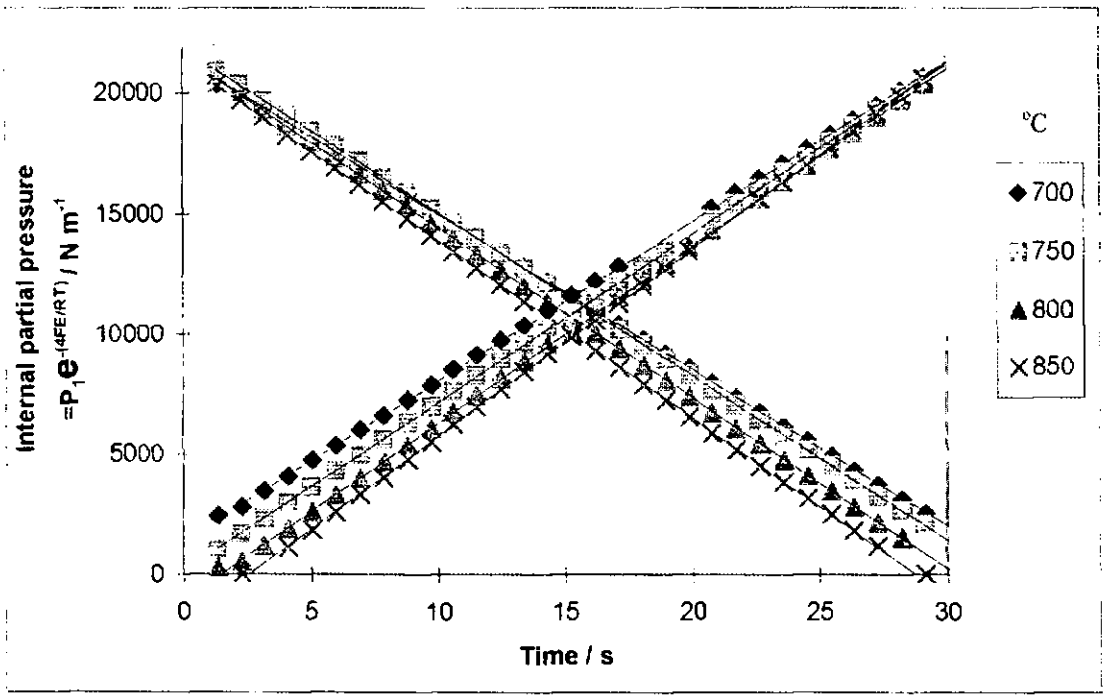

Figure F37 Positive and negative pumping test
internal oxygen partial pressure

Pumping rates determined by pressure/time slopes are indicated in table F2, these allow us again to calculate the internal cavity volume. Volumes are obtained by applying the formula:

$$Volume = \frac{IRT}{4F\dfrac{dP}{dt}} \qquad \text{Equation F38}$$

Temperature °C	Outward pumping rate (mbar s^{-1})	-RT/4FV (mbar s^{-1})	Volume (mm^3)	Inward pumping rate (mbar s^{-1})	IRT/4FV (mbar s^{-1})	Volume (mm^3)
700	-648	-654.9	16.1	662	654.9	15.8
750	-681	-688.6	16.2	701	688.6	15.7
800	-710	-777.2	16.3	735	777.2	15.7
850	-739	-755.9	16.4	774	755.9	15.6

Table F2

These values do indicate a slightly higher rate for pumping oxygen back into the cell and correspondingly give lower internal volumes. This may be an indication of some degree of leakage. Unfortunately these do not give sufficient data to determine the leakage mechanism by analysing the temperature dependent nature as performed for steady state and recovery techniques reported below. We do however have a roughly linear change with these few points as predicted from ideal gas theory as stated above. The internal volumes calculated do agree with those obtained by dimensional measurement and current/time integration given above. Also the rates of pressure change are in agreement with those calculated using the above formula.

F2.3 Steady state tests

Results of the steady state tests are shown in figure F38 & F39. The gauge EMF gradually rose over time as the oxygen was depleted. As the partial pressure differential rose, the leakage rate also increased until a point was reached at which the leakage current was equal to the pump current and the pressure differential monitored by the gauge EMF.

Although it is only the final EMF value we are really interested in, the whole trace was recorded to monitor the test progression which, as seen, took in excess of one hour to reach stabilisation with these devices, compared to 15 minutes required in the work of Kaneko et al [61]. This is probably a function of the larger internal cavity obtained in plastic-ceramic sensors. These tests were performed at various temperatures and partial pressures to monitor the effects of these factors on leakage and thus give clues to the leakage mechanism involved. Larger currents of up to 20 mA were employed and gave EMFs which increased steadily up to higher values before dropping back into line with results obtained at lower currents (figure F38).

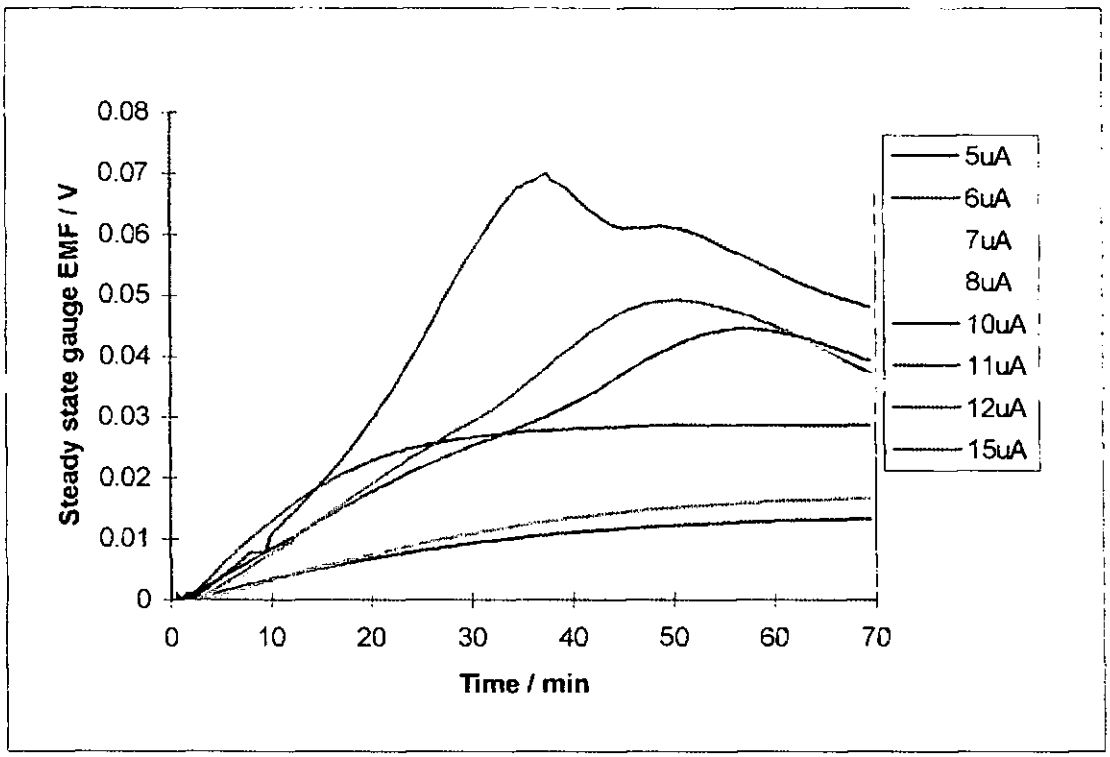

Figure F38 Steady state leakage examination results instability.

Gauge EMFs reached values of 70 mV before dropping back to 40 mV. The immediate thought was that this may have been due to dissociation of H_2O or CO_2. These values compare with results taken from an amperometric device in humid / high CO_2 atmospheres. These results show gauge EMFs of 100 mV rising to 900 mV upon reduction of reducible species. Clearly the EMFs produced via reducible species dissociation are much higher than those seen here and reduction may be dismissed as a cause.

The other possible explanation is that leakage rates increased during the test, reducing the attained partial pressure differential and therefore the indicated gauge EMF. An increase in leakage rates infers either an increase in physical leakage, increased electronic conduction of the electrolyte or an increase in electrode activity. Of these electronic conduction seems the most likely cause due to the higher currents and reduced oxygen concentrations applied. Physical and electrochemical leakage increase mechanisms seem unlikely as similar changes occurred 3 times at the 3 higher currents used. The leakage rate change appears to be reversible. No similar effects were reported by Kaneko et al [61].

At lower pump currents, more sensible and stable results were obtained. Figure F39 shows an example of the steady state results obtained. These results follow much better the expected trend. Upon pump current application, the internal oxygen partial pressure dropped (rose dependent upon pumping direction) until a steady state was attained at

which the pump current equalled the leakage current. The gauge EMF indicates the partial pressure differential necessary for this to be realised for each pump current. This data may then be manipulated and plotted to shed light on the leakage mechanisms involved (see section F2.5). It is interesting to note at this stage that the partial pressures were not symmetrical with respect to positive and negative pumping potentials.

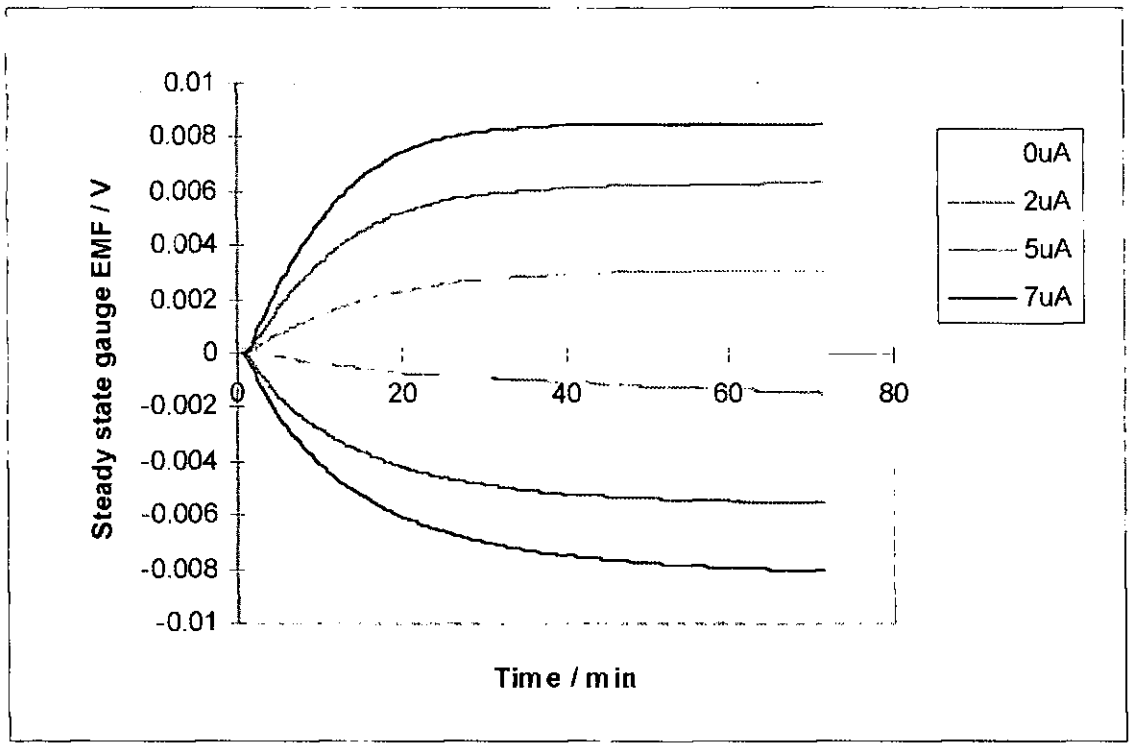

Figure F39 Steady state leakage test

F2.4 Recovery tests

The results from recovery tests showed (fig. F40) that the leakage rate started off high when the oxygen partial pressure differential between inner and outer atmospheres was high. Leakage rates then quickly reduced down towards zero as the partial pressure differential tended toward zero, although equilibration may not have been obtained for tens of minutes. Again the temperature and external partial pressure parameters were used to calculate the internal partial pressure from the gauge EMF via the Nernst equation. Kaneko et al [61] showed that from the decay in gauge EMF, knowing the test parameters and internal cavity volume, it is also possible to calculate the leakage current (see section F2.5). Tests were repeated for temperatures ranging from 700 to 850°C and in oxygen concentrations from 21 to 6%.

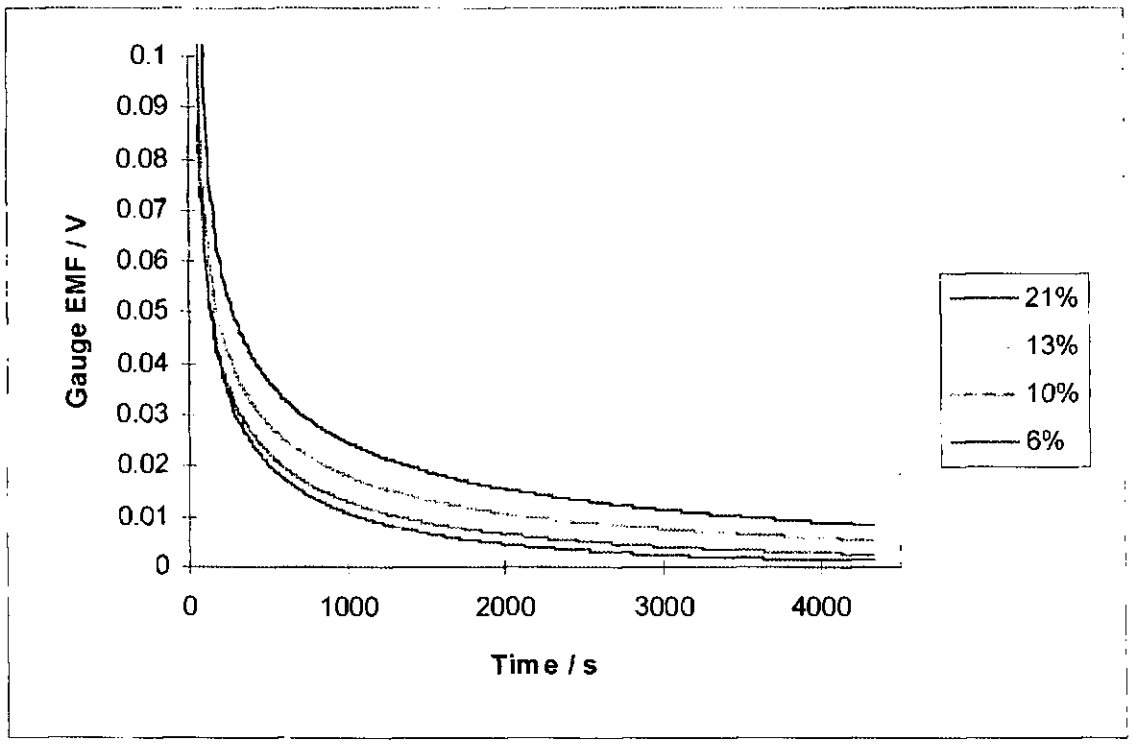

Figure F40 Dynamic recovery leakage test

F2.5 Leakage assessment

A comparison of the leakage data obtained from steady state and recovery leakage tests is given in (fig. F41). The data depicted were taken from the same sensor in air on two separate occasions. The first set of data are the results of steady state leakage tests, the second set are for recovery tests. The recovery data have been converted from EMF, time and volume data to EMF and leakage current data using the formula:

$$I = \frac{16F^2VP_1}{R^2T^2}\exp(-4FE/RT)\frac{dE}{dt} \qquad \text{Equation F39}$$

Although the data do not match completely, there does exist a degree of agreement between the data sets and certainly the same linear trends were followed with a similar temperature dependence. Both methods indicate a good linearity in accordanee with theoretical expectations however, the steady state method returns points crossing the origin whereas the recovery method does not. This gives slightly more faith in the steady state method whieh also as a steady state method, is not dependent on accurate timings although this is not thought to be the route of the disagreemcnt. The actual root causc of this anomaly has not been identified and was not examined further.

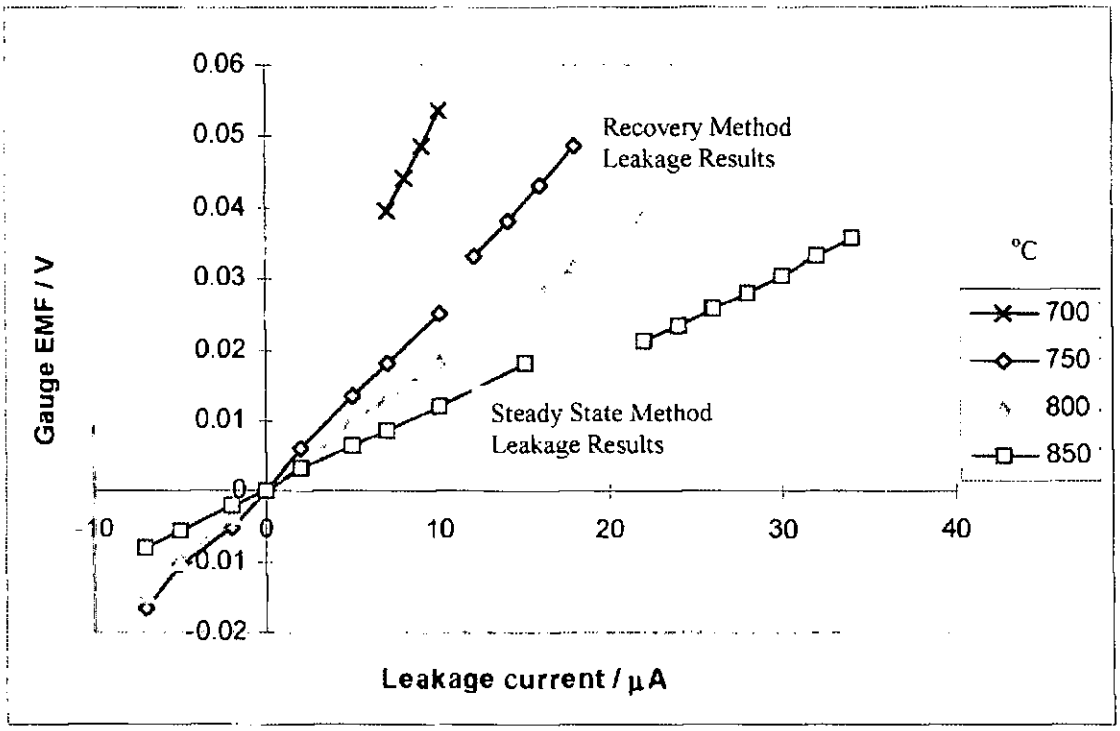

Figure F41 Leakage data comparison chart

We can use the data obtained from leakage tests to investigate the nature of leakage mechanism involved. An introduction to and an explanation of these analyses can be found in section B1.2. This work follows that of Kaneko et al [61] who used similar analyses to investigate leakage processes. If the process is dominated by a physical leakage mechanism then the leakage current would have been linearly related to the partial pressure differential (P_1-P_2) and would have been largely independent of temperature. From figure F42 we see this was not the case and physical gas leakage can be discounted as a major factor. Secondly we can test for semi-permeability by plotting the leakage current versus $P_1^{1/4}$ - $P_2^{1/4}$ (fig F43). Here we did see a certain degree of linearity at lower temperatures but this linearity broke down at high and low currents, especially at higher temperatures where semi-permeability would be expected to be at its most significant. Also literature suggests that the currents obtained (up to 5.6 $\mu A/mm^2$) were far higher than may be expected from this mechanism [61]. Also the dependence upon P_1 would suggest that this was not the dominant leakage cause, as oxygen concentration would not be expected to affect electrolyte permeability until much lower concentrations. Provided these assumptions are correct, we are led to believe that the dominant factor in device leakage must be electrochemical leakage. This was a surprising conclusion since, although similar tests conducted by Kaneko et al [61] using a gold sealed sensor, also showed electrochemical leakage as a dominant cause, those devices incorporated a larger leakage three phase boundary (TPB). The gold seal TPB extended around the entire sensor circumference, whereas the leakage TPB in these plastic-ceramic sensors was confined to the circumference of the conducting wire. This result may be explicable, at least in part, by the fact that gold, as used in the seal, is not a catalytic material whereas platinum, as used in the wires, is highly catalytic to oxygen ion dissociation. Copcutt & Maskell [129] used amperometric sensors employing a gold seal and a laser drilled diffusion pore in an attempt to measure SO_2 levels. They found that their sensors also suffered a large degree of electrochemical leakage. The high currents obtained in sulphur atmospheres suggested electronic conduction of the electrolyte in sulphur atmospheres.

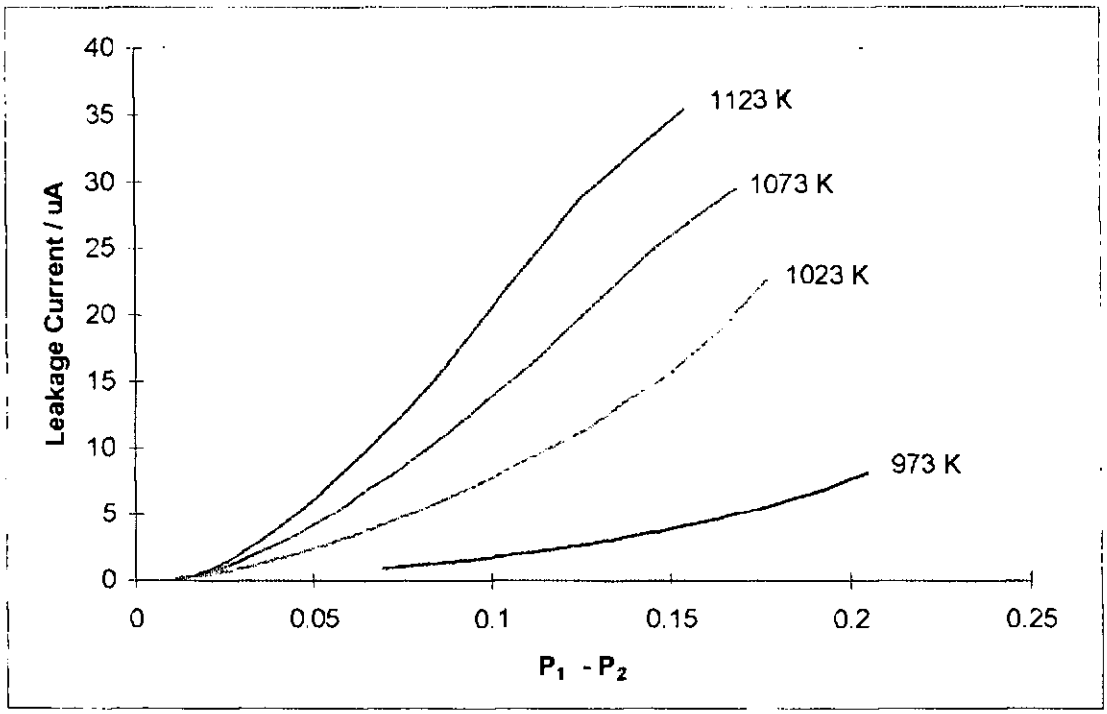

Figure F42 Test for physical leakage mechanism

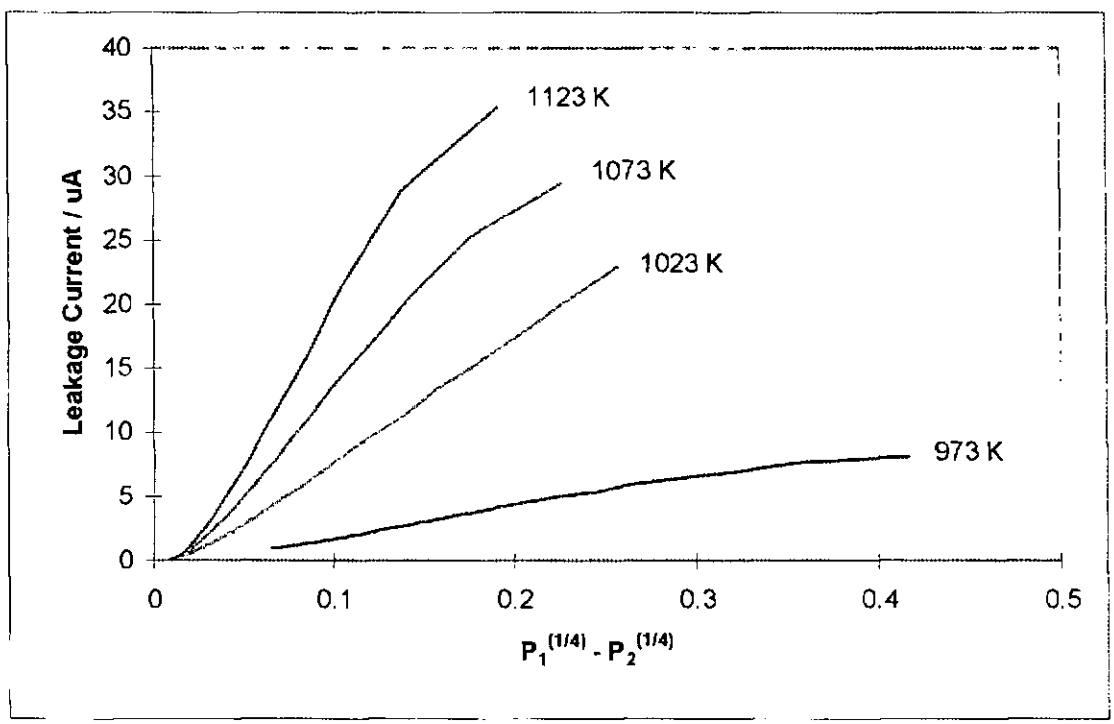

Figure F43 Test for semi-permeability leakage mechanism

To investigate the leakage phenomenon further, two small patches of electrode material were painted onto the sensor exterior and electrically connected to the internal electrode connection wire. In this way the effective leakage TPB was significantly increased. The calculated TPB length of two 100 μm diameter platinum wires = 0.62 mm. The calculated TPB length of a gold seal = 50 mm. Estimated TPB length of two ×4 mm^2 Pt cermet electrodes = 5152 mm (according to platinum electrode micrograph estimations see section 5.8). Leakage rate results were recorded using the recovery method for this device with one and then two leakage electrodes connected. Tests were also performed with high temperature glass used to block, firstly the wire connection TPBs, and secondly the entire sensor circumference. The results are compared figure F44. These show a dramatic

increase in leakage with the addition of subsequent leakage electrodes, and a significant reduction in leakage when the wire TPBs were glassed with leakage electrodes disconnected. A surprising result was that addition of further glass to block the entire seal actually increased the leakage currents obtained for a given gauge EMF. Closer examination shows that leakage rates di/dV actually remained unchanged but it is the intercept of the plot that has moved. Indicating that an additional (unidentified) leakage mechanism was present that had worsened upon glass application. The fact that leakage current versus gauge EMF plots do not pass through the origin supports this hypothesis. Prior to application of leakage electrodes, similar plots from the same sensor did have a point at the origin (see figure F41). Benammar & Maskell [60] found that the seal of a gold seal pump gauge could be improved by an external coating of glass to block three phase boundaries.

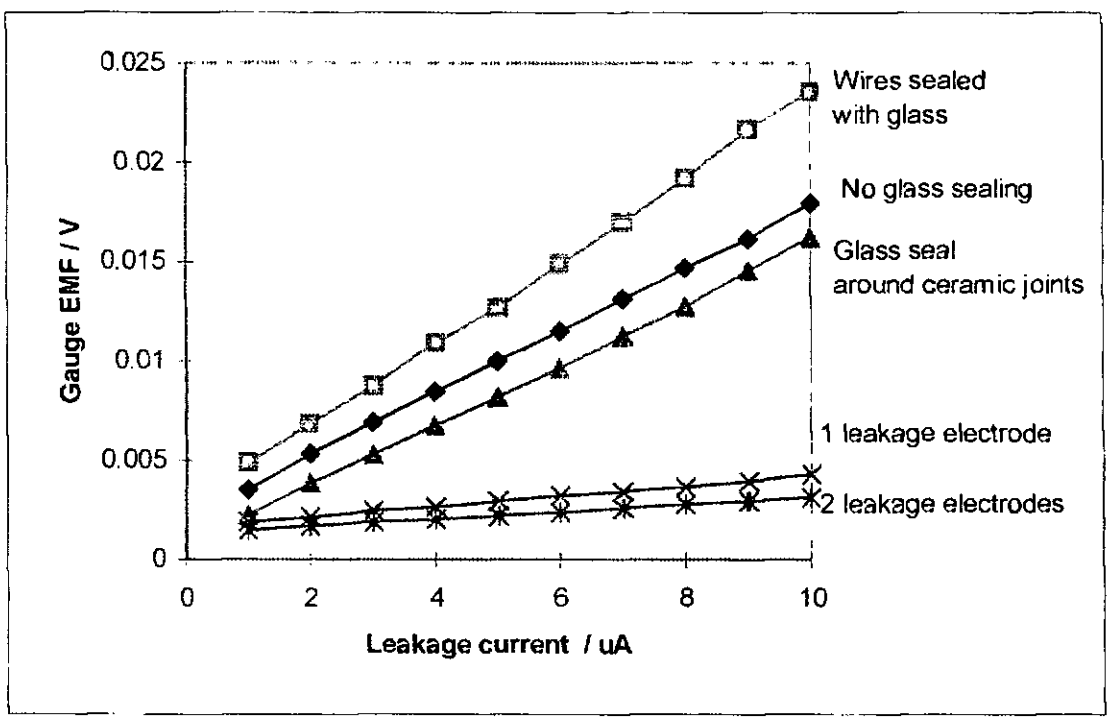

Figure F44 Data comparison of sensor with altered leakage characteristics

Furthermore, from the leakage current / EMF data of the original tests, it was possible to calculate the two electrode rate constants and the electrolyte resistance of the device (k_1, k_2 and R_L). Again see section B1.2 for details. A value for k_1+k_2 was obtained by plotting dE/dI versus $P_1^{-1/2}$, the gradient of which gave a k_1+k_2 value of approximately 1000 Ω $atm^{1/2}$ (see figure F45).

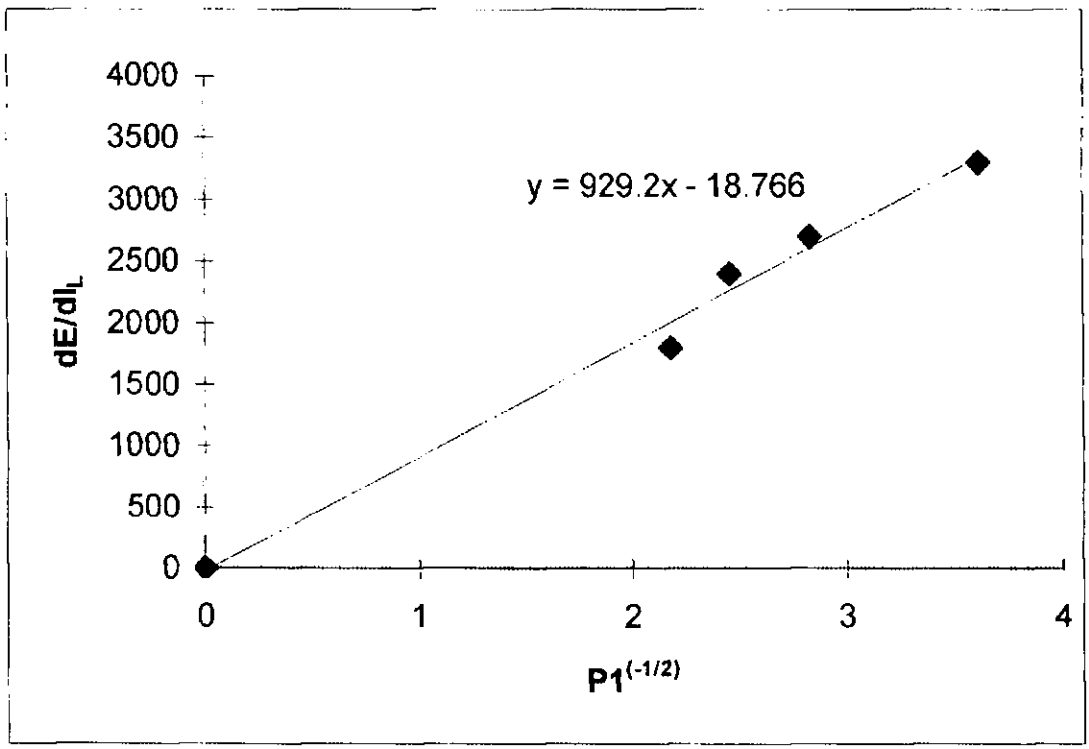

Figure F45 Determination of $k_1 + k_2$ value

A value for k_2 was given by the plot of E/I versus $P_2^{-1/2}$. For each oxygen concentration examined, this plot had virtually zero gradient and therefore we deduce that k_2 was small compared to k_1 which thus $\approx 1000\ \Omega\ atm^{1/2}$ (see figure F46).

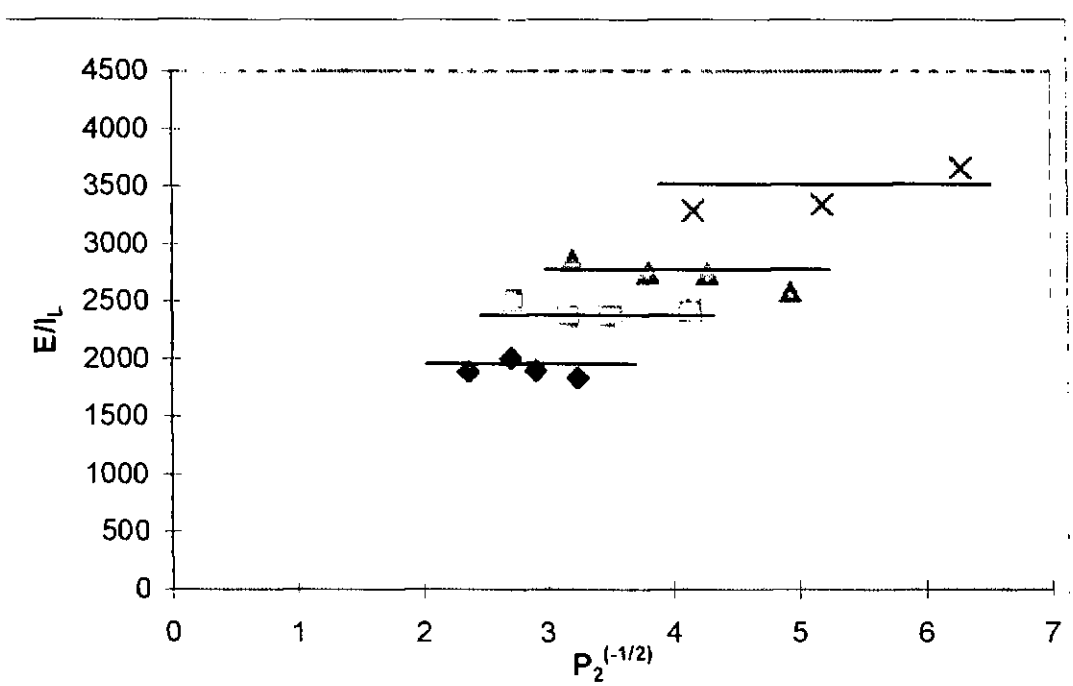

Figure F46 Determination of k_2 value

A plot of $P_1^{-1/2}$ versus the intercept of E/I versus $P_2^{-1/2}$ gives a line of gradient = k_1 and intercept = R_L again returning values of 1000 $\Omega\ atm^{1/2}$ and –550 Ω respectively. The intercept of –550 Ω represents a negative resistance, clearly this cannot be the case, and the results may be explained by the large uncertainty of this plot (see figure F47). An R^2

value of 0.987 was obtained for the straight line fit of this plot with a long extrapolation required to obtain this value.

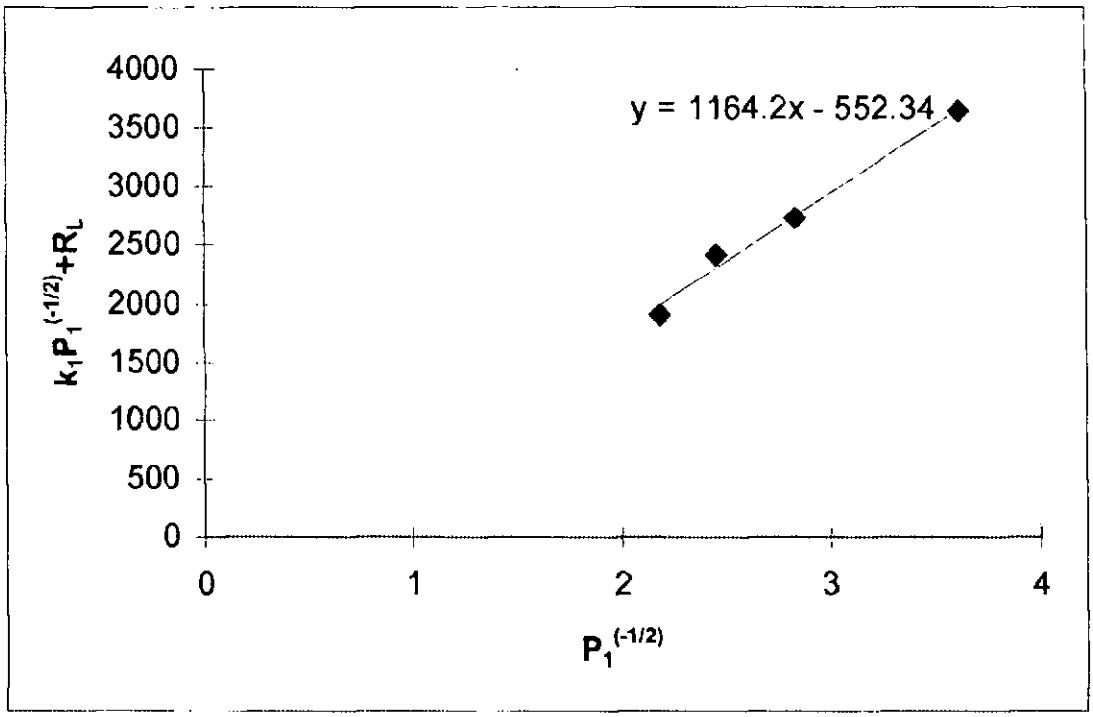

Figure F47 Determination of K_1 and R_L values

The R_L value does however indicate, as expected that the resistance of the electrolyte at these temperatures was not large (a fact backed up by impedance measurements see section 3.1.1). Figure F48 demonstrates that the calculated values do indeed tie up with the measured values for each data point recorded. This is somewhat to be expected since the calculated values were obtained directly for this data but, that the data does tie up for all data points at each P_1 is indicative of practice matching theory.

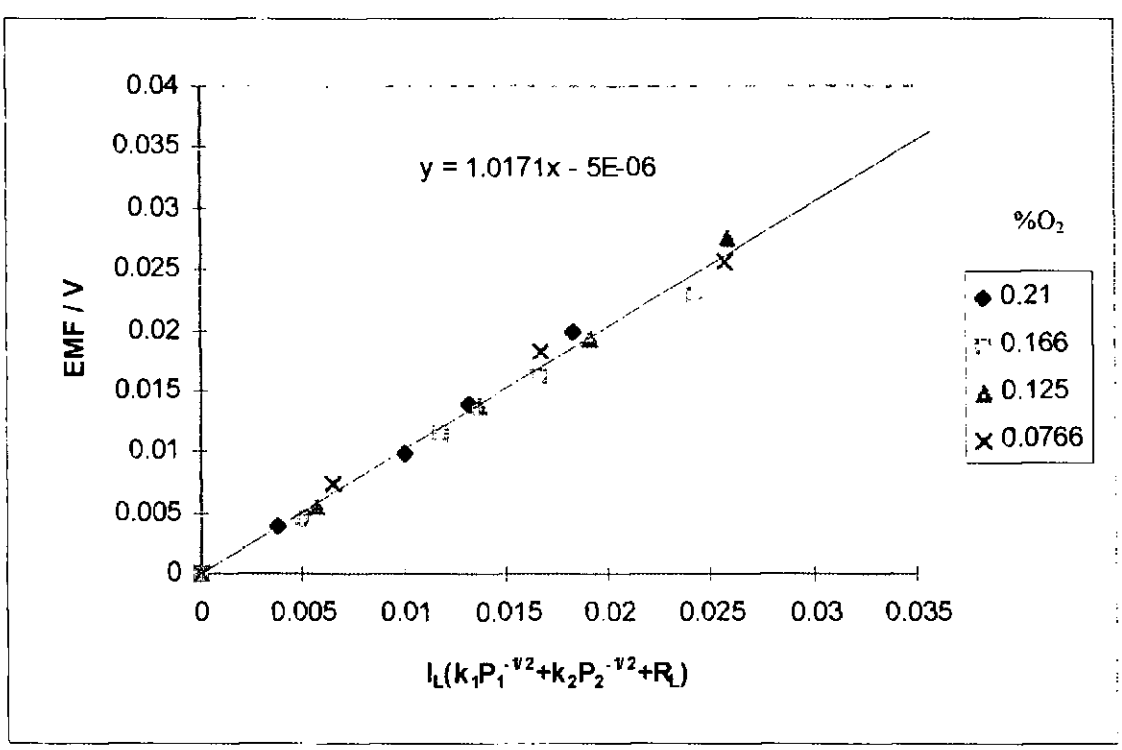

Figure F48 Assessment of electrode rate constant values

The results of Kaneko et al [61] are compared to values obtained in this work in table F3.

			Kaneko	This work
Seal rate constant	k_1	≈	4 kΩ $atm^{1/2}$	1 kΩ $atm^{1/2}$
Electrode rate constant	k_2	≈	1.5 kΩ $atm^{1/2}$	0 kΩ $atm^{1/2}$
Electrolyte resistance	R_L	≈	500 Ω	0 Ω

Table F3

The electrode resistance coefficients in Kaneko's work gave 3:1 ratio but different metals and imprecise area estimates made analysis difficult.

This comparison supports the theory that leakage rates in gold seal devices were indeed lower than in plastic-ceramic sensors. This is probably due to the catalytic nature of the connection wires as previously suggested. Haaland [23] found that the principle and significant leakage mechanism in his pump-gauge was that of electrochemical leakage through the platinum metal seal. A further finding of this work is that electrode and electrolyte resistances appear to have been reduced for these new devices. The electrolyte used here is a similar fully stabilised zirconia of similar dimensions, suggesting improved sintering, whilst my electrodes are platinum cermet compared to Kaneko's platinum metal, suggesting an electrode microstructure improvement. A definitive test would involve the fabrication of a device with non-catalytic gold connection leads, poisoned platinum connection leads or the successful blocking of leakage TPBs using glass. Attempts to seal the platinum wires using glass were unsuccessful due to a mismatch in thermal expansion coefficient and that glass, in contact with platinum electrodes can gave anomalous voltage readings.

F3 H_2O / CO_2 sensing

The following work has been published Maskell & Page [147].

F3.1 H_2O effects

The literature survey (section B1.3) suggested that, if present, humidity would reveal itself, in amperometric sensors, as a second limiting current plateau. Such a second current limit plateau had not been observed in the work carried out this far. One effect that had been seen in both fully sealed and amperometric pump-gauges, was a large step in gauge EMF after the initial plateau. At first this was suspected to be an effect of semi-permeability developing or of water used during fabrication being sealed into the devices. Further experiments using atmospheric, bottled and dried gases (Fig. F29) showed that these effects were due to moisture, introduced through the compressed gas supply. The presence of moisture may be expected to give such a result, considering the well-known step in potentiometric sensor EMF at stoichiometry of H_2 / O_2 gas mixtures however, as no secondary limiting current was apparent, a further examination was performed.

Below are given the redox O_2/H_2 reactions which allow ionic currents to be drawn. The first of these shows that the current is limited by the supply of oxygen molecules which controls the primary limiting current. In the absence of oxygen molecules and at sufficient applied potential, the second reaction will come into play, providing additional oxygen ions for the secondary current plateau. In this case it is the supply of water molecules which controls the increased magnitude for the secondary current plateau.

$$O_2 + 4e^- \leftrightarrows 2O^{2-}$$
$$H_2O + 2e^- \leftrightarrows H_2 + O^{2-} \qquad \text{Equation F40}$$

Considering now the gauge potentials, in the first instance (oxygen reduction) the potential is set by the difference in oxygen levels between the cell electrodes. The reference electrode potential is set by free oxygen partial pressure of the test atmosphere, the measuring electrode potential is set by the free oxygen partial pressure inside the sensor cavity. In the second instance (water reduction) the reference electrode potential is again set by free oxygen partial pressure of the test atmosphere but the measuring electrode potential is set by the H_2/H_2O couple established inside the sensor cavity.

Results of these tests (figure F49) show pump current and gauge EMF versus pump potential, using a four electrode amperometric sensor. Tests were performed using atmospheric air, a mixture of 21% oxygen / 79% nitrogen from bottled gas supplies and air passed through a column of calcium chloride to remove water. The results indicate that atmospheric H_2O gave a negligible effect on limiting current under these conditions but a had large effect on the gauge EMF where water was present. The fact that no secondary step was seen after drying demonstrated that the effect was due to H_2O and not CO_2 (although, if CO_2 were present in sufficient quantities a similar effect would be expected). Omerod et al [148] suggested respective atmospheric water and carbon dioxide levels of 1.5 and 0.03% and we would therefore expect a factor of 5 times less effect for CO_2 than H_2O at atmospheric levels. The impression that this test left was that a very sensitive H_2O sensor could be achieved using a conventional 4 electrode device. No such device has been reported in the literature. Logothetis et al [81] did comment upon the level of second gauge EMF although no results or analyses were presented.

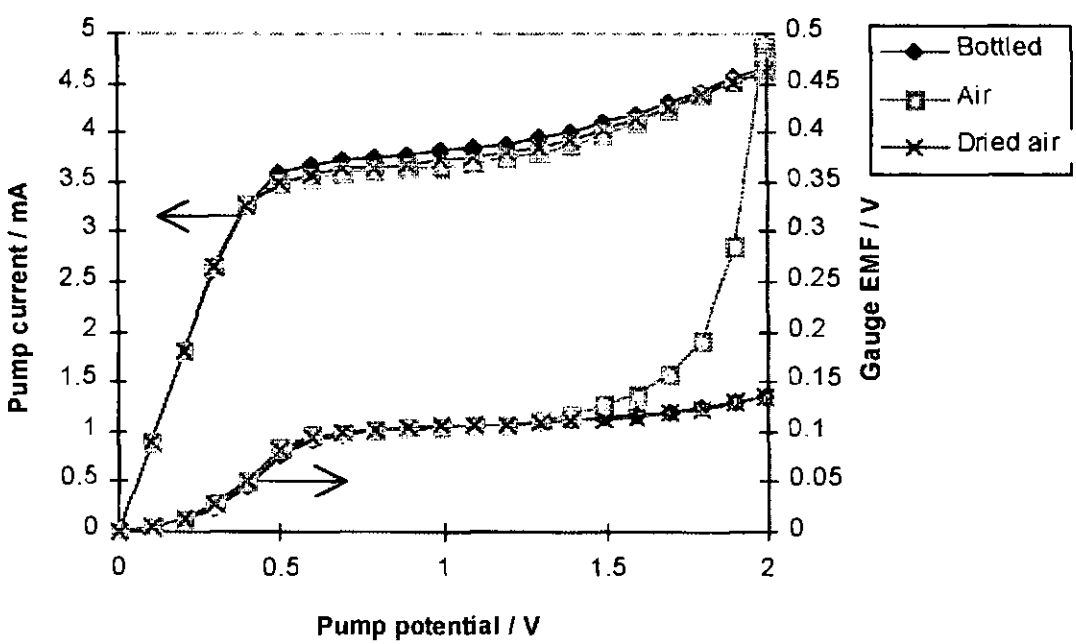

Figure F49 Sensor response to atmospheric, dried and bottled gases

Following the above result, a test-rig was specifically adapted for measurements in humid atmospheres (section C1.3.2) and more detailed experiments performed to identify the controlling factors.

F3.1.1 Oxygen concentration

A series of tests were performed to investigate the influence of O_2 concentration (see section E3.1. for experimental details). The results (figs. F50 & F51) showed the expected double limiting current plateaux, and also a double limiting plateau for the gauge EMF. It is worth noting that current and potential differentials were relatively unaffected by these significant changes in oxygen levels. A substantial second current limit is observed in these results as humidity levels introduced were significantly higher than atmospheric levels. Using a psychrometric chart, atmospheric water contents are estimated at 1.0 mole % (approximately 30% RH at 25°C, of the order of those quoted by Omerod et al [148]) compared to levels used in this work of 7.3 mole %. Interestingly, the second current plateau was initiated at a pump potential dependent upon oxygen concentration. Closer examination shows that the initial plateau remains flat over a similar pump potential range. This leads us to suspect that the shift was due to I.R. potential drop as a result of the larger currents required for diffusion limitation rather than a change in thermal decomposition voltage. The same trend in EMF step is also observed, and can be explained by the same factors.

Another interesting feature is that the secondary gauge EMF plateaux are initiated at lower pump potentials than those for pump currents, whilst primary pump and gauge plateaux occur at similar potentials. This leads us to suspect that the gauge is more sensitive than the pump to the presence of humidity. Analysis of these plateaux lengths returns values of 600 mV for the current and 400 mV for the gauge. These voltages can be partially attributed to the ohmic voltage component due to the current flow, which increased with increasing oxygen concentration, and the ionic resistance of the zirconia; the voltage component due to this effect can be estimated from the slopes of the current voltage curves at zero pump current. Carrying out such an exercise leads to an expected voltage separation of the curves for 2 and 21% oxygen in figure F51 of 400 mV. Examination of figure F51 indicates a separation, best estimated where slopes are highest of 600 mV indicating that there are additional components of pump voltage besides the ohmic one. Part of the remaining 200 mV is due to the change in effective reference gas between 2 and 21% oxygen; this accounts for approximately 50 mV (using the Nernst equation) of the 200 mV. The remaining 150 mV is probably electron transfer overvoltage. For the case where the oxygen concentration was only 2%, currents due to oxygen reduction were relatively small and so, as a result were the voltage drops due to the ionic resistance of the pump and the electron transfer overvoltage; thus, it is concluded that an electrode voltage of about 600 mV relative to a reference electrode in a gas containing oxygen is required to bring about the water dissociation reaction, equation F42.

It is interesting that the slope of the curve of gauge EMF at the onset of water reduction is proportionately very steep compared to that for the pump current. This again indicates that the gauge cell (potentiometric) is substantially more sensitive to the presence of a reducible species than is the pump cell (amperomctric) in this region.

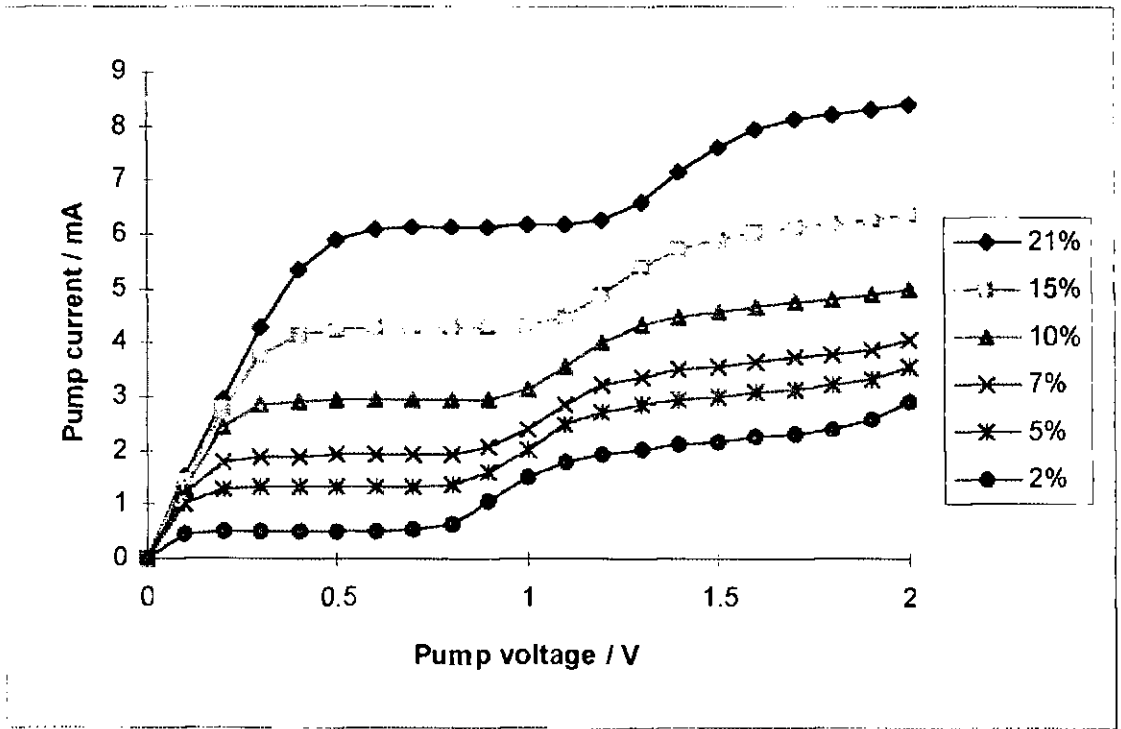

Figure F50 Pump current behaviour with oxygen variation in humid atmospheres

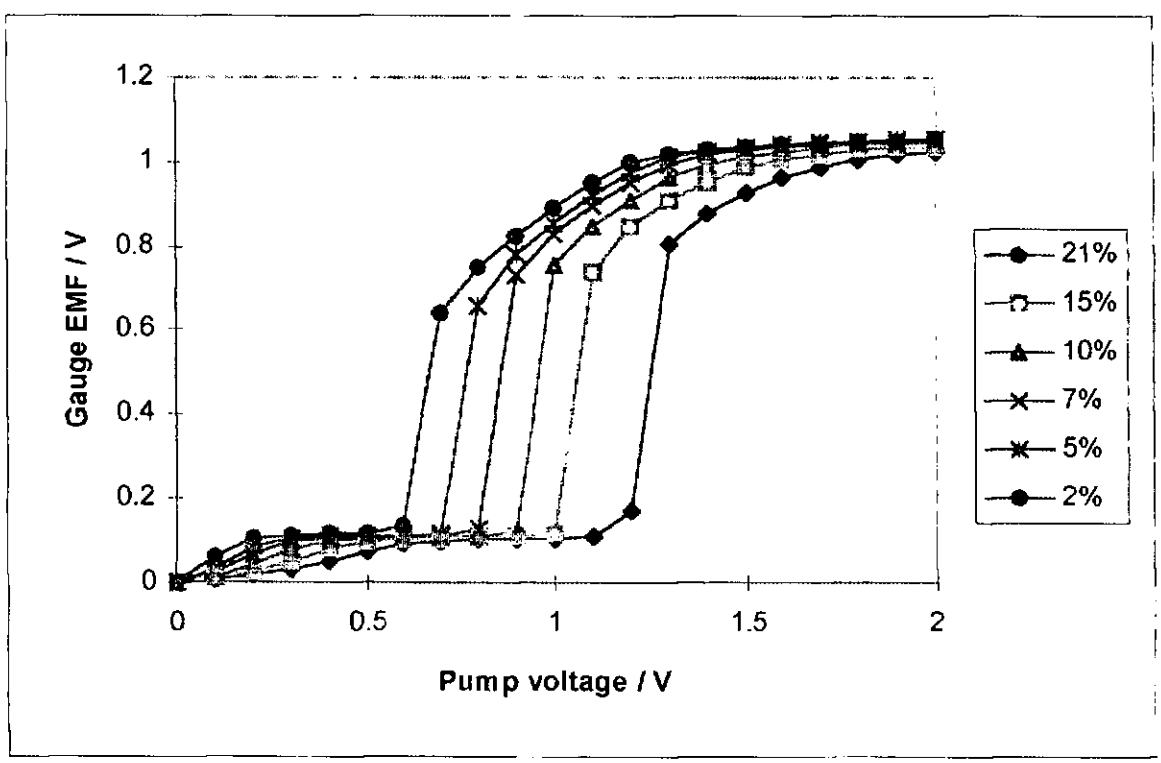

Figure F51 Gauge EMF behaviour with oxygen variation in humid atmospheres

F3.1.1.1 Water content calculation

Test atmosphere water contents are calculated from water bath temperatures, psychrometric tables and physical constants taking into account the relative molecular masses (RMM) and the dilution of gases by the H_2O species.

$$x'' = x' \times RMM_{Air}/RMM_{Water} \qquad \text{Equation F41}$$

$$X_{H2O} = x''/(x''+1) \qquad \text{Equation F42}$$

Where x' is the moisture content in kg/kg derived from psychrometric tables, x" is the mole fraction of water prior to consideration of dilution, X_{H2O} is the actual molar fraction of water.

Similarly, oxygen concentrations are also affected by the dilution effects of the additional moisture.

$$X_{O2} = X_{O2}' - (X_{O2}' \times X_{H2O}) \qquad \text{Equation F43}$$

Where X_{O2} and X_{O2}' and X_{H2O} are the oxygen mole fractions, after and before accounting for dilution effects, and the mole fraction of water respectively.

Dry air has a composition with mole fractions of 0.21 oxygen and 0.79 nitrogen (argon and other minor inert components have been summed and taken simply as nitrogen). If water vapour is then added to the air so that the mole fractions become X_{H2O} for water vapour and for air, $X_{Air} = (1-X_{H2O})$, then the mole fraction of oxygen $X_{O2} = 0.21(1-X_{H2O})$. The limiting current for oxygen reduction assuming no change in diffusion coefficient is given by equation F43.

$$I_{lim} = \left(\frac{4FDSP}{RTL}\right)\ln(1 - X_{O2}) \qquad \text{Equation F43}$$

approximating to

$$I_{lim} = \left(\frac{4FDSP}{RTL}\right)(X_{O2}) \qquad \text{Equation F44}$$

Taking the latter equation for simplicity and substituting the reduced oxygen mole fraction $0.21(1-X_{H2O})$ for X_{O2}, equation F45 becomes

$$I_{lim} = \left(\frac{0.84FDSP}{RTL}\right)(1 - X_{H2O}) \qquad \text{Equation F46}$$

Thus the limiting current in humid atmospheres should be related to the mole fraction of water in the air with a negative slope of (0.84FDSP/RTL). Table F4 below gives the conversions required to relate the water bath temperature to the reduction in oxygen concentrations as a result of dilution with water vapour. Table F5 below gives the conversions required to relate the oxygen concentration before humidification to the reduction in oxygen concentrations as a result of dilution with water vapour.

Dry	25	30	35	40	46	51	57	Water bath temperature °C
0	0.02	0.027	0.037	0.049	0.069	0.091	0.128	Moisture content kg/kg
0	3.22	4.382	5.900	7.862	11.101	14.709	20.622	x' %
0	3.12	4.198	5.568	7.289	9.991	12.823	17.097	X_{H2O} %
21	20.34	20.118	19.830	19.469	18.902	18.307	17.410	Diluted oxygen level %

Table F4 Values for levels of air with added water

21	15	10	7	5	2	Initial oxygen level %
7.289	7.289	7.289	7.289	7.289	7.289	X_{H2O} %
19.469	13.906	9.271	6.450	4.635	1.854	Diluted oxygen level %

Table F5 Values for levels of O_2/N_2 with moisture added. Water bath at 40°C

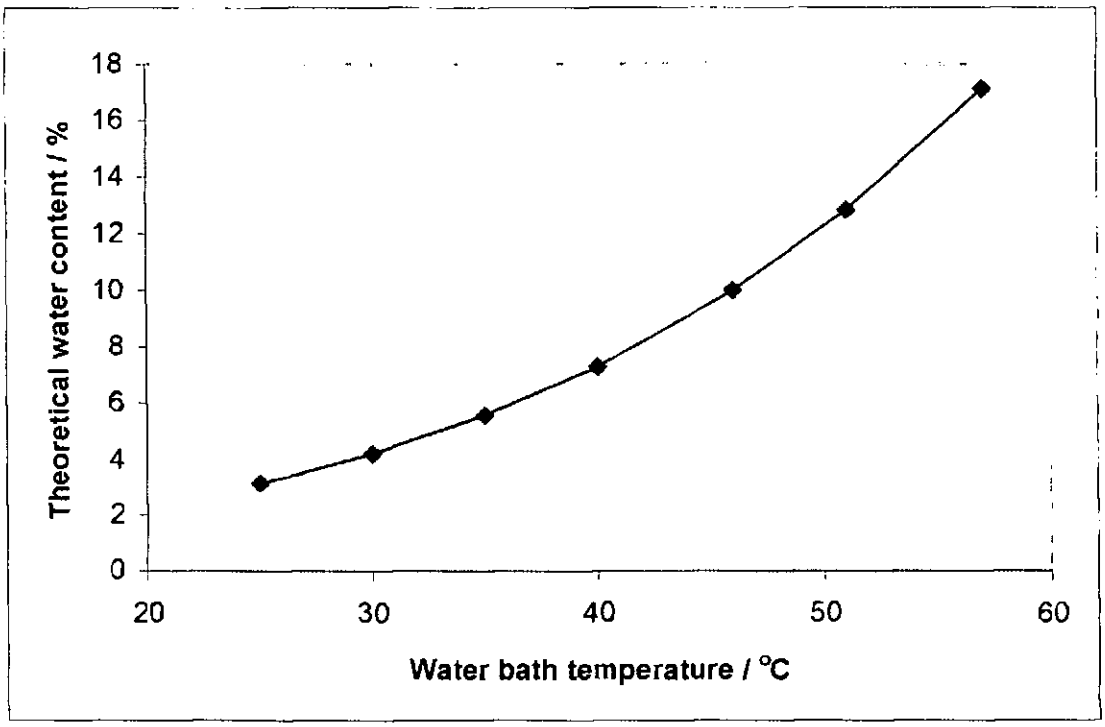

Figure F52 Translation of water bath temperature to percentage water content of gas

F3.1.1.2 Humidity sensing characterisation

Following the work of Takahashi et al [73], the levels of the two pump current plateaux were plotted versus $-\ln(1-X_{O2})$ (fig. F53) to give two linear plots of similar slope, intersecting at zero and a level above zero correlating with the humidity level in the absence of oxygen. This upper intersection occurs at 1.87 mA.

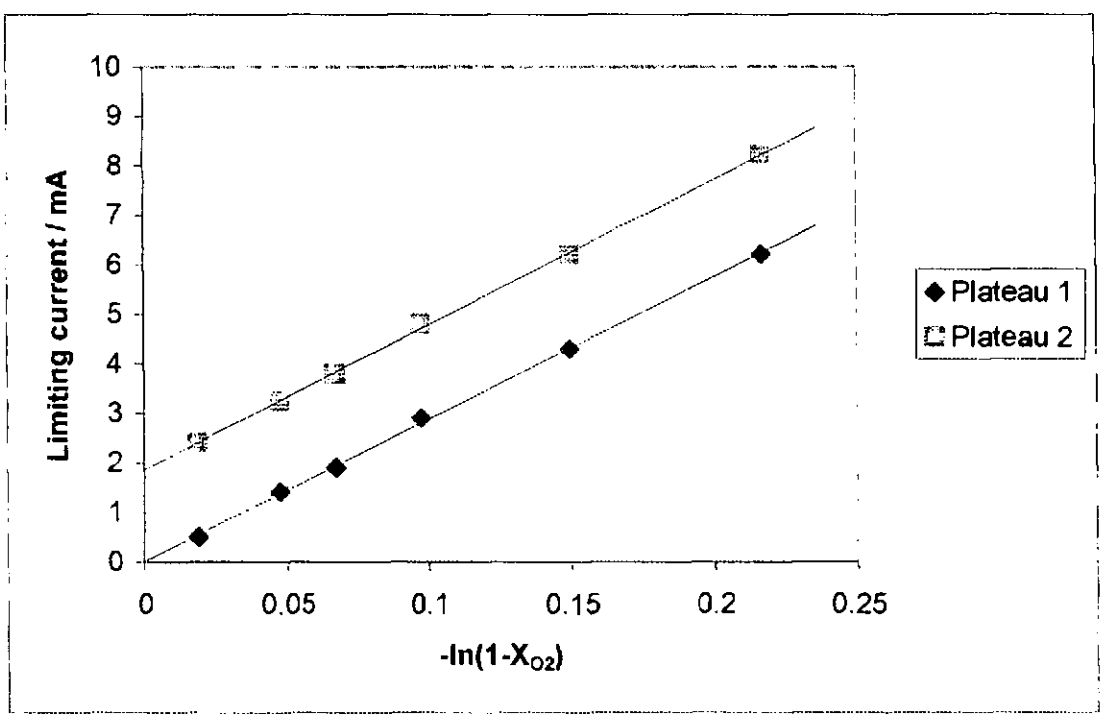

Figure F53 Effect of oxygen variation on both limiting pump currents

This current may be reinterpreted as a flow of water into the internal cavity using Fick's first law of diffusion replacing the factor 4 with 2 as only two moles of electrons are required to dissociate 1 mole of water, and using a diffusion coefficient for water in

nitrogen. The equations defining the limiting current for the primary and secondary plateaux are given in equations F47 & F48 respectively.

$$I_{O2} = \frac{4FD_{O2}SP_bX_{O2}}{RTL} \qquad \text{Equation F47}$$

$$I_{H2O} = \frac{2FD_{H2O}SP_bX_{H2O}}{RTL} \qquad \text{Equation F48}$$

Since both of these contain a similar set of physical constants, these may be used to perform a verification that the sensors characterisation by the above equations does hold.

$$\frac{FSP_b}{RTL} = \frac{I_{O2}}{4D_{O2}X_{O2}} = \frac{I_{H2O}}{2D_{H2O}X_{H2O}} \qquad \text{Equation F49}$$

(#a) (#b) (#c)

Using this analysis with input values of:

F	=	96500 C mol^{-1}	I_{O2}	=	6.91 mA
S	=	2.14×10^{-8} m	D_{O2}	=	1.95×10^{-4} m^2s^{-1}
P_b	=	101325 N m^{-2}	X_{O2}	=	21 %
R	=	8.314 J K^{-1} mol^{-1}	I_{H2O}	=	1.87 mA
T	=	1073 K	D_{H2O}	=	2.96×10^{-4} m^2s^{-1}
L	=	1.65×10^{-3} m	X_{H2O}	=	7.3 %

Table F6

Using equation F51 and comparing to the plotted results (figure F53), we get correlation values of #a = 14.216, #b = 42.186 and #c = 43.271. The two values for free oxygen and water dissociation agree closely however the first term is some way from agreement. It is most likely that this disagreement lies in the diffusion barrier S/L ratio as pump currents seen here are almost twice those seen in similar devices. Back calculating to get an estimate of S/L ratio required for agreement we see that a value of 3.9×10^{-5} m rather than the estimated 1.3×10^{-5} m is needed. This in turn would be realised by a diffusion barrier diameter of 0.34 mm rather than 0.2 mm expected. Whilst this is a substantial difference it is not beyond belief, and taking previous results and experience into account seems the most plausible explanation.

The diffusion coefficients for the above analysis are defined by:

$$D = D_0 \times \left(\frac{T}{T_0}\right)^{\alpha} \times \left(\frac{P_0}{P}\right) \qquad \text{Equation F50}$$

Where D, T, a, P are the diffusion coefficient, operation temperature, temperature coefficient and barometric pressure respectively. Values of D_0 and α are given for relevant gases in table F7, from which we see similar temperature coefficient from all but CO_2 and significantly high diffusion coefficients for H_2.

Temperature coefficient (α)						Diffusion coefficient at STP (D_0)				
Primary gas	Secondary gas					Secondary gas				
	O_2	H_2O	CO_2	H_2	CO	O_2	H_2O	CO_2	H_2	CO
Air	1.75	1.75	2	1.75		0.178	0.219	0.138	0.611	
N_2	1.75			1.75		0.181	0.256	0.144	0.674	0.192
O_2				1.75					0.697	
CO_2	2	2		1.75	1.75	0.139	0.202		0.55	0.137
CO	1.75			1.75		0.185			0.651	

Table F7 Gas pair diffusion coefficient data [130]

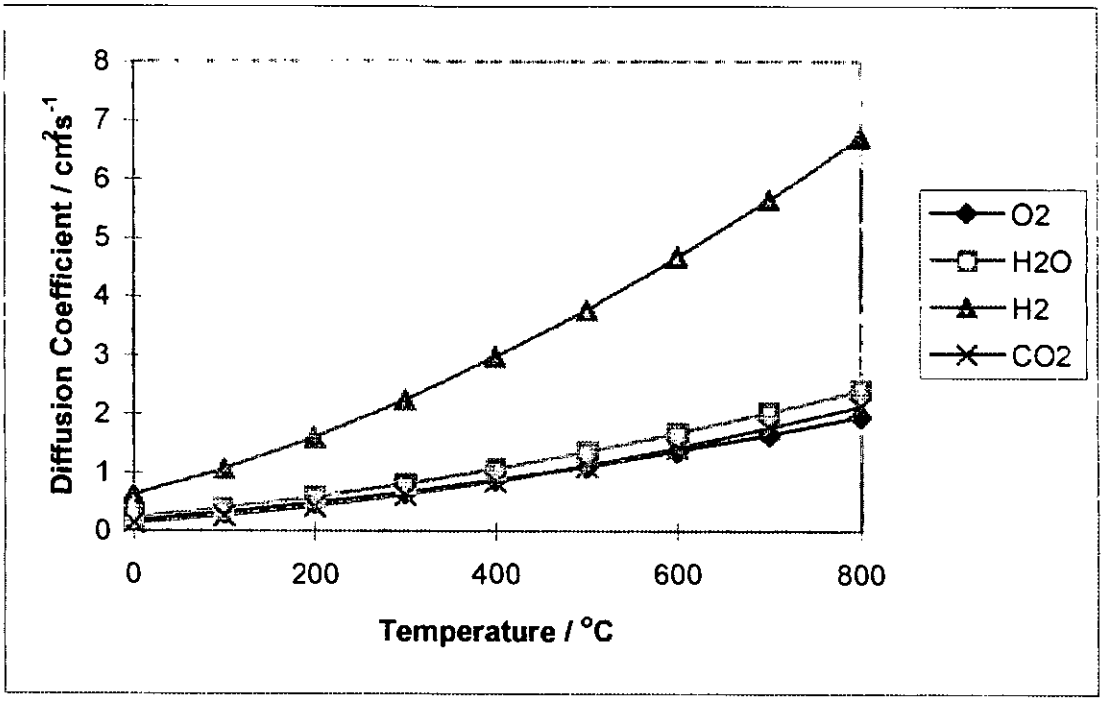

Figure F54 Gas diffusion coefficient with species in air

F3.1.1.3 Analysis of gauge cell measurements

The limiting current data for the primary plateaux given in the above analyses were taken from the intercepts of exponential type plots as discussed in section F1.3. These exponential plots are derived from combining the pump cell measurements with those of the gauge cell. In brief these plots extrapolate data from the low leakage (low pump potential) region to the high pump potential where semi-permeability can be significant. Thus we can predict the true limiting currents given by both the slope and intercept of the linear regions. In addition to predicting the true limiting currents, these plots can also be used to indicate problems with the sensor as seen in section F1.4 where high oxygen concentrations produced a curvature in these plots. In this case the good linearity of these plots gives added confidence to the readings obtained.

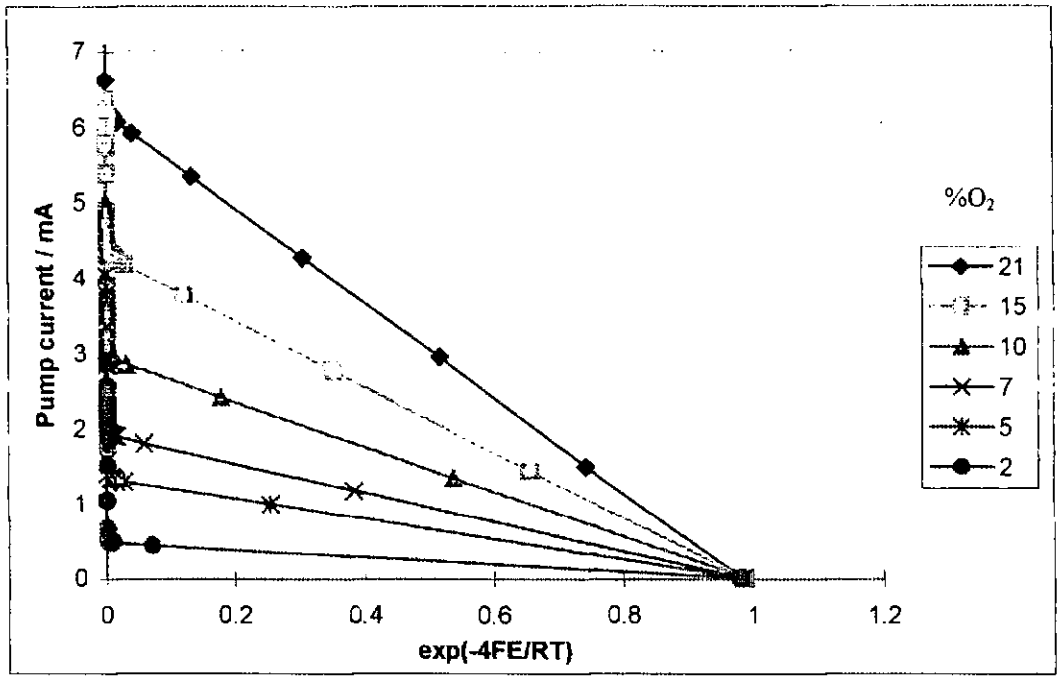

Figure F55 Exponential plot for oxygen concentration variation to show true limiting currents

We now turn our attention to the data obtained from the gauge electrodes. The two EMFs of the split gauge cell are plotted against $-\ln(1-X_{O2})$. Both the EMF plots (fig. F56) follow a linear relationship with the same negative slope. The level of the differential seen in figure F51 is maintained at around 70-80 mV. The second plateau shows a value of around 1volt, this is approximately 10 times the EMF recorded at the primary plateau, falsely indicating a residual oxygen pressure of 1 oxygen molecule in 3×10^{19} (1 molecule in ≈ 4 cm^3). This logically supports the theory that the EMF plateau differential is set up by H_2/H_2O couple rather than residual oxygen partial pressure as sensor internal cavity volume is only of the order of 16 mm^3.

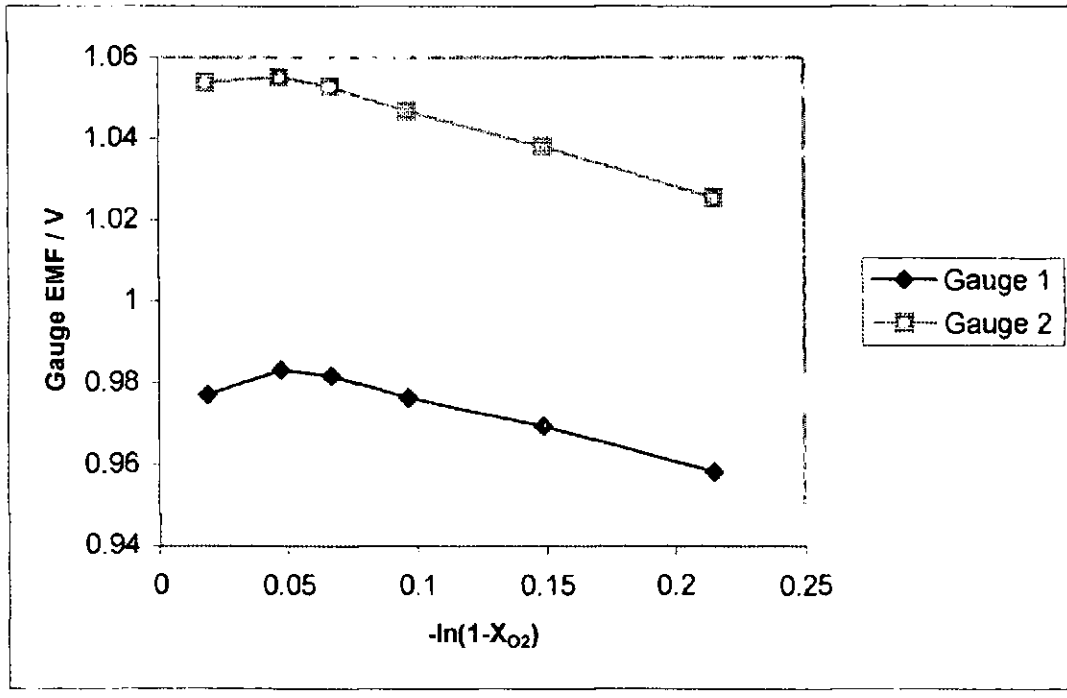

Figure F56 Effect of oxygen variation on the two secondary limited gauge EMFs

In figure F57 the recorded EMF for both of the split electrode gauges is translated into internal oxygen partial pressure for oxygen concentrations of 19.3, 9.7 and 4.6%. The gauge near to the diffusion hole is represented by solid markers whilst the remote cell is depicted by open markers. The data shown represents only data for the primary oxygen reduction EMF plateau as data for the secondary plateau would indicate un-representatively low pressure indications. At primary plateau levels we see a constant differential between the two gauge cells irrespective of oxygen concentration but a steady decrease in internal oxygen pressure with external oxygen pressure. The rough impression that these diagrams give is that there exists an approximate drop of two orders of magnitude between the internal and external oxygen concentrations across the diffusion barrier to attain the limiting condition. A further drop is seen across the internal sensor electrode face with distance from the diffusion barrier.

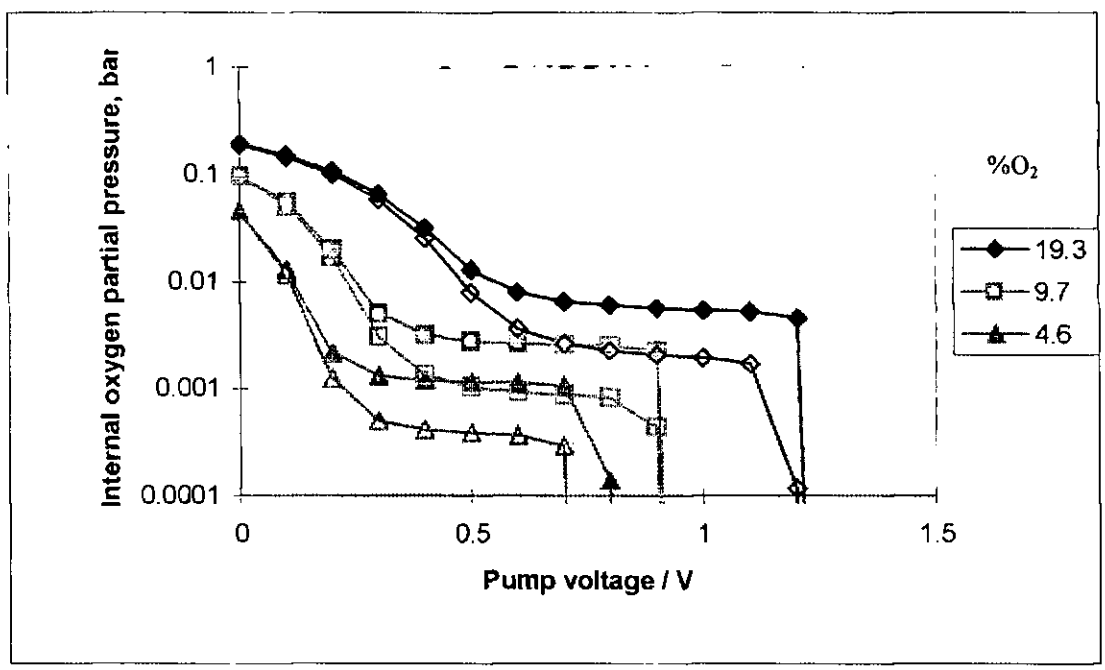

Figure F57 Oxygen concentration dependence of internal partial pressure

F3.1.2 Temperature variation

Reducing the operating temperature of amperometric sensors had the effect of increasing both electrolyte bulk resistance and electrode interface resistance. These translate into the characteristic curves of the sensor by requiring increased pump voltages in order to pump sufficient oxygen to attain a limiting current plateau and for water reduction to occur. Results of the sensor in humidified air over a range of temperatures is given in figures F58 & F61. At 650°C, these effects were sufficient to prevent resolution of the secondary plateau at pump voltages of up to 2 V. Operation at lower temperatures could be realised by a reduction of the S/L ratio, effectively providing a more restrictive diffusion barrier, allowing lower pump currents which may be attained at lower temperatures. Temperature effects on the second limiting current plateaux (fig. F58) are not obvious due to the effects of semi-permeability playing a significant role above 800°C.

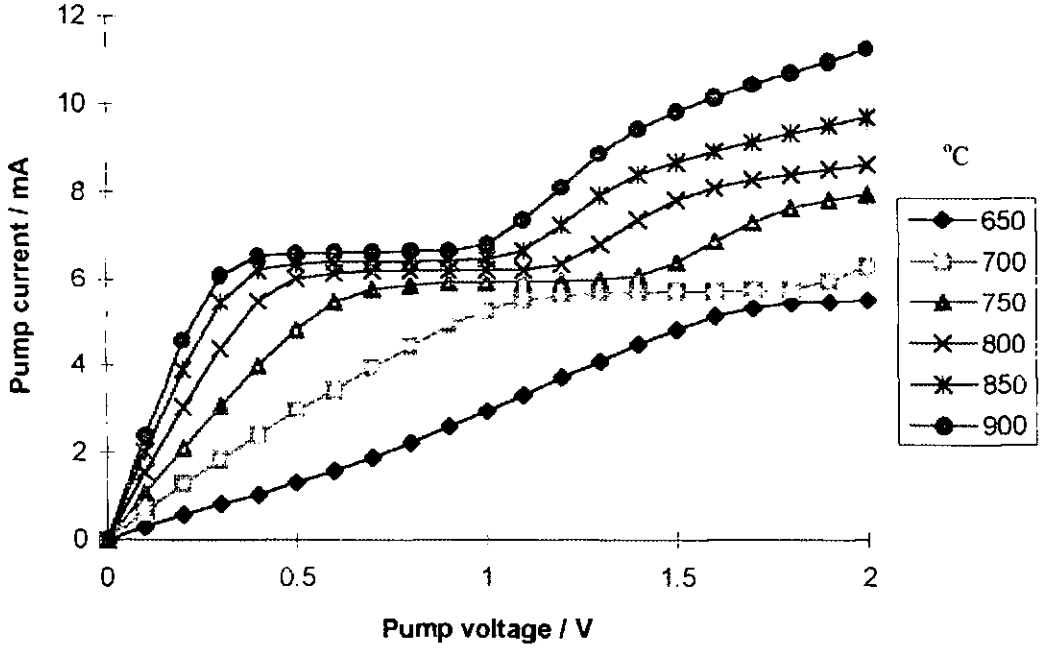

Figure F58 Pump current behaviour with temperature variation in humid atmospheres

F3.1.2.1 Analysis of temperature coefficient

Analysis of temperature dependence of the primary current plateau show, in accordance with theory (see section F1.2), a temperature coefficient of $\alpha = 1.72$ (fig. F59), in line with theoretical diffusion temperature coefficients of alpha = 1.75 as discussed in section F1.2. This also shows that a sensible temperature coefficient can be obtained from plastic/ceramic sensors and so the previous deviation is not a peculiarity of this novel manufacture technique. The alpha coefficient for H_2O/N_2 gases is similar to that of O_2/N_2 [130] (table F7) so a similar temperature coefficient of operation would be expected. Note that at the stage of the primary limiting current, hydrogen gas has not yet been evolved and so does not affect gaseous diffusion or temperature dependence.

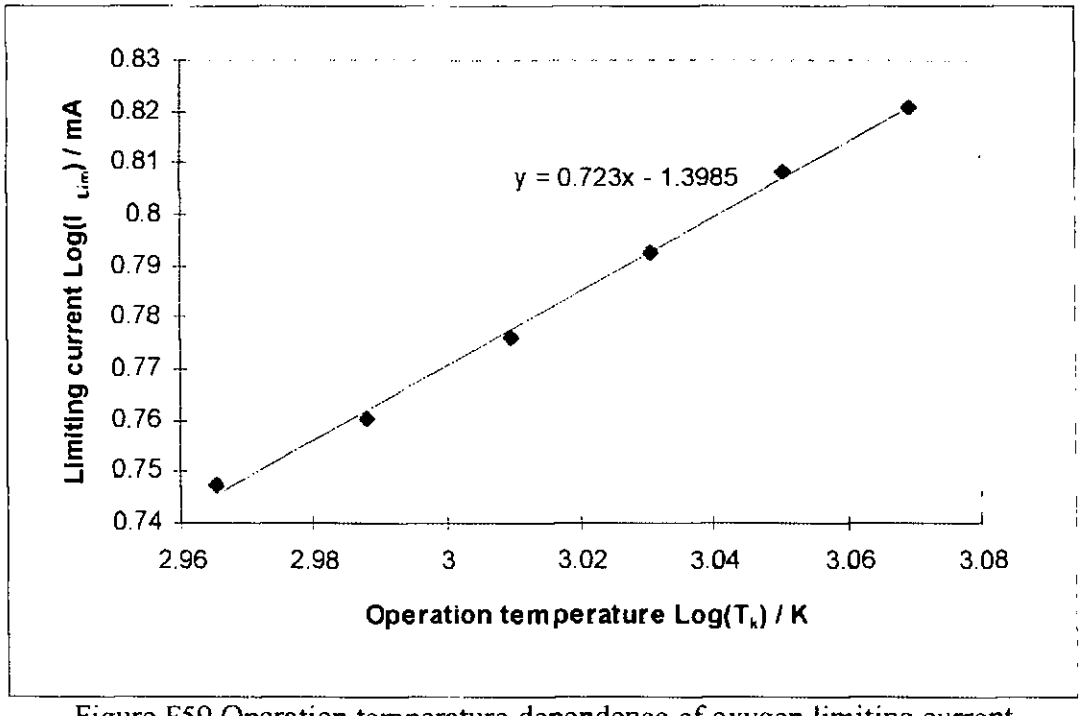

Figure F59 Operation temperature dependence of oxygen limiting current

F3.1.2.2 Electrolyte impedance calculation

By calculating the slope of the current/voltage curves taken at low pump potentials, we obtain an idea of cell resistance using Ohm's law. The data obtained in such a manner is presented below in Arrhenius format. Such a chart could be expected to reveal a straight line, the slope of which gives the activation energy for the process. The resultant plot is superficially linear but with a clear curvature present. This may be explained by the fact that we actually have a composite of three separate processes, discussed chapter 4, of electrode interface, electrolyte grain and electrolyte grain boundary polarisations.

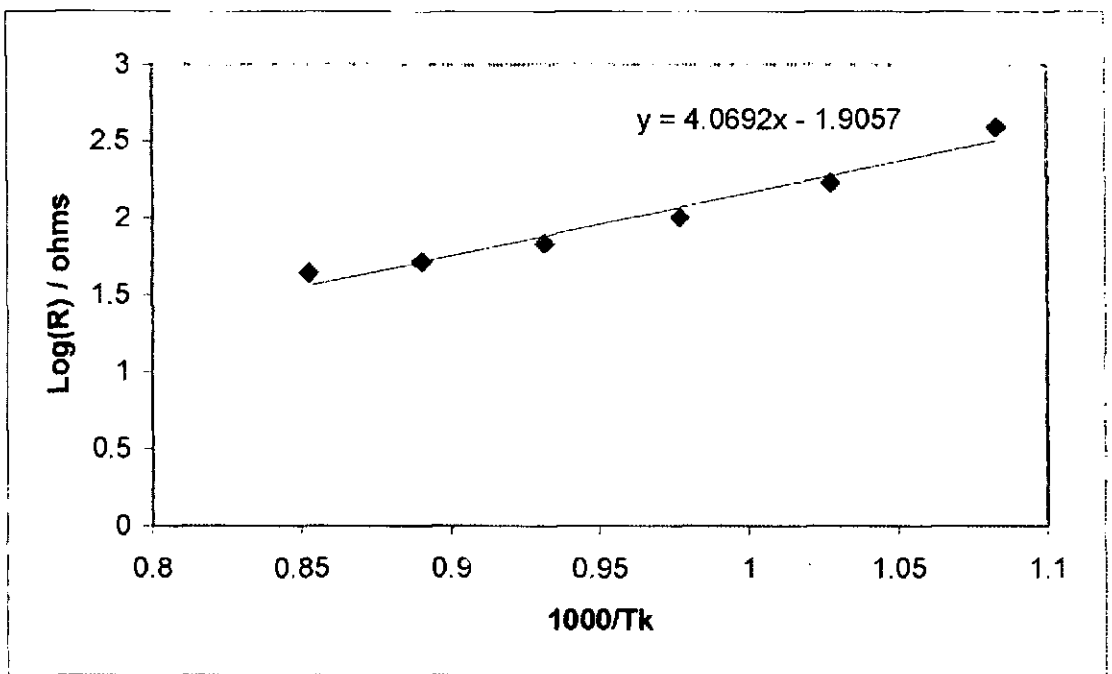

Figure F60 Initial current / voltage indication of cell resistance with temperature variation plotted in Arrhenius format

F3.1.2.3 Analysis of gauge cell measurements

The gauge EMF on the other hand does not suffer the effects of semi-permeability as gauge potentials involved remain small at less than one volt irrespective of pump potential (fig. F61). The use of a high impedance voltmeter ensured that current flow was negligible. This enables us to see that the temperature effects on gauge EMF (primary and secondary plateaux) are indeed small, with similar levels obtained for both plateaux throughout the temperature range examined. Again, the secondary EMF plateaux are initiated at lower pump potentials than those of pump currents.

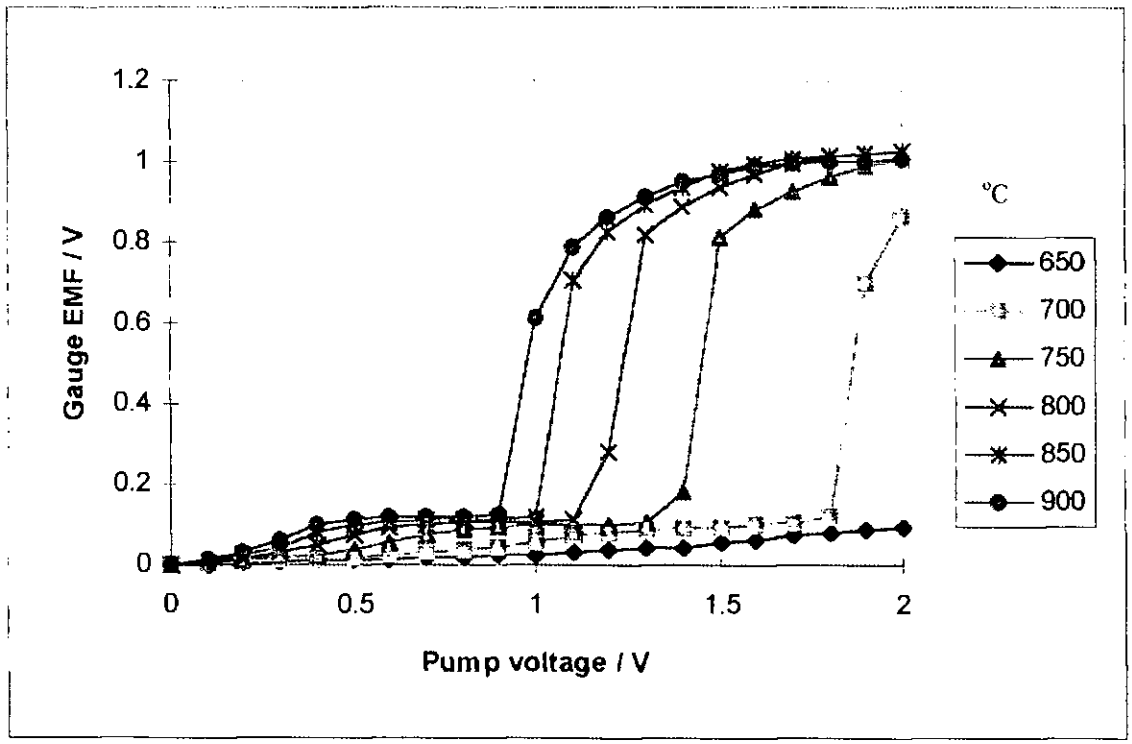

Figure F61 Gauge EMF behaviour with temperature variation in humid atmospheres

Figure F62 demonstrates the exponential type plot through which true primary limiting currents are taken. Whereas in the previous exponential plot of figure F55, we saw the anticipated linearity in low pumping region, in this case we see a significant curvature occurring at lower temperatures (<750°C). Previously seen curvature of these plots has been explained as a flow of gas through the diffusion pore as a result of high oxygen concentrations. In this case however, the curvature is in the opposite direction and is more likely attributable to poor electrode activity and low pump cell efficiency at reduced temperature. One clear indication given by this plot is that of low temperature sensitivity of these devices with a drop of about 15% in limiting current over the range of 250°C or < 0.07 % / °C.

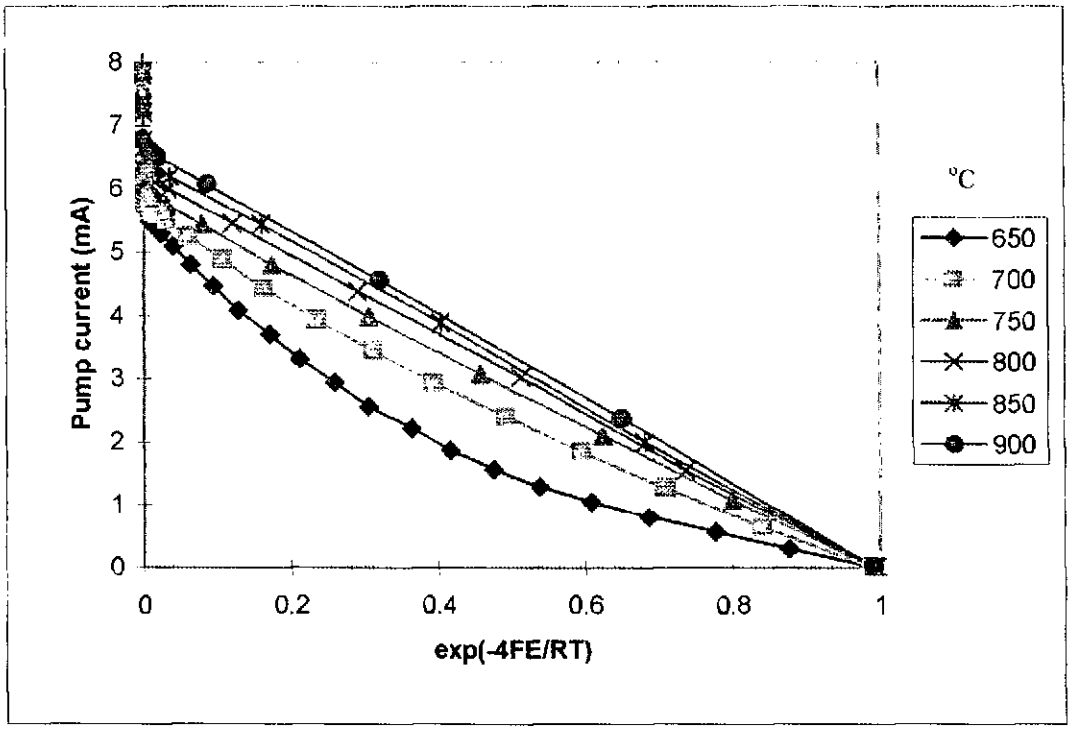

Figure F62 Exponential plot for operation temperature variation to show true limiting currents

The sensor used in this work had a split internal gauge electrode. Using both gauge EMFs, the data were converted to internal partial pressures using air as the reference gas (fig. F63). Plotting these versus pump potential, we see a similar level attained at each temperature, prior to the occurrence of the second plateau. A constant differential between the two gauges was also observed. This indicates that the effects of temperature have very little influence on the overall diffusion mechanisms where humidity is present but not dissociated.

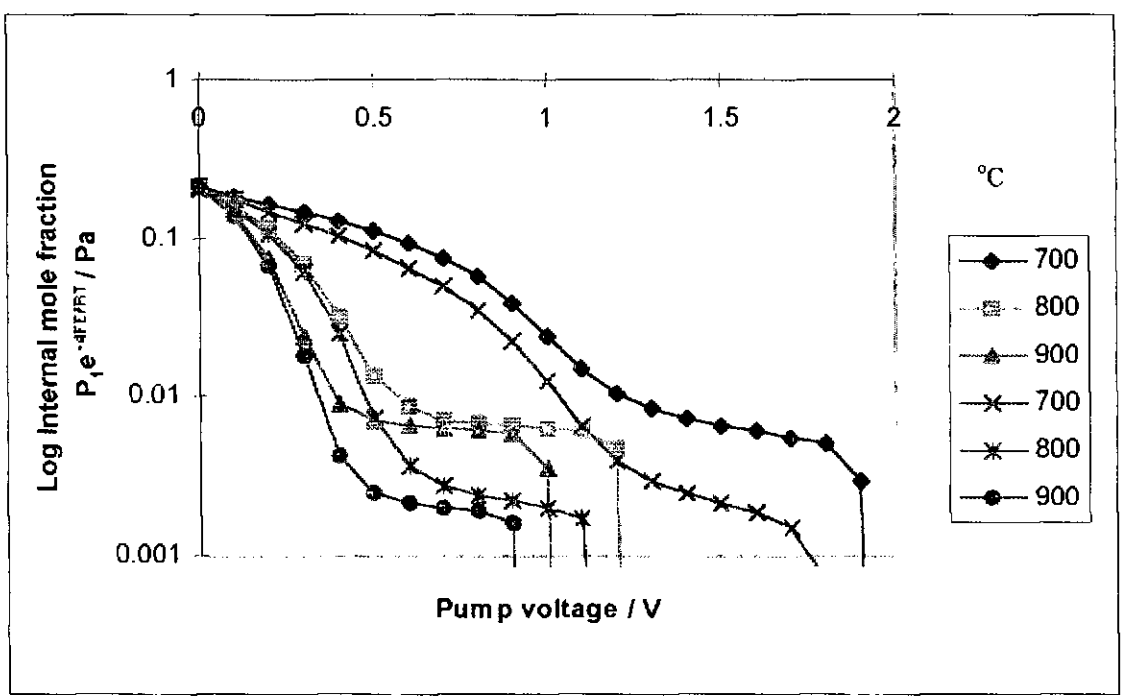

Figure F63 Operation temperature dependence of internal partial pressure

F3.1.2.4 Assessment of thermal decomposition voltage

The thermal decomposition voltages for H_2O and CO_2 are compared in figure F64 this comparison is made from theoretical equations for these coefficients presented by Usui et al [89]. The comparison shows that for the range of temperatures covered by this work there exists a steady decline in decomposition voltage which is of similar values for both reducible species. The decomposition voltage is dependent upon Faradays constant and Gibbs free energy which is in turn temperature dependent. A point of interest occurs at 830°C at which the decomposition voltages for both gases is identical. Unfortunately insufficient data have been obtained within relevant temperature ranges for a detailed comparison with these equations.

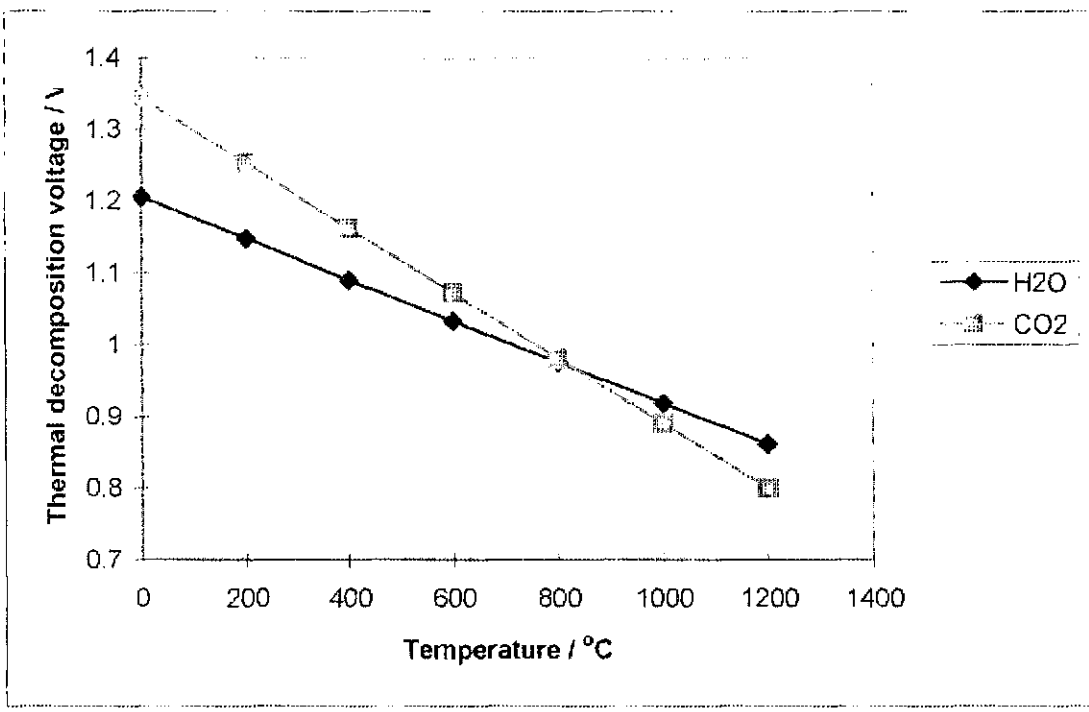

Figure F64 Comparison of temperature dependence of the thermal decomposition voltage for H_2O and CO_2

$$E_x = \frac{1000G_x}{-2F} \qquad \text{Equation F51}$$

$$G_{H_2O} = -247.657 + 0.0552T_K \qquad \text{Equation F52}$$

$$G_{CO_2} = -283.328 + 0.08753T_K \qquad \text{Equation F53}$$

F3.1.3 Humidity variation

Having established oxygen and temperature dependence of operation in humid atmospheres, the sensor was operated in atmospheres of varying humidity. The pump characteristics (fig. F65) again show a double current plateau. The legend in figures indicate measured water bath temperature used in gas humidification (see table F8 for conversion to mole %). Pump currents are seen to be very similar for pump potentials below 0.4 V. This indicates that gas humidity levels have little effect on cell resistance. In these tests both plateaux were affected by humidity, contrary to the work of Takahashi et al [73]. This discrepancy may be explained because, in this work, water was added to the oxygen/nitrogen gas mixture, effectively decreasing the partial pressure attributable to the oxygen and nitrogen components. In Takahashi's work the oxygen partial pressure was

kept constant and water reduced nitrogen partial pressure alone. In this work, the current plateau orders reversed upon water decomposition as the dilution effects of water presence were negated by the evolution of oxygen from the water dissociation. The currents of the second plateaux do appear to have been affected to a certain extent by semi-permeability, indicated by a significant positive slope to the secondary current limit plateau. By maintaining a constant temperature the effects seem to be humidity independent and for the most part can be ignored.

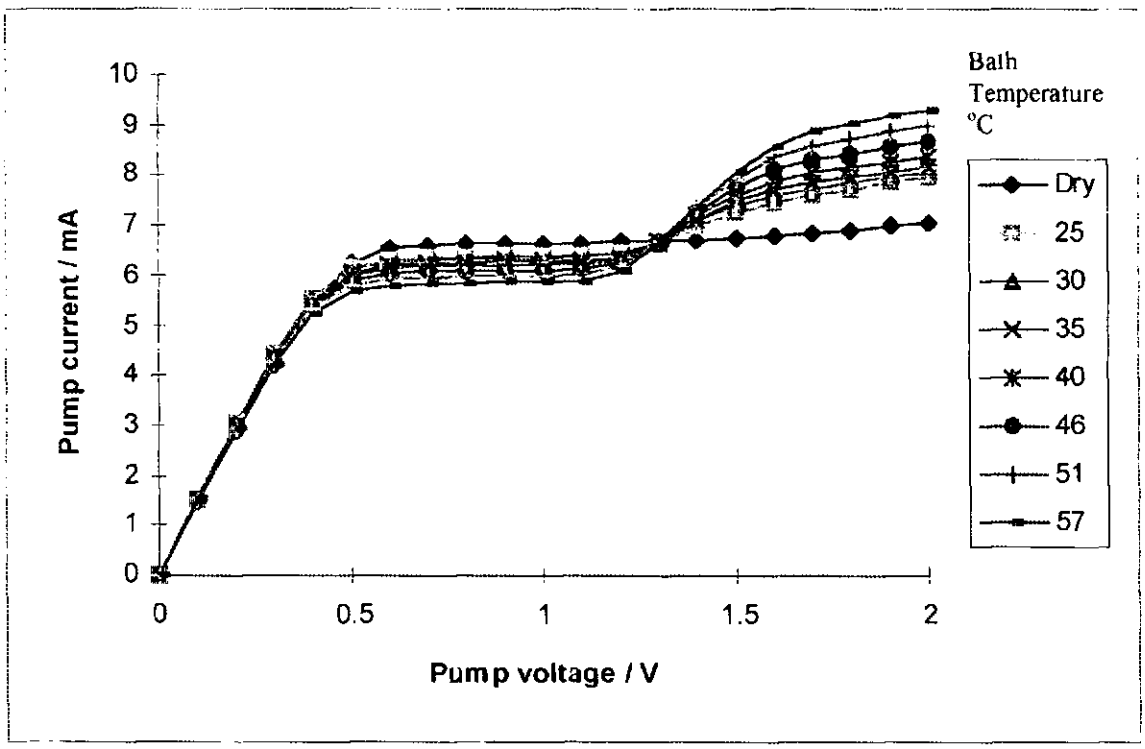

Figure F65 Pump current behaviour with humidity variation

F3.1.3.1 Water content correction

Figure F66 shows the relation between primary limiting current and oxygen concentration for the humidity variation experiments. This shows the dilution effect of the introduced water on the free oxygen concentration for which we would expect to see a straight line according to theory and previous experience using these devices. This leads us to the conclusion that, despite the precautions taken, the air introduced to the test-rig had not attained 100% relative humidity. This plot can, however, be used to back-calculate to give a measurement of humidity. We have shown the linearity of the sensor to free oxygen concentration, and we know that the air contained 21% oxygen prior to humidification, so we can confidently predict the moisture content of the humidified gases.

$$\text{Fraction of } H_2O = (1 - I_{dry}/I_{humid}) \qquad \text{Equation F54}$$

Where I_{dry} = primary limiting current in dry air and I_{humid} = primary limiting current in humidified air.

Using this method we obtain the values in the table below:

Bath Temperature °C	Dry	25	30	35	40	46	51	57
Theoretical mole % water	0	3.12	4.198	5.568	7.289	9.991	12.823	17.097
Oxygen dilution mole % water	0	3.966	4.535	5.544	6.620	8.178	9.870	11.628

Table F8

These results are depicted in figure F67 showing the re-calculation effect on primary, secondary and differential limiting current. The re-calculated water contents are shown by solid markers, the psychrometrically calculated values by open markers. The re-calculated values show a far stronger linearity, giving confidence to this method. The differential current shows a non-zero intercept which indicates a significant degree of electrolyte semi-permeability at a pump voltage of 2 V, where the secondary limiting currents are measured.

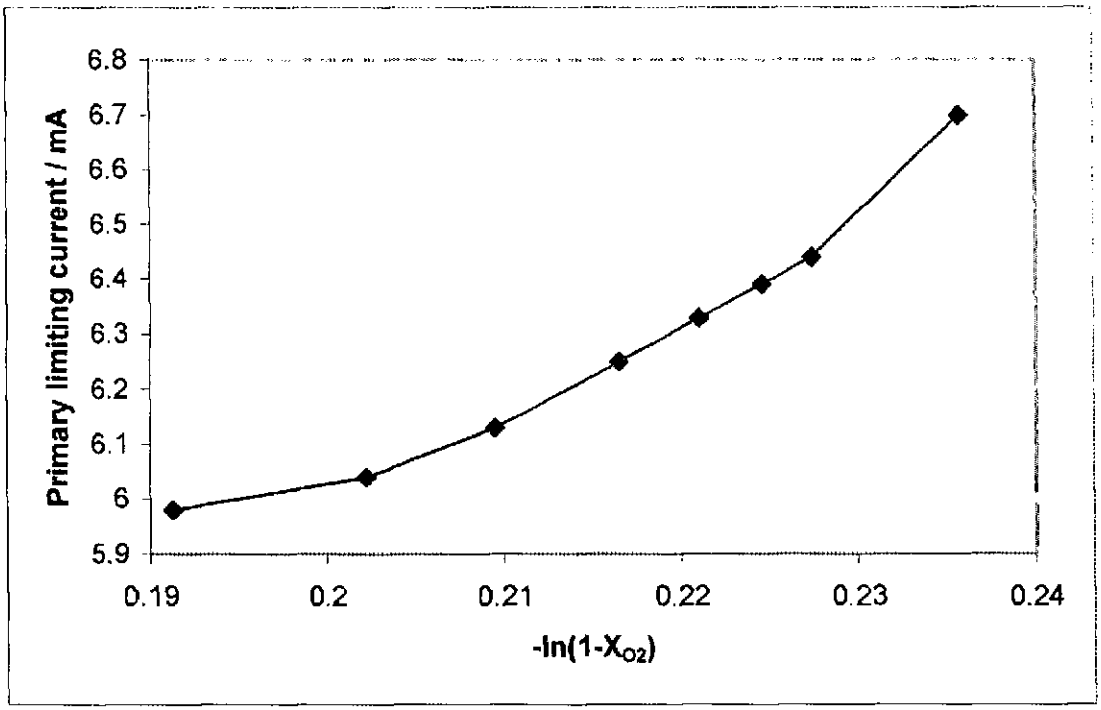

Figure F66 Primary limiting current versus diluted oxygen levels

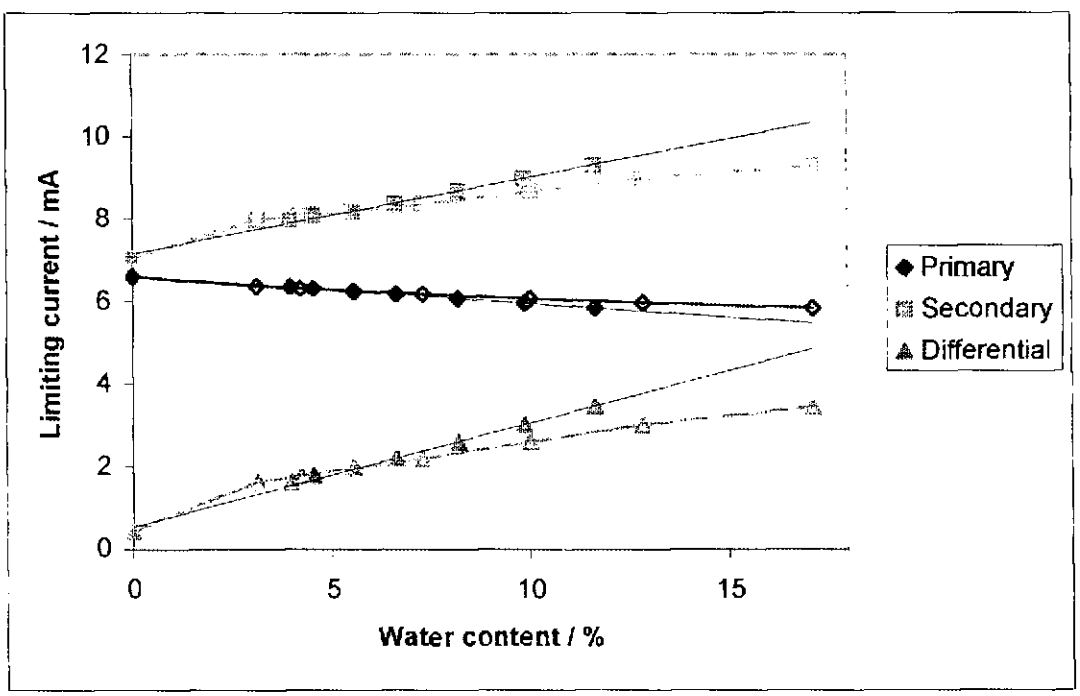

Figure F67 Primary limiting current versus diluted oxygen levels

F3.1.3.2 Analysis of gauge cell measurements

In considering the gauge EMFs (fig. F68) we see that the plots at each humidity are virtually identical up until 1.1V when deviations provide slightly higher EMFs for higher

humidities. This trend is to be expected as internal/external partial pressure differential is virtually humidity independent prior to dissociation. It is, however notable that the differences above 1.1 V are small. This can be attributed to the potential being set by the H_2/H_2O couple rather than by a concentration cell and therefore has a given potential independent of concentration. Once again we see that secondary gauge EMFs are initiated at lower pump potentials than secondary pump currents confirming the greater sensitivity of the gauge cell compared to the pump cell. The potential at which the decomposition occurs is also moisture content independent as anticipated by its dependence on the thermal decomposition voltage and cell impedance both of which are constant in this range. The sensor operated in a dry atmosphere shows only the primary plateau for both pump currents and gauge EMFs.

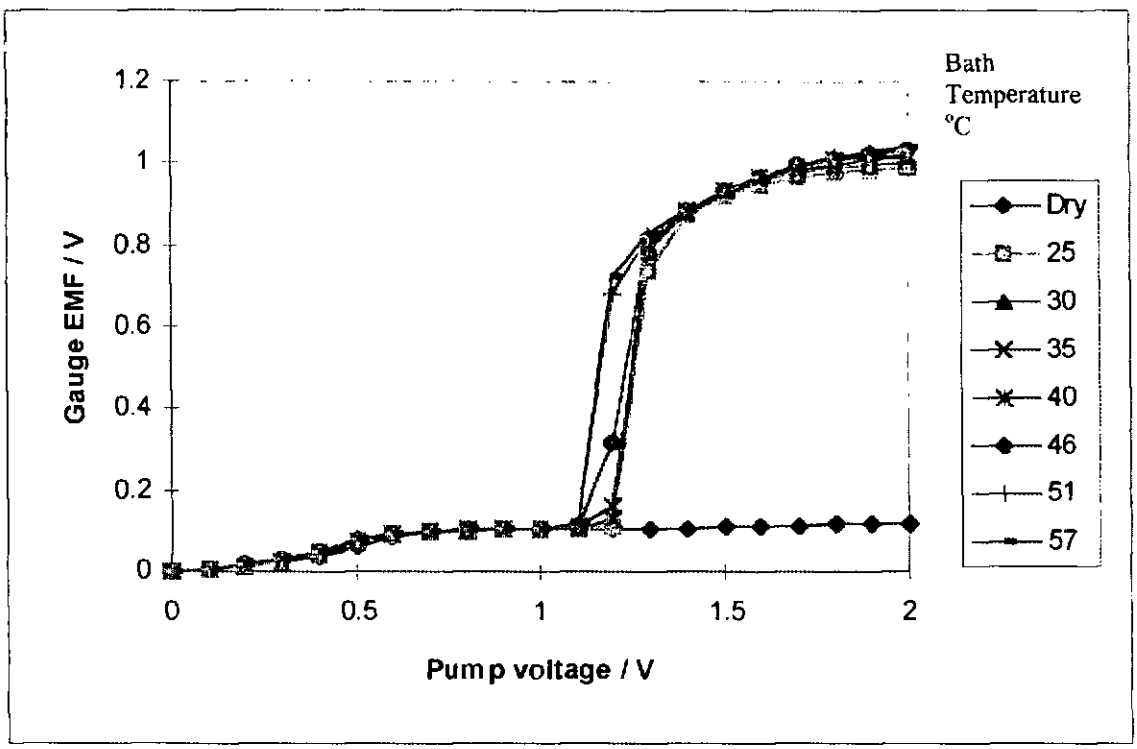

Figure F68 Gauge EMF behaviour with humidity variation

As described in previous sections, the gauge EMF can be used alongside the pump current to show the extent of semi-permeable leakage and check that the cell is working as expected. Figure F69 shows the exponential plot for this set of measurements. This plot returns satisfactorily linear plots in the region prior to the secondary limiting plateau for each humidity level assessed. Slightly decreasing slopes are obtained as humidity increases, again expected due to the dilution of oxygen species in this region. The graph shows that humidity has no significant influence on the semi-permeability leakage mechanism.

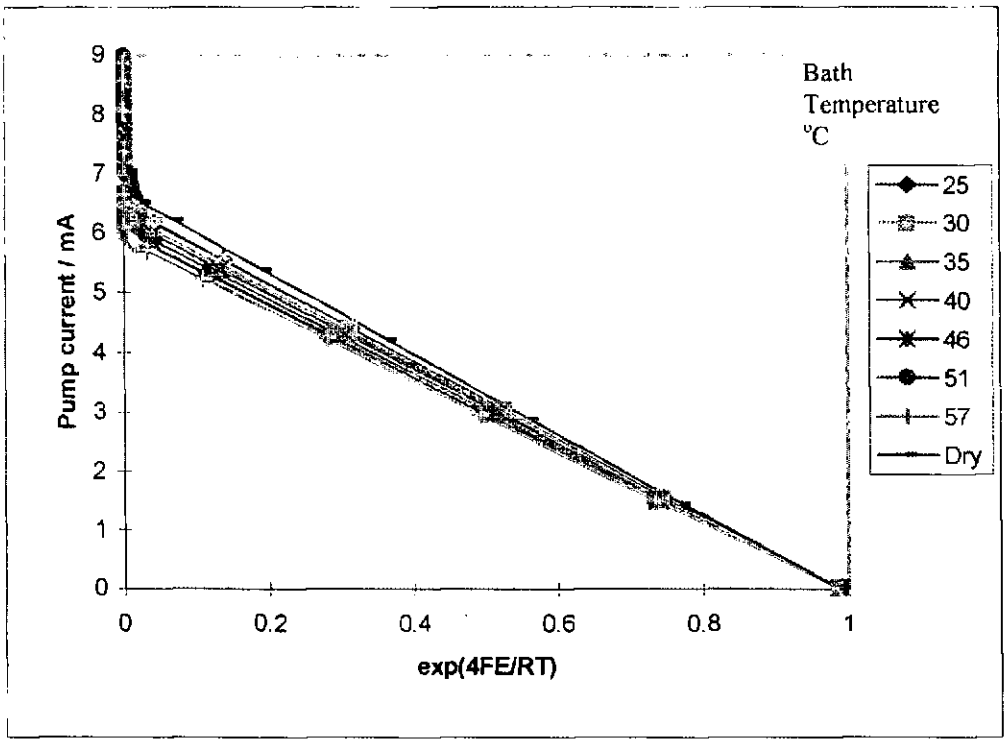

Figure F69 Exponential plot for humidity content variation to show true limiting currents

We have also previously shown that the gauge EMF can be used to provide a reading of internal oxygen partial pressure developed inside the sensor. In figure F70, the gauge EMFs recorded for humidity variation experiments are converted to give such a reading. Again the plot does not give any surprises with a small drop in internal oxygen pressures as humidity is added and oxygen diluted. This figure clearly shows that the sudden drop in measured partial pressure is attributable to the presence of humidity. We have previously established however that this sudden drop does not give a true indication of oxygen levels as the internal potential is set by the H_2/H_2O couple at this point.

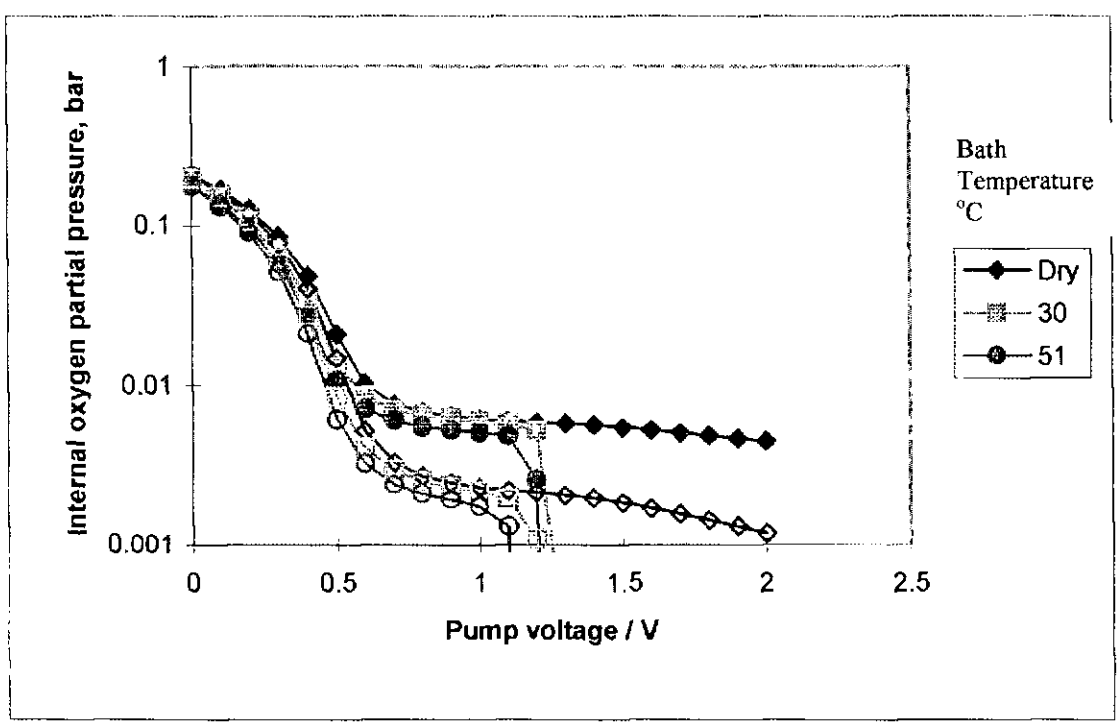

Figure F70 Humidity dependence of internal partial pressure

Considering the pump currents, the secondary minus the primary current limit differentials are plotted against mol% H_2O. These show a linear relationship as predicted by Takahashi et al [73]. For initial data, this linearity was seen to give a non-zero intercept, and so further tests were carried out using lower humidities. The resultant plot (fig. F71) showed that the linearity only holds for mole fractions greater than 0.02. Below this limit, differentials fell back towards zero more rapidly. These lower humidities were realised by mixing humidified air with dried air so it is doubtful that this trend is an artefact of the test procedure. This may therefore be a further indication that, despite the precautions taken, the atmospheres used did not attain 100% saturation.

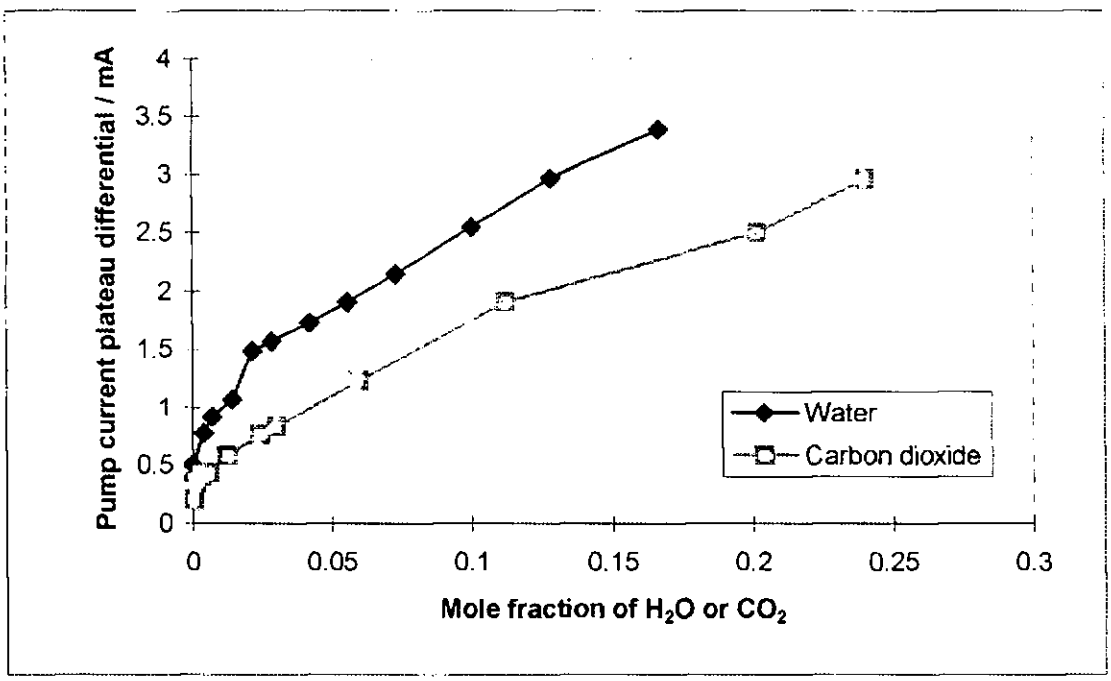

Figure F71 Pump current differential versus mole fraction
(H_2O derived from pyschrometric tables)

The H_2O mole fractions used in figure F71 were derived from psychrometric tables by measuring the temperature of the water that the oxygen/nitrogen mixture had been passed through and assuming 100% saturation. If saturation had not been obtained, this would explain the curvature seen at lower H_2O mole fractions. This was assessed by utilising the drop in primary limiting currents to indirectly measure the mole fraction of water present by the decrease in oxygen partial pressure. Figure F72 shows the same data as that in figure F71 presented but using humidity mole fractions derived from calculations of oxygen dilution (see table F8) rather than those derived from pyschrometric tables. This shows a clear straightening of the humidity curve with a non-zero intercept related to the degree of non-physical leakage occurring between the 0.7 and 2 V pump potential at which the pump currents were measured.

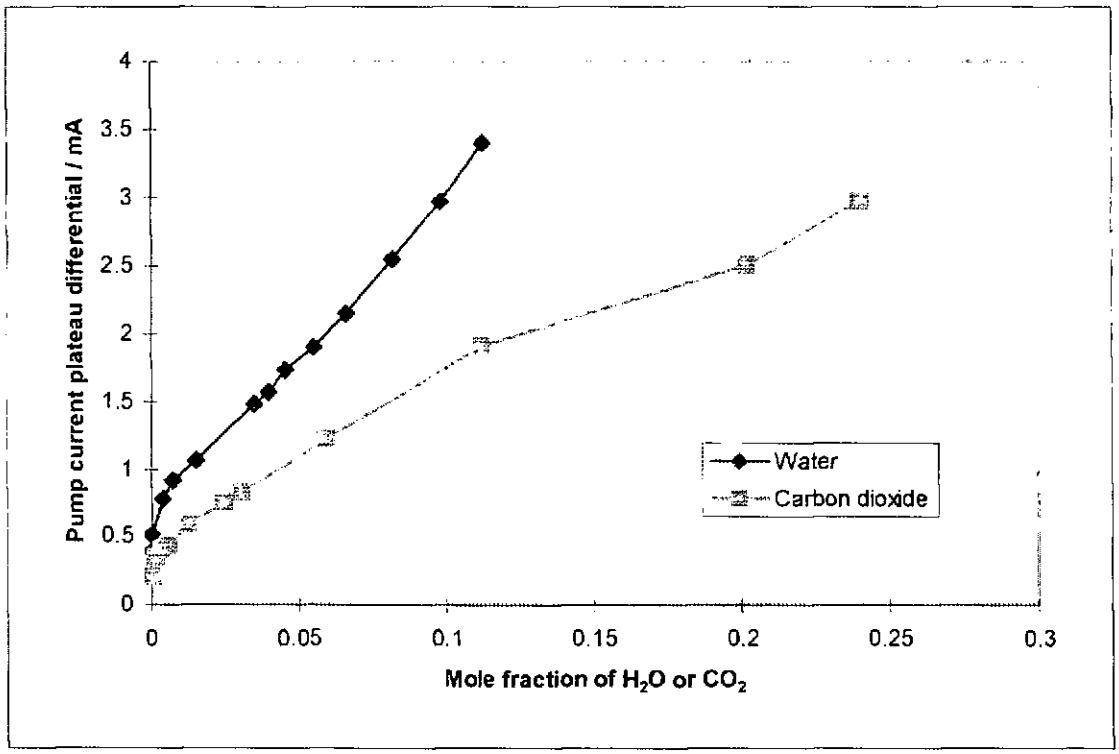

Figure F72 Pump current differential versus mole fraction
(H_2O derived from oxygen dilution calculations)

Gauge EMFs for the humidity variation measurements are presented in figure F73 along with similar data for CO_2 by plotting gauge EMF against mole fraction of the reduced species. This plot shows that the gauge EMF is extremely sensitive to the presence of H_2O, showing an increase in excess of 800 mV for levels above 0.01% such that readings with gauge EMF between 50 and 800 mV proved difficult to obtain. After this initial step, the EMF shows little dependence on humidity level and so, whilst the gauge is unsuitable as a sensor for quantitative measurement, it may be utilised effectively as an H_2O detector or along side the pump cell to enhance measurement. Whilst there are various H_2O sensors/detectors currently available with greater sensitivity / lower cost, this device has features of high temperature operation, a useful and clear indication of humidity presence and oxygen / water amperometric sensor capabilities.

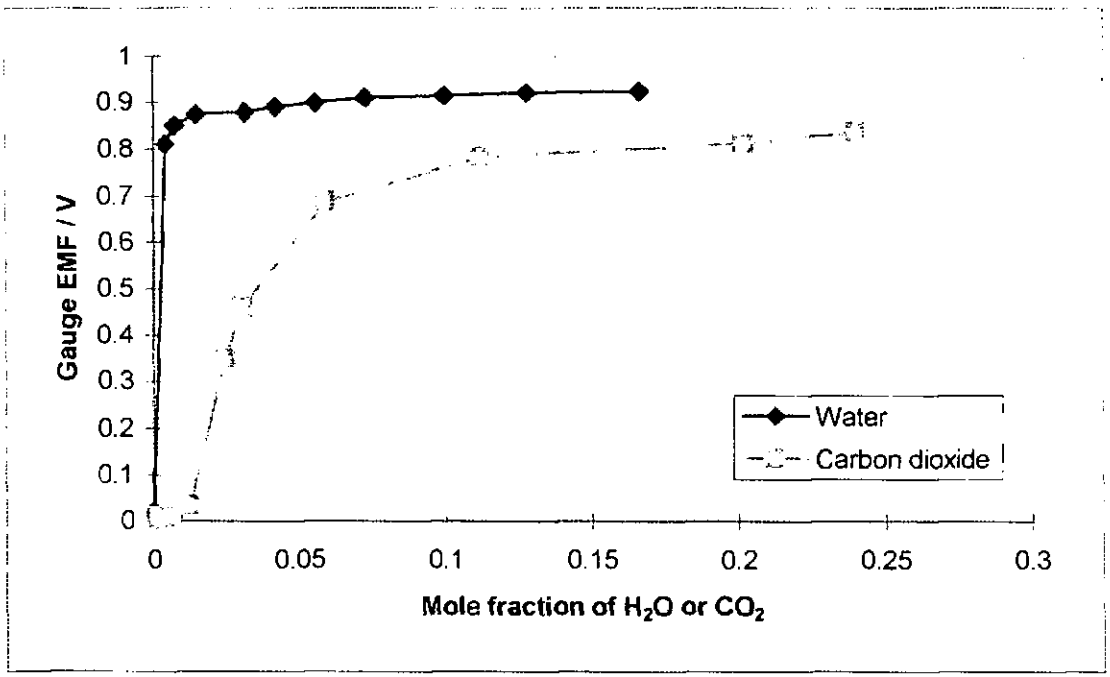

Figure F73 Ultimate gauge EMF versus mole fraction
(H_2O derived from psychrometric tables)

In figure F74 we convert the above graph to account for the revised humidity levels indicated by oxygen dilution calculations (table F8) in an identical manner to those used for current differentials rather than pyschrometric tables. A similar result to that found prior to the re-calculation is obtained.

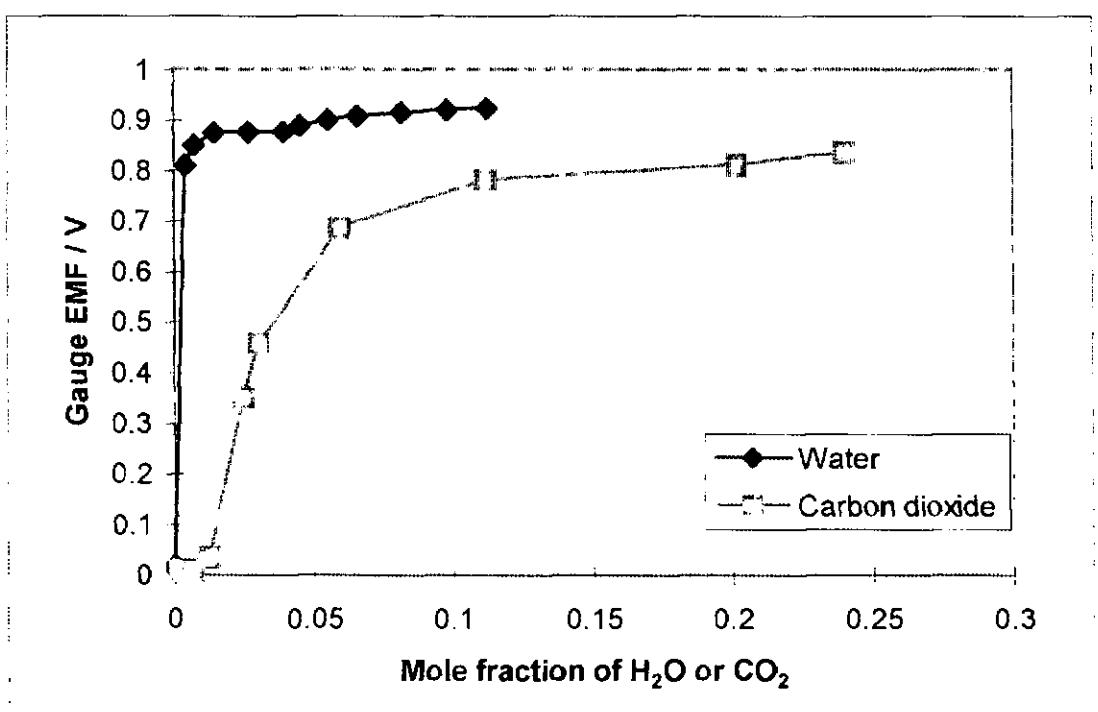

Figure F74 Ultimate gauge EMF versus mole fraction
(H_2O derived from oxygen dilution calculations)

F3.2. CO_2 effects

The above work concerning humidity assumed that the effects seen were due solely to H_2O as CO_2 at atmospheric levels are significantly smaller than those for H_2O. In order to check the validity of this assumption, the experiments were repeated using CO_2 in place of H_2O.

F3.2.1 Effects on pump cell

The current / voltage curves obtained for CO_2 were similar to those obtained for H_2O. The results of pump current plateau differential are compared with the similar results for H_2O in figures F71 & F72. The notable differences between H_2O and CO_2 characteristic curves are a slight instability in limiting plateaux, variation in cell impedances and the higher pump potential required for dissociation. One would expect to see the same linearity as obtained for H_2O as the reduction processes would be similar for both. However whilst similar trends were observed, current differentials were reduced overall and secondary plateaux were not clearly sustained below 2 V pump potential. This may be explained as a difference in diffusion coefficients of the gases involved (see table F7). In addition there exists the possibility of carbon or carbon monoxide poisoning that is known to occur with platinum electrodes. C/CO poisoning could be expected to increase electrode interface impedance but leave limiting currents unaffected. Whilst cell impedance (indicated by the initial slope of I/V curves) is not as consistent as that seen with H_2O, there is no clear trend to the variation. Limiting currents are clearly affected but this is due, primarily, to oxygen dilution by CO_2.

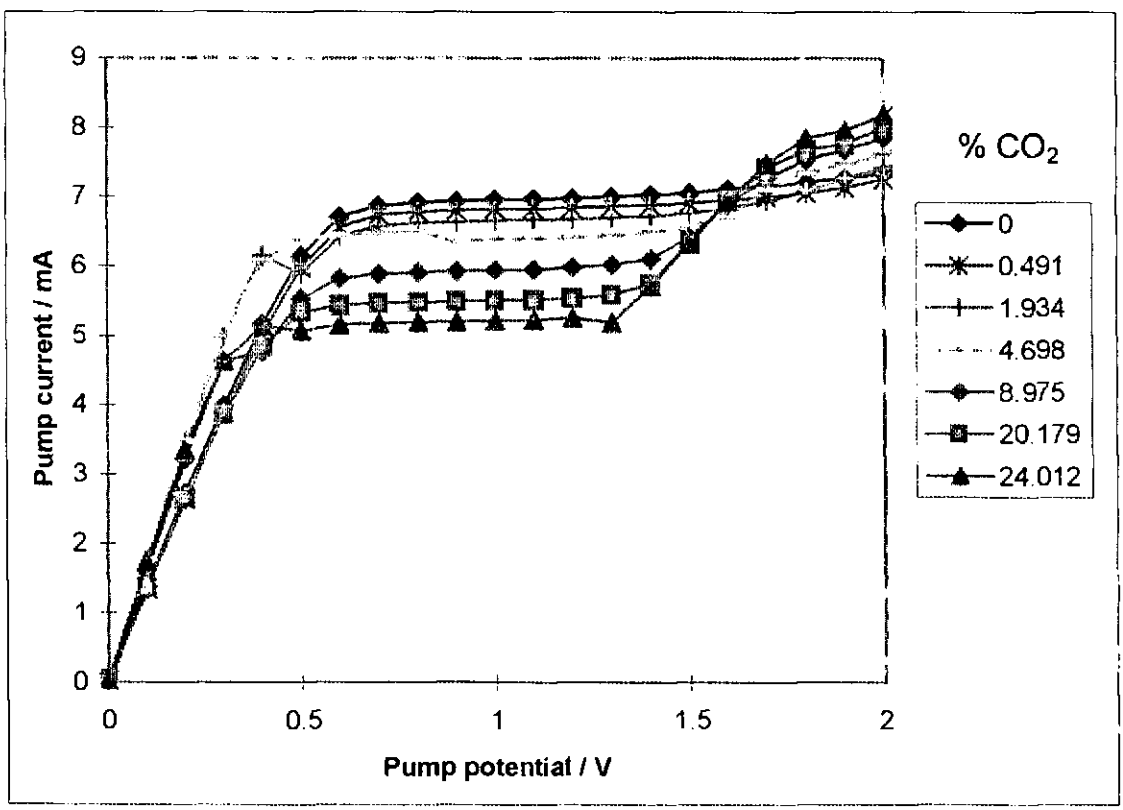

Figure F75 Pump characteristics in CO_2 atmospheres

Okamoto et al [71] studied the CO adsorption onto Pt/YSZ electrodes. CO was found to adsorb onto Pt sites and at low temperature, around 350°C, resulting in non-Nernstian output as CO blocked oxygen reduction sites. Potentials generated in potentiometric cells in these experiments were reportedly caused by mixed potential of oxygen and CO_2 reductions. The reduction was also found to be accompanied by an increase in temperature. Local temperature changes as a result of CO_2 reduction were not monitored in

the work presented here but this could account for the instability seen in characteristic graphs, both in terms of cell impedance and limiting plateaux. The low temperature sensitivity of these devices, previously demonstrated, would suggest that this is not the case. Another point worth noting is that for both CO_2 and H_2O reaction mechanisms there is no flow of gas through the diffusion barrier as there would be with oxygen, as for each mole of species reduced, one mole of the reduced species is produced. For this reason we do not use the $-\ln(1-X_v)$ conversion for these graphs.

Thermal decomposition voltages have been calculated and plotted in the previous section. This plot (figure F64) showed that the two gases (H_2O & CO_2) show similar decomposition voltages around 830°C. Insufficient data were recorded over temperature ranges for CO_2 to comment upon verification of this phenomenon.

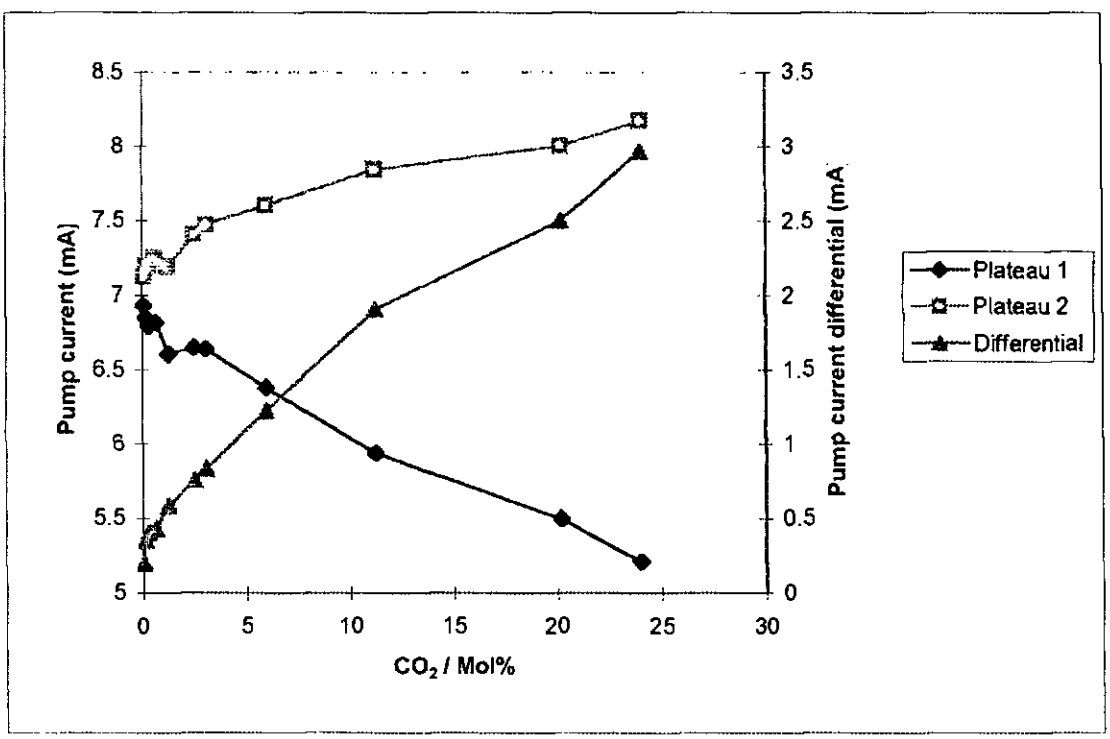

Figure F76 Pump current behaviour with CO_2 variation

In both H_2O and CO_2 cases, the reduction process involves 2 electrons per molecule unless the full reduction to carbon occurs. Etsell & Flengas [55] plotted oxygen partial pressure versus temperature for CO/CO_2 mixtures showing the point of carbon deposition (figure F77). Carbon deposition is thought not have occurred as no third current plateau is observed and the current differential is smaller than that for H_2O, not larger. In the case of water, H_2 is evolved and may diffuse out, in the case of CO_2, CO is evolved or C deposited. Note the significantly higher values for H_2 diffusion coefficient compare to that of other common gases (table F7). The effect of reducible gases diffusion rates through the porous barrier were also deemed influential on the currents drawn in the work of Takahashi et al [73].

Copcutt & Maskell [13] used an amperometric sensor without a gauge in $CO_2/CO/N_2$ atmospheres. A dip in pump potential 2nd plateau was seen and assumed to be due to CO blocking of electrode three phase boundary sites, no such dip was seen in the work presented here. They found that pump currents were very sensitive to operating temperature in the fuel rich region. Electrode conductivity was seen to improve sharply at

700°C due to a change in CO stability. Similar effects may account for the instability seen in the I/V characteristic charts presented here

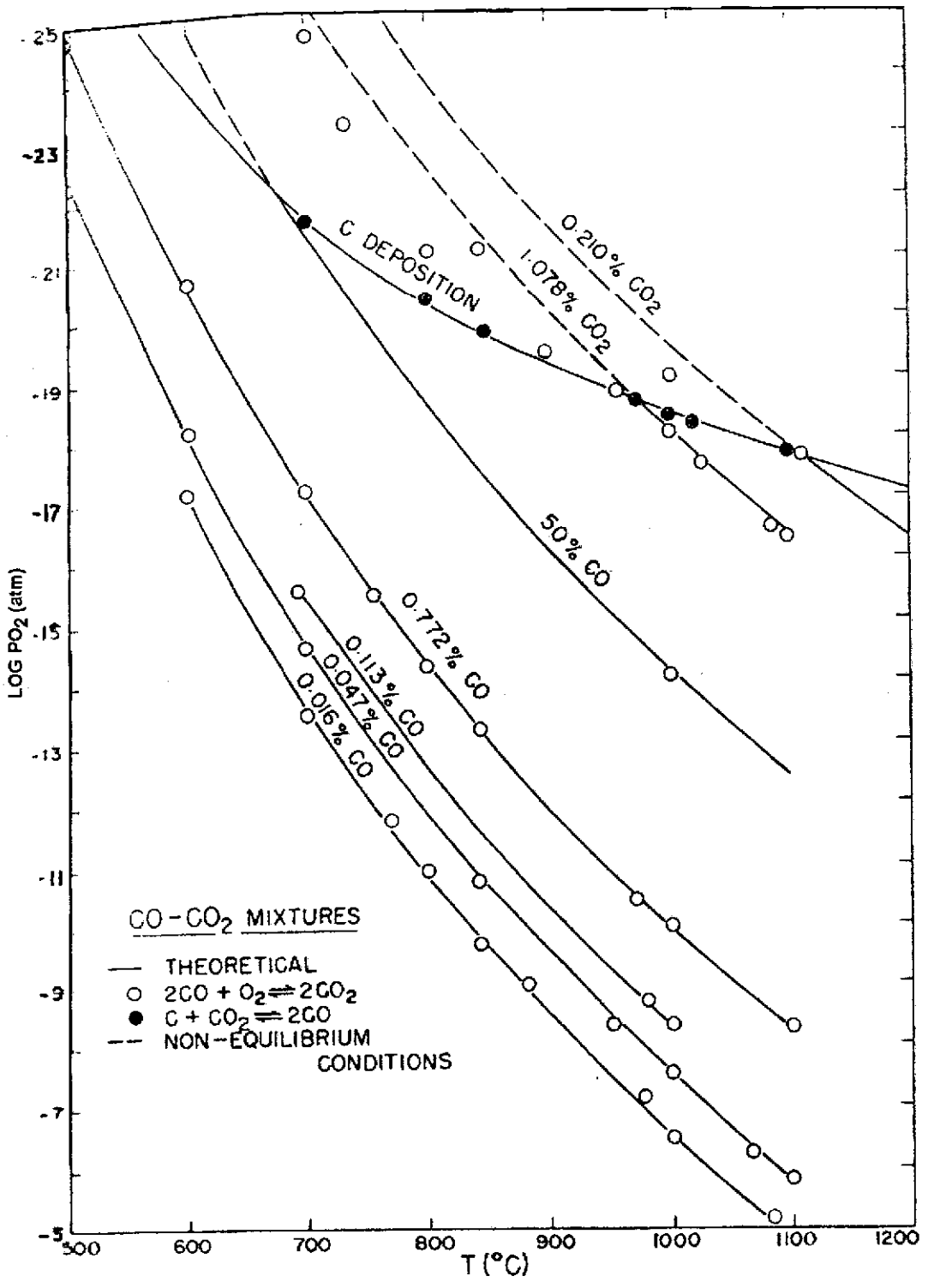

Figure F77 Carbon deposition diagram

$$CO_2 + 2e^- \leftrightarrows CO + O^{2-}$$
$$CO + 2e^- \leftrightarrows C + O^{2-} \qquad \text{Equation F55}$$
$$CO_2 + 4e^- \leftrightarrows C + 2O^{2-}$$

F3.2.2 Effects on gauge cell

The effects of CO_2 on the gauge EMF are shown in figure F78. Again the pump / gauge voltage curves are similar to those for H_2O and again, dissociation occurs at higher pump potentials than for H_2O. The ultimate gauge EMF shown in figure F73 is given in comparison to the H_2O results to highlight the differences. CO_2 measurements show a much lower sensitivity than those for H_2O. Lower gauge EMFs may again be attributable to the reducible gases effect on diffusion coefficient or electrode poisoning by CO. In this case it is more likely attributable to the lower potential of the CO/CO_2 couple compared to the H_2/H_2O couple. The reduced sensitivity shown may indicate higher exchange currents for the H_2/H_2O than the CO/CO_2 mixtures.

The concentration at which gauge EMF begins to reveal a significant second plateau shows gauge EMF sensitivity to H_2O and CO_2 which occurs at 0.004 and 0.02 mol% respectively. From these graphs we can see why no second plateau was seen in gauge EMF or pump current for dried atmospheric air through dissociation of CO_2. CO_2 does not show second plateaux until levels exceeding those found in the atmosphere. In comparison the greater sensitivity to water, along with the higher species atmospheric levels, does lead to the detection of atmospheric humidity.

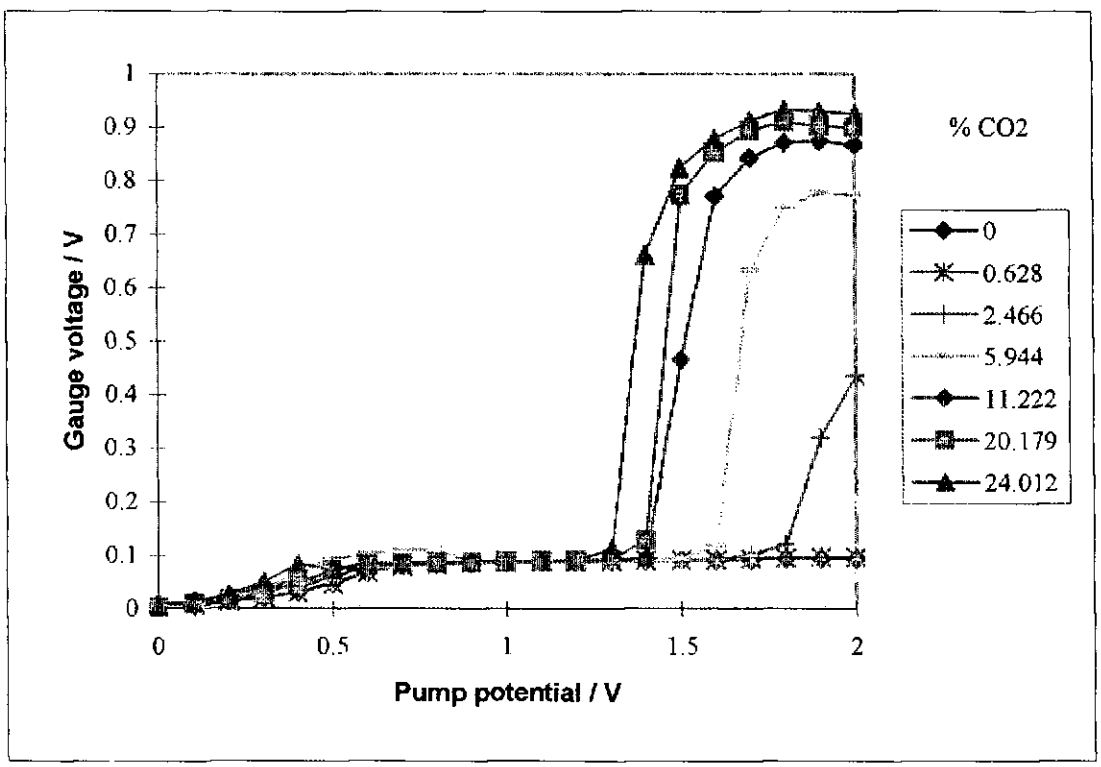

Figure F78 Gauge EMF behaviour with CO_2 variation

Anderson & Graves [149] reported the steady state characteristics of potentiometric cells with reactive gas mixtures. Potentiometric cell EMFs were plotted against O_2/H_2 and O_2/CO ratio and showed an EMF of some 200 mV larger for H_2 than CO which also occurred at a lower A:F ratio (see figure F79). Comparing the work of Anderson & Graves with figure F73, it is clear that the large increase in gauge voltage obtained in this work indicates the stoichiometric point with a similar magnitudes of increase for both H_2/H_2O and CO/CO_2. Both works also indicate a less sharp step for CO/CO_2 than for H_2/H_2O.

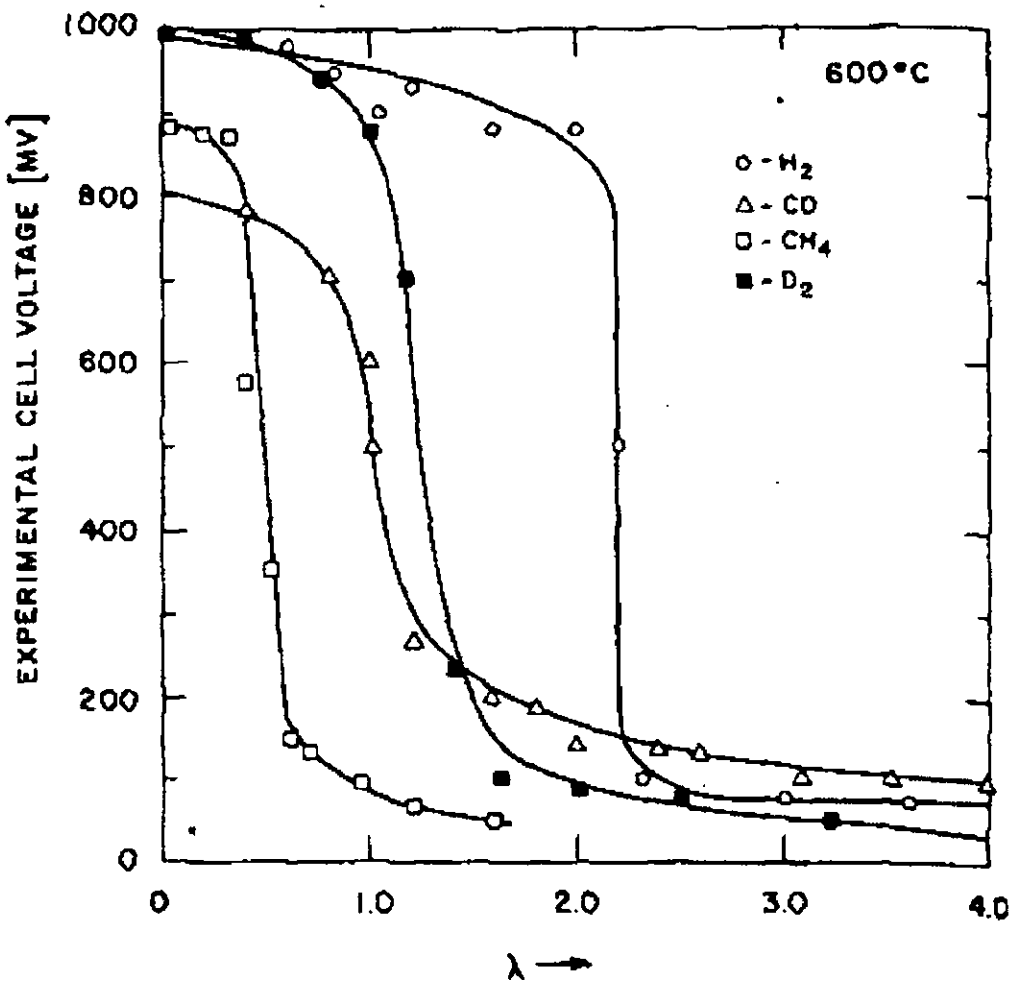

Figure F79 Anderson & Graves chart of gauge EMF vs. A:F ratio

F4 Sensor Evaluation Summary

In this chapter we have reported the factors affecting the performance of amperometric sensors over a range of conditions. A novel sensor fabrication technique has been demonstrated which has the potential to deliver relatively low cost, reproducible, robust and reliable sensors. Sensor characteristics have been examined and reported over a wide range of temperatures and gas concentrations. The upper and lower limits of sensor operation have been examined, revealing potential problems and indicating suspected causes of, and possible solutions to these problems. Existing sensor theory has been extended to allow for the operation of sensors at high oxygen gas concentrations whilst, at the opposite end, sensors have been fabricated and characterised for measurement at low oxygen concentrations. A new configuration of split electrode sensor has been proposed and demonstrated. This new configuration has allowed further investigation of sensor operation. Possible areas for improvement of both electrode and electrolyte components have been suggested and investigated.

An SEM analysis of electrolytes has been performed and found to be beneficial in the understanding of the manufacture and sintering behaviour of the zirconia plastic-ceramic material. Plastic-ceramic sintering temperature has shown a marked effect on mechanical and electrical properties of the fired specimen. The beneficial effects of sintering temperature undergo diminishing returns past 1350°C but improvements are still seen for temperatures as high as 1550°C. Scanning electron microscopy has also been utilised in the development of in-house production of plastic-ceramic and has enabled us to

demonstrate along with, physical measurements, that a material similar or better than the commercial materials has been and can be produced with minimal equipment and cost.

We have demonstrated a technique of electro-depositing a fresh platinum layer, on both external and internal electrodes, with the effect of reducing cell resistance. This has demonstrated the levels of improvement required in amperometric devices to make the process worth while however the beneficial effects are clear and a detailed study could pay dividends.

Work presented in this section has demonstrated that physical leakage of plastic-ceramic sensors is not a significant factor in sensor operation. This leads us to believe that the plastic-ceramic sinters to near full density and that the joints between separate components are leak free. In creating fully sealed devices we have also shown that gases evolved within the sensor, as organic components burn off, do not build in pressure so as to cause mechanical failure during firing. This can be explained by the ceramic remaining relatively porous until the sintering stage after which the ceramic is cooled and the pressure differential between the internal cavity and external atmosphere would put the device into compression. Keeping heating / cooling rates low also allows time for pressure release. Finally we have used the pump-gauge to investigate sensor component performance compared to gold seal devices fabricated by Kaneko et al. In this work we have shown advantages in using platinum cermet electrodes as opposed to pure metal electrodes and shown the improved ionic conductance of the plastic-ceramic fully stabilised zirconia. This work has also indicated that electrochemical leakage is greater for these sensors over those employing a gold seal. This is attributed to the catalytic nature of the platinum connection wires.

Further we have shown here the potential of both two electrode and four electrode amperometric sensors to be used as multi-functional sensors. The sensitivity of the gauge EMF to reducible species has not previously been demonstrated. In addition we have shown that this EMF is more sensitive to H_2O than to CO_2, thus at normal atmospheric levels the effects of CO_2 may be ignored and the device used as a humidity detector. The reason for the second EMF plateau is that the potential becomes set by the H_2/H_2O or CO/CO_2 couple rather than the residual oxygen partial pressure.

To: The Librarian, Tottenham

From: The University Research Office, Tottenham

Date: 24 February 2003

THESIS COPIES

I am sending you ~~one~~ two copies of the following thesis:

Name: Julian PAGE

Degree: Doctor of Philosophy

The hard-bound copy is the copy of the thesis for the degree of ~~BPhil, MPhil,~~ PhD which all research degree students must lodge in the University Library.

Additionally, PhD students (only) have the option of participating in the British Library scheme for doctoral students which brings doctoral theses to a wider public. For this, they have to complete an Agreement Form which they complete, hand to this office, and we forward it to the British Library. As part of this scheme, an extra copy of the thesis is required - produced in SOFT-BOUND- form.

The soft-bound copy is Middlesex University's copy for inter-library loan either direct to British Library, Boston Spa, or to another university library if they submit to the University Library the appropriate British Library form.

I can confirm that the above-named student has opted to participate in the British Library Scheme by completing the appropriate Agreement Form.

pp University Research Officer